

Springer Proceedings in Earth and Environmental Sciences

Robert Zakinyan
Arthur Zakinyan *Editors*

Physics of the Atmosphere, Climatology and Environmental Monitoring

Modern Problems of Atmospheric
Physics, Climatology and Environmental
Monitoring

 Springer

Springer Proceedings in Earth and Environmental Sciences

Series Editors

Natalia S. Bezaeva, The Moscow Area, Russia

Heloisa Helena Gomes Coe, Niterói, Rio de Janeiro, Brazil

Muhammad Farrakh Nawaz, Department of Forestry and Range Management,
University of Agriculture, Faisalabad, Pakistan

The series Springer Proceedings in Earth and Environmental Sciences publishes proceedings from scholarly meetings and workshops on all topics related to Environmental and Earth Sciences and related sciences. This series constitutes a comprehensive up-to-date source of reference on a field or subfield of relevance in Earth and Environmental Sciences. In addition to an overall evaluation of the interest, scientific quality, and timeliness of each proposal at the hands of the publisher, individual contributions are all refereed to the high quality standards of leading journals in the field. Thus, this series provides the research community with well-edited, authoritative reports on developments in the most exciting areas of environmental sciences, earth sciences and related fields.


Robert Zakinyan · Arthur Zakinyan
Editors


Physics of the Atmosphere, Climatology and Environmental Monitoring

Modern Problems of Atmospheric Physics,
Climatology and Environmental Monitoring

 Springer

Editors

Robert Zakinyan 
Faculty of Physics and Technology
North-Caucasus Federal University
Stavropol, Russia

Arthur Zakinyan 
Faculty of Physics and Technology
North-Caucasus Federal University
Stavropol, Russia

ISSN 2524-342X

ISSN 2524-3438 (electronic)

Springer Proceedings in Earth and Environmental Sciences

ISBN 978-3-031-19011-7

ISBN 978-3-031-19012-4 (eBook)

<https://doi.org/10.1007/978-3-031-19012-4>

© The Editor(s) (if applicable) and The Author(s), under exclusive license to Springer Nature Switzerland AG 2023

This work is subject to copyright. All rights are solely and exclusively licensed by the Publisher, whether the whole or part of the material is concerned, specifically the rights of translation, reprinting, reuse of illustrations, recitation, broadcasting, reproduction on microfilms or in any other physical way, and transmission or information storage and retrieval, electronic adaptation, computer software, or by similar or dissimilar methodology now known or hereafter developed.

The use of general descriptive names, registered names, trademarks, service marks, etc. in this publication does not imply, even in the absence of a specific statement, that such names are exempt from the relevant protective laws and regulations and therefore free for general use.

The publisher, the authors, and the editors are safe to assume that the advice and information in this book are believed to be true and accurate at the date of publication. Neither the publisher nor the authors or the editors give a warranty, expressed or implied, with respect to the material contained herein or for any errors or omissions that may have been made. The publisher remains neutral with regard to jurisdictional claims in published maps and institutional affiliations.

This Springer imprint is published by the registered company Springer Nature Switzerland AG
The registered company address is: Gewerbestrasse 11, 6330 Cham, Switzerland

Contents

Results of 65-Years Project of Hail Suppression in Russian Federation	1
Magomet T. Abshaev, Ali M. Abshaev, and Aminat M. Malkarova	
Lightning Protection and Attack by Ground Lightning in the Territory of the Northern Caucasus	29
A. Kh. Adzhiev and Z. M. Kerefova	
Vibrational Regimes in the Atmosphere	37
I. S. Afanasyev, R. G. Zakinyan, and Yu. L. Smerek	
Long-Term Variations of Meteorological Parameters According to the Data of High-Altitude Weather Stations of the Central Caucasus	47
A. H. Aliev, N. N. Skorbezh, and A. G. Tlatov	
Adaptation of Tourist and Recreational Zones of Mountain Territories to Climate Change: Tasks and Methods for Their Solution	55
A. B. Ashabokov	
The Current State of Convective Cloud Physics and Active Effects and the Main Directions of Its Development	69
B. A. Ashabokov, L. M. Fedchenko, and V. A. Shapovalov	
On the Solution of the Problem of Formation and Approval of Target Indicators of Development of the Agro-Industrial Complex	83
M. B. Ashabokova and Kh. M. Temirkhanova	
Formation of Migration Flows Under Conditions of Global Climate Change	97
M. B. Ashabokova	

The Modern Climate of Pyatigorsk Resort	107
G. Kh. Badakhova, M. V. Barekova, V. I. Volkova, Yu. L. Smerek, and G. L. Kaplan	
Applying Recurrent Neural Networks for Short-Term Surface Temperature Forecasts Making	123
D. S. Efremenko, A. D. Kuznetsov, and O. S. Serouhova	
Humidity of the Surface Air Layer as the Main Factor of the Formation of the Basic Climate Forming Elements	131
Ya. A. Ekba, A. K. Akhsalba, and L. V. Khintuba	
Analysis of the Effect of the Sensitivity Value on the Results of Studies of Rapid Atmospheric Processes in Multifrequency Microwave Radiometric Sounding of the Atmosphere	141
E. V. Fedoseeva, I. N. Rostokin, G. G. Shchukin, and I. Yu. Kholodov	
The Gabor Filter Application in Satellite Analysis of “Invisible” Orographic Waves	149
N. V. Fedoseeva and T. E. Simakina	
On the Transfer of Heavy Particles by Intense Winds	157
L. Kh. Ingel	
Precipitation Measurement by Radar and Ground Methods	167
V. S. Inyukhin and K. B. Liev	
Ground Radar Method for Measuring Precipitation Under Complex Relief Conditions	175
V. S. Inyukhin, Yu. V. Suspitsyna, and V. V. Suslov	
Radar Methods for Determination of Hail Microstructure	185
V. S. Inyukhin and E. A. Cherednik	
Measuring Precipitation Fields Using Radar and Rain Gaugers	195
V. S. Inyukhin and S. A. Kushchev	
Sochi Airport Thunderstorm Forecast	203
I. A. Ivanova, M. V. Khaibullov, O. N. Toptunova, and O. V. Volobueva	
The Maximum Hail Size Assessment Regression Model by Predictive Fields of Meteorological Parameters	215
A. Kh. Kagermazov and L. T. Sozaeva	
Snow Cover and Snowstorms Regime on the Stavropol Upland	223
G. L. Kaplan, G. Kh. Badakhova, M. V. Barekova, and Yu. L. Smerek	
Investigations of the Formation of the Ice Phase on the Particles of the Reagent and Zinc Oxide Taking into Account the Influence of the Electric Field Strength	233
B. M. Khuchunaev and S. O. Gekkieva	

Comparison of the Results of Approximation of the Vertical Profiles of the Refractive Index in the Atmosphere Over St. Petersburg and Moscow 241
 A. D. Kuznetsov, O. S. Seroukhova, S. V. Kryukova, and T. E. Simakina

Investigation of the Influence of the Interaction of Convective Clouds With the Surrounding Atmosphere on the Evolution of Their Parameters 249
 V. N. Lesev, B. A. Ashabokov, L. M. Fedchenko, and V. A. Shapovalov

On the Relationship Between Critical Wind Velocity and Wind Direction and the Size Distribution of Dust Microparticles 259
 E. A. Malinovskaya and O. G. Chkhetiani

Relationship Between Microphysical Characteristics and Turbulence in Winter Clouds 269
 V. V. Petrov, N. V. Bazanin, D. V. Kirin, V. V. Volkov, and A. M. Strunin

Case Study of Mesoscale Convective System on August 7, 2021 Over the Center of the European Territory of Russia by Remote Sensing Data 277
 A. A. Strygin and A. E. Vyazilov

Modern Climate Changes in the North Caucasus Region 289
 A. A. Tashilova, B. A. Ashabokov, L. A. Kesheva, and N. V. Teunova

Long-Term and Seasonal Changes in Atmospheric Transparency and Their Impact on Astronomical Observations on the Shatdzhatzmaz Plateau 299
 A. G. Tlatov, D. V. Dormidontov, and R. N. Kirpichev

Peculiarities of Climate Change in Central Africa 307
 Mamy Magbini Tokpa and V. A. Lobanov

Electrical Structure and Dynamics of a Thunderstorm with Hail in the North-West of the Russian Federation by Three-Dimensional Simulation data 327
 M. L. Toropova, N. E. Veremei, Yu. P. Mikhailosvkii, and A. A. Sin'kevich

Measurement of Cloud Water Content from a Research Aircraft 339
 V. V. Volkov, V. V. Petrov, and N. O. Krutikov

Analytical Solution of a Two-Dimensional Model of Dry Air Convection in a Stratified Atmosphere 347
 Robert G. Zakinyan, Arthur R. Zakinyan, and L. M. Kulgina

Statistical Analysis of Thunderstorm and Hail Activity in the Stavropol Territory 361
 M. V. Zharashuev

Results of 65-Years Project of Hail Suppression in Russian Federation



Magomet T. Abshaev , Ali M. Abshaev , and Aminat M. Malkarova

Abstract The article provides brief information on the history of the development of hail suppression works in the USSR and the Russian Federation, the main provisions of the currently used Russian automated rocket technology to prevent hail, the characteristics of a modern anti-hail protection system, including the radar parameters of seeding objects (hailstorms), the average annual number of seeding objects, the consumption of rockets and glaciogenic agents for seeding objects of different hail categories, the results of assessing the physical effectiveness of long-term protection against hail, the main problems and prospects for further improvement of rocket technology.

Keywords Hail · Hailstorm · Hail suppression · Seeding concept · Criteria · Physical efficiency · Problems and prospects

1 Introduction

According to the World Meteorological Organization [1] and the United Nations [2], over the past 50 years, there have been more than 11,000 natural disasters related to weather and climate, which have led to the death of 2 million people and economic losses about 3.6 trillion dollars. Global climate change has resulted in a fivefold increase in disasters and a sevenfold increase in economic losses in these 50 years. In the last 20 years, there has been an increase in the number of weather-related disasters by 1.83 times. The main increase is due to extreme convective storms,

M. T. Abshaev · A. M. Abshaev (✉)
Hail Suppression Research Center «Antigrad», Nalchik, Russia
e-mail: abshaev.ali@hsrc-antigrad.com

M. T. Abshaev
e-mail: abshaev@mail.ru

A. M. Malkarova
Department of Scientific Research and Weather Modification of Roshydromet, Moscow, Russia
e-mail: a.malkarova@meteorf.ru

accompanied by destructive hail, thunderstorms, flash floods, landslides, tornadoes and squalls.

Security measures taken in developed countries in recent decades have reduced the number of victims of natural disasters by about 20 times [2]. This was facilitated by the development of modern systems of observation, monitoring and early warning of weather related dangers. However, about 20–25 thousand people continue to die every year, and the number of victims and lost housing reaches several million [1]. Such high risks can be significantly reduced through preventive measures, including forecasting, monitoring, early warning and prevention of natural hazards, which are many times cheaper than natural disaster response measures. These measures should become an integral part of programs for sustainable economic development, ensuring safe life and adaptation to changing natural conditions. This is urged by the Sendai Framework for Disaster Risk Reduction 2015–2030. Sendai Framework for Disaster Risk Reduction [3], adopted by United Nations members in 2015.

In many regions, hail destroys from 3 to 18% of agricultural production annually. It causes great damage to flora, fauna, various buildings and communications. There are cases when hail storms cause material losses of more than 1 billion dollars [4]. According to WMO registries 1990–2000 [5] more than 30 countries are implementing scientific and operational hail suppression programs covering an area of about 95,000 km², of which about half are in China.

To protect small areas from hail, shelters made of metal or nylon nets have long been used. The modern cheapening of nets has made it possible to increase the area of protection up to several tens of km². But to protect large areas, methods are used to modify hail storms by seeding them with glaciogenic and hygroscopic reagents, including:

- Method of ground generators (France, Brazil, Hungary, Spain, Italy, Switzerland);
- Aviation method (USA, Austria, Germany, Greece, Canada, Kenya, South Africa);
- Artillery method (China, Mongolia, and earlier Russia, Azerbaijan, Armenia, Georgia, Tajikistan and Uzbekistan);
- Rocket method (Russia, Azerbaijan, Armenia, Argentina, Bulgaria, Brazil, Hungary, Georgia, Romania, Italy, Macedonia, Moldova, Slovenia, Serbia, Tajikistan, Ukraine, Uzbekistan, Croatia, etc.).

These technologies have had and have various modifications based on different physical principles implemented to varying degrees. The scientific foundations of hail suppression remain at the level of physical concepts, among which the most common are:

- complete crystallization of supercooled LWC;
 - favorable competition (Sulakvelidze [6]);
- increase size of cloud droplets and freeze they (Bartishvili et al. [7]);
- accelerating precipitation in new growth areas of storms, where hail may originate in future (Abshaev [8]).
- dynamic suppress the updraft (Vulfson and Levin [9]);

- lowering of the trajectory of growing hailstones (Browning and Foote [10, 11]).

To evaluate the effectiveness of anti-hail projects in different countries and projects, different parameters and criteria are used. This makes it difficult to compare the results of different projects and assess the current hail suppression potential.

One of the largest and long-term projects aimed at reducing damage from hail and related hazardous phenomena is the anti-hail project, launched in the USSR in 1956 on the initiative of academic Fedorov [12], which provided protection for 10.6 million hectares and continues to this day. Only the French ANELFA project, which was launched in 1952 and applied to protect 5 million hectares with 650 ground-based glaciogenic aerosol generators, can be compared in duration and scale with this project [13].

From 1956 to 1962, on the basis of field, laboratory and theoretical studies of hail storms, the first ideas about the mechanism of hail formation and the basis of artillery and rocket methods of hail control were developed. In 1962–1963 author's tests of these methods were carried out, in 1964–1966 experimental protection, and since 1967, in accordance with the Decree of the Council of Ministers of the USSR, industrial protection against hail of large areas was started.

This stage ended with the creation of three different methods of hail suppression: artillery [6] and rocket [11] methods with glaciogenic seeding, as so combined artillery with glaciogenic and hygroscopic seeding [7]. The physical basis of all these methods was the concept of favorable competition, which involved increasing the concentration of hail embryos, believing that this would lead to competition for available water, limiting the growth of hail embryos due to lack of cloud water and the formation of small hail that would melt in the warm part of the atmosphere. The artillery method was used until 1991 in the North Caucasus, Azerbaijan, Armenia, Georgia, Tajikistan and Uzbekistan. The rocket method was used in Moldova, Crimea and Ukraine, and the combined method in Georgia.

In the period 1980–1984 the Hail Suppression Research Center, organized in 1980 at the High Mountain Geophysical Institute for the scientific and methodological management of all anti-hail services has created a unified technology of hail suppression. This technology was based on:

- new concept of hail suppression, which provides for the acceleration of precipitation in areas of new growth—areas of future hail formation [8];
- new seeding schemes for hailstorms of various structures, based on the classification of hailstorms according to the features of their spatial structure and development dynamics [14–16], as well as the classification of seeding objects (SO) into 4 categories depending on the degree of their hail hazard [15, 17];
- unified radar methods [18] and technical means of hail detection, including dual-wavelength S/X band radar MRL-5 [19], multi contour device BOMO for hailstorms radar analysis;
- new unified methods of evaluation physical and economic efficiency of hail suppression [20];

- unified guiding documents regulating the organization and conducting of anti-hail operations;
- centralized professional training and certification of specialists in seeding of hailstorms, radar, rocket and artillery technology and hail forecasts at annual courses;
- annual inspections of all anti-hail services with an assessment of the quality of technology implementation, elimination of methodological, technical and organizational problems;
- regular analysis of unsuccessful operations and elimination of their organizational and technical causes;
- systematic introduction of new scientific and practical achievements.

The next important step was the creation of automated hail suppression technology [15, 17, 21] based on software-hardware complexes for processing radar information and managing anti-hail operations ASU-Antigrad (1993), Merkom (1995), ASU-MRL (2005) and ASU-DMRL-10 (2015). These tools provide automation of operations for radar detection of hailstorms and hail-hazardous storms, recognition of categories of seeding objects (SO), development and execution of commands for rocket seeding, documentation of hailstorms parameters, seeding materials and radar scan files of three-dimensional space [15, 17, 21, 22].

In the period from 1984 to 2015, automated rocket systems were created that can provide a high rate of storms seeding by AgI aerosols. They include multi-barrel remote-controlled rocket launchers MS-280 N, Elia, Elia-2, Elia-3, Elia-4 [17, 22, 23] and environmentally friendly rockets Krystal, Nebo, Alazan-ChM15, Alazan-5, Alan-2, Alazan-6, Alazan-9, Alazan-8 and As. New radars have been created, equipped with a program for managing anti-hail operations:

- Doppler S-band radar DMRL-10 [24], designed for anti-hail work and storm warning in regions with intense thunder and hail processes;
- Rapid-scan Doppler S-band radar complex Sopka-2 [24], which has a phased array antenna that provides space scan every 10 s.

Some of these radars, rocket complexes and automation systems are in use in Russia and several other countries, and the newest of them can provide upgrades to existing hail suppression systems.

2 The Main Provisions of the Automated Rocket Technology of HS

2.1 *Conceptual Models of Hailstorms*

Hailstorms are divided into single cell, multicell, intermediate (hybrid) and supercell types with right-sided [10, 14, 17, 25, 26, etc.] and left-sided development [16, 17,

etc.]. Convective cells (CC) in storms of different types have different spatial structure and duration of existence due to differences in the three-dimensional structure of the wind in the atmosphere.

Studies of the fine structure of hailstorms also showed [26, 27] that each powerful hail cells consists of many small-scale structures formed due to the development of feeder clouds on the upwind flank, the radar echoes of which are traced against the background of the main radar echo and have their own trajectory of movement inside the storm. The variety of types of hail storms, each of which is a cluster of convective cells, having its own structure, continuously changing in time and space, cannot be adequately theoretical modeled, therefore, the existing methods of hail suppression are based on empirical models of hailstorms, built on the basis of radar, aviation and ground observations.

The process of hail formation can be conventionally divided into four stages: the formation of the conditions necessary for the hail origin; formation of hail embryos; hail growth and hailfall [17]. In accordance with these stages, four zones can be conditionally distinguished in hailstorms:

- zone of formation of conditions for hail initiation located in new cells of all types of storms and in feeder clouds of supercell, hybrid and multicell storms, where updrafts formed, droplet water is accumulated, and gravitational growth of cloud particles begins;
- zone of hail embryos formation, located in a relatively weak updraft in the layer from the isotherm level of -5°C to the isotherm level of -40°C , having a rather high content of liquid water content (LWC);
- hail growth zone located in the area of the most powerful radar echo hanging over the bounded weak echo region (BWER) or WER in the layer between the levels of isotherms from 0 to -40°C , where the most powerful updrafts;
- hailfall zone located in the area of the highest radar reflectivity and downdrafts in the layer from the earth's surface to the isotherm level of -40°C .

2.2 Physical Principle of Hail Suppression

Modern Russian automated rocket technology is based on the concept of precipitation acceleration in new growth areas of developing and mature hailstorms [15, 17]. It is assumed that premature precipitation leads to the washing out of areas of future hail formation and the dynamic suppression of updrafts that are weak in these areas. This concept and the corresponding schemes for seeding hailstorms were first proposed in 1966, first published in 1973 [8], reported at a meeting of the WMO CAS Expert Working Group on Physics, Chemistry and Weather Modification in 1977. The testing of new seeding schemes in practice of hail suppression has begun in 1966 [8]. Gradually, the scale of application expanded, and since 1980, this concept and the corresponding technique for seeding hailstorms gradually supplanted the schemes for seeding hail initiation and growth zones, which corresponded to the concept of competition.

Acceleration of precipitation formation is stimulated by massive seeding of ice-forming particles in areas of new growth of hailstorms and creating an initial concentration of glaciogenic particles of about $3 \cdot 10^{10} - 10^{11} \text{ m}^{-3}$ in rockets trails in order to form such a high initial concentration of ice crystals (at least 10^8 m^{-3}), which will inevitably lead to aggregation of crystals, followed by their granulation with cloud drops and the formation of a high concentration of snow pellets (graupels) [17, 28].

It should be noted that the Alberta project [29–31] also provides for the glaciogenic seeding of developing feeder clouds near the level of $-10 \text{ }^\circ\text{C}$ in order to create increased concentrations of crystals, accelerate the growth of snow pellets, which, as a result of competition, will lead to the formation and earlier precipitation of small hail that can melt, reaching the ground in the form of rain.

2.3 Seeding Objects (SO)

Seeding objects (SO) are hail and hail dangerous cells of all types of hailstorms with right-sided and left-sided development [15, 17], in which volumes with identical microphysics are seeded, located in areas of new growth, where conditions for hail generation are formed:

- in single-cell storms, these are the areas of the first radar echo of newly developing cells;
- in supercell and hybrid storms, these are areas of new growth and development of feeder clouds located on the windward flank of the radar echo canopy*;

***Note:** The radar echo canopy is hereinafter referred to as the radar echo area located above the BWER or WER, i.e. the region of the radar echo hanging over the region of the power updraft.

- in multicell storms, these are the areas of the first radar echo of new cells, as well as the windward flank of the radar echo canopy of mature hail cells.

Seeding areas of radar echo, where hail has already originated, grows and falls, is prohibited due to the fact that this leads to an acceleration of hail growth, an increase in its size and intensity.

2.4 SO Categories

Seeding objects (SO), regardless of the type of hailstorm, according to Table 1, are divided into 4 categories [15, 17, 20]:

- SO I category—potentially hail dangerous convective cells, the first radar echo or radar echo maximum of which originates above the $0 \text{ }^\circ\text{C}$ isotherm level (i.e. above the melting line) and have tends to develop;

Table 1 Criteria for recognition SO of different categories

SO category	Criteria					
I	$0 < \Delta H_{Z_m} < 5$	$15 < Z_m < 45$	$\Delta q_m \geq 0,5$	$\Delta M_{25} > 10^3$	$d\Delta q_m/dt > 0$	$d\Delta M_{25} > 0$
II	$\Delta H_{35} > 3$	$Z_{max} \geq 45$	$\Delta q_m \geq 2$	$\Delta M_{35} > 2 \cdot 10^4$	$d\Delta q_m/dt > 0$	$d\Delta M_{35} > 0$
III	$\Delta H_{45} \geq 3$	$Z_{max} \geq 55$	$\Delta q_m > 8$	$\Delta M_{45} > 2 \cdot 10^4$	–	–
IV	$\Delta H_{45} > 4$	$Z_{max} > 65$	$\Delta q_m > 16$	$\Delta M_{55} > 2 \cdot 10^5$	–	–

Table 1 uses the following designations for the parameters and their dimensions

Z_{max} (dBZ)—maximum reflectivity of SO

ΔH_{Z_m} (km)—height of Z_{max} above the 0 °C isotherm level (H_0)

ΔH_{35} and ΔH_{45} (km) are the heights of the upper boundary of the radio echo volumes with $Z = 35$ and 45 dBZ above the H_0

Δq_m (kg/m²)—the maximum value of vertically integrated water content (VIL) above the H_0 level
 ΔM_{25} , ΔM_{35} , ΔM_{45} and ΔM_{55} (kton)—integrated water content of radar echo volumes with $Z = 25, 35, 45$ and 55 dBZ, located above the H_0 level, respectively

$d\Delta q_m/dt$ (kg/(m²min))—growth rate of VIL above the H_0 level

dM_{25}/dt and dM_{35}/dt (kton/min) are the rate of increase in the integral water content of radar echo volumes above the H_0 level with $Z = 25$ and 35 dBZ, respectively

- SO II category—hail dangerous convective cells that tend to develop;
- SO III category—hail convective cells, from which hail falls according to radar data;
- SO IV category—heavy power hail convective cells, from which intense hail falls.

2.5 Seeding Schemes

Seeding schemes are differentiated taking into account the structural features of hailstorms with right hand and left hand development, the nature of the distribution of the hail formation process in space [15, 17].

Interruption of the discrete propagation of the hail formation process during single-cell hailstorms is carried out by seeding convective cells originated over 0 °C at the stage of their first radar echo no later than 2–5 min after its origin.

Interruption of the discrete–continuous propagation of the hail formation process in multi-cell hailstorms is carried out by seeding newly developing cells and subsequent hail interruption from a mature hail cells.

Interruption of the process of continuous propagation of hail formation in supercell hailstorms is carried out by seeding the upwind flank of their radar echo canopy and feeder clouds closest to the main body of the storm:

- on the right upwind flank in case of cells with right-hand developmental (see Fig. 1);
- on the left upwind flank in case of cells with left-hand development.

2.7 Seeding Height

Seeding is usually performed at level of minus (6 ± 3) °C, corresponding to the crystallizing threshold of the used reagents and favorable for growth, aggregation and multiplication of ice crystals. When the first radar echo of new cells and the overhanging radar echo of mature hail storms are located above the -6 °C isotherm, seeding is performed at the level of their lower boundary, bounded by $Z = 15$ dBZ [17].

2.8 Time of Seeding

Seeding is carried out within 1–2 min after identification of SO [23]. The delay reduces seeding efficiency due to changes in location and hailstorm intensification.

2.9 Dosage of the Seeding Agent

It is desirable that the initial concentration of ice-forming nuclei in the rocket seed plume be about $n_0 > 3 \cdot 10^{10} \text{ m}^{-3}$. At such concentration of ice-forming nuclei, according to theoretical modeling data [17, 28], during the first 5 min after seeding, an energetic transformation of the microphysical parameters of the cloud medium occurs, the formation and growth of ice crystals up to sizes of about 60–80 μm , their aggregation, an increase in ice content, and a decrease in LWC, etc. High turbulence in the seeding volume reduces the effect of seeding on the course of microphysical processes. Numerical experiments [28] have shown that under real conditions of liquid water content and turbulence, the initial concentration $n_0 \geq 10^{11} \text{ m}^{-3}$ is the key to effective hail prevention. If the used anti-hail rockets do not provide such an initial concentration, then the distance between the seeding trajectories should be reduced to 0.5 km, and in the case of SO category IV duplicate seeding should be used [17].

2.9.1 Multiplicity and Frequency of Seeding

SO of I categories are seeded once, SO of II categories—twice after 7 min (i.e. after 2 radar scan cycles), SO of III categories of low and medium power—three times every 7 min, powerful SO of III categories and SO of IV category—four times every 3.5 min.

Table 2 Technical characteristics of selected anti-hail rockets

Specifications	Alazan-6	Alazan-9	Loza	As
Caliber (mm)	82,5	60	55	57
Rocket flight length (mm)	1402	1200	910	520
Initial flight weight of the rocket (kg)	8,8	4,5	2,8	1,41
Starting speed (m/s)	26	50	65	85 ± 5
Start of seeding route (km)	3,5–4,5	3,5–4,5	–	0,0
End of seeding route (km)	10,5	9,5	7,5	10,7 ± 0,6
Seeding path length in 1-km layer (km)	7,0	6,0	4,5	9,0 ± 0,5
Reagent mass (g)	630	400	400	830
Amount of AgI (g)	26,4	12,0	40	16,6
Yield of ice-forming particles at –10 °C	6.6·10 ¹⁵	3·10 ¹⁵	1.2·10 ¹⁶	1.6·10 ¹⁶
Cloud seeding duration (s)	30 ± 3	40 ± 4	30	47 ± 4
Security system	explosion	explosion	explosion	no exploding
Mass of explosive (g)	240	130	100	0

2.9.2 Methods of Hail Detection and Recognition of SO

One- and two-wavelength radar methods [18] based on measurements of one-dimensional, two-dimensional and three-dimensional cloud parameters [8, 17].

2.9.3 Seeding Means

Rapid-firing automated anti-hail rocket launchers and environmentally friendly rockets. The characteristics of selected rockets are shown in Table 2.

2.9.4 Seeding Control

Seeding is controlled using radar data processing and decision support system ASU-MRL [21] that automates the detection and measurement of a complex of one-dimensional, two-dimensional and three-dimensional cloud parameters, SO recognition, generation, transmission and control of the execution of rocket seeding commands, control of the physical efficiency of seeding.

The procedure for using the automated rocket hail suppression technology is set out in the manual [17] and nine guiding documents of Russian Hydrometeorological Service (Roshydromet).

3 Organization of Anti-Hail Protection

Industrial antihail protection in the North Caucasus of the Russian Federation has been carried out since 1967. Protection is carried out by the Krasnodar, Stavropol and North Caucasian Paramilitary Services for active influence on meteorological and other geophysical processes of Roshydromet, which finances them from the federal budget. But the costs of services for the purchase of rockets, fuel and lubricants are paid by customers, which are the ministries of agriculture of the Krasnodar and Stavropol Territories, the republics of Adyghea, Karachay-Cherkessia, Kabardino-Balkaria and North Ossetia-Alania.

Anti-hail services consist of several detachments, each of which has 15–20 rocket sites and one command site, usually equipped in a radar site. The staff of the command sites includes 3 teams on duty, consisting of 5–6 people, including the head and operators performing anti-hail operations, a radar and automation engineer. Rocket site serve 2 technicians in each of 2 shifts. Carrying out anti-hail operations is allowed to specialists who have been trained according to a special training program corresponding to the function performed, who have experience and periodically undergo retraining and certification. The most experienced specialists who know the basics of cloud physics, radar meteorology, technologies and technical means of hail suppression are allowed to lead anti-hail operations.

The hail suppression usually starts on April 15th and ends on October 1st. During the protection period, duty shifts of command and rocket sites are at their posts around the clock in full readiness for anti-hail operations. Every day at the command sites begins with a morning meeting, at which the weather forecast, the state of readiness of equipment and personnel are discussed, the elimination of possible interference is planned, and, depending on the likelihood of hail, a preliminary application is submitted to the regional air traffic control service (ATC) about the possibility and expected time carrying out anti-hail firing. Regardless of the forecast, the duty shift of the command site carries out round-the-clock radar control of the clouds development, maintains contact with rocket sites and Aviation Traffic Control (ATC), which gives permission for anti-hail firing. For many years of interaction between anti-hail services and ATC services, the procedure for using airspace has been adjusted in such a way that ATC prohibitions on anti-hail firing in the presence of hail danger are extremely rare. This allows you to start seeding hail clouds that threaten the protected area at any time of the day or night immediately after their detection. In the afternoon, the forecast is updated according to the data of the second radiosonde, released at 12:00 UTC.

The morning and updated forecasts contain an analysis of the thermodynamic and synoptic situations, the expected heights of the lower and upper boundaries of convection, the speed and height of the maximum updrafts, and the formulation of the hail forecast. In addition, the direction and speed of the leading air flow, the height of the isotherms 0, -6°C and the height of the tropopause are given, which are entered into the ASU-MRL for automatic radar recognition of the categories of SO, selection of the seeding height, and generation of commands for rocket seeding.

The method and technical means of hail suppression improved over the years, the area of protection gradually increased. Tables 3 and 4 present the characteristics of the protection system in the period from 2001 to 2021. From Table 3 it follows that the area of protected area (PA) during this period varied from 1.9 to 2.66 million ha, where the share of cultivated area is 74.3%. The main areas are occupied by grain crops (wheat, barley, and corn), orchards, vineyards, sugar beets and vegetables. There are 12 command posts and 173 rocket posts in the three services. The number of permanent personnel of the services is about 1,130 people, of which 720 are technicians of rocket posts.

Rocket sites are located on the PA at a distance of 10–20 km from each other. From the side of the predominant intrusion of hail clouds, they cover a buffer zone 6–10 km wide. The seeding radius of sites is 10–10.5 km. The seeding area is 32–40 thousand hectares, of which about half is occupied by prohibited shooting sectors in the direction of cities, zones without seeding within a radius of 4–5 km and zones of mutual overlap. With their deduction, each rocket site actually protect 15–20 thousand hectares.

According to long-term meteorological observations, most often hail in the region falls between 16:00 and 18:00 local time. The annual maximum of hail fall frequency is observed in May—June, the second maximum—in August [20]. Days with hail were counted as days when hail was observed at least one of the 42 meteorological stations, 66 meteorological sites, 184 rocket and command sites located on the protected territory, or damage to crops from hail was noted at least at one of the thousands of agricultural enterprises.

From Fig. 2b and Table 4 it follows that the average annual number of days with hail in the region is 36 days. The average annual number of days with seeding is 42 and exceeds the number of days with hail by an average of 18% (see Fig. 2b). This means that the seeding of hail and hail-dangerous clouds was carried out with some reinsurance. However, after the introduction of the new guiding document GD 52.37.731 “Organization and implementation of anti-hail protection” since 2011, this reinsurance has decreased to 3%.

According to Table 4 and Fig. 3a, on average, 685 SO were sown per year, including 16 SO of I category, 227 SO of II category, 367 SO of III category and 75 SO of IV category. That is, on average, 241 SOs were sown with purpose to prevent hail formation and 442 with purpose to interrupt hail fallout. An analysis of the place of origin shows that about 30% of seeded SO of III category and 55% of SO of IV category invades the protected area at a mature stage, while the rest originate and develop in the protected area.

This means that, in violation of the requirements of GD 52.37.731 on the priority seeding of SO of categories I and II, in order to prevent their development to the hail stage, in practice they are seeded less than SO of categories III and IV. The reason for this is the frequently repeated cases of late detection of SO of I category due to the long duration of the radar scan cycle, which is 3.5–4.0 min, as well as the desire to save rockets. However, instead of saving rockets, this leads to a decrease in seeding efficiency and an increase in rockets consumption, since many times fewer rockets are spent on preventing the development of SO of I and II categories than on

Table 3 Protection area, equipment and personnel of anti-hail services of Roshydromet in 2017

Service name	Protection area, (Thousand has)		Number of command sites	Number of rocket sites	Number of technical means (Pcs.)			Number of personal	Cost of protection, (Rub./ha)
	total S_T	cultivated S_C			MRL-5 radars	rocket launchers	VHF radio station		
Krasnodar	895,2	707,4	6	68	6	130	178	504	224,2
Stavropol	839,0	660	2	44	2	70	113	237	163,8
North Caucasian	921,4	616	3	61	5	153	204	392	129,0
Total:	2655,6	1983,4	11	173	13	353	485	1133	172,1

Table 4 Statistical characteristics of the anti-hail system in the period 2001–2021

Parameter name	Minimum	Maximum	Medium
Protected area (thousand ha)	1907	2656	2363
Number of days with hail in the region	26	45	36
Number of days with seeding in a season	30	51	42
The number of seeded SO of all categories:	480	1080	682
• SO I category	2	93	13
• SO II category	89	398	227
• SO III category	240	527	367
• SO IV category	28	106	75
Annual consumption of anti-hail rockets (Pcs.)	7869	16,184	11,913
Annual consumption of agent (kg)	5194	10,681	7863
Annual consumption of AgI (kg)	416	956	629
Average consumption of rockets for seeding (Pcs.)	14	25	17,5
• SO I category	3	9	5
• SO II category	6	27	10
• SO III category	10	70	22
• SO IV category	21	300	77
Average consumption of agent for seeding 1 SO (kg)	9,0	16,5	11,5
The average number of IFN introduced into 1 SO (Pcs.)	$9,1 \cdot 10^{16}$	$1,7 \cdot 10^{17}$	$1,2 \cdot 10^{17}$
• SO I category	2,0·1016	6,0·1016	3,3·1016
• SO II category	4,0·1016	1,8·1017	6,6·1016
• SO III category	6,6·1016	4,6·1017	1,5·1017
• SO IV category	1,4·1017	2,0·1018	5,1·1017

the subsequent cessation of hail fall from SO of categories III and IV. This is also evidenced by the fact that out of the annual consumption of rockets, only 0.4% of the SO of I category, accounts for 14% of the SO of II category, and the remaining 85.6% falls on SO of III and IV categories.

The annual consumption of anti-hail rockets, as follows from Table 4 and Fig. 3b, varies from 7 869 to 16 184 pieces and averages 11 913 pieces. The average annual expenditure for the defense of 1 000 km² is about 5 000 rockets.

In the last 15 years, Alazan-6 rockets were mainly used, which contain 0.66 kg of AD-1 pyrotechnic composition with 8% AgI content. With this in mind, the annual consumption of the agent varied from 5 194 to 10 681 kg, averaging 7 863 kg. In this case, the average annual consumption of AgI is 629 kg. Laboratory tests of the ice-forming efficiency of the composition AD-1 [17, 23] have shown that the yield of ice-forming nuclei (IFN) from 1 rocket is $6.6 \cdot 10^{15}$ at a temperature of -10 °C. It follows from Fig. 3b that, on average, about 17 SO of different categories were seeded per day and about 280 rockets were used, which contain $1.8 \cdot 10^{18}$ IFN, active at a temperature of -10 °C.

In the ANELFA project, 650 ground-based acetone generators emit about $4.7 \cdot 10^{18}$ IFN active at a temperature of -15 °C for 1 day with seeding for 10 h [13]. Given that at a temperature of -10 °C the number of active IFNs would be several times

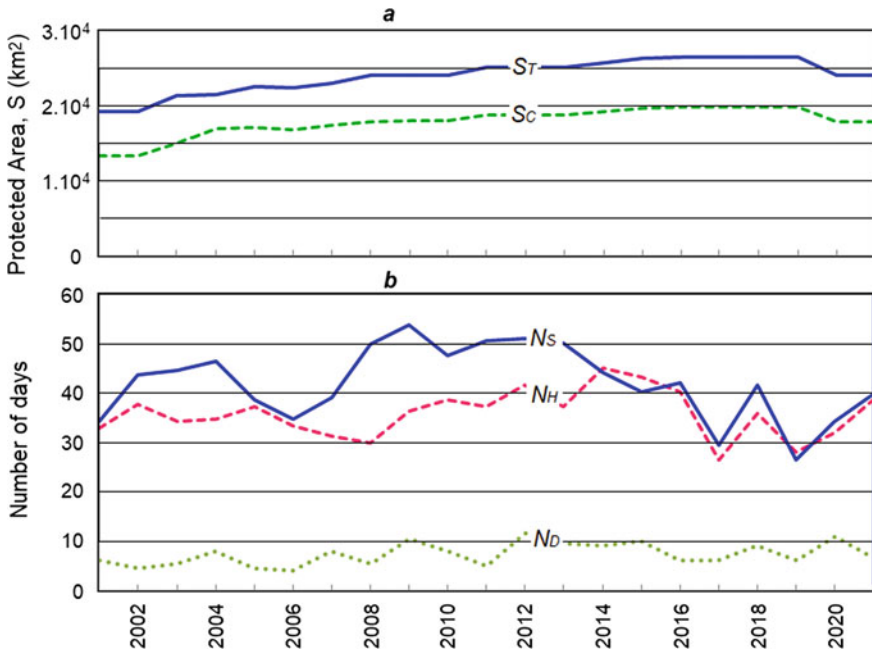


Fig. 2 Time course: **a** area of antihail protection: total (S_T) and cultivated part (S_c); **b** number of days: with hail in the region (N_H), with seeding (N_S) and with hail in the protected area

less, it can be said that the number of IFNs introduced by ground-based generators is comparable to the number of IFNs introduced by 280 rockets consumed in 1 day. In Alberta Hail Suppression Project [30], on the same day with inoculation with onboard generators and fired squibs, about 50 kg of reagent was consumed for inoculation of 7 SO with a total yield of IFN about $1.5 \cdot 10^{18}$. Those the amount of IFN introduced into hail storms by rocket, ground and air seeding methods is approximately the same. But the difference is that the rockets contribute this amount of IFN directly to the volumes of future hail formation, to the required height and to the required place. Ground-based generators bring them into the surface layer of the atmosphere, believing that the updrafts will raise the IFN in the area of negative temperatures. Aerial seeding is more targeted at seeding specific storms, but when seeding from the level of the base or top of developing towers, the reagent gets to the required height with some delay, which reduces the seeding efficiency.

Figures 4 and 5 show the distribution of seeded SO of different categories according to their maximum radar reflectivity Z_{max} and the height of the upper boundary of the radar echo with $Z = 35$ and $Z = 45$ dBZ above the level of the melting line and vertically integrated water content (VIL) of the cloud layer above the melting line. These distributions are single-vertex. One it is shown that the higher the category of seeded cells, the higher the values of these parameters, as one would expect.

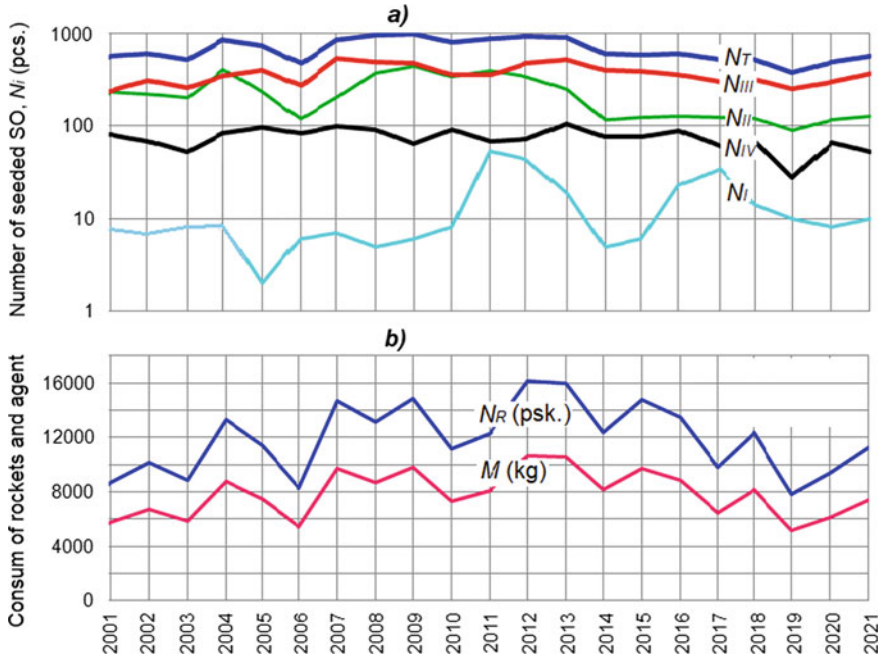


Fig. 3 Temporary trend: **a** the annual number of sown SO of different categories N_i ; **b** the annual consumption of rockets N_R (Pcs.) and reagent M (kg)

4 Project Evaluation

The methodology we use for evaluation of hail suppression technologies [8] includes following aspects:

- i. Radar assessment during hailstorms seeding operation in order to decide whether to stop or continue seeding.
- ii. Express assessment of the avoidable damage during the protection period to determine the extent of the damage prevented by the seeding of a separate hailstorm.
- iii. Assessment of the physical efficiency of technology in a season or a multi-year protection period to determine the degree of hail losses reduction.
- iv. Assessment of the economic efficiency of the technology over a season or a multi-year protection period to determine its payback and profitability.
- v. Assessment of the statistical significance of effect at a given level of importance.
- vi. Assessment of the environmental safety of technology.

The methodology of such a multilevel assessment is described in detail in the monograph [20]. It shows that the massive rocket seeding of areas of future hail formation leads to changes in the radar characteristics of storms, including changes in the spatial structure of storm hail, the disappearance of the radar echo canopy over

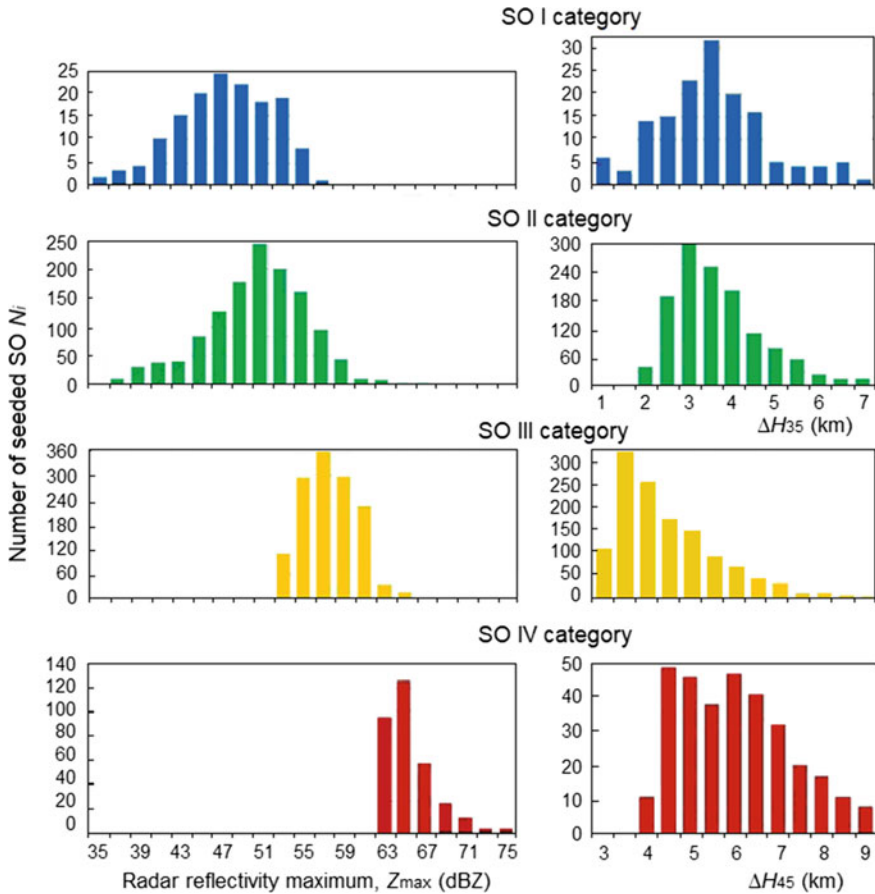
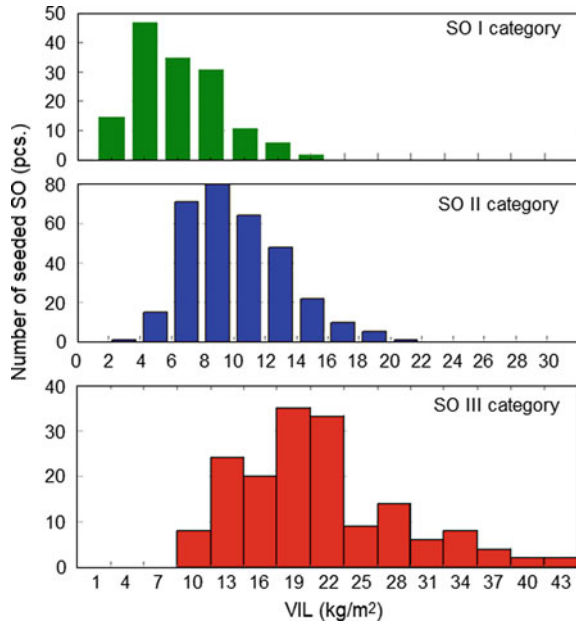


Fig. 4 Distribution of the number of seeded SO of different categories depending on: **a** maximum reflectivity Z_{max} ; **b** thicknesses of ΔH_{35} and ΔH_{45} layers

the BWER (or WER), a decrease in volumes with $Z > 55$ dBZ, corresponding to the volumes of the hail growth and hailfall zones, reduction of vertically integrated liquid (VIL) and volumetrically integrated water content M_{Zi} , reduction of the duration of the hail state of storms, reduction of the precipitation area, hail size and kinetic energy, degree of plants damage. Similar reactions to seeding of hailstorms are noted in the Alberta Project [30, 32].

Evaluation of physical and economic efficiency of the project was carried out by the method of historical series by comparing the areas of damage S_i (ha), the degree of damage K_i (%) before protection and during protection [17, 20], assuming that the hail climatology during these periods had not changed. Before 1991, the data on the areas and degree of damage were determined at the place of damage by a commission consisting of representatives of the Ministry of Agriculture, which

Fig. 5 Distribution of the number of seeded SO of I, II and III categories depending on the vertically integrated water content (VIL) of the cloud layer above the melting line



commissioned the works, the affected farm, the state insurance agency and the anti-hail service. Since 1992, the data of representatives of agriculture are mainly used. These data are used to calculate the average annual crop losses from hail before protection N_C (%) and during protection N_S (%) and physical efficiency E_f (%) [20] according to the formulas

$$N = 100 \frac{\sum_0^n S_i K_i}{\sum_0^n S_{ki}},$$

$$E_f = 100 \left(1 - \frac{N_S}{N_C} \right),$$

where S_{ki} is the cultivated area occupied by crops and green spaces.

Average annual yield losses in the 10-year period before protection (control period), were [20]:

- in the protection zone of the Krasnodar anti-hail service $N_C = 6.27\%$;
- in the protection zone of Stavropol anti-hail service $N_C = 3.65\%$;
- in the protection zone of the North Caucasus anti-hail service $N_C = 6.25\%$.

Taking into account the areas of the protected territories of these three services, the average annual hail losses in all the territory protected by them in the control years are about $\overline{N_C} = 5.4\%$. In years of protection from 2002 to 2021, average annual crop losses were $\overline{N_S} = 0.72\%$, ranging from 0.23 to 2.07%. The average physical efficiency of project from 2002 to 2021 is $\overline{E_f} = 86\%$.

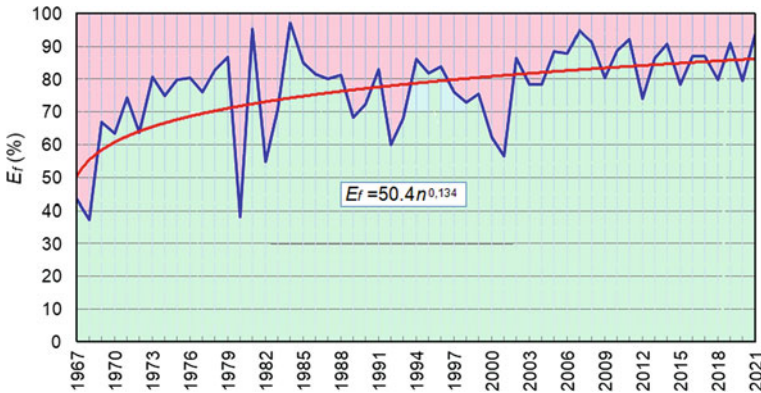


Fig. 6 Time course of physical effectiveness of anti-hail protection in the North Caucasus. In the approximation $E_f = 50.48n^{0.134}$ (%), n means the ordinal number of the year of protection since 1967

Figure 6 shows that from 1967 to 2021, the physical efficiency increased as technology and technical means improved and reached an average of $E_f = 86\%$. I.e., losses in the protected area over the past 20 years decreased on average 7.1 times.

Assessment of the statistical significance of this effect was carried out by the bootstrap method and t -test, which are widely used to assess the effectiveness of projects with purpose of hail prevention and rain enhancement [33, 34, etc].

Using the bootstrap method, two large samples simulating the general series $\{N_{Si}\}$ and $\{N_{Ci}\}$ were generated by repeating the empirical samples of hail losses before protection (N_C) and during protection (N_S) 1,000,000 times. A given number of experimental units were extracted from these samples using a uniformly distributed random number generator, and the effect value E_f was estimated [8]. Repeating this procedure many times gives the physical efficiency E_f at different significance levels, the probability density distribution of the effect $P(E_f)$, the significance level of the effect α , the probability of the effect at a given significance level $P(\alpha_0)$ and the confidence interval $(-1, \bar{E}_\gamma)$, where γ is the confidence level.

The t -test examination showed [20] that with the observed temporal variability of hail losses before and during years of protection (σ_C/\bar{N}_C), σ_S/\bar{N}_S and σ_S/σ_C) and the available length of observation series (N_C , N_S) the actual efficiency $E_f = 86\%$ significantly exceeds the t -test criteria $E_{Cr} = 27\%$ i.e. $E_f > E_{Cr}$. Consequently, the t -test exam is successfully met and the length of the statistical data series (N_C , N_S) is sufficient to claim that the resulting effect is the result of seeding of hail storms rather than their natural variability. Moreover, with a natural variability of 0.5 (typical of the North Caucasus region), the length of the data series (10 years before protection and 55 years during protection) is sufficient to confirm the effectiveness of protection at the level of significance $\alpha = 0.05$, two years of protection. In fact, the duration of protection is 55 years, including 20 years of automated protection with an average efficiency of about 86%.

Thus, the bootstrap and *t*-test methods confirmed a statistically significant reduction in hail losses in the North Caucasus as a result of anti-hail operations. Similar results were obtained in all regions of application of the considered technology in the CIS countries and Argentina [20], except Brazil, where, due to unskilled implementation of the technology, the reduction of hail losses was 24%, which is comparable with the level of their natural variability.

The decreases in efficiency seen in Fig. 6 are observed in years with an increased number of heavy supercell hailstorms when damage hail events were observed in the protected area. In all such cases, a thorough analysis of the features of the hailstorms, the quality of the implementation of seeding technology, the presence of scientific, technical and organizational problems that may affect the result of seeding was carried out. Generalization of the results of such analyses shows [17] that the main reasons limiting the efficiency of hail prevention are:

(A) **Scientific challenges:**

- long period (about 6–8 min) for realization of the precipitation acceleration chain initiated by glaciogenic seeding, including time of crystal formation and growth, time of their aggregation, time of aggregates' envelopment by cloud droplets, time of formation and falling a snow graupel [17];
- emergence of unknown or insufficiently studied features of hail storms.

(B) **Technical challenges:**

- (1) Volumetric radar scans cycle equal to 3.5–4 min. In the case of rapidly developing storms this duration did not provide timely detection of SO of I category. Because of this, the anti-hail services have seeded few of SO of I category, which are most effective and require less rockets.
- (2) The manually operated TKB-040 and Elia-MR rocket launchers cannot provide the required seeding rate for powerful and large-scale fast-developing hailstorms. In such cases insufficient number of rockets are introduced into hailstorms than the technology requires. For example, as shown in Fig. 7, on August 30, 2008, at each seeding of SO of III category, an average of 3 times less rockets were applied than required. Since the desired effect of weakening the storm was not achieved, the seeding was repeated many times. As a result, instead of a three-time seeding with a total consumption of 45 rockets, a 17-time seeding was performed with a total consumption of 76 rockets. At the same time, in addition to increasing the consumption of rockets, hail damage was not completely prevented.
- (3) The completeness of seeding is also reduced by the fact that the used anti-hail rockets Alazan do not seed clouds on the trajectory until it reaches an altitude of 3 km, so an unseeded circle 4–5 km in diameter remains around rocket sites, which is not always overlapped by neighboring rocket sites. It would also be desirable to increase the ice-forming efficiency of used rockets by 3–5 times, or to use rocket as instead that has radius of the unseeded circle less than 1.5 km, and the ice forming nucleus yield 2–3 times higher than that of the Alazan rockets.

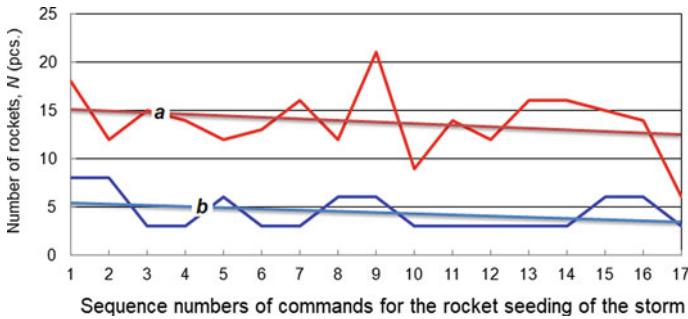


Fig. 7 Example of difference between required **a** and real **b** rockets consumption for seeding SO of III category 30.08.2008. The straight lines are trend lines

(C) *Organizational challenges:*

- Existence of forbidden sectors and non-shooting areas on protected territories (their elimination requires creation of additional 4–5 rocket sites in each anti-hail service).
- Insufficient length or lack of buffer zone from the side of their predominant invasion of hailstorms, does not allow to seed their upwind flank, where the initial stages of hail formation take place. This can be clearly seen in Fig. 8 on a fragment of SO of IV category seeding; in which most of the seeding area is unseeded because the rocket sites do not reach it, although the fallout zone has already reached the boundary of the protected area.
- In some years, the amount of funding for the services does not allow the purchase of the required number of anti-hail missiles and forces them to save at the expense of efficiency. For example, in 1991–1992 and 2000–2001, this led to a shortage of anti-hail missiles and a reduction in the quality of training of the entire anti-hail system. This, in turn, led to a drop in anti-hail effectiveness of up to 56–60%.

The combined effect of the above causes leads to incomplete seeding of OV of categories III and IV. A detailed analysis [8, 17] showed that during seeding of powerful category IV hail clouds only 25–30% of the required number of rockets is injected into them in time, as shown in Fig. 7. This leads to a decrease in the seeding effect, an increase in the number and duration of seeding and to an overestimated expenditure of rockets. The seeding effect of powerful hailstorms is often limited to a reduction in size and intensity of hail, narrowing the hailfall band without completely interrupting hail.

It should be noted that insufficient seeding reduces the effectiveness of all hail suppression technologies. For example, ground-based generators may not be turned on if hail is not predicted by the forecast. Aerial seeding is limited when visibility is poor in night, mountainous and difficult meteorological conditions [11] and in 40% of cases seeding cannot be performed. Nevertheless, in the ANELFA project, ground-based generators provide up to 50% reduction in the kinetic energy of hail

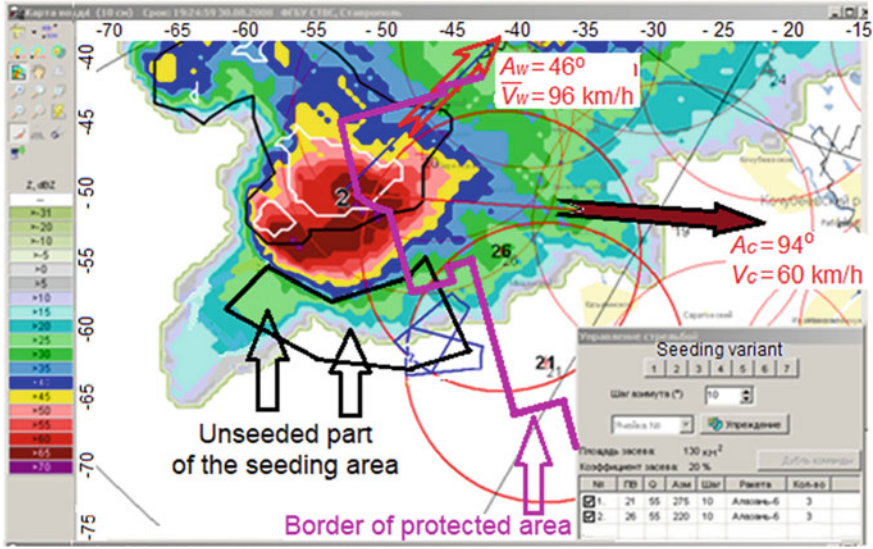


Fig. 8 Example of seeding the SO of IV category invading the protected area on 30.08.2008. It is clearly seen that the radius of rocket site action (red circles) does not allow to seed most of the seeding area bounded by the black broken line. The blue trapezoids show the seeding boundaries of two trios of rockets launched from rocket sites No. 21 and No. 26. Here A_w and \bar{V}_w are the direction and speed of the average wind in the 700–500 MB layer. A_c and V_c are the direction and speed of movement of hailstorm

[13]. In the Alberta project, a comparison of the radar parameters of seeded and unseeded storms [6, 30] showed that aircraft seeding leads to a reduction of VIL, area of radar echo with $Z > 60$ dBZ, size and time of hail fallout.

The economic effect of hail suppression E_e in the North Caucasus increased as the physical efficiency of protection and the cost of agricultural products increased. From 2016 to 2021, the annual economic effect is about $E_e = 3.5\text{--}4.5$ billion rubles and recoups the cost of operation by an average of 7.2 times. At the same time, the volume of preserved production of homestead farms, which reaches 50% of the production of large farms, is not taken into account. It is also not taken into account that prevention of hail leads to reduction of duration and intensity of flash floods, thunderstorms and squalls, causing damage comparable to the damage from hail. The cost of protection ranges from \$400 to \$600/km², of which about 40% goes to the purchase of anti-hail rockets, and 50% to personnel, et al.

5 Prospects for Improvement

The effectiveness of rocket technology of hail suppression has been improving for 55 years as the technology and technical means have improved. However, in the last

15 years this tendency has not been observed because the action for the improvement of the protection system has been suspended. Hail suppression equipment has not been updated since 1990 and does not provide full seeding of most powerful, large-scale, rapidly developing hailstorms. Re-establishing a trend of increasing protection effectiveness requires further improvement in the physical principles and strategy of hailstorm seeding and technical modernization of the protection system to improve the quality of seeding technology. The first-priority tasks in this regard are:

1. The use of at least one Sopka-2 rapid scan radar in each anti-hail service, which can provide timely detection and seeding of SO of I category [24]. Modernization of the outdated MRL-5 radars with installation of anti-hail control systems ASU-MRL, or replacement of MRL-5 with the new Doppler radars DMRL-10 [21, 24].
2. Replacement of manually controlled rocket launchers with automated high-speed units of the Elia-2 or Elia-4 type with wireless remote control [17, 22], in order to provide the required efficiency of seeding powerful and fast-developing hailstorms.
3. Creation of ASU-Hail robotic hardware-software complexes on the basis of the listed technical means (Fig. 9). Field tests of the ASU-Hail complex in the North Caucasus Service in 2015–2017 showed [22] that it provides implementation of low-personnel technology of hail suppression (without permanent personnel of rocket sites). Such integrated automation of anti-hail operations can improve the quality of technology implementation, its efficiency and reduce the cost of protection by reducing the number of personnel by 3–4 times [33].

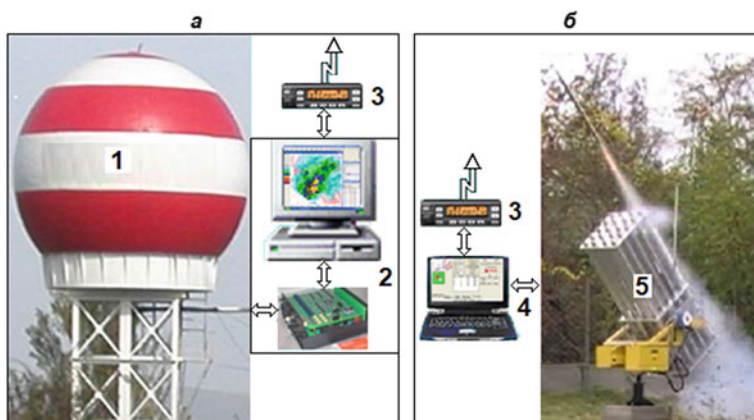


Fig. 9 Robotic anti-hail system: **a** equipment of command site; **b** equipment of rocket site (there can be up to 48 such sites at one command site). 1—S-band radar (upgraded MRL-5M or DMRL-10 or Sopka-2); 2—Hardware-Software complex ASU-MRL for processing radar information and control of anti-hail operations; 3—radio modem for data exchange between command and rocket sites; 4—Notebook; 5—automated rocket launcher Elia

6 Conclusion

The described hail suppression rocket technology was created as a result of 65 years of continuous field, laboratory and theoretical research of hailstorms and summarizing 55 years of experience of its application in various climatic conditions (in Russia, Moldova, Azerbaijan, Armenia, Georgia, Tajikistan, Uzbekistan, Ukraine as well as in Argentina and Brazil [20]) over a total area of more than 115,000 km². Over the past 20 years, this technology has provided a statistically significant 86% reduction in hail losses. There are prospects of further increasing its efficiency by improving the scientific and technical basis of the created anti-hail system.

In a long-term project ANELFA which started in France in 1952, seeding the ground atmosphere with ground generators of ice-forming aerosol leads to a 50% reduction in the kinetic energy of hail over an area of about 50,000 km² [13]. In the US state of North Dakota, aircraft seeding hail damage has been reduced by 44–47% on an area of about 30,000 km² [35, 36]. Aircraft seeding of hailstorms in Canada resulted in a 20% reduction in hail losses over an area of approximately 60,000 km² [30–32]. In the republics of former Yugoslavia the reduction of damages by 60–70% by the rocket method was achieved on about 122 700 km² areas [37, etc.]. Similar results have been obtained in Bulgaria [38]. The largest project of hail protection in the world in China was started in the province of Xinjiang in 1968. Later, the area of protection gradually increased up to 500,000 km², covering areas prone to hail in almost all the provinces of China. The effectiveness of this project varies somewhat from province to province. For example, in Xinjiang Province, hail damage is reduced by 73%.

Thus, large and long-term hail suppression projects in Russia, France, USA, Canada, China, CIS countries, Yugoslavia and Bulgaria have yielded statistically significant reductions in damage. At the same time, one can often find very pessimistic assessments of hail suppression in the scientific literature.

It is obvious that the effectiveness of hail suppression depends on the physical validity and quality of the technology used. The quality of technology implementation and completeness of implementation of the physical principles underlying the technology are not unimportant factors either. It was shown above, that the rocket and other technologies do not provide the complete seeding of chemical agents in the required volumes. None of the technical means used makes it possible to cover the required volume in the required time (1–2 min) in large-scale supercell storms. Not full seeding leads to insufficient seeding efficiency of such storms, although in terms of timely detection and selection of seeding locations, it is the easiest case. Reduced effectiveness of protection due to incomplete seeding of hailstorms complicates the evaluation of the performance of the physical principles of hail prevention. Randomization methods for such assessments are not acceptable due to the high variability of storm parameters and the big influence of accuracy and completeness of seeding [20].

The use of incorrect technologies or their inadequate implementation leads to an ambiguous assessment of the potential of various weather modification technologies. There are many such examples, but the USA National Hail Research Experiment (NHRE) [10, 26] and the Grossversuch-IV experiment [39], which were conducted to assess the scientific prerequisites and effectiveness of old Soviet methods of hail suppression, can be cited as better known ones. In the NHRE in 1972–1976, Sulakvelidze’s method [6] was evaluated based on the concept of competition, which involved artillery seeding of hail initiation and growth zones in the so-called large droplet “accumulation zone”. The Grossversuch-IV experiment in 1972–1976 tested the rocket method used in Moldova [11].

Both of these experiments gave ambiguous and, in fact, negative results. The reason for this was that, along with a good program of instrumental measurements and scientific evaluations, the seeding operations in the NHRE and Grossversuch IV experiments did not fully reproduce the methods tested. Artillery and rocket methods provided for the seeding of mature hail cells and all developing cells, which made it possible to prevent their development to the hail stage and ensured some success for these methods. In the NHRE and Grossversuch IV experiments, only mature hail cells were seeded in the region of strong updrafts and the central part of the radar echo with $Z > 45$ dBZ, where hail has already formed and is growing. Such seeding, instead of limiting the growth of hail, leads to an acceleration of its growth, an increase of hail size and kinetic energy, which was obtained in these experiments [39, 40]. The seeding agent dosage in NHRE and Grossversuch IV was significantly lower than in the methods tested. For example, in Grossversuch IV, the consumption of Soviet rockets Oblako and PGI-M was 5–10 times less than in Moldova and Georgia.

On the other hand, both tested methods did not provide hail interruption from mature hail storms, since seeding of hail initiation and growth zones excludes such result. Such seeding cannot lead to favorable competition for available water between the smallest aerosol particles of the crystallizing agent and the growing hailstones. Therefore, in the 1980s, we moved from the concept of competition to the concept of accelerating precipitation [8] and to seeding in storms only zones of new growth. The seeding of the hail growth zone is considered as one of the major mistakes of the seeding operators.

Thus, the Grossversuch IV and NHRE experiments quite naturally gave negative results, and gave rise to pessimism in assessing the hail suppression potential. This pessimism persists to this day and is reflected in the statement of the World Meteorological Organization [41]. Such pessimism is also evident in the evaluation of weather modification projects to increase precipitation, disperse fog, etc., and is supported by observers who usually do not participate in the field projects [42 et al.] Such pessimism inhibits funding and development of weather modification methods and technical means, contrary to the UN Sendai Framework Program, which calls for a set of measures to significantly reduce mortality, casualties and economic losses by using new technologies [3]. Climate change and the increase in the frequency and intensity of hail and associated tornadoes, thunderstorms, floods and flash floods also require building capacity to monitor and prevent them.

Acknowledgements This article was prepared on base of the data processing from the annual reports of the Krasnodar, Stavropol and North Caucasus hail suppression Services of Roshydromet, as well as annual reports on scientific and methodological management of anti-hail operations by Hail Suppression Research Center “Antigrad” and High-Mountain Geophysical Institute of Roshydromet. The authors express their deep gratitude to all those who participated in the preparation of these reports and are very grateful to the numerous participants of the long-term research of hailstorms and regional projects of hail suppression.

Data Availability Concept development and manuscript preparation, M.T.A.; analysis of experimental data and preparation of illustrations, A.M.A.; general supervision, collection and statistical evaluation of project results, A.M.M.

Funding The work was done on the authors’ initiative without financial support.

Data Availability Final data on the hail suppression project in the North Caucasus are available upon request. An example of annual reports of anti-hail Services and an example of a scientific and methodological guidance report can also be provided upon request, as there are 120 books even in the last 30 years.

Conflicts of Interest The authors declare no conflicts of interest.

References

1. State of Climate Services 2020 Risk Information and Early Warning. WMO-No. 1252 (2020).
2. United Nations. International Day for Disaster Risk Reduction, Geneva, 13 October 2020.
3. Sendai Framework for Disaster Risk Reduction (2015–2030). United Nations, Sendai, Japan (2015).
4. Adam B. Smith: 2021 U.S. billion-dollar weather and climate disasters in historical context. *Observing & Predicting*. January 24 (2022).
5. Register of National Weather Modification projects 2000. WMP Report series No. 38. WMO/TD- **1094**.
6. Sulakvelidze G.K.: Heavy rainfall and hail. *L. Gidrometeoizdat*, (1967).
7. Bartishvili I.G., Bartishvili G.S., Gudushauri Sh.L., Lominadze V.P.: On the issue of combined impact on the warm and supercooled part of the cloud for prevent hail. *Proc. of ZakNIGMI*, **2**, 7–22 (1967).
8. Abshaev M.T., Dadali Yu.A.: Some issues of impact on hailstorms. *Proc. of VGI*, **22**, 104–116 (1973).
9. Vulfson N.I., Levin L.M.: Destruction of developing cumulus clouds using explosions. *Izv. Academy of Sci. of the USSR, Physics of the Atmosphere and Ocean*, Vol. 8, **2**, 156–166 (1972).
10. Browning K., Foote G.B. Airflow and hail growth in supercell storms and some implications for hail suppression. *Q. J. R. Meteorol. soc.* 1976, **102**, 499–533.
11. Bukhnikashvili A.V., Gaivoronsky I.I., Kartsivadze A.I. et al.: Methodology for prevention of hail processes and results of experiments in the Alazani Valley. *Proc. of the All-Union Conf. on active influence on hail processes*. Tbilisi, 76–87 (1964).
12. Fedorov E.K.: Active influences on meteorological processes. *Bulletin of the Academy of Sciences of the USSR*, **9**, 73–78 (1962).
13. Dessens J., Berthet C., Sanchez J.L., Hermida L., Merino A.: Hail prevention by ground-based silver iodide generators: Results of historical and modern field projects. *Atmos. Res.*, **170**, 98–111 (2016). doi:<https://doi.org/10.1016/j.atmosres.2015.11.008>.

14. Abshaev M.T.: Structure and dynamics of development of hailstorms in the North Caucasus. Proc. of VGI, Vol. 53, 6–22 (1982).
15. Abshaev M.T.: Automated rocket technology of hail suppression. 8th WMO Sci. Conf. on Weather Modification, Casablanca, Morocco. 335–338 (2003).
16. Abshaev M.T., Nunez J.M.: Hailstorms principal differences between some regions of the Northern and Southern hemispheres and the operating procedures at present. Proc. 6th WMO Sci. Conf. on Weather Modif., Paestum, Italy, 101–104 (1994).
17. Abshaev A.M., Abshaev M.T., Malkarova A.M., Barekova M.V.: Manual on hail prevention. Nalchik, Printing House (2014).
18. Abshaev M.T.: Radar detection of hail. Izv. An. USSR, FAO, Vol. 18, 5. 483–494 (1982).
19. Abshaev M.T., Burtsev I.I., Shevela G.F.: Manual for the use of radars MRL-4, MRL-5 and MRL-6 for hail suppression. L., Gidrometeoizdat (1980).
20. Abshaev M.T., Malkarova A.M.: Evaluation of hail prevention effectiveness. St. Petersburg: Gidrometeoizdat (2006).
21. Abshaev M.T., Abshaev A.M., Kotelevich A.F., Sirota N.V.: Automated system for processing radar information for the purposes of storm warning and weather modification. Proc. of the XXVII All-Russian Symposium of Radar Research natural environments. St. Petersburg, 211–225 (2011).
22. Abshaev M.T., Abshaev A.M., Chochoev H.H., Kuznetsov B.K.: New advances in automation of antihail rocket technology. Proc. of 10th WMO Conf. Weather Mod. Bali, Indonesia, 279–282 (2011).
23. Abshaev M.T., Stasenko V.N., Nesmeyanov P.A., Dubinin, Korneev V.P. Russian hail suppression rocket systems: main technical and performance characteristics, development concept/8th WMO Sci. Conf. on Weather Modification. Casablanca, Morocco. Vol. 2. 311–314 (2003).
24. Abshaev A.M., Abshaev M.T., Efremov V.S., Vylegzhanin I.S.: New radars for research and weather modification. Proc. of 2nd Int. Conf. Innovative methods and means of research in the field of atmospheric physics, hydrometeorology, ecology and climate change. Stavropol, 265–271 (2015).
25. Chisholm A.J., and J.H. Renick: The kinematics of multicell and supercell Alberta hailstorms, Alberta Hail Studies, Research Council of Alberta Rep. 72 2, 24 31. (1972).
26. Foote B, Browning K.A., K.A. Borland, S.A. Chengnon et al.: Hail. A review of hail science and hail suppression. Meteorological Monograph, Vol. 16, No 38. Amer. Met. soc. Boston, Mass., 277 p. (1977).
27. Barge B.L., Bergwall F., Goyer G.G., Renick J.H.: Fine scale structure of convective storms – Implications for cloud seeding in Alberta.–Atmospheric Sci. Report 76–3, Alberta Weather Modif. Board. Red deer, Alberta (1976).
28. Abshaev A.M., Abshaev M.T., Sadykhov Y. A.: Diffusion of artificial aerosol in Cu cong clouds. Russ. Meteorol. Hydrol. 18–24 (2004).
29. English, M.: Results of hail suppression research in Alberta, Canada. Prep. 11th Conf. Weather Modif. Amer., Met. Soc., Edmonton, Alta. 98–101 (1987).
30. Gilbert D.B., Boe B.A. and T.W. Krauss: Twenty Seasons of Airborne Hail Suppression In Alberta, Canada. J. Weather Modification, Vol. 48, 68–92 (2016).
31. Krauss T.W., and J.D. Marwitz: Precipitation processes within an Alberta supercell hailstorm. J. Atmospheric Sciences, **41**, 1025-1034 (1984).
32. Sankha Subhra Maitra: Methods for Evaluation of the Alberta Hail Suppression Project Using Radar Observations. University of North Dakota Theses, Dissertations, (2021).
33. Buykov M.V., Kuzmenko A.G.: Analysis using bootstrap of the results of an experiment on the weakening of hailstorms. Proceedings of the UkrNII. **221**, 13-29 (1987).
34. Ventzel E.S.: Probability Theory: Textbook for Higher Education Institutions. Moscow: Higher School, (1999).
35. Smith P.L.: Hail suppression activity around the world. Preprints of the Symposium on Plan. Inv. Weather Modif. Atlanta, Published by the Amer. Met. Soc. Boston, Mass. (1992).
36. Smith P.L., Johnson L.R., Priegnitz D.L., Mielke P.W.: Statistical evaluations of the North Dakota cloud Modification Project. 6th WMO Sci. Conf. On Weather Modif. Paestum, Italy, Vol. 1. 281–284 (1994).

37. Rakovec J., Gregorcic B., Kranic A., Melcinda T., and L. Kazkez-Bogataj: Some results evaluation of hail suppression of Slovenia, Yugoslavia. *J. Appl. Met.* **41**. 157 -171 (1990).
38. Simeonov P.: Study on some effect of Bulgarian hail suppression operational project: statistical evaluation. 8th WMO Sci. Conf. on Weather Modification, Casablanca, Morocco. 299–302 (2003).
39. Federer B., Waldvogel A., Schmidt W. et al.: Main results of Grossversuch-4. *J. Climate Appl. Met.* Vol. 25. 917-957 (1986).
40. Auf der Maur A., Germann U.A: Re-Evaluation of the Swiss Hail Suppression Experiment using Permutation Techniques shows Enhancement of Hail Energies when Seeding. *Atmosphere*, 12, 1623. (2021). doi.org/<https://doi.org/10.3390/atmos12121623>.
41. WMO Statement on the Status of Weather Modification. web.archive.org. (2017).
42. Wieringa J. and Holleman I.: If cannons cannot fight hail, what else? *Meteorologische Zeitschrift*, 15, 3, (2006).

Lightning Protection and Attack by Ground Lightning in the Territory of the Northern Caucasus



A. Kh. Adzhiev and Z. M. Kerefova

Abstract Lightning is a powerful electrical discharge in the atmosphere, which occurs due to the potential difference inside a thundercloud or between a cloud and the ground. To prevent the detrimental effects of lightning, lightning protection measures are organized. The effectiveness of them largely depends on a well-executed grounding system. In the above work, an experimental and theoretical study of the physical and statistical characteristics of thunderstorm activity and the susceptibility of the territory and objects to lightning, characteristic of the territory of the North Caucasus, was carried out. A map of the average annual lightning strike rate of the territory of the North Caucasus has been constructed.

Keywords Thunderstorms · Lightning protection · Susceptibility map · Lightning detector · Instrumental research · Duration of thunderstorms

1 Introduction

A lightning discharge between a cloud and the ground is one or more successive partial discharges (pulses). Usually these are (3–4) pulses with a characteristic duration of about 40 microseconds each, separated by a characteristic interval of about 40 ms. Each impulse consists of a leader (pre-discharge) and a return (reverse) strike. It is the leaders who pave the way for impulses. The leader preceding the first impulse is called the step leader, and the leaders preceding subsequent impulses are called swept leaders [1, 2]. They appear in the atmosphere at an electric field strength of about 3 kV/cm [3, 4], which is an order of magnitude lower than the field strength for the electrical breakdown of air under normal conditions ($E \approx 30$ kV/cm). Fields with $E \approx 30$ kV/cm are not observed in the free atmosphere. In the theory of thunderstorms, the issue of the emergence of lightning leaders is the least studied. Lightning is often associated with the occurrence of fires, destruction of buildings, damage to power lines, disruption of the movement of aircraft and trains, etc. A direct lightning strike

A. Kh. Adzhiev · Z. M. Kerefova (✉)
High Mountain Geophysical Institute, 2 Lenin Ave, Nalchik, Russia
e-mail: zknyaz-kbsu@mail.ru

© The Author(s), under exclusive license to Springer Nature Switzerland AG 2023
R. Zakinyan and A. Zakinyan (eds.), *Physics of the Atmosphere, Climatology and Environmental Monitoring*, Springer Proceedings in Earth and Environmental Sciences, https://doi.org/10.1007/978-3-031-19012-4_2

on a person usually leads to death. In general, a thunderstorm is a complex atmospheric phenomenon, the signs of which are multiple electrical discharges (lightning) between oppositely charged areas of a cloud—cloud discharges, different clouds—intercloud discharges, or between clouds and the ground—ground discharges. As a rule, very often thunderstorms are accompanied by strong squally winds, heavy rainfall and hail. The operational determination of its location, intensity, direction and speed of movement is of great practical importance for many branches of human economic activity. In particular, for meteorological support for aviation, lightning protection of energy facilities, etc. The problem of monitoring the electrical activity of convective clouds is one of the urgent and complex problems of modern atmospheric physics. The needs of aviation, meteorology and a number of other areas of science and technology are inextricably linked with this problem. The importance of this task is due to the need to ensure the safety of aircraft and power facilities from lightning, prevent forest fires and eliminate the possibility of lightning current impact on electrical networks.

One of the indicators of the reliability of overhead power lines, buildings, structures and other lightning-dependent objects is their lightning resistance. Overhead power lines, due to their great length and height, are very vulnerable objects for the effects of lightning. To develop measures to improve the reliability of lightning protection of operated and designed facilities, statistical data on lightning activity and its characteristics are needed: the number and location of lightning strikes, the amplitude, duration and polarity of the current pulse. The availability of reliable statistical data on the intensity of thunderstorm activity in the areas of operating and projected lightning-dependent facilities will improve their lightning protection. The risk of lightning damage to various objects can be reduced if, at the design stage, when choosing the route for the passage of power lines, the location and parameters of objects, statistical data on the intensity of thunderstorm activity are taken into account. Currently, the intensity of thunderstorm activity in the Russian Federation is determined by regional maps of the average annual duration of thunderstorms in hours, compiled according to long-term observations at meteorological stations of Roshydromet visually and by ear [5].

2 Methods

The aim of the work is to build a map of the average annual ground lightning strike rate in the North Caucasus using the LS 8000 instrumental observation data. Lightning is one of the most dangerous natural phenomena, the consequences of which can lead to explosions, fires, electric shock to people.

The location of the impact is difficult to predict. Lightning currents always choose the shortest path to the ground with the least resistance, then the potential objects of the discharge will be significantly elevated buildings and their elements that have good conductivity and are connected to the ground. There are different types of

lightning rods: rod, cable and mesh. To protect against secondary manifestations of lightning, fuses and surge arresters are used in the form of electromagnetic impulses.

The problem of monitoring the electrical activity of convective clouds is one of the urgent and complex problems of modern atmospheric physics.

The number of lightning strikes per year of various objects depends on its geometric dimensions and the number of lightning strikes on the earth's surface per year n , $1/(\text{km}^2 \text{ year})$ in the territory where the object is located.

The expected number N of lightning strikes per year is calculated using formulas (1, 2 and 3): for concentrated buildings and structures (chimneys, derricks, towers)

$$N = 9\pi h^2 n \cdot 10^{-6}, \quad (1)$$

for buildings and structures of rectangular shape

$$N = [(S + 6h)(L + 6h) - 7, 7h^2] n \cdot 10^{-6} \quad (2)$$

where h is the highest height of a building or structure, m ; S , L —respectively the width and length of the building or structure, m ; n —the average annual number of lightning strikes per 1 km^2 of the earth's surface (specific density, lightning strikes into the ground) at the location of a building or structure.

For buildings and structures of complex configuration, as S and L , the width and length of the smallest rectangle in which a building or structure can be inscribed in plan are considered.

The number of lightning strikes per year into a power transmission line with a length l , km , with an average height of the upper wire or cable suspension h_{av} , m :

$$N = 4nh_{cp}l \cdot 10^{-4}, \quad (3)$$

The density of lightning strikes to the ground, expressed in terms of the number of strikes per 1 km^2 of the earth's surface per year, is determined according to meteorological observations at the location of the object. If the density of lightning strikes to the ground n , $1/(\text{km}^2/\text{year})$ is unknown, it can be calculated using the following formula:

$$n = 6, 7 \cdot \frac{T}{100}, \quad (4)$$

where T is the average annual duration of thunderstorms in hours, determined from regional maps of the intensity of thunderstorm activity.

3 Results

In recent decades, along with visual [1–3] methods of observing thunderstorms, instrumental methods [4–7] have been increasingly used.

In this work, for the first time in Russia, the lightning direction finding network (GPS) LS 8000 of the VGI was used to determine the statistical distributions of the number of days with a thunderstorm, the duration of thunderstorms and their spatial variations in the North Caucasus. GPS LS 8000 manufactured by Vaisala, Finland, is a difference-range system of the LPATS type [8].

The lightning detection system of the Federal State Budgetary Institution “VGI” consists of four lightning direction finders and a central point for receiving, processing information and archiving. Since 2020, GPS has been supplemented with two more sensors.

Each lightning direction finder (sensor) has two sensors—low-frequency (LF) and high-frequency (VHF).

According to the data received from LF and VHF sensors, the central processor, after processing these data, provides information about the lightning strike, the number of days with thunderstorms and the duration of thunderstorms. The GPS ensures the reception of information about lightning from the entire territory of the North Caucasus, their archiving and transmission of information to consumers.

Most often, thunderstorms at observation points (a point with a radius of up to 20 km) last 1–2 h, but in some cases they last 4–5 h or more and the number of days with a thunderstorm is from 20 to 80 days. In the North Caucasus as a whole, the average duration of a thunderstorm is about 4 h per thunderstorm day.

On the territory of the North Caucasus, from January to April and from October to December, the highest frequency of thunderstorms, as a rule, occurs from 12:00 to 19:00. In other periods of the year, thunderstorms occur during the day in the territory under consideration.

An analysis of daily data on the duration of thunderstorms based on instrumental measurements of the GPS LS 8000 showed that the average duration of one thunderstorm in the south of the territory under consideration increased by about 8...0.10 min over 10 years. Similar conclusions were made by the authors of [9] based on data from weather stations.

Table 1 shows the frequency distribution of thunderstorms during the day.

The average duration of one thunderstorm in the south of the territory under consideration has increased over 10 years by about 8...0.10 min. To create a map of the average annual lightning strike rate of the territory of the North Caucasus, a sample was made for the period from 2008 to 2019 of cases of lightning strikes on the earth’s surface, Fig. 1.

Table 1 Frequency of thunderstorms during the day in the North Caucasus

Time (h)	1–4	5–8	9–12	13–16	17–20	21–24
% Thunderstorm	6	4	17	38	25	10

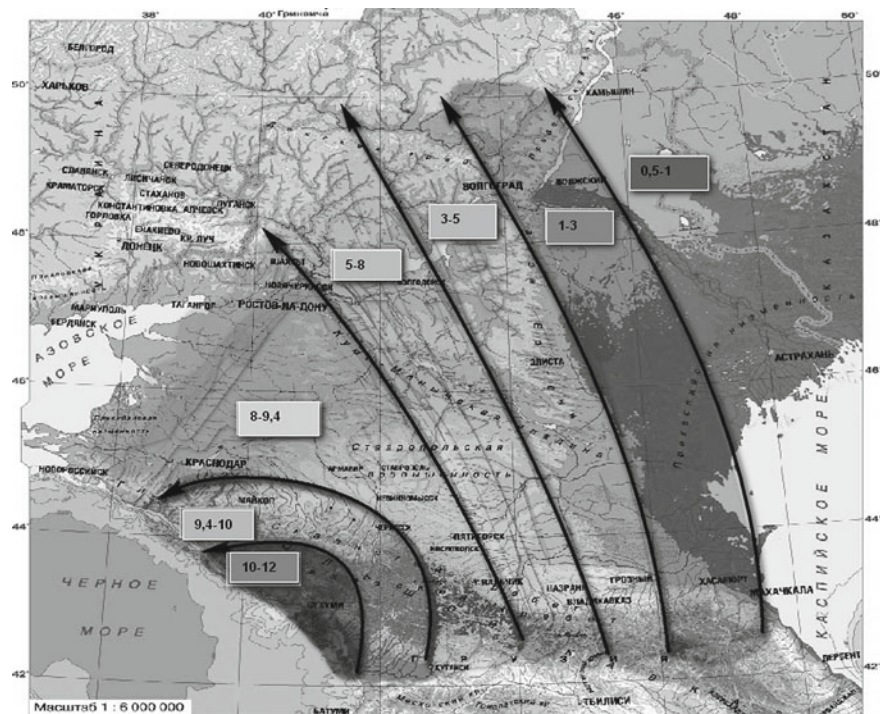


Fig. 1 Map of the average annual ground lightning damage to the earth's surface in the North Caucasus, built on the basis of instrumental observations LS 8000

The created map made it possible to identify areas on the territory of the North Caucasus with maximum and minimum damage to the earth's surface by cloud-to-ground lightning discharges.

When creating the map in Fig. 2, we also used data on the duration of thunderstorms and expression (4).

In the North Caucasus, from west to east, the number of strikes of various objects by lightning per year increases. At the same time, concentrated buildings and structures up to 50 m high, these are masts, pipes, television towers, in the west, according to instrumental data, are struck once every 1.5 years, in the east—in 15 years, such objects are struck by lightning. Likewise for other objects. Rectangular buildings and structures in the south are affected about once a year. In the East in 10 years once. High-voltage power lines 100 km long in the west are struck 4 times a year. In the east—at 2.5 years.

Figure 2 shows that the average annual susceptibility of the earth's surface of the North Caucasus by ground-based lightning varies from 10–12 strikes/km² year in the south to 0.5–1 strikes/km²*year in the northeast.

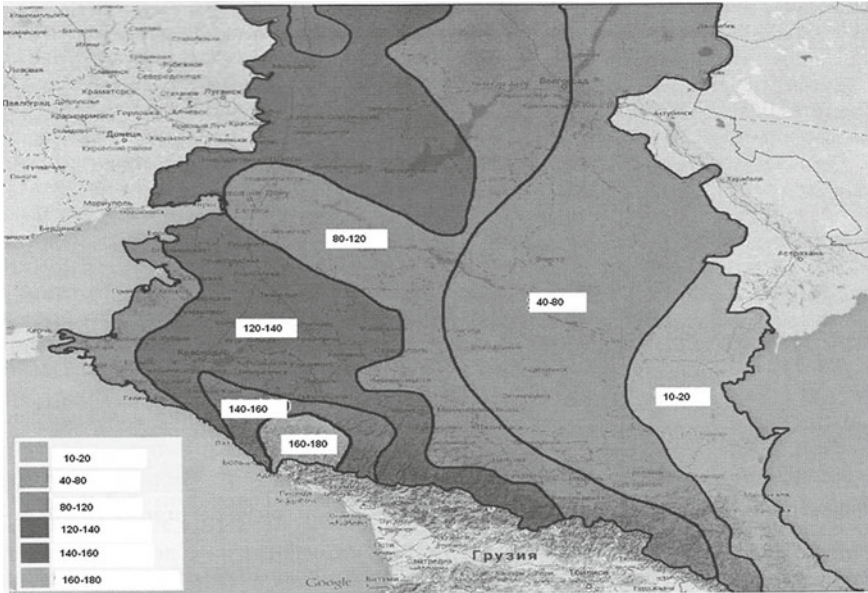


Fig. 2 Map of the average annual duration of thunderstorms in hours according to instrumental observations

Using the data on the map (Fig. 1) and formulas (1)–(3), an assessment was made of the lightning strike rate of various objects in the North Caucasus. For comparison, similar calculations were made using a climate map.

4 Conclusions

There is a tendency to reduce the average annual specific strike rate of the earth from south to north. The highest average annual lightning strike rate of the earth up to 12 strikes/km² year hours according to instrumental measurements of GPS LS 8000 in the area of the Black Sea coast of Russia (up to 8 strikes/km² year according to meteorological stations) and the lowest strike rate of 1 strike/km² year in the northeast.

The North Caucasus remains an area of increased thunderstorm activity, as evidenced by both the rather high frequency of thunderstorm processes in general, and the scale and intensity of individual processes.

References

1. Instructions for hydrometeorological stations and posts. Gidrometeoizdat, Leningrad (1985). [in Russian].
2. Guidance document. Instructions for hydrometeorological stations and posts. Issue 3. Part II. Processing of materials of meteorological observations. Gidrometeoizdat, St. Petersburg (2001). [in Russian].
3. Guide to meteorological instruments and methods of observation. WMO **8**, 778. (2014).
4. Mareev, E.A., Trakhtengerts, V.I.: Mysteries of atmospheric electricity. *Priroda* **3**. 24–33 (2007) [in Russian].
5. Trakhtengerts, V.Y., Iudin, D.I., Kulchitsky, A.V., Hayakawa, M.: Electron acceleration by a stochastic electric field in the atmospheric layer. *Phys. Plasmas* **10**(8), 3290–3296 (2003).
6. Price, C. and Rind, D.: Possible implications of global climate change on global lightning distribution and frequencies. *Journal of Geophysical Research* **99**, 10823–10831 (1994).
7. Grandt, Ch.: Global thunderstorm monitoring by using the ionospheric propagation of VLF lightning pulses with applications to climatology: Diss. Bonn, 134–142 (1999).
8. Adzhiev, A.K., Stasenko, V.N. & Tapaskhanov, V.O. Lightning detection system in the North Caucasus. *Russ. Meteorol. Hydrol.* **38**, 1–5 (2013).
9. Badakhova, G.Kh. Lashmanov, Yu.K., Shmigelsky, V.A.: Dynamics and modern regime of thunderstorm activity over the Central Ciscaucasia. *Science. Innovation. Technology.* **4**, 117–130. (2018) [in Russian].

Vibrational Regimes in the Atmosphere



I. S. Afanasyev , R. G. Zakinyan , and Yu. L. Smerek 

Abstract The article considers the influence of the daily rotation of the Earth on the oscillatory processes in the atmosphere. When considering axial rotation, diurnal changes in air temperature are taken into account. If the frequency of Brunt–Väisälä coincides with the frequency of the daily rotation of the Earth or their difference is insignificant, then phenomena such as resonance or beats occur. In a standard atmosphere, the Brunt—Väisälä frequency is many times greater than the axial rotation frequency, so these cases are very rare. However, such high-intensity fluctuations can lead to significant periodic temperature changes at the considered point.

Keywords Brunt–Väisälä frequency · Temperature difference · Temperature gradient difference · Dynamic heating · Velocity · Ascending flows · Amplitude · Beats · Resonance

1 Introduction

The oscillatory processes of high intensity are periodically observed in the atmospheres of the planets. The studies of the oscillatory regimes of the Earth's atmosphere, taking into account the influence of axial rotation, which affects the occurrence of beats and resonances, are relevant.

The methods of mathematical modeling of the motion of an air particle have been widely used to describe atmospheric processes. They are based on equations describing the dynamics and statics of air, and expressions characterizing the dependence of meteorological quantities on space and time.

The atmosphere is a stratified gas, meaning that its density almost always changes with height. The equation of statics is used to describe the stationary atmosphere. When disturbances occur, the particles deviate from the equilibrium position and oscillations occur, characterized by the Brunt—Väisälä frequency (or buoyancy

I. S. Afanasyev (✉) · R. G. Zakinyan · Yu. L. Smerek
North-Caucasus Federal University, 1 Pushkin Str, 355017 Stavropol, Russia
e-mail: afanasevigor278@gmail.com

frequency). That is, two main forces act on a particle of unit mass: the force of gravity \mathbf{g} and the force of Archimedes $-\frac{1}{\rho}\nabla p$ [1, 2].

If the oscillatory regime of the atmosphere is synchronized with the axial rotation of the planets, then phenomena such as beats and resonance are observed. These phenomena are quite rare on Earth, so it is interesting to know the probability of their occurrence, frequency, features of such oscillations and their characteristics.

The objectives of the research work are to obtain a solution to the system of equations describing the oscillatory motion, taking into account the influence of the axial rotation of the planet, and to analyze high-intensity oscillations. The purpose of the work is to study the oscillatory processes occurring in the Earth's atmosphere, to study such phenomena as beats and resonance, and to determine the conditions for their occurrence.

2 Methods of Research

2.1 Basic Equations

Let us consider air as an ideal liquid [3]. Its motion is characterized by the Euler equation, written in an inertial frame of reference:

$$\frac{\partial \mathbf{v}}{\partial t} + (\mathbf{v}, \nabla)\mathbf{v} = \mathbf{g} - \frac{1}{\rho}\nabla p. \quad (1)$$

In the state of statics, Eq. (1) takes the form [4]:

$$\mathbf{g} - \frac{1}{\rho_e}\nabla p_e = 0. \quad (2)$$

Let small disturbances occur in the atmosphere, that is, $p = p_e + p'$, $p' \ll p_e$, $\rho = \rho_e + \rho'$, $\rho' \ll \rho_e$. Then Euler's equation takes the form:

$$\frac{d\mathbf{v}}{dt} = -\frac{1}{\rho_e}\nabla p' + \frac{\rho'}{\rho}\mathbf{g}. \quad (3)$$

Accordingly, in the projection on the axis OZ , based on (2), the expression is valid (let us also assume that there is no horizontal movement) [5]:

$$\frac{dw}{dt} = -\frac{1}{\rho_e}\frac{dp'}{dz} - \frac{\rho'}{\rho}g. \quad (4)$$

Consider the interaction of air flow with the surrounding atmosphere, and their pressures are mutually compensated, so $p = p_e$ or $p' = 0$. We also consider that the equation of state of dry air is valid, and then we obtain the relation:

$$\frac{\rho_e}{\rho} = \frac{T}{T_e}. \quad (5)$$

Let's introduce the temperature difference $\Delta T = T - T_e$, and so T (and T_e) varies with height according to a linear law [6], then the expression for ΔT takes the form:

$$\Delta T = \Delta_0 T - \Delta \gamma z, \quad (6)$$

where $\Delta \gamma = \gamma_a - \gamma$ —difference between dry adiabatic and vertical temperature gradient [1], $\Delta_0 T = T_0 - T_{e0}$ —temperature difference at altitude $z = 0$.

Here it is assumed that the axial rotation of the Earth does not play a role. Because $p' = 0$ in the example under consideration, then, substituting relation (5) into the equation of motion (4) and differentiating (6) with respect to time, we obtain a system of equations describing oscillatory processes in the atmosphere:

$$\frac{dw}{dt} = \alpha g \Delta T, \quad \frac{d\Delta T}{dt} = -\Delta \gamma w, \quad (7)$$

where $\alpha = 1/T_{0e} \approx 1/T_0$ —thermal expansion coefficient.

From the system (6) and (7) follow the equations of harmonic oscillations for the vertical velocity component w and for temperature fluctuations ΔT :

$$\frac{d^2 w}{dt^2} = -N_{BV}^2 w, \quad \frac{d^2 \Delta T}{dt^2} = -N_{BV}^2 \Delta T, \quad (8)$$

where N_{BV} —the Brunt—Väisälä frequency, set by the ratio [7]: $N_{BV} = \sqrt{\alpha g \Delta \gamma}$.

2.2 Basic Parameters of Atmosphere

1. Autoconvection gradient: $\gamma_A = g/R_d$, where R_d —specific gas constant for the planet.
2. Coefficient α —temperature reciprocal characteristic. For some layer of the atmosphere, we obtain the average value of the coefficient $\bar{\alpha} = 1/\bar{T} = 1/\left(\frac{T_i + T_{i-1}}{2}\right)$, where T_i is the temperature of the upper boundary of the zone, T_{i-1} —temperature of the lower boundary of the zone.
3. Dry adiabatic gradient: $\gamma_a = g/c_p$, where c_p —specific heat capacity of a mixture of gases of the planet's atmosphere.
4. Vertical temperature gradient: $\gamma = -dT/dz$.
5. Frequency N_{BV} and the period of Brunt—Väisälä oscillations for each layer or near the surface.

3 Research Results and Discussions

Let us take into account the daily temperature fluctuations due to the rotation of the Earth around its axis, with a frequency $\omega_0 \approx 7,27 \cdot 10^{-5} \text{s}^{-1}$. In other words, the planet will be exposed to the influence of the Sun, periodically changing during the day [8, 9].

Due to the rotation of the planet around its axis, diurnal temperature fluctuations arise (for convenience, we will assume that these fluctuations occur according to the harmonic law according to the harmonic law). Then for the temperature difference we get:

$$\Delta T = \Delta_0 T + \Delta T_0 \cos(\omega_0 t + \psi_0) - \Delta \gamma z, \quad (9)$$

where $\Delta_0 T = T_{i0} - T_{e0}$ is the temperature difference near the surface $z = 0$; T_{i0} —the temperature of the air flow that has arisen in the atmosphere; T_{e0} —static ambient temperature, $\Delta \gamma = \gamma_a - \gamma$ —difference between dry adiabatic and vertical temperature gradient, ψ_0 —phase determined by the time of day.

Taking into account dependence (9), we similarly obtain a system of equations describing the fluctuations of air in the atmosphere, based on the equation of motion of dry air:

$$\begin{aligned} \frac{d^2 \Delta T}{dt^2} + N_{\text{BV}}^2 \Delta T &= -\omega_0^2 \Delta T_0 \cos(\omega_0 t + \psi_0), \quad \frac{d^2 w}{dt^2} + N_{\text{BV}}^2 w \\ &= -\alpha g \omega_0 \Delta T_0 \sin(\omega_0 t + \psi_0) \end{aligned} \quad (10)$$

Solutions of Eqs. (3) and (4) can be represented as:

$$\begin{aligned} \overline{\Delta T}(t) &= \Delta_0 T \cos(N_{\text{BV}} t + \varphi_0) - \frac{\omega_0^2}{N_{\text{BV}}^2 - \omega_0^2} \Delta T_0 \cos(\omega_0 t + \psi_0), \\ \overline{w}(t) &= w_{\text{max}} \sin(N_{\text{BV}} t + \varphi_0) - \frac{\omega_0}{N_{\text{BV}}^2 - \omega_0^2} \alpha g \Delta T_0 \sin(\omega_0 t + \psi_0). \end{aligned} \quad (11)$$

$\varphi_0 = \text{arctg}(w_0/w_{\text{max}0})$ —initial phase of natural oscillations.

So $\overline{w}(t) = dz/dt$, then the dependence of particle coordinates on time from is equal to:

$$z_i(t) = z_{\text{max}i} [\cos \varphi_0 - \cos(N_{\text{BV}} t + \varphi_0)] - \frac{\alpha g \Delta T_0}{N_{\text{BV}}^2 - \omega_0^2} [\cos \psi_0 - \cos(\omega_0 t + \psi_0)].$$

In what follows, for convenience, we take $\varphi_0 = \psi_0 = 0$.

For standard atmosphere ($N_{\text{BV}} \gg \omega_0$) the rotation of the Earth around its axis does not play a significant role when considering fluctuations in the temperature difference and velocity, that is, in expressions (11), the second term can be neglected. However, this affects the movement of air particles.

It can be shown that when $N_{\text{BV}} - \omega_0 \rightarrow 0$ there is an increase in the oscillation amplitudes, which can be seen from expressions (11). Consider fluctuations in the

temperature difference $\overline{\Delta T}(t)$ in the presence of external influences in more detail (11), including beats and resonance.

If $N_{BV} = \omega_0$ (resonance condition), then $\Delta\omega = 0$, and for $\Delta\gamma_{\text{res}}$ we get $\Delta\gamma_{\text{res}} = \omega_0^2/\alpha g$.

For example, when $T_{0e} = 273 \text{ k} (\alpha = 1/T_{0e})$ we get $\Delta\gamma_{\text{res}} \approx 1,443 \cdot 10^{-7} \text{ K/M}$. Let us assume in this work that $\alpha = \text{const}$.

Let us make a remark: for beats and resonance $\Delta\gamma \approx \Delta\gamma_{\text{res}}$, and $\Delta\gamma_{\text{res}} \ll \Delta\gamma_{\text{norm}}$, so the conditions corresponding to $\Delta\gamma \rightarrow 0$.

Given the connection, it is convenient to introduce the parameter ε : $\varepsilon = \frac{N_{BV}^2 - \omega_0^2}{\omega_0^2} = \frac{\Delta\gamma - \Delta\gamma_{\text{res}}}{\Delta\gamma_{\text{res}}}$, then the equation of fluctuations of the temperature difference and velocity (11) can be conveniently represented as:

$$\begin{aligned} \overline{\Delta T}(t) &= \Delta_0 T \cos(N_{BV}t) - \frac{1}{\varepsilon} \Delta T_0 \cos(\omega_0 t) \cdots \overline{w}(t) \\ &= w_{\text{max}} \sin(N_{BV}t) - \frac{1}{\varepsilon} \alpha g \Delta T_0 \sin(\omega_0 t) \end{aligned} \tag{12}$$

3.1 Beats

Beating is a phenomenon that occurs when two harmonic oscillations of a similar frequency are superimposed and is expressed in a periodic decrease and increase in the amplitude of the total signal. The frequency of change in the amplitude of the total signal is equal to the difference between the frequencies of the two original signals. Beats arise because one of the two signals is constantly behind the other in phase, and at those moments when the oscillations occur in phase, the total signal is amplified, and at those moments when the two signals are out of phase, they cancel each other out.

At certain values of the Brunt-Väisälä frequency, beats can be observed in the atmosphere of planets. For this, the condition: $N_{BV} = \omega_0 + \Delta\omega$, $\left| \frac{\Delta\omega}{\omega_0} \right| \ll 1$.

Let us analyze when the amplitude increases. Consider beats using an example when the amplitudes of the added oscillations are equal:

$$\Delta T_{\text{max}} = \frac{1}{\varepsilon_{b0}} \Delta T_0 \tag{13}$$

where the parameter ε_{b0} —it's such a value ε_b , in which it is fair (13).

At fixed ΔT_0 и $\Delta T_{\text{max}} - \varepsilon_{b0} = \text{const}$. In other words, with a single value $\Delta\gamma_{b0}$ beats occur with equal added amplitudes, so ε_{b0} —key parameter.

Then the oscillation equation can be represented as [6]:

$$\Delta T(t) = -2 \cdot \Delta_0 T \sin\left(\frac{\Delta\omega}{2}t\right) \sin(\omega_0 t) = 2 \cdot \Delta_0 T \sin\left(\frac{\varepsilon\omega_0}{4}t\right) \sin(\omega_0 t). \quad (14)$$

In general, with a decrease $\Delta\omega$, $\Delta\gamma$ —the beat period increases. Beat amplitude at equal amplitudes: $\Delta T_{\text{var}}(t) = 2\Delta T_{\text{max}} \sin\left(\frac{\Delta\omega}{2}t\right)$.

If the summed amplitudes are not equal ($\Delta\gamma_{\text{beats}} \neq \Delta\gamma_{\text{beats}0}$), then it's convenient to introduce the ratio coefficient $\eta = \frac{\left(\frac{\Delta T_0}{\varepsilon_b}\right)}{\Delta T_{\text{max}}} = \frac{\varepsilon_{b0}}{\varepsilon_b} = \frac{\Delta\omega_{b0}}{\Delta\omega_b} = \frac{\Delta\gamma_{b0} - \Delta\gamma_{\text{res}}}{\Delta\gamma_b - \Delta\gamma_{\text{res}}}$, where $\varepsilon_{b0} = \frac{\Delta T_0}{\Delta T_{\text{max}}}$ — ε_b with equal amplitudes ($\eta = 1$), which follows from (12). Then expression (12) for the temperature difference takes the form:

$$\overline{\Delta T}(t) = \Delta T_{\text{max}}[\cos(N_{\text{BV}}t) - \eta \cos(\omega_0 t)], \quad (15)$$

Let us consider examples in more detail for various η , but permanent ΔT_0 and ΔT_{max} (so $\varepsilon_{b0} = \text{const}$). We write expression (15) as: $\overline{\Delta T}(t) = \Delta T_{\text{max}}[\cos\left(\left(1 + \frac{\varepsilon}{2}\right)\omega_0 t\right) - \eta \cos(\omega_0 t)]$ and let's draw graphs.

Let $\varepsilon_{b0} = 0, 1$ ($\Delta\gamma = 1, 587 \cdot 10^{-7} \frac{\text{K}}{\text{m}}$) and $\Delta T_{\text{max}} = 1 \text{ K}$. In Fig. 1 it is shown that if we decrease $\varepsilon_{\text{beats}}$ (or $\Delta\omega/\omega_0$, $\Delta\gamma \rightarrow \Delta\gamma_{\text{res}}$), then the amplitude will increase in $\eta \pm 1$ paz, and will fluctuate within these limits [10]. Therefore, when $\eta \gg 1$ the beat graph resembles harmonic oscillations with large (but practically constant) amplitudes, i.e. dependence (15) takes the form:

$$\overline{\Delta T}(t) \approx -\eta \Delta T_{\text{max}} \cos(\omega_0 t), \quad (16)$$

The amplitude changes over time by no more than a factor of 2 (which happens when $\varepsilon_b = \varepsilon_{b0}$). It is also seen that the beat period is inversely proportional to, so $\varepsilon_{\text{beats}}$ increases:

$$T_{\text{beats}} = \frac{4\pi}{\Delta\omega} = \frac{4\pi}{\left(\frac{\varepsilon_b\omega_0}{2}\right)} = \frac{8\pi \cdot \Delta\gamma_{\text{res}}}{\omega_0} \frac{1}{\Delta\gamma - \Delta\gamma_{\text{res}}}.$$

In general, with a decrease $\Delta\omega$, $\Delta\gamma$ —the beat period increases. Beat amplitude at equal amplitudes: $\Delta T_{\text{var}}(t) = 2\Delta T_{\text{max}} \sin\left(\frac{\Delta\omega}{2}t\right)$.

3.2 Resonance

Resonance, the phenomenon of a sharp increase in the amplitude of forced oscillations in any oscillatory system, which occurs when the frequency of periodic external action approaches certain values determined by the properties of the system itself. In the simplest cases, resonance occurs when the frequency of external action approaches one of those frequencies with which natural oscillations occur in the system resulting from the initial shock. The nature of this phenomenon significantly depends on the properties of the oscillatory system.

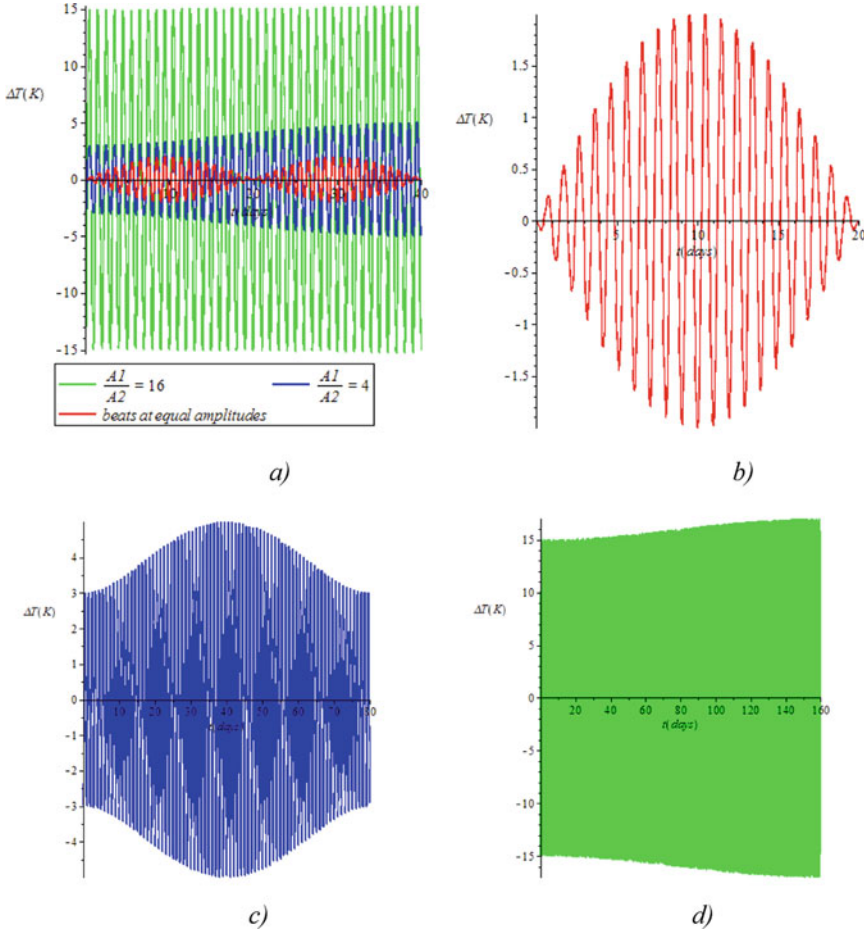


Fig. 1 Comparison of the beats ($\varepsilon = 0,025$ and $\varepsilon = 0,00625$ at $\varepsilon_0 = 0,1$) the temperature difference: **a** general view, $\varepsilon_{b0} = 0,1$, $\Delta\gamma_{res} = 1,443 \cdot 10^{-7} \frac{K}{m}$; **b** $\eta = 1$, $\varepsilon_b = 0,1$, $\Delta\gamma = 1,587 \cdot 10^{-7} \frac{K}{m}$, 40 days. (period); **c** $\eta = 4$, $\varepsilon_b = 0,025$, $\Delta\gamma = 1,479 \cdot 10^{-7} \frac{K}{m}$, 160 days; **d** $\eta = 16, \varepsilon_b = 0,00625$, $\Delta\gamma = 1,452 \cdot 10^{-7} \frac{K}{m}$, 640 days

The basic condition of resonance in the atmosphere at a given temperature $T_{0e} = 273 \text{ K} (\alpha = 1/T_{0e})$: $\Delta\gamma = \Delta\gamma_{res} = 1,443 \cdot 10^{-7} \frac{K}{m}$. Also, a certain period of time is needed for its onset. Let's show it in more detail.

At resonance, the Brunt-Väisälä frequency is equal to the cyclic frequency of rotation of the Earth around its axis ($N_{BV} = \omega_0$), then the equation for the temperature difference (10) takes the form:

$$\frac{d^2 \Delta T}{dt^2} + \omega_0^2 \Delta T = -\omega_0^2 \Delta T_0 \cos(\omega_0 t + \psi_0). \quad (17)$$

In other words, it makes no sense to use expressions (11), because the amplitude grows indefinitely. For expression (12), it is taken into account that when $\varepsilon = 0$ (resonance) a replacement is being made $\varepsilon \rightarrow \varepsilon_{\text{res}}(t) = 2/(\omega_0 t)$.

One of the particular solutions is an expression in the form (by introducing a coefficient $n = \Delta_0 T / \Delta T_0$) [10]:

$$\overline{\Delta T}(t) = \Delta_0 T \cos(\omega_0 t) - \frac{\omega_0 t}{2} \Delta T_0 \cos(\omega_0 t) = \Delta T_0 \left[n - \frac{\omega_0 t}{2} \right] \cos(\omega_0 t). \quad (18)$$

Accordingly, $\Delta T_{\text{var}}(t) = \Delta T_0 \left[n - \frac{\omega_0 t}{2} \right] = \Delta T_0 \left[n - \frac{\pi t}{P} \right]$, where $P = 24$ h—the period of the axial rotation of the Earth. The amplitude of the oscillations will decrease for some time $t_P = \frac{n}{\pi}$ days and then it will change the sign (Fig. 2).

Resonance occurs when: $t \gg \frac{2n}{\pi}$ days In this case, an approximation is acceptable: $\overline{\Delta T}(t) \approx -\frac{\omega_0 t}{2} \Delta T_0 \cos(\omega_0 t)$, that is, after a considerable time, the ratio does not play any significant role, only the value of the amplitude of daily temperature differences is important ΔT_0 .

According to the graphs, we can see a sharp increase in the amplitude when the Brunt–Väisälä frequency is equal to the cyclic frequency of rotation of the planets around its axis.

Thus, we have considered the change in the amplitude characteristics of the oscillations at different frequencies which depends on. Real oscillations are much more complicated, since they oscillate with variable frequencies, because at different heights there may be its own value $\Delta \gamma$. The axial rotation of the Earth plays a special role in $\Delta \gamma$, which are of the order, because there are beats and resonance. If $N_{\text{BV}} \ll \omega_0$, then the fluctuations occur only due to the rotation of the planet around its axis (Table 1).

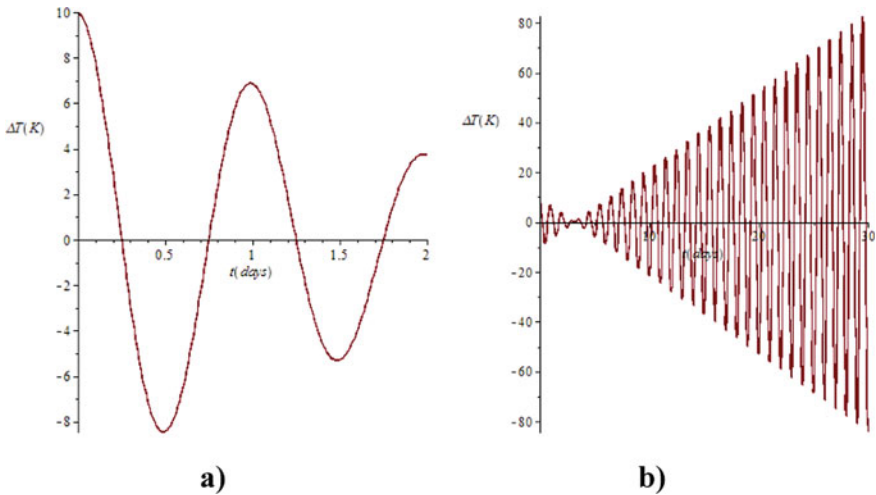


Fig. 2 Oscillations at: $\Delta T_0 = 1$ K, $\Delta T_{\text{max}} = 10$ K, $N_{\text{BV}} = \omega_0$, **a** $t < t_P$; **b** $t \gg 2t_P$

Table 1 Observed phenomena at different Brunt–Väisälä frequencies and temperature gradients

Frequencies	$\Delta\gamma$	Phenomena
$N_{BV} \gg \omega_0$	$\Delta\gamma \gg \Delta\gamma_{res}$	Daily temperature changes don't play a role
$N_{BV} \approx \omega_0$	$\Delta\gamma \sim \Delta\gamma_{res}$	Beats
$N_{BV} = \omega_0$	$\Delta\gamma = \Delta\gamma_{res}$	Resonance
$N_{BV} \ll \omega_0$	$\Delta\gamma \ll \Delta\gamma_{res}$	Fluctuations occur due to daily temperature changes

4 Conclusion

Brunt–Väisälä frequencies N_{BV} related to the temperature gradient difference $\Delta\gamma$ dependence (9), and under standard conditions these values are equal to $\Delta\gamma_{norm} = 0,004$ K/m and $N_{BVnorm} = 0,012$ s⁻¹. Consequently, the rotation of the Earth around its axis usually does not affect atmospheric fluctuations in speed and temperature difference, since its cyclic frequency $\omega_0 \approx 7,27 \cdot 10^{-5}$ s⁻¹, i.e. $\omega_0 \ll N_{BV}$.

However, there is a case when the difference between the above frequencies is extremely small or zero (this is possible when $\Delta\gamma \ll \Delta\gamma_{norm}$). Then there is an increase in the amplitude of the oscillations, i.e. beating or resonance. In these cases, they talk about high-intensity fluctuations. This is possible when the vibrational regime of the atmosphere is synchronized with the axial rotation of the planets, i.e. when $\omega_0 \approx N_{BV}$.

Accordingly, when $(\Delta\omega/\omega_0) \rightarrow 0$ there is an increase in the amplitude, which first leads to beats ($\Delta\gamma \approx \Delta\gamma_{res}$), and then, with a further decrease in this ratio, to resonance ($\Delta\gamma = \Delta\gamma_{res}$). Note that to observe the beats, the oscillation amplitudes must be comparable, their period reaches the order of several days. In addition, it takes a long time for resonance to occur.

An oscillation formula was also obtained that takes into account the axial rotation of the Earth, which includes the parameter ε :

$$\overline{\Delta T}(t) = \Delta T_{max} \cos(N_{BV}t) - \frac{1}{\varepsilon} \Delta T_0 \cos(\omega_0 t).$$

In this formula, a direct relationship is established between the specified and resonant values of the temperature gradient difference and frequencies:

$$\varepsilon = \frac{\Delta\gamma - \Delta\gamma_{res}}{\Delta\gamma_{res}} = \frac{N_{BV}^2 - \omega_0^2}{\omega_0^2}.$$

For beats we get: $\varepsilon_{beats} = \frac{\Delta\gamma_{OHeH} - \Delta\gamma_{res}}{\Delta\gamma_{res}} \approx \frac{2\Delta\omega}{\omega_0}$, with $\varepsilon_{beats} \ll 1$.

For the case of resonance we have: $\varepsilon \rightarrow \varepsilon_{res}(t) = 2/(\omega_0 t)$ (12), (18).

Acknowledgement This research was supported by the North-Caucasus Center for Mathematical Research under agreement No. 075-02-2021-1749 with the Ministry of Science and Higher Education of the Russian Federation.

References

1. Blake, D., Robson, R.: Physical principles of meteorology and environmental physics: global, synoptic and micro scales. Singapore. World Scientific Publishing Company Ltd. (2008).
2. Rabinovich, M.I., Trubetskov, D.I.: Introduction to the theory of vibrations and waves. – Moscow. Nauka, (1984) [in Russian].
3. Landau, L. D., Lifshits, E.M.: Fluid Mechanics. Elsevier (1987).
4. Matveev, L.T.: Fundamentals of General Meteorology: Physics of the Atmosphere. Israel Program for Scientific Translations. Jerusalem. Israel. (1967).
5. Ryzhkov, R.D., Avanesyan, K.S., Smirnova, L.N., Zakinyan, R.G.: To the two-dimensional model of heat convection of dry air in the atmosphere. Science. Innovations. Technologies. **1**, 117–130 (2019) [in Russian].
6. Saveliev, I.V.: General Physics Course. Vol. 1: Mechanics, oscillations and waves, molecular physic. Moscow. Nauka (1970) [in Russian].
7. Simakhina, M.A.: Conditions of occurrence and method of calculating the parameters of convection in the atmosphere: dissertation of the candidate of physical and mathematical sciences. Stavropol (2010) [in Russian].
8. Sidorenkov, N.S.: Celestial-mechanical factors of the weather and climate change. Moscow: Geophysical Processes and the Biosphere. **14**(3). 5–26 (2015) [in Russian].
9. Sidorenkov, N.S.: The interaction between Earth's rotation and geophysical processes. Weinheim. WILEY-VCH Verlag GmbH & Co. KGaA, (2009).
10. Landau, L.D., Lifshits, E.M.: Mechanics. Elsevier (1982).

Long-Term Variations of Meteorological Parameters According to the Data of High-Altitude Weather Stations of the Central Caucasus



A. H. Aliev, N. N. Skorbezh, and A. G. Tlatov 

Abstract The analysis of changes in meteorological parameters according to the data of two high-altitude weather stations of the Central Caucasus “Klkhorsky Pass” 1960–2020 and “Shatdzhatmaz” 1950–2020 was carried out. The weather stations are located at an altitude of about 2000 m. It has been established that in recent decades, the thermal regime of the high-altitude zone of the Central Caucasus is characterized by an increase in air temperature, which is most noticeable in recent decades and is 1.4° at the Klkhorsky Pass weather station and 2.2° at the Shatdzhatmaz weather station. Humidity data from the Klkhorsky Pass weather station show a long-term variation lasting about 35 years with highs near 1985 and 2010. Perhaps this is due to the Brückner cycle.

Keywords Temperature trend · Precipitation · Sunny hours · Humidity · Wavelet analysis

1 Introduction

In recent years, many studies have shown the existence of accelerated climate change that has affected the entire Earth, in particular the most vulnerable ecosystems, such as mountainous areas. Over the past 100 years, the global average air temperature has increased by $0.74 \pm 0.18^{\circ}\text{C}$, and, for example, in the Alps, the temperature increase has almost doubled [1–3].

The purpose of this work was to study long-term climate changes for the Central Caucasus region. The mountain ranges of the Greater Caucasus stretch between the Black Sea and the Caspian Sea. In the axial part, their length is about 1100 km, the width reaches 180 km. Almost the entire northern slope of the Greater Caucasus

A. H. Aliev · N. N. Skorbezh · A. G. Tlatov (✉)
Kislovodsk Mountain Astronomical Station of the Pulkovo Observatory, Kislovodsk, Russia
e-mail: tlatov@mail.ru

A. H. Aliev · N. N. Skorbezh
Department of Theoretical and Mathematical Physics, North-Caucasus Federal University,
Stavropol, Russia

© The Author(s), under exclusive license to Springer Nature Switzerland AG 2023
R. Zakinyan and A. Zakinyan (eds.), *Physics of the Atmosphere, Climatology and Environmental Monitoring*, Springer Proceedings in Earth and Environmental Sciences, https://doi.org/10.1007/978-3-031-19012-4_4

and part of its southern slope up to the Psou River are located within the modern border of Russia. The Greater Caucasus is divided into 3 parts: the Western one from the Black Sea coast to the sources of the Kuban River, the Central one from Elbrus to the meridional segment of the Terek River valley east of Mount Kazbek and the Eastern one from the Daryal Gorge to the coast of the Caspian Sea. The main (Watershed) and Lateral ridges with heights exceeding 3000 m in a significant area and reaching over 5000 m in the central part are framed from the north by lower Rocky, Pasture, Black and other ridges. In the central and western part of the Greater Caucasus, gradually decreasing, the fringing ridges extend mainly parallel to the Main Ridge, separated by wide depressions. In the Eastern Caucasus, the Lateral Ridge significantly exceeds the Watershed. From it and on the southern slope from the Main ridge fan-shaped ridges of the second order depart. In the Greater Caucasus, there are several high-altitude belts with characteristic relief forms for each. The highlands and midlands include landscapes with glacial relief at elevations from 2000 m. The Central Caucasus region plays an exceptional role in the formation of the water balance of the region: rivers flowing into both the Caspian, Azov and Black Seas originate here. It is also home to one of the most famous winter recreation centers in Russia—the Elbrus region, the occupancy and comfort of recreation on which are associated, among other things, with climatic conditions. In this regard, the continuation of studies of long-term changes in meteorological data is of scientific interest and has applied significance [4].

The article [5] analyzes the changes in climatic parameters of high-altitude meadow landscapes of the North-Eastern Caucasus according to the data of the weather station “Sulak, Vysokogornaya” for 1931–2013. A significant increase in air temperature has been revealed in the last decade, although in general temperature changes of different signs (relative warming and cooling) from one year to another reduce the influence of temperature on high-altitude landscapes. Precipitation changes are cyclical and manifest themselves in the presence of periods with significant precipitation deviations from the norm. A significant increase in air temperature against the background of precipitation close to normal, observed in the last decade, led to partial degradation of the glaciation of the North-Eastern Caucasus. The climatic feature of high-altitude landscapes is that they are located within the free atmosphere, the lower boundary of which is drawn at altitudes of more than 1000 m, where the influence of the underlying surface decreases. This is manifested in the fact that the direction and repeatability of the prevailing winds are modified here in comparison with the lower altitude tiers [5].

In [6], long-term changes in temperature and precipitation for 1960–2015 were analyzed according to the data of the weather stations “Klukhorsk Pass” and “Shatdzhatmaz”. Statistical changes in air temperature (up to 0.8 °C) were revealed against the background of precipitation changes close to cyclical.

In this paper, we have extended the considered data period of high-altitude weather stations and expanded the range of analyzed parameters. So in addition to temperature and precipitation, we included data on humidity and the number of recorded hours of sunshine.

2 Observational Data and Results

On the territory of the Central Caucasus, there are quite a few meteorological stations in the mountainous part. To analyze climate changes in the mountainous part of the Central Caucasus, we used data from the Shatdzhatmaz (2070 m) and Klukhorsky Pass (2037 m) weather stations located on the northern slope of the Greater Caucasus as reference weather stations. Despite similar absolute heights near the free atmosphere, they are confined to different positions.

Klukhorsky Pass weather station is located in a rather narrow gorge in the upper reaches of the Teberda River basin, where the main natural complexes are upper montane forests. The Shatdzhatmaz weather station is located on a plateau, where the main type of vegetation is grass communities of meadow and meadow-steppe type. To identify the temporal variability, along with a graphical representation, the average values and deviations from them for 10 years were determined.

Figures 1 and 2 show the temperature values according to the data of the Shatdzhatmaz weather station and the Klukhorsky Pass weather station. The average values obtained by averaging with a sliding window of 11 years and changes in the global temperature are also presented.

As we can see from the above data, the average annual temperature on Shatdzhatmaz in the period 1950–2020 is 2.88 °C. The coldest was 1992, when the temperature dropped to 0.93 °C. The warmest was 2010 with a temperature of 5.1 °C. At the Klukhorsky Pass weather station, the average temperature for the period 1960–2020 was 4.12 °C, which is 0.1 °C higher than the data [3].

The long-term trend in Figs. 1 and 2 illustrates the trend of increasing air temperature from the early 1990s to the present. During this period, the temperature increase for the Shatdzhatmaz weather station was ~2.2 °C, and for the Klukhorsky Pass weather station ~1.43 °C.

Figure 3 shows the total precipitation of Shatdzhatmaz weather station and the Klukhor Pass. The amount of precipitation in the area of the Klukhorsky Pass weather

Fig. 1 Annual temperature values according to the Shatdzhatmaz weather station. The average values obtained by averaging with a sliding window of 11 years and changes in global temperature are also presented

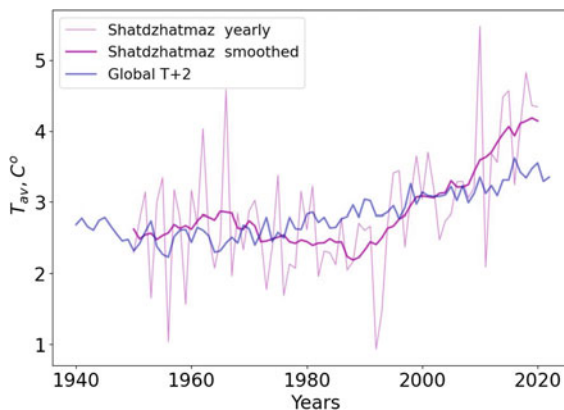
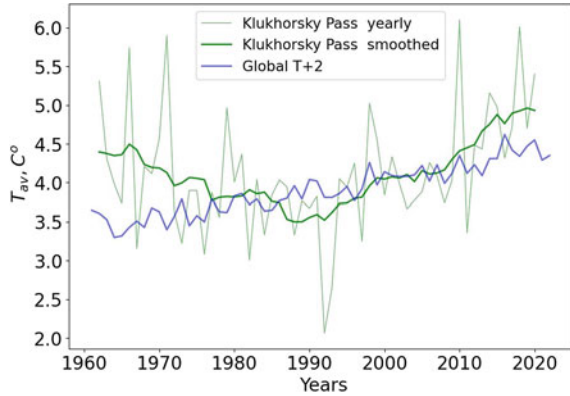


Fig. 2 The same as in Fig. 1, but according to the Klukhorskoy pass weather station



station is more than 2 times more than at the Shatdzhatmaz weather station. Therefore, the number of sunny hours at the Shatdzhatmaz weather station is significantly higher than at the Klukhorskoy Pass weather station (Fig. 4). The highest humidity on Shatdzhatmaz was observed in 2002 (Fig. 5). In June of this year there was a flood.

Despite the greater amount of precipitation at the Klukhorskoy Pass weather station, the humidity in this area is significantly less than in the area at Shatdzhatmaz weather station. Humidity data from the Klukhorskoy Pass weather station show a long-term variation lasting about 35 years with highs near 1985 and 2010. Perhaps this is due to the Brickner cycle (BC). In some cases, the duration of e BC may vary from 25 to 50 years. For our data, periods close to BC are found in the humidity data both according to the data of the Shajatzmaz and Klukhorskoy Pass weather stations (Fig. 6).

Fig. 3 Precipitation values according to the Shatdzhatmaz and Klukhorskoy pass weather stations

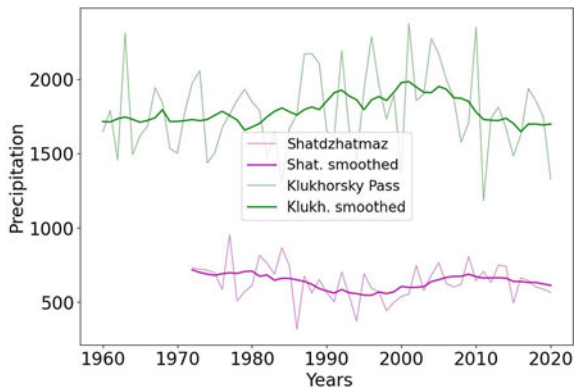


Fig. 4 The number of sunny hours according to the weather stations Shatdzhatmaz and Klukhorsky pass

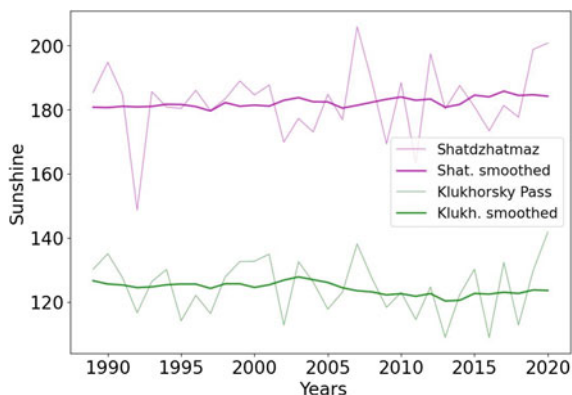
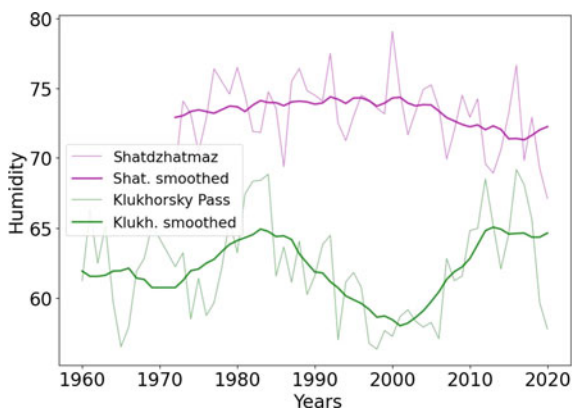


Fig. 5 Humidity according to Shatdzhatmaz and Klukhorsky pass weather stations

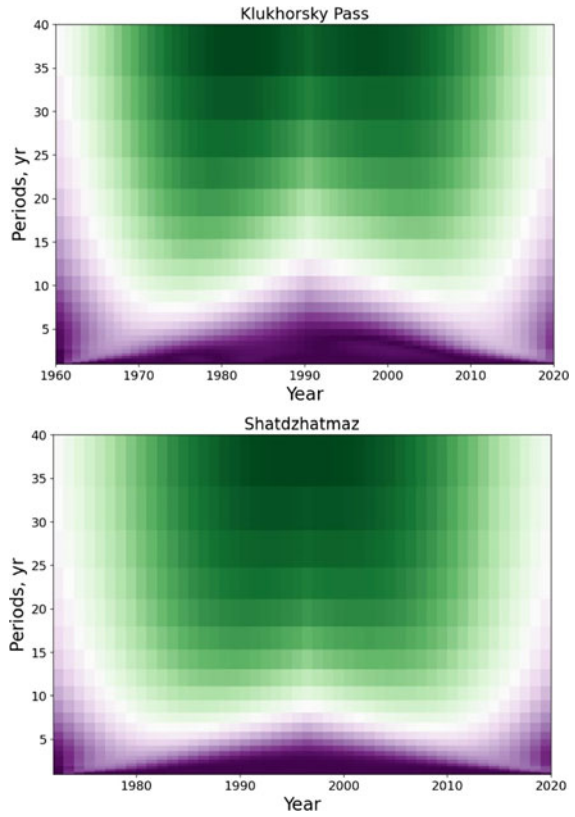


3 Conclusions

The thermal regime of the high-altitude zone of the Central Caucasus is characterized by an increase in air temperature, which has been most noticeable in recent decades and is $1.4\text{ }^{\circ}\text{C}$ at the Klukhorsky Pass weather station and $2.2\text{ }^{\circ}\text{C}$ at the Shatdzhatmaz weather station, while the amount of annual precipitation (Fig. 2) remains fairly stable, but changes significantly over time, which it manifests itself both at the level of the year and individual seasons and months of the year. This conclusion is close to the conclusions of [3], but according to our data, the amplitude of long-term variations has increased significantly.

For climate, the minimum detection time is recognized as a 30-year period. The main issue that is currently being discussed is the ability of modern climate changes to be so significant that they can lead to a change in the landscape structure of the region, or they can be considered as climatic heterogeneities. Long-term climate fluctuation, expressed in the transition from cold and humid years to warm and dry

Fig. 6 Wavelet analysis of humidity data from Shatdzhatmaz and Klukhorsky pass weather stations



over an average 35-year period. Back in the 17th century, this cycle was noticed in the temperature conditions of northwestern Europe.

At the end of the 19th century, E. Brückner found [7] that the cycle has a broader planetary character, and, in particular, established it in fluctuations in the level of the Caspian Sea, during precipitation, in the retreat and advance of glaciers of a number of mountain systems. It is believed that in the 20th century BC was almost not detected [8]. It is possible that its amplitude has decreased, and it is overlapped by stronger climate fluctuations. Doubts were also expressed about its real existence. However, our analysis of humidity observations at high-altitude observatories may indicate the reality of such cyclicity in high-altitude regions.

References

1. Auer, I., Böhm, R., Jurkovic, A., Lipa, W., Orlik, A., Potzmann, R., Schoner, W., Ungersbock, M., Matulla, C., et al.: Historical instrumental climatological surface time series of the Greater Alpine Region 1760-2003. *Int. J. Climatol.* **27**, 17–46, (2007). doi: <https://doi.org/10.1002/joc.1377>.
2. Cannone, N., Guglielmin, M., Casiraghi, C., Malfasi, F.: Salix shrub encroachment along a 1000 m elevation gradient triggers a major ecosystem change in the European Alps. *Ecography*, **2022**, 2, (2022), doi: <https://doi.org/10.1111/ecog.06007>
3. Sekeryapan, C.: Freshwater ostracods from an alpine wetland in south-central Anatolia, Turkey. *Limnologica*. **93**, 125963, (2022), doi: <https://doi.org/10.1016/j.limno.2022>.
4. Ataev, Z.V., Bratkov, V.V.: Modern climate changes of the North Caucasus semi-desert landscapes. *South of Russia: ecology, development*. **3**, 15–20, (2010).
5. Abdugaliyev, A.A., Ataev, Z.V., Bratkov, V.V.: Modern climate changes of high-mountain landscapes of the north-eastern Caucasus. *Izvestiya of Dagestan State Pedagogical University. Natural and exact sciences*. **31**(2), 86–94, (2015).
6. Kravchenko, I.V.: Evaluation of the Current Climate Change in the Mountainous Part of the Central Caucasus. *Izvestiya of Dagestan State Pedagogical University. Natural and Exact Sciences*. **10**(2), 92–101, (2016).
7. Brückner, E.: Klimaschwankungenseit 1700. *Geographische Abhandlungen*, **4**, 35-38, (1890).
8. Macdowall, A.: Brückner's Cycle and the Variation of Temperature in Europe. *Nature*, **66**, 77–78 (1902). doi: <https://doi.org/10.1038/066077c0>.

Adaptation of Tourist and Recreational Zones of Mountain Territories to Climate Change: Tasks and Methods for Their Solution



A. B. Ashabokov 

Abstract The work is devoted to the problems of reducing risks in tourist and recreational areas of mountainous areas associated with climate change. The main factors through which this global factor can influence this area of activity are discussed. Such slope processes as snow avalanches and mudflows are considered as such factors in mountainous areas. It is noted that the reduction of risks in the tourist and recreational zones of mountainous areas associated with climate change requires adaptation of the functioning of these zones to climate change. In this case, it is considered appropriate to consider this problem for two cases. In the first case, this problem is considered for a functioning tourist and recreational zone, and in the second case, for the zones being created, taking into account the consequences of climate change. The formulations of the tasks of adapting the existing tourist and recreational zones of mountainous regions to climate change are given, the features of information support and methods for solving these problems are discussed. A method for solving one of these problems is presented, namely, the development of models for reducing risks in the tourist and recreational zone associated with such a climatic factor as snow avalanches. It is noted that the features of the information support of this problem, which consist in the presence of uncertainties, make it natural to search for a solution to this problem within the framework of decision theory. The statement of this problem is given.

Keywords Tourist and recreational zone · Adaptation to climate change · Avalanches · Risk reduction

1 Introduction

Adaptation of systems to climate change requires the study of climate change, the mechanisms of its influence on systems and its consequences, the formulation of adaptation tasks and the development of methods for their solution, the development

A. B. Ashabokov (✉)

Department of Natural Phenomena, High-Mountain Geophysical Institute, Lenin Ave, 2, 360002 Nalchik, Russia

e-mail: Azret.Ashabokov.1994@mail.ru

of methods for reducing risks in various fields of activity associated with this factor, etc. It is also important to note that it will affect not only sectors of the economy, but also management systems at all levels, the political system of states, education and healthcare systems, and others.

If the need to stabilize and then reduce the content of greenhouse gases in the atmosphere is understandable in order to counter climate change, then the need to adapt various systems requires clarification. It is related to the fact that all systems, regardless of their nature (environmental, economic, social, political, etc.), are subordinate to the earth's climate system. Therefore, the most important structure-forming factor for these systems is the interaction with the climate system [1]. For their existence, these systems, including the tourist and recreational sphere of activity, must adapt to changes in the external environment, must change the structure and parameters. Those systems or areas of activity that will not be able to adapt to its changes will cease to exist. This is connected with the fact that the adaptation of systems to climate change is defined as one of the ways to counter this global factor.

It should be noted that in recent years there has been a noticeable increase in attention to these problems, the number of publications devoted to solving problems in these areas is increasing rapidly. However, achievements in the direction of formulating the tasks of adaptation of various fields of activity to climate change and the development of methods for their solution are still quite limited.

The purpose of the research in this paper is to formulate the tasks of adapting the functioning of tourist and recreational zones of mountainous areas to climate change, to analyze the information support and methods for their solution, and to develop a model for reducing risks in touristic and recreational zones of mountainous areas associated with such climatic factors as snow avalanches and mudflows.

2 Literature Review

Global warming of the Earth's climate has become a factor that can have a tremendous impact on the processes taking place in society and in the natural environment. There are a lot of works devoted to the study of climate change. One of the first climatologists who predicted global climate warming due to the emission of anthropogenic carbon dioxide into the atmosphere is the American climatologist J. Hansen [2]. Of the works devoted to the study of climate change in Russia, one can note [3–5]. Climate change is already having a noticeable impact on various areas of activity, on the natural environment, on human health, etc. Therefore, much attention has been paid to the study of the consequences of this factor; among the works of this area of research, one can note the works [6–9]. They are expected to be especially significant for mountain areas. Moreover, there are quite a lot of mechanisms of influence of this factor on the spheres of activity in these areas, and the main of them can be considered the influence through dangerous slope processes (avalanches, mudflows, rockfalls, etc.). It is important to note that to resist the impact of climate change, if scientifically sound and urgent measures are not taken, neither society nor the global ecological

system is able, its consequences can be catastrophic [6]. This is related to the fact that the goal of the Paris Climate Conference (2015) was to develop an agreement that would allow at the first stage to slow down climate warming, and then stop it. As such measures, the conference proposed the stabilization of the content of greenhouse gases in the atmosphere at levels that would prevent dangerous anthropogenic impact on the climate, and the adaptation of various systems to its change [6, 10].

2.1 Material and Research Methods

The results of the analysis and forecast of climate change and its consequences for various fields of activity, methods for assessing the risks associated with avalanches and mudflows were used as material for research. The formulation of the task of reducing risks in tourist and recreational areas of mountainous areas associated with climate change is based on the use of decision theory.

3 Goals and Objectives of Adaptation of Various Fields of Activity to Climate Change

The adoption of the Paris climate agreement means that the next 2–3 decades should be a transitional period for humanity, during which the transition of society to a new model of development should be carried out. This model can be called adaptive and it consists in the fact that society must “coordinate” all its actions with the natural environment, adapt them to its changes. During the transition period (until approximately 2050), the content of greenhouse gases in the atmosphere should be stabilized, which, according to experts, will make it possible to keep the increase in global temperature within 1.5 °C and prevent a climate catastrophe [6].

The measures proposed at the Paris Climate Conference to achieve these goals have been noted above. One of them is the adaptation of various fields of activity to climate change. At the same time, adaptation to climate change, for example, of a sector of the economy, involves solving a fairly wide range of problems: developing an adaptation plan for the sector, reducing its vulnerability to climate change, reducing the impact of its functioning on the climate, and using the beneficial effects of climate change.

Adaptation plans for various fields of activity, including tourism and recreational activities, can be considered as plans for their development over a given period of time, taking into account the impact of climate change, i.e., plans in which the solution of the noted tasks should be provided. From here it is possible to formulate the goals of adapting systems (economic, social, environmental, etc.), including tourist and recreational ones, to climate change. They consist in finding such trajectories of their development, on which the structure of these systems at each moment of time

will correspond to the prevailing natural and climatic conditions, while remaining able to perform their functions. In addition, the impact of systems functioning on the climate on a given trajectory should gradually decrease or remain within acceptable intervals.

Note that the goals and objectives of the adaptation of sectors of the economy and other areas of activity should be taken into account when formulating and solving the problems of adaptation plans.

As for the size of the time interval (adaptation interval) for which an adaptation plan for a particular area of activity should be developed, it cannot exceed the time period in which solutions to the problems of forming an adaptation plan can be obtained. The problem lies in the fact that the features of information support do not allow obtaining such solutions to these problems, on the basis of which it is possible to make sufficiently reliable decisions in the medium and long term. For tourist and recreational zones, the value of this interval, in our opinion, should be about 5 years. For different fields of activity, adaptation intervals may be different.

It is important to note that in organizing the solution of complex and interdisciplinary tasks aimed at developing and implementing adaptation plans, monitoring the implementation of these plans and analyzing the effectiveness of adaptation measures taken, management bodies at all levels should participate, and decisions made at various levels should be consistent with each other.

4 Tasks of Adaptation of the Tourist and Recreational Sphere to Climate Change

The factors through which climate change can affect tourism and recreational activities are different in different climatic zones. In mountainous areas, the main of these factors are dangerous slope processes (avalanches, mudflows), the occurrence of which, as is known, is associated with various reasons (heavy precipitation in the form of rain or snow, fluctuations in meteorological parameters, and others). As an example, it can be noted that showers of unprecedented intensity were observed in 2021 in many regions of our country, especially in the Krasnodar Territory. They were accompanied by dangerous weather events (floods, strong winds, mudflows, hailstorms), which led to great destruction. In this regard, the intensive development of mountain territories against the background of climate warming and, as a result, the growth of activity and the destructive power of slope processes, significantly increases the relevance of developing effective ways to reduce risks in various fields of activity and improve human safety in these areas. This is due to the fact that attention to these problems has increased markedly in recent decades.

Slope processes can cause damage or destruction of objects in mountainous areas, damage to roads, power lines, water and gas pipeline systems, etc. There are many cases when they lead to the complete destruction of objects, harm the health of people or lead to their death. Therefore, the risks associated with these processes

can be of a social, economic and environmental nature [3]. Nevertheless, it cannot be said that the conditions for the occurrence of these processes have been studied at a level that makes it possible to reliably predict their occurrence and manage the risks associated with them. This can be explained by the fact that they belong to the so-called “rare” phenomena and, in addition, the conditions for their occurrence in a complex way depend on many factors, which makes obtaining information for studying the formation of these phenomena a rather serious problem.

The problem of adaptation of tourist and recreational zones to climate change should be considered for two cases. In the first case, this problem is considered for functioning tourist and recreational zones, and in the second case, for zones being created, taking into account the consequences of climate change. Note that in the second case, it is possible to create such zones with lower exposure and vulnerability to climatic factors.

Below are the formulations of the objectives of the climate change adaptation plan for the tourist and recreational zones operating in the mountainous areas. In this case, slope processes (avalanches, mudflows) are considered as climatic factors through which climate change affects these zones, and, thus, the problem of adaptation is reduced to reducing the risks associated with them, taking into account changes in their activity, destructive power and spatial distribution.

The tasks that arise on the way to solving this problem can be formulated as:

1. analysis and forecast of climate change in the adaptation interval;
2. study of the conditions for the occurrence of slope processes (or climatic factors) that can have a negative impact on the objects of the tourist and recreational zone, on infrastructure facilities;
3. analysis and forecast of the impact of climate change on the conditions for the occurrence of these factors in the adaptation interval;
4. study of the mechanisms of the impact of slope processes on the objects of the tourist and recreational zone, on infrastructure facilities;
5. analysis and forecast of the exposure and vulnerability of objects of the tourist and recreational zone and infrastructure facilities to climatic factors in the adaptation interval, taking into account climate change and the development of this zone in a given period of time;
6. determination of a set of measures (actions) with the help of which it is possible to reduce the exposure and vulnerability of objects of the tourist and recreational zone to climatic factors;
7. development of models for reducing risks in the tourist and recreational zone associated with climatic factors;
8. modeling the functioning of the tourist and recreational zone in the adaptation interval under various scenarios for the transformation of the characteristics of climatic factors and the use of various measures to reduce risks;
9. decision-making on the choice of the most appropriate strategy to reduce risks in the tourist and recreational area associated with climate change;

Regarding the tasks of other groups, it can be noted that they can be considered areas in which research should be carried out to develop methods and technologies that can reduce the impact of climate change on the objects of the tourist and recreational complex and, conversely, the impact of this area of activity on the climate.

To reduce the vulnerability and exposure of the tourist and recreational zone to the influence of slope processes (the second group of tasks), all possible methods should be used, from the creation of various kinds of engineering structures to the organization and implementation of work to actively influence these processes. Therefore, the goal of research in this direction should be to improve existing and create new ways to reduce the vulnerability and exposure of tourist and recreational areas to the influence of climatic factors.

As for the tasks of the third group, they involve the study of the mechanisms of influence of this sphere of activity on the climate, the creation of climate-saving and environmentally-saving technologies and methods to reduce the impact of tourism and recreational activities on the climate. The main attention in research in this area, in our opinion, should be given to reducing greenhouse gas emissions into the atmosphere, reducing energy consumption and environmental pollution.

Regarding the effects of climate change that favor the functioning of tourist and recreational zones, it can be noted that their list is rather limited. Such consequences may be associated with an increase in air temperature in different seasons of the year, especially in spring and winter seasons, which in some cases will expand the time interval during which the operation of the tourist and recreational zone is possible, reduce energy consumption, etc.

5 Analysis of Methods for Solving the Problems of Adaptation of Tourist and Recreational Zones to Climate Change

Let us dwell on the content and methods for solving the above tasks of the plan for adapting the tourist and recreational zone to climate change.

1. The solution of the first task (analysis and forecast of climate change in the adaptation interval) is aimed at determining the dynamics of climatic factors through which climate change affects the functioning of the tourist and recreational zone. Conducting research in this direction is based on the use of time series of climatic variables, which make it possible to determine the parameters of these factors. In [3], to analyze climate change in various climatic zones of the south of the ETR, time series of meteorological parameters were used that characterize the temperature regime in the surface atmosphere (average, maximum, and minimum air temperatures) and the regime of atmospheric precipitation (the amount and intensity of precipitation, the number of days with precipitation above a certain value) in different seasons of the year and for the year. For the

field of activity considered in this paper, climatic changes in certain meteorological parameters should be studied for more limited time periods. Mathematical and statistical methods [10] can be used to analyze the dynamics of climatic variables, and existing methods for forecasting time series can be used to predict their dynamics. In [3], for this purpose, the singular-spectral method [11] was used.

2. The purpose of solving the second problem is to determine the conditions for the occurrence of climatic factors (for example, conditions that determine avalanche activity) that pose a threat to the sustainable functioning of objects of the tourist and recreational zone. The solution of this problem is connected with the use of a large amount of information. The main methods for obtaining such information are: theoretical studies and mathematical modeling of various scenarios for the occurrence of slope processes, the use of data from field studies of avalanche conditions. It is also possible to use data obtained as a result of laboratory and field experiments. An important feature of the data obtained as a result of such studies is the presence of uncertainties associated with their incompleteness and measurement errors. As a result of research, models of the occurrence of climatic factors under certain conditions of snow cover and atmosphere should be obtained. Models in this case, as noted, can be obtained in the form of integral functions that combine the parameters that determine the conditions for the occurrence of these factors (avalanches, mudflows, etc.).

As an example, it can be noted that the activity of snow avalanches depends on many parameters (one of them is the snowiness of winters). After determining these parameters, it is advisable to construct an integral function that combines these parameters. This function can be called a model for the occurrence of snow avalanches. It can be used to solve various problems, for example, to predict avalanches.

3. The purpose of solving the third task is to determine the natural and climatic conditions in which the tourist and recreational zone will operate in the adaptation interval. The need to solve this problem is due to the fact that the parameters that determine the conditions for the occurrence of climatic factors (slope processes) are quite sensitive to climate change. In this regard, under the influence of climate change, the role of one or another of them may be strengthened or weakened, and, as a result, the number of parameters that determine these conditions can be expanded or narrowed.

As an example, we should note that the authors of [12–14] found changes in the conditions of avalanche formation as a result of climate warming. At the same time, changes in these conditions are caused by changes in the parameters determining the precipitation regime and the air temperature regime, including an increase in the frequency of abnormally warm winters. This also applies to snow cover, which decreases due to climate change, as well as to the ratio of air temperature to precipitation during the cold season. As you know, these parameters are considered to be the key determinants of avalanche activity. The result of reduced winter snowiness, for example, may be a decrease in avalanche danger associated with a reduction in

the number of particularly large avalanches, which can have a negative impact on the functioning of tourist and recreational areas [15].

At the same time, climate change can occur in complex ways. According to the authors' research [3], since 2009, no negative (below 0 °C) absolute maximum temperatures have been recorded at the Terskol high altitude weather station (2144 m asl); the record value of the absolute maximum winter temperature (+11.5 °C) was recorded in 2016. At the same time, a decrease in all seasonal and annual absolute minimum temperatures was observed in 2006–2018, with the most notable decrease in spring absolute minimum temperatures (−1.0 °C/year, D = 54%).

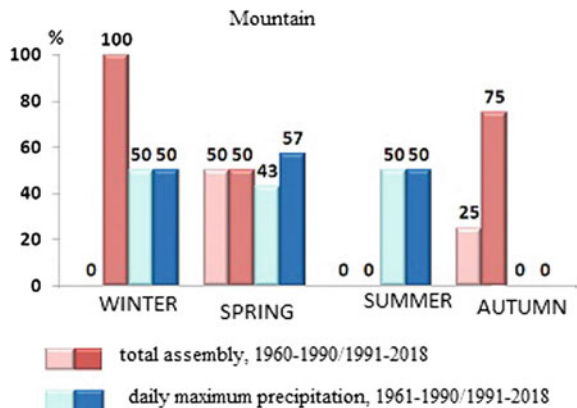
In addition, the main contribution to the increase in the number of precipitations sum extremes in the mountain zone was made by the winter (0%: 100%) and autumn (25%: 75%) seasons; the number of extremes of daily precipitation maximums has not changed in the modern period compared to the baseline. Obviously, such changes in the air temperature regime influence the activity of avalanche processes.

Figure 1 Shows changes in the number of precipitation maximums (%) in different seasons in the mountainous climatic zone of the southern ETR in the baseline 1961–1990 and modern 1991–2018 periods.

Let us also note that a study of the impact of climate change on the parameters included in the model of interaction between climatic factors and objects in the tourist and recreation zone requires forecasting the dynamics of the parameters determining these factors during the adaptation interval, studying changes in the exposure and vulnerability of these objects during this interval, taking into account changes in these parameters. The works devoted to this problem include [3, 16, 17].

4. The necessity of solving the fourth task (study of mechanisms of slope processes impact on objects of tourist-recreational zones, as well as their consequences) is connected with the fact that mechanisms of climatic factors impact on objects of tourist-recreational zone, vulnerability of objects of tourist-recreational zone by these mechanisms depend in a complex way on characteristics of these factors and objects of tourist-recreational complex. In this regard, there is a need to study

Fig. 1 Changes in seasonal precipitation extremes (%) in the mountainous climatic zone of the southern ETR in the baseline period 1961–1990 and the current 1991–2018



the mechanisms of impact of each climatic factor on these objects and select the most important ones among them.

The solution of this problem requires the use of a sufficiently large amount of information on the parameters characterizing climatic factors, as well as the consequences of their impact on various objects. Therefore, for this purpose it is necessary to use existing databases on conditions of occurrence of climatic factors and their interaction with various objects in tourist and recreational areas, at the same time it is necessary to continue collecting these data. It should also be noted that the peculiarities of these data (incomplete parameter series, the presence of errors in them and the difficulty or even impossibility of conducting experiments to obtain them) become a source of certain difficulties in solving the problem.

5. The need to solve the fifth problem is that the parameters of climatic factors and conditions of their occurrence are quite sensitive to climate change. Therefore, climate change may result in strengthening or, on the contrary, weakening of mechanisms of influence of climatic factors on objects of the tourist and recreation zone within the adaptation interval, and, as a consequence, in this interval an increase or decrease of exposure and vulnerability of objects of the tourist and recreation zone to these factors. In this regard, when planning adaptation of the zone to climate change, it is necessary to analyze and forecast changes in the parameters of climate factors, as well as the exposure and vulnerability of various objects to these factors during the adaptation interval.

The data and methods outlined in the previous task will be used to solve this problem.

6. The purpose of solving the sixth task is to determine the set of actions that can be used to reduce risks in the tourist and recreational zone associated with the impact of a particular climatic factor. Such actions can be aimed at reducing the exposure or vulnerability of facilities in this area of activity to climatic factors. At the same time, for each climatic factor, it is necessary to find the corresponding set of actions, bearing in mind that in the process of adaptation of all spheres of activity, their functions should be performed, the main of which should be the improvement of people's well-being [18].

Due to the peculiarities of the information support of the problem (the impossibility of accurately determining the conditions for avalanches), it is more promising to consider this problem within the framework of decision theory [19].

7. The purpose of solving the following problem is to develop models for reducing risks in the tourist and recreational zone associated with the impact of climatic factors. The solution of this problem requires a comparative analysis of the effectiveness of risk reduction methods (actions) for each climatic factor. At the same time, such an analysis should be carried out for all states in which the conditions for the occurrence of a climatic factor may be.

Note that in the general case, depending on the available information, this problem is formulated as a decision-making problem under conditions of risk or uncertainty.

Depending on the problem being solved, there may be cases when the choice of the most appropriate way to reduce risks can be carried out by an expert method. In [15], the problem of calculating the risks associated with slope processes is considered, and some approaches to their calculation are proposed.

8. The purpose of solving the eighth task is to model the functioning of the tourist and recreational zone in the adaptation interval under various scenarios of the transformation of the characteristics of climatic factors and the use of various methods to reduce risks. As a result, indicators of the functioning of the tourist and recreational zone are determined, corresponding to various scenarios for the transformation of the characteristics of climatic factors in the adaptation interval.
9. The purpose of solving the ninth task is to use the results of solving the previous task to choose the most appropriate of the many ways to reduce risks in the tourist and recreational zone (in terms of the criterion used) associated with climatic factors.

6 Setting the Task of Reducing Risks in Tourist and Recreational Zones of Mountainous Areas Associated with Climate Change

Let us consider in the general case the formulation of the problem of reducing risks in the tourist and recreational zone associated with avalanches. As already noted, the features of information support, which consist in the impossibility of accurately determining the moment of descent and the characteristics of snow avalanches, make it natural to search for a solution to this problem within the framework of decision theory. In this regard, to develop a model for reducing risks in the tourist and recreational zone associated with the noted climatic factor, the approach described in [3] is used below. In this paper, it was used to record models of risk reduction in agriculture associated with droughts and hailstorms. The analysis showed that the models are quite effective, and their practical use does not require significant costs.

For specific climatic factors and specific sectors of the economy, including tourist and recreational areas, the risk reduction model can be considered as a single-criteria decision-making problem. This makes it much easier to write and implement.

The recording of the model can be represented as the following steps:

- definition of a set of actions $A_1, A_2, A_3, \dots, A_M$, with the help of which it is possible to reduce the risks associated with the considered climatic factor;
- determination of patterns of formation of conditions for the occurrence of climatic factors in the interval of adaptation;
- calculation of outcomes S_{ij} , corresponding i -to the action and j -to the state of the conditions for the occurrence of a climatic factor in the adaptation interval ($i = 1, 2, \dots, M; j = 1, 2, \dots, N$);
- choice from the available set of valid actions A_i ($i = 1, 2, \dots, M$) the most acceptable (or acceptable). Such a choice is made taking into account the values of

the outcomes corresponding to possible actions that lead to risk reduction, and various states of the conditions for the occurrence of the climatic factor. For this purpose, existing criteria can be used [19].

In the case of such slope processes as snow avalanches or mudflows, these tasks are considered for a specific avalanche source or a specific mudflow basin. Let us dwell briefly on the content of these tasks.

The formulation of the first task assumes that in order to reduce the risks associated with the considered climatic factor (in the case of snow avalanches, for example), it is possible to use a variety of actions $A_1, A_2, A_3, \dots, A_M$. The effectiveness of these actions is different and they depend on the conditions that contributed to the emergence of the climatic factor, and the implementation of each of the actions is associated with certain costs of limited resources. It should also be noted that the quality of the decision to reduce the risks associated with a specific climatic factor will depend on the successful formation of a set of actions. $A_1, A_2, A_3, \dots, A_M$.

In the case of the second task, it is assumed that the conditions that contribute to the emergence of one or another climatic factor can be in states $U_1, U_2, U_3, \dots, U_N$. Here are the possible cases:

- definition of states U_j and the values of their corresponding probabilities p_j ($j = 1, 2, \dots, N$) possibly based on long-term observations; - possible states U_j are determined on the basis of long.
- term observations, and the available information is not sufficient to determine the corresponding probabilities p_j ($j = 1, 2, \dots, N$).
- In the first case, based on the available information, it is possible to represent U_j in the form, for example, of a discrete random variable (Table 1). This makes it possible to write a risk reduction model in the form of a decision-making task under risk conditions.

In the second case, the information support for the problem, as noted, does not allow this probability distribution to be determined and the risk reduction model is written as a decision-making problem under uncertainty [19].

Let us focus on the third task. To analyze the effectiveness of actions from a set of $A_1, A_2, A_3, \dots, A_M$ an assessment of the effects (or outcomes) of each under different conditions of the climate factor is necessary $U_1, U_2, U_3, \dots, U_N$ (in the case of avalanches, conditions for avalanches). This means that each pair of (A_i, U_j) must be matched with a value of S_{ij} ($i = 1, 2, \dots, M; j = 1, 2, \dots, N$), which is called the outcome and has the meaning of the efficiency corresponding to the i -th action under the j -th condition of occurrence of the climate factor U_j . The outcome can be, for example, the amount of damage that the climate factor will cause to the tourism and

Table 1 Conditions of occurrence of the climate factor and their corresponding probabilities their respective probabilities p_i

N	U_1	U_2	U_3	–	U_N
p_i	p_1	p_2	p_3	–	p_N

Table 2 S_{ij} outcomes corresponding to actions A_i and conditions U_j of the climate factor conditions

	U_1	U_2	U_3	–	U_N
A_1	S_{11}	S_{12}	S_{13}	–	S_{1N}
A_2	S_{21}	S_{22}	S_{23}	–	S_{2N}
A_3	S_{31}	S_{32}	S_{33}	–	S_{3N}
–	–	–	–	–	–
A_M	S_{M1}	S_{M2}	S_{M3}	–	S_{MN}

recreation area, or, conversely, the reduction in damage from this factor when using the i -th action. Changes in this or that social or environmental indicator can also be used. The problem of risk assessment is considered in [15].

To solve the next problem (i.e. the problem of choosing the most acceptable one(s) from the set of actions $A_1, A_2, A_3, \dots, A_M$), Table 2 is produced, which can be considered a decision-making model for reducing risks in the tourist and recreational area related to the climate factor.

Note also that the elements of the sets $U_1, U_2, U_3, \dots, U_N$ should be such characteristics of climatic factors that allow calculating the values of outcomes S_{ij} ($i = 1, 2, \dots, M; j = 1, 2, \dots, N$). The existence of sets $A_1, A_2, A_3, \dots, A_M$ & $U_1, U_2, U_3, \dots, U_N$ makes it possible to define outcomes. Knowing them, the choice of the most acceptable of the set of measures can be made using one of the known criteria [19].

In the case of avalanches, the elements of the action set $A_1, A_2, A_3, \dots, A_M$ are the possible ways of reducing the risks associated with them; the elements of the set of states are the probabilities p_j ($j = 1, 2, \dots, N$) of avalanches with characteristics j . As a set of avalanche activity states, in our opinion, we can use a four-point scale, which is based on the use of avalanche ejection range and is widely used in the analysis of avalanche consequences [12]:

1. small avalanches that stop within the avalanche collection area or on the slope;
2. medium-sized avalanches that stop within the limits of mineral fans;
3. large avalanches capable of blocking mineral fans;
4. especially large (often catastrophic avalanches) that go beyond the limits of mineral fans.

Then for each avalanche it is necessary to determine the probabilities corresponding to these states. For this purpose, one can use the data that are collected as a result of many years of research.

7 Conclusion

Thus, in this study the formulations of the tasks of adapting the existing tourist and recreational zones of mountainous regions to climate change are given, the features

of information support and methods for solving these problems are discussed. A method for solving one of these problems is presented, namely, the development of models for reducing risks in the tourist and recreational zone associated with such a climatic factor as snow avalanches. The results of the analysis and forecast of climate change and its consequences for various fields of activity, methods for assessing the risks associated with avalanches and mudflows were used as material for research. The formulation of the task of reducing risks in tourist and recreational areas of mountainous areas associated with climate change is based on the use of decision theory.

References

1. Mesarovich, M., Takahara, Y.: General systems theory. Mathematical foundations, Moscow. Mir (1978) [in Russian].
2. Hansen J, Sato M, Ruedy R, et al.: Dangerous human-made interference with climate: a GISS model study. *Atmos. Chem. Phys.* **7**, 287–312 (2007) [in Russian].
3. Ashabokov, B.A., Fedchenko, L.M., Tashilova, A.A., Kesheva, L.A., Teunova, N.V.: Spatio-temporal climate change in the south of the European territory of Russia, assessment of its consequences, methods and models of adaptation of the agro-industrial complex. Nalchik. Fregat LLC, 476 (2020) [in Russian].
4. Bulygina, O.N., Korshunova, N.N., Kuznetsova, V.N., Razuvaev, V.N., Trofimenko, L.T.: Analysis of climate variability in Russia in recent decades. *Proceedings of VNIIGMI-WDC*, Issue 167, 3–15 (2000) [in Russian].
5. Gruza, G.V., Rankova, E.Yu.: Climate variability and change in Russia. *Izvestiya RAS. Physics of the Atmosphere and Ocean.* **39** (2), 1–20 (2003) [in Russian].
6. Bedritskii, A.I., Korshunov, A.A., Khandozhko, L.A. *et al.* Fundamentals of optimal adaptation of Russian economy to hazardous weather and climate impacts. *Russ. Meteorol. Hydrol.* **34**, 195–201 (2009).
7. Kattsov, V.M., Semenov, S.M.: Earth's climate: factors of change and causes of concern in Sat. The second assessment report of Roshydromet on climate change and its consequences on the territory of the Russian Federation. Moscow. 10–17. (2014) [in Russian].
8. Oleinikov, A.D., Volodicheva, N.A.: On the increase in avalanche disasters in the areas of degradation of mountain glaciation. *MGI. Issue* **99**. 89–93 (2005) [in Russian].
9. Taha, H.: Introduction to Operations Research. Moscow. Mir. 496 (1985).
10. Golyandina, N.E.: Caterpillar Method- SSA Time Series Forecast. St. Petersburg: Publishing House of St. Petersburg State University, 52 (2004) [in Russian].
11. Nasledov, A.D.: SPSS 19: professional statistical data analysis. St. Petersburg. 400 (2011) [in Russian].
12. Fedchenko, L.M., Ashabokova, M.B., Ashabokov, B.A.: A method to reduce agricultural losses based on the difference in damage to agricultural crops by hail. Reports of the All-Russian Open Conference on Cloud Physics and Active Influences on Hydrometeorological Processes. Nalchik. Print Center publishing house, September 08–10. 490–495 (2021) [in Russian].
13. Oleinikov, A.D.: Snow avalanches in the Greater Caucasus under conditions of general climate warming. *MGI. Issue.* **93**, 67–72 (2002) [in Russian].
14. Oleinikov, A.D., Volodicheva, N.A.: Modern trends in the snow avalanche regime of the Central Caucasus (on the example of the Elbrus region). *Ice and Snow.* **59** (2), 191–200 (2019) [in Russian].
15. Andreev, Yu.B., Bozhinsky, A.N., Sidorova, T.L.: Methodology for mapping the probable damage from avalanches and mudflows. *Bulletin of Moscow State University. Ser, Geography.* **5**, 67–69 (1997) [in Russian].

16. Ashabokov, B.A., Fedchenko, L.M., Tashilova, A.A., Shapovalov, A.V., Khavtsukov, A.Kh., Balkarova, S.B.: *Modeling Risk Reduction in Agriculture Associated with Dangerous Agrometeorological Phenomena in International scientific and practical conference AgroSMART. Smart solutions for agriculture, KnE Life Sciences, 223–231 (2019)* [in Russian].
17. Pachauri, R.K., Meyer, L.A.: IPCC: Climate Change. Synthesis Report. Contribution of Working Groups I, II and III to the Fifth Assessment Report of the Intergovernmental Panel on Climate Change [core group of authors. Geneva, Switzerland, 163 (2014)].
18. Seliverstov, Yu.G., Shnyarkov, A.L., Glazovskaya, T.G.: Assessment of avalanche risk for the population of mountainous regions of Russia. Snow cover and snow avalanches. 41–44 (2010) [in Russian].
19. Kattsova, V.M.: Report on climate risks in the Russian Federation. St. Petersburg. **106** (2017) [in Russian].

The Current State of Convective Cloud Physics and Active Effects and the Main Directions of Its Development



B. A. Ashabokov , L. M. Fedchenko, and V. A. Shapovalov

Abstract The reasons for the slowdown in the development of the convective cloud physics and active influences on them in recent decades are discussed. As the results of the analysis showed are that the present period of time is a transitional one for this scientific direction: there is a transition from the stage of studying “elementary” processes in clouds to the stage of studying the formation and development of clouds as a whole, considering their systemic properties. The main tasks arising at the coming stage of its development are formulated. It is noted that such tasks include aggregating the results of studying “elementary” processes in clouds and studying the role of systemic properties of clouds in the formation of macro- and microstructural characteristics of clouds. The state of research on the development of numerical models of convective clouds, within which the aggregation of “elementary” processes in clouds is carried out, is touched upon. As for the study of the role of the system properties of clouds in the formation of their macro- and microstructural characteristics, the study of the role of the interaction of clouds with the atmosphere surrounding them (the property of the hierarchy of systems) and the interaction of processes in clouds, which are the most important structure-forming factors for clouds, seems to be the most important and difficult task in this area of research. Methods and some results of research in this direction are presented, which confirm the significant role of these factors in the formation and development of clouds, in the formation of their macro- and microstructural characteristics.

Keywords Convective cloud physics · Directions of development · The role of system properties · Research results

B. A. Ashabokov (✉) · L. M. Fedchenko · V. A. Shapovalov
High Mountain Geophysical Institute, Lenin Ave., 2, 360002 Nalchik, Russia
e-mail: ashabokov.boris@mail.ru

© The Author(s), under exclusive license to Springer Nature Switzerland AG 2023
R. Zakinyan and A. Zakinyan (eds.), *Physics of the Atmosphere, Climatology and Environmental Monitoring*, Springer Proceedings in Earth and Environmental Sciences, https://doi.org/10.1007/978-3-031-19012-4_6

1 Introduction

The second half of the last century was a period of rapid development of cloud physics and active influences on them, and it should be noted that significant fundamental and applied results were obtained in this scientific direction in a relatively short period of time. To date, the most of the microphysical processes in clouds have been studied and formalized theoretically and under laboratory conditions, and a huge amount of material has been accumulated in field studies of the formation and development of convective clouds in natural conditions and under active influence. Various cloud models have been developed, including both three-dimensional and non-stationary numerical models with a detailed account of the processes, which make it possible to study the evolution of convective clouds in natural conditions and simulate the active impact on them [1–10]. Various concepts of active influence on the processes of precipitation formation in clouds have been proposed and implemented.

But, despite all these successes, the current state of the physics of convective clouds and active influences on them is complex and ambiguous, approximately since the beginning of the 90 s. In the twentieth century, its development slowed down. The reason for the negative phenomena in the development of this scientific direction is not economic or other problems, it is of a deeper nature. As the results of the analysis [11] showed, the main reason due to which it ended up in this state is that at the present time there is a transition from the stage of studying “elementary” processes in clouds to the stage of studying the formation and development of convective clouds in general considering their system properties [1]. Further progress in the development of this scientific direction requires the solution of qualitatively new problems using new methods and methodologies.

No less complex and ambiguous is the state of active influences on convective clouds [1]. The technologies used for this purpose are still based on the use of concepts proposed in the twentieth century, which are based on the ideas of their authors about the processes of cloud and precipitation formation. Given that clouds are extremely complex physical systems, such concepts cannot be sufficiently substantiated and reliable.

2 The Current State of Convective Cloud Physics (Literature Review)

A consequence of the stagnant phenomena in cloud physics can be considered the fact that, since the early 1990s, it has not been possible to obtain such fundamental scientific results that would contribute to the development of existing ideas about the laws of formation of macro- and microstructural characteristics of clouds [1]. In this connection, there is an urgent need for a detailed analysis of the development of this scientific direction in order to determine ways to bring it out of this state, the formulation of the main directions of its development and the tasks corresponding to these

directions. Serious attention should be paid to the development of methodologies and methods of solving the problems of these directions.

A detailed analysis of the cloud physics state was carried out in [12] in the first half of the 1980s of the twentieth century, i.e. in the period when it was developing quite intensively. The main attention in the work was paid to the analysis of the research state on microphysical processes in clouds. The possibilities of including one or another of them in numerical cloud models were discussed.

We should also note the work [13], which presents the results of the analysis of the state of cloud physics in the early 1990s. The main attention in this work was paid to the analysis of the physics state of hail clouds and active effects on them, as well as methods for studying cloud formation and development.

Comparison of the results obtained in these works showed that the state of convective cloud physics has not undergone significant changes for about ten years, i.e., no significant fundamental results in this scientific field have been obtained over a sufficiently long period of time.

In order to find out the causes of negative phenomena in the development of cloud physics, an analysis of its current state was carried out in [1]. Another method was used for this purpose. This is due to the fact that the method (analysis of the state of research on individual processes in clouds) used in [12, 13] does not allow us to clearly identify the state and features of the development of this scientific area. Considering that clouds refer to complex physical systems, the analysis of cloud physics development in this work was carried out in terms of stages, methodologies and methods of systems research [1].

Let us dwell on this method. The methodology of systems research regardless of their nature is based on the use of such fundamental methods as decomposition and aggregation [14, 15]. At the first stage, as a result of decomposition of systems, their main elements (or “elementary” processes in the case of physical systems) are identified and studied. The next stage is to aggregate (combine) the results of the previous stage and study the system as a whole, considering its system properties. When determining the directions of research at this stage, it should be borne in mind that the main purpose of studying systems is to establish the regularities of formation of their structure. Achieving this goal requires the definition of the main factors that are structure-forming for the system under consideration, the mechanisms of influence of these factors on the system, a detailed study of their role in the structure formation of the system. Such factors are the interaction of system elements among themselves (the property of emergence) and the interaction of systems with the external environment (the property of hierarchy) [15].

This methodology was also used to study the current state of stages of development of the laws of cloud formation and development. Then, the main stages of the study of cloud formation and formation of their macro- and microstructural characteristics can be formulated as follows:

- study of “elementary” processes occurring in clouds and leading to cloud formation and development;
- aggregating the results of “elementary” processes studies;

- determining the factors that are structure-forming for clouds and study the mechanisms of their influence on cloud formation processes;
- studying the role of structure-forming factors in forming the macro- and microstructure of clouds;
- studying the regularities of cloud formation and development in general, considering their systemic properties.

At each of these stages, in accordance with the tasks to be solved, it is necessary to use appropriate methodologies and techniques [1].

An analysis of the stages listed above shows that the first of these stages (i.e., the study of “elementary” processes in clouds), in which the main attention in recent decades has been paid to the study of microphysical processes in clouds, is currently being completed. As a result, as was noted, many of these processes have been studied at a high level, which made it possible to formalize them. At the same time, studies were carried out to develop mathematical models of clouds, which included the results of studies of microphysical and other processes.

We can say that significant progress has been made in the development of numerical cloud models. To date, full multidimensional cloud models have been developed and implemented, in which the processes of hermos-hydrodynamics and microphysics and electrical processes are considered in detail [1, 5–7, 12]. These models are actively used to study various issues of cloud physics [4, 9, 11, 16–21]. Note that numerical models aggregate fundamental results obtained at the first stage of cloud physics development.

It is important to note that at the oncoming stage of development of cloud physics and active effects on clouds, the role of mathematical modeling increases significantly. This is due to the fact that the aggregation of the results of studies of “elementary” processes in clouds and the study of clouds as a whole is possible only on the basis of mathematical cloud models.

The state of active impacts on clouds to control the processes of precipitation formation is also complex and ambiguous. This issue is discussed in more detail below. Here we will only note that the technologies used for active influence on convective clouds so far are based on limited knowledge about the formation of macro- and microstructural characteristics of clouds, relying on concepts developed several decades ago.

Based on the above, it can be argued that one of the stages in the development of cloud physics (the stage of studying “elementary” processes in clouds) is now completed and the transition to the next stage, in which qualitatively new tasks will be solved. In the same way, there is a transition from the currently existing concepts of active impact on clouds to methods derived from rigorous studies of cloud formation and development in natural conditions and under active impact.

3 Research Results

3.1 The Main Trends of Cloud Physics and Active Influences on Clouds

The transition of any scientific field from one stage of development to another cannot be a jump, it will take a certain period of time. This also applies to the physics of clouds and active effects on them. Its current state, as noted above, is characterized by the fact that research has begun and is being conducted (although still limited) on various issues that belong to the second stage of its development. At the same time, the study of “elementary” processes in clouds has not been completed—there are still many such processes that remain insufficiently studied or not fully understood [22]. Among them, there are such processes that are still not fully understood even at the qualitative level [12]. Therefore, when formulating research directions, along with the problems of the coming stage of development, the study of the remaining unstudied processes should be included. As an example, we can mention processes of primary droplet and crystal formation, processes of crystal phase formation in clouds, processes of interaction of reagent particles with cloud medium, processes related to electrification of particles in clouds, etc.

3.2 Results of Studies of the Role of System Properties of Convective Clouds in the Formation of Their Macro- and Microstructural Characteristics

Let us further dwell on the structure-forming factors and methods for studying their role in the processes of cloud and precipitation formation [15]. Such factors, as noted above, are the interaction of clouds with the surrounding atmosphere and the interaction of processes in clouds among themselves. If the mechanisms of the interaction of clouds with the surrounding atmosphere are more or less understood, the mechanisms of the interaction of processes in clouds cannot be considered understood at a level sufficient for their effective study. This also applies to the methodologies and methods for studying their role in forming the macro- and microstructural characteristics of clouds.

Let us dwell on some results of studies of the role of interaction of clouds with the surrounding atmosphere in cloud formation and development, which have been conducted for several years at “High Mountain Geophysical Institute”. The studies were carried out on the basis of a three-dimensional model of convective clouds with detailed consideration of thermo-hydrodynamics and microphysics processes [1]. For example, calculations were carried out to study the influence of two mechanisms of interaction between clouds and the surrounding atmosphere on cloud formation processes. The first mechanism is caused by the structure of the wind field in the

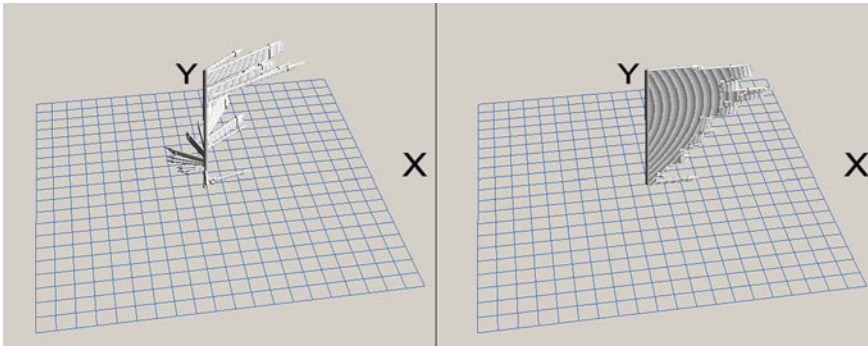


Fig. 1 Real (left) and model (right) structures of the wind field in the atmosphere used for the calculations

atmosphere, and the second by the aerosol composition of the atmosphere, namely, the content of aerosol particles in the atmosphere, which have ice-forming properties. Regarding the research methodology in this direction, we note that it consists in a comparative analysis of the cloud parameters, which are formed in the atmosphere with real and model wind field structures.

Below are some results of calculations to study the role of the first mechanism of cloud-atmosphere interaction in cloud formation and development [1, 11, 16]. Cloud calculations were performed for different structures of the wind field in the atmosphere: for the real structure obtained by aerological sounding of the atmosphere (Fig. 1, left) and the model structure obtained by varying the wind speed vector direction by height with its values unchanged (Fig. 1, right).

In the figure, we can see that the structure of the wind field in the model case has greatly simplified. Obviously, such changes in the wind field cannot but affect the character of the interaction of the cloud with the surrounding atmosphere. They lead to its weakening, i.e., in the model case, the atmosphere impedes the development of the cloud less.

Let us briefly dwell on the results of the calculations, which are described in detail in [11, 16]. Figure 2 shows isolines of the velocities of vertical air flows in the clouds and near-cloud space in the vertical plane passing through the center of the clouds along the OX axis. The figure corresponds to 20 min of their development, the left figure corresponds to the real wind field structure in the atmosphere, and the right one to the model structure. Without dwelling on the quantitative differences in the cloud parameters, we note that the velocity fields of upward and downward airflows in both cases have a rather complex structure. The structures of air currents, significantly changing over time (Figs. 2 and 3).

Comparison of the isolines of vertical air flow velocities at 20 min of cloud development corresponding to the real and model structures of the wind field in the atmosphere (Fig. 2) shows that, in the second case, the maximum rates of upward and downward air motions in the cloud are noticeably higher than in the first case. It can be seen in the figures, in the case of the model wind field structure in the

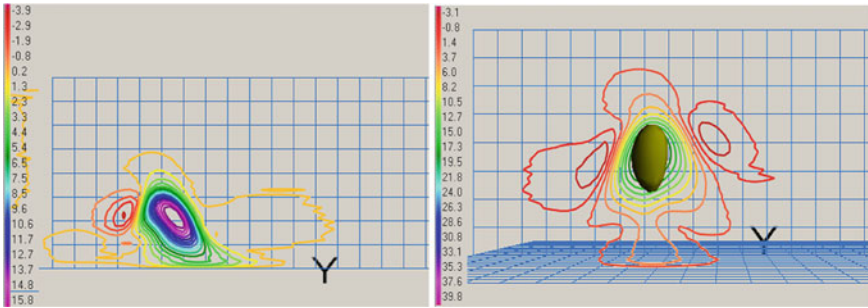


Fig. 2 Isolines of different values of the velocity of upward air flows in the vertical plane at the 20th minute of cloud development in the cases of real (left) and model (right) wind field structure in the atmosphere

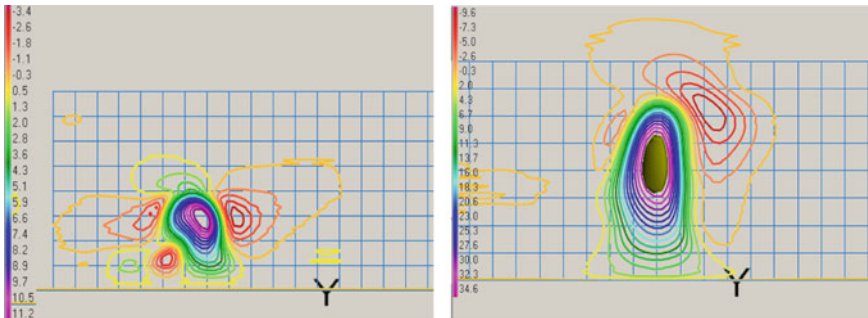


Fig. 3 Isolines of different values of upward air velocities in the vertical plane at 20 (left) and 30 min (right) of cloud development in the case of a model field structure

atmosphere, an isosurface of the upward sweat velocity of 35 m/s is depicted in the central part of the upward air flow zone in the cloud. In the real case, the maximum velocities of ascending air movements do not reach this value.

Figure 3 shows isolines of the same parameters at 30 min of cloud development. Comparison of Figs. 2 and 3 shows that the fields of velocities of vertical air flows in the cloud and around the cloud, corresponding to the considered wind fields in the atmosphere, differ qualitatively. The structure of the field of this parameter in the cloud and near-cloud space, corresponding to the real wind field in the atmosphere, has a more complicated character. This is explained by the fact that the real wind field structure is significantly more complex than the model wind field structure.

As for the maximum values of the cloud parameters (Table 1), they are appreciably greater in the cloud corresponding to the model structure of the wind field in the atmosphere. As noted, this is due to the fact that in this case, the interaction of the cloud with the atmosphere is less intense, i.e., in this case, the atmosphere impedes the development of the cloud less.

Table 1 Maximum values of cloud parameters corresponding to different variants of wind distribution in the atmosphere

Parameter	Real wind field structure in the atmosphere			Model wind field structure in the atmosphere		
	20	30	40	20	30	40
Time, min	20	30	40	20	30	40
W_{\max} , m/s	17.9	12.8	7.9	44.4	39.3	39.0
HW_{\max} , km	3.5	5.0	5.0	6.5	7.0	6.75
Q_{\max} , g/m ³	6.63	8.7	6.9	11.8	11.1	10.9
HQ_{\max} , km	4.75	5.25	4.5	7.0	6.75	6.5
Z_{\max} , dBZ	37.6	64.7	64.3	60.0	62.8	66.6
HZ_{\max} , km	4.25	5.25	3.75	6.5	6.0	5.5

The role of the wind field structure in the atmosphere in the processes of cloud formation was also investigated in the case when the wind speed in the atmosphere at all heights was varied with its direction unchanged. According to the results of the calculations, even in this case, changes in the wind structure noticeably affect the processes of cloud formation. It was also obtained that an increase in wind speed in the upper atmospheric layers prevents cloud formation, and starting from some values of wind speed, the cloud is not formed.

We also modeled the influence of another mechanism of interaction between the cloud and the atmosphere on the processes of cloud formation, namely, the influence of the aerosol composition of the atmosphere on these processes. The studies were carried out by varying the intensity of the crystal source in the cloud, i.e., the influence of the content of aerosol particles in the atmosphere, which have ice-forming properties, on cloud formation processes was simulated. According to the results of calculations, this mechanism also affects the processes of cloud formation in the atmosphere, cloud parameters.

As for the study of the role of interaction of cloud processes in cloud formation and development, there are serious difficulties in this case. To carry out research in this direction, in many cases we have to use indirect manifestations of a given structure-forming factor. Therefore, their study may require the development and use of special cloud models, which contain indirect manifestations of this or that structure-forming factor.

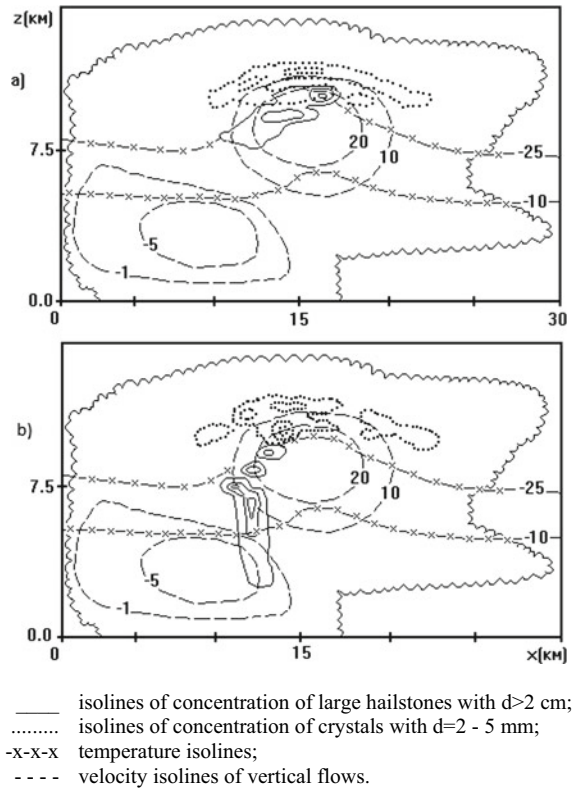
Below are some results of studies of the role of deformation of the fields of thermodynamic parameters in the cloud in the formation of the microstructure of powerful convective clouds in which hail is formed. As noted, the deformation of these parameter fields is the result of a complex interaction of cloud processes among themselves. A two-dimensional model of microphysical processes in mixed clouds against the background of given thermo-hydrodynamics was used for the studies. This way of accounting for thermo-hydrodynamic processes in the model allowed us to consider different degrees of deformation of the fields of thermodynamic parameters in the cloud. The motion and growth of hailstones in powerful hail clouds were also studied. Immediately note that, as the results of calculations have shown, in the

absence of deformation of the fields of the noted parameters, hail in the cloud is practically not formed or their formation requires unrealistically high-water content in the cloud.

Figure 4 shows the isolines of the vertical component of the velocity of air flows in the cloud and the pattern of hail growth in powerful clouds, which were obtained as a result of calculations.

The maximum value of the vertical component of the velocity of air flows $V_z(x,z)$ is about 35 m/s. The figure shows that the growth of hail particles occurs in the zone, which is formed in the cloud under the influence of the interaction of dynamic, thermodynamic and microphysical processes. This zone, which can be called a zone of hail particles motion and growth, is located, as seen in the figure, between isotherms of $-10^{\circ}\text{C} \div -25^{\circ}\text{C}$. In addition, due to temperature field deformation and horizontal movement of hail particles from the region with maximum upward fluxes to the rear part of the cloud with lower $V_z(x,z)$ values, the zone of hail motion and growth in clouds is more extended. Its shape corresponds to the typical radio echo structure in the plane of the cloud motion direction given in (21). The results obtained within the framework of the model used agree quite well with the experimental data of different authors on the study of the mechanism of hail nucleation and growth.

Fig. 4 Isolines of cloud parameters at $t = 18$ min (a) and $t = 24$ min (b)



According to the results of isotopic analysis of hailstones, for example, modal values of hail nucleation temperature on croup nuclei are $-20\text{ }^{\circ}\text{C} \div -25\text{ }^{\circ}\text{C}$, and on droplets approximately $-10\text{ }^{\circ}\text{C}$. According to the same studies, hail growth occurs in the temperature range $-10\text{ }^{\circ}\text{C} \div -25\text{ }^{\circ}\text{C}$. In addition, the calculations show that the time from the formation of hail particles with $d > 2\text{ cm}$ to the time of their falling out of the cloud is about 6–8 min, which also agrees with the observational data. Note also that the formation of a layered structure of hail particles, in our opinion, may be associated with a change in their growth regime during their movement in the temperature range.

The obtained results also indicate that the division of the cloud in the vertical or horizontal section into different zones (hail nucleation zone, hail growth zone, etc.), as it is currently accepted, is conditional and does not reflect the real picture of these processes.

Using several variants of the fields of thermodynamic parameters in numerical experiments has shown that the shape and size of the zone of nucleation and growth of hail particles are significantly affected by the deformation of the cloud thermodynamic fields under the influence of upward flows and the heat of water phase transitions. As hail particles move in this zone, they interact with air streams and the droplets contained in them in a complex way. The obtained scheme of hail formation and growth, as noted above, does not contradict the experimental data.

The figure shows that in the zone of motion and growth of large hail particles, the isolines of their concentrations form closed areas that do not intersect. This means that the intensity of hail precipitation will change periodically. At the same time, the cloud model used does not contain any cyclic process. Therefore, it can be assumed that the cyclic nature of cloud precipitation is also the result of the interaction of cloud processes.

In (6), the interaction of electrical and microphysical processes in clouds was investigated. It should be noted that electrical processes in clouds are also the result or manifestation of interaction of cloud processes.

Features of existing technologies of active impact on convective clouds were noted above. They show that the transition to technologies based on the use of impact methods derived from rigorous studies of cloud evolution *in vivo* and under active impact can be considered as one of the most important problems of modern cloud physics and active impact on clouds.

Challenges encountered in the development of cloud sedimentation control methods can be formulated as follows:

- finding a local region in the cloud in which conditions are favorable for active influence in order to achieve the goal;
- finding the concentration of reagent particles that should be provided in this area at each moment of time, i.e. finding the dynamics of reagent introduction into the cloud.

It is important to note that the formulation as independent tasks of developing a method of controlling the processes of precipitation formation in clouds is conditional, because the concentration of reagent particles, which should be provided as

a result of exposure, and the place and time of introduction of these particles in the cloud are interrelated.

Solving the mentioned problems by modeling different variants of the reagent application to the cloud will meet serious difficulties. This is especially true for the second problem. Nevertheless, the most common method nowadays can be considered simulation of different variants of reagent particle introduction into the cloud and choosing the most effective of them in terms of achieving the goal of exposure. The options for introducing the reagent into the cloud may differ in the values of the parameters of the source of the reagent particles that are introduced into the cloud model. Depending on the method used to introduce the reagent into the cloud, the source may be a point source, a linear source, or may have a more complex shape. Note also that a wide variety of cloud models are used for studies based on this approach. Obviously, it is possible to solve the noted problems in this way in a very approximate way. In this connection, serious attention should be paid to the development of effective approaches to the development of methods for controlling the processes of precipitation formation in clouds, which has not been given enough attention in cloud physics and active effects on clouds so far. At the same time, all approaches should be based on extensive use of mathematical modeling. Cloud models to be used to solve this problem should be sufficiently complete, they should allow modeling the active effects with different types of reagents and different ways of their introduction into the cloud.

According to the authors, in the case of hail clouds, the most promising approaches for solving this problem are those based on the use of optimal control theory and bifurcation theory [14, 23].

4 Conclusions

Considering the current state of cloud physics and active effects on clouds, it is possible to note the following directions of its development:

- continuation of the study of “elementary” processes in clouds;
- improvement of existing and development of new numerical models of convective clouds, development of effective methods of model input data formation and methods of calculations;
- determine the main structure-forming factors for clouds, study the mechanisms of their impact on cloud and precipitation formation processes;
- development of effective methodologies and methods and study of the role of interaction processes in clouds in forming their macro- and microstructural characteristics;
- development of effective methodologies and methods and study of the role of interaction of clouds with the surrounding atmosphere in forming their macro- and microstructural characteristics;

- investigating the regularities of formation of macro- and microstructural characteristics of clouds as a whole considering system properties;
- development of methodologies and methods of research on the development of effective methods of active influence on convective clouds in order to control the processes of precipitation formation in them;
- development of scientifically based technologies for cloud precipitation control.

References

1. Belova, L.K., Drofa, A.S.: Study of the impact of hygroscopic reagents on the convective cloud by numerical simulation // Proceedings of GGO. Issue. 282. 184–201 (2016) [in Russian].
2. Dovgalyuk, Yu.A., Veremey, N.E., Zatevakhin, M.A., Ignatyev, A.A., Sinkevich, A.A., Toropova, M.A.: Example of calculation results of the evolution of precipitation-forming convective cloud using the full three-dimensional model // Proceedings of GGO. Issue. 282. 92–115 (2016) [in Russian].
3. Kogan, E.L.: Three-dimensional numerical model of a dripping rain cloud, taking into account microphysical processes // Proceedings of the USSR Academy of Sciences, Physics of the Atmosphere and Ocean. V. 14, **8**, 876–886 (1978).
4. Kogan, E.L., Mazin, I.P., Sergeev, B.N., Khvorostyanov, V.I.: Numerical modeling of clouds. Moscow: Gidrometeoizdat. (1984) [in Russian].
5. Kupovykh, G.V., Ashabokov, B.A. et al.: Numerical Modeling of Electric Characteristics of Convective Clouds // Izvestiya Vuzov. North Caucasus Region. **6**, 65–68 (2012) [in Russian].
6. Pastushkov, R.S., Schmeter, S.M.: Influence of vertical motions in powerful convective clouds on the wind field. // Izv. of the USSR Academy of Sciences. FAO. Vol. IV, **3**. 283–291 (1968) [in Russian].
7. Chlodniok, M., Klitsch, A., Kubicek, M., Marek, M.: Methods of analysis of nonlinear dynamic models. Mir. Moscow (1991) [in Russian].
8. Cotton, W. R., Stephen, M. A., Nehrkorn, T., Tripoli, G. J.: The Colorado State University three-dimensional cloud mesoscale model. Part II: An ice phase parameterization. J. Res. Atmos. **16**(3), 295–320 (1982).
9. Mesarovich, M., Takahara, Y.: General systems theory: mathematical foundations. Mir. Moscow (1978).
10. Straka, J.: Cloud and Precipitation Microphysics: Principles and Parameterizations. Cambridge University Press. Cambridge (2009).
11. Ashabokov, B.A., Fedchenko, L.M., Shapovalov, A.V., Shapovalov, V.A.: Physics of clouds and active effects on them. Nalchik: “Printed Yard”, (2017) [in Russian].
12. Sinkevich, A.A., Kraus, T.V., Pavar, S.D., Veremey, N.E., Dovgalyuk, Yu.A., Kurov, A.B., Gopalakrishnan, V.: Study of the impact of strong aerosol pollution of the atmosphere on the development of cumulonimbus rain cloud using a three-dimensional model // Proceedings of GGO. Issue. 170, 197–210 (2014) [in Russian].
13. Ashabokov, B.A., Kalazhokov, H.H.: Numerical Modeling of Hail Clouds. Moscow: Gidrometeoizdat, (1992) [in Russian].
14. Andronov, A.A., Leontovich, E.A., Gordon, I.M., Mayer, A.G.: Bifurcation theory of dynamical systems on a plane. Moscow: Nauka, (1967) [in Russian].
15. Ashabokov, B.A., Fedchenko, L. M., Shapovalov, A.V., Kalov, Kh. M., Kalov, R. Kh., Tashilova, A.A., Shapovalov, V.A.: Mathematical modeling of the influence of the wind field structure in the atmosphere on the cloud formation processes. Atmospheric and Climate Sciences, **1**, 84–96 (2018) [in Russian].

16. Ashabokov, B.A., Shapovalov, A.V.: Convective clouds: numerical models and results of modeling in natural conditions and under active influences. Nalchik: KBNTs RAS (2008) [in Russian].
17. Veremey, N.E., Dovgalyuk, Yu.A., Zatevakhin, M.A., Ignatyev, A.A., Morozov, V.N., Pastushkov, R. S.: Description of the basic numerical unsteady three-dimensional model of a convective cloud // Proceedings of GGO. Vol. 282. 45–91 (2016) [in Russian].
18. Pastushkov, R.S.: Model of active influences on convective clouds by ice-forming aerosols. Current state and prospects for development // Proceedings of GGO. Issue. 582. 128–157 (2016) [in Russian].
19. Schmeter, S.M.: Thermodynamics and physics of convective clouds. Hydrometeoizdat. Leningrad (1987) [in Russian].
20. Karacostas, T., Spiridonov, V., Bampzelis, D., Pytharoulis, I., Tegoulis, I., Tympanidis, K.: Analysis and numerical simulation of a real cell merger using a three-dimensional cloud resolving model. *Atmospheric Research* **169**, 547–555 (2016).
21. Klemp, J.B., Wilhelmson, R.B.: The simulation of three-dimensional convective storm dynamics. *J. Atmos. Sci.* **35**(6), 1070–1096 (1978).
22. Khvorostyanov, V.I., Curry, J.A.: Thermodynamics, Kinetics, and Microphysics of Clouds. Cambridge University Press (2014).
23. Dovgalyuk, Y.A., Veremei, N.E., Vladimirov, S.A., Drofa, A.S., Zatevakhin, M.A., Ignatiev, A.A., Morozov, V.N., Pastushkov, R.S., Sinkevich, A.A., Stasenko, V.N., Stepanenko, V.D., Shapovalov, A.V., Shchukin, G.G.: The concept of developing a three-dimensional model of precipitation-forming convective cloud. II: Microphysical block model // Proceedings of GGO. Vol. 562. 7–39 (2010) [in Russian].

On the Solution of the Problem of Formation and Approval of Target Indicators of Development of the Agro-Industrial Complex



M. B. Ashabokova  and Kh. M. Temirkhanova

Abstract The purpose of the work is to analyze the problem of adaptation of various fields of activity to climate change, to formulate the tasks of adapting the agro-industrial complex (AIC) and to analyze the features of information support and methods for solving the tasks of its adaptation plan, to develop a method for solving one of the tasks of this plan the formation and coordination of target indicators of the development of the agro-industrial complex. To solve the above problems, the results of the analysis of climate change in the territory of the North Caucasus, the model for optimizing the functioning of the “crop industry—processing industry” system, developed to form and agree on target indicators for the development of the regional agro-industrial complex, were used. It is noted that at the regional level it is not advisable to limit adaptation to climate change only to agriculture, this problem at this level should be considered for the “agriculture—processing industry” system, taking into account the relationship between its elements, the goals of adapting this system to climate change are formulated. The formulations of the tasks of the adaptation plan for the regional agro-industrial complex are given, the approach to solving the problem of forming and coordinating the target indicators of the agro-industrial complex is outlined, some calculation results are given. The main results of the work are: the formulation of the tasks of adapting the agro-industrial complex to climate change, the model for optimizing the functioning of the “crop industry—processing industry” system, developed to solve the problem of forming and coordinating target indicators for the development of the regional agro-industrial complex.

Keywords Climate change · Agro-industrial complex · Objectives of the adaptation plan · Formation and coordination of target indicators

M. B. Ashabokova (✉) · Kh. M. Temirkhanova
High Mountain Geophysical Institute, Lenin Ave., 2, 360002 Nalchik, Russia
e-mail: ashabokova.marina@rambler.ru

© The Author(s), under exclusive license to Springer Nature Switzerland AG 2023
R. Zakinyan and A. Zakinyan (eds.), *Physics of the Atmosphere, Climatology and Environmental Monitoring*, Springer Proceedings in Earth and Environmental Sciences, https://doi.org/10.1007/978-3-031-19012-4_7

1 Introduction

In recent decades, much attention has been paid to the analysis and forecast of climate change, which is gaining momentum at a rapid pace and becoming a factor capable of influencing all areas of activity and the environment. Of the large number of works devoted to these problems, we can note the works [1, 4, 5, 7, 10–13, 17–21]. The influence of this factor on the weather-dependent sectors of the economy, on the processes in the climate system, on the well-being and health of people is already noticeable [3, 6, 9, 14–16, 19]. It is important to note that no system is able to resist this factor. If urgent and evidence-based measures are not taken, the consequences can become catastrophic [19]. The goal of the Paris Climate Conference (2015) was to develop an agreement that would stop climate warming by reducing the anthropogenic impact on it.

As measures to achieve this goal, stabilization of the content of greenhouse gases in the atmosphere at levels that would prevent dangerous anthropogenic impact on the climate system and adaptation of the functioning of various systems to climate change are considered [19].

The agricultural sector is a rather complex economic system. One of the elements of the external environment in which it operates is the natural environment, which makes this sector of the economy extremely sensitive to climate change. Therefore, the discrepancy between the structure of the agro-industrial complex and rapidly changing natural conditions will lead to a gradual decrease in efficiency, and then to the destruction of this sector of the economy. Related to this is the need to adapt to climate change.

As for the goals of adapting sectors of the economy to climate change, including the agro-industrial complex, they should be to find such a trajectory for their development so that at each moment of time their structure and indicators best correspond to the conditions of the external environment. At the same time, along this trajectory, they should be able to perform their functions, which are to improve the well-being of people [8].

It should be noted that not only sectors of the economy need to adapt to climate change. This also applies to management systems, education and health systems, and so on.

2 Literature Review

Global warming of the Earth's climate has become a factor that can have a tremendous impact on the processes taking place in society and in the natural environment. It is important to note that modern climatic changes, in addition to changes in average values (slow change), are manifested in a sharp change in the frequency and intensity of extreme climatic events, both temperature and precipitation, leading to droughts or floods [1, 4, 7, 10, 12, 17, 18, 21]. At the same time, one of the first climatologists

who predicted global climate warming due to the emission of anthropogenic carbon dioxide into the atmosphere is the American climatologist J. Hansen [5]. Of the works devoted to the study of climate change in Russia, it can be noted [4, 5, 11, 13, 21]. Climate change is already having a noticeable impact on various areas of activity, on the natural environment, on human health, etc. Therefore, much attention has been paid to the study of the consequences of this factor; among the works of this area of research, one can note the works [3, 6, 9, 16]. They are expected to be especially significant for mountain areas. Moreover, there are quite a lot of mechanisms of influence of this factor on the spheres of activity in these areas, and the main of them can be considered the influence through dangerous slope processes (avalanches, mudflows, rockfalls, etc.). It is important to note that unless scientifically based and urgent measures are taken, neither society nor the global ecological system is able to resist the impact of climate change, its consequences can be catastrophic [19]. This is related to the fact that the goal of the Paris Climate Conference (2015) was to develop an agreement that would allow at the first stage to slow down climate warming, and then stop it. As such measures, the conference proposed the stabilization of the content of greenhouse gases in the atmosphere at levels that would prevent dangerous anthropogenic impact on the climate, and the adaptation of various systems to its change [19]. This is due to the fact that research is being carried out in such areas as the analysis of climate change and its consequences, the search for effective methods for adapting various fields of activity to climate change, reducing the risks associated with extreme weather events, etc. Of the works in this area of research, one can note [2, 8, 14].

3 Formulating the Tasks of Adapting the Regional Agricultural Sector to Climate Change

The adoption of the Paris Agreement, one might say, means that a stage in the development of society has begun, which differs from all previous stages. It provides for the transition of society to a new development model, which can be called adaptive, i.e., it is forced to “coordinate” all its actions with the natural environment, to adapt them to its changes. The adaptation plan for sectors of the economy, including agriculture and the agro-industrial complex, can be considered as a plan for their development, but taking into account the consequences of changes occurring in the elements of the external environment (natural, economic, demographic, and others) [4].

As for the sphere of food production, at the regional level it will be inappropriate to be limited to the adaptation of one agriculture; plans for the adaptation of the agro-industrial complex as a whole should be developed and implemented. This is due to the fact that the sustainability and, as a result, the profitability of this industry is relatively low. Therefore, the problem of adaptation to climate change should be considered for the “agriculture—processing industry” system, taking into account

the relationship between its elements. Such an approach to solving this problem will increase the efficiency of the system and its elements, and increase the income of the region.

It is necessary to dwell on the choice of a period of time (adaptation interval) for which an adaptation plan for the sector of the economy should be developed and implemented. Its length should not exceed the length of the time interval in which the tasks of forming an adaptation plan can be solved quite reliably. First of all, this refers to the task of determining the conditions of the external environment (natural, economic, political, social, demographic, etc.) that influence its development. In the case of the agro-industrial complex, this interval, apparently, cannot exceed 5–7 years.

The tasks of adapting the agro-industrial complex of the region can be divided into groups [4]: the tasks of forming an adaptation plan to climate change; tasks related to reducing the vulnerability of the agro-industrial complex by climate change; tasks related to reducing the impact of the agro-industrial complex on the climate; tasks aimed at using the favorable effects of climate change to improve the efficiency of the agro-industrial complex.

1. The tasks of developing a plan for adapting the agro-industrial complex to climate change:
 - 1.1. analysis and forecast of climate change and the dynamics of climatic factors affecting the productivity of agricultural crops;
 - 1.2. building models of agro-climatic resources, determining their dynamics in the adaptation interval;
 - 1.3. analysis and forecast of changes in external and internal conditions (natural, economic, technological, political, social, demographic, etc.), under the influence of which the agro-industrial complex of the region will develop;
 - 1.4. development of a model and solution of the problem of formation and coordination of target indicators for the development of the agro-industrial complex in the considered period of time;
 - 1.5. determination of climate-saving agrotechnical measures, with the help of which it is possible to bring crop yields due to natural factors to target indicators;
 - 1.6. development of a model and study of various scenarios for the production and processing of crops in the adaptation interval in order to determine the most promising of them;
 - 1.7. development of a method and selection of the most appropriate scenario for adaptation of the agro-industrial complex to climate change;
 - 1.8. optimization of the structure of support services (services for the supply and maintenance of technical facilities and equipment, the supply of fertilizers, the construction of various facilities, scientific support for the agro-industrial complex, training and retraining of specialists, etc.) taking into account climate change;

- 1.9. choice with systems of target indicators, development of methods and analysis of the effectiveness of adaptation measures and monitoring the implementation of plans for adaptation of the agro-industrial complex to climate change, improvement of adaptation plans.
2. Tasks, the solution of which is aimed at reducing the negative impact of the agro-industrial complex on the climate:
 - 2.1. monitoring the balance of greenhouse gases at various stages of crop production in order to establish the mechanisms of influence of agriculture to the climate system;
 - 2.2. development of nature- and climate-saving means of production and processing of agricultural products;
 - 2.3. development of efficient technologies for tillage and crop production, minimizing the impact of the industry on the climate;
 - 2.4. development of effective climate-saving technologies for processing agricultural products;
 - 2.5. development of technologies for the use and disposal of industrial waste in agriculture, minimizing their impact on the climate;
 - 2.6. development and use of climate-saving technologies for recycling waste from the processing industry;
 - 2.7. monitoring the balance of greenhouse gases in various ways of using and disposing of crop waste;
 - 2.8. development of effective methods and means of combating diseases and pests of crops and animals that do not affect ecological systems.
3. Tasks, the solution of which is aimed at reducing the vulnerability of the agro-industrial complex by climate change:
 - 3.1. creation of shelter belts that contribute to the accumulation of moisture in the soil, the creation of a microclimate favorable for agricultural crops;
 - 3.2. search for ways to preserve the region's water resources, optimize their use in the agro-industrial complex;
 - 3.3. breeding highly productive agricultural crops that are resistant to fluctuations in the natural conditions of their production;
 - 3.4. study of the trend in the frequency and characteristics of hazardous weather events, the exposure and vulnerability of agriculture to these events;
 - 3.5. improving existing and developing new methods to reduce risks in agriculture associated with extreme weather events;
 - 3.6. analysis and forecast of changes in the activity of diseases and pests of agricultural crops and animals traditional for the region, forecast of the emergence of new species in the region;
 - 3.7. Development of effective methods and means of combating diseases and pests of crops and animals that do not affect the environment.
4. Tasks, the solution of which is aimed at using the favorable effects of climate change to improve the efficiency of the agro-industrial complex:

- 4.1. looking for ways to use the increase in the likelihood of mild winters in agriculture (in order to improve the efficiency of the industry);
- 4.2. development ways using extended growing season to improve efficiency industries;
- 4.3. study of the possibility of producing more valuable crops in the region;
- 4.4. study of the effect of increasing the content CO_2 in the atmosphere on crop productivity;
- 4.5. study of changes in the need of agricultural crops for fertilizers and water with an increase in the content CO_2 in the atmosphere.

The stated method of dividing the tasks of AIC adaptation into groups is not the only one. Tasks in each group can be detailed, as well as increase or decrease their number in groups.

4 Methods for Solving the Problems of Forming a Plan for Adapting the Agro-Industrialcomplex to Climate Change

Let us dwell on information support and methods for solving the problems of forming plans for adapting agricultural sectors to climate change.

1. The purpose of solving the first problem is to study the dynamics of natural factors that form crop yields in given areas. In this regard, when solving this problem, a complex of the main of these factors should be used as climatic variables, on the basis of which it is possible to build a model of the agroclimatic resources of these territories.
2. The productivity of agricultural crops in a complex way depends on a complex of natural factors [4, 6]. The purpose of solving the second problem is to build integral functions that link crop yields with natural factors (models of agroclimatic resources). They are used to determine the dynamics of agro-climatic resources in the adaptation interval. To build such models, you can use existing models, adjusting them to the natural and climatic conditions of specific areas, or build new ones, taking into account the peculiarities of the influence of each natural factor on crop yields [4].

To solve this problem, long-term data on natural factors are used, under the influence of which crop yields are formed (time series of the same meteorological parameters that characterize the regime of precipitation and air temperature in different seasons of the year). Long-term data on crop yields formed by these factors are also used.

3. The purpose of solving the third problem is to determine the conditions for the functioning of the agro-industrial complex in the adaptation interval, which include natural, production-economic, political and other conditions. They can be determined by processes taking place in the country and regions (conditions

due to internal factors), as well as processes observed in world dynamics (external factors).

The first two tasks were devoted to determining the natural conditions for the functioning of agriculture in the adaptation interval. To determine other conditions, it is necessary to use information that characterizes the production of agricultural products at all levels, the cost of production and processing of these products, demand, supply and sales prices for agricultural products at all levels, the development and availability of technologies for the production and processing of agricultural products, etc. This information should be taken into account when developing a plan for adapting the industry to climate change (to form target indicators for production, to assess the optimal volumes of agricultural production, etc.). To solve this problem, expert methods seem to be more promising.

4. The purpose of solving the following problem is to determine and agree on the target indicators of the “agriculture—processing industry” system [4]. When forming them, the possibilities of their achievement should be taken into account, which depend on many factors, ranging from the agro-climatic resources of the region’s agricultural lands to the financial and economic state of the system. In addition, they must be coordinated with each other within the framework of available resources, requirements imposed on production volumes, etc.

At the same time, target indicators of agriculture are directly determined, namely, crop yields, target indicators of the processing industry should be determined on the basis of agricultural indicators, taking into account their relationship, preferably optimizing the functioning of this system.

The solution of this problem requires the development of a model that links the indicators of agriculture and the processing industry. For this purpose, it is promising to use a model for optimizing the structure of products produced by the “agriculture—processing industry” system. As an optimality criterion, one can use, for example, the maximum profit or income of the system. Such an approach to solving this problem will improve the efficiency of the functioning of the system as a whole and its elements.

5. The purpose of solving the fifth task is to develop climate-saving agrotechnical measures, with the help of which it is possible to bring crop yields due to natural factors (the lower limit of the range of yield changes) to target indicators (the upper limit of this interval). The solution of this problem is not related to the direct use of climate information. But in certain situations, such a need may arise.
6. As a result of solving the sixth task, scenarios for the development of the “agriculture—processing industry” system over the adaptation interval should be determined, corresponding to possible scenarios for changing the conditions for its functioning. The need for such studies is due to the fact that in the conditions of the functioning of the agricultural sector in the adaptation interval, which are determined as a result of solving problem 3, there may be significant uncertainties. To solve this problem, at the first stage, the trajectory of changes in agro-climatic resources in the adaptation interval is determined. At the second stage, the most

probable scenarios for changes in the conditions for the functioning of the “agriculture—processing industry” system are determined. Then, along the trajectory of changes in agro-climatic resources, scenarios for the development of this system are modeled, corresponding to scenarios for changing the conditions for its functioning. The use of expert methods is promising for determining scenarios for changing the conditions for the functioning of the agro-industrial complex.

7. After receiving scenarios for the development of the agro-industrial complex that correspond to the most probable scenarios for changes in the conditions for its functioning, it becomes necessary to choose the most appropriate one from this set. The purpose of solving the seventh problem is to choose this scenario. The solution of this problem is connected with the use of a complex of indicators of the agro-industrial complex. The choice of the most suitable scenario may require the development of a special method. As such a scenario, you can choose the one in which the indicators of the agro-industrial complex will be closest to the target indicators of its development.
8. The solution of the eighth task is to adapt the functioning of support services to possible changes in the conditions and technologies for the production of products, indicators of the system “agriculture—processing industry”. The goal of adaptation is to be able to perform its functions effectively during the adaptation interval.
9. Target 1.9 can be considered separately from the other targets of the industry adaptation plan. This is due to the fact that the analysis of the effectiveness of adaptation measures and control over the implementation of adaptation plans, in our opinion, should be carried out by a service specially created for this purpose. The results of such an analysis should be used to improve plans for adaptation of the agro-industrial complex.

5 Methods and Results of Solving the Problem of Formation and Coordination of Target Indicators for the Development of the Agro-Industrial Complex on the Adaptation Interval

Let us dwell on the method and some results of solving task 1.4, which, in our opinion, is one of the most difficult tasks of the agro-industrial complex adaptation plan.

The purpose of solving task 1.4 is to form and agree on target indicators for the development of the agro-industrial complex, from which target indicators for crop yields are directly determined. The rest of the indicators depend on these indicators and should be determined taking into account the interconnections between the branches of the agro-industrial complex, and it is desirable to determine their optimal values, which requires the development of a model for the functioning of the “agriculture—processing industry” system.

Let us dwell on the recording of this model for the production and economic system, the elements of which are crop growing and processing crop products of the industry. Assume that agriculture produces n -types of agricultural crops, and in the processing industry m -types of products. At the same time, agricultural products are used as raw materials in the processing industry. In order to simplify the model, we limited ourselves to taking into account the use of land and financial resources in it. Let us introduce the notation: x_1, x_2, \dots, x_n —arable land occupied by agricultural crops, $x_{n+1}, x_{n+2}, \dots, x_{n+m}$ —volumes of production by the processing industry.

When writing the objective function, it was assumed that the profit of the agro-industrial complex is approximately equal to the profit of the processing industry:

$$\Pi = \sum_{j=1}^m (c_{n+j} - z_{n+j})x_{n+j} \rightarrow \max, \quad (1)$$

where P —is the profit of the processing industry, c_{n+j} —selling price per unit j -th type of product, z_{n+j} —unit production cost j -th type of product.

The system of constraints is written as:

- restriction on the use of land resources for the production of crops:

$$\sum_{i=1}^n x_i \leq x_0, \quad (2)$$

- restrictions that take into account the observance of crop rotation in agriculture:

$$x_i = \alpha_i x_0, \quad (i = \overline{1, n}), \quad (3)$$

where α_i —share of arable land occupied i culture.

- restrictions on crop production

$$Y_i x_i \geq u_i, \quad (i = \overline{1, n}), \quad (4)$$

where Y_i —productivity and u_i —minimum production volume i -th culture.

- restrictions that take into account the use of financial resources of the industry:

$$\sum_{i=1}^n Y_i s_i x_i \leq \Phi_0^{(1)}, \quad (5)$$

where s_i —production cost i -th culture.

- restrictions considering crop processing technology:

$$\sum_{j=1}^m \alpha_{i, n+j} x_{n+j} = Y_i x_i, \quad (i = \overline{1, n}), \quad (6)$$

where $\alpha_{i,n+j}$ —volume i -th crop spent on the production of a unit of production of the type j ;

- restrictions placed on the use of limited financial resources in the processing industry:

$$\sum_{j=1}^m x_{n+j} z_{n+j} \leq \Phi_0^{(2)}, \quad (7)$$

- restrictions imposed on the volume of production in the processing industry:

$$x_{n+j} \geq v_j, \quad (j = \overline{1, m}). \quad (8)$$

In order to study the possibility of solving problem 1.4 on the basis of model (1)–(8) for the natural-climatic and production-economic conditions of the agro-industrial complex of the KBR, calculations were carried out. At the same time, it was assumed that in the adaptation interval, the indicators of the regional agricultural sector should be at the level of the developed countries of Europe. The following crops were used in the calculations: winter wheat, grain crops, corn, sunflower, potatoes, sugar beets, vegetables, fruits, grapes, medicinal herbs. The yields of these crops in German agriculture were used as target indicators to be achieved in 2030. For example, it was assumed that the yield of wheat should reach 74 c/ha, barley 56 c/ha, corn 92 c/ha, potatoes 403 c/ha, sugar beet 593 c/ha, tomatoes 1244 c/ha, grapes 57 c/ha. These indicators are achievable for the conditions of the region under consideration.

Let us designate the areas of arable land occupied by the marked crops: (x_1) area of winter wheat, (x_2) grain crops (without winter wheat and corn), (x_3) corn, (x_4) sunflower, (x_5) potatoes, (x_6) sugar beet, (x_7) vegetable crops, (x_8) gardens, (x_9) vineyards, (x_{10}) medicinal herbs; $x_{11}, x_{12}, \dots, x_{55}$ —volumes of production by enterprises of the processing industry.

As products of agricultural processing were considered:

- wheat: bread (x_{11}) , bakery products (x_{12}) , flour (x_{13}) , groats (x_{14}) , pasta (x_{15}) , alcohol (x_{16}) , starch (x_{17}) , confectionery products (x_{18}) ;
- grain crops: malt (x_{19}) , beer (x_{20}) , alcohol (x_{21}) , groats (x_{22}) , bread (x_{23}) ;
- corn: flour (x_{24}) , groats (x_{25}) , flakes (x_{26}) , alcohol (x_{27}) , starch (x_{28}) , oil (x_{29}) ;
- potato: frozen potatoes (x_{30}) , dried potatoes (chips) (x_{31}) , alcohol (x_{32}) , starch (x_{33}) , oil (x_{34}) ;
- beet: sugar (x_{35}) , canned food (x_{36}) ;
- vegetables: juices (x_{37}) , tomato (x_{38}) , canned food (x_{39}) , cosmetics (x_{40}) ;
- sunflower: oil (x_{41}) , halvah (x_{42}) , meal (x_{43}) , kazinaki (x_{44}) ;
- fruit: juices (x_{45}) , jam (x_{46}) , jam (x_{47}) , alcohol (x_{48}) , guilt (x_{49}) , vinegar (x_{50}) , dried fruits (x_{51}) , medicines (x_{52}) ;
- grape: juices (x_{53}) , guilt (x_{54}) , raisin (x_{55}) .

Processing of medicinal herbs in the model is not provided.

Denote financial costs for the processing of listed agricultural crops and $x_{66}-x_{74}$ —for the production of agricultural crops; x_{75}, x_{76} —the volume of financial resources of the processing and agricultural industries.

It can be seen that the processing industry produces 45 types of products.

6 Results

The results of calculations of some AIC indicators at the end of the adaptation interval (per 1000 ha of arable land) are shown in Table 1. Target indicators are, as noted, crop yields and production volumes of the processing industry, i.e., variables x_1, x_2, \dots, x_{55} , given in the table.

Table 1 Production and economic indicators of the agro-industrial complex in the third period of time

Areas of arable land occupied by agricultural crops (ha)			
$x_1 = 364,0$	$x_2 = 200,0$	$x_3 = 143,0$	$x_4 = 147,8$
$x_5 = 3,5$	$x_6 = 40,0$	$x_7 = 38,0$	$x_8 = 0,25$
$x_9 = 33,0$	$x_{10} = 0,5$		
Volumes of production in the processing industry (c)			
$x_{11} = 877,0$	$x_{22} = 10$	$x_{33} = 14,0$	$x_{44} = 10,0$
$x_{12} = 14,0$	$x_{23} = 165,0$	$x_{34} = 0,0$	$x_{45} = 14,7$
$x_{13} = 1370,0$	$x_{24} = 10,0$	$x_{35} = 115,0$	$x_{46} = 0,0$
$x_{14} = 0,0$	$x_{25} = 12,0$	$x_{36} = 0,0$	$x_{47} = 10,0$
$x_{15} = 10,0$	$x_{26} = 10,0$	$x_{37} = 141,7$	$x_{48} = 0,0$
$x_{16} = 21,0$	$x_{27} = 21,0$	$x_{38} = 310,0$	$x_{49} = 2,1$
$x_{17} = 15,0$	$x_{28} = 19,0$	$x_{39} = 10,0$	$x_{50} = 10$
$x_{18} = 10,0$	$x_{29} = 6,44$	$x_{40} = 31,0$	$x_{51} = 10$
$x_{19} = 190,31$	$x_{30} = 0,0$	$x_{41} = 30$	$x_{52} = 10$
$x_{20} = 10,0$	$x_{31} = 215,4$	$x_{42} = 10,0$	$x_{53} = 10,0$
$x_{21} = 10,0$	$x_{32} = 0,0$	$x_{43} = 949,2$	$x_{54} = 31,0$
			$x_{55} = 10,0$
Financial costs for the processing of agricultural crops (thousand rubles)			
$x_{56} = 53,310,7$	$x_{59} = 4507,7$	$x_{62} = 13,809,9$	$x_{64} = 600,0$
$x_{57} = 2000,0$	$x_{60} = 2300,0$	$x_{63} = 1264,3$	$x_{65} = 2117,5$
$x_{58} = 463,3$	$x_{61} = 1866,7$		
Volumes of crop production (c)			
$x_{66} = 2478,2$	$x_{69} = 200,0$	$x_{71} = 4140,0$	$x_{73} = 20,0$
$x_{67} = 300,0$	$x_{70} = 974,0$	$x_{72} = 300,0$	$x_{74} = 186,0$
$x_{68} = 1053,2$			

The calculation results show that the largest area in the structure of sown areas at the end of the adaptation interval will be occupied by wheat, grain crops and corn.

It can also be noted that the production volumes of some crop processing products are insignificant or equal to zero, which indicates the inexpediency of their production. These include, for example, wheat groats (x_{14}), frozen potatoes (x_{13}), oil (x_{34}) etc. The indicators of the processing industry in Table 1 should be used to improve its structure.

7 Conclusions

The problems of adaptation of various fields of activity to climate change have now become the focus of attention not only of researchers, but also of the world community. But, despite this, there is still no consensus on the tasks that arise on the way to solving this problem, on the methods for solving them. This also applies to the problem of adapting agriculture to climate change. Despite the fact that various approaches to solving this problem have been proposed, many issues, including the formulation of the tasks of adapting agricultural production, have not yet been resolved.

The main results of this work, devoted to the problem of adaptation of the regional agro-industrial complex to climate change, can be formulated as follows:

- an analysis of the problem of adaptation of the regional agro-industrial complex to climate change was carried out, it was proposed to consider this problem at the regional level not only for agriculture, but for the “agriculture—processing industry” system. This approach is more appropriate in terms of improving the efficiency of this system.
- formulated the goals of adapting sectors of the economy, including the agro-industrial complex, to climate change;
- the concept of an adaptation interval is introduced, the value of which should not exceed the length of the time interval on which the tasks of forming an adaptation plan can be solved quite reliably;
- the tasks of the plan for adapting the agro-industrial complex to climate change are given, as well as the results of the analysis of the features of information support and methods for solving the tasks of the adaptation plan;
- the method and results of solving one of the tasks of the agro-industrial complex adaptation plan are given, namely, the task of forming and coordinating target indicators for the development of a regional agro-industrial complex in the adaptation interval for the natural-climatic and production-economic conditions of a particular region.

References

1. Aleshina, M.A., Semenov, V.A., Chernokulsky, A.V.: The role of global and regional factors in changing the extremeness of summer precipitation on the Black Sea coast of the Caucasus based on the results of experiments with a climate model. *Fundamental and applied climatology*, volume 3, 59–75 (2019) [in Russian].
2. Ashabokov, B.A., Shapovalov, A.V., Tashilova, A.A.: Analysis of Changes in the Natural and Climatic Conditions of the Functioning of the Construction Industry (Operation of Buildings and Structures) in the Region. *Materials Science Forum* **931**, 1031–1036 (2018).
3. Ashabokov, B.A., Fedchenko, L.M., Tashilova, A.A., Shapovalov, A.V., Khavtsukov, A.Kh., and Balkarova, S.B.: «Modeling Risk Reduction in Agriculture Associated with Dangerous Agrometeorological Phenomena» in International scientific and practical conference AgroS-MART. - Smart solutions for agriculture, *KnE Life Sciences*, 223–231 (2019) [in Russian].
4. Ashabokov, B.A., Fedchenko, L.M., Tashilova, A.A., Kesheva, L.A., Teunova, N.V.: Spatial-temporal climate change in the south of the European territory of Russia, assessment of its consequences, methods and models of adaptation of the agro-industrial complex. Nalchik: Fregat LLC, (2020) [in Russian].
5. Bardin, M.Y., Ran'kova, E.Y., Platova, T.V. *et al.* Modern Surface Climate Change as Inferred from Routine Climate Monitoring Data. *Russ. Meteorol. Hydrol.* **45**, 317–329 (2020).
6. Barvitenko, Yu.N., Roslyakov, A.I., Elizarova, I.O.: Features of the influence of weather factors on the population's accessibility for medical care for diseases of the cardiovascular system // Proceedings of the Intern. scientific conference "Regional effects of global climate change", Voronezh, June 26–27, 365–369 (2012) [in Russian].
7. Bazelyuk, A.A.: Dangerous hydrometeorological phenomena in the south of the European territory of Russia // Natural and social risks in the coastal zone of the Black and Azov Seas. Triumph, Moscow. 33–42 (2012) [in Russian].
8. Bedritskii, A.I., Korshunov, A.A., Khandozhko, L.A. *et al.* Fundamentals of optimal adaptation of Russian economy to hazardous weather and climate impacts. *Russ. Meteorol. Hydrol.* **34**, 195–201 (2009).
9. Belova, V.A., Larina, E.S.: Demographic consequences of global climate change for Russia in the 21st century. Regional effects of global climate change (causes, consequences, forecasts). Proceedings of the international scientific conference, Voronezh, June 26–27, 375–377 (2012) [in Russian].
10. Climate change: The physical science basis. Contribution of Working Group I to the Fifth Assessment Report of the Intergovernmental Panel on Climate Change (pp. 1029–1136). Cambridge, United Kingdom and New York, NY, USA: Cambridge University Press. (2013).
11. Gruza, G.V., Rankova, E.Yu.: Climate variability and change in Russia. Proceedings of the Russian Academy of Sciences, *Physics of the Atmosphere and Ocean*, 39 (2), 1–20 (2003).
12. Hansen, J, Sato, M, Ruedy, R, *et al.*: Dangerous human-made interference with climate: a GISS model study. *Atmos. Chem. Phys.* **7**, 287–312 (2007).
13. IPCC 2014: Climate Change 2014: Synthesis Report. Contribution of Working Groups I, II and III to the Fifth Assessment Report of the Intergovernmental Panel on Climate Change [core group of authors, R.K. Pachauri and L.A. Meyer (ed.)]. Geneva, Switzerland, (2014).
14. Kelly, P.M., Adger, W.N.: Theory and practice in assessing vulnerability to climate change and facilitation adaption. *Climate Change* **47**, 325–352 (2000).
15. Koukhta, A.E., Maksimova, O.V. Effects of Growing Season Climatic Factors on Scots Pine Increment for the Middle Volga Region and the White Sea Coast. *Russ. Meteorol. Hydrol.* **47**, 50–58 (2022).
16. Libin, I.Ya., Perez, P., Oleinik, T.L., Prudnikova, R., Treiger, E.M.: Possible impact of global climate change on social processes and the Russian economy. *International Journal of Applied and Fundamental Research.* **9**, 105–108 (2013).
17. Matveeva, T.A., Gushchina, D.Y. & Zolina, O.G. Large-scale indicators of extreme precipitation in coastal natural-economic zones of the European part of Russia. *Russ. Meteorol. Hydrol.* **40**, 722–730 (2015).

18. Meredith, E.P., Semenov, V.A., Maraun, D., Park, W., Chernokulsky, A.V.: Crucial role of Black Sea warming in amplifying the 2012 Krymsk precipitation extreme. *Nature Geoscience*, **8**, 615-620 (2015).
19. Perevedentsev, Y.P., Vasil'ev, A.A., Sherstyukov, B.G. *et al.* Climate Change on the Territory of Russia in the Late 20th–Early 21st Centuries. *Russ. Meteorol. Hydrol.* **46**, 658–666 (2021).
20. Report on climate risks in the Russian Federation. St. Petersburg, ed. V.M. Kattsov, (2017). [in Russian]
21. Zolina, O.G., Bulygina, O.N.: Modern climatic variability of extreme precipitation characteristics in Russia. *Fundamental and applied climatology*, **1**, 84–103. (2016) [in Russian].

Formation of Migration Flows Under Conditions of Global Climate Change



M. B. Ashabokova 

Abstract *Object:* to analyze the mechanisms of the impact of climate change on demographic processes and to determine methods for reducing their consequences for the demographic state of society. *Methods:* review of literature data on the results of analysis and forecast of climate change, as well as its consequences for human health. Also, analysis of the influence of other global factors on the demographic state of society. *Results:* the analysis of the problem of adaptation to climate change of demographic processes was carried out. *Conclusions:* under the influence of climatic factors, powerful migration flows from the islands and coastal zones of the oceans will be formed. Due to the rise in the level of the world ocean and the increase in the power of hurricanes, the likelihood of the disappearance of island nations in the oceans will increase significantly. Also, under the influence of these phenomena, there will be an expansion of the area of the coastal zone along the oceans with unfavorable living conditions. With the frequent and intense impact of these factors, the flows that will be directed to neighboring countries that are less affected by these factors.

Keywords Changing of the climate · Agriculture · Agro-industrial complex · Adaptation · Goals, objectives of the adaptation plan · Information support · Methods and results of the solution

1 Introduction

The climate of the earth in recent decades has been changing at an unprecedented rate and is becoming a factor that can have a tremendous impact on processes in society and the natural environment. It already affects the natural environment, various fields of activity, people's health and demographic processes, and so on. To resist this global factor, if effective and urgent measures are not taken, neither society nor the global ecological system is able to. Stabilization of the concentration of greenhouse gases

M. B. Ashabokova (✉)

High Mountain Geophysical Institute, Lenin Ave., 2, 360002 Nalchik, Russia
e-mail: ashabokova.marina@rambler.ru

© The Author(s), under exclusive license to Springer Nature Switzerland AG 2023
R. Zakinyan and A. Zakinyan (eds.), *Physics of the Atmosphere, Climatology and Environmental Monitoring*, Springer Proceedings in Earth and Environmental Sciences, https://doi.org/10.1007/978-3-031-19012-4_8

in the atmosphere at levels that would prevent dangerous anthropogenic impact on the climate and adaptation of various fields of activity to its change are currently considered as such measures [8].

This global factor will also have a tremendous impact on the demographic state of society, both on a local and global scale, and there are a lot of mechanisms for the influence of this factor on demographic processes [20]. This is connected with the fact that at present there is an urgent need to study these mechanisms and develop methods to reduce their consequences for the demographic state of society. It should be noted that in recent years there has been a noticeable increase in attention to this problem.

2 Literature Review

Global warming of the Earth's climate has become a factor that can have a tremendous impact on the processes taking place in society and in the natural environment, on human health and demographic processes. An extremely large number of works by both foreign and domestic scientists are devoted to the study of climate change. One of the first climatologists, who for the first time predicted global warming due to the emission of anthropogenic carbon dioxide into the atmosphere, is considered the American climatologist Hansen [8]. Works [1, 7, 12, 17, 20] and others are devoted to the study of climate change in Russia. Climate change is already having a noticeable impact on various areas of activity, on the natural environment, on human health, and on demographic processes [3, 4, 7, 9, 19]. In this regard, attention to the study of the consequences of this factor for various fields of activity and the environment, to the development of methods to reduce the risks associated with it is constantly increasing. Of the works in this area of research, the works [2, 13, 16] can be noted. Reference [2] outlines one approach to reducing risks in agriculture associated with extreme weather events. It was developed within the decision theory [2]. They are expected to be especially significant for mountain areas. Moreover, there are quite a lot of mechanisms of influence of this factor on the spheres of activity in these areas, and the main of them can be considered the influence through dangerous slope processes (avalanches, mudflows, rockfalls, etc.). It is important to note that to resist the impact of climate change, if scientifically sound and urgent measures are not taken, neither society nor the global ecological system is able, its consequences can be catastrophic [9]. This is related to the fact that the goal of the Paris Climate Conference (2015) was to develop an agreement that would allow at the first stage to slow down climate warming, and then stop it. As such measures, the conference proposed stabilization of the content of greenhouse gases in the atmosphere at levels that would prevent dangerous anthropogenic impact on the climate, and adaptation of various systems to its change [9, 12].

We also note that climate change is not the only global factor that has influenced society and the environment. Such factors are environmental pollution, the depletion of the planet's resources and the rapid growth of the world's population. Modeling

the consequences of these factors for the development of society has shown that they will be extremely serious [5, 6, 14, 15]. It should also be noted that the coincidence of the global demographic transition that has been going on for a number of years [10, 11] with the emergence of the noted factors can lead to a significant increase in the negative impact of these factors on demographic processes.

3 The Impact of Climate Change on Demographic Processes

The report of the Intergovernmental Panel on Climate Change (IPCC) notes that in the next two decades, global temperatures are likely to rise by 1.5 °C and exceed the key goal of the Paris Agreement, which is considered critical to reduce the risk of climate catastrophe [12].

As for demographic processes, the study of the direct impact of climate change on them encounters serious difficulties associated with the limited or even lack of necessary information. This is due to the lack of information about the impact of this global factor on demographic processes (on such indicators as fertility and mortality rates), and the difficulty of collecting such information. The exception can be considered the impact of climate change on migration processes, which can be estimated in various ways, but even in this case it is possible to estimate it rather approximately.

In our opinion, it may be promising to use for this purpose the results of an analysis of the influence of this factor on people's health, although even in this case it cannot be said that all the mechanisms of its influence on this indicator fully studied or even understood at a qualitative level. Therefore, the present period of time can be considered a period of accumulation of information and knowledge about the impact of climate change on human health and demographic processes.

To assess the influence of environmental factors on demographic processes, let us dwell on some features of the current stage of the development of society, which qualitatively distinguish it from all previous stages.

One of these features can be considered the fact that for the first time in the history of its development, society was under the influence of a complex of global factors that pose a threat not only to development, but also to the existence of modern civilization [8]. Such factors are: environmental pollution, depletion of the planet's resources, population growth and global warming. It should be noted that in the history of the development of modern civilization, situations have repeatedly arisen when it was influenced by a combination of factors (natural disasters, crises, wars, epidemics, climate change, etc.). But such a situation, when her existence was threatened, and, through her own fault, arises for the first time. The noted factors were local in nature and could not affect global development, nature itself was able to recover from external influences. Therefore, the assessment of the consequences of the global factors noted and the development of effective methods to reduce the risks associated with them have become extremely relevant problems.

Another feature of the current stage of the development of society is that the present period of time can be considered a period of global demographic transition: society is transitioning to a qualitatively new demographic state. This process began in the 60s of the twentieth century: trends appeared in demographic processes indicating the beginning of fundamental changes. Moreover, such a transition is carried out with a simultaneous decrease in mortality and fertility. The duration of the transient process, as noted in [2, 9], is determined by the double duration of the characteristic time of a person's life (40–45 years), i.e., the demographic transition will last about 80–90 years (until 2040–2050). In many economically developed countries, the demographic transition can be said to have already been completed, and in most developing countries this process is either beginning or ongoing.

It should be noted that this demographic transition has an important feature: it was influenced by the noted global factors, which can qualitatively change the natural course of this process. Therefore, the consequences of the noted global factors for the future demographic state of society may turn out to be unpredictable. Especially this is concerns consequences changes climate. In this regard, due to the importance of the demographic state of society (population size, its structure, etc.), which determines the possibility of ensuring the conditions for its development in the impending extremely harsh conditions, the relevance of research in these areas is constantly increasing.

The possible consequences of the noted global factors for the demographic state in the world can be judged by the results of modeling their influence on world dynamics. Figure 1 shows a scenario for the global development of society, taking into account the influence of the first three of the noted factors: environmental pollution, depletion of the planet's resources, and an increase in the population of the Earth [13]. It can be noted that, starting approximately from the middle of this century, a rapid drop in all indicators is expected, including the population of the Earth.

Such studies were also carried out by other authors, for example, the authors of [1, 18]. Note that the results obtained in these works agree with each other. They

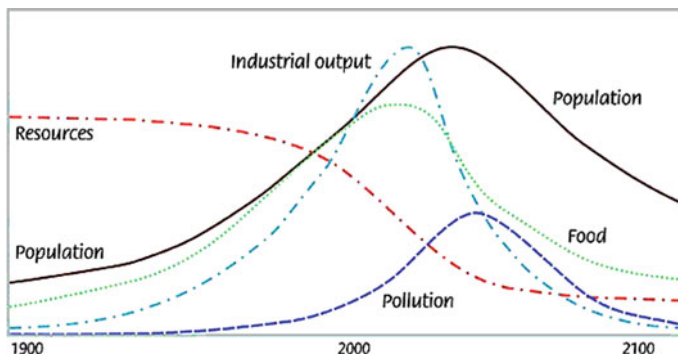


Fig. 1 One of the scenarios of world dynamics, taking into account the influence of the first three factors, obtained as a result of modeling

show that unless urgent and effective measures are taken, the end of our civilization is inevitable.

Obviously, when taking into account the impact of climate change, the consequences of which for world dynamics will be much more serious than the factors listed, the rate of decline in the indicators of development of society will be even more significant than in the case in Fig. 1.

As for the trend in the growth of the population of the Earth, then, as you can see in the figure, it will change to the opposite under the influence of global factors. But due to the fact that the ability to withstand global challenges and provide conditions for the development of society depends on the size and quality of the population, maintaining demographic indicators at the minimum required level will apparently become a serious problem.

Let us dwell on the mechanisms of the influence of climate warming on demographic processes. The effects of climate change may be related [12]:

- with “slow” climate changes (temperature regime, precipitation regime, greenhouse gas content in the atmosphere, etc.);
- with adverse weather events, the frequency and intensity of which are increasing due to climate warming.

It is important to keep in mind that the gradual warming of the climate will result in an increase in the number of global factors that will oppose the development of society and have a serious impact on the demographic situation on various scales. As an example, the following factors can be noted, which, if action is not taken, will be added to those noted above:

- a shortage of fresh water, which is aggravating rapidly and covering new territories;
- activation of existing dangerous infectious diseases, expansion of the habitat of their carriers, the emergence of new species;
- large-scale migration flows that will be shaped by climate change.

Regarding the shortage of fresh water, it should be noted that it will directly affect the economy in many regions of the planet and, above all, the industries producing and processing agricultural products, which cannot but affect human health and demographic processes. In addition, the lack of quality drinking water will have a direct impact on human health and thus on demographic indicators (fertility and mortality) and migration processes.

Of particular danger to the countries of northern latitudes (including Russia) is the thawing of permafrost [12, 14], which is accelerating. It can lead to the destruction of buildings and structures, roads, pipelines. It will also lead to air, soil, water pollution, which cannot but affect the health of the population and demographic processes. In addition, in these regions, the probability of destruction of water supply and sewerage and other engineering communications will increase, which will be one of the reasons for the mixing of rainwater and wastewater and, as a result, the growth of dangerous bacterial infections. Taking into account the negative consequences of permafrost thawing for the economy of the region and the country as a whole, it is highly likely

that there will be a need to evacuate the population from these regions. Obviously, the consequences of these processes for the health of the population and the demographic state of these regions and the country will be negative.

We also note that the present moment in time may be the beginning of the emergence of an extremely dangerous global factor. It will be due to the fact that as a result of climate warming, as noted, the activation of dangerous infectious diseases is taking place. One of the sources of carriers of these diseases is the thawing of permafrost and glaciers, which will result in the release of carriers of such diseases that have been in them for thousands of years, to which a modern person may completely lack immunity. Thus, in the future, severe infectious diseases like COVID-19, apparently, will be constant companions of mankind. This factor, in the absence of effective methods of confrontation, will significantly affect people's health, the demographic state of society and, in general, the development of society.

Thus, we can say that under the influence of the mentioned factors, demographic processes at all levels will change qualitatively, which will lead to the same changes in the number and structure of the population. The trend in the dynamics of the Earth's population will be reversed. Because of the fact that the possibilities of development of society and of coping with global challenges depend on the number and quality of the population, maintaining demographic indicators at a certain level may become an extremely urgent problem.

4 The Mechanisms of the Influence of Climate Change on Migration Processes

Let us dwell further on the migration flows that will be formed under the influence of climate change. The most powerful of them will be sent from the coastal zones of the continents, from islands in the oceans, from mountainous areas that, due to climate change, may become dangerous or even uninhabitable, from areas where there will be no fresh water, etc. We are talking about the migration of not one or two million people, but hundreds of millions (according to the UN, at least 1 billion people). Obviously, the consequences of migration processes will be extremely serious. They will influence the structure and national composition of the population of many regions of the planet, their socio-economic structure. They can cause large-scale armed conflicts.

As noted, climate change will affect the demographic state of society in numerous ways [10, 11]. Many of them are insufficiently studied, there are those that have not yet shown themselves. Therefore, let us briefly dwell on the formation of migration processes under the influence of extreme weather events, the frequency and power of which, as noted, increase due to climate change (the second mechanism of the impact of climate change on processes in society and the natural environment). This

is evidenced by data on the number of these phenomena in 1980–1999 and 2000–2019. If the number of these phenomena in the first of these periods of time was 3656, in the second it increased to 6681 [15].

It can also be noted that in the period of time 2000–2019. 7348 major natural disasters were recorded, which claimed the lives of 1.23 million people, the total number of victims of these events reaches 4.2 billion people (many of them more than once), and the economic damage from them amounted to about 2.97 trillion USD USA.

For comparison, here are some data on the consequences of these phenomena for 1980–1999: 4212 natural disasters were registered, the death toll was approximately 1.19 million people, the total number of victims was about 3.25 billion people, total economic damage 1.63 trillion USD USA.

This has led to the fact that the damage from these events has now significantly exceeded the ability of the world community to provide assistance to the victims.

As for the Russian Federation, the number of extreme weather events on its territory increases annually by 6–7%. Direct and indirect damages from them amount to 4–5% of the gross national product, i.e., they amount to trillions of rubles annually [14].

Such a trend of changing the characteristics of these phenomena and their consequences cannot but negatively affect the development of various fields of activity and society as a whole, migration processes and the demographic structure of society. This also applies to areas such as health care, agricultural and food production and other areas of activity that have a direct impact on public health and demographic processes [5, 6, 11].

It is believed that in the future the nature of the development of socio-economic systems at all levels will be determined by the consequences of these phenomena.

The most powerful migration flows under the influence of these phenomena will be formed from the islands and coastal zones of the oceans. The reason for this would be that due to rising sea levels and increasing hurricane power, the likelihood of island nations disappearing from the oceans is greatly increased. In the same way, under the influence of these phenomena, there will be an expansion of the coastal zone along the oceans with unfavorable living conditions.

We have assessed the characteristics of migration processes in the Western Pacific, including islands located in the ocean. At the same time, data on the population of the countries indicated in Table 1 were used.

According to our estimates, migration processes in this region will cover a significant part of the population of these countries—at least 150–200 million people. These processes will be especially acute in the PRC, where practically the entire population occupies about half of the country's territory. In addition, many large cities of the country are located on the coast (Table 2), which significantly increases their vulnerability to extreme weather events.

Note that the scale of migration flows will be determined by the nature of the impact of climatic factors on these cities. With the frequent and intense impact of

Table 1 Population in the countries of the Western Pacific

Country	Population, persons
Japan	126,340,199
Philippines	112,659,031
Papua New Guinea	9,281,845
Australia	26,230,534
Indonesia	279,760,056
Malaysia	33,235,652
Cambodia	17,199,667
Laos	7,487,838
Thailand	70,290,274
Myanmar	55,206,409
China	1,452,857,665
South Korea	51,792,304
North Korea	26,021,261
New Zealand	4,878,521
Taiwan	23,902,428

Table 2 Population of Chinese cities located on the coast

Country	Population, persons
Hainan	10,081,232
Guangzhou	13,839,587
Zhanjiang	6,900,000
Shantou (Swatow)	4,312,192
Xiamen (Amoi)	3,707,090
Fuzhou	3,671,192
Ninping	2,890,000
Wenzhou	3,604,446
Shanghai	20,242,992
Suzhou	4,330,000
Qingdao	5,818,255
Yantai	2,511,053
Tianjin	13,929,152
Jingzhou	3,000,000
Dalian	5,871,474

these factors, the flows that will be directed to neighboring countries that are less affected by these factors. The probability that these flows will affect the territory of Russia is quite high.

5 Conclusions

Analysis of the effects of global factors, including global climate change, on societal development. As the results of studies have shown, the consequences of these factors for the demographic state of society will be negative. In addition, as a result of climate warming, there are increased opportunities for the emergence of new global factors, the impact of which on demographic processes will be negative. These include such factors as the formation of large-scale migration processes from those regions of the planet in which natural conditions will make the conditions in them unsuitable for living. The most important of these factors is climate warming, under the influence of which there is an increase in the frequency and destructive power of dangerous weather phenomena. These factors include the activation of existing dangerous infectious diseases, the expansion of the habitat of their carriers, the emergence of new species. Therefore, the development of scientifically based methods to reduce the consequences of the noted factors becomes relevant for ensuring the development of society.

References

1. Ashabokov, B.A., Fedchenko, L.M., Tashilova, A.A., Kesheva, L.A., Teunova, N.V.: Space natural-temporal climate change in the south of the European territory of Russia, assessment of its consequences, methods and models of adaptation of the agro-industrial complex. Nalchik, Fregat LLC, (2020) [in Russian].
2. Ashabokov, B.A., Fedchenko, L.M., Tashilova, A.A., Shapovalov, A.V., Khavtsukov, A.Kh., and Balkarova, S.B.: «Modeling Risk Reduction in Agriculture Associated with Dangerous Agrometeorological Phenomena» in International scientific and practical conference AgroS-MART.—Smart solutions for agriculture, KnE Life Sciences, 223–231 (2019) [in Russian].
3. Belova, V.A., Larina, E.S.: Demographic consequences of global climate change for Russia in XXI century.—Regional effects of global climate change (causes, consequences, forecasts)//Proceedings of the international scientific conference, Voronezh, June 26–27, 375–377 (2012) [in Russian].
4. Carly Ray and Xue Ming: Climate Change and Human Health: A Review of Allergies, Autoimmunity and the Microbiome. *Int. J. Environ. Res. Public Health*, **17**(13), 4814 (2020).
5. Egorov, V.A., Kallistov, Yu.N., Mitrofanov, V.B., Piontkovsky, A.A.: Mathematical models of global development. *Gidrometeoizdat, Leningrad* (1980) [in Russian].
6. Forrester J.: *World dynamics*. Wright-Allen Press (1971).
7. Grishchenko, I.V.: Observed climate change and its impact on public health in the Arkhangelsk region. Abstracts of the reports of the international scientific conference on regional problems of hydrometeorology and environmental monitoring. Kazan, October 2–5, 123 (2012) [in Russian].
8. Hansen, J., Sato, M., Ruedy, R., *et al.*: Dangerous human-made interference with climate: a GISS model study. *Atmos. Chem. Phys.* **7**, 287–312 (2007).
9. IPCC 2014: *Climate Change 2014: Synthesis Report*. Contribution of Working Groups I, II and III to the Fifth Assessment Report of the Intergovernmental Panel on Climate Change [core group of authors, R.K. Pachauri and L.A. Meyer (ed.)]. Geneva, Switzerland, (2014).
10. Kapitsa, S.P.: Demographic transition and the future of mankind. *Bulletin of Europe* **21** (2007).
11. Kapitsa, S.P.: Population Growth as a Global Problem//Global Environmental Problems at the Turn of the 21st Century. Ed. A. L. Yanshin. Nauka. Moscow (1998) [in Russian].

12. Kattsov, V.M., Semenov, S.M.: The Earth's Climate: Drivers of Change and Causes of Concern. The second assessment report of Roshydromet on climate change and its consequences on the territory of the Russian Federation. Moscow, 10–17 (2014) [in Russian].
13. Kelly, P.M., Adger, W.N.: Theory and practice in assessing vulnerability to climate change and facilitation adaptation. *Climate Change*, **47**, 325–352 (2000).
14. Malkov, S.Yu., Markova, A.A.: Impact of climate change on global demographic dynamics: statistical analysis of empirical data. *History and Synergetics: Mathematical Models of Social, Economic and Cultural Dynamics*/Ed. ed. S.Yu. Malkov, A.V. Korotaev. 2nd ed., rev. and additional—M.: KomKniga, 49–75 (2010) [in Russian].
15. Meadows, D., Randers, J., Meadows D.: *Limits to Growth. 30 years later*. Akademkniga. Moscow (2007) [in Russian].
16. Nikiforova, A.: UN: the number of natural disasters has doubled in 20 years and this is not the limit//Hitech. 2020 URL: <https://hitech.fm/2020/10/13/climate-disasters> (2021).
17. Report on climate features in the territory of the Russian Federation for 2017. Moscow: Roshydromet. (2018) [in Russian].
18. Taha, H.A.: *Operations Research. An Introduction*. Pearson (2017).
19. Zholudeva, V.V.: Statistical assessment of the impact of climate change on social and demographic processes (on the example of the Yaroslavl region). *Statistics and Economics* **16**(6), 57–66 (2019).
20. Zolina, O.G., Bulygina, O.N.: Modern climatic variability of extreme precipitation characteristics in Russia. *Fundamental and applied climatology*, **1**, 84–103. (2016) [in Russian].

The Modern Climate of Pyatigorsk Resort



G. Kh. Badakhova, M. V. Barekova, V. I. Volkova, Yu. L. Smerek,
and G. L. Kaplan

Abstract The problem of climate change is currently attracting the attention of specialists in various scientific branches. The great interest is the analysis of the consequences of climate change on the development of various sectors of the economy. For balneology, this problem is also relevant, since the climate is often one of the important therapeutic factors in resort regions. Pyatigorsk, along with other cities of the ecological resort region Caucasian Mineralnye Vody, is famous not only for its mineral water sources, but also for its healing climate. However, systematized data on the climate of Pyatigorsk are contained only in issues of the Handbook on the Climate of the USSR and refer to the observation period up to 1966. Due to the climate changes taking place on the planet, these data, of course, are outdated. This article is devoted to the study of the current climate and the temporal dynamics of changes in the main climatic characteristics of the Pyatigorsk resort. The article describes modern climate and the temporal dynamics of the change of major climatic characteristics of Pyatigorsk resort. Data on the temperature regime, precipitation regime, snow cover, wind, as well as data on the frequency of adverse and dangerous weather phenomena are analyzed.

Keywords Pyatigorsk resort · Modern climate · Balneology · Climatic characteristics

G. Kh. Badakhova (✉)
Stavropol Hydrometeorology and Environmental Monitoring Center, 53B Kulakov Av, 355047
Stavropol, Russia
e-mail: badahovag@mail.ru

M. V. Barekova
High-Mountain Geophysical Institute, 2 Lenin Av., 360030 Nalchik, Russia

V. I. Volkova · Yu. L. Smerek
North-Caucasus Federal University, 1 Pushkin str., 355014 Stavropol, Russia

G. L. Kaplan
Terra Space Lab, 6 Reading str., Tel-Aviv, Israel

1 Introduction

Pyatigorsk is one of the oldest resorts in Russia, the date of its foundation is considered 1780. In 1717 Peter I sent the first special expedition to the Caucasus to study and describe the healing waters in the land of Beshtaugorian Circassians. In 1773 was published a detailed scientific description of Pyatigorye and its healing factors. In 1780 on the place of present-day Pyatigorsk a fortress Konstantinogorsk was built. In the healing springs were taken baths, but the water was not drunk, because their properties had not been studied. In 1809 Dr. F. P. Gaaz discovered the Elizavetinsky spring. He studied the composition of its waters and waters of other springs and determined their therapeutic properties. Since 1809 the mineral waters of the Caucasus began to be drunk for medicinal purposes [10].

Gaaz described his research in his book [13]. He devoted two chapters to the description of flora and climate of Alexander waters. He wrote down all weather contrasts in his diary of meteorological observations. Leaving the Caucasus, Gaaz left his instruments with the Scottish colonists: barometer, thermometer and weathervane. And one of the colonists, Peterson, began to conduct meteorological observations. Gaaz set up a similar barometer in Georgievsk with Wilhelms, a pharmacist in the pharmacy. Peterson and Wilhelms sent Gaaz the results of their observations. F. P. Gaaz can be safely called not only the pioneer of regular meteorological observations in the Caucasian Waters, but also the first climatologist of this region.

In the middle of XIX century the systematic study of the Pyatigorsk resort began. A great contribution to the study and systematization was made by F. A. Batalin [7]. He described in detail Lake Proval and its thermal waters, discovered several new springs. In addition, F. A. Batalin made, albeit very brief, a description of some elements of the climate of the resort. Thanks to these researches, Pyatigorsk became a balneological and mud resort of national importance.

In Soviet times, within this oldest recreational area of Russia a unique system of balneological resorts (Pyatigorsk, Kislovodsk, Essentuki, Zheleznovodsk) was formed, unequalled in the volume of recreational activities, traditions, experience in organizing spa treatment, scientific research in the field of balneology.

2 Materials and Methods

The present study was based on the weather observation data recorded by weather station Pyatigorsk in 2001–2020 and data from the Handbook on the Climate of the USSR [15–17]. Meteorological data for some years [26] and some other publications [9, 11]. In the process of analysis basic statistical characteristics of meteorological parameters were calculated: average, maximum and minimum values for different time periods, recurrence and duration of the phenomena, as well as changes in the characteristics of their regime and trends of these changes. The study based on physical-statistical and regression analysis methods [23].

Trends of current variations in climatic parameters are analyzed. The characteristic of prevailing tendency of long-term air temperature variations are given. The trend of the average air temperature is estimated by the regression analysis. The obtained trends of air temperature, precipitation total and frequency of different weather events are clearly revealed.

3 Analysis and Discussion

Air temperature. The average annual temperature in Pyatigorsk is about 10 °C. The frost-free period lasts more than 200 days, early autumn frosts are usually short and shallow, and late spring frosts are most often isolated cases of a very weak frost in the second or third decade of April [3].

Winter is generally comfortable enough. Very severe frosts at the resort does not happen. The average winter temperature is +0.2 °C. The coldest winters were in 2008 and 2012, when the average minimum temperature of the three winter months was –6.4 and –6.8 °C, respectively. The warmest winter months were in 2010, with an average maximum temperature of 17.3 °C for the period. Table 1 shows average and extreme temperature characteristics of winter months for 2001–2020.

During the winter there are an average of 70 days with a minimum air temperature below 0 °C (and another 20 days outside the calendar winter). However, there are few really cold days: only 8 days with minimum air temperatures below –10 °C are recorded on average (actually, from 13 days in 2008 to the absence of such low temperatures in seven of the 20 years under consideration). The average monthly number of days with the minimum temperature below –15 °C is 1–2 days in January (actually—from 9 days in 2008 to none in 11 years of the period), 1 day in February (from 9 days in 2012 to none in 15 of 20 years), in December in 2002 there were 6 such days, and no more temperatures below –15 °C in the new century. The thermometer dropped below –20 °C three times in January 2006 and twice in January 2014, and three times in February 2012 and once in February 2014. The thermometer fell to –25 °C on February 7 and 8, 2012, but the frost did not reach the level of dangerous phenomena [5, 28].

Table 1 Temperature characteristics of calendar winter

Air temperature, °C	December	January	February	Winter
Average maximum	4.3	2.6	4.0	3.6
Average minimum	–2.5	–3.9	–3.1	–3.2
Absolute maximum	19.1	16.7	22.9	22.9
Absolute minimum	–19.5	–22.2	–25.6	–25.6
Average of absolute highs	14.8	12.2	16.2	14.4
Average of absolute minima	–10.0	–11.4	–12.0	–11.1

Table 2 Temperature characteristics of calendar spring

Air temperature, °C	March	April	May	Spring
Average maximum	9.3	15.4	21.5	15.4
Average minimum	1.3	5.7	11.8	6.3
Absolute maximum	30.0	30.1	32.5	32.5
Absolute minimum	−11.5	−7.7	0.8	−11.5
Average of absolute highs	20.6	24.8	29.0	24.8
Average of absolute minima	−5.7	−0.8	6.1	−0.1

During the winter months, there are an average of 36 days with maximum air temperatures above 5 °C, 14 days with temperatures above 10 °C, and 3 days with temperatures above 15 °C.

It should be noted that the meteorological winter (the period between the steady transition of the average daily air temperature through 0 °C down and up) in Pyatigorsk is much shorter than the calendar winter. On average, it lasts less than 70 days in the new century, from December 15 to February 19. This is due to changes in the atmospheric circulation regime during transient periods [24, 33] and an increase in air temperature, including in the winter period [4].

Spring. The average spring temperature in Pyatigorsk is about 11 °C, ranging from 5.3 °C in March to 16.7 °C in May. The amplitude of recorded air temperature values exceeds 40 °C (Table 2). On average, there are 14 days during the calendar spring when the minimum air temperature was below 0 °C. Of these, 12 days occurred in March, and in 20 years in March there were five days with minimum air temperatures below −5 °C and one day with temperatures below −10 °C. However, the maximum temperatures in March are positive for 26 days, with 16 days of air warming to 5 °C or higher. In a month there are on average 9 days with maximum air temperatures above 10 °C and 3 days with temperatures above 15 °C. On March 24, 2008, a record temperature of 30.0 °C was registered for March.

The average monthly temperature in April is about 11 °C. In April, there are 1–2 days on average with subzero minimum temperatures, the maximum daily temperatures are always positive and usually (28 days per month) are above 5 °C. During the month there were 23 days with maximum air temperatures above 10 °C and 12 days with temperatures above 15 °C.

May is almost a summer month in Pyatigorsk. Negative temperatures were not recorded in the new century in May. The minimum temperatures fell below 5 °C only in the first 10 years of the new century, below 10 °C they fall only for 8 days. Days with a maximum temperature of 15 °C and above in May averaged 25, with a temperature of 20 °C and above—15. In 7 of the 20 years analyzed, temperatures above 30 °C were recorded in May.

Summer. The summer weather is also quite comfortable, without long periods of heat, strong winds and prolonged rain. The average summer temperature is 22.1 °C. July is the hottest month, while June is the coolest (Table 3). Of the 92 days of the

Table 3 Temperature characteristics of the calendar summer

Air temperature, °C	June	July	August	Summer
Average maximum	26.1	29.5	30.1	28.6
Average minimum	15.8	18.4	18.4	17.5
Absolute maximum	36.7	40.6	39.2	40.6
Absolute minimum	6.0	9.5	10.3	6.0
Average of absolute highs	32.5	35.8	36.1	34.8
Average of absolute minima	10.8	13.5	13.6	12.6

calendar summer in Pyatigorsk there are an average of 74 days with a maximum air temperature of 25 °C and above, 36 days with a maximum air temperature of 30 °C and above, and 8 very hot days with a maximum air temperature of 35 °C and above. Despite the rather strong daytime heating, nighttime temperatures fall below 20 °C almost daily.

The first month of summer is the least hot. Every year in June there are an average of 26 days with a minimum daily temperature below 20 °C. The air only warms up to 25 °C for 19 days. There are only five hot days in a month when the maximum air temperature rises to 30 °C and above, and only one very hot day with a maximum daily temperature of 35 °C and above.

July is traditionally considered the “peak” of summer, the hottest month of the year. Nevertheless, in July, on average, the thermometer will drop below 20 °C for 23 nights. As for the daytime temperatures in July, the temperature usually exceeds 25 °C for an average of 27 days during the daytime, the thermometer reaches 30 °C every year for 14 days, and there are 2–3 days per month when the temperature rises to 35 °C and above, but the highest number of days was in 2007—11 days. There have been a total of 54 such hot July days in 20 years. On July 31, 2015, the absolute maximum temperature of 40.6 °C was recorded in Pyatigorsk.

Since the mid-1990s there has been a pronounced tendency for August temperatures to rise [5], and in the new century August has become the hottest month in Pyatigorsk. In August, there are an average of 28 days with maximum daily temperatures above 25 °C. There are an average of 17 hot days per month when the thermometer goes over 30 °C. There have been 73 very hot days, with temperatures reaching 35 °C and above in 20 years, which is considerably more than in July, traditionally the hottest month of the year. In the second decade of the new century, heat waves were more frequent than in the first [21].

Autumn. The autumn period in Pyatigorsk is characterized by a fairly comfortable temperature regime. The average autumn temperature exceeds the average spring temperature and is almost 14 °C (Table 4).

September is essentially still a summer month, with average temperatures around 20 °C. Even the minimum temperatures dropped below 5 °C only 5 times in 20 years. On average, maximum temperatures exceeded 15 °C for 27 days, 20 °C for 17 days, and 25 °C for 6 days. Absolute maximums exceeded 30 °C in 17 years of the period

Table 4 Temperature characteristics of calendar autumn

Air temperature, °C	September	October	November	Autumn
Average maximum	24.5	16.7	9.2	16.8
Average minimum	13.7	8.0	2.0	7.9
Absolute maximum	38.3	32.3	24.7	38.3
Absolute minimum	1.0	-7.5	-15.7	-15.7
Average of absolute highs	32.9	27.4	19.9	26.7
Average of absolute minima	7.1	0.4	-5.5	0.7

under consideration. In 20 years, about 40 days with maximum daily temperatures of 30 °C and above were recorded.

October is already autumnal month, but with a very comfortable and suitable weather for the resort: the average temperature is about 14 °C, in addition, in October, as a rule, there is the so-called “Indian summer”. In 20 years, there were only 25 cases when the minimum temperature dropped to negative values, while in 11 years of the period under consideration there were no such low temperatures. But the maximum temperatures exceed 10 °C for 23 days, exceed 15 °C for 12 days, and exceed 20 °C for 4–5 days.

November is naturally the coldest of the fall months. The average monthly temperature is about 6 °C. Negative minimum temperatures are recorded for 8 days on average, but maximum temperatures are positive almost all month (27 days on average), exceeding 5 °C for 20 days, 10 °C for 8 days and exceeding 15 °C 2–3 times a month. Temperatures rise above 20 °C on average 3–4 times a month in November, but in 2001 there were 14 such warm days.

Atmospheric precipitation. There is an average of 605.6 mm of precipitation in Pyatigorsk throughout the year. The largest amount of precipitation in the new century was in 2016—775.2 mm, the least in 2006—418.5 mm, which is respectively 128% and 69% of the climatic norm, i.e. the values of anomalies are relatively small and almost identical.

An average of 159 days of precipitation are recorded per year, with the highest annual number of days being 176 (2008) and the lowest being 138 (2019 and 2020). The discrepancy is half as large as the discrepancy in precipitation amounts and is 111% and 87%, respectively, i.e., it is also within the same limits.

Warm period of the year (April–October) accounts for 73.3% of annual precipitation (445.5 mm), while cold period (November–March) accounts for 26.7% (160.1 mm). Days with precipitation averaged 92 in the warm period and 67 in the cold period.

The difference in the distribution of precipitation is more noticeable by season (Table 5). Annual precipitation is distributed as follows: winter—13%, spring—30%, summer—35%, autumn—22%.

Although average seasonal precipitation amounts vary widely, the number of days with precipitation varies very little from season to season. Naturally, this causes

Table 5 Seasonal characteristics of the precipitation regime

Characteristics of the precipitation regime	Winter	Spring	Summer	Autumn
Average seasonal amount of precipitation, mm	80.3	181.7	208.7	134.9
Maximum seasonal amount of precipitation, mm	116.3	286.5	381.0	252.0
Least seasonal amount of precipitation, mm	31.2	111.2	58.6	49.4
Maximum daily precipitation, mm	17.6	37.0	93.6	60.7
Average seasonal amount of days with precipitation	40	44	38	37
Highest seasonal number of days with precipitation	53	53	49	51
Lowest seasonal number of days with precipitation	28	28	29	26

marked differences in the average daily precipitation per day with precipitation (the so-called precipitation density). Thus, in winter the average rainfall per day is 2.0 mm, in spring—4.1 mm, in summer—5.5 mm, in autumn—3.6 mm.

During 20 years of the new century in Pyatigorsk there were 21 cases of monthly sum of precipitation more than 100 mm (7 cases each in May and June) and 4 cases with monthly sum of precipitation more than 200 mm (1 in May, 3 in June) [20]. During this period, there were also 13 cases when monthly precipitation did not exceed 10 mm, of which six cases were in winter, five in autumn and one each in spring and summer.

The amount of precipitation in winter is almost equally distributed on a monthly basis: January—24.9 mm, February—24.6 mm, December—30.8 mm. January and February account for only 4% of annual precipitation. The highest and lowest monthly precipitation amounts differ more markedly. Thus, the highest monthly precipitation is 46.0 mm in January, 69.1 mm in February, and 71.3 mm in December. Minimum monthly precipitation was 8.5 mm in January, 5.0 mm in February, and 5.1 mm in December. Absolute maximum daily precipitation is 16.6 mm in January, 16.1 mm in February, and 17.6 mm in December.

On average, there are 40 days of precipitation during the calendar winter in Pyatigorsk, with 18 days of rain. Days with precipitation in the winter months are almost equal: 14 in January and 13 each in February and December. The greatest number of days with precipitation in 20 years: in January-22, in February-19, in December-21. The lowest number of days with precipitation in 20 years: in January-7, in February-8, in December-5.

The richest spring month is May, with 84.5 mm of precipitation (47% of spring precipitation and 14% of annual precipitation). In March it falls 42.9 mm, in April 53.4 mm. The highest and lowest precipitation totals were: March—107.0 mm and 13.3 mm; April—95.3 mm and 21.1 mm; May—202.5 mm and 24.2 mm. The average monthly number of days with precipitation is 14 in March and April and 16 in May. The highest and lowest number of days with precipitation are 21 and 10 in March, 19 and 6 in April, and 22 and 6 in May, respectively.

The rainiest month is June, which accounts for half of the summer rainfall (17% of the annual amount)—101.7 mm. Next is July—65.2 mm, then August—39.7 mm.

The highest and lowest monthly precipitation totals were in the same order: 264.9 mm and 11.5 mm, 140.0 mm and 11.0 mm, 101.3 mm and 4.0 mm.

In the same order is the average monthly number of days with precipitation: 15, 12 and 11, respectively. The highest and lowest number of days with precipitation were 21 and 8 in June, 20 and 4 in July, and 16 and 5 in August.

Precipitation also decreases in autumn from the first month to the third: September to September—53.8 mm, October—44.2 mm, November—36.9 mm. The highest and lowest monthly precipitation totals were: September—199.2 mm and 7.0 mm, October—90.3 mm and 3.7 mm, November—69.1 mm and 6.5 mm.

Average monthly number of days with precipitation: 12 in September and October, 13 in November. In September, the greatest number of days with precipitation - 19, the least - 3, in November-18 and 7, respectively. October recorded the largest difference in the values of this indicator for 20 years: 26 days with precipitation in 2010 and 1 day with precipitation in 2005.

Snow cover. Stable snow cover in Pyatigorsk is extremely rare. The average date for the first day of the year with snow cover is November 24, but over the winter there are on average only 45 days with snow cover: 15 days in January and 13 days each in February and December. The actual number of days with snow cover varies significantly from year to year. Thus, the least number of days with snow cover for the three months of calendar winter was recorded in 2019 and was 13 days, the greatest—72 days—was recorded in 2008. Monthly, the highest number of days with snow cover was 26 days in January (2006, 2008), 28 days in February (2012) and 28 days in December (2001). The least number of days with snow cover in January was recorded in 2005—1 day, in February there was no snow cover in 2019, in December no snow cover was formed in 2005 and 2010. The average of the highest snow cover height is 13 cm.

Wind. The average annual wind speed in Pyatigorsk is 2.8 m/s. Winter and spring are windier, with an average wind speed of 3.3 m/s during this period. During the winter months, the average wind speed is markedly similar: 3.3 m/s in February and 3.0 m/s in January and December. In spring, in March and April, the speeds are approximately the same—3.3 and 3.2 m/s, respectively, and in May the wind speed is noticeably lower and more close to the values characteristic of the summer period—2.7 m/s. Wind speeds are still decreasing in summer, reaching 2.4 m/s in June and August and 2.3 m/s in July. Wind speeds increase again in the fall: 2.5 m/s in September, 2.6 m/s in October, and 2.8 m/s in November [6].

Maximum wind speeds in all months except September exceed 20 m/s. In ascending order, the distribution is as follows: September—19 m/s, July—20 m/s, February and December—21 m/s, January and November—22 m/s, April and May—23 m/s, October—24 m/s, July—25 m/s, March and August—26 m/s.

However strong wind (with a speed of 15 m/s or more) is very rare in Pyatigorsk: on average 3 days per fall, 4 days per winter, 5 days in spring and summer, i.e. an average of 17 days per year. Monthly, the highest number of days with strong winds are as follows: 3 days each in September and October, 4 days each in January, February and November, 5 days each from May to August, 8 days each in March

and April, and 11 days in December (2015). The highest annual number of days with strong winds in the new century is 33 (2015), the lowest—9 days (2005).

Dangerous and adverse weather phenomena. According to Roshydromet criteria [28], dangerous phenomena are the following: strong heat—air temperature 40 °C and above; strong downpour—amount of precipitation 30 mm or more for 1 h or less; strong rain—amount of precipitation 50 mm or more for 12 h or less, very strong wind—wind when reaching speed in gusts not less than 30 m/s.

Hazardous weather events are very rare in Pyatigorsk at present. Thus, a heat wave as a dangerous phenomenon was recorded only once: on July 31, 2015 the thermometer reached 40.6 °C. Severe downpours of the hazardous event level were not observed during the period 2001–2020. Heavy rains were observed: in June 2002—80.4 mm, in July 2009—93.6 mm, in September 2009—60.7 mm, in June 2013—58.8 mm, in June 2016—103.0 mm. There were no very strong winds in the new century in Pyatigorsk.

Unfavorable weather events are recorded much more often. Hot days, which can be classified as unfavorable phenomena, occur quite often: on average, there are 36 days during the calendar summer with maximum air temperature above 30 °C, including 7 days with maximum air temperature above 35 °C. The hottest days are most often in August.

Fogs. Fogs occur annually in Pyatigorsk: an average of 52 days with fog per year: 40 days in the cold and 12 days in the warm period of the year. November and December are the foggiest, with an average of 9 days of fog per month. The calendar winter has an average of 24 days with fog [19]. There was not a single winter without fog during the period under review; there were no fogs only in 2002 in February and in 2015 in December. The lowest number of winter days with fog was 7 (2016), the highest was 44 (2005). Autumn has an average of 16 days with fog, ranging from 35 days in 2003 to 3 days in 2020 [27]. In spring, there is an average of 11 days with fog. No spring days with fog were recorded in 2012, while in 2006 there were 27. Over a 20-year period, there were 2 days of fog in the summer in 2002, 2003, 2005, and 2008, and 1 day in 2004. In other years, no summer fogs were recorded.

Particularly unfavorable weather conditions include long periods of prolonged, daily fog. Practically every year in Pyatigorsk there are two or three 6-day periods with daily fog. In the first decade of the new century, there were three 10-day periods and one 11-day period with daily fogs.

Snowstorms. Snowstorms are extremely rare in Pyatigorsk. In 20 winters of the new century there were only 7 days with snowstorms. In 2004 there were 2 days with a snowstorm in February, in 2006 there was 1 day in January, in 2014 there was 1 day in January, in 2018 there were 2 two days in January and in 2019 there was 1 day in February. There were no snowstorms in December, which distinguishes Pyatigorsk from the average conditions in Stavropol Krai, where the greatest number of days with snowstorms most often falls in December [19].

Thunderstorm processes. Thunderstorms in Pyatigorsk occur in the warm period of the year, from April to October. Only four thunderstorms were recorded during the

cold season in 20 years: three days in March (2004, 2013 and 2016) and one day in January (2007). There were an average 26 days with thunderstorms during the warm period. In October, there are thunderstorms once every four years; in the other months of the warm period, thunderstorms occur every year from two days in April to seven days in June. Two percent of thunderstorms are accompanied by hail.

Climate change. Comparison of the main climatic characteristics of Pyatigorsk for different long-term periods shows that global climate change has not bypassed the resort and affected both the rainfall regime and the temperature regime, and the mode of various, including unfavorable weather phenomena. Comparison of the characteristics of the precipitation regime of 1936–1955 [26] and 2001–2020 20-year periods showed that in Pyatigorsk resort there was quite a noticeable increase in the average annual amount of precipitation, which amounted to 58 mm. By seasons, these changes are as follows: an increase of 22 mm in winter, 28 mm in spring, 19 mm in autumn, and a decrease of 11 mm in summer.

It should be noted that the amount of winter precipitation at the beginning of the XXI century is 45% more than in the first half of the XX century and 10% more than in its second half (Fig. 1) [5, 12, 15, 18].

The shares of seasonal precipitation in the annual total increased by 2% in winter, by 3% in spring, and by 1% in fall; the contribution of summer precipitation to the annual total decreased by 6%. Precipitation frequency increased by an average of 11 days per year: increased by 7 days in spring, by 4 days in summer, by 2 days in fall, and decreased by 2 days in winter. The frequency of intensive precipitation

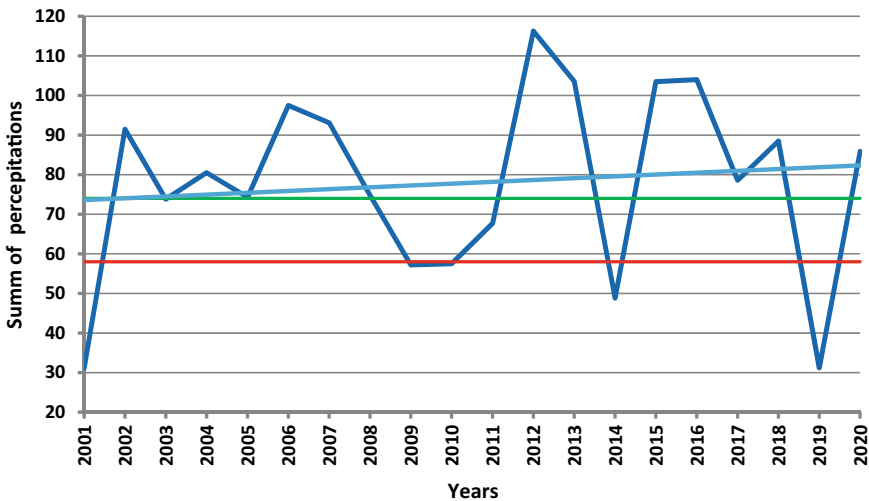


Fig. 1 Winter precipitation totals. 1—average winter precipitation in 1931–1960; 2—average winter precipitation in 1961–1990; 3—trend of winter precipitation in 2001–2020; 4—The course of winter precipitation totals in 2001–2020

increased, and the frequency of months with extremely low precipitation decreased [25].

Comparison of modern data with data of [16] also showed that there was not only a 20% increase in annual precipitation, but also some redistribution of precipitation between warm and cold periods of the year: the share of precipitation of cold period increased from 20 to 27%, the share of precipitation of warm period decreased from 80 to 73%.

Studies conducted in other regions of Russia [2, 14, 22, 29, 30, 31, 32, 34, 35 etc.] also record a relative decrease in the amount of warm period precipitation. One of the reasons for the decrease in the amount of precipitation during the warm period of the year is, among other things, an increase in the warm period temperature.

Comparison of average, average maximum and average minimum summer temperatures for the first 20 years of the XXI century with the same characteristics of the middle of the XX century (1936–1965) [15] showed that in modern climatic conditions calendar summer is characterized by significantly higher air temperatures [21].

Figure 2 and Fig. 3 shows graphs of 20-year mean maximum (Fig. 2) and mean minimum (Fig. 3) air temperatures (line 1), their long-term mean values in the middle of the XX century (line 2) and at the beginning of the XXI century (line 3), as well as trends in air temperature during the calendar summer (line 4). Both graphs show that there is an increase in summer temperatures at the resort of Pyatigorsk. Figure 2 shows that the summer average maximum temperature twice during the 20 years of the new century was lower than the average of the middle of the last century, once was equal to it and 17 times was significantly higher.

Figure 3 shows that the summer average minimum air temperature in all past years of the new century was higher than the summer average minimum air temperature of the period 1936–1965.

The equations of air temperature trends were obtained:

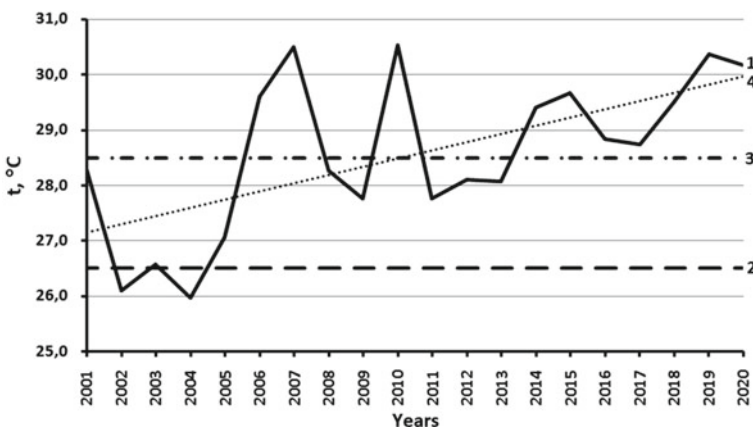


Fig. 2 Characteristics of the summer average maximum air temperature

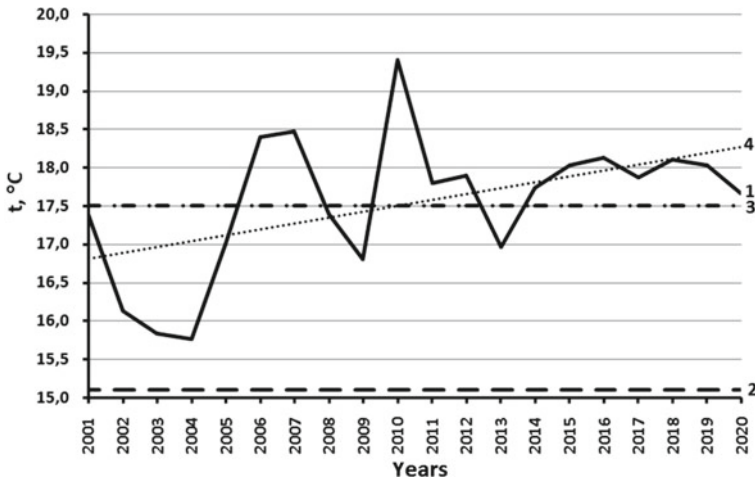


Fig. 3 Characteristics of the summer average minimum air temperature

for the average maximum $y = 0.129x + 27.00$;

for the average minimum $y = 0.076x + 16.73$.

Trend equations of average maximum and average minimum air temperatures show that there is a well-defined, stable trend of air temperature increase during the calendar summer, with the rate of increase of maximum temperatures higher than the rate of increase of minimum temperatures. The fact that the temperature characteristics of the second decade of the new century surpass those of the first decade also indicates that the warming process continues.

But the warming is not only in the summer. Winter temperatures increased even more markedly than summer temperatures, with winter warming occurring earlier [4]. The degree of warming in December is unprecedented.

Changes in the atmospheric circulation regime and changes in the temperature regime caused by it have led to the fact that the actual time limits and the duration of the seasons began to differ significantly from the calendar ones. Thus, due to a later start and an earlier end, the duration of the meteorological winter in the entire Stavropol Territory, including Pyatigorsk, was significantly reduced, and the trend has continued, despite some colder March observed in recent years. An increase in the temperature background of the transition period February–March led to an earlier onset of spring [33].

There is also a shift of dates of stable transition of average daily temperature through 15° upwards ($15^\circ\uparrow$) and downwards ($15^\circ\downarrow$) and corresponding change of duration P (days) of meteorological summer as a period between these two dates (Table 6) [5, 15, 20].

Table 6 Duration of meteorological summer in different multiyear periods

1936–1965			1966–2000			2001–2020		
P	15°↑	15°↓	P	15°↑	15°↓	P	15°↑	15°↓
106	27.05	10.09	91	08.06	07.09	116	26.05	19.09

The duration of the frost-free period increased due to the warming of autumn months: the dates of the last single spring frosts remained almost unchanged, but the first autumn frosts were recorded much later [3].

Continued significant increases in temperature [4, 5, 20] have resulted in a doubling of the number of days with fog in spring and fall in 2011–2020 compared to 2001–2010, a complete absence of fog in the summer after 2008, and a 22% decrease in the number of days with fog in winter. A total of 640 days with fog were recorded for 2001–2010, and for 2011–2020—392 days.

It should be noted that the frequency of thunderstorms is steadily decreasing in Pyatigorsk, as well as in all of the CMW region, except Kislovodsk. In the first half of the twentieth century, the average annual number of days with thunderstorms was 46 days, i.e., almost twice as many as at present.

Unfortunately, along with the positive climatic changes in Pyatigorsk, the environmental situation is worsening. And, if in previous years, environmental tensions were created by emissions of enterprises (with which by now the situation has somewhat improved), and then—an increasing number of motor transport, now a great threat to the resort environment is the building of forest park zones of Beshtau and Mashuk, which will most negatively affect the environmental state of the resort and mineral sources of Pyatigorsk [1, 8].

4 Conclusions

The average annual temperature in Pyatigorsk is about 10 °C, the average winter temperature is about +0.2 °C, the average summer temperature is about 22 °C. There is an average of 605.6 mm of precipitation in Pyatigorsk throughout the year. An average of 159 days with precipitation are recorded per year.

Hazardous weather events are very rare in Pyatigorsk at present. Thus, a heat wave as a dangerous phenomenon was recorded only once, there were no very strong winds and severe downpours in the new century, heavy rains were observed five times.

Changes in the temperature regime caused by it have led to the fact that the actual time limits and the duration of the seasons began to differ significantly from the calendar ones. The mean spring onset dates shifted to earlier date, the duration of winter and a number of days with snow cover decreased, the duration of the frost-free period and the duration of summer increased.

The quantity of precipitation in a warm period decreased on the background of increasing of total year precipitation. Similar climatic changes have been noted not only in other areas of Stavropol Region, but also in many other regions of Russia.

References

1. Assman, D.: Sensitiveness of man to the weather. Gidrometeoizdat, Leningrad (1966) [in Russian]
2. Bratkov, V.V., Zaurbekov, Sh.Sh., Ataev Z.V.: Monitoring of the current climate changes and the assessment of their consequences for the landscapes of the Northern Caucasus. News of the Russian Academy of Natural Sciences. **2**, 7–16 (2014) [in Russian]
3. Badakhova, G.Kh., Kaplan G.L.: Monitoring, analysis and forecast of frost-free period duration in different agroclimatic zones of Stavropol Territory. Materials of 74th regional scientific and practical conference “State and prospects of agricultural sector of Southern Federal District”. Stavropol, 118–122 (2010) [in Russian]
4. Badakhova, G.Kh., Kaplan G.L.: Trends in winter temperatures in the Central Caucasus. Actual directions of fundamental and applied research. SIC “Academic”. 45–48 (2017) [in Russian]
5. Badakhova, G.Kh., Kaplan G.L.: Changes in temperature and precipitation regime in Stavropol Region for the past 30 years. “International exchange of scientific knowledge, innovations, technologies”: Collection of articles on the mat. inter. scientific and practical conference. Apex, Irkutsk. 5–9 (2018) [in Russian]
6. Badakhova, G.Kh., Kaplan G.L., Kravchenko N.A.: Climatological analysis and prediction of the conditions of the distribution of impurities in the air basin of the Caucasian Mineral Waters. Natural and engineer sciences. **4**, 241–246 (2009) [in Russian]
7. Batalin, F.A.: Pyatigorsk region and Caucasian Mineral Water. St. Petersburg (1861) [in Russian]
8. Belozеров, V.S.: Ecological Problems of the CMW Resort Area. Theses of reports of Regional Scientific Conference. Stavropol. 68–69 (1989) [in Russian]
9. Belozеров, V.S.: Caucasian Mineral Water: evolution of the system of cities of the Eco-Resort Region. Vash Vibor, CIRZ, Moscow (1997) [in Russian]
10. Bogoslovsky, V.S.: Pyatigorskian and related with mineral waters. Moscow (1989) [in Russian]
11. Brockhaus, F.A., Ephron, I.A.: Encyclopedic Dictionary. Joint Stock Company Printing House “Publishing Business”, Brockhaus-Efron, St. Petersburg. **50**, 939 (1898) [in Russian]
12. Dinevich, L., Kaplan, L., Badakhova, G., Kaplan, G.: The issue of climate change. Modern High Technologies. **2**, 60–63 (2013) [in Russian]
13. Gaaz, F.P.: Ma visite aux eaux d’Alexandre en 1809 et 1810. Moscow (1811)
14. Golubiatnikov, L.L., Denisenko, E.A.: The effect of climatic changes on a vegetative cover of the European Russia. News of the Russian Academy of Sciences. A series geographical. **2**, 57–68 (2009) [in Russian]
15. Handbook on the Climate of the USSR. Vol. 13. Part 2. Air and Soil Temperatures. Gidrometeoizdat, Leningrad (1966) [in Russian]
16. Handbook on the Climate of the USSR. Vol. 13. Part 4. Air Humidity, Precipitation, Snow Cover. Gidrometeoizdat, Leningrad (1968) [in Russian]
17. Handbook on the Climate of the USSR. Vol. 13. Part 5. Cloudiness and Atmospheric Phenomena. Gidrometeoizdat, Leningrad (1968) [in Russian]
18. Kaplan, G. L.: Research of modern changes of a regional climate and their influence on landscapes of Stavropol Territory: the dissertation on a rank of the candidate of geographical sciences. High-mountainous geophysical institute. Nalchik (2010) [in Russian]
19. Kaplan, G.L.: Adverse and dangerous weather phenomena in winter and their impact on the economy of the Stavropol Territory. Proc. of the V Int. conf. “Problems of environmental safety and conservation of natural resource potential”. Stavropol. 156–160 (2008) [in Russian]

20. Kaplan, G.L., Badakhova, G.Kh.: Dynamics of climate change in the Caucasian Mineral Waters in the twentieth century. Materials of the II International Conference "Problems of Environmental Security and Conservation of Natural Resource Potential". Stavropol. 161–163 (2005) [in Russian]
21. Kaplan, G.L., Badakhova, G.Kh., Kravchenko, N.A.: Influence of climate change on characteristics of summer period in landscapes of Stavropol. Hydrometeorology, climate change, and environmental monitoring: current problems and solutions. Materials of interdisciplinary scientific and practical conference. Tashkent. 47–50 (2021) [in Russian]
22. Khlevina, S.E.: Climate change in the 20th Century in the Volga-Vyatka region. Materials of the 8th Scientific Conference of the Moscow State University. Saransk. 26–28 (2003) [in Russian]
23. Kobysheva, N.V., Narovliansky, G.Ya.: Climatological processing of meteorological information. Gidrometeoizdat, Leningrad (1978) [in Russian]
24. Kononova, N.K.: Atmospheric circulation as factor natural disasters in Northern Caucasus in XXI century. Geopolitics and ecogeodynamics of regions. Vol 8. 1–2. 72–103 (2012) [in Russian]
25. Kravchenko, N.A.: Climate of Mineralovodskaya Plain // Problems of effective use of scientific potential of the society. Digest of articles based on the results of the International Scientific and Practical Conference. Orenburg 2021. Sterlitamak, AMI. 8–10 (2021) [in Russian]
26. Meteorological data for some years. Issue 13. Rainfall and daily precipitation for 1936–1960 years. Gidrometeoizdat, Leningrad (1962) [in Russian]
27. Nesudimova, M.R.: Unfavorable weather conditions at the Pyatigorsk resort. Innovation science. 2, 65–67 (2022) [in Russian]
28. Procedures for Roshydromet organizations and institutions in case of dangerous natural (hydrometeorological and heliophysical) phenomena. Gidrometeoizdat, St. Petersburg (2000) [in Russian]
29. Sherstukov, B.G., Salugashvili, R.S.: New trends in climate change in the Northern Hemisphere of the Earth in the last decade. The Proceedings of the VNIIGMI-MCD. 175, 43–51 (2010) [in Russian]
30. Teslenok, S.A., Khlevina, S.E., Teslenok, K.S.: Regional displays of air temperature changes in the geosystems of forests and forest-steppe on the right bank of the Volga and the South of Western Siberia // Problems of hydrometeorological support of economic activity in a changing climate: materials of the International scientific conference. Minsk. 151–153 (2015) [in Russian]
31. Vinogradov, B.V.: Desertification is the problem of the Russian steppe zone. Step bulletin. 3 (1999) [in Russian]
32. Vinogradova, V.V., Titkova, T.B., Cherenkova, E.A.: The dynamics of humidifying and heat supplying in transitive landscape zones on satellite and meteorological data in the XXI century beginning. Modern problems of remote sounding of the Earth from space. 2, 162–172 (2015) [in Russian]
33. Volkova, V.I., Badakhova, G.Kh., Berekova, M.V., Kaplan, G.L.: Atmospheric circulation features of the transition period and variations of spring onset dates in the Central Precaucasus. Science. Innovations. Technologies. 1, 125–138 (2021) [in Russian]
34. Zamolodchikov, D., Kraev, G.: The effect of climate change on the forests of Russia. Sustainable forest management. 4, 23–31 (2016) [in Russian]
35. Zolotokrylin, A.N.: Climatic desertification. Science, Moscow (2003) [in Russian]

Applying Recurrent Neural Networks for Short-Term Surface Temperature Forecasts Making



D. S. Efremenko, A. D. Kuznetsov, and O. S. Serouhova

Abstract Today neural networks (NN) are omnipresent and its using is continuously growing in different areas like automation and optimization, researching, health care, engineering etc. This is due to NN possibility to recognize difficult patterns and structures. There are feed-forward and recurrent neural networks (RNN) among various architectures. Former implies only one-directional neuron's relations, later permits bidirectional neuron's interactions which mean possible cycles occurring, similar with cyclic graph. Nowadays RNN are within the best NN architectures for time series predictions. This paper we applied one of RNN architectures, namely long short-term memory (LSTM) for surface temperature time series prediction purposes, producing only short-term forecasts, not more than three hours lead time. Data was sourced from automatic weather station (AWS) archive, located in the Saint-Petersburg. The results obtained from conducted experiments showed LSTM fairly good performance. We also induced an algorithm to train LSTM and tackle with required predictions deadlines.

Keywords Recurrent neural network · Meteorological time series · Preprocessing

1 Introduction

LSTM NN was introduced by Sepp Hochreiter and Jürgen Schmidhuber in their technical report, aiming to overcome gradient vanishing problem occurring while training stage [1, 2]. In common case LSTM consists of following elements: gates (input gate, forget gate, output gate) and cell. Cell remembers and carries time series parameters for an arbitrary time delta (e.g., while training stage). Gates serve input and output cell's data flow, e.g., regulate its ratio, heuristic parameters, information

D. S. Efremenko (✉) · A. D. Kuznetsov (✉) · O. S. Serouhova
Russian State Hydrometeorological University, 98 Malookhtinsky ave., 195196 Saint-Petersburg, Russia
e-mail: reeearth768@gmail.com

A. D. Kuznetsov
e-mail: kuznetsov1946@inbox.ru

© The Author(s), under exclusive license to Springer Nature Switzerland AG 2023
R. Zakinyan and A. Zakinyan (eds.), *Physics of the Atmosphere, Climatology and Environmental Monitoring*, Springer Proceedings in Earth and Environmental Sciences, https://doi.org/10.1007/978-3-031-19012-4_10

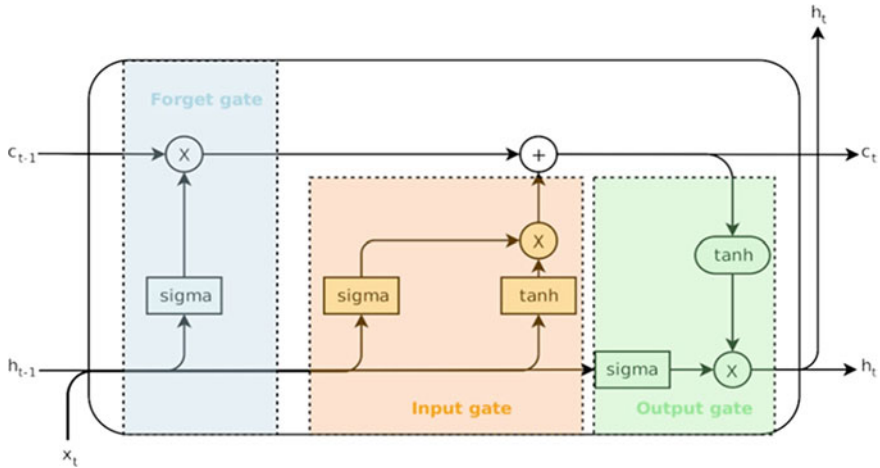


Fig. 1 LSTM principle diagram

quantity. Therefore, every iteration there are several simultaneous operations, to be precisely cell fed by current iteration gradient parameters while accounting previous iteration computed gradient for current prediction.

From Fig. 1, where it's depicted principal LSTM working scheme—«c» with prescriptions are cells from previous and current iterations, that carrying memory and produce new one, based on former, «h» with indexes are previous and current output, « x_t » is input sequence from the dataset, «x» and «+» means point wise multiplication and addition respectively, «sigma» and «tanh» in rectangles are sigmoid and tangential layers, «tanh» in ellipse implies applying hyperbolic tangent function.

It should be noted LSTM usually applying in a couple with linear layer, which transform its output to desirable prediction dimension.

Hence LSTM is promising for surface temperature time series prediction, which in principle is long sequence with complicated structure, where observations order is important.

2 Experiment

2.1 Data

Data for conducting experiments was sourced from AWS, located in the Saint-Petersburg, Russia. It is placed on the Saint-Petersburg's ring road and is a part of ring road AWS net, which produces, saving and storing meteorological data archive, including surface temperature with a measuring resolution as 5 min. Initially we had 3 month duration time series, transitioning from autumn to winter 2015, with

a various omissions. Restoring procedure included spline interpolation, with one restriction—gap between observations should be not more than 30 min. Therefore, after preprocessing we got about two month duration time series, comprising 17,281 observations (hereinafter points) equivalent to 86,405 min length.

2.2 Network Architecture

Experimental NN comprised two layers: LSTM and linear. Later layer employed for transforming LSTM output to target dimension.

To optimize NN while training phase gradient descent (GD) method [3] applied. GD has three parameters: learning rate (LR), dropout and weight decay (WD). LR expressing the degree of GD convergence, and should be chosen carefully, since high value could lead to divergence and small value could dramatically decrease convergence speed. Dropout is using to overcome neurons co-adaptation. Its value is probability of which some elements of NN tensors zero filled based on Bernoulli distribution. WD is intended to multiply with NN neurons weights every time while optimization, applied after each next iteration. We assign LR as 10^{-3} , dropout as 0.2 and WS as 10^{-6} .

2.3 Algorithm Description

Aiming to make 1, 2 or 3 h lead time forecasts, it was decided to train LSTM with one week duration dataset derived from initial surface temperature time series. Since considered problem is short-term forecasts, we trained each NN for only one prediction, i.e., without cross-validation and test stages. Otherwise, we need to train a global prediction model, that is time-consuming task [4].

Forecast making routine comprised the following steps [5]:

- (1) Deriving 7 days duration train dataset from origin time series.
- (2) Transforming train dataset to ranges with minimum and maximum values -1 and 1 respectively. For this we used minimum–maximum scaling procedure [6].
- (3) Splitting 7 days long train dataset to two types of sequences, first type are sequences with 40–100 points' length and each next sequence of this type is shifted by 1 point onward. The second type 1 point length sequences shifted related to appropriate type 1 sequence, respective to an prediction term (e.g. for 3 h prediction it will be shifted 36 point onward relative to type 1 sequence). For training stage we used $N-1$ sequences both mentioned types, where N is total sequences length.
- (4) Train stage, comprised LSTM was fed by 40–100 length sequences of type 1. Linear layer transformed LSTM output to one dimension array including one value and presenting a prediction in a range $[-1, 1]$. Then to decrease a

prediction error all neurons weights should be updated. For that we used standard scheme, i.e., mean square error computed based on NN prediction and real value, after gradient descent method applied for all neurons within all layers.

- (5) Validation stage, that included fed last sequence of type 1 into trained NN, presented a prediction, which compared with linked value of appropriate sequence of type 2. Since prediction lying in range $[-1, 1]$ then its value transformed to real scale, computing reversing for aforementioned step 2. After transforming real and prediction values residuals calculated.
- (6) Shifting 3 h onward origin time series and repeat step 1.

Steps 1–6 were repeated, tentatively moving across surface temperature time series, till to destination of the end of the origin time series. Finally, it was computed 424 forecasts with 1, 2, 3 h lead time for the same time series points and mentioned residuals values.

It is common practice to speed up NN training to use batch processing, which main idea lying in computing training error for a bunch of results in each iteration, that means the more batch length the less training time. In fact, we not applied batch processing and set a batch length value as 1.

2.4 Environment

Neural network was implemented in Python 3 programming language, used pytorch packages [7, 8]. In a preprocessing stage we applied standard Python 3 routines in a couple with scipy scientific package [9].

3 Experiment Results

In Figs. 2, 3, 4 are depicted experiment results fragments for the first 100 predictions. Real observations colored as green line, forecasts as blue and their residuals as red. From these plots analysis it's obvious all conducted forecasts results similarity, which probably related with the same initial NN parameters, equal trained dataset and sequences length.

Basic statistics for experiment are presented in Table 1 where «mean» and «SD» are mean and standard deviation, computed for real observations and relevant forecasts residuals values, «mean abs» and «SD abs» are the similar with one difference residing in results were produced for absolute residuals values. We see all aforementioned parameters similarity and slightly deviations resulted by NN semi-randomness nature, e.g., initial neurons weights are initialized fully randomly.

Averaged forecast consumed time is about 1~2 s.

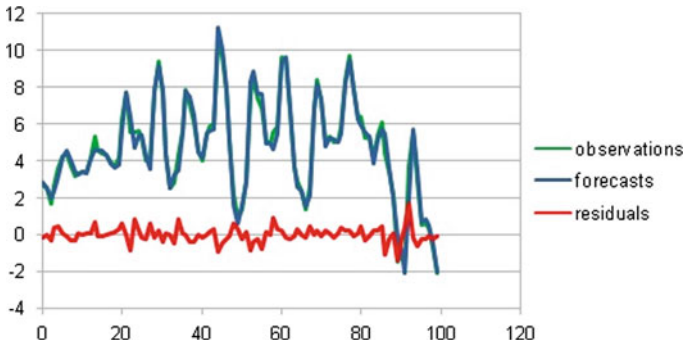


Fig. 2 One hour forecast lead time plot

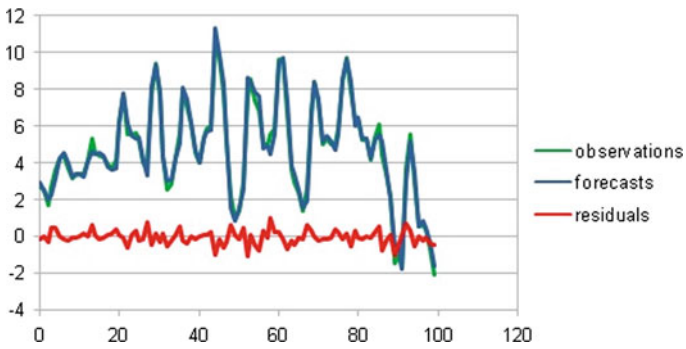


Fig. 3 Two hours forecast lead time plot

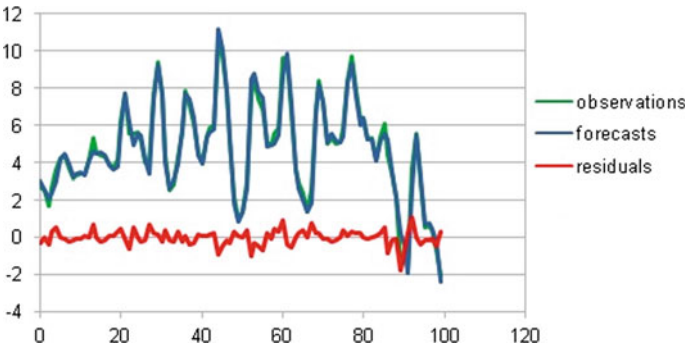


Fig. 4 Three hours forecast lead time plot

Table 1 Experiment results basic statistics

Forecast lead time	Mean	Mean abs	SD	SD abs
1 h	0.00825	0.18500	0.29104	0.22464
2 h	-0.00627	0.17546	0.26054	0.19251
3 h	0.00895	0.17652	0.26926	0.20334

4 Conclusions

In this work we demonstrated applying neural network of RNN architecture, namely LSTM to tackle with surface temperature short-term forecasts tasks. Experiment results demonstrated good enough NN performance in terms of predictions errors, more specifically mean and standard deviation are small. Figures 2, 3 and 4 with depicted forecasts, observations and errors values approved this. Therefore, we guessing LSTM outputs can deal for a longer forecast terms with a good enough performance.

Average forecast time is small and appropriate for making short-term forecasts target despite of we not applied batch processing.

Nevertheless, we noted higher predictions errors for several transition points, related with a fast surface temperature changing. Such cases should be studied separately to tune better NN parameters. In addition, it's not all obvious from the randomness of neurons weights initialization. Consequently, to clarify this we need to perform more numerical experiments targeting to derive averaged results depends on each initial parameters values. Sequence length (type 1 from part 3) potentially should be tuned dynamically, respective to previously conducted training dataset analysis. It needs to be checked results for different learning rate, dropout and weight decay values. Also, this experiment we used mean squared error optimization, which should be compared with another functions (e.g. mean absolute error). Since we not used batch processing it need to be considered in next research.

Although implemented experimental NN architecture is simplest and in essence solving a linear regression equation, still it is promising technique for detecting surface temperature complicated structure. Hence, we can add more layers to experimental NN, to check performance and steadiness.

Finally, an attention should take to importance of studying making another meteorological time series short-term forecasts, like atmosphere pressure and relative humidity applying LSTM technique.

References

1. Robin, M.S.: Recurrent Neural Networks (RNNs): A gentle Introduction and Overview. [arXiv:1912.05911v1](#) [cs.LG] (2019)
2. Hopfield, J.J.: Neural networks and physical systems with emergent collective computational abilities. *Proc. Natl. Acad. Sci. U.S.A.* **79** (8): 2554–2558 (1982)
3. Sepp, H., Jürgen S.: Long short-term memory. *Neural computation* **9**(8), 1735-1780 (1997)
4. Sebastian, R.: An overview of gradient descent optimization algorithms. [arXiv:1609.04747v2](#) [cs.LG] (2017)
5. Emmanuel, A.: Forecasting of Meteorological variables using statistical methods and tools. [arXiv:2103.10936v1](#) [physics.ao-ph] (2021)
6. Alex, S.: Fundamentals of Recurrent Neural Network (RNN) and Long Short-Term Memory (LSTM) Network. [arXiv:1808.03314v9](#) [cs.LG] (2020)
7. Eli, S., Luca, A., Thomas, V.: *Deep Learning with PyTorch*. Manning (2020)
8. Orna, I., Nathan I.: Interpreting neural-network results: a simulation study *Computational Statistics. & Data Analysis* **37**, 373–393 (2001)
9. Pauli, V., Ralf G., Travis E. O., Matt H., Tyler R. and et al. SciPy 1.0 Contributors.: *SciPy 1.0-Fundamental Algorithms for Scientific Computing in Python*. *Nature Methods*. **17**, 261 (2020)

Humidity of the Surface Air Layer as the Main Factor of the Formation of the Basic Climate Forming Elements



Ya. A. Ekba, A. K. Akhsalba, and L. V. Khintuba

Abstract Climate change over the past two decades, driven by a variety of factors, including greenhouse gas emissions, is unprecedented. As the temperature rises, the absolute humidity increases, reaching a maximum in July–August. Based on the close relationship between the values of the average annual temperature and absolute humidity, one can assume that water vapor is the main factor responsible for changing the temperature of the surface air layer.

Keywords Greenhouse gases · Average annual temperature · Absolute and relative humidity · Water vapor · Surface air temperature

1 Introduction

Within the framework of models developed by the Intergovernmental Panel on Climate Change (IPCC), climate change and its consequences in different regions of the world will be different [1]. Thus, the results of rising global temperatures will be a rise in sea level, a change in the amount and nature of precipitation, and an increase in the deserts area. Important consequences for humanity include the threat to food security due to the negative impact on crop yields (especially in Asia and Africa) and the loss of human habitats due to sea level rise [2–4].

It should be noted that, despite the anthropogenic origin of climate warming on Earth, a large role is assigned to natural factors. Among them are variations in the

Ya. A. Ekba · A. K. Akhsalba
Institute of Ecology, Academy of Sciences of Abkhazia, Sukhum, Abkhazia, Georgia
e-mail: ekba-yan@yandex.ru

A. K. Akhsalba
e-mail: Asida_cen@mail.ru

Ya. A. Ekba · A. K. Akhsalba · L. V. Khintuba (✉)
Abkhazian State University, Sukhum, Abkhazia, Georgia
e-mail: LolitaKhintuba@yandex.ru

average annual power of solar radiation and cyclic changes in the orbital parameters of the Earth's motion [5–7].

Surface temperature variations reconstructed from the deuterium series from an ice core [8, 9] showed that the temperature during the Holocene (the last 10 thousand years) did not remain constant and repeatedly exceeded the current value.

It must be pointed out that powerful volcanic eruptions have a significant impact on the temperature regime of the planet, contributing to the activation of the formation of stratospheric aerosol, which significantly lowers the temperature of the surface air layer in the year following the eruption [10, 11].

Climate change will inevitably cause large-scale changes in the planet's ecosystems, and will lead to the need to rebuild the economies of many countries, adapting it to new natural conditions. There is also a strong regional specificity of the ecological situation due to the global climate change.

2 Features of the Temperature Regime of the Territory of Abkhazia

The Black Sea coast has the warmest winter in Abkhazia. The average winter temperature decreases from north to south, as if ignoring the geographic latitude. Local factors are of great importance for the distribution of winter temperatures. The protection of the territory by ridges from the invasion of cold air masses, the influence of the warm Black Sea, and the wide development of foehn winds increase the temperature in winter [12, 13]. During the observation period from 1999 to 2021, two periods can be noted in Abkhazia: the first general increase in atmospheric air temperature from 1999 to 2010, when the average annual temperature reached a maximum (18.4 °C). After that, under the influence of the eruption of the powerful volcano Eyjafjallajökull (Iceland, April 14–19, 2010), the temperature of the SLA in the next 2011 decreased by 3.8 °C and amounted to 14.6 °C (Fig. 1).

After 2011, the SLA temperature began to increase again, reaching its maximum value (16.9 °C) in 2018.

Figure 2 shows the average annual temperatures of the SLA for 10 years, where it is clearly shown that the warmest decade since the beginning of meteorological observations was the 2001–2010 period (ATSLA-16.3 °C). It is worth noting that over the last decade of 2011–2020, the average annual temperature was 15.7 °C, which is 0.6 °C lower than the previous decade, i.e. since 2011, there has been a decrease in the temperature of the SLA, which continues to the present, since 2021 was the coldest year in the last decade.

Therefore, the analysis of the data of the Abkhazian meteorological network for the period from 1999 to 2021 clearly shows that the temperature trends and the nature of their seasonal distributions indicate a significant decrease in average annual temperatures in the last decade [14, 15].

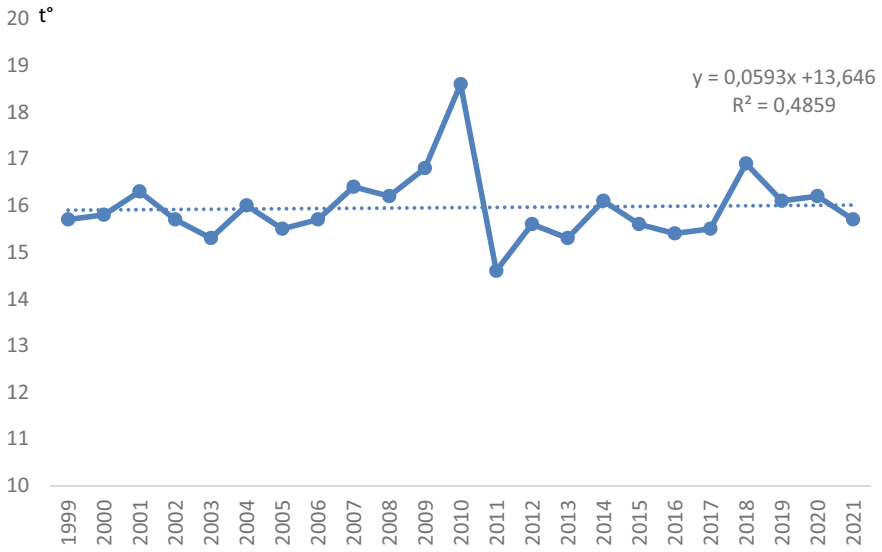


Fig. 1 Dynamics of the average annual temperature of the surface air layer for the 1999–2021 period in Sukhum

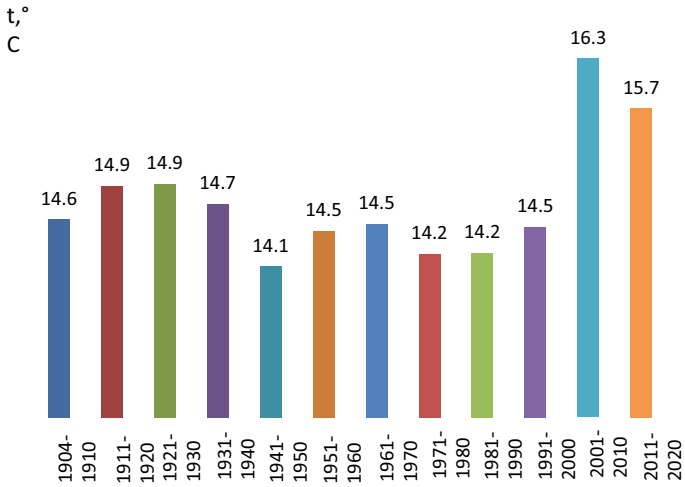


Fig. 2 Average annual air temperatures in Sukhum over 10 years for 1904–2020

3 The Main Characteristics of the Humidity of the Surface Layer of Air in the Territory of Abkhazia

A feature of air humidity—a climate component—is its great instability and pulsation. Analysis of hydro-grams shows that under normal weather conditions, relative humidity values can change by 10–15% in 1–2 min. Turbulent currents and descending and ascending air currents developing in the surface layer of the atmosphere have an exceptional effect on air humidity.

The climate warming observed in the last decade on the territory of Abkhazia has caused a change in meteorological parameters. The annual temperatures have increased. In addition, there has been a significant transformation of the seasonal distribution of precipitation. The minimum is observed in the summer months, especially in July.

In some years, due to the fact that most of the summer precipitation falls with significant variations in the form of short-term showers that do not have time to sufficiently moisten the soil, a lack of moisture is observed in July and August.

Due to the unfavorable moisture balance, the probability of insufficient moisture supply during the summer months in Abkhazia is 46% in June, so atmospheric drought is often observed here during the month. Over the past 20 years, with an increase in temperature, relative humidity has systematically decreased, if in 2002 the average annual relative humidity was 85%, then in 2019 it dropped to 76%.

At the same time, the average annual absolute air humidity changes synchronously with the average annual air temperature (Fig. 3).

The correlation coefficient between the two data series for the last 20 years is over 0.85.

Water vapor and clouds are the largest contributors to surface air warming (SLA). We cannot directly control the amount of water vapor in the atmosphere, because water is everywhere on our planet—it covers 71% of the Earth's surface. Observations show a significant effect on the climate of stratospheric aerosol and water vapor, the total content of which in the stratosphere has steadily increased over a 30-year period [16].

An increase for water vapor in the upper troposphere and lower stratosphere leads to radiative cooling at these levels and causes warming on the Earth's surface [16].

The main essence of the “work” of greenhouse gases is that their molecules are able to absorb infrared photons passing through the atmosphere, i.e. they, in fact, absorb IR photons with different wavelengths. It is this fact that complicates the process of calculating the contribution to the greenhouse effect of each individual gas [17, 18]. The contribution to the greenhouse effect of various air components based on calculations using numerical models of the general circulation of the atmosphere is presented in Table 1.

According to Table 1, on average, the contribution to the greenhouse effect of atmospheric air humidity (HA) is approximately 50%, clouds—25%, carbon dioxide—only 20%. The total contribution of all other gases to PE does not exceed 5%.

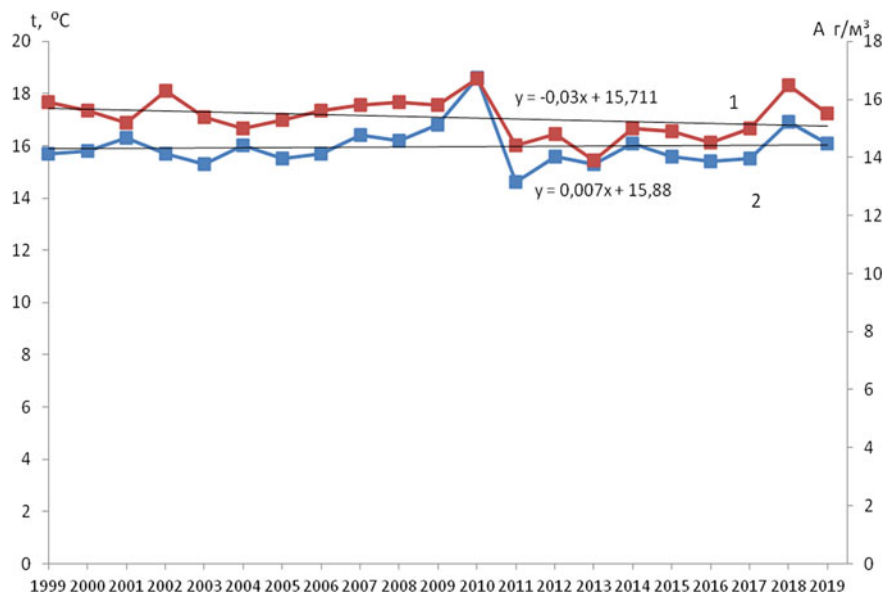


Fig. 3 Distribution of temperature (1) and absolute humidity (2) in Sukhum

Table 1 Contribution of atmospheric components to the greenhouse effect

Source	Contribution of various atmospheric components to the greenhouse effect (%)				
	HA		HA		HA
Schmidt	39.0–61.9	Schmidt	39.0–61.9	Schmidt	39.0–61.9
NASA model	36–66	NASA model	36–66	NASA model	36–66
Average value	37.5–64 (~50)	Average value	37.5–64 (~50)	Average value	37.5–64 (~50)

It is the processes of interaction between the ocean and the atmosphere, which form the variability of the components of vertical moisture exchange. They are the main factor in the formation of interannual HA fluctuations, including its trend.

4 The Main Characteristics of the Humidity of the Surface Air Layer in the Caucasus

Turbulent currents and descending and ascending air currents developing in the surface layer of the atmosphere have an exceptional effect on air humidity.

The degree of air saturation with moisture is one of the calculated parameters of the effective temperature and, therefore, is of great importance in assessing the complex impact of climate on the human body. Atmospheric drought is associated

with relative humidity, which has a depressing effect on crops. The absolute humidity of the air affects the condensation processes and determines their intensity. Absolute humidity and its deficit are the initial data for calculating evaporation losses.

On the territory of the Caucasus, humidity experiences large fluctuations caused by the orographic structure, the type of underlying surface, and the atmospheric circulation processes developing here. High absolute humidity is typical for the territories located on the Black Sea coast, while the humidity deficit is observed in the North Caucasus, especially in the eastern regions of Table 2.

It follows from Table 2 that the minimum relative humidity is observed here in summer: in July, August, and September, and the maximum in spring: in April, May, and June. The average annual values of the relative humidity of the SLA, shown in Fig. 4, demonstrate a steady increase in its average annual values to 83% by 2002 and a corresponding decrease in relative humidity to 65% by 2020. A high moisture deficit of the SLA is called atmospheric drought. Since the late 1990s, more than half of the world's plant landscapes have experienced increasing moisture deficits or drying up.

Due to moisture deficiency, that is, due to low relative humidity and, accordingly, high temperature and absolute humidity, deadwood ignites.

5 Precipitation in the Caucasus

A significant climate-forming factor is the nature of the seasonal distribution of precipitation and their total annual amount. More than half of the annual precipitation (over 60%) falls on the coast of Abkhazia during the growing season, but they cannot create a favorable moisture balance, not only because of the increased influx of solar radiation and increased evaporation at this time, but also due to the nature of precipitation [12, 13]. Most of the summer precipitation falls with significant variations in the form of short-term showers that do not have enough time to moisten the soil of Table 3. Insufficient moisture supply is most often observed in July and August [12].

Despite significant fluctuations in monthly and annual precipitation, reaching 100% or more, a high synchronism coefficient is observed between the extreme values of the average annual precipitation for territories with different types of climates, reaching values of 0.7–0.8. This is the evidence that in the territories of the North and South-Western Caucasus, the same global circulation processes form precipitation. A high correlation, reaching values of 0.7, can be traced between the total average annual precipitation and the average annual relative humidity (Fig. 4), which is a confirmation of the priority role of water vapor in the formation of precipitation.

An even closer relationship is observed between total monthly precipitation and seasonal monthly values of relative humidity (Fig. 5). For Anapa, which is located on the Black Sea coast, this dependence is practically functional.

With the general synchronism of changes in the total average monthly precipitation and average monthly relative humidity, there are certain discrepancies for

Table 2 Values of relative air humidity (f %) by months from 1982 to 2020, in the Caucasus

Cities	f %	Months												
		I	II	III	IV	V	VI	VII	VIII	IX	X	XI	XII	
Sukhum	f %aver	80.1	78.6	78.2	78.3	79.4	79.4	79.4	79.4	73.5	74.6	76.8	78.4	79.3
Sochi	f %aver	73.6	71.3	72.4	73.4	78.8	79.3	79.0	79.0	77.3	75.7	76.3	72.5	71.3
Anapa	f %aver	80.2	77.4	76.3	74.2	77	74.9	69.1	69.1	65.4	69	73.8	77.8	80.1
Tuapse	f %aver	71.5	68.3	69.5	69.6	74.1	73.8	70.6	70.6	67.5	68.0	70.9	68.6	69.8
Stavropol	f %aver	83.9	81.3	76.7	67.0	67.7	63.9	58.0	58.0	56.0	65.8	76.0	82.3	83.9
Vladikavkaz	f %aver	77.9	75.8	74.4	71	73.3	72.3	71.5	71.8	71.8	76.1	77.3	77.6	77.3

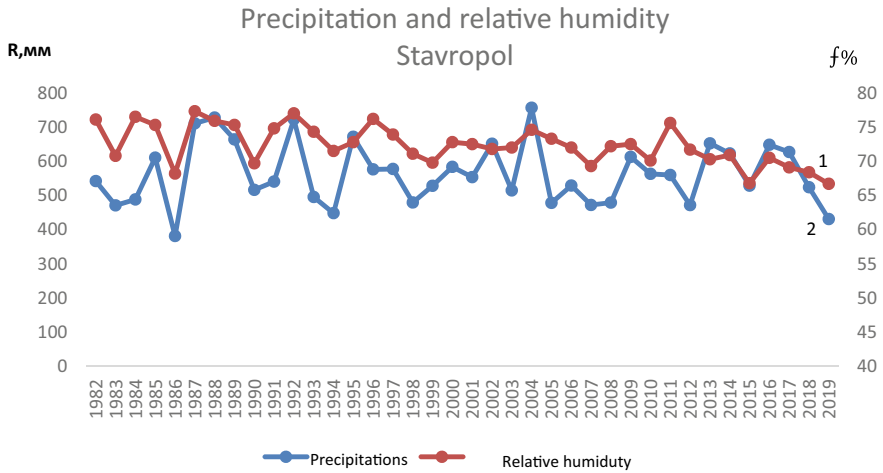


Fig. 4 Average annual values of atmospheric precipitation and relative humidity in Stavropol

Table 3 The values of total monthly precipitation (R, mm) for the 1982–2019 period, by cities of the Caucasus

Cities	R _{MM}	Months											
		I	II	III	IV	V	VI	VII	VIII	IX	X	XI	XII
Sukhum	Rcp	165	147	156	133	122	148	144	153	165	183	180	171
Sochi	Rcp	175	130	143	111	105	104	121	109	143	183	176	177
Anapa	Rcp	61	46	52	39	41	42	35	35	51	53	50	64
Tuapse	Rcp	155	119	118	88	97	96	97	84	122	152	143	164
Stavropol	Rcp	28	28	42	42	73	77	58	38	50	53	38	34
Vladikavkaz	Rcp	30	34	61	94	146	183	114	88	72	64	41	30

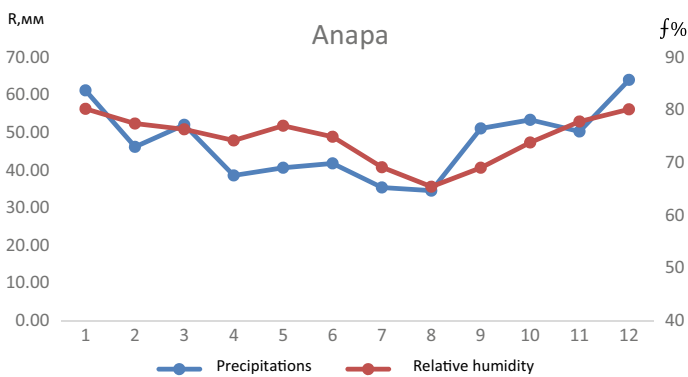


Fig. 5 Seasonal distribution of precipitation and relative humidity in Anapa

some territories, which is explained by the peculiarities of orography and circulation processes. At the same time, the relative humidity changes synchronously with the total average monthly precipitation, and the absolute humidity changes synchronously with the SLA temperature [14].

6 Conclusion

Thus, the relative air humidity is the determining factor responsible for the formation of both seasonal and interannual amounts of precipitation. Taking into account the close relationship between the absolute humidity and the average annual temperature of the SLA, established in [14], it could be stated that atmospheric moisture is the main factor responsible for the formation of the regional climate.

References

1. Bedritsky, A.I.: On the influence of weather and climate on the stability and development of the economy. *Meteorology and Hydrology*. **10**, 5-11 (1997) [in Russian].
2. Budyko, M.I.: Climate and life. L., Gidrometeoizdat. **126**, 472 (1971) [in Russian].
3. Budyko, M.I., Byutner, E.K., Vinnikov, K.Ya., Golitsyn, G.S., Drozdov, O.A., Karol, I.L.: Anthropogenic changes in the global climate. *Meteorology and hydrology*. **8**, 5–14 (1998) [in Russian].
4. Rosgidromet. The second assessment report on climate change and its consequences on the territory of the Russian Federation, Moscow. **703**, 1008 (2014) [in Russian].
5. Gudkovich, Z. M., Karklin, V. P., Smolenitsky, F. M., Frolov, I.E.: What is happening to the Earth's climate? *Russian Ecological Bulletin*. **5**, 34-40 (2012) [in Russian].
6. Isaev, A.A.: Ecological climatology. Textbook for high schools. M. Nauchny Mir. **256**, 458 (2001) [in Russian].
7. Klimenko, A.V., Klimenko, V.V.: Is humanity to blame for global climate change? Russia in the surrounding world. (1998), (Analytical Yearbook). Ex. editor N.N. Marfenin. M.; Publishing house of MNEPU. **43**, 53–66 (1998) [in Russian].
8. Kotlyakov, V.M., Losev, K.S., Ananicheva, M.D.: Comparison of disturbed ecosystems in Russia and other European countries. *Izvestia RAS. Geography series*. **2**, 18-29 (1998) [in Russian].
9. Kotlyakov, V.M., Klige, R.K., Zakharov, V.G.: Global cycles of climatic changes and glaciation of Antarctica.//Global changes in the natural environment (Climate and water regime). Edited by N.S. Kasimov. M. **54**, 70–90 (2000) [in Russian].
10. Kondratiev, K.Ya.: Global ecodynamics and sustainable development, natural science aspects and the “human” dimension. *Russian Geographical Society*. Vol 129, **6**, 1–12 (1997) [in Russian].
11. Surkova, G.V.: Chemistry of the atmosphere. M.: Publishing House of Moscow University, **104**, P. 210 (2002) [in Russian].
12. Ekba, Ya.A., Dbar, R.S., Akhsalba, A.K.: Trends in climate change in the Southwestern Caucasus in the 20th century. Tr. intl. conf. “Biosphere and Man”, Maykop. **39**, 38–41 (2003) [in Russian].
13. Ekba, Ya.A., Akhsalba, A.K.: Modern changes in surface air temperature and atmospheric precipitation regime in the coastal zone of Abkhazia. Reports of the Adyge (Circassian) International Academy of Sciences. Nalchik. (2011), Vol. 13, **2**, 105–111 [in Russian].

14. Ekba, Ya.A., Akhsalba, A.K., Khintuba, L.V.: Global and regional (Abkhazia) manifestations of the greenhouse effect in the atmosphere and on the Earth's surface. Collective monograph "Modern problems of geology, geophysics and geoecology of the North Caucasus", (GEOKAVKAZ-2021). Moscow. Vol. XI. **495**, 493–498 (2021) [in Russian].
15. Ekba, Ya.A., Akhsalba, A.K., Marandidi, S.I.: Peculiarities of formation of surface air temperature (FSAT) on the territory of Abkhazia and Stavropol Region. Reports of the third international scientific conference "Innovative methods and means of research in the field of atmospheric physics, hydrometeorology, ecology and climate change". Stavropol. **214**, 213–216 (2018) [in Russian].
16. Forster, P.M. de F., and K.P. Shine.: Assessing the climate impact of trends in stratospheric water vapor, *Geophys. Res. Lett.*, **29**, 1086, doi:<https://doi.org/10.1029/2001GL013909> (2002).
17. Jiang, J. H., Su, H., Zhai, C., Wu, L., Minschwaner, K., Molod, A. M., Tompkins, A. M. An assessment of upper troposphere and lower stratosphere water vapor in MERRA, MERRA2, and ECMWF reanalyses using Aura MLS observations. *J. Geophys. Res. Atmos.*, **120**, 11,468–11,485 (2015).
18. Hurst, D.F., S.J., Oltmans, H., Vömel, K.H. Rosenlof, S.M.: Davis, E.A. Ray, E.G. Hall and A.F. Jordan. Stratospheric water vapor trends over Boulder, Colorado: Analysis of the 30 year Boulder record. *Journal of Geophysical Research: Atmospheres*. **101**, 116 (D2): D02306, doi:<https://doi.org/10.1029/2010JD015065>. Hurst, D.F., personal communication (2016).
19. Lacis, A.A., Hansen, J.E., Russell, G.L., Oinas, V., Jonas, J.: The role of long-lived greenhouse gases as principal LW control knob that governs the global surface temperature for past and future climate change. *Tellus B*, **43**, 65:19734, <https://doi.org/10.3402/tellusb.v65i0.19734> (2013).

Analysis of the Effect of the Sensitivity Value on the Results of Studies of Rapid Atmospheric Processes in Multifrequency Microwave Radiometric Sounding of the Atmosphere



E. V. Fedoseeva , I. N. Rostokin, G. G. Shchukin , and I. Yu. Kholodov

Abstract The difference in the level and relative temporal variations of input signals of multifrequency microwave radiometric system sets certain requirements to the task of increasing its sensitivity. In general, for low-frequency channels, increase of sensitivity is caused by the requirement of accuracy and reliability of assessment of possible small increments of input signal, and for high frequency measurements perfect identification of the temporal trend of the signal level, especially during studies of fast flowing atmospheric processes. This article is devoted to research of influence of change of sensitivity of multifrequency microwave radiometric system at variation of one of radiometer parameters—time constant of accumulation of an output signal on accuracy of measurements at changing meteorological conditions.

Keywords Microwave radiometric sounding · Sensitivity · Temporal trend · Fast atmospheric processes

1 Introduction

Methods of remote study of the atmosphere allow us to continuously assess its structure, condition, and predict the development of atmospheric processes [1–4]. It is known that contact methods provide, as a rule, a more accurate measurement of the values of the physical characteristics of the atmosphere, but they are incomparably more expensive and make it possible to form a structural model of the atmosphere in a limited spatial area for a limited period of time and can be used for periodic verification of the accuracy of estimates of the state of the atmosphere by remote measurement systems.

E. V. Fedoseeva (✉) · I. N. Rostokin · G. G. Shchukin · I. Yu. Kholodov
Murom Institute of Vladimir State University named after A.G. and N.G. Stoletov, 23 Orlovskaya St., 602264 Murom, Russia
e-mail: elenafedoseeva@yandex.ru

G. G. Shchukin
Mozhaysky Military Space Academy, 13 Zhdanovskaya St, 197198 St. Petersburg, Russia

Remote sounding is a more affordable way of continuous monitoring of its state under the condition of obtaining a more smoothed structural-spatial model of the atmosphere, but it provides a possibility of operative assessment of the conditions of occurrence and assessment of the characteristics of rapidly proceeding atmospheric processes during the formation of dangerous atmospheric phenomena.

Microwave radiometric sensing is a method of passive investigation of the atmosphere, which is based on measurements of its radiothermal radiation. The spectrum and power of this radiation depend on the meteorological parameters and spatial and structural characteristics of the observed area. This relationship is based on the construction of algorithms for the reconstruction of altitude-azimuth profiles of atmospheric parameters when obtaining correlation estimates and regression ratios of meteorological parameters and the measured radio brightness temperature—the power characteristics of the input radio noise signal of the system performing microwave radiometric sensing. Small values of the power of the measured radio noise radiation determine the importance of the task of constructing highly sensitive microwave radiometric systems that provide the possibility of measurements in conditions of internal and external noise interference [5–7].

Microwave radiometric measurements of the atmosphere with several frequency ranges make it possible to obtain more information to assess the state of the atmosphere by the magnitude of the power of the radio noise radiation generated by it. It is known that meteorological parameters—temperature, humidity, moisture content, precipitation have a different predominant effect on the magnitude of this power in significantly different frequency ranges [1–3]. It is known that the power of radio-noise radiation of the atmosphere strongly depends on the frequency range. The general trend is that the higher the central frequency of the measurement range, the higher the value of the input power. Besides, there are frequency ranges, in which the generated input power of noise signal is maximal in comparison with neighboring frequencies, that is caused by peculiarities of meteorological parameters influence, for example, 3.5 GHz (for thermodynamic temperature estimation) and 22 GHz (for humidity research). Microwave radiometric sensing of the atmosphere in the region of relatively low frequencies is performed in order to solve the problems of detecting and evaluating the parameters of precipitation zones in the studied area. For such studies, it is possible to carry out measurements at frequencies from 3.5 to 10 GHz.

The difference in the magnitude of the signals and their relative changes over time for a microwave radiometric system operating in several frequency ranges sets certain requirements for the task of increasing its sensitivity. In general, for low-frequency channels, an increase in sensitivity is due to the requirement of accuracy and reliability of estimating possible small increments of the input signal, and for high-frequency measurements, a more perfect detection of the time trend of the signal level, especially in studies of fast-flowing atmospheric processes.

This article is devoted to the study of the influence of changes in the sensitivity of a microwave radiometric system operating in several frequency ranges when varying one of the parameters of the radiometer—the time constant of the output low-frequency filter integrator on the accuracy of measurements under changing weather conditions.

2 Materials and Methods

The limiting accuracy of measuring the power of radio-noise radiation of the atmosphere by microwave radiometric systems is characterized by the value of sensitivity, expressed in the values of radio-luminous temperature. The potential sensitivity of the microwave radiometric system is the minimum power of the input measured noise signal, which the receiver of the system, the radiometer, can distinguish against the background of its own noise [5–7]. As a measure of the accuracy of microwave radiometric measurements in radiometry, the value of the relative limiting sensitivity is proposed [2], defined by the expression:

$$\delta = (1 + T_R/T_A)/q \quad (1)$$

where T_R radiometer noise temperature; T_A —antenna temperature; $q = \sqrt{\Delta f \cdot \tau}$ —radiometric gain; Δf —frequency band width of the high-frequency path of the radiometer; τ —the accumulation time constant of the output filter integrator of the radiometer.

Expression (1) defines the dependence of the value δ from noise parameters of a radiometer T_R , from size of input noise power of the microwave radiometer system, characterized by size and from radiometric gain q . The values T_R and T_A depend on the characteristics and parameters of the microwave radiometric system, as well as their value is affected by the conditions of measurement. The value q can be increased by increasing the time constant of accumulation in the formation of a measurement base in discrete form when the output signal passes through the ADC on the PC.

The increase in the time during which the accumulation of the output signal of the microwave radiometric sensing system of the atmosphere is carried out is associated with an increase in the smoothing effect in time dependencies, which determines the need to assess its effect on the conditions for tracking fast-flowing atmospheric processes.

The issue of changing the sensitivity of the microwave radiometric system as a result of additional software-implemented processing of discrete samples of measurement results was considered on the example of a system with reception on a common antenna mirror in three frequency ranges, in which sequential selection of signals in a common antenna irradiator is performed [4–6]. The central frequencies at which reception is carried out in the microwave radiometric system are as follows: 3.5, 10 and 22 GHz. A significant difference in frequencies determines a significant difference in the value of the antenna temperature and, accordingly, the level of output signals of the three channels of the system. In addition, for these frequencies, the degree of influence of meteorological parameters on the power level of the recorded radiothermal radiation of the atmosphere is different. In particular, the output signal of the channel, which receives at 3.5 GHz, at the standard for the microwave radiometric system time constant of 1 s, mainly reacts to the presence of the precipitation zone in the sounding area.

3 Analysis and Discussion

In Picture 1 shows the daily course of the output signals of three channels of the microwave radiometric system, recorded on June 12, 2021 during measurements in the Vladimir region at a point with coordinates 55°26'N, 42°03'E in the south-west direction. During the measurements, there was a significant change in weather conditions—a change in humidity, precipitation, which determined the complex form of changes in the time of the output signals of the microwave radiometric system.

The analysis of the dependencies presented in Fig. 1 showed the presence of general trends of output signals change in time, with individual features for each channel. At a frequency of 22 GHz, the output signal has a more complex dependence on the general trend of change compared to the rest, which may be due to local variations in meteorological parameters—humidity and precipitation intensity in the studied zone of the atmosphere. At a frequency of 10 GHz, the time-dependent curve of the signal magnitude has a more smoothed shape, which can be explained by an increase in the spatial region, mainly determining the level of radiothermal power generated by the atmosphere at the receiving point. Weak relative changes per day of the output signal at a frequency of 3.5 GHz are due to the influence of large-scale spatial atmospheric processes—extended precipitation regions.

Thus, the levels and rates of change of the signals recorded at the three outputs of the microwave radiometric system are different, which suggests a different approach to improving the accuracy of measurements by increasing sensitivity when the signal accumulation time changes.

The presence of rapid signal changes at the channel output at 22 GHz of the microwave radiometric system determines the limitation on increasing the time constant of the accumulation of the output signal, especially since the signal level

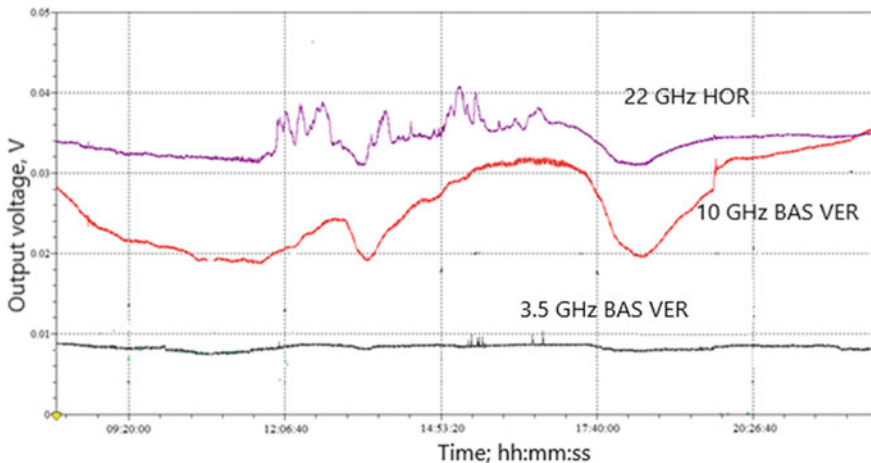


Fig. 1 Output signals of the microwave radiometric system recorded during the day on June 12, 2021

is quite large compared to the other channels. The most smoothed time dependence of the signal at a frequency of 3.5 GHz at its small value suggests the possibility and necessity of increasing sensitivity by generating an output signal at a constant accumulation time significantly greater than 1 s.

Figures 2, 3 and 4 show programmatically generated output signals of a microwave radiometric system with two values of 0.1 s accumulation time, equal to the period of ADC formation of output digital signals for subsequent processing on a PC, and 20 s, i.e. with an increase in the time constant by 200 times.

For a comparative analysis of the degree of change in the sensitivity of the microwave radiometric system due to changes in the time during which the accumulation of the radiometer signal was performed, a special numerical estimate was proposed $\bar{\delta}U$, equal to the ratio of the average deviation of the output signal from its mean value:

$$\bar{\delta}U = \frac{\sum(U_i - \bar{U}_i)}{\sum U_i} \tag{2}$$

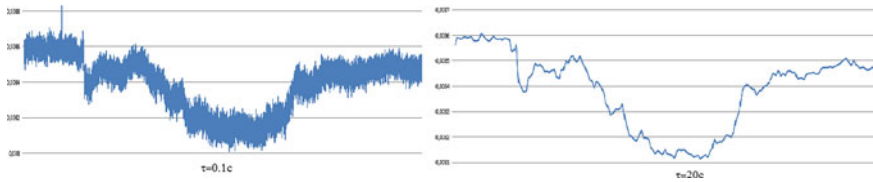


Fig. 2 Time course of the output signal of the microwave radiometric system at a frequency of 3.5 GHz

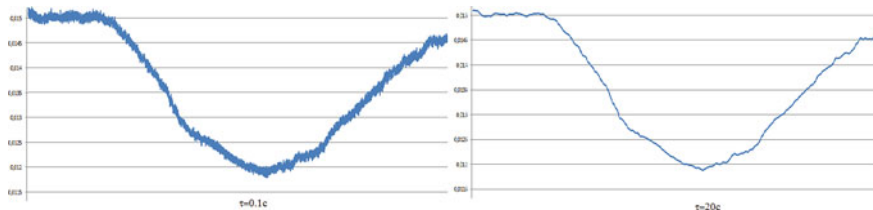


Fig. 3 Time course of the output signal of the microwave radiometric system at a frequency of 10 GHz

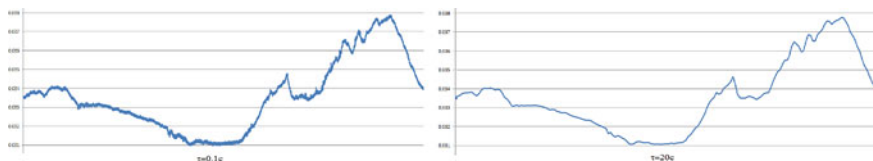


Fig. 4 Time course of the output signal of the microwave radiometric system at a frequency of 22 GHz

where U_i —current value of output voltage of the system; \overline{U}_i —output voltage averaged over a given time interval.

Introduction of the specified quantity allows to estimate change of sensitivity of the system by primary measurements of an input signal. Numerical analysis of the measurement data shown in Figs. 2, 3 and 4 showed that for the frequency of 3.5 GHz the value of the proposed estimate is 0.23 for $\tau = 0.1$ s and 0.18 for $\tau = 20$ s, for 10 GHz frequency—0.16 and 0.07, for 22 GHz frequency—0.25 and 0.2. Thus, the sensitivity of the channel with a frequency of 3.5 GHz has increased the most, which corresponds to the data of the dependencies shown in Picture 2. According to Picture 2 increasing the sensitivity by increasing the time constant to 20 s allows you to more accurately record changes in the time of the output signal at a frequency of 3.5 GHz.

Analysis of the daily records of the output signals shown in Figs. 2, 3 and 4 showed that an increase in the time during which the accumulation of signals is programmatically performed leads to an increase in the sensitivity of all three channels through which reception was carried out in the microwave radiometric system. The spread of random values of signals is significantly reduced and a certain trend of signal change is clearly manifested when weather conditions change. But for the channel with frequency 22 GHz the indicated increase of accumulation time up to 20 s turned out to be limiting from the position of tracking of temporal changes of the signal, because in certain moments small changes in the output signal are weakly manifested, which can lead to underestimation of the system response to changes in the state of the atmosphere, fixed in this range. Thus, in Fig. 4, the areas of the time dependence in which the initial rapid changes in the output signal are smoothed out and ultimately missed in the processing are highlighted in red. With further increase, the effects of averaging lead to the omission of a greater number of such sharp transitions in the signal, which may ultimately lead to an incorrect assessment of the meteorological situation under conditions of rapidly developing atmospheric processes.

4 Conclusions

The results obtained as a result of the conducted studies confirmed the possibility of increasing the sensitivity of microwave radiometric measurements by increasing the time of accumulation of the output signal, programmatically implemented in the system for collecting and processing radiometric information for remote sensing of the atmosphere, with the introduction of certain restrictions due to the rate of change in time of signals recorded at the output of the microwave radiometric system, especially when observing rapidly developing atmospheric processes. The direction of intelligent change of accumulation time for different channels is promising with operational tracking of relative changes in time of output signals to make a decision on increasing the accuracy of measurements and preventing the omission of signal changes due to the presence of rapidly developing processes in the atmosphere.

Acknowledgements The study was supported by grant № 21-19-00378 from the Russian Science Foundation, <https://rscf.ru/project/21-19-00378/>.

References

1. Stepanenko, V.D., Shchukin, G.G., Bobylev, L.P.: Radiotepolocacion in meteorology. Hydrometeoizdat, Leningrad (1987) [in Russian]
2. Basharinov, A.E., Gurvich, A.S., Egorov S.T.: Radiation of the Earth as a Planet. Nauka, Moscow (1974) [in Russian]
3. Ware, R.R., Carpenter, J., Guldner, J., Liljegren, T., Nehrkorn, F., Solheim, Vandenberghe, F.: A multi-channel radiometric profiler of temperature, humidity and cloud liquid. *Radio Science*, **38**, 8079–8032 (2003)
4. Westwater, E.R., Crewell, S., Matzler, C.: Surface-based Microwave and Millimeter wave Radiometric Remote Sensing of the Troposphere: A Tutorial. *IEEE Geos. and Rem. Sens. Soc. Newsletter*. **27**, 16–33 (2005)
5. Falin, V.V.: Radiometric microwave systems. Luch, Moscow (1997) [in Russian]
6. Tsybulev, P.G.: Data Collection and Control System of a New Generation for Radio Astronomy Observations in the Continuum at the RATAN-600 Radio Telescope: Development Observation, Measurements. *Astrophysical Bulletin*. **66**, 118–133 (2011)
7. Camps, A., Corbella, I., Bara J., Torres F.: Radiometric sensitivity computation in aperture synthesis interferometric radiometry. *IEEE transactions on geoscience and remote sensing*. **36**, 680–685 (1998)
8. Rostokin, I.N., Fedoseyeva, E.V., Fedoseyev, A.A.: Issues of construction of multifrequency microwave radiometric system of remote sensing of cloudy atmosphere with compensation of background radiation. *Radiotechnical and telecommunication systems*. **1**, 5–11 (2015)
9. Fedoseeva, E.V., Rostokin, I.N., Shchukin, G.G., Rostokina, E.A.: Multi-band microwave radiometric sensing of remote rain zones. *Journal of Physics: Conference Series*. **1632**, (2020). 012012 doi:<https://doi.org/10.1088/1742-6596/1632/1/012012> (2020)
10. Rostokin, I.N., Fedoseyeva, E.V., Shchukin, G.G., Rostokina, E.A.: Tasks and principles of organization of data collection and processing system of multifrequency microwave radiometric system of weather formations state control with compensation of background noises. *Radio engineering and telecommunication systems*. **1**, 3–16 (2017)

The Gabor Filter Application in Satellite Analysis of “Invisible” Orographic Waves



N. V. Fedoseeva  and T. E. Simakina 

Abstract “Invisible” mountain waves are a particularly dangerous type of atmospheric disturbances associated with a high risk of aircraft operation in conditions of orographic turbulence. The paper presents the experience of using a digital Gabor filter to improve the quality of detection of “invisible” orographic waves in satellite images in water vapor channels. In the course of the work, an archive of 20 MODIS/Aqua, Terra multispectral images with “invisible” orographic waves for 2000–2020 was formed. The results of numerical experiments demonstrate the successful extraction of mountain waves in satellite images using the Gabor filter. The Gabor filter is resistant to scaling, rotation, brightness and contrast changes.

Keywords Orographic waves · Gabor filter · Satellite analysis · Water vapor channels

1 Introduction

When an air flow in the earth’s atmosphere interacts with a topographic barrier, disturbances being the source of various wave processes arise. One type of such processes is stationary waves, called orographic waves, occurring in a moving wind flow. They are generated above mountain range and are observed in leeward areas [1–3]. Banded clouds above the crests of lee waves occur under conditions of sufficient relative humidity. Depending on the height of the mountain barrier, stratocumulus, altocumulus, less often cirrus clouds can be formed.

Turbulence can originate at the crests of mountain waves, but it does not always happen, since wave motion is a type of laminar motion. The transition from one form of motion to another can occur very abruptly, and it is usually observed in layers where there is large wind velocity gradient orthogonal to the mountain barrier. The presence of clouds indicates the movement of air and turbulence.

N. V. Fedoseeva (✉) · T. E. Simakina
Russian State Hydrometeorological University, Saint-Petersburg, Russia
e-mail: n.fedoseeva@rshu.ru

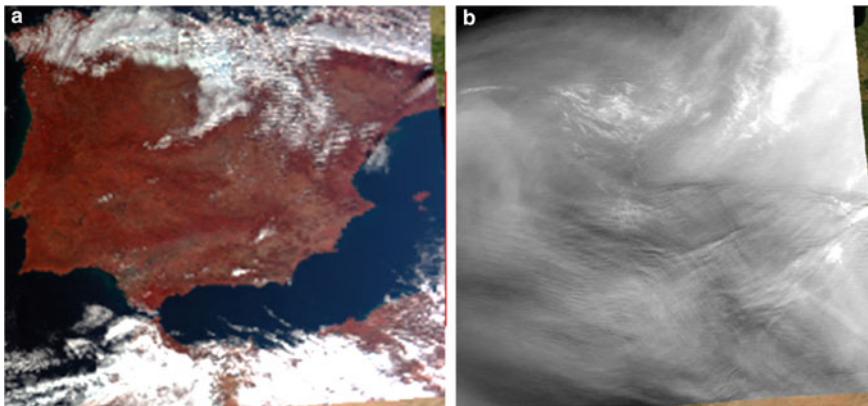


Fig. 1 **a** image in true colors, **b** image in the water vapor channel ($7.3 \mu\text{m}$), 29.12.2004/ 13:15 UTC

The occurrence of turbulence is possible not only when clouds form, but also when the sky is cloudless. Clear-air turbulence often occurs near the tropopause due to vertical waves in dry environments. Areas prone to turbulence are most likely to be found at the crests and troughs of the wave, while at middle levels the air currents remain undisturbed and laminar. Like all gravitational waves, mountain waves are capable to break, causing especially strong turbulence [4].

In this regard, orographic waves are an extremely dangerous type of atmospheric movements for aircrafts operation. This is especially true in conditions of insufficient humidity, when banded clouds are not formed, and the lee waves remain invisible to both the pilot and the radar. Detection of “invisible” mountain waves is possible with satellite imagery in the spectral ranges located in the far IR absorption band of water vapor [5]. Figure 1a shows a multispectral satellite image in true colors, Fig. 1b—image of the same territory in the water vapor channel. The image on the left shows the cloudless Iberian Peninsula, the image on the right demonstrates the alternation of stripes of orographic waves parallel to the mountain range.

The paper presents the experience of using a digital Gabor filter [6, 7] to improve the quality of detection of “invisible” orographic waves in satellite images in water vapor channels. In the course of the work, an archive of 20 MODIS/Aqua, Terra multispectral images with “invisible orographic waves for 2000–2020 was formed.

2 Results and Discussion

The process of formation of atmospheric mountain waves is associated with a violation of the stability of thin layers of air, which have almost the same parameters and do not mix for long periods of time. The first of the lee waves originates over the mountain that causes it, with a series of waves of the same horizontal wavelength

propagating downstream. Numerous evenly spaced lee waves are often visible where they are not obstructed by other mountains, such as over the sea [8, 9].

Lee waves most often occur when a deep airflow with stronger winds at higher levels and stably stratified air at lower levels passes over a long mountain range with a steep leeward slope at or near a right angle to the direction of the airflow. Then the strongest updraft occurs not over the windward slope, but in front of the first leeward wave. Mountain waves are characterized by a periodic change in pressure, temperature and height of an idealized air mass in the atmospheric air flow [9, 10].

In meteorology, there are two main types of lee waves: trapped lee waves and vertically propagating lee waves [11]. Trapped lee waves have horizontal wavelengths from 5 to 35 km. They exist in a layer with high static stability and moderate wind speeds, usually in the lowest 1–5 km of the troposphere. Trapped waves occur when the wind speed over an orographic obstacle increases sharply with height and when stability decreases in the layer immediately above the mountain top. Since the energy of the waves is trapped in a stable layer, these waves can propagate far downwind from the mountain crest.

For vertically propagating waves, the energy of the wave propagates vertically rather than horizontally as in the case of trapped waves. They form in broad mountain ranges under conditions of considerable atmospheric stability due to the depth of the atmosphere. These are the so-called uncaptured lee waves. Uncaptured waves occur when the static stability increases over the top of the mountain and when there is little wind shear with height [12]. As a rule, they extend vertically to the upper layers of the troposphere and are deflected back in height relative to the mountain range. They indicate the presence of turbulence in the upper layers of the troposphere. Sometimes wave crests can extend beyond the upper limits of the troposphere into the stratosphere. Due to their greater vertical extent, the energy of the waves is dissipated more quickly downstream compared to trapped lee waves, resulting in a smaller overall horizontal extent of the wave pattern. Vertically propagating waves are often accompanied by strong downwind winds (e.g. foehn and bora).

The following conditions are favorable for the formation of orographic waves:

- (1) The direction of the wind varies within 30 degrees from perpendicular to the mountain obstacle and does not change with height;
- (2) On the crest of the ridge, the wind speed reaches 50 km/h and increases with height;
- (3) There are stable layers of inversion or isotherm at a height of 1–3 km from the summit.

The characteristics of lee waves are generally determined by the characteristics of the air flow and the orographic obstacle: the flow velocity, the orientation of the flow relative to the ridge, the stratification of the air mass, and the height of the ridge relative to the surrounding underlying surface. The air flow speed should not exceed 8–15 m/s at the level of the ridge in accordance with the height of the mountain obstacle; the most optimal heights for the formation of mountain waves vary from 500 m to 2 km.

The length of the lee waves is directly proportional to the wind speed. There is also an inverse relationship with the stability of the air flow stratification. The weaker the wind and the greater the stability, the shorter the wavelengths. Stronger winds produce longer waves with smaller amplitude. Mountain ranges with very steep slopes and a large vertical drop on the leeward side create waves with the greatest amplitude. Lower, more streamlined mountains produce lower amplitude waves.

Wave amplitudes, according to observational data, vary from hundreds of meters to 2000 m, but mostly range from 300 to 500 m.

Mountain waves can be observed at high altitudes even in the case of a low mountain obstacle. They can be traced not only in the troposphere, but even in the stratosphere, up to 5 times the height of the mountain range. At the same time, they can be observed at horizontal distances 20 times greater than the height of the obstacle [1, 3].

The most favorable for the occurrence of orographic waves are rectilinear extended mountain ranges, since the air flow partially flows around individual mountains of small extent, which leads to a weakening of the flow disturbance. If the mountain range is not straight, more turbulence in the flow will be observed in the sections of the mountain range that are concave with respect to the direction of the flow. This is due to the fact that the bulk of the air is forced to cross the ridge, instead of flowing around it [2].

Waves on satellite images in steam-water channels are represented by areas of sharp transitions in the brightness range. Such a transition can be considered as a single oscillation of a periodic signal with a certain spatial frequency. Gabor filters belong to the family of band pass filters. Such filters are able to detect the frequency range of a signal in a certain interval and direction, they are widely used for image analysis [13–16]. Thus, Gabor filters can be used to define boundaries of a specific length, width, and direction. In this work, a 2-dimensional Gabor filter was used to process satellite images.

The Gabor filter kernel is the product of a Gaussian and a harmonic function [13]:

$$g_{\xi, \eta, \lambda, \theta, \varphi}(x, y) = \exp\left(-\frac{x'^2 + \gamma^2 y'^2}{2\sigma^2}\right) \cos\left(2\pi \frac{x'}{\lambda} + \varphi\right), \quad (1)$$

$$x' = (x - \xi)\cos\theta - (y - \eta)\sin\theta, \quad (2)$$

$$y' = (x - \xi)\sin\theta - (y - \eta)\cos\theta. \quad (3)$$

Equations (2) and (3) describe the rotation of the filter through an angle θ radians. By changing the angle of rotation, it can change the direction of waves detection.

The Gaussian signal centered at wavelength λ is the Fourier transform of the Gabor function.

The filter response at the center of the window (ξ, η) is obtained by convolving Eq. (1) and the brightness of the original image in the vicinity of Ω around (ξ, η) :

$$r_{\xi,\eta,\lambda,\theta,\varphi} = \iint_{\Omega} f(x, y) g_{\xi,\eta,\lambda,\theta,\varphi}(x, y) dx dy, \tag{4}$$

where: ξ, η —filter window center coordinates;
 x, y —pixel coordinates in the filter window;
 γ —the eccentricity of the wave region, depending on the size of this region;
 λ —wavelength under the cosine corresponding to the spatial frequency of the detected periodic patterns;

$\theta \in [0, \pi)$ —orientation of the normal to the region of parallel patterns (this normal is the x' axis of the Eq. (2);

φ —phase shift that determines the symmetry of the function (under the cosine).

Thus, the Gabor function filters the brightness of the image based on the specified spatial frequency λ^{-1} .

As a result of multiplication in the frequency domain, the amplitudes of the output signal frequencies close to the frequency of the sinusoidal signal increase, while others are attenuated. If the filter is convolved with a signal with a frequency significantly higher or lower than the center frequency of the filter, then ideally the signal amplitude should be zero. This is because the positive and negative parts of the signal cancel each other out in the convolution integral. In this case, the filter kernel should have a constant component as close as possible to zero, defined as the average value of the filter kernel.

Filter windows $15 \times 15, 10 \times 10$ and 5×5 pixels were used in all experiments. It makes no sense to use filter windows of large sizes, since the values of $g(x, y)$ quickly approach zero with increasing distance from the center of the filter window.

The ability to distinguish brightness differences in the wave process on a satellite image is determined by the amplitude of the filter kernel. If the amplitude is too large, the filter will be insensitive to small details, if it is not enough, it will no longer be invariant to illumination.

The possibilities of detecting and contrasting mountain waves in satellite images using the Gabor filter are illustrated in Figs. 2, 3, 4 and 5. The figures show fragments of images of the Modis/Terra spectroradiometer in the thermal IR range of the spectrum in the absorption band of water vapor. The information of such a channel makes it possible to detect mountain waves that are not accompanied by the formation of clouds [5]. As a result of which they are not identifiable in the images of the visible range. The maximum weight function of the water vapor channel at a wavelength of $7.3 \mu\text{m}$ falls at a height of about 500 hPa; the brightness is due to the emission of water vapor in the middle troposphere.

Mountain waves originated on the lee side of the Atlas Mountains. On the right side of Figs. 2, 3, 4 and 5 show the results of the Gabor filtering $15 \times 15, 10 \times 10$ and 5×5 pixels respectively, with different parameters. Since the spatial orientation of mountain waves is determined primarily by the orientation of the mountain range

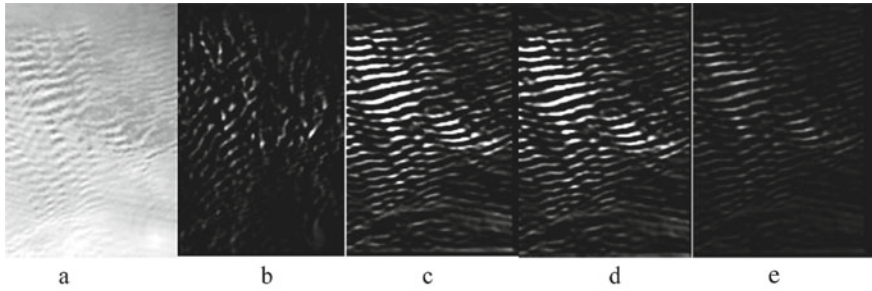


Fig. 2 Applying a 5×5 pixel Gabor filter. **a** Original image in the water vapor channel; **b** $\theta = 25$, $\sigma = 25$, $\lambda = 8$, $\gamma = 1.5$; **c** $\theta = 1$, $\sigma = 25$, $\lambda = 8$, $\gamma = 1.5$; **d** $\theta = 1$, $\sigma = 5$, $\lambda = 8$, $\gamma = 1.5$; **e** $\theta = 1$, $\sigma = 5$, $\lambda = 18$, $\gamma = 1.5$

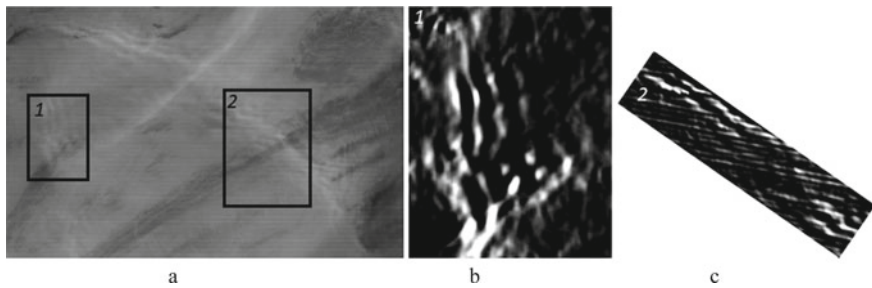


Fig. 3 Applying a 15×15 pixel Gabor filter. **a** Original image in the water vapor channel; **b** $\theta = 5.98$, $\lambda = 15$, $\gamma = 1$; **c** $\theta = 5.23$, $\lambda = 15$, $\gamma = 0.3$

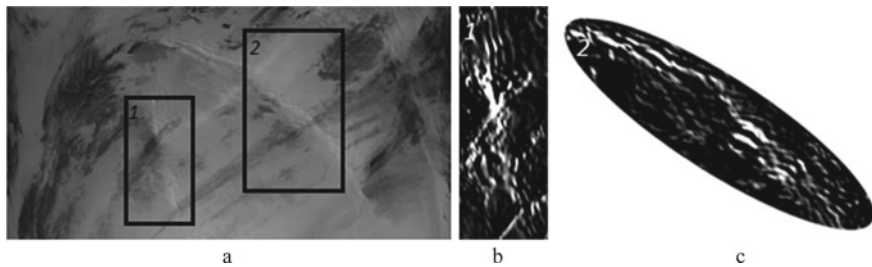


Fig. 4 Applying a 10×10 pixel Gabor filter **a** Original image in the water vapor channel; **b** $\theta = 1.7$, $\lambda = 15$, $\gamma = 1$; **c** $\theta = 5.49$, $\lambda = 15$, $\gamma = 0.3$

and, secondly, by the direction of the wind, the values of the Gabor filter parameter θ for a particular sub-satellite scene were set in advance. For the Atlas Mountains, this value was 0.4 radians, since the mountains stretched almost along the latitude from the west-southwest to the east-northeast.

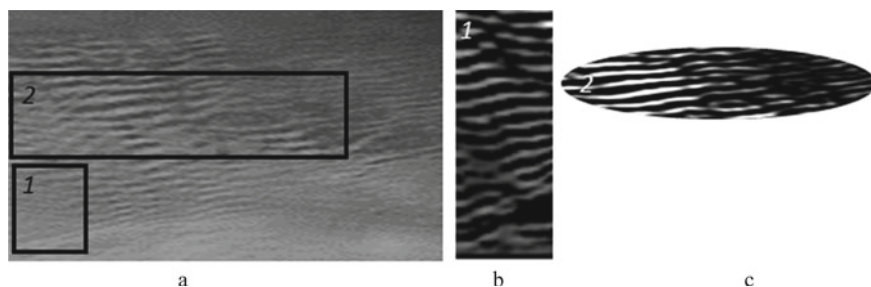


Fig. 5 Applying a 5×5 pixel Gabor filter **a** Original image in the water vapor channel; **b** $\theta = 1.0$, $\lambda = 18$, $\gamma = 1.5$; **c** $\theta = 1.0$, $\lambda = 8$, $\gamma = 1.5$

3 Conclusions

The results of numerical experiments demonstrate the successful extraction of mountain waves in satellite images using the Gabor filter. The Gabor filter is resistant to scaling, rotation, brightness and contrast changes.

References

1. Durran, D.R.: Mountain Meteorology: Lee Waves and Mountain Waves. In: Encyclopedia of Atmospheric Sciences. **1–6**, 2998 (2014).
2. Whiteman, C.D.: Mountain Meteorology: Fundamentals and Applications. New York: Oxford University Press, 355 (2000).
3. Menchaca, M.Q., Durran, D.R.: Mountain Waves, Downslope Winds, and Low-Level Blocking Forced by a Midlatitude Cyclone Encountering an Isolated Ridge. *Journal of the Atmospheric Sciences* **74**(2), 617–639 (2017)
4. Guarino, M.V.: Mountain wave breaking in atmospheric flows with directional wind shear. A thesis submitted for the degree of Doctor of Philosophy. 147 (2017).
5. Fedoseeva, N.V., Efimova, Yu.V., Kuroplina, V.I.: Detection of invisible mountain waves with satellite water vapor imagery. *Proc. Conf. Modern problems of hydrometeorology and sustainable development of the Russian Federation*. 173–174 (2019) [in Russian].
6. Tadic, V. et al.: A Note on Advantages of the Fuzzy Gabor Filter in Object and Text Detection. *Symmetry*. **13**(4), 678–694. (2021) DOI:<https://doi.org/10.3390/sym13040678>
7. Erwin at all.: The Enhancement of Fingerprint Images using Gabor Filter. *Journal of Physics: Conf. Series* **1196** 012045 (2019) DOI:<https://doi.org/10.1088/1742-6596/1196/1/012045>.
8. An Introduction to Atmospheric Gravity Waves. *International Geophysics*. **102**, 1–321. (2012)
9. Colfescu, I. at all.: The Dynamics of Observed Lee Waves over the Snæfellsnes Peninsula in Iceland. *Monthly Weather Review* **149**, 1559–1575 (2021).
10. Hupe, P. at all.: Mountain-Associated Waves and their relation to Orographic Gravity Waves. *Meteorologische Zeitschrift* **30**(1), 59–77 (2021) DOI: <https://doi.org/10.1127/metz/2019/0982>.
11. Lott F.: A New Theory for Downslope Windstorms and Trapped Mountain Waves. *Journal of the Atmospheric Sciences*. **73**(9), 3585–3597 (2016)
12. Turner, H.V., Teixeira, M.A.C., Methven, J.: The effect of a stable boundary layer on orographic gravity-wave drag. *Quarterly Journal of the Royal Meteorological Society*, 147, 321–340. (2021)

13. Madhavi, D., Ramesh Patnaik, M.: Image Retrieval Based on Tuned Color Gabor Filter Using Genetic Algorithm. *International Journal of Applied Engineering Research*. **12**(15), 5031-5039. (2017)
14. Varghese, P., Saroja, A.S.: Image enhancement using different forms of hex-Gabor filter: a comparative analysis. *European Journal of Molecular & Clinical Medicine*. **7**(11), 1483-1491. (2020)
15. Sultan, Al-K.O.: A Gabor filter texture analysis approach for histopathological brain tumour subtype discrimination. *ISESCO JST journal*. **12**(22), 14 (2017).
16. Nazarkevycha, M., Nazarkevychb, H., Karovic, V.: Ateb-Gabor Filtering Method in Fingerprint Recognition. *Procedia Computer Science* **160**, 30–37. (2019).

On the Transfer of Heavy Particles by Intense Winds



L. Kh. Ingel 

Abstract The nonlinear problem of the acceleration of heavy particle picked up by a fast flow in a gravity field is studied analytically. This problem is interesting, in particular, in connection with dangerous convective phenomena in the lower atmosphere (heavy wind gusts, tornadoes). Heavy particles/objects carried by intense winds are one of the main hazards associated with such phenomena. The corresponding theoretical problems are complicated by the nonlinear dependence of the hydrodynamic resistance on the velocity of the particle relative to the medium, and were studied, as a rule, by numerical methods. The paper considers an analytical model that makes it possible to establish some general regularities of particle acceleration in the non-stationary flows. According to the solutions derived, the characteristic time of the acceleration of a particle during a fast intensification of the flow is an order of magnitude of the ratio of the particle settling velocity in the gravity field to the acceleration of gravity.

Keywords Heavy particles transfer · Intense winds · Nonlinear model · Hydrodynamic resistance · Analytical model · Non-stationary flows

1 Introduction

The present work theoretically investigates several features of the heavy (inertial) particles motion in the air during rather fast changes of the background wind velocity. One of the possible applications is the calculation of the dynamics for heavy particles/objects (debris, hydrometeors, soil particles, etc.), picked up by squall wind gusts and tornado. As it is known, one of the hazards in episodes with hurricane winds is associated with fast moving particles/objects picked up by the wind. There

L. Kh. Ingel (✉)

Research and Production Association «Typhoon», 4 Pobedy Str., 249038 Obninsk, Russia
e-mail: lev.ingel@gmail.com

Obukhov Institute of Atmospheric Physics, Russian Academy of Sciences, 3 Pyzhevskii lane,
119017 Moscow, Russia

are not rare the situations when the wind velocity changes sharply. For example, if a tornado with horizontal dimensions of about 50 m moves horizontally with the velocity 10 m/s, the question is of practical importance: to what extent in a matter of seconds will certain particles/objects picked up by the wind have time to accelerate. Another possible application is the calculation of heavy particles settling in the shear flows, when the forces of the flow on the particle change rapidly.

The transfer of heavy particles/objects under strong winds has been studied in a number of works (see, for example, [1–10] and the bibliographies in these publications). In particular, attention is paid to the existence of different categories of wind-borne objects with significantly different aerodynamic properties: “compact”, “flat (sheet)”, “rod-shaped” [6]. In the present work, we have in mind mainly the first of these categories, so for brevity we usually talk about “particles”.

Due to the complexity of the corresponding mathematical problems, they were studied, as a rule, by numerical methods. Therefore, the clear analytical models are need even for several idealized situations. The available results are restricted in a number of other respects. In several works, for example, in [1, 9], analytical calculations are performed, but only for small (Stokes’) particles having linear resistance law. For larger particles, it is necessary to take into account a nonlinear character of hydrodynamic resistance that complicates a problem significantly. In [8] we succeed to advance by analytical methods into the region of larger particles (up to Reynolds number values about 10^3 ; that is suitable, for example, to water drops about 1 mm in size). These results are limited by the assumption that the viscous relaxation time of particles is small compared to the vortex rotation period. To describe the movement of large particles, the models of hydrodynamic resistance, more or less hypothetical, are used. In the case of tornadoes, consideration is usually limited to axisymmetric problems.

In [4] attention is paid to the fact that the Doppler radars actually register not the air movement but the heavy particles motion, which, generally speaking, differs from the air movement. Therefore, an issue on the motion of heavy particles in a tornado under conditions of a strong centrifuging has assumed a great importance. This problem is important for a number of other applications too. It is claimed that the presence of some amount of the heavy particles in a tornado can affect its dynamics significantly. According to the published estimations, mass of heavy particles picked up and transferred by a tornado in several cases can reach and exceed 10^7 kg [11]. The presence of heavy particles/objects in the air is the factor strengthening a wind pressure to the buildings and increasing other dangers related to a tornado. The movement and spatial distribution of the particles carry a lot of information in an optical range too. This is used, in particular, in the study of “dust devils” [9].

However, taken into account a rapid transfer of the vortex, the problem is actually far from an axial symmetry. In general, it seems that during the movement of sufficiently massive particles, which are unable to adapt to the flow during the rotation of the vortex, the assumption about the axial symmetry of the problem is far from always adequate.

2 The One-Dimensional Problem of the Acceleration of a Massive Particle Under a Sharp Gust of Wind

Let us consider a simplest case, when the horizontal flow, in which a particle is located, increases sharply. The horizontal projection of the particle movement equation in the absence of another horizontal forces besides hydrodynamic resistance, can be written as

$$\frac{du}{dt} = -c[u - U(t)]. \quad (1)$$

Here t is the time, $U(t)$ is the velocity of horizontal flow, u is the component of a particle velocity toward the flow, c is the coefficient of resistance. The latter essentially depends on the particle velocity relatively medium (except the case of sufficiently small “Stokes” particle), that makes the problem nonlinear even in such, extremely simplified, statement. For a wide range of Reynolds numbers, a linear dependence of this coefficient on the absolute value of the particle velocity relative to the medium $|v|$ is usually assumed [3, 4, 6, 8]:

$$c = |v|/l, \quad (2)$$

here l is some spatial scale. The latter can be estimated, for example, if the rate of stationary settling of the considered particle in a medium at rest is known. In this case, obviously, the relation is

$$-w|w|/l = g,$$

here w is the vertical component of velocity, g is acceleration of gravity, the vertical axis z is directed upward. From here the scale l can be express through the absolute value of settling rate W :

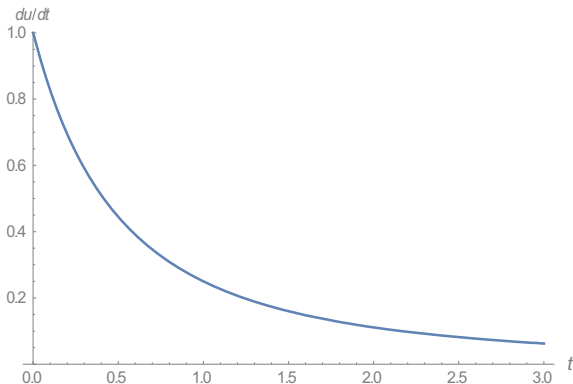
$$l = W^2/g. \quad (3)$$

If we assume that the settling rate of the considered particle in a medium at rest W is known (extensive experimental and theoretical studies are devoted to settling rates), then system (1)–(3) is closed without using additional hypotheses about hydrodynamic resistance. Such an approach to studying the motion of particles was proposed in [4]; it seems successful and will be used below.

Subtracting from the left and right parts of (1) the value $A \equiv dU(t)/dt$, taking into account the above, we arrive at the Riccati equation:

$$\frac{d\Upsilon}{dt} = -\frac{\Upsilon|\Upsilon|}{l} - A(t), \quad (4)$$

Fig. 1 The dependence of a particle acceleration (normalized on $(u_0 - U)^2/l$) on time (normalized on $T_1 \equiv l/(U - u_0)$)



where Υ denotes the deviation of particle velocity from flow velocity $u - U(t)$. It is assumed that at the initial moment $t = 0$ a certain value of the particle velocity is given u_0 ; $\Upsilon_0 = u_0 - U(0)$.

The Eq. (4) admits an explicit analytical solution in a number of the important cases. First of all, of interest is the simplest case, when at the initial moment the particle lags behind the flow of the medium, whose velocity is constant at $t > 0$, and the equation of motion takes the form

$$\frac{d\Upsilon}{dt} = \frac{\Upsilon^2}{l}. \tag{5}$$

The solution takes the form

$$u - U = \frac{u_0 - U}{1 - (u_0 - U)t/l}, \quad \frac{du}{dt} = \frac{(u_0 - U)^2}{l[1 - (u_0 - U)t/l]^2}. \tag{6}$$

The dimensionless dependence of acceleration on time is shown in Fig. 1.

Under the fast flow affect, the particle is accelerated gradually. Its velocity approaches to the flow velocity during time about

$$T_1 = \frac{l}{U - u_0} = \frac{W^2}{g(U - u_0)}. \tag{7}$$

It should be noted that the particle the faster “catches up” with the flow, than the greater was its initial “lag” $-\Upsilon_0 = U - u_0$, since in this case the particle experiences a more intense effect of this flow, therefore, the acceleration du/dt strongly depends on the initial difference in velocities. If, for example, the particles are the large hails with diameter about 5 sm and free settling velocity $W = 25$ m/s [4], $U - u_0 = 40$ m/s, then $l \approx 60$ m, $T_1 \approx 1.5$ s. For $u_0 = 0$ the solution (6) formally, up to notation, coincides with the corresponding solution [3]. However, it has much more general

character, since, unlike [3], it does not assume a spherical shape of the particle and a specific resistance model corresponding to this geometry; it is enough to know the value of W .

3 Case of Uniformly Accelerated Flow

If $U = U_1 + At$, where U_1, A are constant, the Eq. (4) is also solved by separation of variables. For definiteness, we consider the case $A > 0, \Upsilon_0 < -(lA)^{1/2}$ (it is assumed that at the initial moment the particle lags far enough behind the accelerating flow). By introducing the dimensionless variable $V = \Upsilon/v_*$, where the velocity scale is $v_* = (lA)^{1/2} = W(A/g)^{1/2}$, the solution can be represented in the form

$$V = -\frac{1 + \Pi \exp(-t/T_2)}{1 - \Pi \exp(-t/T_2)}, \tag{8}$$

here

$$T_2 = \frac{1}{2} \left(\frac{l}{A} \right)^{1/2} = \frac{1}{2} W(gA)^{-1/2}, \quad \Pi = \frac{V_0 + 1}{V_0 - 1}.$$

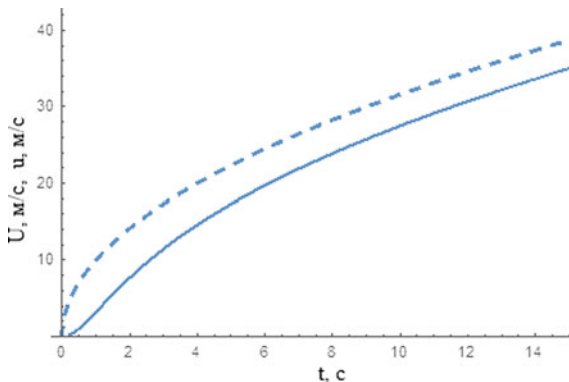
After a transition period of the order of magnitude T_2 , the particle motion enters into the regime with a constant lag behind the flow:

$$u|_{t \rightarrow \infty} \rightarrow U_1 + At - W \left(\frac{A}{g} \right)^{1/2}.$$

4 An Example with Flow Intensification According to a Power Law

For the power dependence $U(t)$, solution of the Eq. (4) can be expressed through the special functions. In particular, with root dependency $U(t) = at^{1/2}$, the solution is expressed in terms of Bessel and gamma-functions. Without giving here a rather cumbersome analytical expression (it is easily reproduced, for example, using the ‘‘Mathematica’’ computer system), we present the dependencies $U(t)$ and $u(t)$ with $W = 10$ m/s, $a = 10$ m/s^{3/2}, $u_0 = 0$ (Fig. 2). The lag of the particle from the flow velocity slowly decreases with time. As it is easy to see from (4), far from the initial moment, there is an approximate balance of last two terms of this Eq. (4), so that $|\Upsilon| \propto t^{-1/4}$.

Fig. 2 The example of particle velocity versus time (solid line) with an increase in the flow velocity according to the root law (dashed line)



5 Accounting for the Influence of the Vertical Motion of a Particle on the Resistance Coefficient

According to (2), it is assumed that the hydrodynamic resistance depends on the particle velocity modulus relative to the medium. Above, only the horizontal motion of the particle was taken into account. In some cases, this can be justified for not too long-time intervals, when the particle picked up by the horizontal flow did not have time to pick up the vertical velocity. Taking into account the vertical motion, the modulus of the particle velocity increases and, consequently, the resistance coefficient arise too. Therefore, the particle is accelerated by the flow more quickly than in the “one-dimensional” model (4), which, thereby, can serve as a minorant estimate of horizontal velocity acquired by the particle.

Taking into account the vertical motions, a more general system of equations should be considered

$$\frac{d\Upsilon}{dt} = -\frac{\Upsilon(\Upsilon^2 + w^2)^{1/2}}{l} - A(t), \quad \frac{dw}{dt} = -\frac{w(\Upsilon^2 + w^2)^{1/2}}{l} - g.$$

Let’s go on to dimensionless variables $v = \Upsilon/W$, $\omega = w/W$, $\tau = t/T$, где $T = W/g$. The system of equations at $U = \text{const}$ takes the form

$$\frac{dv}{d\tau} = -v(v^2 + \omega^2)^{1/2}, \quad \frac{d\omega}{d\tau} = -\omega(v^2 + \omega^2)^{1/2} - 1. \tag{9}$$

The minorant estimate was implemented above: there is considered the case when there is no vertical motion of the particle, and the modulus of its velocity, the resistance coefficient, and the entrainment of the particle by the flow are minimal. Let us now make a majorant estimate. We consider the opposite limiting case, when a gust of horizontal wind picks up the particle settling with the maximum possible absolute value of the vertical velocity $-W$, and assume that this velocity remains unchanged in the future. In this case, the horizontal projection of the motion equation in the

dimensionless variables has the form:

$$\frac{dv}{d\tau} = -v(v^2 + 1)^{1/2}. \tag{10}$$

The general solution:

$$v = \frac{2C \exp \tau}{\exp(2\tau) - C^2}, \tag{11}$$

here C is the constant of integration. Taking into account the initial condition $v|_{\tau=0} = v_0$,

$$C = \frac{-1 \pm (1 + v_0^2)^{1/2}}{v_0}. \tag{12}$$

In the case under consideration $v_0 < 0$, in (12) one should choose the upper sign:

$$C = \left[-1 + (1 + v_0^2)^{1/2} \right] / v_0 < 0.$$

$C > 0$ corresponds to another sign; this solution has no physical meaning, since it leads to the possibility of positive values (11), i.e., to the possibility of a particle forestalling of its accelerating flow. Figure 3 shows the dependencies $v(\tau)$ with various contributions of the vertical movement into the coefficient of hydrodynamic resistance. The lower curve corresponds to the minorant estimate (the solution (6)), when the vertical movement is not taken into account, so that the resistance is determined only by horizontal movement and is minimal. On the contrary, the upper curve corresponds to the majorant estimate, in which the particle settling is given maximal from the very beginning ($w = -W$), so that its contribution to hydrodynamic resistance is somewhat overestimated (the solution (11)). Two intermediate curves are derived by numerical solution of the system (9). The dotted line corresponds to the case when there is no vertical motion at the initial moment, so that it does not immediately begin to contribute to the hydrodynamic resistance. On the contrary, the dashed line corresponds to the case $w_0 = -W$, but, in contrast to the upper line, the settling velocity with $t > 0$ is not assume to be constant, and this is calculated. The w variations affect the resistance coefficient; therefore, the top two curves are somewhat different. The proximity of all these curves indicates the adequacy of the considered above simplified analytical models.

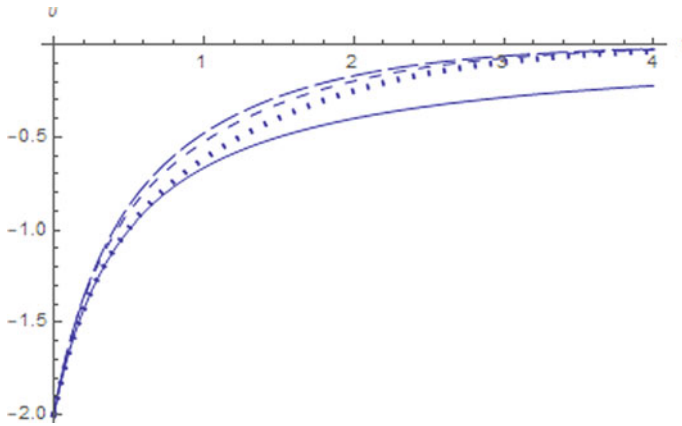


Fig. 3 An approximation of the particle velocity to the flow velocity with the initial velocity difference $u - U = -2W$ (this is explained in the text)

6 Conclusion

The results obtained allow us to justify a simple estimate of the time period during that the heavy particle picked up by a fast flow begins to move and “catches up” with the flow: $T = W/g$. Taking into account the vertical motion of the particle, its velocity approaches the flow velocity exponentially with time. Without taking into account the particle settling (that in some situations is justified at the initial stage), the mentioned velocities approach each other according to a slower algebraic law (the solution (6)); moreover, they approach the faster, the greater the initial difference is between the particle and flow velocities. In this case, the characteristic time is expressed by relation (7).

References

1. Ostrovskiy, L.A.: Dynamics of the concentrations of heavy and light particle in vortex flows. *Izv. Atmos. Ocean Phys.* **28**, 950–956 (1990)
2. Pleshanov, A.S.: On the Theory of Hydrodynamic Stability of Tornadoes. Informenergo, Moscow (1993) [in Russian]
3. Holmes, J.D.: Trajectories of spheres in strong winds with application to wind-borne debris. *J. Wind Eng. Ind. Aerodyn.* **92**, 9-22 (2004)
4. Dowell, D.C., Alexander, C.R., Wurman, J.M., Wicker, L.J.: Centrifuging of hydrometeors and debris in tornadoes: Radar-reflectivity patterns and wind-measurement errors. *Mon. Wea. Rev.* **133**, 1501-1524 (2005). doi:<https://doi.org/10.1175/MWR2934.1>
5. Lebedeva, N.A., Osiptsov, A.N.: Structure of inertial-admixture accumulation zones in a tornado-like flow. *Fluid Dyn.* **44**, 68-79 (2009)
6. Baker, C.J., Sterling, M.: Modelling wind fields and debris flight in tornadoes. *J. Wind Eng. Ind. Aerodyn.* **168**, 312-321 (2017). <http://dx.doi.org/https://doi.org/10.1016/j.jweia.2017.06.017>

7. Baker, C.J., Sterling M.: A conceptual model for wind and debris impact loading of structures due to tornadoes. *J. Wind Eng. Ind. Aerodyn.* **175**, 283-291 (2018)
8. Ingel, L.Kh.: On the dynamics of inertial particles in an intensive atmospheric vortex. *Izv. Atmos. Ocean Phys.* **57**, 551–558 (2021). DOI: <https://doi.org/10.31857/S0002351521060067>
9. Snow, J.T.: On the formation of particle sheaths in columnar vortices. *J. Atmos. Sci.* **41**, 2477–2491 (1984)
10. Maruyama, T., Noda, M.: Tornado-borne debris. *J. Appl. Wind Eng.* **37**, 124–129 (2012). doi:<https://doi.org/10.5359/jawe.37.124>
11. Bodine, D.J., Maruyama, T., Palmer, R.D., Fulton, C.J., Bluestein, H.B., Lewellen, D.C.: Sensitivity of tornado dynamics to debris loading. *J. Atmos. Sci.* **73**, 2783–2801 (2016). doi:<https://doi.org/10.1175/JAS-D-15-0188.1>

Precipitation Measurement by Radar and Ground Methods



V. S. Inyukhin  and K. B. Liev 

Abstract Errors of radar measurement of precipitation are investigated at the High-Altitude Geophysical Institute with the help of a locator and a network of pluviographs. It is shown that the radar, subject to its correction by ground data, is a very reliable and accurate measuring device. The radar method of measuring precipitation has an advantage over ground measurements, it covers a large area (within a radius of 128 km), efficiency (in real time). Studies have shown that the radar, provided it is calibrated with ground data, is a very reliable and accurate measuring device. The conducted comparisons of radar and ground measurements of precipitation showed that almost always the matching coefficient is greater than one and on average for seven years it varied from 1.3 to 1.5. This suggests that the radar systematically underestimates the size of the thickness of the precipitation layer by 1.3–1.5 times. The average relative error of measuring total precipitation for the summer season by radar method does not exceed 42%.

Keywords Precipitation · Data comparison · Meteorological data · Meteorological radar · Precipitation meter

1 Introduction

The main goal when using any method of measuring precipitation is to obtain data representative of the study area. Therefore, it is important to choose the location for the precipitation meter station, its type, as well as the possibility of preventing losses caused by evaporation and wind exposure. For the application of more complex methods, for example, using meteorological radars and satellites, information about measurement errors is needed.

V. S. Inyukhin (✉) · K. B. Liev
High-Mountain Geophysical Institute, 2 Lenin Avenue, Nalchik, Russia
e-mail: inuhin51@mail.ru

K. B. Liev
e-mail: buffy_li@mail.ru

To determine the capabilities of the radar method for determining precipitation parameters, it is necessary to compare radar data with ground-based observation [1–5].

The aim of the authors of this work was to study methods for measuring the amount and intensity of precipitation, as well as to analyze comparisons of the results obtained by ground and radar methods.

2 Materials and Methods

Since 2007, the FSBI “VGI” has been conducting studies of precipitation using the MRL-5 radar and ground indicators. Until 2011, pluviographs P-2 were used as ground indicators.

In 2011, the hardware and software complex “Network of automatic small-sized weather stations” was created in the VGI, located in the vicinity of Nalchik on an area of $12 \times 12 \text{ km}^2$. The complex is designed for simultaneous measurement and transmission to the central server of the main meteorological parameters. The list of components used for the hardware and software complex of the network of automatic small-sized weather stations includes:

- 10 automatic wired weather stations Vantage Pro2, Davis;
- 10 devices with protocol support IP – WeaterLinkIP (6555);
- 10 netbooks ASUSEeePC 1001P;
- 10 GPRS modems for data transmission over the Internet;
- PC CPU AMD SocketAM3 Phenom II X4 965;
- Server CPU AMD SocketAM3 Phenom II X4 965.

The Vantage Pro station used measures the following parameters:

- wind speed and direction;
- air temperature;
- rain intensity;
- total precipitation;
- air humidity;
- atmospheric pressure.

Currently, precipitation meters are used for ground-based precipitation measurement at weather stations, which measure precipitation amounts over a certain period of time (Fig. 1).

The automatic Vantage Pro station performs all measurements in continuous mode, which allows you to determine the time of the beginning and end of rain, the course of changes in precipitation intensity, the course of changes in the amount of precipitation. All this data is saved and can be displayed on the screen.

To carry out ground-based measurements, a network consisting of 10 small-sized automatic Vantage Pro weather stations operating in continuous mode was deployed. The computer interface of the station is designed for a memory capacity of 2560



Fig. 1 Meteorological site with the Tretyakov sedimentation meter in the foreground

records of all parameters with date and time indication. Figure 2 shows the layout of weather stations in the vicinity of Nalchik.

Radar measurements of precipitation are based on the use of the so-called I-Z ratio.

$$Z = A \cdot I^\beta \tag{1}$$

In this work, the meteorological two-wave radar MRL-5 was used (wavelength $\lambda = 10$ cm is used), located at the VGI research site, with an effective range of 130 km.

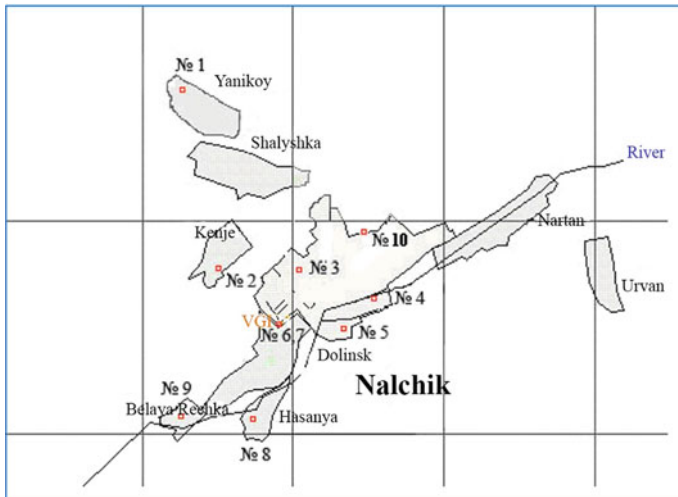


Fig. 2 The layout of the network of weather stations in the vicinity of Nalchik

Radar methods for measuring rain parameters have a number of advantages over ground-based methods: efficiency and greater scale of measurements, the ability to accumulate all information about precipitation for any period of time. In addition, the accumulated and processed information can be quickly transferred to the interested consumer. But radar methods do not have a sufficiently high measurement accuracy. This is due to large variations in the coefficients and (1) depending on the type of precipitation, their intensity, the region of observations, etc. [6–8]. To improve the accuracy of radar measurements of precipitation, various schemes are used that combine a radar and a ground-based precipitation network. This allows you to calibrate the locator in real time. For example, a method is known, which consists in determining the parameter A in the ratio (1) for the i -th element of the area and the j -th time interval according to the formula:

$$A_{ij} = I_{ij} / Z_{ij}^b. \quad (2)$$

Parameter b is considered unchanged. This technique is widely used in the USA, England and other Western countries. Another calibration method is based on the use of radar scale coefficients (so-called matching coefficients), which can be represented as the ratio:

$$M = \frac{I_H}{I_P}, \quad (3)$$

where I_P , I_H —the average precipitation layer over the cell area according to radar and ground data, respectively.

3 Research Results

As mentioned above, precipitation studies were conducted in the VGI from 2007 to 2014 using a ground-based network of precipitation meters and an MRL-5 radar. Table 1 shows data on the coefficient of matching M between radar and ground data for 8 years (2007–2014).

The analysis of the table shows that almost always the coefficient of agreement is greater than one and on average over seven years has varied from 1.3 to 1.5. This suggests that the radar systematically underestimates the size of the precipitation layer by 1.3–1.5 times.

To assess the accuracy of radar measurements of precipitation, the average relative error of measuring the precipitation layer by radar ε_2 as a percentage is calculated for rain.

$$\varepsilon_2 = \frac{1}{n} \sum_{i=1}^n \frac{|R_i - H_i|}{H_i} \cdot 100. \quad (4)$$

Table 1 Values of the matching coefficient for 8 years (2007–2014)

Years	Period			
	June	July	August	Season
2007	–	1.1	0.9	1
2008	1	2.3	1.1	1.5
2009	1.2	0.9	1.4	1.2
2010	1.2	1.4	1.2	1.2
2011	–	1.2	1.5	1.3
2012	1.2	1.3	1.3	1.2
2013	1	1.1	1.2	1.1
2014	2	2.5	1.6	2.1
On average for 8 years	1.3	1.5	1.3	1.3

In this case, the precipitation layers measured by the radar R_i and the precipitation meter H_i in the i -th of n observation points are compared.

Table 2 provides data on the relative errors of radar measurements of precipitation.

The table shows that the average relative error of radar determination of the precipitation layer is 41.63% per season.

In parallel, the influence of precipitation types on the magnitude of the measurement error was investigated. Rains, thunderstorms and downpours were considered [9–11]. There are also heavy and weak rains. Table 3 shows data for light rains. The data are provided for three years 2009, 2011 and 2014.

Table 4 shows data for heavy rains for the same years.

Analysis of the data in Tables 3 and 4 shows that with radar measurements of light rains, the error is on average 47.75%, which is slightly higher than the average for seven years. And with radar measurements of heavy rains, the error on average is 39.85%, which is slightly lower than the average for seven years.

Table 2 Relative errors of precipitation measurement for 8 years (2007–2014)

Years	Period			
	June (%)	July (%)	August (%)	Season (%)
2007	–	44.92	35.85	40.39
2008	40.35	39.20	41.15	40.18
2009	45.82	45.72	46.30	46.01
2010	38.24	37.42	36.44	36.93
2011	47.55	47.55	41.69	44.62
2012	37.65	38.54	37.71	38.13
2013	42.70	34.06	47.86	40.96
2014	42.55	47.44	41.80	44.62
On average for 8 years	42.12	41.42	41.85	41.63

Table 3 Comparison of precipitation layers measured by ground and radar methods for light rains

Date	n	\bar{H} , mm	\bar{R} , mm	σ (%)	M
10.06.2009	2	1.00	0.60	40.00	1.10
29.06.2009	2	1.30	0.60	53.85	1.00
15.07.2009	5	1.30	1.20	7.69	0.90
22.07.2009	8	0.90	0.80	11.11	1.00
27.07.2009	4	1.20	2.70	125.00	0.60
18.08.2009	9	1.70	1.10	35.29	1.00
02.07.2009	6	1.50	2.30	50.00	0.70
21.07.2009	7	0.70	1.20	77.10	0.60
31.07.2009	8	0.70	0.90	33.90	0.80
27.08.2009	7	2.20	2.90	31.82	0.80
02.07.2011	6	1.50	2.30	50.00	0.70
21.07.2011	7	0.70	1.20	77.10	0.60
31.08.2011	8	0.70	0.90	33.90	0.80
13.08.2011	5	2.70	1.50	44.44	1.80
08.06.2014	8	1.10	0.20	78.90	4.80
21.06.2014	5	0.20	0.30	43.80	0.70
22.06.2014	4	1.6	1.2	21.80	1.30
24.06.2014	4	1.9	0.5	72.40	3.60
27.06.2014	8	0.70	0.90	24.00	0.80
29.06.2014	6	0.40	0.20	53.60	2.20
04.07.2014	4	3.00	1.30	57.50	2.40
08.07.2014	4	1.90	0.90	53.00	2.10
09.07.2014	6	0.40	0.10	76.70	4.30
18.07.2014	5	0.20	0.20	0.00	1.00
20.07.2014	4	1.20	2.20	79.10	0.60
22.07.2014	8	0.20	0.10	41.70	1.70
29.07.2014	5	1.00	0.10	85.30	6.80
12.08.2014	5	0.60	0.80	33.30	0.80
29.08.2014	5	2.20	1.50	31.80	1.50
22.08.2014	8	0.40	0.20	50.00	2.00
23.08.2014	6	1.60	1.50	6.30	1.10
Average error value				47.75	1.62

Table 4 Comparison of precipitation layers measured by ground and radar methods for heavy rains

Date	n	\overline{H} , mm	\overline{R} , mm	σ (%)	M
03.07.2009	7	3.4	3.0	10.60	1.1
10.07.2009	5	3.3	2.8	15.20	1.2
11.07.2009	4	17.0	11.3	33.80	1.5
12.07.2009	6	20.0	8.8	56.20	2.3
04.08.2009	6	6.7	3.0	55.22	2.2
16.08.2009	4	4.4	5.8	31.82	0.8
17.08.2009	6	4.2	2.8	33.33	1.5
18.08.2009	7	3.9	2.0	48.72	2.0
25.08.2009	8	9.8	5.6	42.86	1.7
26.08.2009	6	45.7	25.0	45.30	1.8
21.07.2011	6	3.3	1.3	60.61	0.9
03.07.2011	7	3.4	3.0	10.60	1.1
10.07.2011	5	3.3	2.8	15.20	1.2
11.07.2011	4	17.0	11.3	33.80	1.5
12.07.2011	6	20.0	8.8	56.20	2.3
04.08.2011	6	6.7	3.0	55.22	2.2
16.08.2011	4	4.4	5.8	31.82	0.8
17.08.2011	6	4.2	2.8	33.33	1.5
18.08.2011	7	3.9	2.0	48.72	2.0
25.08.2011	8	9.8	5.6	42.86	1.7
26.08.2011	6	45.7	25.0	45.30	1.8
10.06.2014	4	19.5	7.7	60.30	2.5
18.06.2014	6	12.7	13.1	2.50	1.0
26.06.2014	7	3.8	2.8	26.10	1.4
06.07.2014		7.7	6.4	16.40	1.2
07.07.2014	7	6.1	8.5	29.50	1.4
19.07.2014	4	12.1	4.6	25.30	1.3
21.07.2014	7	22.6	3.9	82.90	5.9
28.07.2014	7	6.5	2.0	69.40	3.3
05.08.2014	5	19.0	8.3	56.30	2.3
06.08.2014	4	16.2	5.2	67.90	3.1
10.08.2014	6	23.6	11.7	50.40	2.0
19.08.2014	4	15.2	9.1	40.10	1.7
20.08.2014	4	4.6	2.8	39.10	1.6
21.08.2014	7	4.0	3.5	12.50	1.1
25.08.2014	7	4.4	6.6	50.00	0.7
Average error value				39.87	1.77

4 Conclusions

The conducted comparisons of radar and ground measurements of precipitation showed that almost always the matching coefficient is greater than one and on average for seven years it varied from 1.3 to 1.5. This suggests that the radar systematically underestimates the size of the thickness of the precipitation layer by 1.3–1.5 times.

The average relative error of measuring total precipitation for the summer season by radar method does not exceed 42%. The radar measures weak rains worse. The average error is 48%. In heavy rains, the error is 40%.

References

1. Abshaev, M.T., Inyukhin, V.S., Liev K.B.: Some results of rain measurement by radar and ground methods. *Proceedings of the VGI*. 92, 55-64 (2008). [in Russian].
2. Borovikov, A.M., Kostarev, V.V., Mazin, I.L., Smirnov, V. I., Chernikov, A. A.: Radar measurements of precipitation. Hydrometeoizdat, Leningrad (1967). [in Russian].
3. Volynets, L.M., Zabolotskaya, T.N.: On the choice of parameters in the Z–I ratio for radar measurement of precipitation. *J. Tr. UkrNIGMI*. **118**, 135 - 144 (1972). [in Russian].
4. Doviak, R., Zrnich, D.: Doppler radars and meteorological observations. Hydrometeoizdat, Leningrad (1988). [in Russian].
5. Inyukhin, V.S., Kapitannikov, A.V., Aksenov, S.A., Live, K.B.: The use of radar data on the precipitation field for the operational forecast of rain floods. Reports of the All-Russian Conference on Cloud Physics and active impacts on hydrometeorological processes. St. Petersburg: Hydrometeoizdat, 189–202 (2006). [in Russian].
6. Inyukhin, V.S.: Radar characteristics of rain. *Proceedings of the VGI*. 94, 54-60 (2006). [in Russian].
7. Inyukhin, V.S.: Automated radar measurements of rains. *Proceedings of the All-Russian Conference on Mudflows: October 26–28, 2005, Moscow*, LKI Publishing House, 302–310 (2008). [in Russian].
8. Stepanenko, V.D.: Radar in meteorology. Hydrometeoizdat, Leningrad (1966). [in Russian].
9. Inyukhin, V.S., Kushchev, S.A., Liev, K.B. et al. Radar studies of the distribution of the formation zones of the first radar echo of hail clouds. *Izv. Atmos. Ocean. Phys.* **52**, 615–621 (2016).
10. Inyukhin, V.S., Liev, K.B., Dolova, M.L., Dumaeva, L.V.: On the accuracy of radar measurements of the total amount of atmospheric precipitation on the territory of Kabardino-Balkaria according to the data of 2010-2011. *J. Engineering surveys* **8**, 50-54 (2012). [in Russian].
11. Liev, K.B., Malkarov, A.S.: Comparison of radar and ground-based precipitation measurements based on the results of 2010 in the mountainous regions of Kabardino-Balkaria. *News of universities of the North Caucasus region. Natural Sciences*, **6**, 36–40 (2011). [in Russian].

Ground Radar Method for Measuring Precipitation Under Complex Relief Conditions



V. S. Inyukhin , Yu. V. Suspitsyna , and V. V. Suslov

Abstract It is well known that the radar reflectivity of the precipitation zone Z is related to the intensity of precipitation I . The heavier the precipitation, the higher its reflectivity. The presence of such a relationship makes it possible to determine both the very fact of the presence of precipitation and its intensity from the measured Z values. By measuring the intensity of precipitation at different points in time, it is possible to calculate the amount of precipitation. The error of radar measurement of precipitation amounts can be easily determined by comparing radar readings with data from ground-based precipitation gauges. In this case, the data of the precipitation gauge are taken as “true” and are, as it were, reference. Recently, a large amount of work has been done to compare the intensities and amounts of precipitation measured by contact (precipitation network) and remote (radar) methods. It was found that along with good matches, there were significant differences in precipitation parameters. This is due to the large heterogeneity of precipitation and the previously unknown parameters of the Z – I ratio. Therefore, radar data is usually corrected by ground data. To reduce errors in radar measurements of precipitation, such measurements are made as close as possible to the Earth’s surface, at a level of 0.5–1.0 km. However, in conditions of rough terrain in the mountains and foothills, this condition often cannot be met.

Keywords Precipitation · Ground radar method · Under complex relief

V. S. Inyukhin (✉) · Yu. V. Suspitsyna · V. V. Suslov
High-Mountain Geophysical Institute, 2 Lenin Avenue, Nalchik, Russia
e-mail: inuhin51@mail.ru

Yu. V. Suspitsyna
e-mail: suspitsyna35@yandex.ru

V. V. Suslov
e-mail: victorygi@yandex.ru

1 Introduction

To measure the intensity and amount of precipitation over large areas, it is necessary to deploy a dense network of ground-based precipitation gauges to obtain an adequate precipitation field on the ground. Radar, in contrast to precipitation gauges, has a number of advantages: the efficiency of collecting, processing and presenting information about precipitation; large viewing area in one cycle. The disadvantage of the radar method for measuring precipitation is a large error in determining the intensity of precipitation I by the value of radar reflectivity Z , since the coefficients in the I - Z ratio are not known in advance [1–5]. At the same time, when studying rains, it is necessary to take into account the fact that atmospheric precipitation falls on the ground in the form of spatially extended spots, i.e., form fields of precipitation. At each point, the precipitation field is characterized by a certain set of parameters, for example, the intensity of precipitation, their amount, etc. Often the task of precipitation measurements is reduced to determining the characteristics of this field. To solve such problems, the radar-ground method of precipitation measurement is optimal [6].

The purpose of this work: to discuss the possibilities of the ground-based radar method for measuring the amount of precipitation in difficult terrain.

2 Materials and Methods

Radar measurements of precipitation were carried out on an automated radar MRL-5, at a wavelength of $\lambda = 10$ cm.

A network consisting of 10 Vantage Pro small-sized automatic weather stations was used as ground-based precipitation meters. The weather station includes a rain gauge. Automatic weather station, performs all measurements in a continuous mode, which allows for continuous monitoring of meteorological values.

Instrumental errors in the readings of these rain gauges are determined by the instrument's passport error of 0.2 mm. In addition, ground-based precipitation measurement errors are well known and can be reduced to the following reasons:

- losses due to deformation of the wind field above the rain gauge inlet (2–10%);
- loss of liquid due to wetting of the inner walls of the collector and the liquid remaining in the container after its emptying (2–10%);
- losses due to evaporation from the container (0–4%);
- splashing (1–2%).

Therefore, it is necessary to determine the error of the instrument used empirically.

3 Research Results

The easiest way to compare the errors of two different types of instruments is to compare two instruments side by side. In [7], the data of a comparative analysis of the errors of the Davis Vantage Pro2 meteorological station and the P-2 pluviograph installed nearby are given. The studies were carried out for 2 summer months (26 days with rain). The analysis showed that the average relative measurement error at the weather station was 14.41%. The comparisons made show that the errors in the readings of two dissimilar rain gauges are basically within the measurement errors for ground-based indicators. In another experiment, two Vantage Pro2 weather stations were installed in the immediate vicinity of each other, at a distance of 7 m, on the territory of the FSBI «HMGI» [8].

The measurement data of total precipitation obtained at both weather stations for the entire observation period showed that:

- average monthly relative measurement error was 1.4%;
- the maximum relative measurement error was 16.7%.

Comparisons of the measurement data of two adjacent precipitation gauges showed that automatic precipitation gauges have an acceptable precipitation measurement accuracy.

For radar measurements of precipitation, the meteorological radar MRL-5 is used, located at the research site of the FSBI «HMGI» “Kyzburun”. The amount of precipitation is measured using the «Meteo-X» automated radar system, which provides calculation of precipitation intensity fields I (mm/h) within a radius of 125 km.

Precipitation measurements were made automatically. The round-robin cycle was repeated every 3.5 min during the entire rain that fell in the Nalchik region. The measurement results were presented on the monitor screen in the form of a field of precipitation intensity or a field of accumulated precipitation during the rain. Figure 1 shows the “Precipitation” program window with the calculated precipitation field for June 18, 2009. The height of the level of construction and display of the precipitation field was chosen as close as possible to the ground level. When conducting research, it was assumed that the size distribution function of drops corresponded to the Marshall-Palmer distribution [9]. The relationship between precipitation intensity and reflectivity measured by radar can be represented by the relationship:

$$Z = A \cdot I^\beta. \quad (1)$$

The layer of water that fell during the rain was determined by the radar by summing the values $I_j \cdot \Delta t_j$, received in each review cycle.

Ground and radar measurements were compared in time and space within the same rain.

To improve the accuracy of measuring precipitation fields, the radar is calibrated with data from a ground-based precipitation network. Currently, various methods of calibration are used. For example, a method is known that consists in determining the

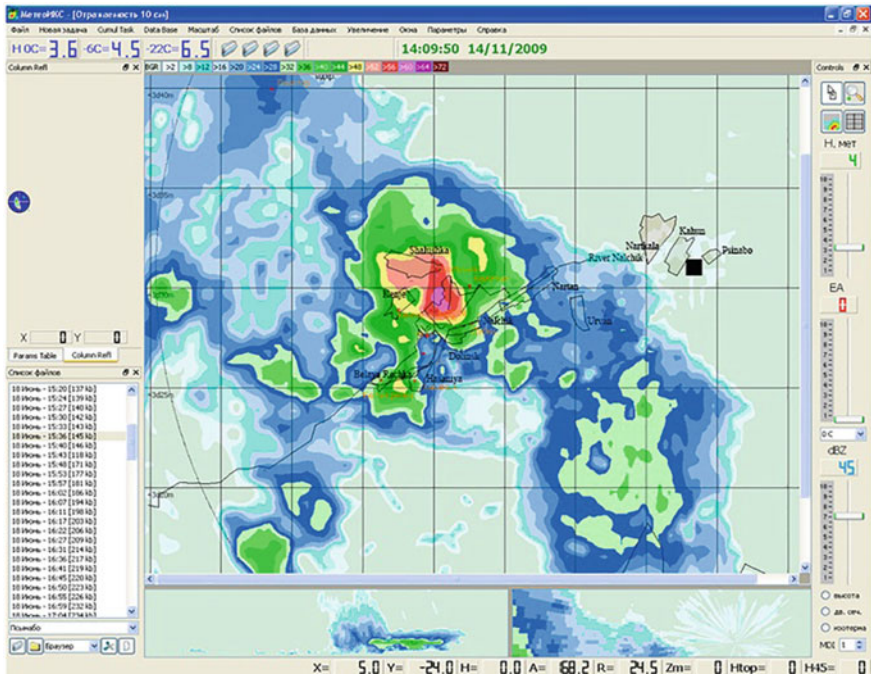


Fig. 1 General view of the “Precipitation” program window

parameter A in relation (1) for the i -th element of the area and the j -th time interval according to the formula:

$$A_{ij} = I_{ij} / Z_{ij}^b. \quad (2)$$

The parameter b is assumed to be unchanged. This technique is widely used in the USA, England and other Western countries. Another calibration method is based on the application of radar scale factors (so-called matching factors), which can be represented as a ratio:

$$M = \frac{I_P}{I_H}, \quad (3)$$

where I_P , I_H —average over the area of the cell layer of precipitation according to radar and ground data, respectively.

In the proposed radar-ground method for measuring precipitation, a slightly different method is used, the essence of which is as follows [10].

1. During the rain, data on the precipitation layer obtained from n pluviographs are entered into the computer database. In the process of radar observations at the same points, the total precipitation is calculated \bar{I}_P , and their values are entered

into the database. Thus, in the data table, each ground value \bar{I}_H is assigned to the radar value I_P . Based on the data obtained, a linear regression equation is constructed:

$$I_H = \alpha \cdot I_P + b. \tag{4}$$

- The coefficients α and b of the linear regression equation are determined by the formulas:

$$\alpha = \frac{N \sum_{i=1}^N I_{Hi} I_{Pi} - \sum_{i=1}^N I_{Pi} \cdot \sum_{i=1}^N I_{Hi}}{N \cdot \sum_{i=1}^N I_{Pi}^2 - \left(\sum_{i=1}^N I_{Pi}\right)^2},$$

$$b = \frac{\sum_{i=1}^N I_{Hi} \cdot \sum_{i=1}^N I_{Pi}^2 - \sum_{i=1}^N I_{Hi} I_{Pi} \cdot \sum_{i=1}^N I_{Pi}}{N \cdot \sum_{i=1}^N I_{Pi}^2 - \left(\sum_{i=1}^N I_{Pi}\right)^2}.$$

The calculation of the coefficients can be started at $N = 2$. The procedure is cumulative. The more, the more accurate the values of the coefficients. Further, the obtained values of the coefficients α and b are substituted into formula (4).

Figure 2 shows two correlations between ground-based and radar measurements of the precipitation layer in August 2009 [6]. The left figure shows the data uncorrected, the right one is adjusted according to the formula (2).

Additional problems of radar measurement of precipitation in rough terrain are associated with the blocking of radio emission by natural barriers (hills). To measure precipitation at low elevation angles under these conditions, the effect of passive interference is significantly interfering. The desire to measure precipitation zones closer to the earth’s surface inevitably leads to an increase in precipitation intensity measurement errors due to the shielding effect of local objects.

When measuring precipitation, the height of passive interference of natural origin, which interferes with the passage of the radar signal and distorts its value behind the obstacle, should be taken into account. Figure 3 shows the real heights of the terrain along the radar signal propagation paths over the network of precipitation gauges.

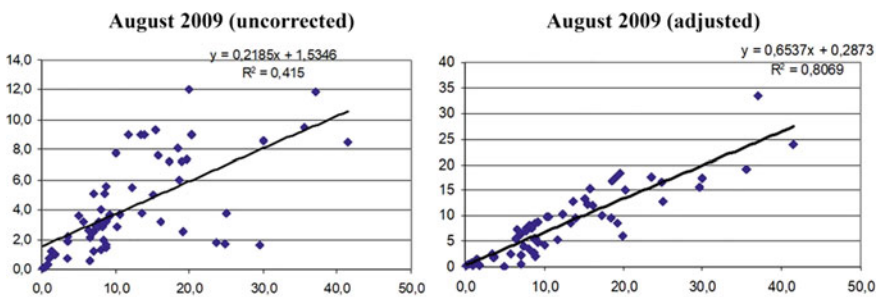


Fig. 2 Communication of ground and radar data

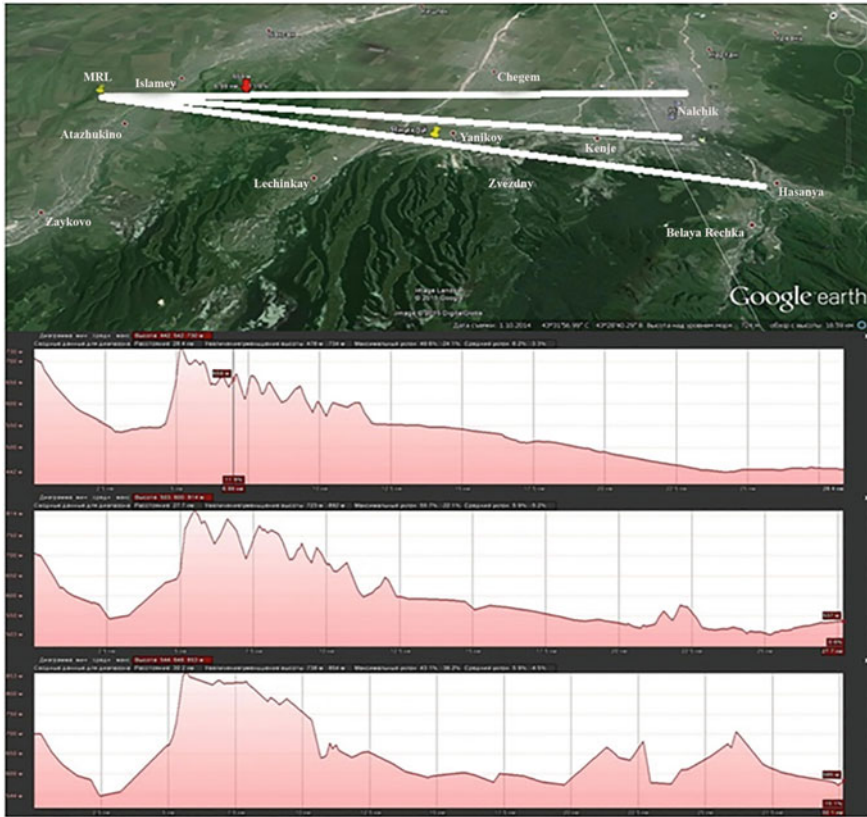


Fig. 3 Elevations of the terrain along three routes: VGI polygon—Aleksandrovka (the highest point is 710 m), VGI polygon—VGI building (the highest point is 814 m) and VGI polygon—v. Hasanya (highest point 850 m)

It can be seen from the figure that in two cases the location of the radar is located slightly below the obstacle. This indicates that the radar signal in these cases at the lower elevation angles behind the obstacle will be obviously distorted.

Figure 4 shows a typical example of a horizontal section of the precipitation field at a height of 1.0 and 2.0 km.

It can be seen from the figure that the precipitation field in the right section is strongly distorted due to the screening of the radar signal by obstacles. Table 1 presents data from radar measurements at various altitudes showing what errors can occur in precipitation measurements.

The table shows that the optimal level of radar measurements in this case is the level of 2 km.

To automate the collection of radar information and find the optimal level of measurements, it is proposed to use a digital map of the area shown in Fig. 5(a).

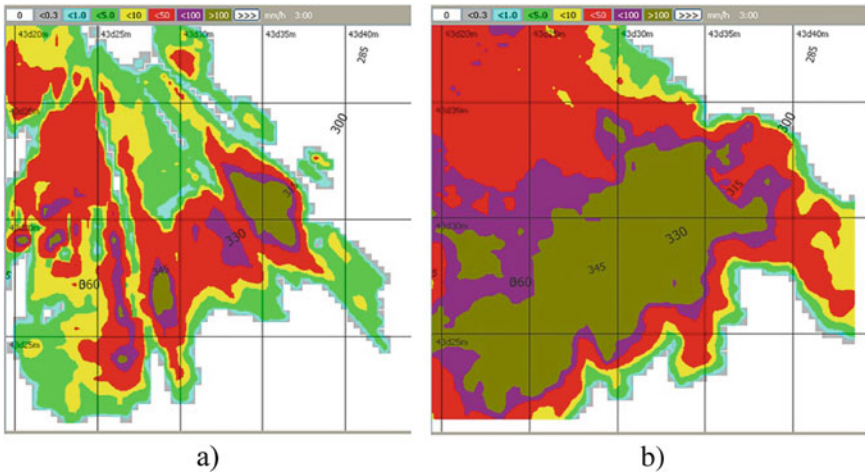


Fig. 4 The field of total precipitation obtained at an altitude of: **a** –1.0 km; **b** –2.0 km.

Table 1 An example of a comparison of radar (at three levels) and ground data on the amount of precipitation for various observation points. Rain on June 18, 2009. The levels of radar measurements above the measurement points P1, P2 and P3 correspond to a height of 1, 2 and 3 km, respectively

Measurement point	Ground data	P1	Error rate 1, %	P2	Error rate 2, %	P3	Error rate 3, %
No. 3	65	24	63.08	54.2	16.62	44.7	31.23
No. 4	30.8	5.2	83.12	22.7	26.30	12.7	58.77
No. 7	63	30.1	52.22	32.9	47.78	25.9	58.89
No. 6	54	24.2	55.19	72.8	34.81	66.4	22.96
No. 1	52	14.1	72.88	63.8	22.69	32.8	36.92
No. 5	48	11.7	75.63	40.5	15.63	35.1	26.88
No. 2	22.6	6.7	70.35	10.2	54.87	9.6	57.52
Average error			67.49		31.24		41.88

Figure 5(b) shows the algorithm of the program for measuring rainfall in conditions of complex terrain.

Methods for measuring precipitation by the radar-ground method in conditions of complex relief include:

1. Selection of a specific radar network from a network of radars that best satisfies the optimal conditions for measuring precipitation at a required point in space.
2. Selection of the optimal elevation angle to obtain a compromise height of the Z-layer measurement in precipitation, which allows measurements to be taken as close to the Earth’s surface as possible and to minimize errors created by local features. Depending on the level of the zero isotherm, the height of the layer can vary from 0.5 to 4.0 km. To exclude reflections from local objects within the

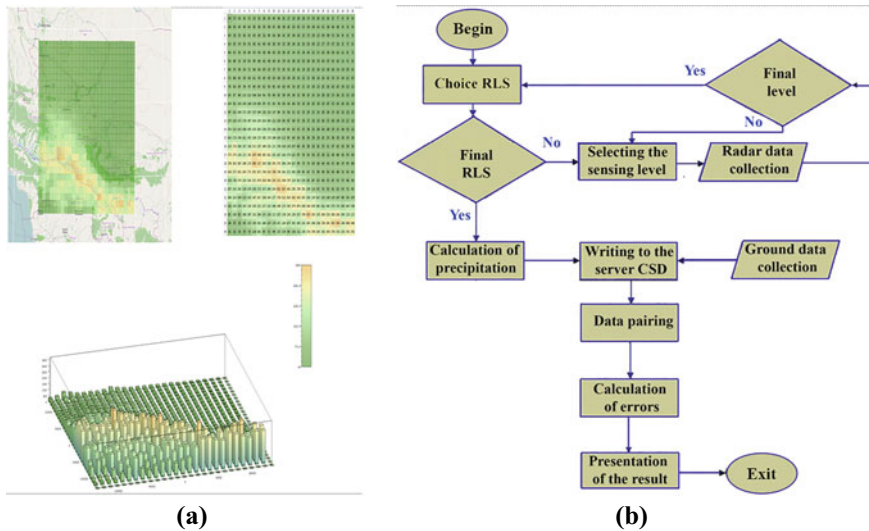


Fig. 5 **a** Three-dimensional map of the heights of the underlying surface. **b** The algorithm of the program for measuring rains in conditions of complex terrain.

viewing radius, a digital map is compiled, which is entered into the computer of the measuring complex.

3. Choosing the optimal value of the $Z-I$ ratio.
4. Carrying out the calibration of the radar station according to ground data from one or more rain gauges. Radar calibration under optimal conditions does not require a large number of rain gauges (pluviographs). The coordination of radar and ground data is carried out on the basis of accumulated precipitation.
5. Carrying out path measurements using two wavelengths. Trace methods can be very promising for measuring total precipitation. By measuring the attenuation at a shorter wavelength, fairly reliable data can be obtained on the average precipitation amounts along the path. When measuring liquid precipitation, the advantages of trace methods compared to contact methods are that they can be used in hard-to-reach areas and over water surfaces.

In the mountains, where obstacles are 2–3 km high, it is possible to increase the accuracy of measurements by using a composite map built using data from several radars of the meteorological network. Figure 6 shows such a compositional cloud map for 07.10.2012, 14:43. The picture was received from four SRLs (indicated by circles) in Maikop, Veseloe, Kyzburun and Ardon. In the center is the Maikop MRL.

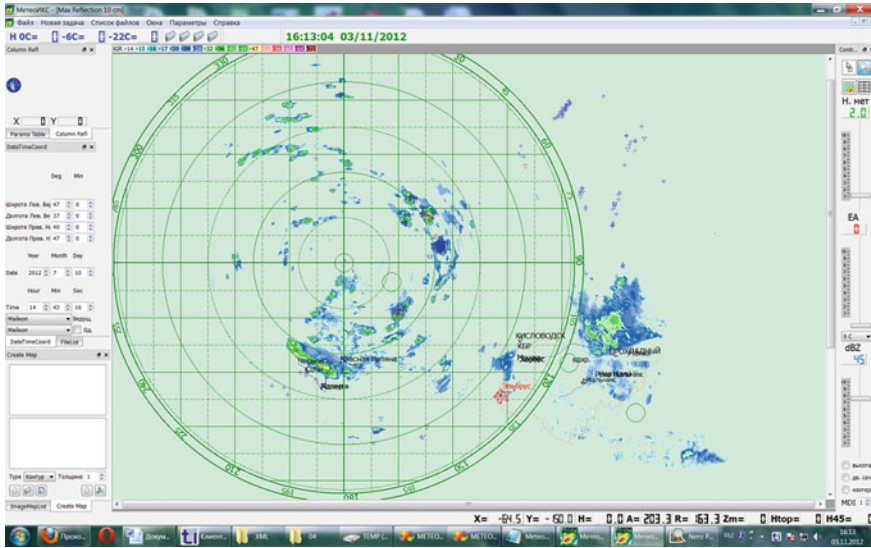


Fig. 6 Composite map of clouds for 10.07.2012, 14:43 The picture was obtained from radar data from four SCRLs (indicated by circles), in Maikop, Veseloe, Kyzburun and Ardon. In the center is the Maikop MRL

4 Conclusions

A ground-based radar method for measuring precipitation in conditions of complex relief is considered. On the rugged terrain of the foothills, it is proposed to use a digital terrain map to automate the collection of radar information and find the optimal level of measurements.

In the mountains, where obstacles are 2–3 km high, it is possible to increase the accuracy of measurements by using a composite map built using data from several radars of the meteorological network.

As experience shows, the use of the radar-ground method significantly increases the accuracy of measuring the amount of precipitation. The presented precipitation measurement method can be used to solve the following problems:

- study of climatological features of the precipitation regime for the observation area;
- study of precipitation fields;
- forecast of floods of stormwater origin;
- mud flow hazard monitoring.

References

1. Borovikov, A.M., Kostarev, V.V., Mazin, I.P., Smirnov V.I., Chernikov A.A.: Radar measurements of precipitation. *Gidrometeoizdat, Leningrad* (1967). [in Russian].
2. Volynets, L.M., Zabolotskaya, T.N.: On the Choice of Parameters in the Z–I ratio for radar measurement of precipitation. *Tr. UkrNIGMI*. **118**, 135 – 144 (1972). [in Russian].
3. Bazalova, T.A.: Meteorological automated radar networks. *Gidrometeoizdat, St. Petersburg* (2002). [in Russian].
4. Stepanenko, V.D.: Radar in meteorology. *Gidrometeoizdat, Leningrad* (1973). [in Russian].
5. Litvinov, I.V.: The structure of precipitation. *Gidrometeoizdat, Leningrad* (1972). [in Russian].
6. Inyukhin, V.S., Live, K.B., Malkarov, A.S., Suslov, V.V.: To the question of the accuracy of radar measurements of total precipitation. *Izvestiya KBNTs RAS*. **3**, 36 - 43 (2011). [in Russian].
7. Inyukhin, V.S., Makitov, V.S., Suslov, V.V.: Comparative analysis of data from radar and ground-based measurements of rainfall. *Izvestiya KBNTs RAS*. **1**(51), 36-44 (2013). [in Russian].
8. Suspitsyna, Yu.V.: The trend of change in the amount of precipitation per month in the summer period by years in the area of the city of Nalchik. *J. Life Safety* **8** (248) 51-56 (2021).
9. Marshall, I.S., Palmer, W.M.: The distribution of raindrops with size. *J. Meteorol.* **5**, 165-172 (1948).
10. Inyukhin, V.S.: Automated radar measurements of rain. *Proceedings of the All-Russian conference on mudflows*. 302–310 (2005). [in Russian].

Radar Methods for Determination of Hail Microstructure



V. S. Inyukhin  and E. A. Cherednik 

Abstract The currently existing radar methods for determining the microphysical characteristics of hail require constant improvement. The purpose of this work is to consider radar methods for determining the hail microstructure (two-wave and single-wave methods). The result of long-term studies of the microstructural characteristics of hail growing in a cloud is presented. A comparison is made of the results of determining the hail size by the two considered methods. The repeatability of some parameters of real hail spectra is determined. More than 600 hail clouds of various intensities that developed over the territory of the KBR and adjacent areas were studied. Based on the results of many years of research, a curve was constructed that describes the correlation between concentrations and the average cubic hail diameter in the growth zone at the moment of maximum development of convective cells.

1 Introduction

Existing radar methods, with varying degrees of reliability, make it possible to indicate hail in a cloud or to estimate the intensity of hail precipitation when it falls. However, in many cases, information about the size and concentration of the growing hail is often needed, as well as the ability to control the change in these parameters over time. This is especially true for carrying out active impacts on clouds, since in this case it is possible to evaluate the seeding efficiency on a real-time scale by changing the hail microstructure.

The two-wave hail detection method is based on differences in the frequency dependence of radio wave scattering by hydrometeors of various sizes. 0.7 cm hydrometeors are considered hail-bearing. The rationale for using the two-wave

V. S. Inyukhin (✉) · E. A. Cherednik
High-Mountain Geophysical Institute, 2 Lenin Avenue, Nalchik, Russia
e-mail: inuhin51@mail.ru

E. A. Cherednik
e-mail: elena.cherednik@mail.ru

radar method to determine the parameters of the microstructure of hail precipitation is given in [1, 3–5] under the assumption that scattering particles are spherical, scattering is single and incoherent. At the same time, it is assumed that the size distribution of hail particles is subject to the law of gamma distribution, while it was assumed that the thickness of the surface water film on hailstones growing in the wet mode, as well as in the melting mode, is equal to a constant (0.05 cm) [2]. In [6, 7], when considering the process of hail melting in the warm part of the atmosphere, patterns of changes in the melt water film on hailstones of various sizes with height were obtained.

The purpose of this work is to consider radar methods for determining the hail microstructure (two-wave and single-wave methods). The result of long-term studies of the microstructural characteristics of hail growing in a cloud is presented.

2 Research Results

When using dual-wavelength radar, the measurement of hail size and concentration in a cloud is based on the dependence of hail size on the ratio of radar reflectivity values at two wavelengths. The reason for using two wavelengths is that the value of radar reflectivity at each wavelength is a function of both hail size and hail concentration. For two wavelengths, in the general case, a system of two equations takes place:

$$\eta_{\lambda 1} = A_1 N d^{\alpha 1}, \quad \eta_{\lambda 2} = A_2 N d^{\alpha 2}. \quad (1)$$

The reflectivity ratio depends only on the hail size.

$$\eta_1 / \eta_2 = A_1 / A_2 d^{\alpha 1 - \alpha 2}. \quad (2)$$

For a water film $h = 0.05$ cm, Eq. (2) can be represented as [2]:

$$\eta_{10} = 3.8 \cdot 10^{-8} N \cdot d^{5.4}, \quad \eta_{3.2} = 6.7 \cdot 10^{-7} N \cdot d^{2.1}. \quad (3)$$

From Eqs. (2) and (3) one can get:

$$d_3 = 2.39 \cdot d^{-0.303}. \quad (4)$$

To take into account the hail attenuation of the radar signal at a wavelength of $\lambda = 3.2$ cm, the relationship between the attenuation coefficient $k_{3.2}$ and the reflectivity η_{10} of the form is often used

$$k_{3.2} = A \cdot \eta_{10}^{\alpha}, \quad (5)$$

where A and α are some coefficients.

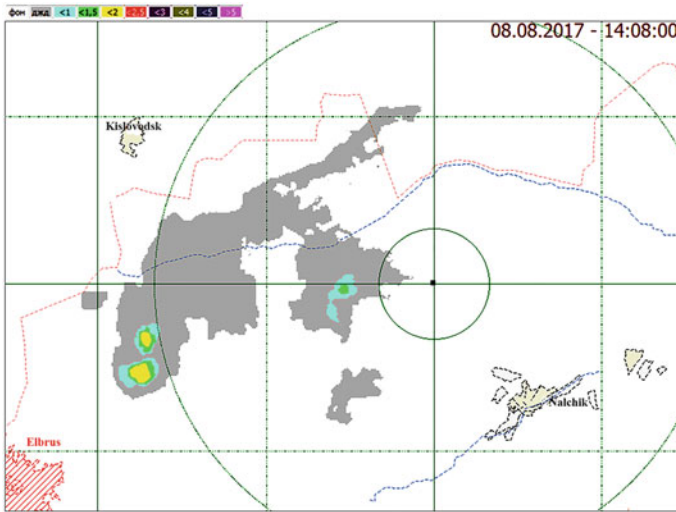


Fig. 1 Horizontal section of a field of average cubic hail on 08/08/2017 14:08, made at a height of 4.4 km

To illustrate the operation of the two-wave method, Fig. 1 shows a horizontal section of the field of the average cubic size of a hail on August 8, 2017 14:08, made at a height of 4.4 km.

Single wave method. The transition to a single-wave dependence can be based on various assumptions and simplifications, leading to an increase in the methodological measurement error. When using dual-wavelength radar, the measurement of hail size and concentration in a cloud is based on the dependence of hail size on the ratio of radar reflectivity values at two wavelengths. The reason for using two wavelengths is that the value of radar reflectivity at each wavelength is a function of both hail size and hail concentration. When developing a single-wave method, it was necessary to find an empirical relationship between the size and concentration of hail in a cloud.

An analysis of a large number of hail spectra obtained on the ground is given in [8]. It shows that the relationship between concentration and size is well described by an empirical dependence of the form:

$$N = Ad_3^\alpha, \tag{6}$$

where A is a constant; coefficient $\alpha \approx 3$.

In [9], 40 hail spectra in a cloud are analyzed, obtained when crossing hail sources by a laboratory aircraft. This is the most reliable data on the growing hail.

If the dependence between N_{gr} and D_{av} , obtained in [9], is reduced to the form (8), then we will obtain the following expression:

$$N = 0.49d_3^{-3.50}. \tag{7}$$

In [10], a family of curves is considered that describes the data of experiments on determining the relationship between the size of hailstones and their concentration, performed by various researchers. Summarizing these data in [10], an expression similar to (9) was obtained:

$$N = 0.56d_3^{-3.40}. \quad (8)$$

Another possibility of obtaining the relationship between the concentration and size of hail appears when conducting two-wave radar studies of the parameters of the microstructure of hail clouds. One of the advantages of this approach is the ability to measure the values of radar reflectivity at two wavelengths at any point in the hail source.

The paper [11] presents the data of two-wavelength radar measurements of hail microstructure on the territory of the KBR and adjacent areas. Research was carried out in 2009–2010 for hail cells during their maximum development. The dependence between N and d_3 , obtained from the results of studies in [11], has the form:

$$N = 0.91 \cdot d_3^{-3.62}. \quad (9)$$

In this case, the correlation coefficient was equal to 0.68.

Theoretical and experimental studies of the formation and development of hail centers show that hail growth occurs mainly in the temperature range from -10 to -25 °C [12]. Under these conditions, the situation is most often realized when we are dealing with the so-called inhomogeneous hail, when only part of the hailstones in the spectrum grows in a wet mode under a water film, while the other part of them remains dry during growth [11–13]. The ratios between the number of hailstones growing in different modes, as well as the thickness of the water film, are determined by the temperature and water content of the cloud.

For such an inhomogeneous hail, the dependence of reflectivity on size and concentration has the form:

$$\eta_{10} = 7.0 \cdot 10^{-8} d_3^{4.83} N. \quad (10)$$

And the theoretically obtained correlation between concentration and size has the form [14]:

$$N = 0.31 \cdot d_3^{-3.64}. \quad (11)$$

Substituting (11) into (10) we obtain for a wavelength of 10 cm the desired dependence of reflectivity on a single parameter—hail size:

$$\eta_{10} = 2.1 \cdot 10^{-8} d_3^{1.19}. \quad (12)$$

From (12) it is possible to obtain a working relation for measuring the average cubic hail size:

$$d_3 = 1.15 \cdot 10^6 \eta_{10}^{0.79}. \tag{13}$$

The resulting single-wave (for wavelength 10) formula can be used to study the microstructure of hail clouds, as well as in anti-hail projects for the operational assessment of the efficiency of seeding hail clouds with a crystallizing reagent.

Let us estimate the errors of the single-wave method. To do this, we will calculate the hail size in real clouds using the two-wave and single-wave methods, and compare the results. Comparison of the results was carried out for a large number of hail clouds, one of them is given in Table 1.

Table 1 Values d_3 measured by the one- and two-wave method in hail clouds developing over the territory of the KBR in June 2011

The date	Z ₁₀	Z _{3,2}	Two wave method d ₃	Single wave method d ₃	Single wave method error, %
05.06	61	53	0.96	1.47	52.87
05.06	59	57	0.66	1.02	54.29
08.06	52	50	0.66	0.29	56.82
08.06	55	46	1.02	0.49	51.77
08.06	55	48	0.9	0.49	45.38
08.06	55	52	0.7	0.49	29.96
09.06	63	50	1.31	2.11	61.19
09.06	53	50	0.7	0.34	51.32
09.06	62	56	0.85	1.76	107.65
09.06	52	51	0.62	0.29	54.05
10.06	57	52	0.8	0.71	11.01
10.06	55	50	0.8	0.49	38.15
10.06	60	52	0.96	1.22	27.45
11.06	57	53	0.75	0.71	5.30
14.06	53	48	0.8	0.34	57.01
14.06	55	45	1.09	0.49	54.68
14.06	53	49	0.75	0.34	54.26
14.06	52	46	0.85	0.29	66.32
17.06	55	55	0.58	0.49	15.60
17.06	54	56	0.51	0.41	20.32
17.06	63	56	0.9	2.11	13.06
23.06	61	59	0.66	1.47	121.99
23.06	59	56	0.7	1.02	44.99
23.06	53	50	0.7	0.34	51.32
30.06	58	54	0.75	0.85	13.59
Mean					51.25

The table shows that, on average, the error of the single-wave method compared to the two-wave method is 50%. In our opinion, further microphysical studies of hail clouds will make it possible to improve the single-wave method.

Long-term automated radar studies of hail clouds made it possible to reveal the repeatability of the main parameters of their microstructure, as was done in [15]. This paper presents the distributions of some microphysical hail parameters obtained in the hail growth zone during the period of maximum development of convective cells in the 2009–2010 season. According to the data of 2009–2010, it was noted that in almost 80% of cases, a small hail with a maximum size of up to 1 cm was recorded in the cloud by radar.

In this work, more than 600 hail clouds of various intensities that developed over the territory of the KBR and adjacent areas were studied. Research was also carried out in the hail growth zone during the period of maximum development of convective cells.

On Fig. 2 shows the repeatability of the average cubic size of a hail growing in a cloud.

From the analysis of the given data, the following distribution characteristics were obtained: the average value of d_3 was 1.20 cm; maximum—3.32 cm; minimum—0.24 cm; standard deviation 0.5. On a more representative sample, it was found that the average size of hailstones, not exceeding 1 cm, accounted for 41% of cases [15]. This difference can be explained by the fact that, possibly, in 2009–2010, processes of low and medium intensity took place.

An important characteristic of hail precipitation is the concentration of hailstones, which, together with their size, is directly related to hail damage. It is known that the concentration of hail particles varies within a fairly wide range: from tenths of a unit to several tens per cubic meter. On Fig. 3 shows the concentration distribution of growing hailstones in the cloud, with the average value being 0.737 m^{-3} ; maximum— 8.4 m^{-3} ; minimum— 0.001 m^{-3} ; standard deviation 1.3.

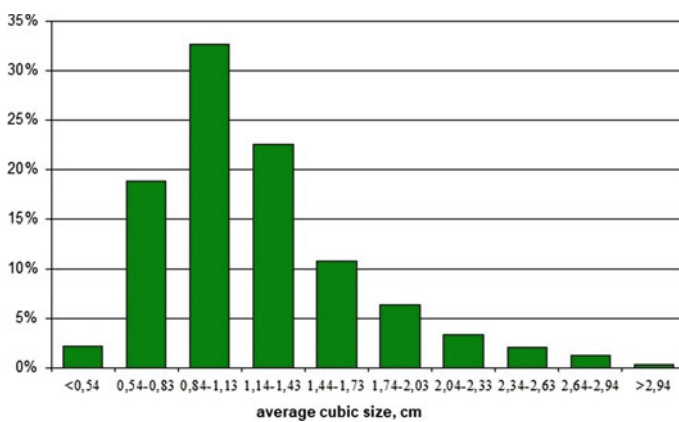


Fig. 2 Repeatability of the average cubic size of hail growing in a cloud

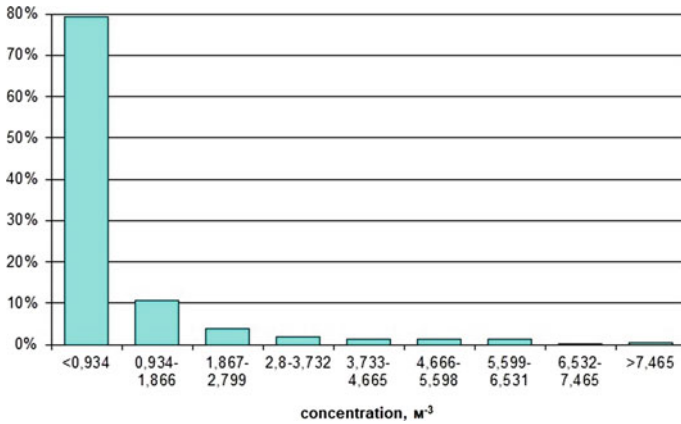


Fig. 3 Distribution of concentrations (N) of growing hailstones in a cloud

It can be seen from the figure that during the period of hail formation in the hail focus, in 78% of cases, the concentration of hail particles is less than 1.0 hailstones per m³. Only in 2% of cases the concentration of hail particles is more than 10 hailstones per m³.

When studying the pattern of hail growth, an important issue is the question of whether there is a relationship between the size of the hail and its concentration. When studying hail on the ground, such a connection was obtained [8]. When conducting this study of the hail microstructure, a correlation was also found between the average cubic size of the hail and the concentration in the growth zone. The correlation coefficient in connection $N - d^3$ was equal to 0.89. In contrast to formula (9), a new correlation formula was obtained: $N = 0.48 \cdot d^{-4.33}$. In this regard, it is necessary to refine the single-wave radar method.

On Fig. 4, based on the results of many years of research, a curve was constructed that describes the correlation between concentrations and the average cubic diameter of hail in the growth zone at the moment of maximum hail development.

3 Conclusions

The currently existing radar methods for determining the microphysical characteristics of hail do not have sufficient accuracy and efficiency, therefore, their constant improvement is required. Restoration of the fields of microphysical characteristics of hail precipitation in a rapidly changing meteorological situation is possible only with the automation of the process of collecting, processing and presenting radar information.

Radar methods for determining hail microstructure are considered. Two-wave and one-wave methods are designed to determine the microstructure of hail in the

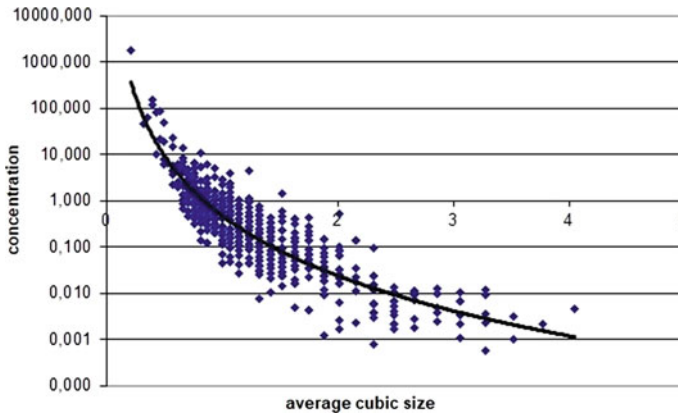


Fig. 4 Dependence of concentrations (N) of growing hailstones in a cloud on the average cubic size of hailstones (d_3)

area of its growth. One of the results of long-term studies of the microstructural characteristics of hail growing in a cloud is presented.

The repeatability of some parameters of real hail spectra is determined: the average size and concentration of hail. From the analysis of the given data, the following distribution characteristics were obtained: the average value of d_3 was 1.20 cm; maximum—3.32 cm; minimum—0.24 cm; standard deviation 0.5. At the same time, the average value of concentration (N) was 0.737 m^{-3} ; maximum— 8.4 m^{-3} ; minimum— 0.001 m^{-3} ; standard deviation 1.3. Based on the results of many years of research, a curve was constructed that describes the correlation between concentrations and the average cubic diameter of hail in the growth zone at the moment of maximum hail development.

References

1. Abshaev, M.T.: Radar measurements of macrostructural characteristics of clouds. Proceedings of the III All-Union Conference on radar meteorology, pp. 96–107. Gidrometeoizdat, Moscow (1968). [in Russian].
2. Abshaev, M.T., Burtsev, I.I.: Guidelines for the use of MRL-4, MRL-5 and MRL-6 radars in the hail protection system. Gidrometeoizdat, Leningrad (1980). [in Russian].
3. Abshaev, M.T. Dadali, Yu.A.: Localization of hail foci in cumulonimbus clouds. Russian Meteorology and Hydrology, **9**, 28–36 (1970).
4. Abshaev, M.T. Dadali, Yu.A., Malbakhova, N.M., Pravosudov, A.V., Chikun, V.N., Shaposhnikov, V.V.: To the question of spatio-temporal distribution of parameters of microstructure and water content of cumulonimbus clouds. Proceedings of VGI, **33**, 67–70 (1976). [in Russian].
5. Inyukhin, V. S.: Two-wave radar studies of hail clouds. Proceedings of the All-Russian Open Conference on Cloud Physics and Active Influences on Hydrometeorological Processes, pp. 151–156. Nalchik (2021). [in Russian].
6. Inyukhin, V.S., Makitov, V.S., Zhekamikhov, Kh.M.: Transformation of the radar characteristics of the melting hail spectrum. Proceedings of VGI, **72**, 42–52 (1989). [in Russian].

7. Inyukhin, V.S.: Radar model of a hail cloud. Radar meteorology and active influences: (collection of articles), pp. 145–162. St. Petersburg, GGO (2012). [in Russian].
8. Khorguani, V.G.: Microphysics of the birth and growth of hail. *Gidrometeoizdat, Leningrad* (1984). [in Russian].
9. Auer, A.H.: Distribution of Graupel and Hail with Size. *Monthly Weather Review* **100** 325–328 (1972).
10. Auer, A.H., Marwitz, J.D.: Hail in the vicinity of organized updrafts. *J. Appl. Meteorol.* **11**, 748–752 (1972).
11. Zhekamukhov, M.K.: Some problems of hailstone structure formation. *Gidrometeoizdat, Moscow* (1982). [in Russian].
12. Mason, B.J.: *The Physics of Clouds*. Oxford University Press. Oxford, UK (2010).
13. Bartishvili, G. S.: Dry and wet regime of hailstone growth during the formation of dense ice. *Trudy VGI*, **24**, 25–36 (1973). [in Russian].
14. Inyukhin, V.S., Makitov, V.S.: Possibilities of using a single-wavelength radar to assess the parameters of the microstructure of hail clouds. *Proceedings of the International Scientific Conference with elements of a scientific school*, pp. 321–328. Stavropol (2013). [in Russian].
15. Inyukhin, V.S.: Repeatability of some microphysical parameters of hail in the seasons of 2009–2010 on the territory of the KBR. *Reports of the All-Russian Conference on Cloud Physics and Active Influences on Hydrometeorological Processes*, pp. 192–199. Nalchik (2011). [in Russian].

Measuring Precipitation Fields Using Radar and Rain Gaugers



V. S. Inyukhin  and S. A. Kushchev 

Abstract The article describes ground-based measurements of precipitation by a network of ground-based precipitation gauges. The main task is to restore the precipitation field from the values measured at reference points (location of precipitation gauges). Precipitation fields were measured using a network of automatic weather stations Vantage Pro2 created at the High Mountain Geophysical Institute. For remote measurement and construction of precipitation fields for various local areas of the territory of the Kabardino-Balkarian Republic (KBR) and adjacent areas, data from a meteorological radar located at the research site of the High-Mountain Geophysical Institute “Kyzburun” are used. The data from it were sent to the FTP server of the High Mountain Geophysical Institute, from where they were further used upon request to construct sediment fields. Similar studies of the precipitation regime were carried out for the catchment area of the Nalchik River. When carrying out radar measurements of precipitation, the entire length of the Nalchik River was conditionally divided into three approximately equal sections: the upper, middle and lower reaches. In this case, the catchment was divided into squares 2×2 km. The conducted studies of precipitation fields for the territory of Nalchik and surrounding villages in June 2012 showed that the average precipitation layer is 31.2% less than that obtained according to the data of the Kabardino-Balkarian Center for Hydrometeorology and Environmental Monitoring. The method of constructing precipitation fields can be used to predict nano-water floods of storm origin and monitor mudflow hazard.

Keywords Precipitation fields · Weather station · Weather radar · Riverbed · Showers

V. S. Inyukhin (✉) · S. A. Kushchev
High-Mountain Geophysical Institute, 2 Lenin Avenue, Nalchik, Russia
e-mail: inuhin51@mail.ru

S. A. Kushchev
e-mail: stasuk6@mail.ru

1 Introduction

When carrying out ground-based measurements of precipitation by a network of ground-based precipitation gauges, the main task is to reconstruct the precipitation field from the values measured at reference points (location of precipitation gauges).

Until the middle of the last century, it was believed that the amounts of precipitation obtained at the point of standing of the precipitation gauge and in the territory near it differ little. More recent studies of precipitation fields have shown that the sums of precipitation at two points can differ significantly from each other. Therefore, it is necessary to estimate the errors of extrapolation of data from one observation point to another point or some territory.

When measuring precipitation, it becomes necessary to solve the following problems:

- according to the data on precipitation layers measured at one point, estimate the layer of precipitation at another point located at some distance from the first one;
- according to data on precipitation layers measured at several points, estimate the layer of precipitation at a point located between them;
- according to the data on precipitation layers measured at one point, determine the layer of precipitation in the area around this point;
- from data on precipitation layers measured at several points located in a certain territory, determine the amount of precipitation for all territories.

2 Methods

Measurement of precipitation fields in a rapidly changing meteorological situation is impossible without automation of the process of collecting, processing and presenting radar information [1–3].

Vantage was created at the High Mountain Geophysical Institute Pro 2 (Fig. 1).

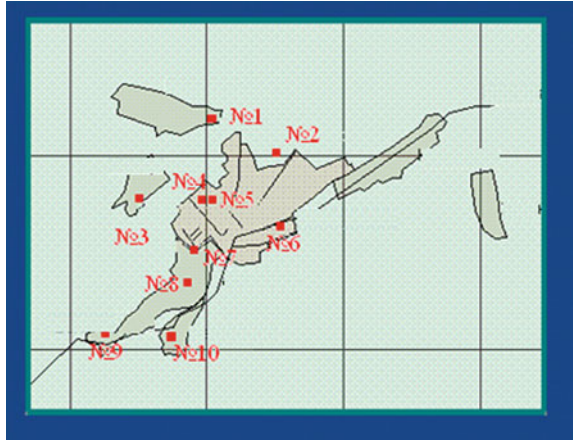
The list of components used for the hardware and software complex of the network of automatic small-sized weather stations includes:

- 10 automatic wired Davis weather stations Vantage Pro2;
- 10 GPRS modems for data transmission via the Internet to the CPU server AMD.

Socket AM 3 Phenom II X 4 965, located in the High Mountain Geophysical Institute building [4].

Weather station Davis Vantage Pro 2 is a professional wire type instrument designed for continuous measurement of meteorological parameters, including the intensity and amount of precipitation.

Fig. 1 Ground network of rain gauges in the area of Nalchik



Since the automatic station Vantage Pro (Fig. 2) performs all measurements in a continuous mode, this allows continuous monitoring of meteorological values, continuous measurement of the intensity and amount of precipitation at the meteorological station.

The created network of meteorological stations is intended for automatic monitoring of precipitation in the observation area and construction of their fields. The field of atmospheric precipitation is the areas of the underlying surface moistened by precipitation falling over various time intervals.

For remote measurement and construction of precipitation fields for various local areas of the territory of the Kabardino-Balkarian Republic, and adjacent areas, radar data are used, located at the research site of the High-Mountain Geophysical Institute “Kyzburun” and the network of meteorological stations described above. The data

Fig. 2 Vantage Pro2 weather station



from scientific research site Kyzburun were sent to the FTP server of the High Mountain Geophysical Institute [1], from where they were further used on request to build sediment fields.

During the rain, data on the precipitation layer obtained from n pluviographs are entered into a computer database. In the process of radar observations at the same points, total precipitation \bar{R}_p is calculated and their values are entered into the database. Thus, in the data table, each ground value y is assigned a radar value x . Based on the data obtained, a linear regression equation is constructed:

$$y = \alpha \cdot x + b. \quad (1)$$

The coefficients α and b of the linear regression equation are determined by the formulas:

$$\alpha = \frac{N \sum_{i=1}^N y_i x_i - \sum_{i=1}^N x_i \cdot \sum_{i=1}^N y_i}{N \cdot \sum_{i=1}^N x_i^2 - \left(\sum_{i=1}^N x_i \right)^2}, \quad (2)$$

$$b = \frac{\sum_{i=1}^N y_i \cdot \sum_{i=1}^N x_i^2 - \sum_{i=1}^N y_i x_i \cdot \sum_{i=1}^N x_i}{N \cdot \sum_{i=1}^N x_i^2 - \left(\sum_{i=1}^N x_i \right)^2}. \quad (3)$$

Radar data readings are carried out automatically using the MeteoX program, which, according to radar data and ground data, builds a single precipitation field over the surveyed area. Then the MeteoX program transferred files with daily precipitation amounts in text format to the FIELD program. The “FIELD” program selects from the general file of the circular view the areas of space that fall on the desired territory, for example, the city of Nalchik. Next, spatial averaging of precipitation over squares of 2×2 km is performed, and a field of precipitation sums for various short periods of time (0.5; 3; 6; 12; 24 h) or longer periods (day, month, season) was built. If necessary, spatial averaging can be changed from a square size of 500×500 m to a size of 10×10 km. Precipitation fields were built in Cartesian coordinates relative to the radar located at the research site of the High Mountain Geophysical Institute “Kyzburun”.

3 Results

In the city of Nalchik and near it, precipitation was measured using a radar and a network of automated weather stations. Radar data corrected by ground data were used to construct precipitation fields. At each point, such a field is characterized by the sum of precipitation $Q(x, y)$ —the thickness of the water layer in mm. The function $Q(x, y)$ is defined at the locations of the rain gauges. In this case, some indicators of the heterogeneity of the precipitation field can be calculated [2]:

- average rainfall per area \overline{Q} ;
- standard deviation σ ;
- average relative variability V ;
- the average absolute difference between the sums of precipitation at the central point (Qc) and at all other points in the study area R .

On Fig. 3 shows maps of precipitation fields for the territory of Nalchik and surrounding villages for June 2012.

Radar data were corrected according to ground-based measurements using formula (1). The following regression relationship was obtained: $R' = 0.4 \cdot R + 88.2$, where R —radar data; R' —corrected radar data. The average layer of precipitation in the region for June was 125 mm, the minimum value 101 mm, and the maximum value 222 mm. In the same studies conducted in July, a correlation of the form was used: $R' = 0.3 \cdot R + 125.4$. The average layer of precipitation in the region for July was 156,2 mm, the minimum value 142 mm, and the maximum value 179 mm. For August, a correlation relationship of the form was used: $R' = -0.6 \cdot R + 54.7$. The average layer of precipitation in the region for August was 41.5 mm, the minimum value 31 mm, and the maximum value 54 mm.

Table 1 shows summary data on precipitation in the region of Nalchik for June 2012.

Analysis of the table shows an important economic result:

- the average layer of precipitation that fell in the city of Nalchik and adjacent villages in June 2013 is 125 mm, which is 31.2% less than that given by the Kabardino-Balkarian Central Hydrometeorological Service;
- the average layer of precipitation in the villages located on the leeward side of the city of Nalchik (v. Kenzhe, v. Yanikoy) amounted to 123 mm for the month, which is 36.92% less than in the villages located on the windward side (village B.Rechka, Khasanya village).

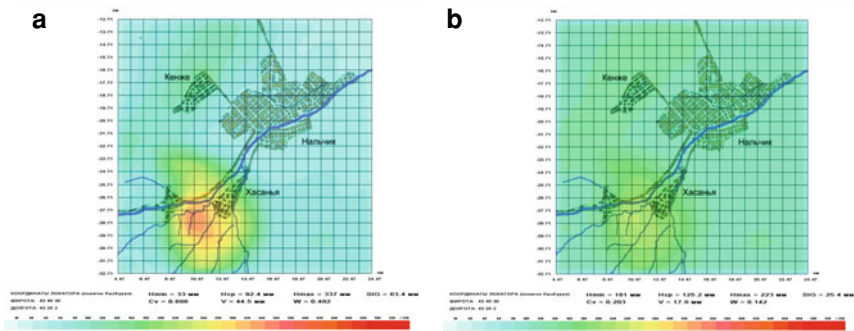


Fig. 3 The field of precipitation that fell on the territory of the city of Nalchik in June 2012: **a** radar data; **b** radar data corrected for ground measurements

Table 1 Summarizing rainfall data for June 2012

	Nalchik and villages	v. Belaya Rechka	v. Hasanya	v. Kenzhe	v. Yanikoy	Nalchik without villages	CGMS data
Min layer, mm	101	183	157	125	108	103	123
Max layer, mm	223	223	209	137	121	138	205
Middle layer, mm	125	203	187	132	114	110	164
σ , mm	8.4	14.4	15.7	3.4	4.2	7.2	
V	0.04	0.06	0.06	0.02	0.03	0.05	
R	7.6	14.6	11.6	2.6	5	4.4	

Similar studies of the precipitation regime were carried out for the catchment area of the Nalchik River. Below are some statistical characteristics of precipitation fields. When carrying out radar measurements of precipitation, the entire length of the Nalchik River was conditionally divided into three approximately equal sections: the upper, middle and lower reaches. In this case, the catchment was divided into squares 2×2 km.

Figure 4 shows the calculated field of accumulated precipitation that fell on the catchment area of the Nalchik River in June 2012.

The method of measuring precipitation fields using radar and ground data can be used to solve the following problems:

1. Study of climatological features of the precipitation regime for the observation area.
2. Study of statistical characteristics of precipitation fields.
3. Forecast of nano-water floods of shower origin.
4. Mudflow hazard monitoring [5].

4 Conclusions

When conducting ground-based precipitation measurements with a network of ground-based precipitation gauges, the main task is to reconstruct the precipitation field from the values measured at reference points (at the locations of precipitation gauges). To do this, ground data on precipitation layers measured at several points in this area must be overlaid with radar data. A network of automatic weather stations Vantage Pro 2 is used to build precipitation fields and radar data located at the scientific research site “Kyzburun”.

Studies of precipitation fields for the territory of Nalchik and surrounding villages in June 2012 showed that the average layer of precipitation in Nalchik and adjacent villages in June 2013 is 125 mm, which is 31.2% less than that obtained according

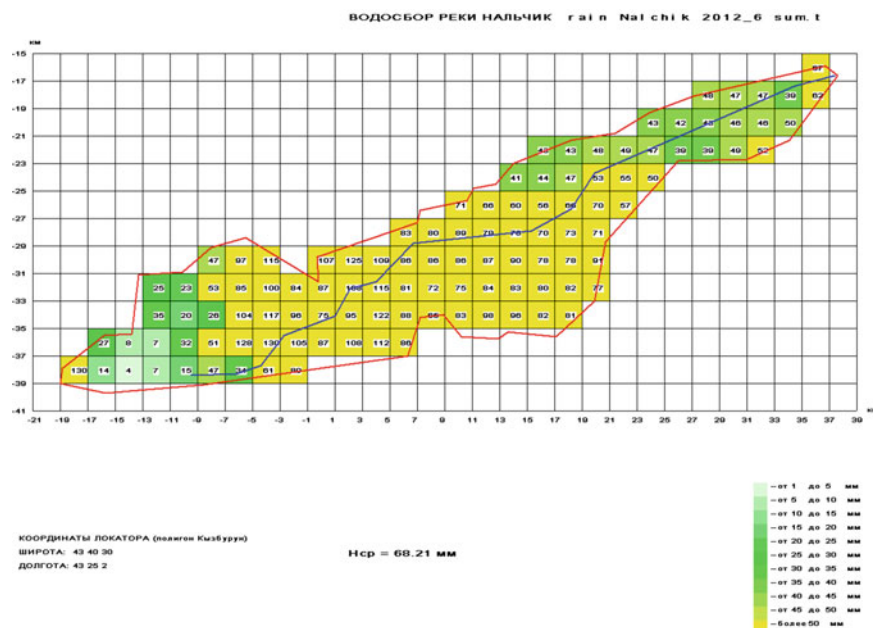


Fig. 4 The field of accumulated precipitation that fell in June 2012 on the catchment area of the Nalchik River

to Kabardino-Balkarskaya Central Hydrometeorological Service. In addition, the average layer of precipitation that fell in the villages located on the leeward side of the city of Nalchik (the village of Kenzhe, the village of Yanikoy) amounted to 123 mm over the month, which is 36.92% less than in the villages located on the windward side (B. Rechka village, Khasanya village), which is in good agreement with the literature data on precipitation fields near large settlements.

The method of constructing precipitation fields can be used to predict nano-water floods of storm origin and monitor mudflow hazard.

References

1. Abshaeв, M. T., Inyukhin, AT. S., Live, K. B.: Some results of rain measurements by radar and ground methods. Proceedings of VGI. **94**. 55 - 64 (2008). [in Russian].
2. Akseнов, S. A., Inyukhin, V. S., Kapitannikov, A. V., Liev K. B.: The use of radar data on the field of precipitation for the operational forecast of rain floods. Proceedings of the All-Russian conference on mudflows. October 26–28, 2005. “LKI”. 49 -57. (2008). [in Russian].
3. Inyukhin, V.S.: Automated radar measurements of rains. All-Russian conference on mudflows. Nalchik. 2005. “LKI”. 49–57. (2008). [in Russian].
4. Inyukhin, V.S., Live, K.B., Berezinsky, I.N., Kapitannikov, A.V.: The program for reading meteorological data from the DavisVantagePro 2 weather station and transferring them to the FTP

- server of a specialized network. Computer program Registration certificate No. 2018615178, 27.04. 2018. (2018). [in Russian].
5. Bogachenko, E.M., Inyukhin, V.S., Malbakhov, A.V.: On the practical experience of measuring rainfall by radar for local forecasting of mudflows. Reports of the All-Russian Conference on Cloud Physics and Active Influences on Hydrometeorological Processes October 24–28. 243–249 (2011). [in Russian].

Sochi Airport Thunderstorm Forecast



I. A. Ivanova, M. V. Khaibullov, O. N. Toptunova, and O. V. Volobueva

Abstract Thunderstorms affect aviation operations. Weather forecasters providing aviation forecasts need to develop the accuracy of forecasting. In addition, according to some studies, thunderstorms are becoming more frequent due to climate change. It has been analyzed those synoptic conditions with thunderstorms occurred at different times of the year. The indices of convective instability of the air mass, successfully predicting the presence and absence of thunderstorms, were considered and systematized.

Keywords Thunderstorm · Forecast · Airport · Meteorological support · Thunderstorms forecasting · Flight safety

1 Introduction

A thunderstorm is one of the most dangerous weather phenomena for aviation [1]. The danger of thunderstorms is due to intense turbulence and strong wind shear, hail, the possibility of an aircraft being struck by lightning, heavy precipitation, which decline the visibility range. Thunderstorms are often accompanied by tornadoes and squalls. Therefore, forecasters providing forecasts for aviation need to develop the accuracy of forecasting such a dangerous phenomenon in order to improve flight safety.

I. A. Ivanova (✉) · M. V. Khaibullov · O. N. Toptunova · O. V. Volobueva
Russian State Hydrometeorological University, 79 Voronezhskaya Street, 192007 Saint Petersburg, Russia
e-mail: ira.nova@mail.ru

M. V. Khaibullov
e-mail: mihail.khaibullov@yandex.ru

O. N. Toptunova
e-mail: olgakolp@yandex.ru

O. V. Volobueva
e-mail: ovvolobueva@rshu.ru

Aviation forecasts are produced every 3 h, each of them is estimated beforehand. All meteorological elements specified in the forecast are evaluated, including thunderstorms. This assessment is made automatically by comparing the information about the thunderstorm in the forecast (indicated or not indicated) with the actual weather data (observed or not observed). The estimate of the entire forecast as a whole may be reduced due to the poor estimate of the forecast of any element, for example, the forecast of a thunderstorm. Moreover, not only the factor of “missing” the phenomenon is important here, but also the factor of “superfluous” phenomenon. Increasing the feasibility of forecasts is relevant for every aerodrome, including Sochi International Airport.

It should be noted that the difficulties of forecasting thunderstorms at this airfield are associated, among other things, with the complex physical and geographical features of the region. Landform plays an important role in the formation of climate and weather there.

The sea in the Sochi area never freezes, and the sea surface temperature exceeds the air temperature for seven months in a row - from September to March. The coastal area is characterized by a high level of relative humidity. Water vapor content here is close to the saturation state.

According to long-term climatic data, there are 50 days a year with thunderstorms in Sochi, including 23 days in summer and 5 days in winter. The maximum of thunderstorm activity is observed in September, when almost every third day thunderstorm occurs. Thunderstorms are divided into intramass and frontal. More often, thunderstorm is formed here as a local phenomenon and to predict it in detail for the next 24 h in accordance with the requirements for the accuracy of aviation forecasts is an incredibly difficult task.

Forecasters around the world have developed many methods of forecasting thunderstorms. Some of them work well only in a certain region (local methods), others do not depend on the location of the forecast. When predicting the possibility of the development of thunderstorm activity, the so-called convective instability indices of the air mass, which are physical and statistical parameters describing the probability and power of the development of convective processes in an unstable stratified atmosphere, are often used as predictors for forecasting dangerous weather events associated with convection.

Based on the results of sounding (wind speed and direction, humidity and air temperature parameters at certain altitudes) the probability of the occurrence of convective phenomenon is estimated. Most of the indices used are designed to predict the presence or absence of thunderstorms as a complex of meteorological phenomena associated with the development of cumulonimbus clouds [2]. This is very useful path to improve forecasts [3, 4] and for research [5–7].

Therefore, as a result of the work, it was necessary to determine the possibility of forecasting thunderstorms at the Sochi airport by the indices of convective instability of the air mass, as well as to identify typical synoptic situations in which there were errors in the forecast of “superfluous” thunderstorms.

2 Research Results

For the work, data from open sources [8–11] for the period 01.06.2020–31.05.2021 was used. Forecasts with thunderstorms were selected there. The selection was made in such a way as to exclude the intersection in time, that is, if there were several forecasts in which a thunderstorm was indicated (within the same date), only the first one was selected for work. The sample was made according to TAF daily forecasts. The actual weather was considered only from regular reports, which are issued every 30 min (METAR). Special SPECI reports were not taken into account. As a result of processing the initial data, Table 1 was formed.

The obtained results show the problem of forecasting thunderstorms at this airfield. Forecasters often indicate “superfluous” thunderstorms in forecasts, working with reinsurance, but taking into account the specifics of the work and the great responsibility they bear, ensuring flight safety, it is quite justified. When conditions are identified as a potential dangerous for the development of thunderstorm activity, the forecaster makes a decision and indicates a thunderstorm in the forecast. For various reasons, a thunderstorm may “not be observed”.

Both cases of “missing the phenomenon” are associated with night thunderstorms in summer, which were observed on warm atmospheric fronts. It is necessary to add that they were still indicated in the forecasts released later. Thus, forecasts of the “presence” of thunderstorms at this airfield can be considered successful.

At the Sochi airport weather forecasters use thunderstorm forecasting methods developed for local conditions. One of them is the method of G. L. Sosin. It is used to forecast thunderstorms in mountainous areas. It is good for assessing the development

Table 1 Assessment of the conformity of the predicted and observed phenomenon

Month	Number of forecasts	Number of periods	The phenomenon observed	The phenomenon not observed	Missing the phenomenon
June	19	36	8	28	
July	20	30	10	20	1
August	17	18	6	12	1
September	17	30	8	22	
October	8	12	5	7	
November	15	18	3	15	
December	15	16	1	15	
January	14	25	2	23	
February	13	20	0	20	
March	13	19	0	19	
April	16	20	3	17	
May	14	16	2	14	
Total	181	260	48	212	2

of intramass convection in the summer. The method is based on the presence of a convectively unstable layer, namely, on the pseudopotential temperature differences between its upper and lower boundaries, taking into account the total dew point depression at the 850 hPa, 700 hPa and 500 hPa levels, and the pseudopotential temperature difference between the 500 hPa level and the lower boundary of the convectively unstable layer taking into account the difference in dew point depression between 850 and 500 hPa levels.

Another local method of forecasting thunderstorms is the method of Akulinina. It has been developed for the Sochi airport zone to assess the occurrence of winter thunderstorms on the coastal section of Dzhubga-Adler.

When a cold front is approached from the Crimea, to find out the possibility of a thunderstorm in the next 6–12 h, this is necessary: according to sounding data in Tuapse, determine the pseudo-potential temperature at the earth and at the level of 850 hPa and calculate the difference between them; calculate the difference between sea surface and air temperature in the same time and use these predictors to determine the possibility of thunderstorms using a special graph. The method can be used from December to February only.

The method of G.D. Reshetov for forecasting frontal thunderstorms is also used. The main predictor is the synoptic situation, additional predictors are: the height of the upper boundary of a possible cumulonimbus cloud cover, the temperature at the level of its top in combination with the thickness of the cloud layer with negative temperatures. Accuracy of these 3 methods is 69–86%.

The analysis of typical synoptic situations with forecast errors of “superfluous” thunderstorms at the Sochi airfield was carried out using the archive of synoptic maps of the open Internet portal [9] and showed that the main part of “superfluous thunderstorms” in summer was predicted in low-gradient baric fields and during the blurred cold fronts passage. In winter, it can be added synoptic situations with the of active cyclones tracks from the southwest and northwest, their warm sectors and rear parts. Most of the “superfluous thunderstorms” refer to the erroneous forecast of summer intra-mass thunderstorms and winter frontal ones. Figure 1 shows a synoptic situation with expected a thunderstorm, but in fact it was not observed.

The satellite data was also used in this research. In particular, The Rapid-Development Thunderstorm (RDT) product, developed by Météo-France within the EUMETSAT NWC-SAF framework [12]. The RDT product outputs storm information on a 15 min interval. For each cloud cell, the RDT product defines a series of parameters capturing the location, shape, cloud top, movement, severity, and life cycle phase. Modern satellite meteorology resources make it possible to determine convective cells at different stages of development, as well as the expected direction and speed of their displacement. This is more useful than using meteorological locator data.

Figure 2 shows as an example a satellite image for 00 UTC on June 12, 2020, when a thunderstorm was indicated in the forecast, but it was not actually observed. Here the color of the contour marks the convection phases: yellow—triggering, orange—triggering from split, red—growing, purple—maturity and blue—decaying, black lines—the direction of displacement. Analyzed satellite image, growing convective

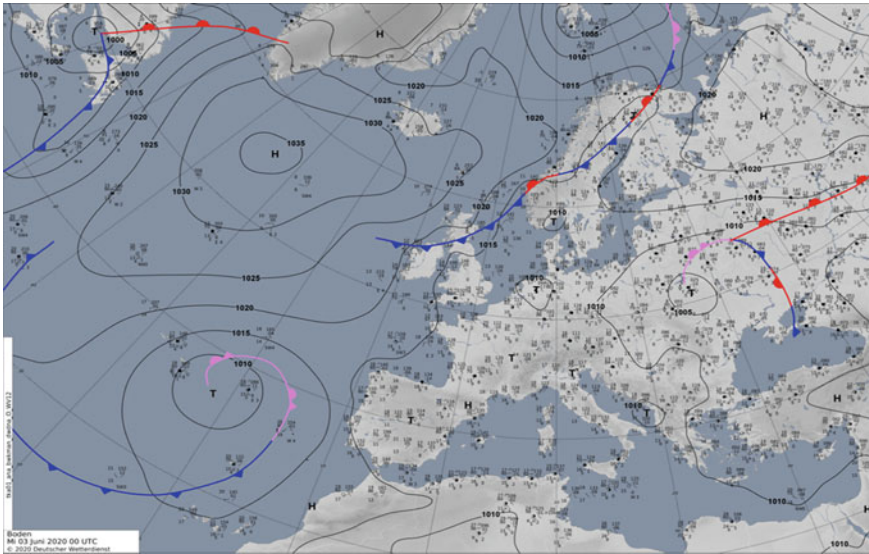
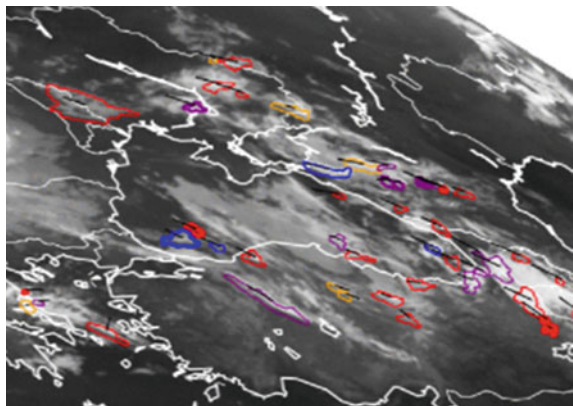


Fig. 1 Surface weather map for 00 UTC 03.06.20 A blurry cold front

cells are observed along the Black Sea coast, near Sochi and shift towards the airfield. In this situation, thunderstorm in the forecast is necessary. Satellite images were examined on selected dates of “extra” thunderstorms, and similar conclusions were made. The data of the open Internet portal [10] was used.

The next stage of the research was the convective instability indices identification that work well as for the forecast of the presence of thunderstorms as the absence of thunderstorms. The indices were calculated based on atmospheric sounding data at station 37,011 “Tuapse” in the terms closest to the thunderstorm forecast period.

Fig. 2 Satellite image for 00UTC 11.06.2020



Already calculated indexes from an open Internet portal were used for the analysis [11]. Then, all the information was classified for the four seasons of the year. Further, the indices confirming the absence of thunderstorms, in cases with “superfluous” thunderstorms, were identified and marked green (according to the quantitative criteria [13]). Then, the most successful of them were identified—those that did not predict a thunderstorm in 75% of cases or more. They are marked blue in the tables.

Here are fragments of this work.

Analysis of the complete data in Tables 2 and 3 revealed those instability indices that well predict the absence of thunderstorms in summer. The most successful are SWEAT and CAPE.

Similar work was done to identify convective instability indices that most successfully predict the absence of thunderstorms in winter.

Analysis of the complete data in Tables 4 and 5 revealed instability indices that predict well the absence of thunderstorms in winter. The most successful are the same two indexes: SWEAT and CAPE, as well as Lifted, Showalter and Vertical Totals.

Table 2 Instability indices and synoptic situation during periods of “superfluous thunderstorms” in summer (SWEAT and others)

Date	Period UTC	Synoptic situation	Showalter	Lifted	SWEAT	Ki	Cross Totals
01–02.06.20	21–05	Warm sector	3.1	3.4	71.19	24.1	18.7
02.06.20	05–09	Warm sector	3.1	3.4	71.19	24.1	18.7
03.06.20	09–16	Blurred cold front	3.91	4.27	110.16	23.1	20.9
04.06.20	10–17	Low–gradient field	3.85	–0.25	91.99	26.5	20.5
04–05.06.20	18–03	Low–gradient field	2.3	–0.83	277.13	20.2	24.4
11.06.20	10–18	Low–gradient field	0.33	–	110.39	24.9	17.1

Table 3 Instability indices and synoptic situation during periods of “superfluous thunderstorms” in summer (CAPE and others)

Date	Period UTC	Synoptic situation	Vertical Totals	Totals totals	CAPE	CINS
01–02.06.20	21–05	Warm sector	28.7	47.4	0	0
02.06.20	05–09	Warm sector	28.7	47.4	0	0
03.06.20	09–16	Blurred cold front	25.1	46	0	0
04.06.20	10–17	Low–gradient field	26.5	47	101.47	–48.58
04–05.06.20	18–03	Low–gradient field	25.3	49.7	178.23	–0.02
11.06.20	10–18	Low–gradientfield	33.1	50.2	–	–

Table 4 Instability indices and synoptic situation during periods of “superfluous thunderstorms” in winter (SWEAT and others)

Date	Period UTC	Synoptic situation	Showalter	Lifted	SWEAT	Ki	Cross Totals
02.12.20	06–15	Cyclone over the Black Sea	4.93	2.17	177.09	21.7	19.3
02–03.12.20	15–06	Cyclone over the Black Sea	2.63	1.76	96.91	25.3	23.5
03.12.20	09–15	Cyclone over the Black Sea	5.48	4.67	31.08	20.9	19.7
03–04.12.20	16–08	Filling cyclone	4.48	2.24	62.16	18.9	20.7
07.12.20	00–06	Baric hollow	3.1	0.97	104.91	21.7	21.7
07.12.20	06–09	Baric hollow	6.22	5.95	19.42	10.7	18.8

Table 5 Instability indices and synoptic situation during periods of “superfluous thunderstorms” in winter (CAPE and others)

Date	Period UTC	Synoptic situation	Vertical Totals	Totals totals	CAPE	CINS
02.12.20	06–15	Cyclone over the BlackSea	28.3	47.6	0	0
02–03.12.20	15–06	Cyclone over the BlackSea	28.5	52	8.97	-115.2
03.12.20	09–15	Cyclone over the BlackSea	26.7	46.4	0	0
03–04.12.20	16–08	Filling cyclone	27.7	48.4	67.25	-104.79
07.12.20	00–06	Baric hollow	30.7	52.4	51.82	-80.35
07.12.20	06–09	Baric hollow	27.8	46.6	0	0

Similar work was done to identify the indices of convective instability of the air mass, confirming the presence of thunderstorms.

Analysis of the complete data in Tables 6 and 7 helped to identify instability indices that predict the presence of thunderstorms during summer. These are Cross Totals, Ki, CINS and Total totals.

Similar work was carried out to identify convective instability indices that most successfully predict thunderstorms during winter.

Due to the limited data amount the presence of thunderstorms during winter, a complete statistical analysis of Tables 8 and 9 was not carried out. However, it should be noted that three indices predict the presence of thunderstorms in all cases. These are the same indexes as in the summer.

Similar tables were compiled for the spring and autumn period. Synoptic situations with “extra” thunderstorms were identified and indices of convective instability of

Table 6 Instability indices and synoptic situation during periods of observed thunderstorms in summer (SWEAT and others)

Date	Period UTC	Synoptic situation	Showalter	Lifted	SWEAT	Ki	Cross Totals
02.06.20	17–21	The influence of the cold front	4.33	–	60.22	15.9	17.3
02–03.06.20	21 – 09	Blurred cold front	2.31	–	125.59	30.3	21.9
13–14.06.20	19 – 06	Low–gradient field	0.8	–	131.08	31.5	20.9
18–19.06.20	22 – 03	Cyclone over the Black Sea	-1.99	-3.41	232.11	34.6	24.8
19–20.06.20	21 – 08	Low–gradient field	1.51	0.18	166.73	33.1	20.9
20.06.2020	18–21	Low–gradient field	3.29	-1.64	126.73	27.1	19.1

Table 7 Instability indices and synoptic situation during periods of the observed thunderstorms in summer (CAPE and others)

Date	Period UTC	Synoptic situation	Vertical Totals	Totals totals	CAPE	CINS
02.06.20	17–21	The influence of the cold front	28.3	45.6	–	–
02–03.06.20	21 – 09	Blurred cold front	26.5	48.4	–	–
13–14.06.20	19 – 06	Low–gradient field	27.9	48.8	–	–
18–19.06.20	22 – 03	Cyclone over the black sea	25.9	50.7	868.9	-22.52
19–20.06.20	21 – 08	Low–gradient field	25.3	46.2	69.65	-98.08
20.06.2020	18–21	Low–gradient field	25.1	44.2	417.16	-0.04

Table 8 Instability indices and synoptic situation during periods of observed thunderstorms in winter (SWEAT and others)

Date	Period UTC	Synoptic situation	Showalter	Lifted	SWEAT	Ki	Cross Totals
23.12.20	04–12	Low–gradient field	2.22	1.77	201.2	15.8	26.9
15–16.01.21	12–06	The northern periphery of the cyclone	8.19	6.78	142.82	10	22.9
18–19.01.21	21–06	Cyclone from the northwest	6.02	6.54	149.64	8.2	25.1

Table 9 Instability indices and synoptic situation during periods of observed thunderstorms in winter (CAPE and others)

Date	Period UTC	Synoptic situation	Vertical Totals	Totals totals	CAPE	CINS
23.12.20	04–12	Low–gradient field	30.8	57.7	0	0
15–16.01.21	12–06	The northern periphery of the cyclone	24.2	47.1	37.32	–10.25
18–19.01.21	21–06	Cyclone from the northwest	27.4	52.5	0	0

the air mass were determined, successfully predicting the presence and absence of thunderstorms.

Generalized results on the justifiability of convective instability indices are given in Tables 10 and 11. Justifiability was calculated as a percentage of the number of cases of successful forecasts for convective instability indices (by the presence or absence of a phenomenon) to the total number of cases with thunderstorms in the forecasts.

Table 10 Justifiability (%) of instability indices in summer and winter

Condition \ Index	Showalter	Lifted	SWEAT	Ki	Cross Totals	Vertical Totals	Totals totals	CAPE	CINS
absence of phenomena, summer	66	51	84	27	34	66	30	81	17
absence of phenomena, winter	94.5	100	87.3	64.5	18.2	78.2	30.1	100	4
presence of phenomena, summer	54.2	52.3	4	79	87.5	20.8	75	4	76.1
presence of phenomena, winter	0	0	0	0	100	0	100		100

Table 11 Justifiability (%) of instability indices in spring and autumn

Condition \ Index	Showalter	Lifted	SWEAT	Ki	Cross Totals	Vertical Totals	Totals totals	CAPE	CINS
absence of phenomena, spring	94	97.7	86	54	28	78	40	97.7	0
absence of phenomena, autumn	81.8	76.7	88.6	45.5	31.8	84.1	34.1	92.9	0
presence of phenomena, spring	0	0	0	80	100	0	20	0	100
presence of phenomena, autumn	50	33.3	12.5	81.3	100	18.8	87.5	13.3	100

An important conclusion from the analysis of Tables 10 and 11: there is some symmetry in the results of the greatest justifiability. Some indexes work well when predicting the presence of thunderstorms, others—when predicting the absence of thunderstorms. These conclusions, along with the available local methods, can be used as an additional predictor when forecasting thunderstorms at the Sochi airport and increase the feasibility of the forecast by reducing the number of “superfluous” thunderstorms in the forecasts. However, it is necessary to divide the “superfluous” thunderstorms according to the following conditions: firstly, a thunderstorm was observed in the study area, but did not go to the airfield and, secondly, there were no thunderstorms (thunderstorm activity did not develop). “Superfluous” thunderstorms in the first case cannot be excluded from the forecast, they will always be present. Further work will be continued in the direction of a detailed study of “superfluous” thunderstorms under the second condition. The proposed scheme can be used as an alternative approach to specifying thunderstorms in the forecast for the next 24 h, taking into account the uncertainty of the development of synoptic processes (Table 12).

The table can be read vertically. The forecaster predicts a thunderstorm at 17 UTC. The forecast is made every three hours starting from 00UTC. A tick marks a thunderstorm in the forecast. Let’s analyze the possible options for specifying thunderstorms in the forecast.

The first variant. It can be noted a thunderstorm at the expected time in each forecast (there are six). In this case, if a thunderstorm takes place, then all six forecasts will be justified by the phenomenon (thunderstorm), and if there is still no thunderstorm, then all six forecasts will not be justified. In the second variant, specify a thunderstorm in one of the terms isn’t noted, and in all the others is noted. In case thunderstorm will be, forecasts for all terms, with the exception of the first one, will be justified, and in the absence of a thunderstorm, only one forecast will be justified,

Table 12 Choosing the optimal indication option in the thunderstorm forecast

Forecast release dates, UTC	Variant 1	Variant 2	Variant 3	Variant 4	Variant 5	Variant 6	Variant 7
00	v	–	–	–	–	–	–
03	v	v	–	–	–	–	–
06	v	v	v	–	–	–	–
09	v	v	v	v	–	–	–
12	v	v	v	v	v	–	–
15	v	v	v	v	v	v	–
18							
21							
Forecast success in the presence and absence of a thunderstorm							
TS+	6/0	5/1	4/2	3/3	2/4	1/5	0/6
TS–	0/6	1/5	2/4	3/3	4/2	5/1	6/0

etc. In the fourth variant, it isn't indicated a thunderstorm in the first three forecasts, in the other three is indicated. And regardless of whether it takes place or not, the overall forecast for the phenomenon will be justified by 50%.

This tactic of indicating thunderstorms in the forecast will increase the number of justified forecasts.

3 Conclusion

Thus, in the presented study the synoptic conditions under which thunderstorms occurred at different times of the year were analyzed. Indicators of the convective instability of the air mass, which successfully predict the presence and absence of thunderstorms, were considered and systematized. It has been established that there is some symmetry in the results of the greatest justifiability. Some indexes work well when predicting the presence of thunderstorms, others—when predicting the absence of thunderstorms. These conclusions, along with the available local methods, can be used as an additional predictor when forecasting thunderstorms and increase the feasibility of the forecast by reducing the number of “superfluous” thunderstorms in the forecasts.

References

1. Bogatkin, O.G.: Fundamentals of Aviation Meteorology: Textbook. RSHU Publishing. 339 (2009). [in Russian].
2. Flymeteo Internet Portal [Electronic resource] - Access mode: <https://flymeteo.org>.
3. Peter L. Watson: Influence of the Characteristics of Weather Information in a Thunderstorm-Related Power Outage Prediction System. **23**, 541-560 (2021). <https://doi.org/10.3390/forecasts3030034>.
4. Mohapatra, M., Sen Roy, S.: Determination of suitable thermodynamic indices and prediction of thunderstorm events for Kolkata, India Sourish Bondyopadhyay. *Meteorology and Atmospheric Physics* **133**, 1367–1377 (2021).
5. Fernando, M., Millangoda, M., Premalal, S.: Analyze and Comparison of the Atmospheric Instability Using K-Index, Lifted Index Total Totals Index Convective Availability Potential Energy (CAPE) and Convective Inhibition (CIN) in Development of Thunderstorms in Sri Lanka During Second Inter-Monsoon. In: Amaratunga, D., Haigh, R., Dias, N. (eds) *Multi-Hazard Early Warning and Disaster Risks*. Springer, Cham. (2021). https://doi.org/10.1007/978-3-030-73003-1_41.
6. Pustovalov, K.N., Gorbatenko, V.P., Nechepurenko, O.E., Nagorskiy, P.M., Oglezneva, M.V.: Spatial and temporal variability of convective instability in the south of Western Siberia, determined on the basis of the total totals index (ERA5 reanalysis), Proc. SPIE 11916, 27th International Symposium on Atmospheric and Ocean Optics, Atmospheric Physics, 119166P (2021). <https://doi.org/10.1117/12.2603446>.
7. DeRubertis, D.: Recent trends in four common stability indices derived from US radiosonde observations. *Journal of Climate* **19**, 309-323 (2006). <https://doi.org/10.1175/JCLI3626.1>.
8. OGIMET Internet Portal [Electronic resource] - Access mode: <https://ogimet.com>.

9. Wetterzentrale Internet Portal [Electronic resource] - Access mode: <https://www.wetterzentrale.de>.
10. EUMETSAT–NWCSAF Internet Portal [Electronic resource] - Access mode: <https://www.nwcsaf.org>.
11. University of Wyoming Internet Portal [Electronic resource] - Access mode: <http://weather.uwyo.edu>.
12. Lee, J.-G., Min, K.-H., Park, H., Kim, Y., Chung, C.-Y., Chang, E.-C.: Improvement of the rapid-development thunderstorm (RDT) algorithm for use with the GK2a satellite Asia-Pacific Journal of Atmospheric Sciences. **56**, 307–319 (2020).
13. Bogatkin, O.G., Toptunova, O.N., Volobueva, O.V., Ivanova, I.A.: Aviation Meteorology Workshop: Textbook. Publishing and Printing Association of Higher Educational Institutions. 154 (2022). [in Russian].

The Maximum Hail Size Assessment Regression Model by Predictive Fields of Meteorological Parameters



A. Kh. Kagermazov and L. T. Sozaeva

Abstract The need to develop new methods for predicting the characteristics of hail processes is dictated, on the one hand, by the trend of growth of convective dangerous weather events due to climate change, on the other hand, by the lack of actual data of aerological sounding due to the location of individual weather stations far enough from each other and the existence of a significant time interval of measurements. In this research instead of upper-air atmospheric sounding data, it is proposed to use the output of the GFS NCEP global atmospheric model, which has sufficient accuracy and the required lead time. The size of the hail is considered as a quantitative characteristic of the hail process. The hail assessment regression model was implemented using statistical analysis methods based on pre-calculated atmospheric parameters that are most responsible for the development of convective phenomena. The model parameters characterizing the statistical significance and practical applicability of the model showed the possibility of applying the proposed model in practice.

Keywords Hail size · Meteorological parameters · Regression model

1 Introduction

The increased requirements to the dangerous weather phenomena forecast necessitate the development of new predicting methods the quantitative characteristics of hail processes [1, 2]. However, in solving this problem, additional difficulties arise related to the definition of criteria for the hail process intensity. It is known that the hail process power is estimated by the size of the crops damage area, but such observations have not been made for a long time. On the other hand, there is a dependence of the dead crops area on the maximum diameter of the falling hail. Based on this, it is assumed to use the maximum diameter of hailstones as the hail processes intensity characteristic.

A. Kh. Kagermazov (✉) · L. T. Sozaeva
High-Mountain Geophysical Institute, 2 Lenin avenue, 360030 Nalchik, Russia
e-mail: vgikbr@yandex.ru

© The Author(s), under exclusive license to Springer Nature Switzerland AG 2023
R. Zakinyan and A. Zakinyan (eds.), *Physics of the Atmosphere, Climatology and Environmental Monitoring*, Springer Proceedings in Earth and Environmental Sciences, https://doi.org/10.1007/978-3-031-19012-4_20

The hail prediction method was originally developed based on the concept of an «ideal forecast», using meteorological parameters of the atmosphere calculated from actual observations. Currently, such data is available only at individual weather stations located far enough apart from each other, which complicates the conduct of research. As part of this work, instead of the atmosphere aerological sounding data, it is proposed to use the output data of global mathematical models of the Earth atmosphere [3–6]. The output data of the GFS model used by us (stratification of temperature, humidity, wind direction and speed fields) have a sufficiently high reliability. This is confirmed by an earlier coincidence degree assessment of the atmospheric stratification predicted values obtained from the global atmospheric model with a lead time of up to three days with the aerological sounding factual data [7].

The purpose of this work is to develop a scheme for maximum hail diameter assessment with a lead time of up to three days. For this, the following challenges are solved:

- calculation of atmospheric parameters most responsible for the development of convective phenomena, according to the global atmospheric model;
- creation of the assessment regression model of maximum diameter of hail that fell to the ground;
- calculation of parameters characterizing the statistical significance and practical applicability of the model.

2 Materials and Methods of Research

The research materials were factual data on dangerous weather phenomena provided by paramilitary services for active impact on meteorological and other geophysical processes (Stavropol, North Caucasus and Krasnodar) in the course of the operational and production work of the National Research University of Roshydromet «Maintenance of the Unified State Data Fund on the state of the environment, its pollution». 30 dates with the fact of hail falling were selected in an area with a radius of 150–200 km from the «Mineralnye Vody» sounding point during the 2021 hail season. These dates were compared with the atmosphere meteorological fields' data according to the global atmospheric model with a lead time of up to three days instead of observational data, namely:

- isobaric surfaces, hPa ;
- heights corresponding to isobaric surfaces, m ;
- ambient air temperature, $^{\circ}C$;
- dew point temperature, $^{\circ}C$;
- wind direction in degrees;
- wind speed, m/s .

These data make it possible to calculate 45 atmospheric parameters known from the existing methods for predicting convection and associated hazardous weather phenomena, including hail. Such a number of features is redundant and makes

the computational prediction procedure laborious. Therefore, the most informative features were selected using the biserial correlation coefficient and factor analysis. Factor analysis of the complex of variables used in the hail prediction makes it possible to distribute them by orthogonal functions. In accordance with the obtained factor decomposition, minimally related groups of parameters are determined, from which the parameters responsible for the development of convection are selected according to the specified coefficient [8, 9].

The research was carried out using the SPSS program designed for statistical data analysis [10].

According to the calculation results, about 10 most informative atmospheric parameters characteristic of convective phenomena were selected:

DTM—maximum temperature difference in the cloud and ambient air;

HM—the level at which the temperature difference in the cloud and the surrounding air is maximum;

DTK—vertical temperature gradient in the layer above the convection level by 4–4.5 km;

SQZ5—total specific humidity in the Earth layer by 5 km;

TDSR5—average moisture deficit in the layer above the convection level by 5 km;

PH1—convection level;

TH1—temperature at the convection level;

DJ—George's Instability Index;

TTMI—Miller Integral sum index;

DSS—the energy characteristic of the sub cloud layer.

Further optimization of the predictors number for convective phenomena intensity assessment, in particular the hail size, was solved by statistical analysis methods. In the final statistical model, those predictors were selected that have the most significant impact on the predicted variable (the maximum diameter of the hail).

To predict the maximum diameter of hail, the global atmospheric model output data with a short-term lead time (up to three days) were used. For each of the hail precipitation dates, the most informative atmospheric parameters were calculated and selected according to the global atmospheric model. As a result, the atmospheric parameters (*DTM*, *HM*, *DTK*, *SQZ5*, *TDSR5*, *PH1*, *TH1*, *DJ*, *TTMI*, *DSS*) were taken into account as independent variables, and the maximum diameter of the hail from observations as a dependent variable.

We will build a regression model in the form:

$$D = f(DTM, HM, DTK, SQZ5, TDSR5, PH1, TH1, DJ, TTMI, DSS) + const, \quad (1)$$

where *const*—is the free term of the regression equation.

The construction of a regression model is reduced to determining the coefficients and the free term of the equation.

3 Calculation Results and Their Discussion

Before the regression analysis, the dependent variable and independent variables values were checked for the normality of the distribution. The verification showed that the distributions of all variables are close to normal. Checking for the difference between the variance (the square of the standard deviation) of variables from zero showed compliance with this condition.

A Pearson correlation matrix was constructed for all variables (D , DTM , HM , DTK , $SQZ5$, $TDSR5$, PHI , THI , DJ , $TTMI$, DSS), which showed the absence of a strong relationship between the variables under researches (multicollinearity). The exceptions to this rule were the independent variables PHI and HM , which were not taken into account in further analysis.

Further, by the method of step-by-step elimination, a model was chosen to estimate the maximum diameter of hail with a lead time of up to three days:

$$D = 16,131 - 0,161 DTM + 0,290 DTK - 0,059 DJ + 0,005 DSS, \quad (2)$$

where DTM is the maximum temperature difference between the cloud and the ambient air;

DTK —vertical temperature gradient in the layer above the condensation level by 4–4.5 km;

DJ —George's Instability Index;

DSS —the energy characteristic of the subcloud layer.

It can be seen from Eq. (2) that the fallen hail maximum diameter depends on the maximum temperature difference in the cloud and the surrounding air, the vertical temperature gradient in the layer above the condensation level by 4–4.5 km, the George instability index and the energy characteristic of the subcloud layer.

Note that the atmospheric parameters included in model (2) reflect the instability reserve, moisture content, and temperature regime in the hail growth zone.

George's Instability Index DJ (indicator of the degree of development of convection) depends on the vertical temperature gradient and the vertical extent of high humidity layers and is equal to:

$$DJ = (T_{850} - T_{500}) + TD_{850} - (T_{700} - TD_{700})$$

where T_{850} —the temperature at the level of 850 hPa, °C;

T_{700} —the temperature at the level of 700 hPa;

T_{500} —the temperature at the level of 500 hPa, °C;

TD_{850} —dew point temperature at 850 hPa, °C;

TD_{700} —dew point temperature at 700 hPa, °C.

The energy characteristic of the subcloud layer (a quantitative characteristic of the state of the lower layer of the troposphere) is equal to the difference between the work performed by the lifting force when moving a unit mass of dry air from the

Table 1 Model summary

<i>R</i>	<i>R</i> Square	Adjusted <i>R</i> Square	Std. Error of the Estimate	Durbin-Watson test	<i>F</i>	Sig
0,780	0,609	0,547	0,60,930	2,084	9,738	0,000

Predictors: (Constant) *DSS*, *DTM*, *DJ*, *DTK*

Dependent variable: *D*

Table 2 Coefficients

Model	Unstandardized Coefficients		Standardized Coefficients	t	Sig	95% Confidence Interval for Beta		Collinearity Statistics	
	Beta	Std. Error	Beta			Lower	Upper	tol	VIF
Constant	16,131	10,380		1,554	0,133	-5,247	37,508		
DTM	-0,161	0,040	-0,509	-4,024	0,000	-0,244	-0,079	0,978	1,023
DTK	0,290	0,072	0,720	4,044	0,000	0,142	0,438	0,493	2,030
DJ	-0,059	0,034	-0,248	-1,741	0,094	-0,128	0,011	0,770	1,299
DSS	0,005	0,002	0,462	2,351	0,027	0,001	0,009	0,406	2,466

earth’s surface to the level of condensation and the work that can be done by the air descending from the level of condensation in the subcloud layer [11].

Tables 1 and 2 present the parameters of the regression equation for estimating the maximum size of hail and its quality indicators.

In Eq. (2), the constant is equal to 16.131 (Table 2), that is, when zeroing the variables on the right side of the equation, the hail diameter will be 16 cm, which is physically incorrect. This situation has developed due to the fact that the dimension of the independent variables differs by two orders of magnitude, so the procedure for standardization of variables (*z* sign) was applied.

A model was constructed for standardized variables in the form:

$$zD = -0,509 zDTM + 0,290 zDTK - 0,059 zDJ + 0,005 zDSS, \quad (3)$$

where the predictors of the equation are the same as in the previous one, but taking into account standardization. Table 3 presents the equation constant and regression coefficients for each predictor, as well as the level of their statistical significance *Sig.*, obtained as a result of testing the null hypothesis that each of them is equal to zero using the Student’s test (*t*). *Sig.* levels. for the coefficients, the models confirm that the independent variables have a statistically significant effect on the maximum diameter of the hail.

The multiple correlation coefficient of the model is 0.780, which indicates a high relationship between the dependent and independent variables (Table 1). The coefficient of determination is 0.609, i.e. 61% of the variation in the maximum hail diameter is explained by the joint variation of atmospheric parameters. In addition,

Table 3 Coefficients taking into account standardized variables

Model	Unstandardized coefficients		Standardized coefficients	t	Sig	95% confidence interval for Beta		Collinearity statistics	
	Beta	Std: Error				lower	upper	tol	VIF
Константа	0,00	0,123		1,554	1,000	−0,253	0,253		
DTM	−0,509	0,126	−0,509	−4,024	0,000	−0,769	−0,248	0,978	1,023
DTK	0,720	0,178	0,720	4,044	0,000	0,354	1,087	0,493	2,030
DJ	−0,248	0,143	−0,248	−1,741	0,094	−0,542	0,045	0,770	1,299
DSS	0,462	0,196	0,462	2,351	0,027	0,057	0,866	0,406	2,466

the value of the Fisher coefficient is $F > 1$, and the level of its significance is $Sig. = 0.01 < 0.05$ —this means that the selected regression coefficients are significant and valid for the general population, and the regression Eq. (3) can be used to estimate the maximum diameter of the fallen hail.

The standardized regression coefficients make it possible to estimate to what extent the values of the maximum hail radius are determined by the values of the atmospheric parameters, i.e. they characterize the specific contribution of each atmospheric parameter to variations in hail intensity characteristics. The standard errors σ indicate that, at a 95% confidence interval, each coefficient can deviate from the mean by two standard errors ($\pm 2\sigma$).

In the table of model coefficients, in addition to all of the above, there is information about the values of tolerance statistics, which are necessary to check the condition of the absence of multicollinearity, i.e. the absence of a relationship between the variables of the model. The value of the indicator *tol* must exceed 0.1, and the value of *VIF*—less than 10. For the constructed model, these indicators confirmed the condition of the absence of the multicollinearity effect and the acceptability of the model for further interpretation.

An important point is the analysis of residuals, that is, deviations of the observed values from the theoretically expected ones. The residuals should obey the normal distribution. This can be verified by plotting a histogram of the residuals. Figure 1 shows a good agreement of the histogram of the residuals with the curve of the normal distribution.

The condition of the residues independence among themselves is checked using the Darbin–Watson autocorrelation test. By constructing a model for predicting the maximum hail diameter, it turned out to be equal to 2.084, which is an indicator of the absence of residues autocorrelation (Table 1).

All indicators characterizing the statistical significance and practical applicability of the regression equations (multiple correlation coefficient, coefficient of determination, residual analysis, etc.) indicate that the maximum hail diameter can be adequately estimated using Eqs. (2) and (3).

Fig. 1 Histogram of standardized residuals with a normal distribution curve

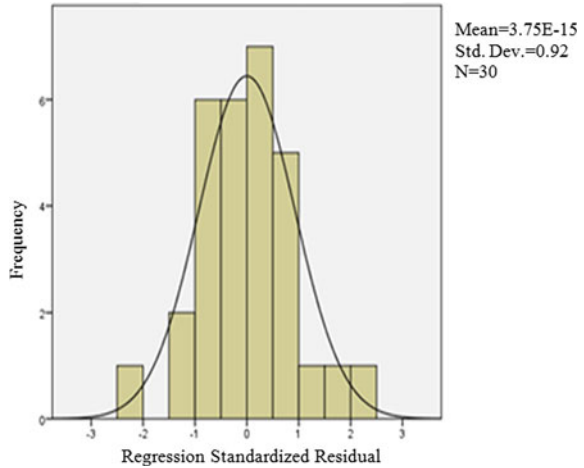


Figure 2 shows the estimated values of the hail diameter calculated by the regression model (3) with a lead time of up to three days in comparison with the observed values.

As can be seen from the figure, the estimated values of the maximum hail diameter are in good agreement with the observational data.

Thus, the constructed model for estimating the maximum hail diameter shows a good match with the observed values and can be used to predict the expected hail process intensity.

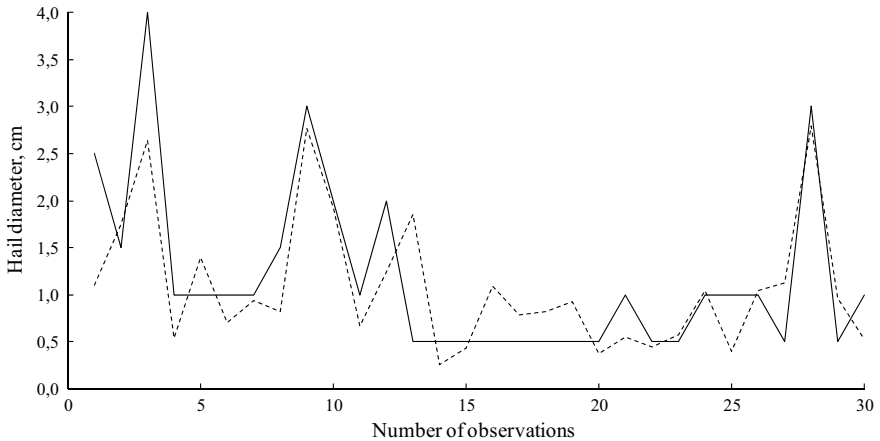


Fig. 2 Hail diameter: solid curves —factual values, dotted curves—estimated

4 Conclusions

The constructed model for estimating the maximum hail diameter shows a good coincidence of the prognostic and observed values of the hail size. All the indicators characterizing the statistical significance and practical applicability of regression equations indicate that the maximum hail diameter of the can be adequately estimated using the compiled equations. Thus, the resulting model for estimating the hail size can be used in paramilitary hail control services.

References

1. Dzombak, B.: Severe hailstorms are costly and hard to predict. *Eos*. 102, (2021). <https://doi.org/10.1029/2021EO158268>
2. Raupach, T.H., Martius, O., Allen, J.T. et al.: The effects of climate change on hailstorms. *Nat. Rev. Earth Environ.* 2, 213–226 (2021). <https://doi.org/https://doi.org/10.1038/s43017-020-00133-9>
3. Dueben, P., Wedi, N., Saarinen, S., Zeman, C.: Global simulations of the atmosphere at 1.45 km grid-spacing with the integrated forecasting system. *Journal of the Meteorological Society of Japan. Ser. II* 98(3), 551–572 (2020).
4. Haiden, T., Janousek, M., Vitart, F., Ferranti, L., Prates, F.: Evaluation of ECMWF forecasts, including the 2019 upgrade. *ECMWF Technical Memorandum*. 853, (2019)
5. Kanamitsu, M., Alpert, J.C., Campana, K.A. et al.: Recent changes implemented into the global forecast system at NMC. *Weather and Forecasting*. 6, 425–435 (1991)
6. Official website of the National Centers for Environmental Prediction. Environmental Modeling Center. [Electronic resource]. [https:// www.emc.ncep.noaa.gov/](https://www.emc.ncep.noaa.gov/) (accessed: 16.04.2021)
7. Kagermazov, A.Kh., Sozaeva, L.T.: Validation the output data of the global model of the atmosphere on data of aerological sensing with increscent lead time. *Nauka. Innovatsii. Tekhnologii*. 4, 125–136 (2020) [in Russian]
8. Kagermazov, A.Kh., Sozaeva, L.T.: Hail forecast on the output data of the global atmospheric model with tree-day advance time. *Trudy VGI*. 598, 204–214 (2020) [in Russian]
9. Kagermazov, A.Kh.: Digital atmosphere. Modern methods and methodology for the study of hazardous meteorological processes and phenomena. *Pechatnyy dvor, Nalchik* (2015) [in Russian]
10. Büyül, A., Zöfel, P.: SPSS: The Art of Information Processing. Analysis of statistical data and recovery of hidden patterns: Per. with him. *DiaSoftYUP*, St. Petersburg. (2005) [in Russian]
11. Belentsova, V.A., Goral, G.G., Terskova, T.N., Fedchenko, L.M., Chepovskaya, O.I.: Aerosynoptic and thermodynamic features of the occurrence and development of intense hailstorms and squalls in the conditions of the North Caucasus. *Trudy VGI*. 51, 88–99 (1982) [in Russian]

Snow Cover and Snowstorms Regime on the Stavropol Upland



G. L. Kaplan, G. Kh. Badakhova, M. V. Barekova, and Yu. L. Smerek

Abstract The paper presents the results of the study of the regime of snow cover and snowstorm phenomena in the Stavropol Upland in the first twenty years of the twenty-first century. It is shown that against the background of increasing winter temperatures, the timing of snow cover appearance shifts to later dates, and periods of continuous snow cover for 30 days or more are observed only in 30% of years. In addition, on the Stavropol Upland there is a decrease in the number of days with snow cover, a decrease in the frequency of years with stable snow cover, and an increase in the frequency of snowless months of the cold period, especially November and December. Also, comparison of the current characteristics of the snowstorm regime with the data for the previous multi-year periods showed that the frequency and duration of snowstorms in the Stavropol Upland decreased, despite an increase in the number of days with strong winds. The main reason for the changes occurring is primarily an increase of air temperature in winter and transitional periods of the year.

Keywords Snow cover · Snowstorms · Strong winds · Air temperature

G. L. Kaplan
Terra Space Lab, 6 Reading str, Tel-Aviv, Israel

G. Kh. Badakhova (✉)
Stavropol Hydrometeorology and Environmental Monitoring Center, 53B Kulakov Av, 355047
Stavropol, Russia
e-mail: badahovag@mail.ru

M. V. Barekova
High-Mountain Geophysical Institute, 2 Lenin Av, 360030 Nalchik, Russia

Yu. L. Smerek
North-Caucasus Federal University, 1 Pushkin str, 355014 Stavropol, Russia

1 Introduction

The Stavropol Upland is the main orographic unit of the Central Caucasus, which is the watershed of the rivers of the Azov and Caspian Sea basins. It occupies almost half of the territory of the region and is a gently sloping folded uplift. The valley of the Kalaus River divides the Stavropol Upland in its high part into two isolated massifs called the Stavropol Heights and the Pre-Kalaus Heights. The Stavropol Heights are located in the central part of the Stavropol Uplands, west of the Kalaus River, and reach 670 m. Here, at an altitude of 451 m above sea level, is the Stavropol weather station, most characteristic of this part of the Stavropol Uplands.

The Stavropol Upland is the place in the region with the greatest number of days with snow cover, the greatest height of snow cover, and the only place where snowstorms are observed annually.

2 Materials and Methods

The material for the research was observation data from Stavropol meteorological station for 1961–2020 and data contained in the Handbook on the Climate of the USSR, as well as the archive of synoptic maps of Stavropol Central Hydrometeorological Service. The data on air temperature, type and amount of atmospheric precipitation, snow cover, wind and snowstorms were considered.

In the process of analysis basic statistical characteristics of meteorological parameters were calculated: average, maximum and minimum values for different time periods, recurrence and duration of the phenomena, as well as changes in the characteristics of their regime and trends of these changes [1, 2].

3 Analysis and Discussion

The climate change occurring on the planet was also reflected in the mode of formation and occurrence of the snow cover both in Stavropol Territory as a whole and in the Stavropol Upland. The main role in this, of course, was played by a change in the temperature background. Table 1 shows values of average monthly and seasonal temperatures for different long-period periods [3–5].

On the Stavropol Upland, in accordance with its geographical location, precipitation falls in solid and liquid form. Although precipitation is predominantly in liquid form, solid precipitation is usually sufficient to form snow cover. A total of 628 days with solid precipitation, 868 days with liquid precipitation and 480 days with mixed precipitation (180 days—wet snow, 300 days—wet pouring snow) were recorded by Stavropol weather station during the cold periods of 2001–2020. Winter months accounted for 75% of days with solid precipitation, 49% of days with liquid

Table 1 Average monthly and seasonal temperature (°C)

Period	January	February	March	November	December	Winter	CP*
Before 1961	−3.7	−3.0	1.6	3.4	−1.1	−2.6	−0.6
1961–2000	−3.4	−2.8	1.7	3.5	−0.6	−2.3	−0.3
2001–2020	−2.1	−1.2	3.7	4.5	−0.2	−1.2	0.9

CP*—Cold Period

precipitation, and 58% of days with mixed precipitation; for the transition months, respectively, 25, 51, and 42% of the days with precipitation of these species. Table 2 shows the values of the average monthly and seasonal number of days with different types of precipitation.

Most of the snow falls from powerful cyclonic systems, which, when sufficiently humid, form over vast areas high sheet clouds and nimbostratus clouds (As-Ns). The speed of such cloud systems is usually at least 15–20 km/h, with snow falling from them lasting several hours. Heavy snowfalls are quite common in northwestern Stavropol Territory, where winter precipitation amounts to 110 to 130 mm. The main cyclone trajectories from the Black Sea pass through these areas. The small amount of snowfall in the eastern parts of the region is due to the relatively rare passage of powerful cyclonic systems, as well as the relatively flat surface of the territory, which causes the Atlantic and Black Sea air masses to sink after they pass over the Caucasus Range and the Stavropol Upland. Although it has relatively long winters, the area is far from major sources of moisture. The rather low temperatures typical of this area greatly reduce the moisture-holding capacity of the air and contribute to a small amount of snow precipitation.

Stavropol has always had cold winters and long periods with snow cover. Back in 1900, Professor N. Dinnik in his climatic description of the Stavropol Province wrote: «The coldest place in Stavropol Province should be considered Stavropol. Usually it snows for 2–2½ months, in exceptional years—even much more. The first frosts occur here around September 10, and the first snow falls in October, but it is

Table 2 Average monthly and seasonal number of days with different types of precipitation in 2001–2020

Month	SP*	LP*	Mixed		
			Total	WS*	WPS*
January	9	7	5	2	3
February	7	7	5	2	3
March	5	12	6	2	4
November	3	10	4	1	3
December	7	8	4	2	2
Cold period	31	43	24	9	15

SP*—Solid Precipitation; LP*—Liquid Precipitation; WS*—wet snow; WPS*—wet pouring snow

very short at this time. It is not uncommon for snow to fall in early April as well. In places 15–20 versts from Stavropol, but below it, winters are much warmer» [6].

At present, the first frosts in the Stavropol Upland are usually observed not earlier than the second half of October, and the frost-free period has lengthened precisely due to shifting the first frosts to later dates [7]. The first snow usually falls in October–November. In the XXI century, the average date of the first snowfall is November 6. But the first snow, as a rule, does not remain lying, but melts under the influence of fairly high daytime temperatures. Snow cover usually forms not earlier than 2–3 decades of November, and in especially warm winters - only in December. In the winter of 2010–2011, snow cover did not appear until January 17, 2011.

Snow cover rarely forms in October. Thus, in the new century, it is noted only in four years out of 21. Snow cover is much more common in November, with 13 in the new century. In December, January and February, snow cover is formed annually. In March in the twenty-first century, it did not form only once, in 2017. Snow cover is much more frequent in April than in October. In the new century, snow lay in April in 7 years, the duration of occurrence was 1–2 days with a maximum of 4 days in 2005.

The last snowfall is usually in the second half of March, usually 1–2 weeks after the snow cover melted. However, once every 4–5 years there is snowfall in April. The most notable snowfall in this regard was on April 21, 2011 (the penultimate one was on March 25).

During the first 20 years of the new century, 1121 days of snow cover were recorded, an average of 56 days per year, including 39 days in the first half of the year and 17 days in the second half of the year. There are 44 days in the calendar winter and 12 days with snow cover in the fall and spring months. Spring had twice as many days with snow cover as autumn (Table 3).

The highest annual number of days with snow cover was recorded in 2012–87 days, the lowest in 2019–30 days. The highest winter number of days with snow cover was 68 (2008), and the lowest was 24 (2005). The year 2005 was notable for the fact that the number of days with snow cover during the calendar winter and outside of it was almost the same—24 and 23 days, respectively—due to 19 days with snow cover in March and 4 days in April.

Even in the highest part of the Stavropol Upland, there are frequent thaws, so periods of uninterrupted snow cover for 30 days or more are observed only in 30% of years. Periods with steady snow cover, interrupted by a maximum of three days for each of the 30 days of snow cover, are also not observed every winter. In the twenty-first century, stable snow cover was formed in 50% of the years. The average

Table 3 Number of days with snow cover

Indicator	January	February	December	Winter	Autumn	Spring	Year
Average	17	14	13	44	4	8	56
Highest	31	29	27	68	21	21	87
Lowest	2	2	2	22	0	0	30

date of establishment is January 1, the average date of destruction is February 12, and the average duration is 42 days.

The dates of formation and destruction of stable snow cover vary greatly from year to year. The earliest stable snow cover was recorded on 8 December 2007, after which the snow cover lasted (with one day interval) until 6 January 2008. The latest stable snow cover was from January 20 to February 19, 2017 (with a two-day break). In the new century, the longest period of stable snow cover lasted 68 days: from 16 January to 23 March (with a total break of three days).

In the first half of the twentieth century, the maximum duration of snow cover in Stavropol was 133 days (winter of 1908–1909) [8]; in the second half of the twentieth century, the highest annual number of days with snow cover was 104 days (1987) [3]. In some winters, stable snow cover is not formed at all throughout the region; snow is repeatedly laid during cold spells and melted during thaws, which occur quite often during the winter.

Sometimes there are almost snowless winters. The minimum number of days with snow cover in Stavropol in 2001–2020—30 days per year and 24 days per calendar winter. November and December are especially often with little snow. During the 20 years analyzed, there was no snow cover at all in November in seven years, and in ten years it was deposited for less than 10 days. In December, the duration of occurrence of less than 10 days was recorded in eight years, while in January and February these indicators are 4 and 5 days, respectively.

Since the formation of a stable snow cover its height gradually increases. However, as analysis of daily data shows, there are fluctuations in snow cover height due to thaws and partial melting of the snow cover, which does not lead to a decrease in the degree of coverage of the area below 5 points. Therefore, the thickness of snow cover on the territory of the region is small. On the Stavropol Upland, its average maximum height is 10–15 cm.

In some years, the maximum height of snow cover during the winter in the Stavropol Upland may reach 30–50 cm, and even 80 cm on the northeastern slopes. Average heights are much smaller than maximum heights and range from 4–5 cm at the beginning of the cold season to 10–14 cm in January–February. During the 20 years of the new century, the average monthly height of snow was: January—18 cm, February—20 cm, March—13 cm, April—4 cm, October—3 cm, November—9 cm, December—12 cm. The highest monthly snow cover height: January—43 cm, February—79 cm, March—51 cm, April—15 cm, November—22 cm, December—35 cm.

An indispensable attribute of the Stavropol winter are snowstorms. Open to all winds, Stavropol is located in the most elevated part of the Stavropol Plateau, and it is the only place in the region where snowstorms are observed annually. They occur in the form of a drifting snow, a blowing snow, or a general snowstorm. Snowstorms can be observed at any time of the day, they are most rare in the morning, and nighttime snowstorms account for 32% of the total duration of snowstorms [9].

In Stavropol, on average, there are 11 days with drifting snow for a total duration of 77 h per year. Drifting snows are observed from November to March, with the highest frequency and duration occurring in January and February. Twice in 20 years

Table 4 Monthly distribution of the number of days with snowstorms and total duration of snowstorms (%)

Parameter	January	February	March	April	November	December
Days with snowstorms	24.6	31.3	17.4	0.5	2.1	24.1
Total duration of snowstorms	20.9	35.2	14.6	0.2	1.3	27.8

there have been drifting snows in April. There was a total of 195 snowstorm days in the 20 years of the new century, i.e., an average of 10 snowstorm days per year. The most snowstorm years were 2006, 2011 and 2012, with 20 days, 18 days and 24 days with snowstorms, respectively. There were no snowstorms at all in 2017.

Table 4 shows the monthly distribution of the number of days with snowstorms, averaged for 2001–2020.

December and February snowstorms are the longest: the average duration of one snowstorm is 6.8 and 6.6 h, respectively. January and March snowstorms do not differ much in duration: 5.0 and 4.9 h. The average duration of November snowstorms was 3.8 h, and the only April snowstorm lasted two hours. Snowstorms lasting more than 10 h continuously occur from time to time almost throughout the region, but snowstorms lasting more than 20 h occur only in the Stavropol Upland. Snowstorms with a continuous duration of 60 h or more are observed only in the Stavropol area on single occasions [9].

Before 1961, there were an average of 16 days with snowstorms [10], in 1961–2000–13 days [3], in 2001–2020–10 days with snowstorms per year. Obviously, there is a decrease in the number of days with snowstorms (Fig. 1). The average annual duration of snowstorms during these periods was 130, 90 and 57 h respectively, i.e., the duration of snowstorms is also decreasing (Fig. 2).

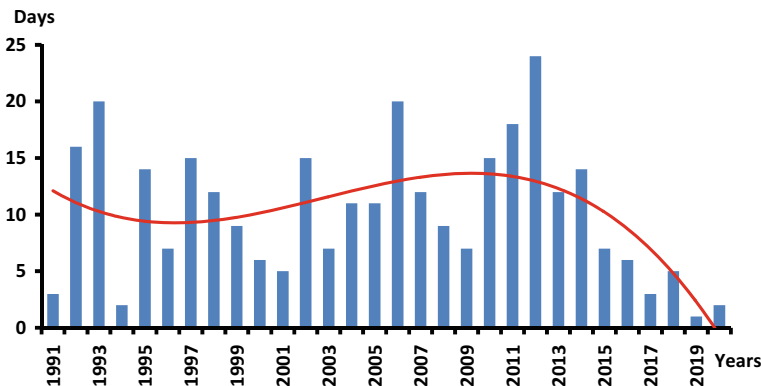


Fig. 1 The 30-year course of the annual number of days with snowstorms

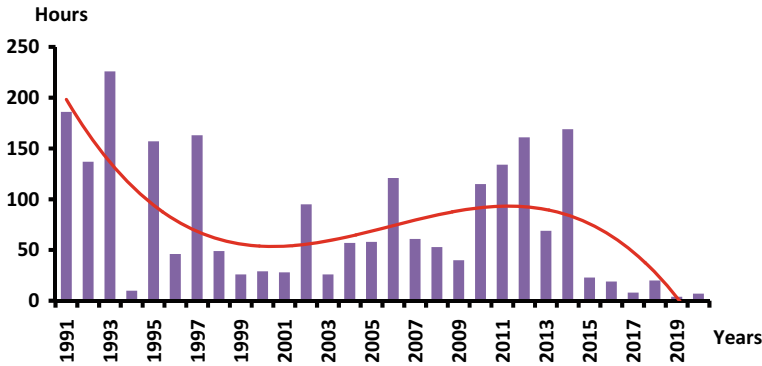


Fig. 2 The 30-year course of the annual duration of snowstorms

Even in the twenty-first century, 112 days with snowstorms were recorded in 2001–2010 and only 83 days in 2011–2020. The cumulative duration of snowstorms is: 674 h in 2001–2010, 466 h in 2011–2020.

The snowstorm phenomena are inseparably connected with the wind. In different sources [11–13] are indicated different critical values of wind speed, at reaching which snowstorms may start. However, the most common position is that most often a general snowstorm begins with solid precipitation when the wind reaches a speed of 7 m/s [14]. As a rule, this level is taken as critical for general snowstorm forecasting [15]. Snowstorms reaching the intensity of hazardous meteorological phenomena and natural hydrometeorological phenomena are predicted at wind speeds of more than 12 and 15 m/s, respectively. As for a low-level snowstorm, the critical speed corresponding to the beginning of a low-level snowstorm will depend mainly on the state of the underlying surface, i.e., on the properties of the snow. Therefore, there is no precise value of the wind speed level in the literature for the onset of a low-level snowstorm.

Let us consider in detail the change of climatic characteristics most closely related to snowstorms—the number of days with strong winds and the temperature of the winter period.

Figure 3 shows a 30-year variation of the number of days with strong wind ($v_{max} \geq 15$ m/s) for the winter period. It follows from the graph that, despite quite significant variations from year to year, in general for the period there is clearly a trend of increasing the number of days with strong wind, especially noticeable in the second 10-year period of the new century.

Table 1 showed that there is a long-term trend of increasing average temperature of winter and transition months. Figure 4 shows the 30-year course of the average maximum temperature of the winter period (by the way, not only on Stavropol Upland, but and on whole Stavropol Region territory) [16].

Comparison of Figs. 1, 2, 3 and 4 shows that, despite the increase in the number of days with strong winds, there is a decrease in the frequency and duration of

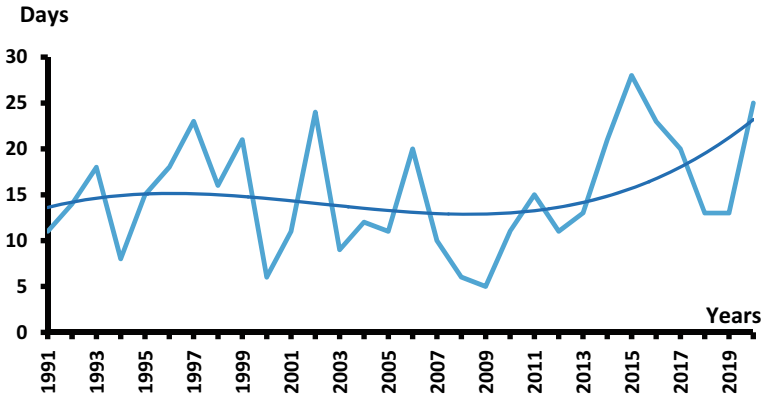


Fig. 3 30-year course of the winter number of days with strong winds

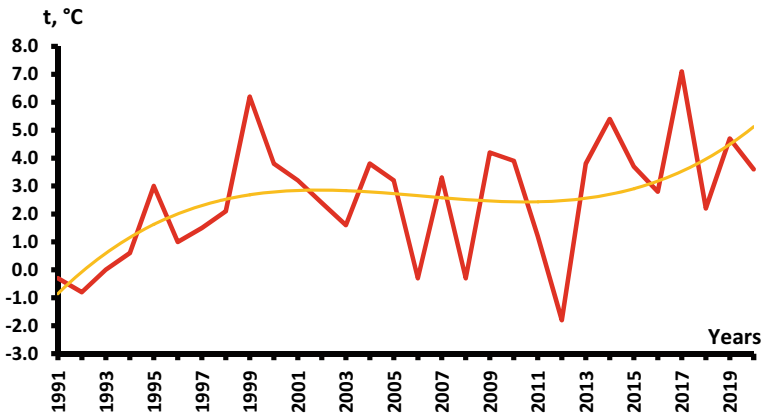


Fig. 4 30-year course of the average maximum winter temperature

snowstorms against the background of increasing winter temperatures, especially noticeable in the second 10-year period of the new century.

Thus, on the Stavropol Upland during the first 20 years of the XXI century has increased significantly the air temperature of the winter and transition months. One of the most important consequences of the temperature increase was a significant decrease in the duration of the meteorological winter [17] as the period between the steady transition of air temperature downward and upward through 0 °C. A reduction in the duration of winter and an increase in its temperature background led to a decrease in the number of days with snow cover, a decrease in the frequency of years with stable snow cover, and an increase in the frequency of snowless months of the cold period, with November and December being the most frequent snowless months.

In addition, a comparison of the current characteristics of the snowstorm regime with the data for previous multi-year periods showed that the frequency and duration of snowstorms on the Stavropol Upland, there is a decrease in the frequency and duration of snowstorms, despite an increase in the number of days with strong winds. Consequently, the decrease in the frequency of snowstorms is mainly facilitated by a significant increase in winter air temperatures and the resulting increase in the frequency of thaws, which leads to compaction of the existing snow cover and a decrease in the frequency of occurrence of conditions favorable for the occurrence of snowstorms, especially low ones.

It should be noted that the identified trends, such as increased winter temperatures, reduced duration of snow cover, shifting the date of spring onset to earlier dates, reduced duration of meteorological winter, reduced frequency of snowstorms were also noted in other regions of Russia [14, 17–23].

4 Conclusion

Thus, in the current study it was shown that in the Stavropol Upland the dates of snow cover appearance are shifted to later dates against the background of increasing winter temperatures, and periods of uninterrupted snow cover occurrence for 30 days and more are observed only in 30% of years. In addition, on the Stavropol Upland there is a decrease in the number of days with snow cover, a decrease in the frequency of years with stable snow cover, and an increase in the frequency of snowless months of the cold period, especially November and December. Also, comparison of the current characteristics of the snowstorm regime with the data for the previous multi-year periods showed that the frequency and duration of snowstorms in the Stavropol Upland decreased, despite an increase in the number of days with strong winds. The main reason for the changes occurring is primarily an increase of air temperature in winter and transitional periods of the year.

References

1. Antonenkov, A.G.: Snow Cover Monitoring: Methodical Guidelines. SPbGTI (TU), St. Petersburg (2003) [in Russian]
2. Kobysheva, N.V., Narovlyznsky, G.Ya.: Climatological processing of meteorological information. Gidrometeoizdat, Leningrad (1978) [in Russian]
3. Badakhova, G.Kh., Knutas, A.V.: Stavropol Territory: Modern Climatic Conditions. Regional networks of communication, Stavropol (2007) [in Russian]
4. Badakhova, G.Kh., Kaplan, G.L.: Changes in temperature and precipitation regime in Stavropol Krai for the past 30 years. “International exchange of scientific knowledge, innovations, technologies”: Collection of articles on the mat. inter. scientific and practical conference. Apex, Irkutsk, 5–9 (2018) [in Russian]
5. Handbook on the Climate of the USSR. Vol. 13. Part 2. Air and Soil Temperatures. Gidrometeoizdat, Leningrad (1966) [in Russian]

6. Brockhaus, F.A., Ephron, I.A.: Encyclopedic Dictionary. Joint Stock Company Printing House "Publishing Business", Brockhaus-Efron, St. Petersburg, **61**, 320–324 (1900) [in Russian]
7. Badakhova, G.Kh., Kaplan, G.L.: Monitoring, analysis and forecast of frost-free period duration in different agroclimatic zones of Stavropol Territory. Materials of 74th regional scientific and practical conference "State and prospects of agricultural sector of Southern Federal District". Stavropol, 118–122 (2010) [in Russian]
8. Handbook on the Climate of the USSR. Vol. 13. Part 4. Air Humidity, Precipitation, Snow Cover. Gidrometeoizdat, Leningrad (1968) [in Russian]
9. Kaplan, G.L.: Adverse and dangerous weather phenomena in winter and their impact on the economy of the Stavropol Territory. Proc. of the V Int. conf. "Problems of environmental safety and conservation of natural resource potential". Stavropol, 156–160 (2008) [in Russian]
10. Handbook on the Climate of the USSR. Vol. 13. Part 5. Cloudiness and Atmospheric Phenomena. Gidrometeoizdat, Leningrad (1968) [in Russian]
11. Dyunin, A.K.: Mechanics of snowstorms. Siberian Branch of AS USSR, Novosibirsk (1963) [in Russian]
12. Gray, D.M., Male, D.H.: Handbook of Snow, 324–343. Gydrometeoizdat, Leningrad (1986)
13. Khromov, S.P., Mamontova, L.I.: Meteorological dictionary. Gydrometeoizdat, Leningrad (1974) [in Russian]
14. Veltishchev, N.F.: Manual handbook on short-term forecasts. Gydrometeoizdat, Leningrad (1986) [in Russian]
15. Bychkova, V.I., Rubinshtein, K.G. Preliminary results of testing the snowstorm short-range forecast algorithm. Russ. Meteorol. Hydrol. **38**, 387–395 (2013).
16. Badakhova, G.Kh., Kaplan, G.L.: Trends in winter temperatures in the Central Caucasus. Actual directions of fundamental and applied research. SIC "Academic", 45–48 (2017) [in Russian]
17. Volkova, V.I., Badakhova, G.Kh., Barekova, M.V., Kaplan, G.L.: Atmospheric circulation features of the transition period and variations of spring onset dates in the Central Precaucasus. Science. Innovations. Technologies. **1**, 125–138 (2021) [in Russian]
18. Bakulina, E.A., Ugryumov, A.I.: Spring reconstructions of circulation in the stratosphere in 1958–2003. Uchenyeyapiski RGMU. **6**, 38–44 (2008) [in Russian]
19. Barashkova, N.K., Kuzhevskaya, I.V., Nosyreva, O.V.: Temperature transition through 0 and 5°C in the south of Western Siberia. Vestnik of Tomsk University. **325**, 191–195 (2009) [in Russian]
20. Belyuchenko, I.S.: Ecology of Krasnodar Krai. KubGAU, Krasnodar (2010) [in Russian]
21. Gavrilenko, N.M.: Features of dates of steady transition of average daily air temperature through 0°C in spring in Ukraine. Proceedings of NIGMI. **32**, 18–26 (1962) [in Russian]
22. Kozeltseva, V.F., Aleshina, A.M., Kuznetsova, N.N.: Spring restructuring of stratospheric circulation rearrangement and steady transition of air temperature through 0, +5°C. Proceedings of the Russian Hydrometeorological Center. **353**, 88–105 (2015) [in Russian]
23. Pogorelov, A.V.: Snow cover of the Greater Caucasus. Akademkniga, Moscow (2002) [in Russian]

Investigations of the Formation of the Ice Phase on the Particles of the Reagent and Zinc Oxide Taking into Account the Influence of the Electric Field Strength



B. M. Khuchunaev and S. O. Gekkieva

Abstract At present, among the many tasks in the field of active influences on clouds, one should single out issues related to the study of reagents and means of influencing clouds. Under laboratory conditions, the crystalline properties of many substances are studied (the pyrotechnic composition of an As rocket with the addition of aerosol particles of a smoke bomb, the pyrotechnic composition with AgI with the addition of graphite, ZnO nanotubes). At the same time, fundamental laboratory experiments are being carried out to study the effect of electricity on the formation of an ice phase on the particles of the reagent and zinc oxide. At present, it is already known that the presence of an electric field in clouds and a charge on reagent particles can affect the specific yield of ice-forming nuclei when working on active influences on cloud processes. Moreover, nanosized particles, as well as particles of reagents, depending on the shape, can increase the electric field near their surface by thousands of times, which can lead to a significant increase in the temperature threshold for the formation of an ice phase on reagent particles.

Keywords Ice phase · Reagent particles · Zinc oxide · Electric field · Active influences

1 Introduction

Questions of the influence of electric forces on the phase and microstructural characteristics of clouds and fogs are of interest to many researchers. However, many aspects of the influence of electric forces on processes in clouds remain unexplored, including the issues of phase and microstructural transformations of water in clouds under conditions of increased ionization of the medium due to electric discharges, the effect of electricity on the formation of an ice phase on reagent particles, etc. [1–4]. Due to the urgency of the problems of developing technologies for active influence on cloud processes, fundamental laboratory experiments are being conducted to study

B. M. Khuchunaev · S. O. Gekkieva (✉)
High-Mountain Geophysical Institute, 2 Lenin Avenue, Nalchik, Russia
e-mail: sgekkieva@list.ru

© The Author(s), under exclusive license to Springer Nature Switzerland AG 2023
R. Zakinyan and A. Zakinyan (eds.), *Physics of the Atmosphere, Climatology and Environmental Monitoring*, Springer Proceedings in Earth and Environmental Sciences, https://doi.org/10.1007/978-3-031-19012-4_22

233

the effect of electricity on the formation of an ice phase on particles of a reagent and zinc oxide. Some of the results of these experiments are presented in this article.

In order to conduct experimental studies of charge formation on AgI reagent particles, a special set of equipment was created, which includes a large cloud chamber, flat capacitor plates, a high-voltage rectifier, a reagent sublimation device, an ultrasonic steam generator, a balance, an optical microscope, and a video camera. A certain technique has been developed to study the effect of the charge on the reagent particles and the electric field on the specific yield of ice-forming nuclei.

2 Method of Influence of Electric Field Strength on Ice-Forming Efficiency of Reagents and Zinc Oxide in Laboratory Conditions

Preliminarily, a certain amount of reagent is weighed on electronic scales. It is loaded onto the metal boat of the reagent sublimation device. Thermo-stated substrates covered with lids are installed at the bottom of a large cloud chamber. An artificial cloud environment is created in the chamber using an ultrasonic steam generator. After that, a high voltage is applied to the capacitor plates from a high-voltage rectifier. Current is applied to the sublimation device; the reagent is dispersed. After sublimation, the air in the chamber is mixed with a fan, and when the first crystals appear in the field of view, the substrates are opened one by one and crystals are deposited on them. Each substrate is examined in the field of an AmScope ME600TZC-18M3 optical microscope, the number of crystals per frame is counted, and then the specific yield is calculated on a computer [5–7].

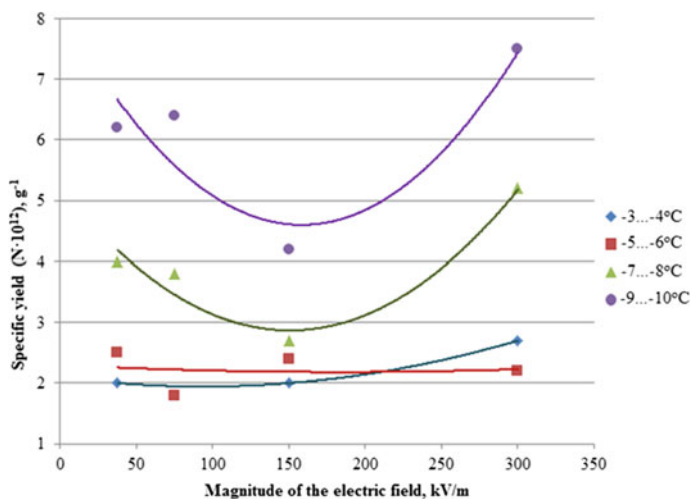
2.1 Laboratory Experiments to Study the Effect of Electric Field Strength on the Ice-Forming Efficiency of the Pyrocomposition AD-1

The experiments were carried out in the temperature range from -10 to -4 °C and at an electric field strength from $3,75 \times 10^4$ to 3×10^5 V/m [8]. Table 1 and Fig. 1 show the dependences of the specific yield of particles of the pyrotechnic composition AD-1 on the electric field strength. Table 1 shows the average values of the specific yield for eight data.

The results of the conducted studies show that with an increase in the electric field strength up to 1.5×10^5 V/m, the specific yield of ice-forming nuclei decreases. With a further increase in the electric field strength, the specific yield of ice-forming nuclei increases. The difference between the maximum and minimum values of the specific output in the temperature range from -10 to -9 °C is 1.6 times. The difference between the maximum and minimum values of the specific output in the temperature

Table 1 Dependence of the specific yield of particles of the pyrotechnic composition AD-1 on the electric field strength

Specific output ($N \times 10^{12}$), g^{-1}				
t, °C	37,5 kV/m	75 kV/m	150 kV/m	300 kV/m
10–9	6.2	6.4	4.2	7.5
7–8	4	3.8	2.7	5.2
5–6	2.5	1.8	2.4	2.2
3–4	2		2	2.7

**Fig. 1** Dependence of the specific yield of particles of the pyrotechnic composition AD-1 on the electric field strength

range from -8 to -7 °C is 1.86 times. The difference between the maximum and minimum values of the specific output in the temperature range from -6 to -3 °C is insignificant. Studies show that in the presence of an electric field, the particles formed during sublimation coagulate with each other. This is the main reason for the decrease in the number of ice-forming nuclei [9]. The increase in ice-forming activity is most likely due to the destruction of crystals under the influence of an electric field. At lower temperatures, ice crystals are more brittle. At temperatures close to 0 °C, ice is more plastic and less prone to breakage. Therefore, the electric field at lower negative temperatures destroys ice crystals more strongly and this leads to an increase in the number of ice-forming nuclei. As part of laboratory studies, a series of experiments were carried out to study the influence of the dependence of the specific yield of ice-forming nuclei of charged zinc oxide particles on temperature. The experiments were carried out in the temperature range from -14 to -5 °C and

Table 2 Temperature dependence of the specific yield of ice-forming nuclei of charged zinc oxide particles

Without electric field		Negatively charged particles		Positively charged particles	
t, °C	Specific output ($N \times 10^{12}$), g^{-1}	t, °C	Specific output ($N \times 10^{12}$), g^{-1}	t, °C	Specific output ($N \times 10^{12}$), g^{-1}
-13.9	2.8	-13.6	0.6	-11.0	6.4
-12.9	1.8	-12.5	0.8	-10.8	4.2
-11.3	2.01	-12.5	1.0	-9.5	5.6
-11.1	0.91	-12.5	0.6	-8.9	0.9
-10.5	2.84	-12.2	0.7	-8.5	1.1
-10.1	5.4	-11.2	0.8	-7.9	4.1
-8.9	1.02	-11.2	2.3	-7.8	3.2
-8.2	1.5	-10	5.5	-6.4	2.3
-7.1	1.1	-8.5	1.4	-6.1	2.6
-6.9	2.9	-8	2.2	-5.7	1.9
-6.8	1.3	-7.9	2.4		
-5.4	2.3	-7	0.8		

the polarities of the capacitor plates “0”, “+” and “0”, “-”. The results are presented in Table 2.

Obviously, the growth of ice crystals on positively charged zinc oxide particles is more active than on negatively charged particles (Fig. 2). Differences are especially noticeable in the temperature range from -13 to -10 °C. At temperatures above -7 °C, negatively charged zinc oxide particles have a greater ice-forming activity than positively charged particles. In the temperature range from -14 to -8 °C, the specific yield of negatively charged zinc oxide particles is less than that of uncharged particles. In the temperature range from -8 to -5 °C, the specific yield of negatively charged zinc oxide particles is greater than that of uncharged particles. In the temperature range from -14 to -5 °C, the specific yield of positively charged zinc oxide particles is higher than that of uncharged particles.

2.2 The Experiments to Study the Effect of Electric Field Strength on the Ice-Forming Efficiency of Zinc Oxide

The series of experiments to study the effect of the electric field strength on the ice-forming efficiency of zinc oxide were carried out in the temperature range from -11 to -5 °C and the electric field strength of 2.25×10^5 V/m. Table 3 and Fig. 3 show the dependences of the specific yield of zinc oxide particles on the electric field strength.

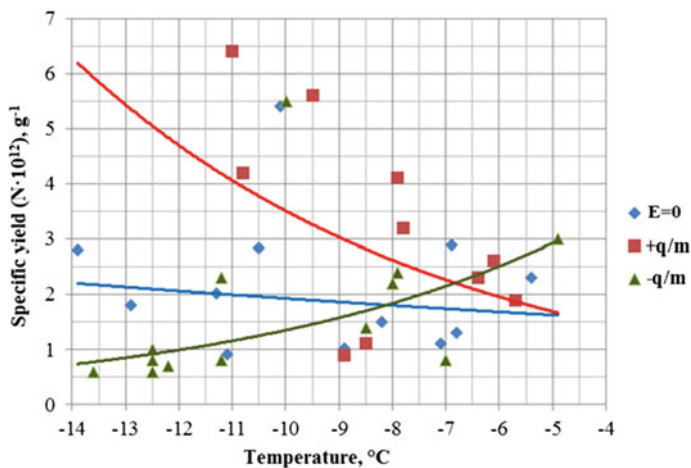


Fig. 2 Dependence of the specific yield of ice-forming nuclei of charged zinc oxide particles on temperature

Table 3 Dependence of the specific yield of zinc oxide particles on temperature in the presence and absence of an electric field

With electric field		Without electric field	
t, °C	Specific output ($N \times 10^{13}$), g^{-1}	t, °C	Specific output ($N \times 10^{13}$), g^{-1}
-8.9	0.53	-11.1	0.091
-8.7	1.2	-10.5	0.28
-7.8	0.66	-10.1	0.54
-7.7	1.1	-8.9	0.1
-7.7	0.53	-8.2	0.15
-7.6	1.1	-7.1	0.11
-7.4	1.4	-7.1	0.29
-5.8	0.96	-6.8	0.13
-5.7	1.5	-5.4	0.23
-5.4	0.89	-	-

The results obtained in the course of laboratory experiments showed that the lowest values of the specific output are observed when conducting experiments without an electric field. At an electric field strength of 2.25×10^5 V/m, a significant increase in the ice-forming activity of zinc oxide is observed. In this case, the values of the specific yield are 3–5 times higher than the specific yield in experiments without an electric field over the entire temperature range. Laboratory studies have shown that sublimation particles of zinc oxide in the presence of an electric field form complexes of nanotubes. Such complexes are ice-forming nuclei; the larger the complex size, the higher the crystal formation temperature [10, 11]. Upon sublimation of ZnO in the presence of water vapor, ice-forming complexes are formed from open nanotubes of

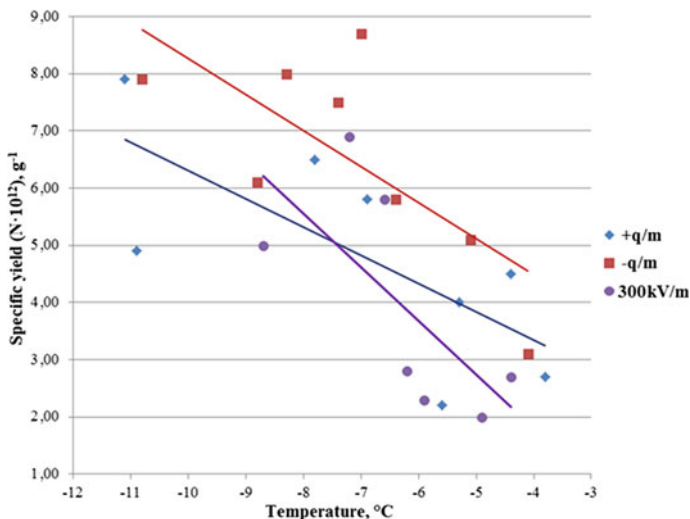


Fig. 3 Temperature dependence of the specific yield of zinc oxide particles in the presence and absence of an electric field

zinc oxide. Upon sublimation of ZnO without water vapor, ice-forming complexes are not formed, although the formation of ZnO nanotubes of very small diameter (~ 1 nm) takes place. These ZnO nanotubes are closed and, due to their small size, cannot be ice nuclei. Consequently, during the sublimation of zinc oxide outside the cloudy environment, ice-forming nuclei cannot be formed. The results obtained show that the growth of ice crystals on negatively charged particles of the pyrotechnic composition AD-1 is more active than on positively charged particles, but slight changes in the values of the specific yield are observed. Conversely, the growth of ice crystals on positively charged zinc oxide particles is more active than on negatively charged particles.

3 Conclusions

As a result of studying the effect of the charge on the particles of the reagent and the electric field on the specific yield of ice-forming nuclei, it was found that the growth of ice crystals on negatively charged particles of the AD-1 pyrotechnic composition is more active than on positively charged particles. However, slight changes in the values of the specific output are observed. In the temperature range from -8 to -4 °C, the specific yield increases from 1.5 to 2.5 times for negatively charged particles and from up to 1.7 times for positively charged particles. In the temperature range from -11 to -8 °C, the specific yield increases by 1.3 times for negatively charged particles and decreases by 1.1 times for positively charged particles. For zinc oxide

particles, it was found that the growth of ice crystals on positively charged particles is more active than on negatively charged particles. Differences are especially noticeable in the temperature range from -13 to -10 °C. But at temperatures above -7 °C, negatively charged zinc oxide particles have a greater ice-forming activity than positively charged particles. At an electric field strength of 2.25×10^5 V/m, a significant increase in the ice-forming activity of zinc oxide is observed. In this case, the values of the specific yield are 3–5 times higher than the specific yield in experiments without an electric field over the entire temperature range.

References

1. Stepanenko, V., Dovgalyuk, Yu., Sinkevich, A., Veremey, N., Ponomarev, Yu., Pershina, T.: Investigation of the influence of electric discharges on phase and microstructural transformations of water in clouds. *J. Meteorology and Hydrology*. 3, 39-50 (2002)
2. Ivlev, L., Dovgalyuk, Yu.: *Physics of atmospheric aerosol systems*. RICH SPBU, Saint Petersburg (1999) [in Russian]
3. *Questions of the physics of clouds*. Collection of selected articles of the MGO. Asterion, St. Petersburg (2008) [in Russian]
4. Vereshchagin, O., Anoshin, A.: *High-voltage electrical technologies*. MEI, Moscow (1999) [in Russian]
5. Emelyanov, V., Nesmeyanov, P., Erlandts, N., Shakirov, I.: Results of the development of new pyrotechnic compositions of ice-forming aerosol for means of active influence on clouds. Proceedings of the jubilee conference, dedicated to the 40th anniversary of the beginning of production works on protection from hail. 259–260, Nalchik (2011) [in Russian]
6. Kachurin, L.: On the probability of formation of ice nuclei in supercooled water. *J. Meteorology and Hydrology*. 8, 48-54 (1976)
7. Guzeeva, T.: *Fundamentals of nuclear physics, radiochemistry and dosimetry: a course of lectures*. (2018). <https://portal.tpu.ru/SHARED/g/GUZEEVA/rabota1/Tab1/lek5-9.doc>. 2018. 06.14.
8. Barthe, C., Chong, M., Pinty, J., Bovalo, C., Escobar, J.: Updated and Parallelized Version of an Electrical Scheme to Simulate Multiple Electrified Clouds and Flashes over Large Domains. *Geoscientific Model Development*. 5(1), 167-184 (2012)
9. Girs, S.: Influence of electrical characteristics of the atmosphere on the initial stage of charging of convective clouds. Collection of selected articles. 50th Anniversary of the Department of Cloud Physics, MGO. 46, 78–86 (2008)
10. Khuchunaev, B., Gekkieva, S., Budaev, A.: Researches of ice-forming efficiency of products of sublimation of pyrotechnic compositions consisting of silver iodide AgI particles and zinc oxide. *IOP Conference Series: Materials Science and Engineering*. Mater. Sci. Eng. 1083 012097 (2021). DOI:<https://doi.org/10.1088/1755-1315/840/1/01> 2014
11. Khuchunaev, B., Baysiev, Kh.-M. Kh, Gekkieva, S., Budaev, A.: Experimental studies of the ice-forming efficiency of the AD-1 pyrotechnic composition with zinc additions. Collection «Proceedings of the MGO». 597, 51–60 (2020). DOI:<https://doi.org/10.1088/1757-899X/1083/1/01> 2097 [in Russian]

Comparison of the Results of Approximation of the Vertical Profiles of the Refractive Index in the Atmosphere Over St. Petersburg and Moscow



A. D. Kuznetsov, O. S. Seroukhova, S. V. Kryukova, and T. E. Simakina

Abstract An approximation of the refractive index vertical profile in the troposphere of St. Petersburg and Moscow has been performed. The coefficients of the exponential regression equation at different times of the day and in different seasons of the year are determined: the value of the refractive index in the surface layer and the exponent responsible for the rate of change of the index with height. The refractive index gradient at the stations under consideration varies within $-33 \div -46$ N-units/km, which corresponds to substandard and superstandard refraction types.

Keywords Refractive index · Vertical profile · Troposphere · Exponential regression

1 Introduction

The use of radio waves is currently very wide. These are communication, radar, radio telemechanics, radio direction finding, radio navigation, ranging, etc. The task of the practical use of radio waves is to ensure reliable communication between objects, which requires information about the electromagnetic energy transmission channel - the tropospheric path.

Wave propagation conditions are affected by atmospheric refraction, characterized by the index of refractive index (IRI) N and depending on the distribution of temperature, pressure, and humidity in the atmosphere. Due to refraction, radio waves propagate along curvilinear trajectories, that is, they pass a longer path in the atmosphere, and the angle of their arrival changes. The change in permittivity with height affects the propagation speed of radio waves [1–4].

A. D. Kuznetsov · O. S. Seroukhova · S. V. Kryukova · T. E. Simakina (✉)
Russian State Hydrometeorological University, 79 Voronezhskaya street, 192007 St.-Petersburg,
Russian Federation
e-mail: tatiana.simakina@gmail.com

A. D. Kuznetsov
e-mail: kuznetsov1946@inbox.ru

Spatial variations in the refractive index due to changes in meteorological parameters affect not only the curvature of the radio wave propagation path, but can lead to the appearance of multipath propagation and to a change in the spectrum of the received signal [5].

The radio-climatic regime of the troposphere over a certain territory affects the accuracy of calculating the slant range to an object in the radar systems software. In this regard, radiometeorological modeling of the troposphere in the meteorological radars coverage area is one of the important tasks of increasing the efficiency and reliability of cloud sounding and detection of dangerous atmospheric phenomena. Modeling implies an approximation of the vertical refractive index profile, on the basis of which refraction in the troposphere can be taken into account [6–10].

2 Methods

In the absence of information about the altitude profiles of meteorological parameters, the standard radio atmosphere is used to set the vertical profile of the IRI [1]. In this model, a pressure of 1000 hPa at the Earth's surface decreases with altitude by 120 hPa/km; the temperature at the Earth's surface $T = 288$ K decreases with altitude by 5.5 deg/km; relative humidity is 60% and does not change with height. The upper limit of the troposphere is 11 km. In such a normal troposphere, the index of refractive index changes linearly with height and its vertical gradient is -40 N-units/km. At a height of 9 km, the value of the refractive index is constant and amounts to a value of 109 [7].

Irregular variation of meteorological parameters with height under real conditions leads to a complex dependence of the refractive index on height. In some layers, the decrease in the IRI turns out to be sharper; in other layers, the index may increase. Deviations from the normal troposphere are especially large at heights up to 2–3 km in summer, when temperature inversions and cloud layers are often formed, which are areas of high humidity [5, 7].

With vertical profiles in the troposphere different from the standard radio atmosphere, the law of change in the index of refractive index with height can be approximated by an exponential dependence [8]

$$N(z) = N_0 e^{-\alpha z} \quad (1)$$

The exponential model does not separate the refractive index into dry and wet components, in contrast to the bi-exponential model, where the exponential law of decrease in IRI with height is applied to two components separately [7]. The bi-exponential model well approximates the vertical profile of the IRI in the equatorial, subequatorial, tropical and subtropical areas with hot and warm climates.

The paper presents a method for calculating the coefficients of Eq. (1) and an approximation of the vertical IRI profiles for different seasons in the troposphere of St. Petersburg and Moscow.

The stages of calculation of dependence coefficients (1) according to aerological sounding data.

1. According to the aerological data of temperature, pressure and humidity measured at different heights z , the vertical profile of the index of refractive index $N(z)$ was calculated [1]:

$$N = \left\{ \left[\frac{78.5}{T} \left(p + \frac{4800e}{T} \right) \right] - 1 \right\} 10^6$$

2. A step $\Delta\alpha$ was set for the coefficient α_i , with which the coefficient will change from the minimum value α_{\min} to the maximum α_{\max} .

$$\Delta\alpha = \frac{\alpha_{\max} - \alpha_{\min}}{k}$$

The direct enumeration method repeatedly calculated the approximation of the profile $N(z)$ with the values of the coefficients α_i .

$$\alpha_i = \alpha_{\min} + \Delta\alpha \times i, \quad i = 1, 2, \dots, k$$

3. After carrying out calculations with all k -values of the coefficients α_i , k -values of residuals between the actual profile $N(Z)$ and its approximation were calculated

$$E_i = \sum_{j=1}^m [N(z_j) - N_0 \times \exp(-\alpha_i z_j)]^2, \quad i = 1, 2, \dots, k; \quad j = 1, 2, \dots, m \tag{2}$$

where m —number of levels at which the values of meteorological quantities are given;

$N_0 = N(z_1)$ – the index of refractive index value calculated from the values of meteorological quantities near the Earth’s surface.

4. The analysis of residuals was performed according to the dependency graph of function (2) on the argument k in the range of the coefficient $[\alpha_{\min}, \alpha_{\max}]$. Three cases are possible:

- growth of the values of the function E_i on the entire interval $[\alpha_{\min}, \alpha_{\max}]$;
- decreasing values of the function E_i without approaching zero;
- the presence of a pronounced one or more minima in the values of the function E_i on the segment $[\alpha_{\min}, \alpha_{\max}]$.

In the first and second cases, the calculation was repeated with a new range of coefficients $[\alpha_{\min}, \alpha_{\max}]$, shifted to the right or left towards the expected minimum. Such changes in the boundaries of the range must be repeated until the “behavior” of the function E_i corresponds to the third case. The minimum value of the function E_k

must be zero. If this is not the case, it is necessary to narrow the range of change in α and reduce the step of changing the argument $\Delta\alpha$, thereby increasing the accuracy of the approximation.

3 Results and Discussion

In this work, the simulation of the atmospheric IRI in the altitudinal layer of 0–6000 m above the earth’s surface was performed at two points - St. Petersburg and Moscow, separated by 712 km, with simultaneous measurements with an interval of 12 h during 2019. The results of the approximation of IRI profiles by season and by time of day are presented in Table 1.

The interval of IRI variation at the station height (initial level) N_0 is in the range of 301–325 N-units, not noticeably different at two stations. The value of the parameter α varies for different seasons within a wider range for St. Petersburg (0.11–0.16) than for Moscow (0.11–0.14). Figure 1 shows the distribution spectrum of the coefficient α for two stations.

The correlation between the values of α in the IRI approximation equations during the day and night is weak (Fig. 2a). In general, the values of α at night are higher than during the day. No correlation was found between the α values in St. Petersburg and Moscow (Fig. 2b).

Table 1 Results of approximation of IRI profiles by seasons at two points

Season	Term	Saint-Petersburg			Moscow		
		Equation	σ_α	σ_{N_0}	Equation	σ_α	σ_{N_0}
January	Day	$N(z) = 314e^{-0,12z}$	0,004	2,1	$N(z) = 308e^{-0,12z}$	0,003	1,7
	Night	$N(z) = 314e^{-0,13z}$	0,004	1,3	$N(z) = 308e^{-0,12z}$	0,001	1,5
April	Day	$N(z) = 301e^{-0,11z}$	0,008	9,5	$N(z) = 303e^{-0,12z}$	0,009	9,8
	Night	$N(z) = 311e^{-0,12z}$	0,006	6,5	$N(z) = 310e^{-0,12z}$	0,009	5,0
July	Day	$N(z) = 325e^{-0,14z}$	0,008	7,2	$N(z) = 312e^{-0,13z}$	0,015	13,5
	Night	$N(z) = 330e^{-0,14z}$	0,006	5,3	$N(z) = 323e^{-0,14z}$	0,010	6,5
October	Day	$N(z) = 316e^{-0,13z}$	0,005	4,5	$N(z) = 317e^{-0,13z}$	0,010	4,1
	Night	$N(z) = 319e^{-0,13z}$	0,005	4,3	$N(z) = 321e^{-0,14z}$	0,009	5,5

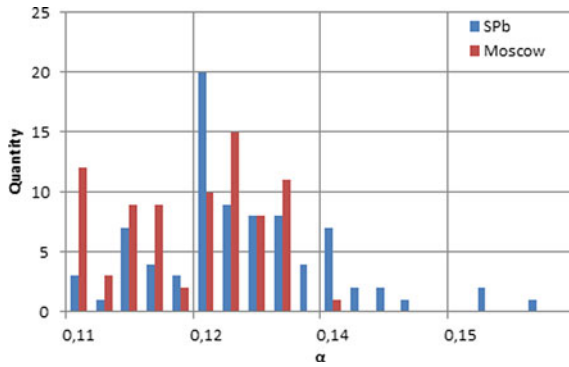


Fig. 1 Distribution of alpha parameter values at two stations

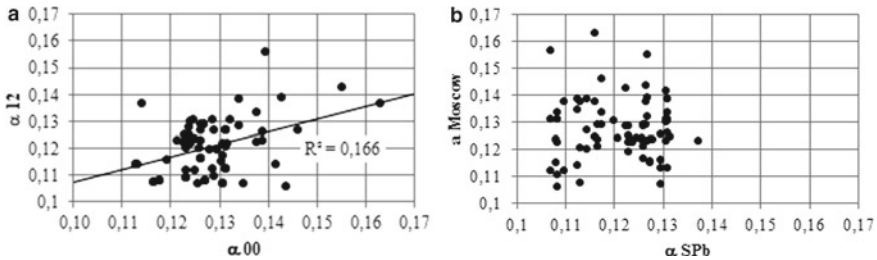


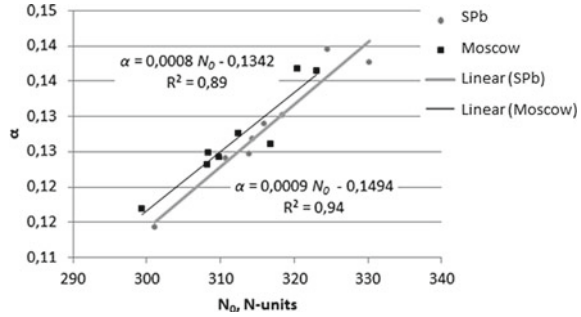
Fig. 2 Scatterplots of the parameter alpha values at night and daytime (a); at two stations (b)

The reciprocal of the parameter α —the so-called height scale [7]—is measured in kilometers and determines the height at which the IRI decreases by a factor of e . The height scale values for Moscow and St. Petersburg vary within 2 km. The maximum value was calculated in St. Petersburg in April during the day and amounted to 9.1 km, the minimum—also in St. Petersburg in July at night—6.3 km. In general, in the more northern city of St. Petersburg, the height scale values are larger, which indicates a less sharp decrease in the refractive index with height and, accordingly, a lower refraction, all other things being equal [7].

There is a direct linear relationship between the regression equation parameters values—Fig. 3. The greater the value of the surface IRI, the greater the rate of its change with altitude. The resulting linear equations $\alpha = f(N_0)$ for the two stations are close, which makes it possible to calculate the surface IRI from ground-based measurements of meteorological parameters, and, having determined the exponent α , restore the IRI profile.

The difference between the obtained refractive index profiles and the standard profile is within 2–20 N-units and is due to layered inhomogeneities [6], primarily clouds. The refractive index in them differs from the refractive index in neighboring areas; on such inhomogeneities, the energy of radio waves is scattered in different directions. The thickness of the deviations layer of the indices in the real troposphere

Fig. 3 Relationship between the parameters of the exponential model for two stations



from the standard is from meters to several kilometers. The movement of layered inhomogeneities in space, which can occur at velocities from 2 to 30 m/s, causes fluctuations in the refractive index.

The found regression equation coefficients also make it possible to determine the gradient of the refraction index. It is due to the type of troposphere refraction that affects the trajectory of the radar beam. The refractive index gradient decreases with height. At the lower level this parameter determines the meteorological regime of the surface layer. Thus, at a gradient value of minus 157 N-units/km, corresponding to superrefraction, conditions appear for the occurrence of temperature inversions.

At the stations under consideration during the year the IRI gradient varies within the range of minus 33–46 N-units/km, which corresponds to a positive refraction—Fig. 4. With positive refraction the gradient of the refractive index is negative, the radius of curvature of the radar beam is a positive value, and the wave propagation path is convex upward. The range of ground radio systems with positive refraction increases. To take into account the influence of atmospheric refraction during the propagation of radio waves near the Earth’s surface on the line-of-sight range, the concept of the Earth’s equivalent radius is introduced [1].

Positive refraction, depending on the magnitude of the refractive index gradient, is divided into low, normal and high. When the gradient value is from 0 to –40 N-units/km, one speaks of substandard refraction, in this case the equivalent radius of the Earth is greater than the true one, but less than 8500 km. With standard refraction, the IRI gradient is –40 N-units/km, the equivalent radius of the Earth is 8500 km. Standard tropospheric refraction increases line-of-sight range by 15%.

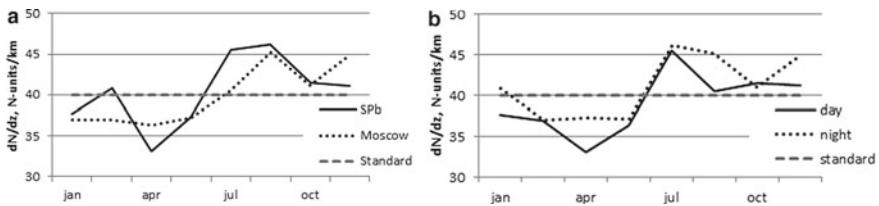


Fig. 4 Time course of the IRI gradient: at different stations (a); at different times of the day (b)

Superstandard refraction is observed when the gradient is in the range from -157 to -40 N-units/km, the equivalent radius of the Earth is greater than 8500 km.

If we compare the troposphere in the regions under consideration with the standard radio atmosphere (the IRI gradient is indicated by a dotted line in Fig. 4), we can note the following. In St. Petersburg, the troposphere is more often close to the standard radio atmosphere than in Moscow. On the other hand, deviations from the standard radio atmosphere are more pronounced here. At both stations a substandard type of refraction is observed in April and a superstandard type in July.

4 Conclusion

The resulting equations for the change in IRI with height make it possible to reconstruct the its profile in the territories under consideration from ground-based data on temperature, humidity, and pressure in different seasons in the absence of aerological data.

References

1. Kiselev, V.N., Kuznetsov, A.D.: Methods for sensing the environment (atmosphere) (St. Petersburg, ed. RGGMU) 429 (2004) [in Russian].
2. Temporary guidelines on the use of information from the Doppler meteorological radar DMRL-S in synoptic practice. Second edition. Moscow, 121 (2017) [in Russian].
3. Oleinikov, V.N., Solyashik, O.A., Evseev, D.B.: Estimation of some characteristics of turbulent processes in the troposphere by the radar method. *Applied Radioelectronics*. 3(1), 35–40 (2004) [in Russian].
4. Meshcheryakov, A.A., Gosenchenko, S.G., Kizhner, L.I.: Influence of the variability of the troposphere refractive index on the line-of-sight range and the error in measuring the coordinates of radar targets. *Bulletin of the Tomsk Polytechnic University. Mathematics and mechanics. Physics*. 318(2), 59–63 (2011) [in Russian].
5. Ostrovsky, E.V., Fridzon, M.B.: Fine structure of the vertical humidity profile affecting the propagation of radio waves in the troposphere. *Scientific Bulletin of MSTU GA, series Radiophysics and radio engineering*. 133, 30–39 (2008) [in Russian].
6. Zabolotny, N.S., Goldina, V.N.: Using mathematical models to determine the refractive index of the atmosphere. *Izvestiya Vuzov. Geodesy and Aerial Photography*. 2, 30–33 (1987) [in Russian].
7. Kizhner, L.I., Maltseva, N.A.: Parameters of the vertical profile of the troposphere refractive index over the northern part of the Atlantic Ocean. *Bulletin of the Tomsk State University*. 175–180. (2012) [in Russian].
8. Kuznetsov, A., Seroukhova, O., Simakina, T., Kryukova, S.: The vertical profile of the refraction coefficient for microwave radiation in the troposphere and its variability. *Journal of Physics: Conference Series* 1991, 012008 (2021), doi:<https://doi.org/10.1088/1742-6596/1991/1/012008>.

9. Mytsenko, I.M.: Study of the propagation of FM band radio waves over the ocean surface during a solar eclipse. *Radiophysics and Electronics*. 12 (1), 192–194 (2007) [in Russian].
10. Novikov A.V., Akulinichev Yu.P.: Model of the space-time field of the refractive index of the surface layer of the atmosphere. *Electronics, measuring equipment, radio engineering and communication. Reports of TUSUR*. 1 (21), part 2, June. 36–44 (2010) [in Russian].

Investigation of the Influence of the Interaction of Convective Clouds With the Surrounding Atmosphere on the Evolution of Their Parameters



V. N. Lesev, B. A. Ashabokov, L. M. Fedchenko, and V. A. Shapovalov

Abstract The article investigates the role of the cloud system properties based on a comparison of the results of calculations of the formation and development of clouds corresponding to the real and model structures of the wind field in the atmosphere. In this case, the hierarchy property is considered, i.e., the interaction of convective clouds with the surrounding atmosphere, due to the structure of the wind field in the atmosphere. A three-dimensional unsteady model of thunderstorm clouds with a detailed account of microphysical processes was used for the research. The results of numerical experiments are presented in order to study the role of the interaction of convective clouds with the surrounding atmosphere.

Keywords Thunderstorm clouds · System properties · Role · Hierarchy property · Interaction of clouds with the surrounding atmosphere · Three-dimensional model

1 Introduction

The interaction of clouds with the atmosphere is quite diverse, some of its types are well known, but their role in the processes of cloud formation is explained at a qualitative level. There are also mechanisms that are not understood at a sufficient level. To date, there is no consensus on the mechanisms of influence of the wind structure in the atmosphere on the processes of cloud formation. The paper [1] describes the mechanism of formation of powerful convective clouds, according to which the main contribution to their formation is made by updrafts. According to some other authors

V. N. Lesev

Kabardino-Balkarian State University Named After H. M. Berbekov, 173 Chernyshevsky str, 360004 Nalchik, Russian Federation

B. A. Ashabokov

Institute of Informatics and Problems of Regional Management, KBNTS RAS, 37a I. Armand str, 360000 Nalchik, RF, Russian Federation

L. M. Fedchenko · V. A. Shapovalov (✉)

High Mountain Geophysical Institute, 2 Lenina Ave., 360030 Nalchik, Russian Federation
e-mail: vet555_83@mail.ru

[2, 3], one of the mechanisms is that precipitation from clouds tilted by wind shear falls sideways from the updraft, which means that it is not slowed down by falling precipitation particles and as a result of a decrease in air temperature due to their evaporation. At the same time, other researchers have not found a clear correlation between the probability of hail and wind shifts in the upper troposphere [4, 5]. Such differences in the estimates of the role of wind shear in the development of clouds, according to the authors [6, 7], are due to the fact that of the many factors affecting the formation of clouds, only wind shear is considered. And as shown in [8], when assessing the effect of wind shear on convective clouds, thermal stratification must also be taken into account. Powerful convection intensifies under the influence of vertical wind shifts and at the same time there is some (critical) value at which it intensifies most strongly. Weak convection, after a certain value, is suppressed.

It has long been noticed that the characteristics of convective clouds and the features of their interaction with the surrounding atmosphere strongly depend on the structure of the wind field. In the zone of formation of convective clouds, the most intense pulsations of the horizontal and vertical components of wind speed are observed. They are most intense in the layer 1–2 km below the upper boundary of the cloud, as well as in the zone where ascending and descending flows are adjacent. In addition, their secondary maximum may be located in the vicinity of the zero isotherm. Its occurrence is due to a decrease in the stability of thermal stratification, which occurs due to air cooling due to melting of ice particles.

In some cases, clouds are able to grow due to upward movements caused by the relative movement of the cloud, even at subzero temperatures of the intra-cloud air. Such dynamic convection has a stronger effect on the development of powerful convective clouds, and it may be one of the mechanisms of selective growth of large clouds at the expense of small ones. Since new cells are formed on the side of the cloud, the trajectory of the visible cloud movement does not coincide with the direction of the wind in the convection layer [6, 9]. Only small clouds mostly move in the direction and at the speed of the average wind in the cloud layer, although they also have erratic wanderings with a weak wind. They may be due to the fact that the apparent movement of clouds caused by the growth or destruction of cloud cells is superimposed on the low transfer rate. Large clouds in the northern hemisphere often shift to the right of the wind direction; the angle of displacement in some cases may exceed 15–20 °C. The speed of movement of such clouds may differ from the wind speed by tens of percent.

The effect of wind shear in the atmosphere on the relative velocity of cloud movement was studied in [10–12]. The presence of wind shear in the atmosphere leads to an external flow around the cloud. Under the influence of flow in the zone of updrafts, a pressure disturbance occurs, which, according to the results of the evaluation in [13], is small near small clouds with small wind shifts, and next to powerful clouds its values reach several hectopascals. These results were confirmed in [14–16] and others. Obviously, this will affect the development of the cloud. It may consist in the fact that the cloud-induced disturbance of the pressure field should contribute to the development of downward flows in the rear of the cloud.

Let us focus on the results of studies of the influence of the convective clouds interaction with the surrounding atmosphere on the evolution of their parameters.

2 The Results of Calculations

The studies were carried out on the basis of a three-dimensional model of thunderstorm clouds with a detailed account of the processes [3, 9]. The dimensions of the spatial area in the calculations were set from 60 to 100 km horizontally and 16 km vertically. The grid step along the X , Y , Z coordinates was 250–500 m. The X —axis was directed to the east, Y —to the north, Z —vertically. The cloud was initiated by setting a thermal pulse at the earth's surface with overheating = 1–4 °C, the shape and size of the pulse also varied in numerical experiments.

During the calculations, data from the aerological sounding of the atmosphere at the Mineralnye Vody airport were used, and in some cases three-dimensional data obtained using the Global Forecast Model (GFS) were used. Days were chosen when showers, thunderstorms, hail were observed within the radius of the probe's representativeness. For comparison with real clouds, data from radar observations from meteorological radars DMRL-S (Stavropol, Mineralnye Vody) and MRL-5 (Nartkala, Kabardino-Balkarian Republic) were used.

Calculations were carried out for the real and model structure of the wind field in the atmosphere. Calculations of cloud formation and development were carried out in the following cases:

- the real structure of the wind field obtained as a result of atmospheric sounding is used (2021.05.13);
- the model structure of the wind field is used, obtained by increasing the wind speed in the first variant, the direction of the wind speed vector does not change at all altitudes;
- cloud formation occurs in a calm atmosphere (the wind speed in the atmosphere is zero).

The calculation results corresponding to the first case are shown in Figs. 1, 2 and 3. The view of the wind field from above and from the side in the vertical plane is shown in Fig. 1.

In Fig. 1 it can be noticed that the direction and speed of the wind vary in height in a complex way. The maximum value of the wind speed in the atmosphere in the upper part is 45 m/s, and its maximum value in the middle part of the region is noticeably less – 8 m/s.

The turbulence coefficient takes the maximum value (can reach 500 m²/s or more) at the 30 min of cloud development, and the minimum value (about 150 m²/s) at the end of the cloud decay stage at the 50th minute of its evolution.

Figure 2 shows isosurfaces with a water content of 0.35 g/m³ at 20 min of cloud development. The formation of the area in the cloud in which the water content is concentrated occurs in the central part of the zone of ascending air flows. The lower

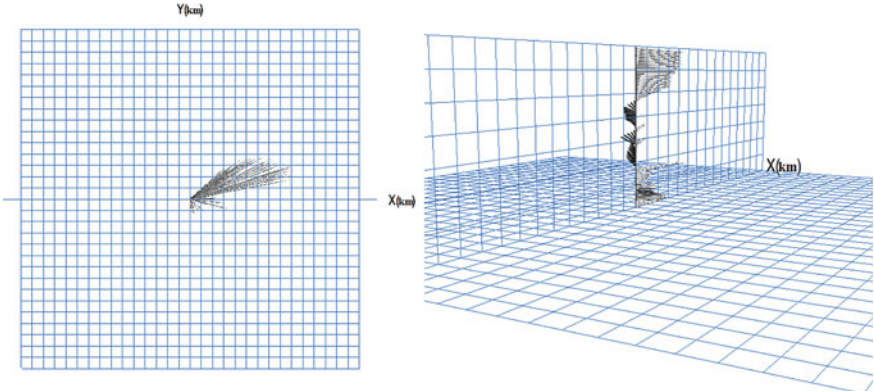


Fig. 1 Wind field in the atmosphere according to atmospheric sounding data (top view on the left; vertical view on the right)

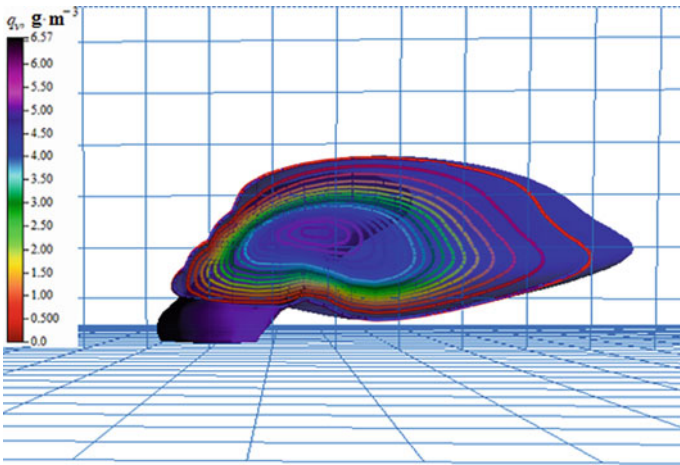


Fig. 2 Isosurface of water content of 0.350 g/m^3 and vertical component of velocity of 5.00 m/s against the background of the water content isoline in the vertical plane at the at the 20th minute

boundary of the considered water content isosurface and the value of the maximum water content are located above the earth's surface, i.e. precipitation from the cloud does not fall out at this time. The isosurface of the vertical component of the velocity of the ascending flows of 10.0 m/s is also shown here against the background of the water content isolines in the vertical plane.

Figure 3 shows the isosurface of the vertical water content of 0.350 g/m^3 and the isolines of the vertical component of the velocity of 10 m/s against the background of the isolines of water content in the vertical plane at 30 min of cloud evolution.

A comparison of Figs. 2 and 3 shows that the maximum value of the velocity of the ascending air flows, as well as the height above the earth's surface on which it is

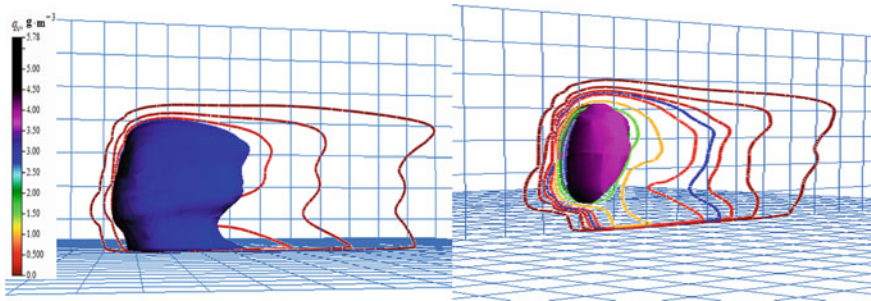


Fig. 3 Isosurface of water content of 0.350 g/m^3 against the background of water content isolines in the vertical plane (left) and isosurface of the vertical component of the velocity of 10.0 m/s against the background of water content isolines in the vertical plane (right) at the 30th minute

located, compared with their values at the previous time, decreased slightly, while the volume of the cloud covered by the isosurface of the vertical component of the air flow velocity of 10.0 m/s , compared with its the value at the previous time also decreased. But it can be noticed that the upward movements of the air in the cloud at a given time have become more intense. At the same time, there seems to be some expansion of the cloud area covered by the water isolines.

Figure 4 shows the isosurface reflectivity of 45 dBZ at 30th minute of cloud development. The maximum value of reflectivity at a wavelength of 3.2 cm at a given time is 61.4 dBZ and it is located at an altitude of 4.72 km above the earth’s surface in the zone of intense updrafts. The region is located above the boundary of the water and ice isosurfaces.

The trend established for the time moments of 20 and 30 min persists at the time of 40 min, that is, the volume of the cloud covered by the isosurface of the vertical component of the air flow velocity of 10.0 m/s continues to decrease. The maximum value of the velocity of ascending air flows at a given time is 13.7 m/s and it is located at an altitude of 3.85 km above the earth’s surface, and the maximum value

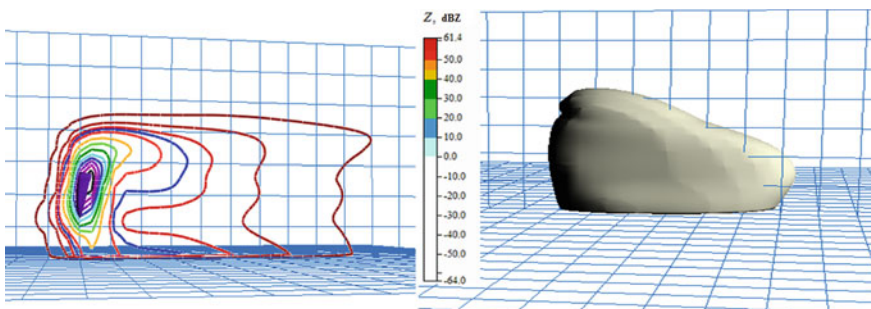


Fig. 4 The isosurface of the vertical component of the velocity of 10.0 m/s against the background of the water line in the vertical plane (left) and the isosurface of the reflectivity of 45 dBZ (right) at 40 min. Maximum reflectivity (3.2 cm): 61.4 dB , $P = 4.72 \text{ km}$

of the velocity of descending air flows is -2.36 m/s at an altitude of 8.57 km. At this point in time, the volume of this area, as can be seen in the figure, has become insignificant—the cloud is apparently already close to destruction. Comparison of Figs. 2, 3 and 4 shows that the maximum value of the velocity of ascending air flows, as well as the height above the earth’s surface on which it is located, compared with their values at the previous time decreased. In addition, there is a decrease over time in the volume of the cloud covered by the isosurface of the vertical component of the air flow velocity of 10.0 m/s. In the same way, such characteristics of these flows as the maximum vertical air velocity and the maximum turbulence coefficient have noticeably decreased. Compared with their values at the 30th minute of cloud development, they decreased almost twice at the 40th minute. In addition, the heights at which these characteristics are located have noticeably decreased. A comparison of the images in Fig. 4 shows that the formation of the reflectivity zone is mainly due to droplets.

The same calculations were carried out for the model structure of wind in the atmosphere. It differed from the real one in that the wind direction did not change with altitude and coincided with the direction of the O_X axis. Table 1 shows the maximum values of cloud parameters corresponding to different variants of wind distribution in the atmosphere (2021.05.13). The table uses the notation: W_E and W_N —the maximum values of the velocity of ascending and descending air flows, H_{W_E} —the height at which the maximum value of the velocity of ascending air flows is located, Q_{max} , Q_{Lmax} , Z_{max} —the maximum values of water content, ice content and reflectivity in the cloud, $H_{Q_{max}}$, $H_{Q_{Lmax}}$, $H_{Z_{max}}$ —vertical coordinates of the maximum values of water content, iciness and reflectivity.

From the table, it can be seen that the maximum value of the vertical flow velocity at the 30th and 40th minutes of cloud development is higher in the case of a model wind structure in the cloud (the wind direction does not change in height), and at

Table 1 Maximum values of cloud parameters corresponding to different variants of wind distribution in the atmosphere (2021.05.13)

Time, min	I—model structure of wind in the atmosphere			II—real structure of wind in the atmosphere		
	20	30	40	20	30	40
W_E , m/s	15.2	17.1	16.4	17.3	16.4	13.7
W_N , m/s	-1.78	-1.80	-2.40	-1.86	-2.26	-1.91
H_{W_E} , km	4	5	5	4	4.5	4.5
Q_{max} , g/m ³	5.48	9.02	9.95	5.78	7.77	3.43
$H_{Q_{max}}$, km	4.5	4.5	3.5	4.50	4	3
Q_{Lmax}	$3 \cdot 10^{-4}$	4.63	3.8	$5 \cdot 10^{-4}$	3.94	6.15
$H_{Q_{Lmax}}$, km	5.5	6.5	6	5.5	6.5	4.5
Z_{max} , dBZ	17.5	65.5	66.2	17.50	17.5	60.80
$H_{Z_{max}}$, km	4.5	4.5	3.5	4.5	4	4

the 20th minute it is higher in the case when the wind direction changes in height. Another picture is observed in the dynamics of the maximum value of the velocity of descending air movements: at the 20th and 30th minutes of cloud development, it is greater in the second case, and at the 40th minute—in the first case. As for the heights at which the maximum value of this parameter is observed, in both cases they are the same and equal to 4 km at the 20th minute of cloud development, and at the 30th and 40th minutes in the first case they are located 0.5 km higher.

It should be noted that an important role in the formation and development of clouds, including the processes of precipitation in them, is played by the amount of water content, in particular, its maximum value. It can be seen from the table that in the case when the wind direction does not change with altitude, the maximum value of water content in the cloud is noticeably greater than when it changes with altitude. This indicates that the concentration and size of droplets are higher in a cloud formed with a constant wind direction in the atmosphere. Also, in this case, this parameter is located at higher levels than in the second case.

As for the maximum value of the ice, at the 20th minute it is insignificant in both variants of the cloud development, although in the second case it is slightly higher than in the first. At the 30th minute it is noticeably larger in the first case, and at the 40th minute, on the contrary, in the second case it became larger than in the first. Taking into account the values of the maximum water content and the levels at which they are in the cloud, it can be noted that in the case when the wind direction does not change with altitude, the conditions for crystal growth and the formation of hailstones are more favorable.

3 Conclusions

The study of the formation and development of convective clouds, taking into account their systemic properties, has begun. The methodology and methods have been developed, numerical experiments have been carried out to study the role of interaction of processes in clouds in the formation of their macro- and microstructural characteristics. The influence of the interaction of convective clouds with the atmosphere due to the structure of the wind field in the atmosphere on the formation of their macro- and microstructural characteristics is investigated. It is found that the structure of the wind field in the atmosphere is a significant factor influencing the formation of thermohydrodynamic parameters of convective clouds. According to the results of calculations, this factor affects the formation of a zone of powerful updrafts in the cloud, the slope of this zone to the horizon. This factor also significantly affects the formation of fields of microstructural parameters of convective clouds. Based on the results of modeling the development of convective clouds with a reversal and without a wind reversal with height, it was found that the structure of the wind field in the atmosphere has a significant impact on the formation of the water content localization area in the cloud. At the same time, the influence becomes weaker with an increase in water content in this zone. The wind influence is less pronounced on

the position and shape of the zone of increased water content values. According to the results of calculations, the nature of the influence of wind in the atmosphere on the formation of the ice localization zone in the cloud is approximately the same as on the formation of the water localization area. And in this case, the influence of the wind decreases with an increase in the value of ice in the area of localization of ice particles.

References

1. Khain, A. P., Prabha, T.V., Benmoshe, N., Pandithurai, G., Ovchinnikov, M. V.: The mechanism of first raindrops formation in deep convective clouds. *Journal of Geophysical Research: Atmospheres*. **118**, 9123-9140 (2013). doi: <https://doi.org/10.1002/jgrd.50641>.
2. Ashabokov, B.A., Fedchenko, L.M., Kupovich, G.V., Shapovalov, A.V., Skorbez, N.N., Shapovalov, V.A.: Model of a convective cloud taking into account the influence of physical processes on its characteristics. *News of higher educational institutions. The North Caucasus region. Series: Natural Sciences*. **172**, 58–62 (2012) [In Russian].
3. Shapovalov, V. A., Kovalev, E. A., Guchaeva, Z. H., Bekkiev, K. M., Kuzmin, V. A.: Formation of macro- and microstructural characteristics of convective clouds depending on the structure of the wind field in the atmosphere. *Bulletin of the Transbaikal State University*. **25**, 21-31 (2019) [In Russian].
4. Cecchini, M. A., de Bruine, M., Vilà-Guerau de Arellano, J., Artaxo, P.: Quantifying vertical wind shear effects in shallow cumulus clouds over Amazonia. *Atmospheric Chemistry and Physics Discussions*. **2022**, 1–33. (2022) doi: <https://doi.org/10.5194/acp-2021-1060>.
5. Koning, A. M., Nuijens, L., Mallaun, C.: Momentum fluxes from airborne wind measurements in three cumulus cases over land. *Atmospheric Chemistry and Physics Discussions*. **2022**, 1-22 (2022). doi: <https://doi.org/10.5194/acp-22-7373-2022>.
6. Dovgalyuk, Yu. A., Veremey, N. E., Zatevakhin, M. A., Ignatiev, A. A., Gopalakrishnan, V., Mikhailovsky, Yu. P., Murugavel, P., Pavar, S. D., Sinkevich, A. A., Toropova, M. L.: Numerical simulation of cloud mergers using a three-dimensional unsteady model of cloud convection. *Proceedings of the Main Geophysical Observatory named after A.I. Voeikov*. **584**, 7–35 (2017) [In Russian].
7. Tolmacheva, N. I.: Investigation of turbulence characteristics in clouds and cloudless atmosphere. *Geographical Bulletin*. **33**, 46-55 (2015) [In Russian].
8. Robe, F. R., Emanuel, K. A.: The effect of vertical wind shear on radiative–convective equilibrium states. *Journal of the Atmospheric Sciences*. **58**, 1427-1445 (2001). doi: [https://doi.org/10.1175/1520-0469\(2001\)058<1427:TEOVWS>2.0.CO;2](https://doi.org/10.1175/1520-0469(2001)058<1427:TEOVWS>2.0.CO;2).
9. Ashabokov, B. A., Fedchenko, L. M., Shapovalov, A.V., Ezaova, A. G.: Results of modeling the influence of wind structure in the atmosphere on cloud formation processes. *Proceedings of the Kabardino-Balkarian Scientific Center of the Russian Academy of Sciences*. **4**, 21-28 (2014) [In Russian].
10. Fan, J., Yuan, T, Comstock, J. M., Ghan, S. J., Khain, A. P., Leung, L. R., Li, Zh., Martins, V., Ovchinnikov, M.V.: Dominant role by vertical wind shear in regulating aerosol effects on deep convective clouds. *J. Geophys. Res.: Atmospheres*. **114**, D22206 (2009). doi: <https://doi.org/10.1029/2009JD012352>.
11. Onishi, R., Takahashi, K., Komori, S.: Influence of gravity on collisions of monodispersed droplets in homogeneous isotropic turbulence. *Phys. Fluids*. **21**, 125108 (2009). doi: <https://doi.org/10.1063/1.3276906>.
12. Weisman, M. L., Klemp, J. B.: The dependence of numerically simulated convective storms on vertical wind shear and buoyancy. *Mon. Weather Rev.* **110**, 504-520 (1982). doi: [https://doi.org/10.1175/1520-0493\(1982\)110<0504:TDonSC>2.0.CO;2](https://doi.org/10.1175/1520-0493(1982)110<0504:TDonSC>2.0.CO;2).

13. Dovgalyuk, Yu. A., Veremey, N. E., Zatevakhin, M. A., Ignatiev, A. A., Sinkevich, A. A., Toropova, M. A.: An example of the results of calculations of the evolution of a sedimentary convective cloud using a full three-dimensional model. Proceedings of the Main Geophysical Observatory named after A.I. Voeikov. **582**, 92–115 (2016) [In Russian].
14. Veremey, N. E., Dovgalyuk, Yu. A., Zatevakhin, M. A., Ignatiev, A. A., Morozov, V. N., Pastushkov, R. S.: Description of the basic numerical nonstationary three-dimensional model of a convective cloud. Proceedings of the Main Geophysical Observatory named after A.I. Voeikov. **282**, 45–91 (2016) [In Russian].
15. Shapovalov, V. A.: Formation and development of powerful convective clouds with various wind characteristics in the atmosphere. News of Saratov University. A new series. Earth Science Series. **18**, 259–264 (2018) [In Russian].
16. Giangrande, S. E., Toto, T., Jensen, M. P., Bartholomew, M. J., Feng, Z., Protat, A., Williams, C. R., Schumacher, C., Machado, L. A.: Convective cloud vertical velocity and mass-flux characteristics from radar wind profiler observations during GoAmazon2014/5. Journal of Geophysical Research: Atmospheres. 121, 12891–12913 (2016). doi: <https://doi.org/10.1002/2016JD025303>.

On the Relationship Between Critical Wind Velocity and Wind Direction and the Size Distribution of Dust Microparticles



E. A. Malinovskaya  and O. G. Chkhetiani 

Abstract Based on the data of field studies of dust aerosol concentration and meteorological parameters, the relationships between wind direction on the aeolian relief and the type of size distribution of transported dust microparticles have been revealed. Based on the field observations, two main cases can be distinguished related to the wind direction with respect to the line of dune ridges: tangential and frontal. At tangential wind direction slightly lower concentrations of fine dust particles are observed in comparison with the frontal wind direction case. This is attributed the electric field increases by increasing the dispersion of particle sizes and enhancing the tunnel effect of charge transfer from larger particles to smaller ones. Relative increase of coarse fraction at tangential wind direction is connected with involvement of larger particles from accumulation zone. The best conditions for generation of microparticles under the influence of electric field are relatively low wind velocities (close to critical). Therefore, during statistical evaluation of the indices in the power law of microparticle size distribution, a sample of data was taken at time moments with wind velocities from 3.5 to 5 m/s. This selection of data makes it possible to clearly highlight existing differences related to the physics of microprocesses in the near-surface soil–air layer for the two wind directions. A significant influence of mutual orientations of aeolian relief inhomogeneities and wind direction on the speed and size composition of dust aerosol emission was revealed. The development of accounting for such effects in the dust-emission blocks of atmospheric models seems relevant.

Keywords Critical wind velocity · Size distribution · Dust microparticles · Saltating particles

E. A. Malinovskaya (✉) · O. G. Chkhetiani
A.M. Obukhov Institute of Atmospheric Physics of RAS, Moscow, Russia
e-mail: elen_am@inbox.ru

O. G. Chkhetiani
e-mail: ochkheti@mx.iki.rssi.ru

1 Introduction

Arid and subarid territories contribute to the appearance of dust aerosol (particles 0.1–5 μm (micrometers) in size) in the atmosphere [1]. Aerosol participates in the processes of moisture condensation and cloud formation, mass transfer of solid and liquid phase substances, and changes in the radiation balance of the Earth [2].

Dust particles are ejected from soil during wind erosion as a result of saltation bombardment of the surface by relatively large particles of about 80–150 μm in size [1]. Their saltation with knocking-out of other particles is observed when a certain critical (threshold) value of wind velocity is reached [3] (about 3.5–5 m/s at a height of 1 m). The splintering (fragmentation) of microparticles occurs at the moment of falling of the saltating particles to the surface [4]. The fine fraction is initially contained in the saltation flow itself [5]. It partially rises into upper layers as a result of convective, diffusive mixing or, possibly, forces of electrostatic nature. Small particles are held on the surface of larger particles by Van der Waals forces of electrostatic nature [6]. The size of the generated microparticles depends on the velocity and mass of the falling saltation particles, which is determined by their potential energy [7] and the features of their distribution on the dune surface.

As a result of wind-sand transport motions near aeolian landforms, zones with different dynamics are distinguished in the surface layer [8]. At the top, the air flow splits [9], and a recirculation zone emerges above the leeward slope [10]. Particles torn off the summit fly over the leeward slope for some distance before falling. Particle accumulation areas appear [11]. There are also larger particles on the leeward slope.

There is a change in electric field strength with increasing wind velocity [12]. This contributes to detachment of particles from the surface and their further ascent [13]. It probably affects microparticles to an even greater. Since the increase in dust concentration correlates with negative field bursts [14]. In [15], relationships of wind regime with changes in concentrations of microparticles with sizes smaller than 0.5 μm were revealed.

Based on the above considerations, we determine that wind velocity and direction, as well as the electric field arising in the wind regime, affect the ratios of dust aerosol concentrations of different sizes in the air. Therefore, the possible influence of various factors on the type of microparticle size distribution is further determined using in-situ data.

2 Data Sources

The data of 2011, 2013, 2016, 2018, and 2020 obtained in summer field campaigns of the A. M. Obukhov Institute of Atmospheric Physics RAS in arid and semi-arid conditions in the Republic of Kalmykia [16] were taken as the basis for the study of the patterns revealed below. A characteristic feature of the relief here is the presence of elongated in the north–northeast direction sand dune ridges with a height of 1–3 m.

The sand area selected for field works, located 5 km to the west of Naryn Khuduk village, is about 1.5 km long and 250–300 m wide.

Aerosol concentrations at two levels of 0.5 m and 2.0 m were measured using a laser aerosol spectrometer LAS-P (9 channels 0.15–1.5 μm) and an aerosol counter OEAS-05 (9 channels 0.2–5.0 μm) designed in the L. Ya. Karpov Institute of Physical Chemistry. The recording frequency was 1 min. In parallel, we carried out accompanying measurements of meteorological parameters: soil temperature, air temperature and wind velocity at 2 and 10 m, pressure, humidity, incident and reflected radiation. The measurement technique and equipment are described in detail in [17].

In 2020, measurements of electric field (recording frequency 1 s.) at the ground surface level were carried out [18]. The flux meter “Field-2” developed at the Voeikov main geophysical observatory was used.

3 To the Relation of the Electric Field with Generation of Microparticles

The electric field changes E as a function of the number of microparticles N_μ from [15]. Here was the assumption that per n_s contact of the moving particle with the surface a charge $n_s q_{\mu k}$ equaled to the threshold value, at which its detachment and free motion above the saltation layer is possible. Accumulated electric field on one microparticle connected with the saltation can be defined as [15]:

$$dE^* = \frac{1}{4\pi \epsilon \epsilon_0} \frac{4n_s^2}{\sigma^2} \frac{\Delta h_s}{h_s} \frac{N_\mu q_{\mu k}}{h^2} \frac{r_\mu^2}{r^2} dN_\mu. \tag{1}$$

Here σ is a fraction of surface particles per unit time, r_μ and r are radii of micro- and saltation particles, ϵ is dielectric permittivity of air, ϵ_0 is electric constant, h is height of particle flow over surface, Δh_s is height of upper sublayer, from which free microparticles are likely to fly out. Exceeding the adhesion forces of microparticles with the surface of the saltating particle under influence of critical value of electric field intensity contributes to the emergence of free microparticles. At the moment of their detachment, the tunnel effect works. As a result, the charges of large particles appear positive [19], micro-particles are negative.

Considering (1) according to the data of measurements for 2020 in [15] the following effects were revealed. At tangential to the dune ridges wind direction there is an increase in the electric field strength. And at weakening of wind speed to critical (Fig. 1) there is a relative decrease of electric field value. The wind direction with an angle of $90 \pm 30^\circ$ with respect to the line of the dune ridges corresponds to the frontal wind direction, and an angle of $0 \pm 30^\circ$ —to the tangential wind direction.

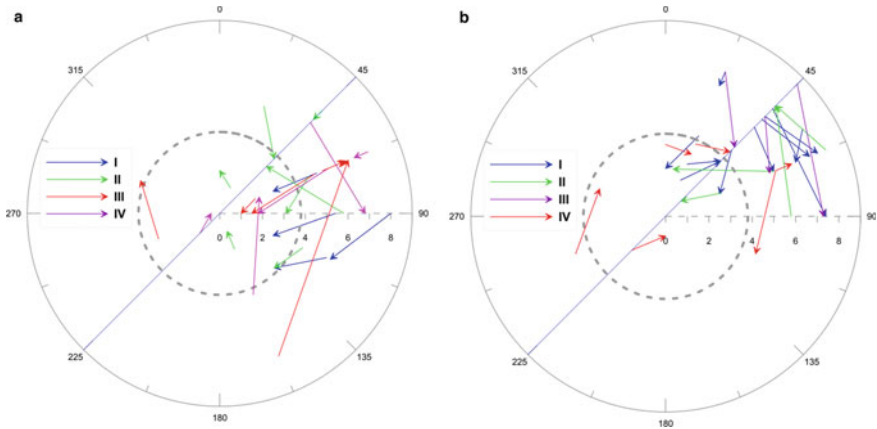


Fig. 1 Relation of changes in wind velocity and direction to changes in the electric field. The inner circle is the threshold wind velocity, the slanted line is the junction line of the windward and leeward slopes. The arrows show changes in wind velocity and direction during an hour until the electric field strength and the number of microparticles change. **a** Vectors of different colors highlight the modes of relative reduction of the electric field with increasing number of particles (I—fast and II—slow) and with decreasing number of particles (III—fast and IV—slow). **b** Vectors of different colors highlight the modes of relative diminishing of the electric field with increasing number of particles (I—slow and II—fast) and with decreasing number of particles (III—slow and IV—fast)

Accordingly, the critical wind velocity and wind direction are important factors influencing changes in the number of microparticles in the surface layer. Below, we consider each of them separately.

4 The Special Role of Threshold Wind Velocity

Figure 2 shows the relation of electric field strength and friction velocity of wind according to observations for 2020 (averaging time 1 min). Appearance of negative and near-zero values when wind velocity increases (up to values exceeding 7–8 m/s— at 2 m height) is associated with appearance of negatively charged aerosol particles in the near-surface layer. It is typical for dust aerosol export not only from desertified territories, but also for unfixed or eroded surfaces [15]. Negative values of electric field strength are more typical for friction velocity values exceeding the critical one. This is due to low bouncing of particles over the surface for small wind velocities. There is a more intensively tunnel transfer of charge from larger particles to smaller ones during impact [20]. In such case, a smaller number of particles are involved in the saltating process. They lose charge as charged microparticles break away [21]. Rapid charging of moving particles takes place with more intensive generation of free aerosol [15]. Its fine fraction is likely to appear. As a result, all moving particles have positive charge. More layers of particles are involved at high velocities. The

hops are higher. The charging process takes longer. The saltation layer becomes more blurred. In this case, microparticles becomes unlikely to detach with loss of charge and emergence of positively charged particles when reaching the critical value of electric intensity. As a result, the particles raised above the surface retain a negative charge. This fact is confirmed by the fact that microparticle concentrations are greater for friction velocities between 0.26 and 0.32 m/s (Fig. 3) than for values above 0.32 m/s.

Fig. 2 Dependence of electric field strength on friction velocity (the threshold friction velocity corresponds to 0.25 m/s) for all observation days in 2020

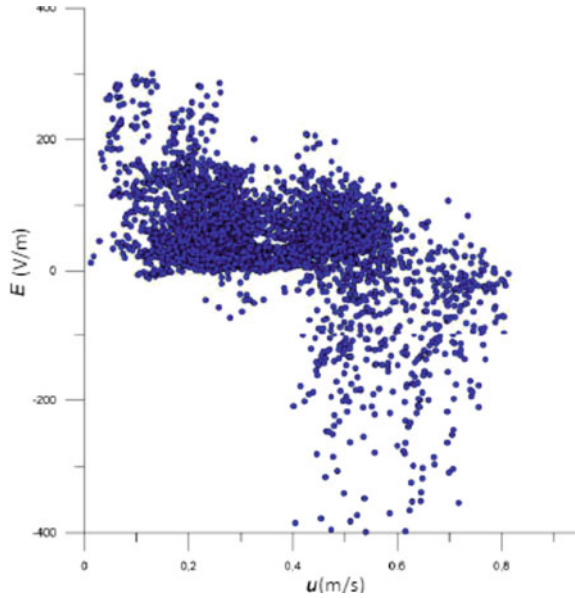
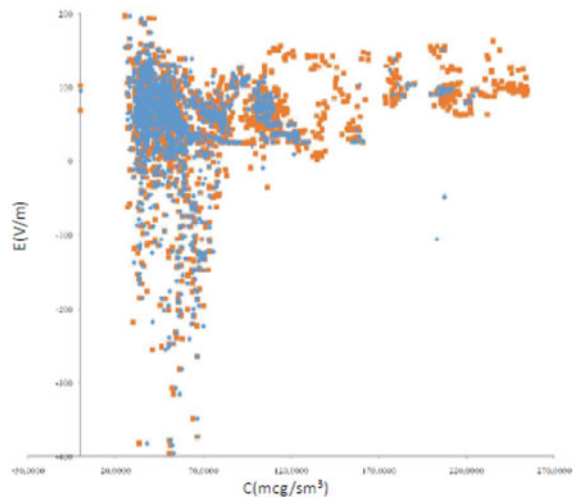


Fig. 3 Dependence of electric field strength on the mass concentration of particles with sizes up to $0.5 \mu\text{m}$ at dynamic velocities >0.32 m/s (gray overlay) and at >0.26 m/s (base)



5 Frontal and Tangential Wind Direction

The tangential wind direction is characterized by an increase in the electric field strength with a decrease in the number of microparticles (Fig. 1b). This leads to the fact that the frontal wind direction generates fine aerosol fraction to a greater extent than the tangential wind direction [22]. For the distributions of the number of microparticles by size, two types (Fig. 4) corresponding to the frontal (a) and tangential (b) directions with respect to the dune ridge lines were identified. The figure shows selectively the distributions for several days according to the data of 2011, 2013, 2016, and 2020. Probably, the tangential direction generates a larger fraction. This is indicated by the rising of the “tail” of the distribution at scales $>0.5 \mu\text{m}$. This is due to the fact that the tangential direction captures larger saltating particles from the accumulation zone. There is a gradual erasure and electrostatic detachment from the particles involved without updating their composition in the frontal direction. As result in the generation of a finer fraction.

As can be seen from Fig. 4, the particle size distribution can be approximated by a piecewise-given power function of the form, $C = A \cdot d^{-n}$ where d is the microparticle size. In [17] it was noted that the existence of such universal power distributions for submicron particles can be explained in the framework of a hierarchical model of fragmentation described by the Kolmogorov equation for mass service systems.

Below we present empirical degree values, approximated by the least-squares method for the 2018 and 2020 data samples for the tangent and frontal wind direction cases for particles larger and smaller than $0.5 \mu\text{m}$. Figure 5 shows the number of degree index values that fall within the 0.4-step intervals. The data were chosen at wind velocity close to the critical value (from 3.5 to 5 m/s at a height of 2 m).

For tangential and frontal directions of fine fraction of microparticles characteristic most frequent values of degree indices coincide with those obtained in [17]

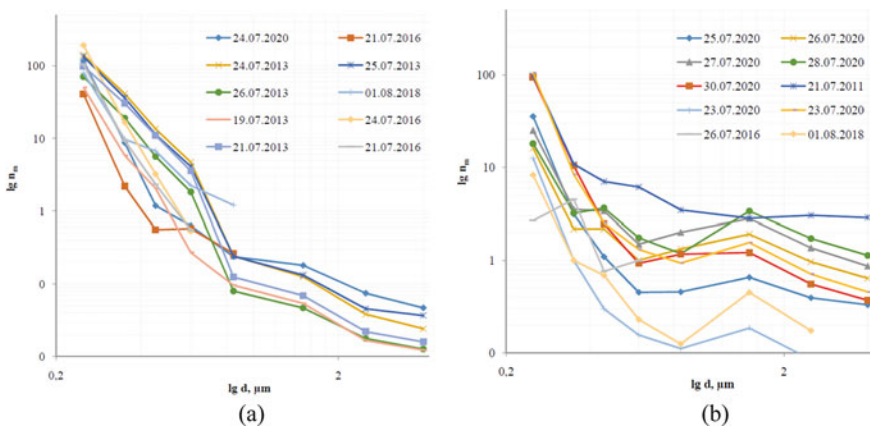


Fig. 4 Size distribution of the number of microparticles n_m in the frontal **a** and tangential **b** flow directions

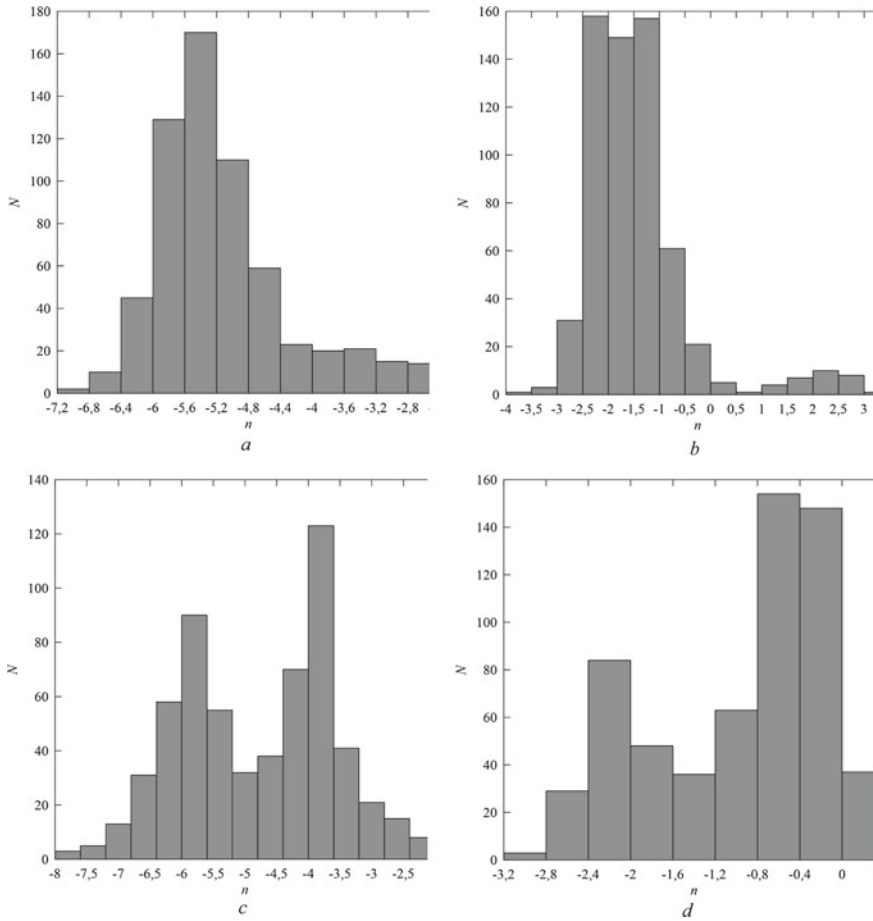


Fig. 5 Number of values, N falling in the intervals for the size distribution of microparticles $C = A \cdot d^n$: a and b for tangential and c and d for windward directions for microparticles less than $0.5 \mu\text{m}$ and greater than $0.5 \mu\text{m}$, respectively (2018 and 2020)

(Fig. 5). It is approximately $-5(-6)$ for small sizes and -2 for larger particles. For the tangential direction, more uniform distributions are observed with the main maximum. It closes to the specified theoretical values, which is probably due to generation of microparticles with increasing electric field. Large fraction of particles is characterized by greater degrees for tangential wind direction than for frontal. It is associated with capture of large particles from the accumulation zone. In some cases here, it is more likely better to use often used log-normal distribution.

6 Conclusions

Based on the data of field studies of dust aerosol concentration and meteorological parameters, the relationships between wind direction on the aeolian relief and the type of size distribution of transported dust microparticles have been revealed. Based on the field observations, two main cases can be distinguished related to the wind direction with respect to the line of dune ridges: tangential and frontal. At tangential wind direction slightly lower concentrations of fine dust particles are observed in comparison with the frontal wind direction case. This is attributed the electric field increases by increasing the dispersion of particle sizes and enhancing the tunnel effect of charge transfer from larger particles to smaller ones. Relative increase of coarse fraction at tangential wind direction is connected with involvement of larger particles from accumulation zone. The best conditions for generation of microparticles under the influence of electric field are relatively low wind velocities (close to critical). Therefore, during statistical evaluation of the indices in the power law of microparticle size distribution, a sample of data was taken at time moments with wind velocities from 3.5 to 5 m/s. This selection of data makes it possible to clearly highlight existing differences related to the physics of microprocesses in the near-surface soil–air layer for the two wind directions.

A significant influence of mutual orientations of aeolian relief inhomogeneities and wind direction on the speed and size composition of dust aerosol emission was revealed. The development of accounting for such effects in the dust-emission blocks of atmospheric models seems relevant.

The authors would like to thank V. A. Lebedev, A. A. Khapaev, L. O. Maksimenkov, B. A. Khartsaev, Y. A. Egorov and I. V. Korolev for their help in organizing and conducting field measurements. Special thanks to G. S. Golitsyn, G. I. Gorchakov, A. V. Karpov, G. G. Petrova, and I. N. Panchishkina for their interest and advice.

Acknowledgements The research was supported by the Russian Foundation for Basic Research (project Micromir 19-05-50110: field measurements, post-processing) and by the Russian Science Foundation (project 20-17-00214: analysis of measurement data, theoretical estimates).

References

1. Shao, Y.: Physics and modeling of wind erosion. Springer, (2009).
2. Maher, B.A. et al.: Global connections between aeolian dust, climate and ocean biogeochemistry at the present day and at the last glacial maximum. *Earth-Science Reviews*. **99**(1–2), 61–97 (2010).
3. Buthner, E.K.: Dynamics of the near-surface air layer. Gidrometizdat, Leningrad (1978). [in Russian].
4. Tatarko, J. et al.: PM_{2.5} and PM₁₀ emissions by abrasion of agricultural soils. *Soil and Tillage Research*, **200**, 104–601 (2020).

5. Liu, X.Y., Ning, W.X., Wang, Z.T.: Theoretical expressions for soil particle detachment rate due to saltation bombardment in wind erosion. *Sciences in Cold and Arid Regions* **12**(4), 234–241 (2020).
6. Kozlov, A.S. et al.: Study of mechanical processes of submicron aerosol formation. *Optics of the Atmosphere and Ocean*. **13**(6–7), 664–666. (2000) [in Russian].
7. Alfaro, S.C. et al.: Modeling the size distribution of a soil aerosol produced by sandblasting. *Journal of Geophysical Research: Atmospheres* **102**(10), 11239–11249. (1997) [in Russian].
8. Michelsen, B. et al.: Two-dimensional airflow modeling underpredicts the wind velocity over dunes. *Scientific Reports*. **5**, 16572 (2015).
9. Parsons, D.R., Walker, I.J., Wiggs, G. F. S.: Park numerical modelling of flow structures over idealized transverse aeolian dunes of varying geometry. *Geomorphology* **59**(1–4), 149–164 (2004).
10. Faria, R. et al.: Wind tunnel and computational ss slope effect on the aeolian erosion of transverse sand dunes. *Aeolian Research* **3**, 303–314 (2011).
11. Anderson, R.S.: The pattern of grain fall deposition in the lee of aeolian dunes. *Sedimentology*, **35**(2) 175–188 (1988).
12. Zheng, X.J., Huang, N., and Zhou, Y.H.: Laboratory measurement of electrification of wind-blown sands and simulation of its effect on sand saltation movement. *J. Geophys. Res.*, **108**(10), 4322 (2003).
13. Gorchakov, G.I. et al.: Electric currents of saltation in winds and flux. *Doklady Earth Sciences*. **410**(7), 1109–1111 (2006) [in Russian].
14. Esposito, F., et al.: The role of the atmospheric electric field in the dust-lifting process. *Geophysical Research Letters*. **43**(10), 5501–5508 (2016).
15. Malinovskaya, E.A. et al.: The relationship between a surface electric field and an arid aerosol under different wind conditions. *Earth Science Reports*. **502**(1), 59–67 (2022) [in Russian].
16. Chkhetiani, O.G. et al.: Analysis of mineral aerosol in the surface layer over the Caspian lowland desert by the data of 12 summer field campaigns in 2002–2020. *Atmosphere* **12**(8), 985 (2021).
17. Chkhetiani, O.G., Gledzer, E.B., Vazaeva, N.V.: Measurements and approximations for submicron-aerosol size distribution functions. *Earth and Space Science*. **8**(6), e2020EA001616 (2020).
18. Petrova, G.G., Petrov, A.I., Panchishkina, I.N.: Formation of the electric structure in the lower layer of the atmosphere: Experimental studies and generalization of the data. *Radiophysics and Quantum Electronics*. **56**(11), 723–738 (2014).
19. Schmidt, D.S., Schmidt, R.A., Dent, J.D.: Electrostatic force on saltating sand. *Journal of Geophysical Research: Atmospheres*. **103**, 8997–9001 (1998).
20. Kok, J.F., Renno, N.O.: Electrostatics in wind-blown sand. *Physical Review Letters* **100**, 014501 (2008).
21. Greeley, R., Iversen, D.J.: *Wind as geological process of Earth, Mars, Venus and Titan*. Cambridge University Press. Cambridge (1987).
22. Malinovskaya, E.A., Chkhetiani, O.G., Maksimenkov, L.O.: Influence of wind direction on the size distribution of aeolian microparticles. *Izvestiya, Atmospheric and Oceanic Physics*. **57**(5), 472–485 (2021).

Relationship Between Microphysical Characteristics and Turbulence in Winter Clouds



V. V. Petrov, N. V. Bazanin, D. V. Kirin, V. V. Volkov, and A. M. Strunin

Abstract The results of full-scale aircraft studies of the relationship between microphysical characteristics and turbulence in supercooled clouds are presented. In zones with the simultaneous presence of supercooled liquid droplets and ice crystals, anisotropy of turbulent pulsations of air flow velocities is observed—the energy of vertical pulsations was greater than the energy of horizontal pulsations, sometimes by more than 2 times. The velocities of the updrafts exceeded 4.5 m/s, which create conditions for the growth of the liquid phase in the presence of ice crystals. In clouds with a mixed phase composition, in areas with increased turbulence intensity, there is a high probability of an aircraft falling into icing due to the presence in these zones of conditions for the generation and growth of the liquid phase in the presence of ice crystals, even for fairly low temperatures.

Keywords Supercooled clouds · Aircraft studies · Turbulence · Liquid droplets · Ice crystals

1 Introduction

By the present time, a large amount of evidence for the long-term existence of zones with supercooled cloud droplets in clouds has been accumulated [1–5]. It is in such zones that dangerous phenomena associated with aircraft icing are observed. However, the information accumulated over the past years about the characteristics of clouds is sometimes insufficient to explain the processes of icing.

Modern means of measuring microphysical characteristics of clouds make it possible to determine the phase composition of cloud particles and the shape of crystals, to measure the integral characteristics of cloud microstructure and thermodynamic parameters of the cloud environment.

V. V. Petrov (✉) · N. V. Bazanin · D. V. Kirin · V. V. Volkov · A. M. Strunin
Central Aerological Observatory, Dolgoprudny, Russia
e-mail: vpetrov555@mail.ru

Created in the Russian Federation, the aircraft-laboratory Yak-42D “Roshydromet” is equipped with modern measuring instruments that allow performing a wide range of studies of the microstructure of clouds in icing conditions [6].

The results of studies of the relationship of microphysical and thermodynamic characteristics of clouds conducted during the cold periods of the year from November to May 2018–2021 are presented.

The major part of flights were performed in Moscow region, at distances up to 200 km from Moscow. Three flights were carried out in the Arctic region near the Kola Peninsula and over the Barents Sea.

2 Research Methodology and Results

The measurements were carried out along the sections of horizontal steady-state flights, without significant changes in the roll angles, pitch and airspeed over the so-called “regimes” from 10 to 50 km in length.

During the flights, measurements in 36 “regimes” were performed in clouds with icing. The total length of the “regimes” in clouds, in areas with icing and mixed-phase precipitation exceeded 3,200 km.

The synoptic conditions under which the studied cloud systems developed were characterized by the influence of atmospheric fronts and the passage of baric hollows.

On 03/22/2021, in Moscow air zone, stratocumulus clouds with penetrating convection were observed, which produced precipitation in the form of snow. The aircraft-laboratory traveled at distances up to 150 km east-southeast of Moscow.

Figure 1 shows the results of measuring vertical flow velocities and temperature pulsations in a cloud layer at $-15\text{ }^{\circ}\text{C}$, at an altitude of 2,050 m, during the flight section between 14:56 and 15:06 on March 22, 2021. The updraft velocities in the zone reached 4 m/s, and the values of temperature pulsations exceeded $1\text{ }^{\circ}\text{C}$.

Figure 2 shows images of cloud particles registered in this zone. The cloud had a mixed-phase structure: con currently, ice crystals in the form of dendrites and plates, as well as a great number of large cloud droplets were present. Water content in this zone reached 0.3 g/m^3 .

Despite the low temperature ($-15\text{ }^{\circ}\text{C}$) and the presence of ice crystals, a great number of large drops were observed in the zone. These factors caused intense icing of the aircraft while in this zone.

Similar situations were more than once observed in other flights with aircraft icing in clouds.

Based on the measurements of pulsations of the thermodynamic characteristics of the atmosphere, statistical characteristics of turbulence in clouds were calculated [7–9]:

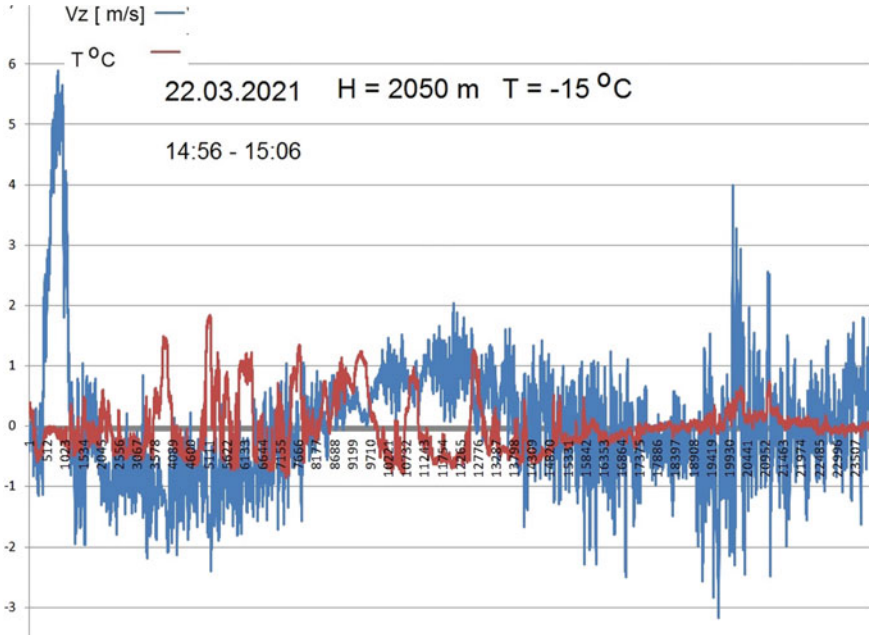


Fig. 1 Vertical flow velocities and temperature pulsations in the zone with icing on 03/22/2021

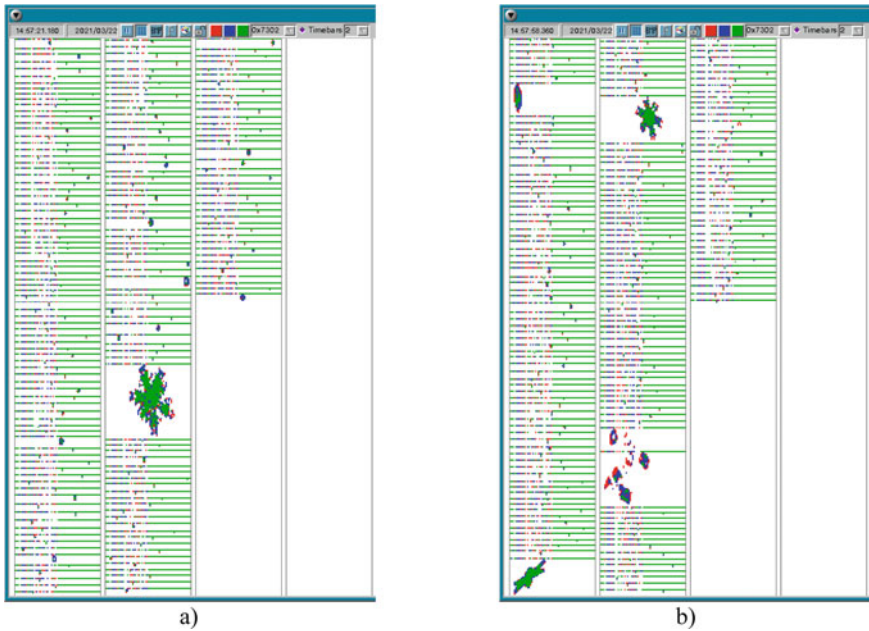


Fig. 2 Cloud particles in the icing zone on 03/22/2021 at 14:57 a) and 14:58 b)

The energy of turbulent pulsations along three axes (X, Y, and Z):	$\sigma_x^2 = \frac{1}{N} \sum_{i=1}^N (V_{xi} - \widetilde{V}_x)^2$	[m ² /s ²]
	$\sigma_y^2 = \frac{1}{N} \sum_{i=1}^N (V_{yi} - \widetilde{V}_y)^2$	[m ² /s ²]
	$\sigma_z^2 = \frac{1}{N} \sum_{i=1}^N (V_{zi} - \widetilde{V}_z)^2$	[m ² /s ²]
Energy of horizontal pulsations	$E_{xy} = \frac{\sigma_x^2 + \sigma_y^2}{2}$	[m ² /s ²]
Energy of vertical pulsations	$E_z = \frac{\sigma_z^2}{2}$	[m ² /s ²]
Turbulence anisotropy	$A = \frac{2E_z}{E_{xy}}$	

Here, V_{xi} , V_{yi} , and V_{zi} are the values of the eastern component of the horizontal wind speed, of the northern and vertical components of the wind speed, respectively. The symbols with a tilde designate the average values of the corresponding wind speed components in the measurement zones.

Anisotropy of turbulent movements in clouds is observed in a large number of zones. The energy of vertical turbulent movements, in many cases, significantly exceeds the energy of horizontal movements.

In Table 1 are presented the microphysical characteristics of the zones, as well as the values of turbulent flow anisotropy (column A).

Interestingly, in all cases of the concurrent presence of supercooled droplets and ice crystals the energy of vertical turbulent movements would be higher than, and even several times as high as that of horizontal movements. Such a coexistence of particles of different phase composition can only occur, if ambient conditions lead to supersaturation over water at negative temperatures in the presence of ice particles. Some papers [10, 11] demonstrate that even at low updraft speeds of 1–2 m/s, ambient conditions can favor supersaturation over water even at fairly high concentrations of crystals and low temperatures.

3 Conclusions

Turbulence is characterized by frequent alternation of updrafts and downdrafts in which air with cloud particles rise or fall. Paper [10] shows that periodic oscillations of vertical flow velocities can lead to periodic activation or evaporation of liquid droplets in mixed-phase clouds. The most interesting feature about this process is that these periodic activations and vaporizations of cloud droplets are not time-limited and can exist for an indefinitely long period. The discovered property of mixed supercooled clouds suggests that in the presence of turbulence in mixed clouds,

Table 1 The relationship between microphysical characteristics of clouds and turbulence

Date	Time of regime	Altitude (m)	Temp (°C)	Cloud type	Microstructure	A
20.02.2018	15:00–15:20	600	-10	Sc	Snow large plates and dendrites	2.445
18.12.2018	14:00–14:35	750	-11	Sc	Plates and dendrites	0.307
05.09.2019	14:08–14:13	4100	-4.5	Ns	Mixed structure: drops-snow-drops	4.229
17.12.2019	13:35–13:42	6800	-38	Ns + As	Compact crystals	0.911
17.12.2019	14:02–14:10	5800	-30	Ns + As	Plates	0.937
17.12.2019	14:20–14:30	4800	-23	Ns + As	Large plates	0.736
17.12.2019	14:51–15:00	3600	-17	Ns + As	Snow, dendrites	0.596
24.12.2020	14:30–14:34	2700	-11	Sc	Large drops!	1.257
24.12.2020	14:35–14:40	1750	-7	Sc	Mixed structure: complicated crystals, droplets	1.752
21.01.2021	14:08–14:12	2000	-10.7	Ns + As	Plates, flat shapes, droplets	7.190
21.01.2021	14:13–14:21	1450	-9.2	Ns + As	Plates, flat shapes, snow	0.545
21.01.2021	14:23–14:33	850	-6.6	Ns + As	Plates, large flat shapes, snow	0.510
04.02.2021	13:48–13:58	4550	-23	As	Mixed phase structure: small droplets, small—crystals	1.300
04.02.2021	15:10–15:30	1950	-8.5	Ns	Large crystals of snow	1.122
04.02.2021	15:50–15:57	775	-6.3	Ns	Snow Dendrites	4.551
25.02.2021	14:20–14:26	1250	-4.5	St	Small grits	0.574
25.02.2021	15:00–15:10	1200	-4.5	St	Snow	0.472
25.02.2021	15:13–15:20	1220	-4.8	St	Different types of crystals	0.544
25.02.2021	15:20–115:27	900–600	-1.8	Sc	compact crystals large drops	4.427
25.02.2021	15:27–15:32	500–280	-0.5	Sc	Drizzle	1.406
04.03.2021	13:43–13:53	1950	-11	As	Pelates sometimes large drops up to 100 μ	0.800

(continued)

Table 1 (continued)

Date	Time of regime	Altitude (m)	Temp (°C)	Cloud type	Microstructure	A
04.03.2021	14:10–14:18	1700	–10	Sc + Cu + Cb	Snow dendrites	1.859
04.03.2021	14:40–14:50	1500	–9	Sc + Cu + Cb	Large plates of snow	1.181
04.03.2021	15:14–15:18	1600	–9	Sc + Cu + Cb	Heavy snow	2.669
18.03.2021	14:03–14:11	1200	–8	As	Compact crystals	0.786
18.03.2021	14:21–14:25	1100	–8.5	As	Large plates and small droplets	9.142
18.03.2021	14:38–14:41	1300	–8.9	As	Snow, large plates (400–500 μ)	1.709
22.03.2021	13:41–13:51	1650	–14.5	Cu + Sc	Snow dendrites up to 600 μ	0.481
22.03.2021	14:11–14:23	1500	–12	Cu	Large dendrites >5000 μ	0.941
22.03.2021	14:56–15:06	2025	–15	Fc	Small drops and large dendrites	1.187
06.05.2021	13:32–13:42	3000	–7	Sc + Cu + Cb	Drops up to 100 μ, then compact crystals	3.283
22.05.2021	11:41–11:51	from 200 to 4500	0 ÷ –15°C	Ac + Cb	First, rain drops large up to 500 μ, then snow Large plates, dendrites up to 700 μ, then compact shapes	2.637
22.05.2021	14:32–14:42	1600	–2	Sc	Large dendrites	4.447
22.05.2021	15:05–15:11	3600	–6	Ac	Plates	6.609
22.05.2021	16:22–16:27	2900	–5	Ns	Plates	6.028
23.05.2021	18:27–18:38	4500–2500	–9	Ac + Cb	Large crystals and small drops	0.795

conditions are formed that favor long-term existence of the liquid phase, even at very low temperatures, which creates conditions for aircraft icing when entering such zones.

References

1. Mazin, I.P.: Physical foundations of aircraft icing. Hydrometeoizdat, Moscow (1957) [in Russian].
2. Pruppacher, H.R., Clett, J.D.: Microphysics of clouds and precipitation. D. Riedel Publishing Company. 714 (1978).
3. Mazin, I.P. Hrgian, A.H., Imyanitov, I.M.: Clouds and cloud atmosphere. Handbook. Hydrometeoizdat, Leningrad (1989). [in Russian].
4. Ice Formation and Evolution in Clouds and Precipitation: Measurement and Modeling Challenges, Meteorological Monographs, **58**: <https://doi.org/10.1175/AMSMONOGRAPHS-D-16-0007.1>. <https://journals.ametsoc.org/mono/issue/volume/58> (2017).
5. Korolev, F.V., Heckman, I., Wolde, M., Ackerman A.S., Fridlind Ann M., Ladino L.A., Lawson Paul, Milbrandt J., and Williams E.: A new look at the environmental conditions favorable to secondary ice production. *Atmos. Chem. Phys.*, **20**, 1391–1429 (2020).
6. Azarov, A.S., Borisov, Yu.A., Vakulovsky, S.M., Danelyan, B.G., Petrov, V.V., Sinkevich, A.A., Strunin, M.A., Fomin, B.A., Khattatov, V.U.: “Aircraft-laboratory of a new generation for research of the atmosphere and the underlying surface”. Collection of scientific papers of International scientific conference with elements of the scientific school “Innovative methods and means of research in the field of atmospheric physics, hydrometeorology, ecology and climate change”, NCFU-VGI-RGGMU, Stavropol, September 23–26, 102–105 (2013) [in Russian].
7. Mazin, I.P., Silaeva, V.I., Strunin, M.A.: Turbulent pulsations of horizontal and vertical components of wind speed in clouds of various forms. *Izv. AN USSR. Ser. Physics of the Atmosphere and Ocean*, **20**, 1, **10–18**. (1984) [in Russian].
8. Volkov, V.V., Strunin, M.A. & Strunin, A.M. Determination of Wind Shear and Turbulence Intensity According to Yak42-D “Roshydromet” Research Aircraft Data. *Russ. Meteorol. Hydrol.* **46**, 640–649 (2021).
9. Strunin, M.A.: Investigation of methods of the thermodynamic condition of atmosphere using aircraft-laboratory. Moscow. Printing Salon “Chance”, (2020) [in Russian].
10. Korolev, A.V., Isaac, G.A.: Phase transformation in mixed phase clouds. *Q. J. Roy Meteorol. Society*, **129**, 19–38 (2003).
11. Korolev, A.V., Mazin, I.P.: Supersaturation of water vapor in clouds. *Journal of Atmospheric Sciences*. **60**, 2957–2974 (2003).

Case Study of Mesoscale Convective System on August 7, 2021 Over the Center of the European Territory of Russia by Remote Sensing Data



A. A. Sprygin  and A. E. Vyazilov

Abstract The article provides an analysis of the case of a mesoscale convective system using remote sensing data of the atmosphere: radar, satellite, lightning detection network and atmospheric electric field. The principle of complex diagnosis of the stages of development of the convective system with the identification of certain diagnostic signatures is applied. The features of the distribution of diagnostic parameters important for nowcasting of dangerous phenomena associated with the formation of stable severe convective structures are revealed.

Keywords Mesoscale convective system · Severe convective storm · Satellite signatures cold-U · Cold-ring · Lightning jump signature · Dangerous convective phenomena · Nowcasting · Atmospheric electric field

1 Introduction

The processes of severe organized convection in the atmosphere that occur under certain thermodynamic and synoptic conditions most often lead to the formation of dangerous convective phenomena and therefore require careful study. Of course, it is important to provide a comprehensive analysis of the manifestation of such processes in diagnostic data of various types: satellite, radar, lightning detection, etc. A number of works are devoted to this topic [1–7]. It is necessary to note the object-oriented approach in such works: the objects of research are not dangerous convective phenomena as such, but cloud systems generating them: mesoscale convective complexes and systems of various types, individual clouds of a certain type (such as supercell cumulonimbus clouds) and other convective storms of various scales. At the same time, the conditions of their formation and decay are analyzed, their

A. A. Sprygin (✉) · A. E. Vyazilov
Research and Production Association “Typhoon”, Obninsk, Russian Federation
e-mail: spralexandr@gmail.com

A. E. Vyazilov
e-mail: vyazilov@typhoon.obninsk.ru

manifestation in diagnostic characteristics at various stages of the life cycle [4, 6, 8, 9], which is important for a better understanding of their genesis and dynamics, as well as the possibility of generating (at certain stages of development) dangerous phenomena. In such studies, it is often possible to select the most important signs of the danger of convective processes, which can be useful in forecasting practice: in short-term forecasting and in the nowcasting of dangerous convective processes and phenomena. This aspect is the most important goal of this work.

As a task of this study, the case study of the formation of severe convective storm formed as part of a quasi-linear mesoscale convective system on August 7, 2021 over the central regions of the European territory of Russia (ETR) was carried out.

Mesoscale analysis was performed using:

1. Data from the DMRL-C Doppler radar network, hosted on the resource [<http://meteorad.ru/maps>] (the system for displaying radar information—METEORAD with authorized access). Maps of weather phenomena and the cloud top height were used. Data source—FSBI “CAO”.
2. Meteosat-10 geostationary satellite data. Images were used (5 min time resolution, IR10.8 infrared channel, with brightness temperature values at the clouds tops), freely available on the resource [<https://meteologix.com/ru/satellite>].
3. Lightning detection data system deployed on the ETR. Data source—FSBI SRC “Planeta”.
4. Atmospheric electric field data in the observation point at the station “Vashutino” (5 km northwest of Obninsk). The data source is FSBI RPA “Typhoon”.
5. The reconstructed temperature, humidity and wind vertical profile near the localization of the storm by the reanalysis data of GFS model (using the RAOB visualization tool).

2 Results and Discussion

The synoptic situation of 07.08.2021 in the area of the mesoscale convective system formation was determined by the presence of an extensive warm sector of the cyclone with southerly flows (advection of unstable stratified moist air masses from the Azov-Black Sea region) and a zone of moderate instability with wind shear. The proximity of a contrasting and sedentary cold front in the west of the ETR created favorable conditions for the development (to the east of the front, in the warm sector of the cyclone) of instability (prefrontal squall) lines oriented parallel to the front, on which convective storms were actively developing.

Cells of active convection began to form, starting from the Kursk region after 08:00 UTC. Initially, these were mostly isolated foci, sometimes united in small clusters, moving with the direction of the leading flow from south to north. After 09:00 UTC, one of the clusters acquired the features of a linearly oriented cluster of thunderstorm cells dominating in development (among neighboring ones).

By about 11:30–11:45 UTC, according to satellite data (Meteosat-10, IR channel 10.8), an area of pronounced convective storm of quasi-elliptical shape with low

brightness temperature formed over the north of the Kaluga region (Fig. 1), within which the so-called cold-U/cold-ring signature [10, 11] was clearly detected—the presence of a U-shaped/ring-shaped region with a relatively colder brightness temperature on the periphery of the storm, encircling an area with a relatively higher temperature in the inner region (the so-called Central Warm Spot (CWS)). These signatures have been studied for various cases of severe convective storms (for example, in [5, 6]), they indicate the probable presence of powerful upward movements within the storm and has a fairly strong correlation with cases of dangerous convective phenomena [6, 10]. Note that the cold-ring/cold-U signature was traced in the storm until 14:25 UTC, while its general (quasi-elliptical) shape changed little from satellite images during the period of the signature’s existence, which is an indirect sign of a possible supercell type of convective storm.

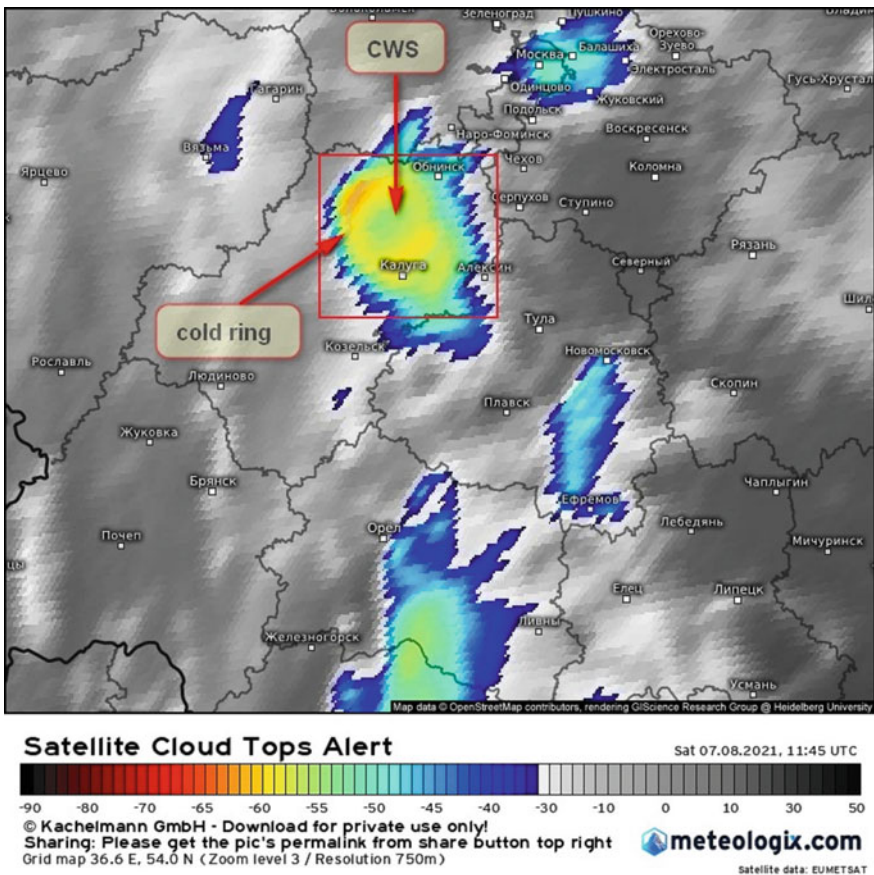


Fig. 1 Severe convective storm (highlighted by a red square) with cold-ring and CWS signatures on Meteosat-10 satellite data, 07.08.2021, 11:45 UTC

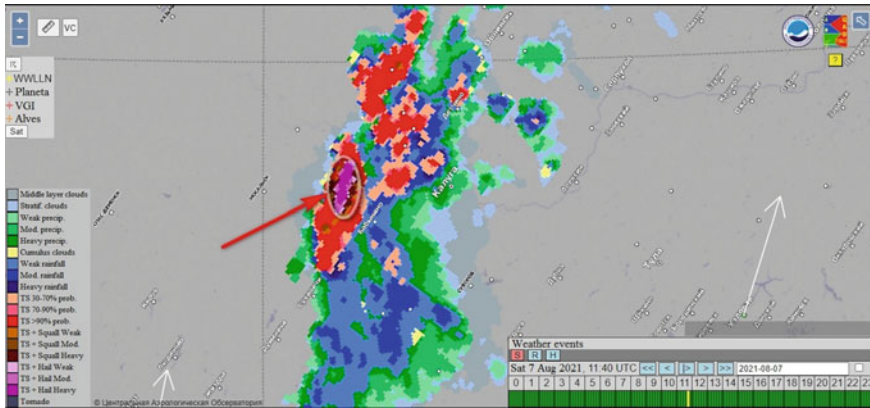


Fig. 2 Severe convective storm as a part of quasilinear mesoscale convective system on radar data. The zone of the most active convection (the “strong squall” cell by gradation of weather phenomena) is shown by the red arrow. DMRL-C radar network data, 07.08.2021, 11:40 UTC

According to the DMRL-C radar network data at this time, within the area of the convective storm detected by satellite data (see Fig. 1), the development of the cell of a “strong squall” was traced (according to the algorithm for recognizing meteorological phenomena, see Fig. 2) within a quasi-linear mesoscale convective system (QLCS). The cloud top height in the hearth exceeded 15 km.

The unstable stratified layer from lifting condensation level to the tropopause level (1.5–12 km), as well as wind shear in speed and direction was existing by the analysis of the temperature, humidity and wind vertical profile by the GFS reanalysis data for a point with coordinates near the center of a severe storm by noted on the DMRL-C data at 12:00 UTC (Fig. 3).

At 13:30 UTC on the territory of the Mozhaisk district of the Moscow region, during the passage of the analyzed severe convective storm, a strong wind, possibly of a squally nature, was recorded by eyewitnesses (and registered in the European database of dangerous phenomena ESWD [<https://eswd.eu>]). So in the Borodino settlement, several huge trees were uprooted, power lines were damaged, part of the roof was torn off. There were also reports in the media about strong gusts of wind along with a strong rainfall in the Mozhaisk itself.

For the analysis of the lightning activity, the convective storm region was allocated, the boundaries of which were determined from satellite data on the zone of a significant gradient of brightness temperature in the IR channel $10.8 \mu\text{m}$ (as shown in Fig. 1, where the storm area is highlighted with a red rectangle). For such spatial areas, data on the position and polarity of lightning discharges (as well as their number—separately for positive and negative discharges) were selected from the lightning detection database of the SRC “Planeta” for all 5 min intervals preceding the timeframe of the corresponding satellite image on which the storm was highlighted.

The data were also compared with the minimum values of the brightness temperature in the IR channel $10.8 \mu\text{m}$ of the Meteosat-10 satellite data, the maximum height

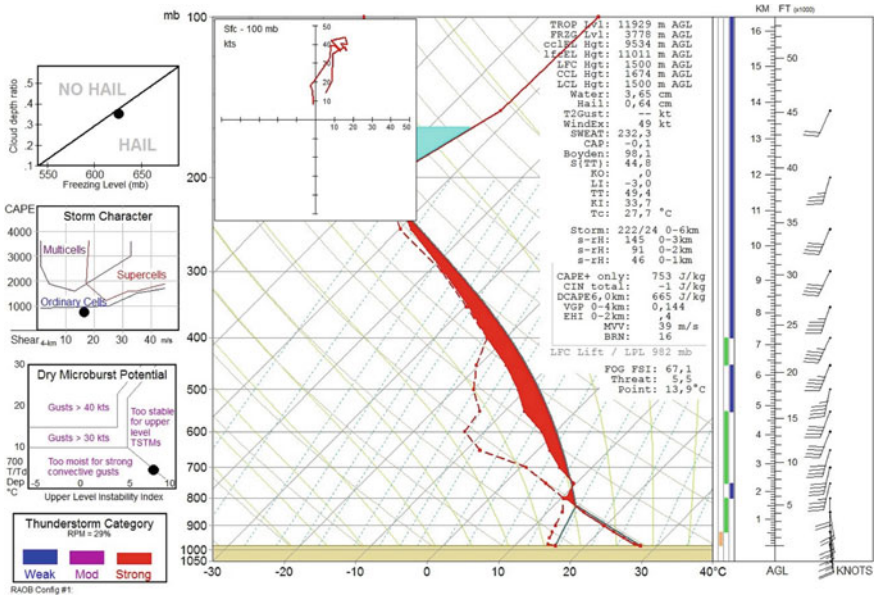


Fig. 3 Skew-T diagram (by reanalysis GFS data for point with coordinates: 54.85 N., 35.65 E), 07.08.2021, 12:00 UTC

of the cloud top height and the type of meteorological phenomena—according to the DMRL-C radar network data. At the same time, the most significant gradation was selected for “meteorological phenomena” (radar output data product) according to their rank in the scale, with some simplification, for example: the gradation “thunderstorm + squall” (of any intensity) was assigned the gradation “SQUALL”, similarly “thunderstorm + hail”—“HAIL”, etc. All types of listed diagnostic data obtained for the track of a convective storm from its initiation to decay (i.e. at all stages of the life cycle) are presented graphically together in Fig. 4.

The following conclusions can be drawn by the complex analysis of the data presented in Fig. 4:

1. The growth of the thunderstorm activity (according to the number of lightning flashes) from initiation to mature stage correlates well with an increase in the cloud top height and a drop in brightness temperature.
2. The ratio of positive and negative discharges during the life cycle of the storm under study was variable, in the mature stage there was a predominance of the proportion of positive discharges, in the dissipation stage—on the contrary.
3. There was a pronounced jump in the total number of discharges at 11:25–11:30 UTC by almost 2 times compared to previous values, mainly due to positive discharges. This type of jumps (the so-called Lightning Jump—LJ signature) are described in [8, 9] and, according to research results, may be a link with the formation of dangerous phenomena. At the same time, there was a change in the gradation on the scale of meteorological phenomena (in the DMRL-C data)

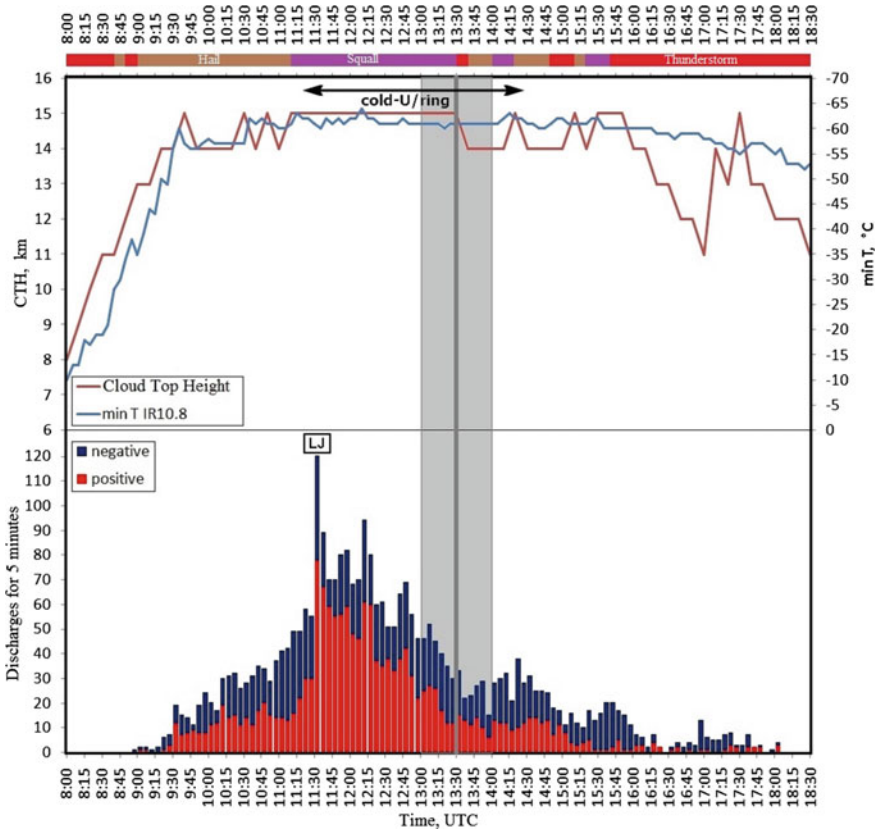


Fig. 4 Distribution of lightning activity by of the SRC “Planeta” lightning detection network: the number of discharges for 5-min intervals with indicating polarity. The Lightning Jump—LJ signature, the values of the minimum radiation temperature (by IR 10.8 MSG-3 data) and the cloud top height (by DMRL-C radar data) of the studied storm are shown. The gradations of weather phenomena by radar data, a period with the observed signatures of cold-U/ring by satellite data (at the top) are shown. The time of registration of dangerous phenomena (strong wind on 13:30 ± 30 min. UTC, based on the characteristics of ESWD messages) marked by the vertical line

from “HAIL” to “SQUALL”, i.e. there was an increase in the degree of general development of the storm cell (an increase in radar reflectivity, an increase in the height of its maximum values, etc.). By the same time, according to satellite data, a cold-U signature was formed, later it transformed into a cold-ring signature, which was continuously observed at the storm until 14:05 UTC, and then existed again in a U-shaped form for another 20 min. Thus, the cold-U/ring signature was observed in the storm during most of its mature stage, when such characteristics as: brightness temperature, cloud top height and radar reflectivity (the values of which can be judged indirectly by gradations of phenomena in recognition algorithms based on the raw data of the DMRL-C) reached extreme values. At the

same time, the advance time (relative to the time of registration of the dangerous phenomena) of the appearance of this signature (cold-U/ring) on satellite images was 2 h 10 min.

4. There was a wave-like distribution of the total number of discharges during the life cycle of the storm under study. Fluctuations in total lightning activity were quasi-periodic (with a period of about 1 h 20 min–1 h 30 min), while there was some correlation of lightning activity maxima with radar gradations of weather events (and hence with radar reflectivity—both general and at certain altitudes, based on algorithms for determining weather phenomena from the original radar data) and, to a lesser extent, with the cloud top height.
5. In the mature stage of storm development, when lightning activity, height and brightness temperature of cloud top reached extreme values, there was a predominance of gradations of recognition of meteorological phenomena “SQUALL” and “HAIL” according to the DMRL-C data.
6. The dangerous phenomena registered near the earth were observed during the decline (after the period of the highest lightning activity) of the total number of discharges, about the time of the first local minimum of activity, about 2 h after the LJ. At the same time, radar characteristics suggested the likelihood of dangerous phenomena, and according to satellite data, the cold-ring signature continued to be observed at this time.

It is also of interest to analyze the spatial distribution of discharges of different polarities in comparison with satellite signatures and localization of recorded dangerous phenomena (DP). To visualize the position of satellite signatures along the storm track, it was decided to use the signature centers, which were determined approximately near the geometric center of the circle (ellipse), the line of which corresponded to the position of the cold ring-shaped signature region. To exclude the error of spatial localization of these centers, the parallax characteristic of geostationary satellite data was taken into account, which in this case was about 25 km (at latitudes 55–56° with cloud top height of cumulonimbus clouds equal to 13–15 km [12]). To analyze the spatial distribution of lightning discharges, the geometric centers of the cold-U/ring signatures and the localization of the registered DP, the maps shown in Fig. 5 were constructed.

The following conclusions by the analysis of the spatial distribution of diagnostic characteristics of the convective storm (see Fig. 5) can be drawn:

1. The densest distribution of discharges was observed in the period approximately from the beginning of the formation of the cold-U/ring signature to the time of DP registration. This is especially true for the distribution of positive discharges.
2. After the time of DP registration, the density (especially positive discharges) decreased significantly, but then less pronounced local density maxima were observed, corresponding to periods of increase in the total number of discharges, as well as variations in radar and satellite parameters noted above, when describing the detected quasi-periodic fluctuations in activity (see above—paragraph 4 of the conclusions in Fig. 4).

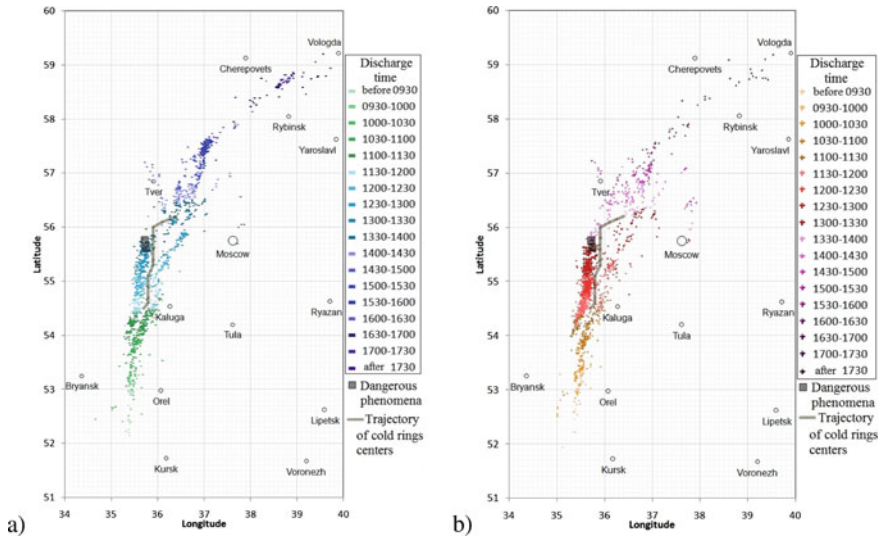


Fig. 5 The distribution of the discharges of negative **a** and positive polarity **b** along the storm track indicating the time interval. The gray line shows the track connecting cold-U/ring signature centers for the entire time interval when the signatures were observed according to satellite data. Gray squares showing localization of registered dangerous phenomena (ESWD)

- It is noticeable that there are two tracks of increased discharge density (both positive and negative) parallel to each other over most of the interval with the cold-U/ring signature. Moreover, the signature centers were localized in the gap of low discharge density, stretched between two parallel tracks of increased density.

To analyze variations in the atmospheric electric field (AEF) in relative proximity to the trajectory of the severe convective storm, data from an electrostatic fluxmeter developed at RPA “Typhoon” [13] and installed at the geophysical station “Vashutino” (Kaluga Region, 5 km northwest of Obninsk) were used. The technical characteristics of this electrostatic fluxmeter were confirmed in a series of experiments on monitoring the vertical component of AEF strength (E_z). It has been established that the achieved level of sensitivity of E_z measurements allows, in particular, to register signals of global electromagnetic Schumann resonances under certain conditions [14]. The fluxmeter at the station “Vashutino” is mounted on a 4^m-high pole. The values of E_z measured at the pole are more than an order of magnitude higher than the values measured directly at the earth’s surface, while the dependence of the measured values linearly depends on the height of the pole [15]. In Fig. 6 shows graphs of the time course of the E_z from 09:00 to 15:00 UTC on August 7, 2021 with per-second averaging of the initial fluxmeter data.

From the comparison of fluxmeter data with radar data, it can be concluded that several characteristic periods have been identified with the peculiarities of the time course of the vertical component of the AEF strength during the passage of various types of convective systems of near or directly above the observation point:

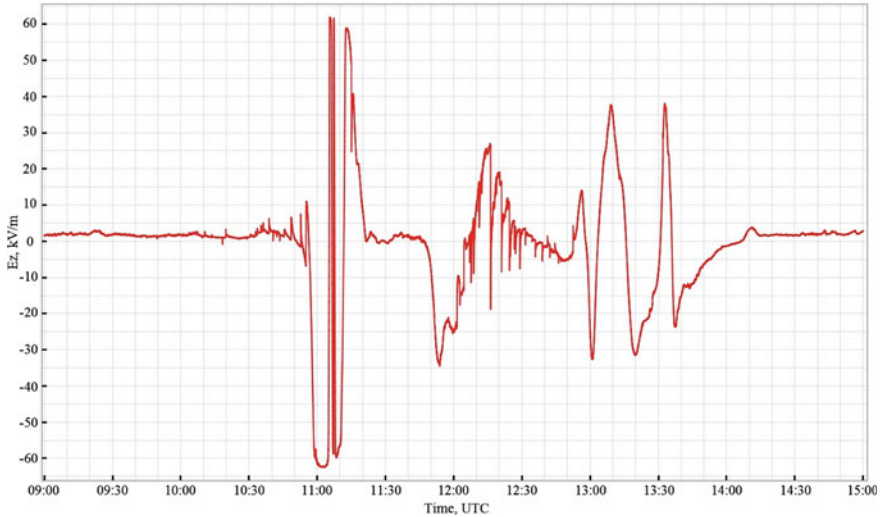


Fig. 6 The time variation of vertical atmospheric electric field. Station “Vashutino”. From 09:00 to 15:00 UTC August 7, 2021

1. In the period from 09:30 to 10:30 UTC, weak (with a gradual increase in amplitude) pulse disturbances of the E_z were observed (Fig. 6) associated with the approach of thunderstorm cell to the observation point.
2. The strongest disturbances of the E_z were observed from about 10:30 to 11:30 UTC (Fig. 6). They are associated with the passage of local thunderstorm cell (not related to the convective system under study) directly through the observation point.
3. In the period from 11:30 to 12:50 UTC, a relatively weaker disturbance of the E_z was observed (Fig. 6) associated with a near thunderstorm at a minimum distance of about 10 km against the background of the passage in relative proximity of the severe convective storm studied in the work as part of a quasi-linear mesoscale convective system (QLCS). The minimum distance to the most pronounced zone of active convection was 50–60 km west of the observation point.
4. From about 12:50 to 14:00 UTC, a low-frequency (with a period of 10–20 min) oscillation of the E_z average amplitude was observed (Fig. 6), characteristic of the passage of a rainfall zone of non-thunderstorm cumulonimbus clouds [16], in this case associated with the southern (rear) periphery of the mesoscale convective system passing during this period directly above the observation point.

In the remaining periods (before 09:30 and after 14:00 UTC), the atmospheric electric field was slightly disturbed (Fig. 6).

3 Conclusions

The case study of severe convection process observed on August 7, 2021 over the territory of central Russia on various types of data allows drawing the following conclusions:

1. For the development of severe organized convection, both favorable synoptic conditions and certain features of the distribution of temperature, humidity, wind profiles, etc. characteristics were observed.
2. As for the classification of the studied severe convective storm, based on the analysis of diagnostic data (the presence of a stable area of high reflectivity according to radar data and a quasi-elliptical shape of the storm that varies little in time and characteristic signatures according to satellite data, a high number and density of lightning discharge distribution), as well as the presence of favorable synoptic, temperature, humidity and wind conditions, it can be done the assumption about the formation of a supercell storm type (with the probable presence of a stable rotating updraft—mesocyclone) inside a quasi-linear mesoscale convective system. A more reliable judgment on the classification of the storm as an “embedded” supercell could be made by a detailed analysis of Doppler radar parameters (which would allow identifying the presence of a mesocyclone), which the authors, unfortunately, did not have.
3. One of the important results of the study is the analysis of the lead time (in relation to the registration of dangerous phenomena) of special signatures that took place in the storm under study (such as cold-U/ring, lightning jump), and often associated with the formation of dangerous phenomena (DP). So, in this study, the value of the lead time for these signatures is about 2 h, which is important for the development of the DP nowcasting schemes. At the same time, it is possible to assume the potential possibility of the formation of DP (in the absence of facts of their registration near the earth for a number of objective reasons) in the period immediately after the detection of signatures due to the potential power and stability of the storm under study, which can be concluded based on diagnostic data in this time period: cloud top height maximum, brightness temperature minimum, hazard gradation by radar data, discharge densities, etc.
4. The spatiotemporal analysis of lightning detection data revealed the periodic nature of the total number and density of discharges (according to the analyzed storm track), possibly associated with periods of intensification of powerful stable convective movements of a long-lived severe storm. It is of interest to identify such features in future work by the analysis of other cases of severe convection.
5. The work additionally analyzes the data of electrostatic fluxmeter (which was located in relative proximity to the areas of movement of the mesoscale convective system) in comparison with radar and lightning detection data. Characteristic periods with the peculiarities of the time course of the vertical component of the atmospheric electric field strength of the are revealed: both separately for the

period of approaching or passing directly over the observation point of thunderstorm and rainfall cells, as well as for the period of passing at some distance from the observation point of severe organized convection cells, which allows us to preliminarily conclude about the possible significance of such data for the nowcasting of convective and thunderstorm processes. This issue also requires further research.

Acknowledgements The authors thank the FSBI SRC “Planeta” for the provision of lightning detection data and FSBI “CAO” for radar data.

References

1. Kalinin, N.A., Shikhov, A.N., Chernokulsky, A.V., Kostarev, S.V., Bykov A.V.: Environments of formation of severe squalls and tornadoes causing large-scale windthrows in the forest zone of European Russia and the Ural. *Russ. Meteorol. Hydrol.* **2**, 83–93 (2021).
2. Novitskii, M.A., Pavlyukov, Y.B., Shmerlin, B.Y. et al.: The tornado in Bashkortostan: the potential of analyzing and forecasting tornado-risk conditions. *Russ. Meteorol. Hydrol.* **41**(10), 683–690 (2016).
3. Proharenja, M.I., Sprygin, A.A.: The using of the method of complex diagnosis and forecast of severe convective structures over the territory of the Republic of Belarus for the summer period 2018. *Natural resources.* **1**, 96–107 (2019) [in Russian].
4. Putsay, M., Simon, A., Szenyán, I. et al.: Case study of the 20 May 2008 tornadic storm in Hungary—remote sensing features and NWP simulation. *Atmos. Res.* **100**(4), 657–679 (2011).
5. Shihov, A.N., Chernokul’skij, A.V., Sprygin, A.A., Azhigov, I.O.: Identification of mesoscale convective cloud systems with tornadoes using satellite data. *Sovremennye problemy d’istantionnogo zondirovaniya Zemli iz kosmosa.* **16**(1), 223–236 (2019) [in Russian].
6. Sprygin, A.A.: Parameters of long-lived severe convective structures in the European territory of Russia and adjacent territories and the possibility of unifying their forecast. *Hydrometeorological Research and Forecasting.* **375**(1), 21–47 (2020) [in Russian].
7. Sprygin, A.A., Proharenja, M.I.: Diagnosis and forecast of convective structures with hazardous phenomena according to modeling and remote sensing data over the territory of Belarus and Central Russia. *Hydrometeorological Research and Forecasting.* **369**(3), 6–22 (2018) [in Russian].
8. Farnell, C., Rigo, T.: The Lightning Jump Algorithm for Nowcasting Convective Rainfall in Catalonia. *Atmosphere.* **11**, (2020). <https://doi.org/10.3390/atmos11040397>.
9. Schultz, C., Petersen, W., Carey, L.: Lightning and severe weather: A comparison between total and cloud-to-ground lightning trends. *Weather and Forecasting.* **26**(5), 744–755 (2011).
10. Setvák, M., Lindsey, D.T., Novák, P. et al.: Satellite-observed cold-ring-shaped features atop deep convective clouds. *Atmos. Res.* **97**(1–2), 80–96 (2010).
11. Basics of operational monitoring and nowcasting of convective storms using satellite imagery. <http://convectivestorm.blogspot.com>.
12. Radová, M., Seidl, J.: Parallax applications when comparing radar and satellite data. The 2008 EUMETSAT Meteorological Satellite Conference. https://www-cdn.eumetsat.int/files/2020-04/pdf_conf_p_s5_22_radova_p.pdf.
13. Boldyrev, A.I., Vyazilov, A.E., Ivanov, V.N. et al.: A highly sensitive field mill for registering weak and strong variations of the electric-field intensity of the Earth’s atmosphere. *Instruments and Experimental Techniques.* **59**(5), 740–748 (2016).
14. Boldyrev, A.I., Vyazilov, A.E., Ivanov, V.N. et al.: Registration of weak ULF/ELF oscillations of the surface electric field strength. *Geomagnetism and Aeronomy.* **56**(4), 503–512 (2016).

15. Chubb, J.: The measurement of atmospheric electric fields using pole mounted electrostatic fieldmeters. *Journal of Electrostatics*. **72**, 295–300 (2014).
16. Pustovalov, K.N., Nagorskij, P.M.: The main types of electric field variations during the passage of cumulonimbus clouds of different genesis. *Optika Atmosfery i Okeana*. **29**(8), 647–653 (2016) [in Russian].

Modern Climate Changes in the North Caucasus Region



A. A. Tashilova, B. A. Ashabokov, L. A. Kesheva, and N. V. Teunova

Abstract This article is devoted to the analysis of changes in the air temperature and precipitation regimes in various climatic zones of the North Caucasus region. Time series of seasonal and annual temperatures in the surface layer of the atmosphere and precipitation for the period 1976–2019 were used to study climate change. It was found that in all climatic zones of the North Caucasus region there was a significant increasing in average annual and seasonal temperatures, especially during the summer season. The change in precipitation regime is not as obvious as the change in temperature. In all climatic zones, both an increase and a decrease in seasonal precipitation, mostly statistically insignificant, were observed. The trend resistance of meteorological parameters was assessed using the normalized range method and its quantitative indicator—the Hurst index. The Hurst index, calculated for the average seasonal temperatures and sum of precipitation, showed a high probability of persistence of the trends, especially for summer temperatures and autumn sum precipitation.

Keywords North Caucasus · Climate change · Air temperature · Precipitation

1 Introduction

Much attention is paid to the study of climate change currently. The consequences of climate change can significantly affect the economic development of society and the safety of people's lives. For Russia 2019 was very warm: the fourth among the warmest in a series of observations since 1936: the average temperature for the year was 2.07 °C higher than the climate norm—the average for 1961–1990. The growth rate of the average annual temperature in Russia was 0.47 °C/10 years. Significant

A. A. Tashilova (✉) · B. A. Ashabokov · L. A. Kesheva · N. V. Teunova
High-Mountain Geophysical Institute, Lenin av., 2, 360030 Nalchik, Russia
e-mail: tashilovaa@mail.ru

B. A. Ashabokov
Institute of Computer Science and Problems of Regional Management, Kabardino-Balkarian
Research Center, Russian Academy of Sciences, I. Armand str., 37a, 360000 Nalchik, Russia

© The Author(s), under exclusive license to Springer Nature Switzerland AG 2023
R. Zakinyan and A. Zakinyan (eds.), *Physics of the Atmosphere, Climatology
and Environmental Monitoring*, Springer Proceedings in Earth
and Environmental Sciences, https://doi.org/10.1007/978-3-031-19012-4_28

climatic anomalies were observed during the year. The spring was very warm with the average temperature for the Russian Federation 2.86 °C above the norm: the fourth value during the observation period [1].

Due to the length of the territory of Russia and the diversity of its natural and climatic features, the consequences of climate change manifest themselves differently in different regions [2]. The climatic features of the North Caucasus region are determined by a number of factors, including zonal and altitudinal zonality, and therefore, the region was divided into four zones depending on the height above sea level (a.s.l.): flat (<500 m a.s.l.), foothill (500–1000 m a.s.l.), mountainous (1000–2000 m a.s.l.) and high-mountain (over 2000 m a.s.l.) zones, where climate change can differ significantly. This article is devoted to the analysis of changes in the air temperature and precipitation regimes in different climatic zones of the North Caucasus region in the period 1976–2019.

It is important to identify trends in the dynamics of such natural and climatic characteristics as the temperature regime of air in the surface layer of the atmosphere and the precipitation regime to analyze climate change. Studies are being carried out on the dynamics of temperature, precipitation, humidity and other climate characteristics based on long-term observations to solve this problem.

2 Materials and Methods

It was used data from time series of seasonal and annual temperatures in the surface layer of the atmosphere and precipitation for 1976–2019 to study climate changes in the North Caucasus region: average temperatures, absolute maximum temperatures, absolute minimum temperatures; amount of precipitation, daily maxima of precipitation and number of days with precipitation of at least 20 mm. The initial data of the listed meteorological parameters is the result of primary measurements at the weather stations (w/stations) of the Roshydromet network, provided by the North Caucasian Hydrometeorological Service Department (HSD), as well as data using the electronic resource <https://rp5.ru>. Time series were studied by methods of mathematical statistics and supplemented with linear trends that characterize the trend of the value under consideration. The studies were carried out for time series of temperature regime and precipitation regime (annual and seasonal) at sixteen considered w/stations. Linear trend coefficients b in our study are expressed in degrees per decade, °C/10 years, or in mm/month/10 years (hereinafter referred to as mm/10 years), D (%) is the contribution to the total variance for 1976–2019.

The quality of the regression model as a whole and by parameters was assessed using the Fisher criterion. The constructed regression equation is significant and can act as a forecast model if the actual value of the Fisher criterion is higher than the theoretical one ($F_{fact.} > F_{theor.}$). The calculation showed that the trend is statistically significant for the coefficient of determination above $R^2 = 0.075$ ($D = R^2 \cdot 100\% = 7.5\%$) for $n = 44$ (for degrees of freedom $df = n - k - 1 = 42$).

An assessment was made of the sustainability of climate change in the course of the study. An indicator of the fractal properties of time series, the so-called Hurst exponent (H), was used as its integral characteristic. Most of the time series of meteorological parameters are non-linear [3–5]. Recently, for the study of nonlinear systems, the so-called normalized range method (R/S - method or fractal analysis) is used, based on the dependence of the normalized range of the parameter on the magnitude of the time increment. The normalized range value scales as the time increment increases, according to a power-law value commonly referred to as the Hurst exponent (H).

The estimate of the Hurst exponent H is calculated by the formula:

$$H = \frac{\lg(R/S)}{\lg(aT)} \quad (1)$$

where R —the range of deviations from the mean, S —the empirical standard deviation, T —the observation period; a —the given constant (Hurst empirically calculated this constant for relatively short time series of natural phenomena as $a = 0.5$).

The larger the value H ($0.5 < H < 1$), the trend is more persistence and more deterministic. Time sequences with $H > 0.5$ belong to the class of persistent (stable), preserving the effect of long-term memory. The series for which $H = 0.5$ have an independent data distribution, are characterized by zero mean and variance equal to 1. The case of $H < 0.5$ is characterized by antipersistence.

A reliable fact is that warming is uneven in time, in addition, it manifests itself differently in different regions. The climate of the North Caucasus region, in addition to the main climate-forming factors, is greatly influenced by the relief and orography of the area. Table 1 presents the physical and geographical characteristics of 16 w/stations, representing all climatic zones of the North Caucasus region.

The synoptic index, geographic coordinates and height above sea level of weather stations are given using official sources (http://meteomaps.ru/meteostation_codes.html—List of indices of meteorological stations (synoptic index); <https://yugmeteo.donpac.ru/Observation/>—Stationary observation points for the state of the environment of the Federal State Budgetary Institution “North Caucasian HSD”).

3 Analysis and Discussion

Many papers [6–8] provide various estimates of changes in the global near-surface air temperature. According to our estimates the warming trend throughout the Caucasus region corresponds to the general direction of global temperature change over the study period 1976–2019.

Summary characteristics of the linear trend are presented in Table 2.

Terskol data on absolute maximums and minimums of temperatures are available only since 2006, therefore they were not included in Table 2.

Table 1 Physical and geographical characteristics of weather stations in the North Caucasus region

No n/n	Synoptic index	Weather stations	Geographical coordinates	Height above sea level (a.s.l.), m
<i>Flat stations</i>				
1	34,945	Izobil'nyi (Stavropol region)	41.5° N; 47.8° E	206
2	37,145	Mozdok (Republic of North Ossetia—Alania)	43.7° N; 44.7° E	136
3	37,144	Prokhladnaya (Kabardino-Balkaria)	43.8° N; 44.1° E	199
4	37,470	Derbent (Dagestan)	42.1° N; 48.3° E	−19
5	37,163	Kizlyar (Dagestan)	43.8° N; 46.7° E	−5
6	37,472	Makhachkala (Dagestan)	42.8° N; 47.6° E	32
7	37,473	Izberg (Dagestan)	42.5° N; 47.9° E	−21
<i>Foothill stations</i>				
8	34,949	Stavropol (Stavropol region)	45.1° N; 42.1° E	452
9	37,047	Cherkessk (Karachay-Cherkessia)	44.1° N; 42.0° E	525
10	37,123	Kislovodsk (Stavropol region)	45.5° N; 42.4° E	890
11	37,212	Nalchik (Kabardino-Balkaria)	43.5° N; 43.7° E	432
12	37,228	Vladikavkaz (Republic of North Ossetia—Alania)	43.1° N; 44.6° E	703
13	37,471	Buinaksk (Dagestan)	42.8° N; 47.1° E	473
<i>Mountain stations</i>				
14	37,193	Teberda (Karachay-Cherkessia)	43.4° N; 41.7° E	1325
15	37,663	Akhty (Dagestan)	41.5° N; 47.8° E	1015
<i>High-mountain station</i>				
16	37,204	Terskol (Kabardino-Balkaria)	42.5° N; 43.3° E	2144

There was a further significant increase in average annual and seasonal temperatures in all climatic zones of the North Caucasus region for 1976–2019. The parameters of linear temperature trends given in Table 2 indicate that, according to the growth rate of the average temperature in 1976–2019 warming in all climatic zones of the region in the summer season exceeds the winter, spring and autumn seasons (significantly in the highland zone). The contribution of the trend to the exflated dispersion of air temperature in the summer season is much higher compared to this

Table 2 Characteristics of the linear trend (*b*, *D*) of the temperature regime at the stations of the North Caucasus region for 1976–2019

Season		Flat zone		Foothill zone		Mountainous zone		High- mountain zone	
		<i>b</i>	<i>D</i>	<i>b</i>	<i>D</i>	<i>b</i>	<i>D</i>	<i>b</i>	<i>D</i>
Year	<i>T^a</i>	0.46	47.2^b	0.57	55.1	0.43	44.2	0.19	13.6
	<i>Min</i>	0.37	1.43	0.26	0.87	0.57	9.83	–	–
	<i>Max</i>	0.78	38.6	0.76	27.2	0.51	10.65	–	–
Winter	<i>T</i>	0.38	12.2	0.49	17.3	0.47	13.9	0.11	0.9
	<i>Min</i>	0.22	0.48	0.61	4.46	0.42	4.93	–	–
	<i>Max</i>	–0.08	0.21	0.35	3.75	0.52	10.46	–	–
Spring	<i>T</i>	0.41	29.1	0.50	29.8	0.34	17.3	0.16	4.3
	<i>Min</i>	0.76	9.88	1.23	19.24	1.17	17.59	–	–
	<i>Max</i>	0.56	15.02	0.44	8.1	0.28	4.76	–	–
Summer	<i>T</i>	0.59	50.2	0.76	57.5	0.53	48.7	0.44	42.1
	<i>Min</i>	0.33	8.92	0.64	28.51	0.54	19.66	–	–
	<i>Max</i>	0.77	37.2	0.75	25.2	0.42	7.29	–	–
Autumn	<i>T</i>	0.42	18.9	0.52	26.4	0.37	17.0	0.05	0.4
	<i>Min</i>	0.33	1.55	0.62	5.20	0.41	2.82	–	–
	<i>Max</i>	0.61	20.5	0.7	14.3	0.15	0.68	–	–

^a*T*—the average temperature, *Min*—the absolute minimum, *Max*—the absolute maximum, *b*—the value of the slope of the linear trend (°C/10 years), *D* (%)—the contribution of the trend to the total variance

^bTrends in bold type are statistically significant at the 5% level.

indicator in other seasons (the highest excess in the high mountain zone, $D = 42.1\%$ in summer and $D = 0.9\%$ in winter).

In the flat, mountain and foothill zones, a statistically significant increase in average annual temperatures occurred during the last years of the period 1976–2019. In the high-mountain zone (Terskol), the average annual temperature growth rate was $0.19\text{ °C}/10\text{ years}$ ($D = 13.6\%$), which also characterizes a steady and statistically significant increase in the average annual temperature.

It should be noted that the growth of the average annual temperature throughout the territory of the Russian Federation coincides with the trends in the growth of annual temperature in the North Caucasus region, especially in the flat zone. As for seasonal changes, the most rapid growth across the entire territory of the Russian Federation was observed in spring ($0.63\text{ °C}/10\text{ years}$), while against the background of interannual fluctuations, the trend is most pronounced in summer ($0.39\text{ °C}/10\text{ years}$: describes 63% total variance) [1]. In contrast, in the region under consideration, the fastest growth was observed in summer for all climatic zones: from $0.44\text{ °C}/10\text{ years}$ ($D = 42.1\%$) in the high mountain zone to $0.76\text{ °C}/10\text{ years}$ ($D = 57.5\%$) in the foothill zone.

In the flat and foothill zones, the growth of average annual temperatures occurred due to the growth of summer and autumn absolute maxima, as well as the growth of spring and summer absolute minima. An increase in spring absolute maximum temperatures was observed only in the flat zone. The increase in the growth of average annual temperatures in the mountain zone occurred due to the growth of winter absolute maxima and the growth of spring and autumn absolute minima. Since the minimum temperatures occur at night, their increase in the spring season leads to a decrease in night frosts. A consequence of the rise in spring lows is that spring warmth arrives earlier, and rising mean summer temperatures drag out summer conditions, shortening autumn.

The change in the precipitation regime is not as obvious as the change in the temperature regime, and, in general, is not statistically significant. In all climatic zones, both an increase and a decrease in seasonal precipitation were observed. Table 3 and Fig. 2 present the characteristics of the linear trend b (D) for 1976–2019 some indicators of the average annual and average seasonal precipitation regime.

In all climatic zones of the North Caucasus region, there was a statistically insignificant increase in annual precipitation. The highest growth rate was in the high-mountain zone ($b = 15.25$ mm/10 years, $D = 1.36\%$). In the flat and foothill zones

Table 3 Characteristics of the linear trend (b , D) of the precipitation regime at the stations of the North Caucasus region for 1976–2019

Season		Flats zone		Foothill zone		Mountain zone		High-mountain zone	
		b	D	b	D	b	D	b	D
Year	R^a	5.32	1.12	0.93	0.01	6.55	1.2	15.25	1.36
	Max	1.1	1.59	-0.04	0.0	0.72	0.91	-	-
	$NR20$	0.05	0.28	0.08	0.49	-0.15	1.23	-	-
Winter	R	5.21	9.62^b	2.47	2.87	0.042	0.0	-3.02	0.25
	Max	0.39	2.02	0.43	3.61	-1.13	3.16	-	-
	$NR20$	0.02	1.33	0.02	3.8	-0.08	1.33	-	-
Spring	R	2.27	1.64	7.27	6.04	10.01	8.9	12.89	3.52
	Max	0.46	0.62	0.02	0.0	0.42	0.36	-	-
	$NR20$	0.07	3.54	0.1	3.12	0.15	5.1	-	-
Summer	R	-4.45	3.0	-7.95	2.75	-2.25	0.6	0.57	0.01
	Max	0.47	0.56	0.42	0.38	-0.59	0.81	-	-
	$NR20$	-0.13	6.79	-0.06	0.46	-0.2	8.04	-	-
Autumn	R	3.12	1.08	-0.34	0.01	-0.66	0.03	5.7	0.66
	Max	1.1	2.23	-0.25	0.29	0.13	0.05	-	-
	$NR20$	0.1	3.58	0.01	0.02	-0.02	0.05	-	-

^a R —the precipitation sum, Max —the maximum daily precipitation, $NR20$ —the number of days with precipitation of at least 20 mm, b —the value of the slope of the linear trend (mm/10 years for R and Max ; n/10 years for $NR20$), D (%)—the contribution of the trend into the total variance

^bTrends in bold type are statistically significant at the 5% level.

the seasonal totals of precipitation in the period 1976–2019 had a positive trend in all seasons, with the exception of summer, where a negative trend was observed. In the mountain zone the negative trend took place in the summer and autumn seasons. The high-mountain zone, unlike the others, is characterized by increase in summer precipitation and decrease in winter precipitation. All changes in precipitation amounts are statistically insignificant, except for the positive trend in the winter season in the flat zone ($b = 5.21$ mm/10 years, $D = 9.62\%$).

Daily precipitation maxima in the flat zone tended to decrease in the autumn and winter seasons, while the summer season is characterized by their growth. Thus, the change in precipitation in response to summer warming was uneven, and this happened mainly during events that are considered extreme.

In the foothill zone daily precipitation maxima decreased in all seasons and in the year as a whole. In the mountainous zone significant decrease in daily precipitation maxima was also observed, especially in the winter season.

In all seasons of the period 1976–2019 in all climatic zones, there was a statistically insignificant increase (50%) and decrease (50%) in the *NR20*.

The normalized range method (fractal analysis) was used to determine the stability of changes in meteorological parameters, for which the Hurst index was calculated using formula 2. The values of the Hurst exponent for average temperature and precipitation in each climatic zone are shown in Table 4.

The Hurst exponent obtained for the series of average annual temperature in the period 1976–2019 took values from $H = 0.5$ in the high-mountain zone in autumn to $H = 0.9$ in the summer in the foothill zone, for the series of precipitation amounts, the Hurst exponent varied from $H = 0.54$ in winter to $H = 0.83$ in spring in the mountain zone, which demonstrates the high trend persistence of the series.

In our work, both in studies [9–11], stability indicators for temperature ($0.68 \div 0.90$) exceed values for precipitation ($0.54 \div 0.74$), which characterizes longer-term changes in air temperature regime compared to precipitation. Our results show that the precipitation series, and especially the temperature series, is not a perfect

Table 4 Values of the Hurst exponent

Season	Flat zone	Foothill zone	Mountainous zone	High-mountain zone
Average temperature				
Winter	0.68	0.76	0.72	0.67
Spring	0.79	0.77	0.70	0.61
Summer	0.89	0.90	0.87	0.86
Autumn	0.78	0.81	0.73	0.50
Amount of precipitation				
Winter	0.69	0.64	0.54	0.55
Spring	0.55	0.67	0.73	0.74
Summer	0.55	0.60	0.61	0.58
Autumn	0.67	0.73	0.71	0.73

Poisson process ($H = 0.5$), on the contrary, there is some long-term correlation between subsequent events and initial ones. Thus, the change in these meteorological parameters, as a phenomenon, carries the dual characteristics of randomness and regularity, and the more H deviates from 0.5, the more regularity appears in the time series.

4 Conclusions

The conducted studies showed that for the studied period 1976–2019 in all climatic zones of the North Caucasus region, there was a further significant increase in average annual and seasonal temperatures. According to the growth rate of the average temperature in 1976–2019 warming in all climatic zones of the region in the summer season exceeds the winter, spring and autumn seasons. The contribution of the trend to the explained variance of air temperature in the summer season is much higher compared to this indicator in other seasons.

The change in the precipitation regime is not as obvious as the change in the temperature regime. In all climatic zones, both an increase and a decrease in seasonal precipitation were observed, mostly statistically insignificant.

The Hurst exponent calculated for the series of seasonal average temperatures and precipitation totals in the period 1976–2019 showed a high probability of continuation of the identified trends, especially for summer temperatures and autumn precipitation totals.

References

1. Report on climate features in the territory of the Russian Federation for 2019. Moscow: Roshydromet (2020) [in Russian].
2. Oganessian, V.V.: Climate changes as risk factors for the Russian economy. Hydrometeorological Research and Forecasts. Moscow, **3** (373), 161–184 (2019) [in Russian].
3. Hurst, H.E., Black, R.P., Simaika, Y.M.: Long term storage: An experimental study. Constable (1965).
4. Mandelbrot, B.: The fractal geometry of nature. Times Books (1982).
5. Kronover, R.M.: Fractals and chaos in dynamical systems. Fundamentals of the theory. Postmarket, Moscow (2000) [in Russian].
6. Hansen, J., Sato, M., Ruedy, R., Lacis, A., Oinas, V.: Global warming in the twenty-first century: An alternative scenario. Proc. Natl. Acad. Sci. USA. **97**, 9875–9880 (2020).
7. Ilyin, Yu.P., Repetin, L.N.: Secular changes in air temperature in the Black Sea region and their seasonal features. Ecological safety of coastal and shelf zones and integrated use of shelf resources. Sevastopol, Russia, 433–438 (2006) [in Russian].
8. Gruza, G.V., Meshcherskaya, A.V.: Changes in the Russian climate over the period of instrumental observations. In: Assessment report on climate change and its consequences on the territory of the Russian Federation. (Bedritsky A.I. and others, ed.), in 2 volumes. Roshydromet. 1, 31–87 (2008) [in Russian].

9. Juan, L.I., et al: Rescaled range (R/S) analysis on seismic activity parameters. *Acta Seismologica Sinica* **14**(2), 148–155 (2001) DOI: <https://doi.org/10.1007/s11589-001-0145-9>.
10. Tashilova, A.A., Ashabokov, B.A., Kesheva, L.A., Teunova, N.V.: Analysis of climate change in the Caucasus region: the end of the 20th—the beginning of the 21st century. *Climate*. **7**, 11, (2019). DOI:<https://doi.org/10.3390/cli7010011>.
11. Ashabokov, B.A., Fedchenko, L.M., Tashilova, A.A., Kesheva, L.A., Teunova, N.V.: Spatial-temporal climate change in the south of the European territory of Russia, assessment of its consequences, methods and models of agrarian-industrial complex (AIC) adaptation. Monograph. Publisher: Fregat LLC, (2020) [in Russian].

Long-Term and Seasonal Changes in Atmospheric Transparency and Their Impact on Astronomical Observations on the Shatdzhatmaz Plateau



A. G. Tlatov , D. V. Dormidontov, and R. N. Kirpichev

Abstract Kislovodsk Mountain Astronomical Station (KMAS) is one of the few observatories in the world where daily observations of the solar corona are carried out. The crown can be observed only in perfectly clear weather at altitudes of more than 2000 m. In this paper, the analysis of the number of days of observations of the corona and their relationship with the data of meteorological parameters in 1957–2022 is carried out. To do this, we used data from the Shatdzhatmaz meteorological station. Both seasonal and long-term variations are present in the data of meteorological parameters, as well as in the variations of corona observations. However, there is no obvious connection with the number of observation days of the corona. The number of days of corona observations can be used to estimate the level of atmospheric aerosols.

Keywords Atmospheric transparency · Solar observations · Solar corona · Meteorological parameters · Atmospheric aerosols

1 Introduction

Astronomical observations require a rather rare combination of geographical and climatic factors. Including: to maximize the number of clear hours for observations, the air would be transparent, without aerosols and calm; the level of turbulence would be as low as possible; the water vapor content in the atmosphere would be as low as possible; there would be no sources of artificial lighting around—“light pollution”. The combination of all these factors has been called “astroclimate”.

In 1947, for observations of the solar corona from the Pulkovo Observatory, an expedition was organized to find a place to install a new, at that time, coronagraph

A. G. Tlatov (✉) · D. V. Dormidontov · R. N. Kirpichev
Kislovodsk Mountain Astronomical Station of the Pulkovo Observatory, Kislovodsk, Russia
e-mail: tlatov@mail.ru

D. V. Dormidontov · R. N. Kirpichev
Department of Theoretical and Mathematical Physics, North-Caucasus Federal University,
Stavropol, Russia

© The Author(s), under exclusive license to Springer Nature Switzerland AG 2023
R. Zakinyan and A. Zakinyan (eds.), *Physics of the Atmosphere, Climatology and Environmental Monitoring*, Springer Proceedings in Earth and Environmental Sciences, https://doi.org/10.1007/978-3-031-19012-4_29

299

telescope. In the vicinity of Kislovodsk town, a place was found—the top of the mountain Shatdzhatmaz, which has many positive qualities. In these places, several more ridges run parallel to the main Caucasian ridge, rising gently from the north side and ending abruptly from the south. This is also the Rocky Ridge to which mount Shatdzhatmaz belongs, which has a large flat top. The gentle ascent from Kislovodsk to this peak allowed a car to pass, so no road construction was required. The same calm relief and flat top do not create air turbulence. With such a relief, western and northern winds blow on a more or less flat surface, and south-easterly winds cross the deep (several hundred meters) valley of the Khasaut River on the way from Mount Kinzal to Shatdzhatmaz. These circumstances significantly affect the local climate and atmospheric-turbulent characteristics [1].

To assess the astroclimate of the area, it is also important to know the magnitude of the “trembling of the atmosphere”, or “seeing”. The atmosphere is in constant motion with changes in temperature, air currents or wind and weather fronts, causing the stars to twinkle. The images of twinkling stars are highly distorted, and this also affects the amount of light reaching us through the air, so it changes from moment to moment, and the star twinkles. If the stars twinkle a lot, this is called “poor” visibility conditions. When the images of stars are stable, this is called “good” visibility conditions. But for observations of the solar corona, this parameter is insignificant.

The astroclimatic characteristics of this place were measured in the late 1950s using the standard technique for photographing stellar traces at that time [2, 3]. The authors demonstrated the advantages of the site in comparison with lower places; at the same time, they clearly realized that the average amplitude of the motion of the stellar image $\sigma \sim 0.3$ arcseconds at the zenith is only indirectly related to the image quality at long exposure. Observations made in 2006–2009 showed that the time of a clear night sky is 1340 h per year [4, 5].

In this paper, we performed an analysis of long-term changes in the number of observational days of the solar corona, which can be observed only in perfectly clear weather at altitudes of more than 2000 m. This is due to the fact that the brightness of the corona during ground observations from Earth is 10–6 times less than the brightness of the solar disk. Therefore, the scattered light in the atmosphere during corona observations should be minimal.

Earlier, on the basis of corona observation data [6], the variation in the level of scattered light of the atmosphere near the solar limb was estimated according to observations on the solar coronagraph of KMAS in the period 1957–2010 and perform comparisons with changes in atmospheric aerosol content and other long-term atmospheric changes [6, 7]. As a result of the analysis, a tendency has been established to increase the amount of scattered light by about 40% over the past 50 years, which may be due to global climate change [8].

In this paper, we consider seasonal changes in the number of observational days of the corona for a period of about 65 years. A comparison with variations of meteorological parameters according to the data of the Shatdzhatmaz high-altitude weather station was also performed.

2 Observational Data

Daily observations of the spectral corona in the FeXIV 5303 Å and FeX 6374 Å lines are carried out at the Kislovodsk Mountain Astronomical Station (KMAS) [9, 10]. KMAS is located near the top of the 2104 m Shatdzhatmaz Mountain (Karachay-Cherkess Republic of Russia, 20 km south of Kislovodsk). The location of the observatory belongs to the Rocky ridge (“rocky”), which runs parallel to the main Caucasian ridge about 50 km away. The Rocky ridge, gradually increasing its height, approaches the Mount Bermamyt (peak height 2642 m) about 20 km west of our site. In the opposite (south-easterly) direction, the ridge declines, but has a noticeable lateral continuation in the form of a high plateau with the summit with a height of 2880 m, removed by 18 km.

Observations of the corona are carried out on the telescope-coronagraph of the Leo system in one photometric system [7]. Observations are conducted in 5° around the solar limb. The intensity is measured at an altitude of $40''$ or $\sim 30,000$ km above the solar photosphere. The technique of determining the absolute intensity of the solar corona in the spectral lines 5303 and 6374 used at KMAS involves determining the level of scattered light resulting from atmospheric and instrumental effects. The obtained values are calibrated when compared with the intensity in the center of the solar disk in the selected spectral ranges, which ensures the stability of the obtained data series. A feature of the shooting is also that it is made in clear cloudless weather.

Other data for us were the data of meteorological parameters of the Shatdzhatmaz high-altitude weather station located nearby (800 m) from the KMAS observation platform.

3 Data Analysis Results

The number of observational days of observation of the solar “green” corona in the spectral line 5303 Å is shown in Fig. 1. In the period 1957–1958, the maximum number of observations was the maximum in the period 2015–2017. The minimum number of observation days corresponds to the period 1965–1971. Also, starting from 2017, we are also seeing a trend towards a decrease in the number of observations.

The number of observation days varies significantly from season to season. Figure 2 shows the seasonal change in the average monthly number of days of observations of the solar corona in the period 1957–2022. The most favorable period is the months from August to October, when the average number of observations reaches 12–13 days per month. The least number of observations occurs in April–May, when the number of observation days drops to 7–8 days.

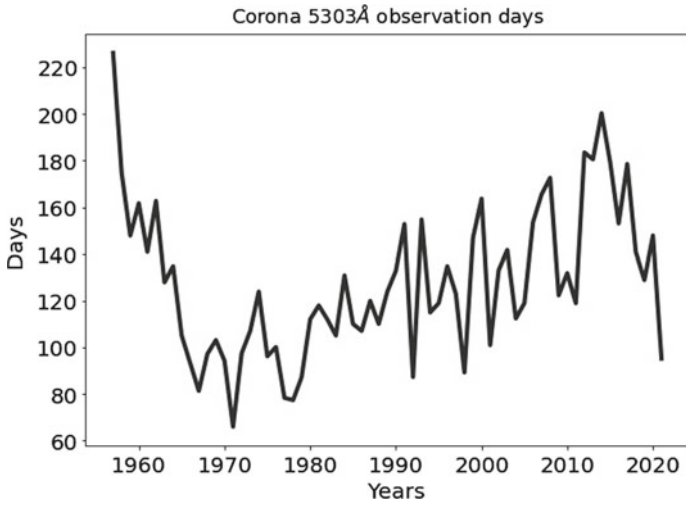


Fig. 1 Change in the number of days of observations of the solar corona, averaged over the year

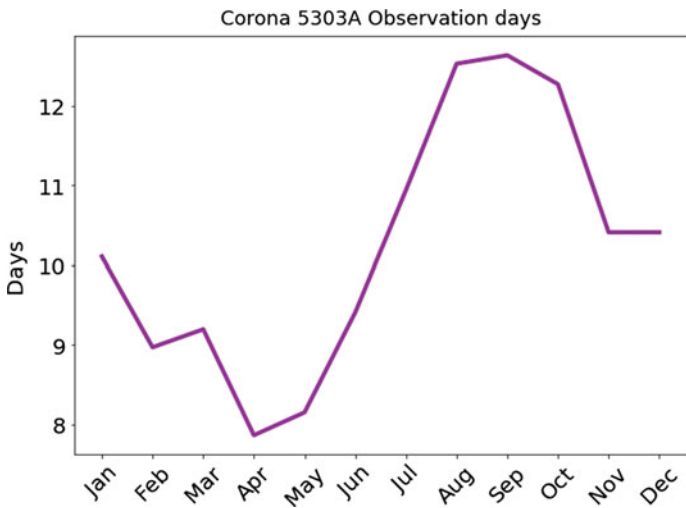


Fig. 2 The average monthly number of observational days of the solar corona in the spectral line 5303 Å according to KMAS data

According to the Shajatmaz weather station in the period 1972–2020. (Fig. 3) The highest temperature near the KMAS observatory is reached in July–August. The greatest amount of precipitation falls in May–June, the highest humidity is reached in June–July.

Figure 4 shows the changes in the annual amplitudes of meteorological parameters, such as average temperature, humidity, precipitation and the number of hours of

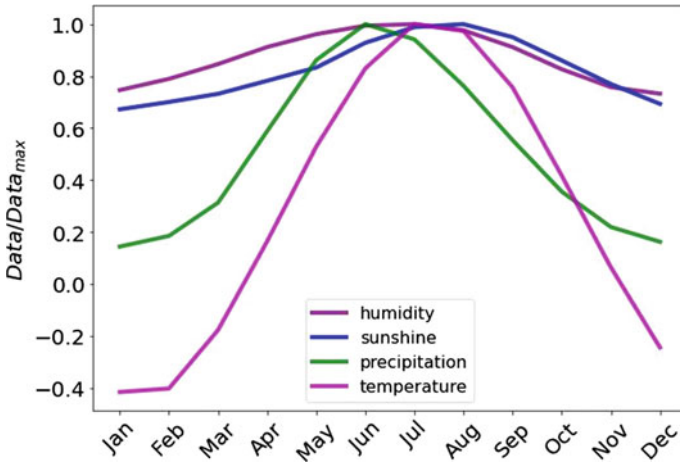


Fig. 3 Relative change of meteorological parameters according to the data of the Shatdzhalmaz weather station in different seasons

sunshine. It can be noted that the greatest annual amplitudes of humidity and precipitation were observed in 82–83 years of the last century, while seasonal temperature fluctuations during this period were minimal. Since the 1990s, there has been an increase in seasonal fluctuations of almost all the considered meteorological parameters.

The change in the number of observation days depending on the number of the month in the period 1957–2022 is shown in Fig. 5. Similar diagrams of monthly values of meteorological parameters are shown in Fig. 6. Maximum temperatures

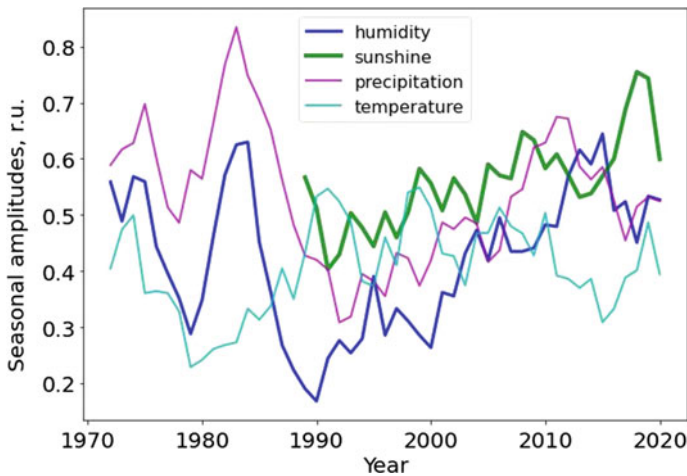


Fig. 4 Variations of annual amplitudes of meteorological parameters

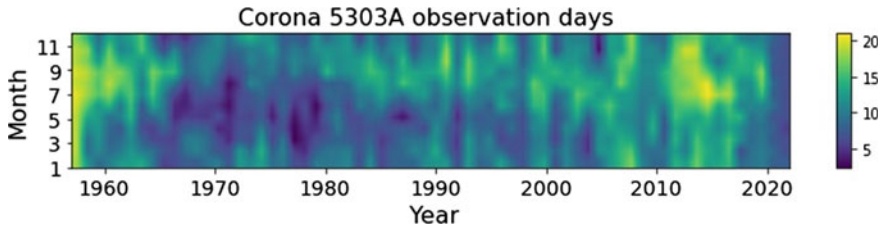


Fig. 5 Change in the number of days of observations of the solar corona by month in the period 1957–2021

were observed in 1998–2000. During this period, a local minimum of precipitation was observed. The greatest amount of precipitation was observed in the spring and summer seasons of 1978. At this time, there was a minimum of observation days of the corona.

4 Conclusions

The analysis of long-term changes in the number of observational days of the solar corona, which can be observed only in perfectly clear weather at altitudes of more than 2000 m, is carried out. It is shown that the most favorable period for corona observations is the period from August to October, when the average number of observations reaches 12–13 days per month. The least number of observations occurs in April–May, when the number of observation days drops to 7–8 days. Other data of the analysis for us were the data of meteorological parameters of the Shatdzhatmaz high-altitude weather station located nearby (800 m) from the KMAS observation platform.

The number of days of corona observations per month and the duration of solar auroras have a maximum in August and September (Figs. 2 and 3). At the same time, the minimum number of days of corona observations falls on April–May, but this minimum is not noted in meteorological parameters. Thus, the transparency of the atmosphere sufficient for observations of the solar corona, which can be estimated by the number of observational days, is not directly related to the meteorological parameters considered, but can complement them for the assessment of aerosols.

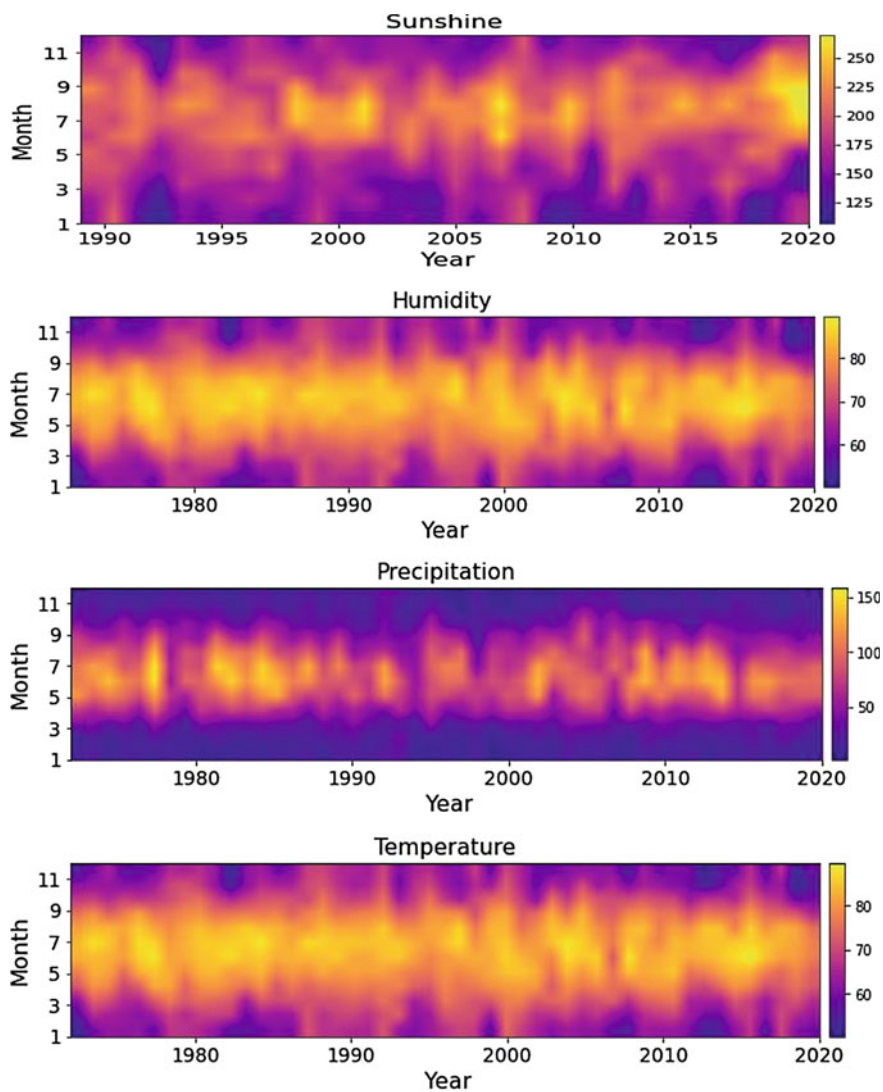


Fig. 6 Dependence of parameters by month according to the data of the Shatdzhatmaz weather station

References

1. Gnevysheva, R. S.: A method for relative determinations of declinations of the sun and the planets with the Erthel-Struve vertical circle at Kislovodsk. *Izvestiia GAO v Pulkove*, **207**, 77, (1991). [in Russian].
2. Darchiya, Sh. P.: Certain Problems in the Method of Studying Astroclimate. *Astronomicheskii Zhurnal*, **41**, 147, (1964). [in Russian].
3. Bol'shakova, G. I., Darchiya, Sh. P.: Fluctuations of shimmer angle, in *Optical Instability*

- of the Earth's Atmosphere. Translated from the Russian, [Opticheskaya neustoichivost' zemnoi atmosfery], Izdatel'stvo "Nauka". Moskva-Leningrad, 1965. Edited by N.I. Kucherov. Jerusalem: Israel Program for Scientific Translations, 66 (1966). [in Russian].
4. Kornilov, V.: How achromatic is the stellar scintillation on large telescopes? *Monthly Notices of the Royal Astronomical Society*, **417**, 2, 1105–1113. (2011). DOI: <https://doi.org/10.1111/j.1365-2966.2011.19329.x>.
 5. Kornilov, V., Shatsky, N., Voziakova, O., Safonov B., Potanin, S. and Kornilov, M.: First results of a site-testing programme at Mount Shatdzhatzmaz during 2007–2009. *Monthly Notices of the Royal Astronomical Society*. **408**, 1233–1248 (2010). DOI: <https://doi.org/10.1111/j.1365-2966.2010.17203.x>.
 6. Aliev, A.Kh., Tlatov, A.G.: Growth in the atmospheric aerosol concentration as a climate forcing agent. *Geomagnetism and Aeronomy*, **52**(8), 1107–1112, (2012). DOI: <https://doi.org/10.1134/S001679321208002>.
 7. Gnevyshev, M.N., Gnevysheva, R.S. Shpitalnaya, A.A.: Method of extraterrestrial observations of the solar corona used at the GAO Mountain Astronomical Station. *Soln. Dannye*, **1**, 101–102, (1958). [in Russian].
 8. Arshinov, M.Yu., Belan, B.D., Kovalevskii, V.K., Plotnikov, A.P., Sklyadneva, T.K., Tolmachev, G.N.: Many-year variability of tropospheric aerosol above West Siberia. *Optics of the atmosphere and ocean*. **13**(6–7) 627–630 (2002).
 9. Makarov, V.I., Tlatov, A.G.: The proportion of hot and cold regions in the polar solar corona during 1957–2002. *Astronomy Reports*. **49**, 932–938, (2005), DOI: <https://doi.org/10.1134/1.2127996>.
 10. Makarov, V.I., Tlatov, A.G., Callebaut, D.K.: Temperature of Polar Corona of the Sun According to Kislovodsk Observations During 1957–2002. *Solar Physics*. **237**, 201–210, (2006). DOI: <https://doi.org/10.1007/s11207-006-1680-2>.

Peculiarities of Climate Change in Central Africa



Mamy Magbini Tokpa and V. A. Lobanov

Abstract The multiyear series of mean monthly air temperatures at 65 meteorological stations in Central Africa are considered to assess the influence of climate change on the dynamics of multiyear mean values. Due to the spatial and temporal heterogeneity of observations, a methodology based on a sequential transition from more reliable to less reliable information, the assessment of the stability of nonstationarity indicators, the selection of areas homogeneous in climate change dynamics, and the quantification of the changes occurred depending on the type of mean value change and on the choice of effective climate models was developed. As a result, we received quantitative estimations of air temperature growth in different seasons, which reach 2.2–2.4 °C in southern mountainous and eastern regions in all seasons and summer monsoon in the coastal areas and spring intermonsoon period in the north. In the central part of the territory, the growth of average temperatures does not exceed 0.5–0.6 °C. Efficient climate models were also selected for the territory for the forthcoming assessment of future temperature.

Keywords Mean monthly temperature · Climate change · Central Africa · Multiyear series modeling · Temperature growth estimates

1 Introduction

Climate change is one of humanity's significant challenges in the twenty-first century [1, 2]. Its impact is now evident in all sectors of public and private activity [3]. The IPCC (Intergovernmental Panel on Climate Change), in its 5th Assessment Report, states that global warming is unequivocally characterized by an increase in the average temperature of the atmosphere and oceans [4]. Moreover, the air temperature increases differently in different latitudes, and the most significant temperature increase was observed in temperate latitudes and the south of Siberia [5]. Based on the latitudinal growth of albedo from the equator to the poles, according to physical

M. M. Tokpa (✉) · V. A. Lobanov
Russian State Hydrometeorological University, St. Petersburg, Russia
e-mail: mtmamy2013@gmail.com; rshu@rshu.ru

© The Author(s), under exclusive license to Springer Nature Switzerland AG 2023
R. Zakinyan and A. Zakinyan (eds.), *Physics of the Atmosphere, Climatology and Environmental Monitoring*, Springer Proceedings in Earth and Environmental Sciences, https://doi.org/10.1007/978-3-031-19012-4_30

307

and mathematical models of climate in the modern warming, one should expect the greatest temperature increase in high latitudes and the smallest in low or equatorial latitudes, which includes the territory of Central Africa considered in this paper. However, in the IPCC reports, the temperature increase in equatorial regions of Africa is highly uncertain, ranging from 0.2 to 2 °C, mainly due to the low reliability of the observational data [6–10].

According to the average scenarios presented in the 5th IPCC report and confirmed by various other climate studies, large areas of Africa will warm more than 2 °C above pre-industrial levels this century [11, 12]. Temperature increases in regions of Africa, including Central Africa, are expected to be higher even than global average temperature increases (by 1.5 and 2 °C), and heat waves are expected to be more frequent and prolonged. Temperature extremes in this region are expected to be higher than the global average, with the most intense warming occurring in the Sahel [13–17]. Several studies have found that trees in the Congo Basin in Central Africa are losing their ability to absorb carbon dioxide, which may lead to an additional increase in temperature [18, 19].

Due to the high uncertainty of the results obtained for the Central African region, this work aims to comprehensively evaluate the quality of the observational data and the estimates of temperature change in this region using statistical methods and models.

2 Climatic Regime of the Territory and Baseline Data

In the present work, we consider the territory of Central Africa, where 65 weather stations with the longest series of observations of average monthly air temperatures were selected (Fig. 1).

The analysis of spatial temperature changes during the year for the considered territory shows the following main situations of its dynamics. In January, relatively low temperatures are observed throughout the region (up to a maximum of 25–27 °C near the Gulf of Guinea), with their lowest values in the northeast and the mountainous southeastern part (20–22 °C) of the territory compared to the center. This situation is due to the influence of the winter phase of the African monsoon, in which the cool and dry air of North Africa moves southward following the movement of the Inter-Tropical Convergence Zone (ITCZ). Then, due to the growth of incoming radiation, the whole area warms up, reaching maximum temperatures in March–April, especially in the northern part (up to 32–33 °C). By summer, the second phase of the African monsoon begins with a shift of the ITCZ to the Northern Hemisphere and a shift of humid Atlantic air following it. The presence of cloudiness and somewhat cooler air from the ocean leads to an overall decrease in temperatures, which is especially noticeable in the western and southwestern parts of the area near the Gulf of Guinea, where temperatures become the same as in the mountainous southeastern part (20–22 °C). In autumn, there is natural radiative heating of the territory during the intermonsoon period, with maximum temperatures in the northern part near the

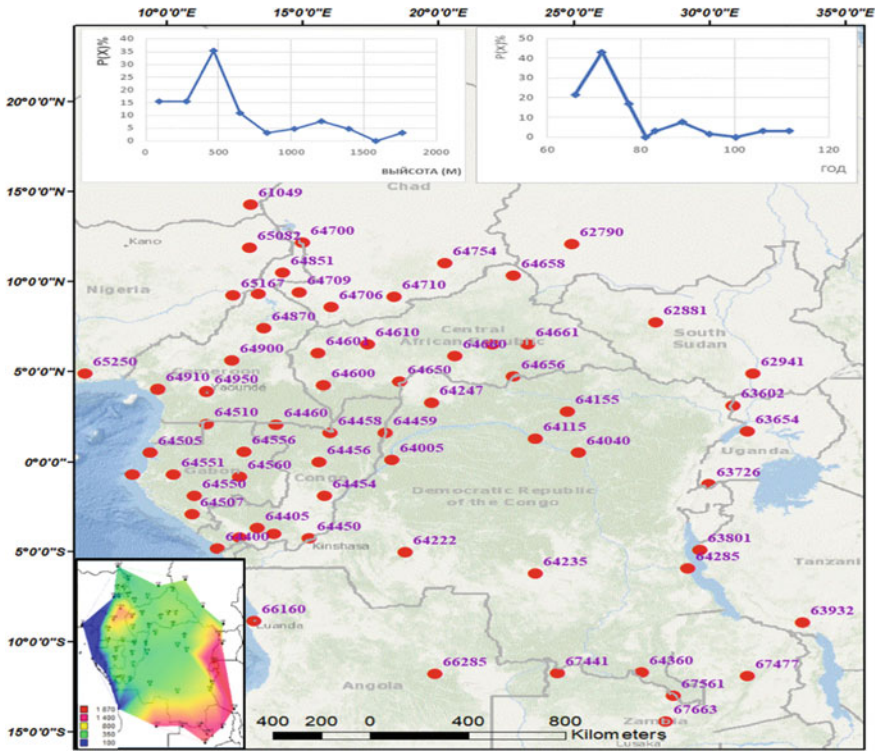


Fig. 1 The map-scheme of weather stations and with small diagrams the distribution of stations by the duration of the series of observations, by height and a map of altitude of station

Sahel (up to 27–28 °C) and minimum temperatures in the mountainous areas (21–22 °C). Temperature variations across the territory range from 7–10 °C in winter to 12–13 °C in April.

In general, it should be noted that throughout the year winter, spring and summer are colder in the mountains and on the sea coast, and spring and summer are warmer in the north than in other parts of the region. As a result, the natural variability (root-mean-square deviation—RMSD) throughout the territory is less than 1 °C, except for the north of the territory in winter and spring and the south in summer and autumn, where the RMSD is slightly greater than 1 °C.

For formalized evaluation of homogeneity and data quality, we applied the statistical criteria of Dixon and Smirnov-Grabbs to evaluate the homogeneity of extremes of empirical distributions and Fisher and Student statistical criteria to evaluate stationarity of dispersions and mean values of two identical parts of the time series [20–22].

As a result, the observation sites were divided into two groups according to the quality of information and duration: 30 sites with long and continuous observation series and the remaining sites with short observation series, unreliable and heterogeneous data, and missing observations.

The methodology based on the construction of regression dependences for the joint period between the short observational series and the longer ones at the reference points has been applied to bring the short observational series to the multiyear period and restore the missing observations [23, 24].

3 Research Methodology

Research methodology is based on approximation of multiyear time series by non-stationary mean models of two types: linear trend and step changes of mean values with an estimation of efficiency of these models in relation to stationary sampling model and modeling itself are described in detail in papers [25–29]. In this case, to assess the effectiveness of the models, such an indicator as the mean square deviation (RMSD) of the model residuals σ_ε is used, and the smaller it is, the better the model is. Moreover, RMSD of the residuals is related to the coefficient of determination of the model (R^2) by the following functional relation:

$$\sigma_\varepsilon = \sigma_y \sqrt{1 - R^2}, \quad (1)$$

where σ_y is the standard deviation of the original series, characterizing the natural variability.

Obviously, for the stationary sample model $\sigma_\varepsilon = \sigma_y$ and $R^2 = 0$. If a nonstationary mean model is more efficient than a stationary sample model, then its $\sigma_\varepsilon < \sigma_y$. Therefore, the relative difference $\Delta = (\sigma_y - \sigma_\varepsilon)/\sigma_y$. Expressed in % can be a measure of the efficiency of any nonstationary mean model. As a first approximation, we can assume that if $\Delta > 10\%$, the nonstationary mean model is more efficient than the stationary mean model. The statistically significant difference between the nonstationary mean model and the stationary model can also be estimated based on the Fisher criterion by comparing the calculated value $F = \sigma_y^2/\sigma_\varepsilon^2$ with the critical F_{cr} at a given significance level α and sample size n [22]. In work [30], the formula connecting Δ and F_{cr} at $\alpha = 5\%$ is given. Thus, at $n = 120$, $F_{cr} = 1.35$ and $\Delta = 13.8\%$, and at $n = 60$, $F_{cr} = 1.53$ and $\Delta = 19.4\%$. When approximating the time series by the step change model of the average, the year of transition from one stationary condition to another is also determined by iterations when reaching the minimum of the sum of squares of deviations from each mean of two parts of the series— T_{cr} .

4 Results and Discussion

4.1 Patterns Obtained Based on Long Series

First, modeling was carried out, and the stability of model parameters was evaluated for the 30 longest series with reliable observational data. The results in the form of average values of the efficiency parameters of nonstationary models r , Δ_{TP} , Δ_{CT} , and T_{CT} are given in Table 1 for two parts of the longest time series: from the beginning of observations until 1960 and from 1961 to 2021.

Table 1 shows that all the nonstationarity in the temperature series occurs after 1960, i.e., in the last period since the second half of the twentieth century. The nonstationarity indices Δ_{TP} and Δ_{CT} are on average $>10\%$ for temperatures in all months of the year, with maximum values of 18–20% in July–September. At the same time, in all cases, $\Delta_{CT} > \Delta_{TP}$ (on average after 1960 $\Delta_{TP} = 11.8\%$, $\Delta_{CT} = 16.4\%$), indicating greater efficiency of the nonstationary model of step changes in the average than the linear trend model in the approximation of time series. On average, the year of such step transitions from one stationary condition to another belongs to the late 1980s and early 1990s. The correlation coefficients r of air temperature with time for all months are statistically insignificant.

Table 1 Results of estimation of stability of model parameters for 30 longest series

Months	Δ_{TP}		Δ_{CT}		r		T_{CT}	
	Before 1960	After 1960	Before 1960	After 1960	Before 1960	After 1960	Before 1960	After 1960
1	7.0	10.0	1.1	13.2	0.06	0.29	1948	1994
2	8.8	10.9	0.8	14.3	0.13	0.35	1946	1995
3	9.9	11	1.5	15.1	0.08	0.39	1948	1995
4	8.9	10.6	1.1	14.7	0.13	0.33	1947	1988
5	7.2	10.3	1.3	15.9	0.09	0.33	1947	1987
6	9.2	11.9	0.1	15.7	0.24	0.4	1946	1991
7	7.0	16.6	0.5	20.4	0.18	0.48	1948	1992
8	6.2	13.9	1.0	18.2	0.08	0.41	1946	1991
9	5.7	12.4	0.3	18.0	0.03	0.35	1945	1991
10	7.2	11.0	0.2	17.6	0.04	0.31	1941	1988
11	9.1	13.0	1.1	18.1	0.02	0.38	1945	1994
12	7.8	10	1.0	15.2	0.1	0.3	1948	1992

4.2 Spatial and Temporal Patterns of the Indicators of Nonstationary Models

For the longest observational series, it was found that all changes occurred in the second half of the twentieth century and, on average, in the late 1980s and early 1990s. Therefore, the observational series only from 1960 was considered for modeling at the remaining sites. As a result, the efficiency parameters of nonstationary models r , Δ_{TP} , Δ_{CT} and the years of transition from one quasi-stationary regime to another T_{CT} were calculated for all observation points and for all average monthly temperatures of the year. Figure 2 shows spatial distributions of correlation coefficients r of mean monthly temperatures with time for all months of the year, which allow us to estimate the evolution of the areas of nonstationary models. With the series duration of 61 years (1961–2021), statistically significant r starts from $r = 0.32$, and therefore second and third gradations of r in Fig. 2 will represent regions of nonstationary mean models.

An analysis of the dynamics of such regions of nonstationary patterns during the year allows us to draw the following conclusions. During the winter monsoon, areas of nonstationary patterns arise along the borders of the territory, occupying about 50% of its total area with a maximum of nonstationarity in February in the east. During the summer monsoon, when humid, warm air masses come from the Atlantic, the area of nonstationary patterns, especially in July and August, occupies up to 2/3 of the total area under consideration and also covers the western coastal regions. During the autumn intermonsoon period, the area of nonstationary patterns gradually decreases and shifts from west to east, comprising only 36% of the total

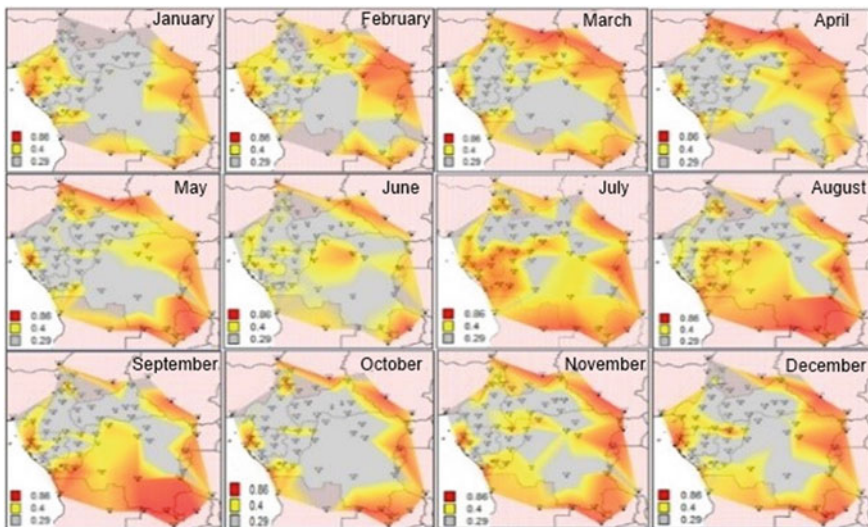


Fig. 2 Spatial distributions of correlation coefficients (r) of air temperature over time during the year

area in October. In general, nonstationary patterns are observed throughout the year in the eastern and southeastern parts of the territory and, as a rule, in the mountainous regions.

4.3 Area Zoning by Type of Climatic Change

Since the model of step changes in average temperature values proved more effective than the trend model, it is necessary to establish the years of step-growth of temperatures and quantify changes in average values. Figure 3 shows that these years vary within a wide range: from the mid-1970s to the early 2000s. At the same time, they are grouped by areas and allow to identify areas homogeneous by type of climate change. In addition, it was found that there may be one-step transition in the multiyear temperature series in some cases, while in others, there may be two.

In addition to T_{cr} , the correlation radius obtained based on the constructed spatial correlation functions of air temperatures for each month was also used as an additional attribute of zoning [22, 30]. As a result, 4 homogeneous areas were singled out according to the dynamics of changes in the average air temperature value; thus, in

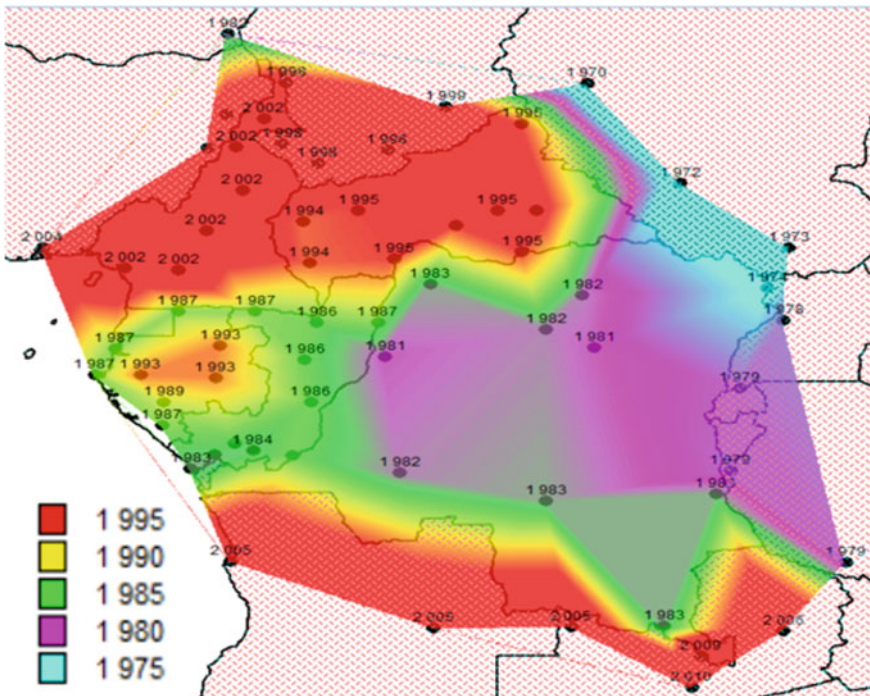


Fig. 3 Spatial distribution of years of transition from one stationary condition to another

the western coastal area № 1 there was a one-step increase in the average temperature in 2002, and the average change $\Delta t_{cp} = 0.7$ °C. In the southern mountainous area № 2, there were two-step increases in temperature in 1984 and in 2002, and each temperature rise was about 0.5 °C. In area № 3, covering the central and eastern parts of the territory, also has two increases in average temperatures in 1977 and 1997, totaling 0.7 °C. In the northern area № 4, there is only one step change in the mean value in 1996, amounting to 0.7 °C.

After developing the classification, its effectiveness should be evaluated, for example, by calculating and comparing the correlation coefficients between the average series in each area and the observation series in all weather stations of the territory in question [31].

4.4 Quantification of Temperature Growth

Quantitative assessment of temperature growth is based on the model view for each period before and after the established year of step changes T_{CT} . If there is a stationary average model for each part of the time series, then the quantification of temperature growth is defined as the difference between the average of the two parts of the time series: $\Delta t_{cp} = t_{cp2} - t_{cp1}$, где t_{cp1} , t_{cp2} are the average temperatures of the first and second parts of the series.

To assess the stationarity of each of the two parts of the time series, correlation coefficients r with time were calculated, which turned out to be statistically insignificant in the vast majority of cases. Therefore, the average series in homogeneous regions and each temperature series at weather stations Δt_{cp} were determined. For the average series in homogeneous areas, it was found that Δt_{cp} varies by 0.7 °C in winter, by 1.2 °C in spring, from 0.8 to 1.0 °C in summer, and from 0.8 to 1.2 °C in fall. However, whether these changes are significant or not can be assessed only by comparing them with natural climatic variability, which is quantitatively expressed by the standard deviation (RMSD) of the whole multiyear series. If the changes in the mean value exceed the RMSD, we can consider them significant. According to the rule of three-sigma for the normal distribution law, a twofold excess of RMSD corresponds to the reliability of concluding the statistical significance of the obtained changes with a probability of 95%. If the obtained changes of average values in areas for different seasons of the year are presented in fractions of RMSD, they would be 0.6 RMSD in winter, 0.9–1.1 in spring, 1.0–1.3 in summer, and 1.1–1.4 RMSD in autumn. Thus, changes in mean multiyear temperatures in summer and autumn are more significant than in spring and winter in relation to their natural climatic variability.

Of course, of the greatest interest are the spatial changes obtained both in Δt_{cp} themselves at the stations and in relation to the RMSD. Examples of such spatial variations of mean long-term temperatures are shown in Fig. 4 for temperatures of mean months of all year seasons, and in relation to RMSD in Fig. 5.

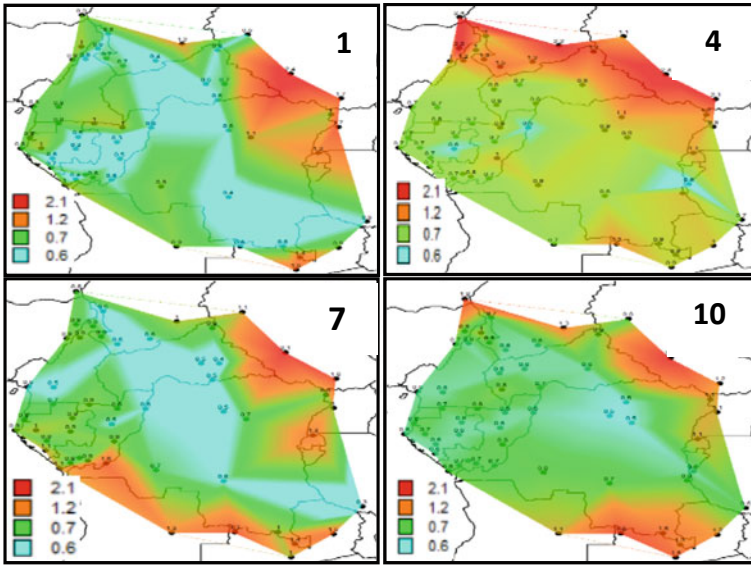


Fig. 4 Spatial distributions of the growth of average long-term temperatures in the middle months of the seasons of the year

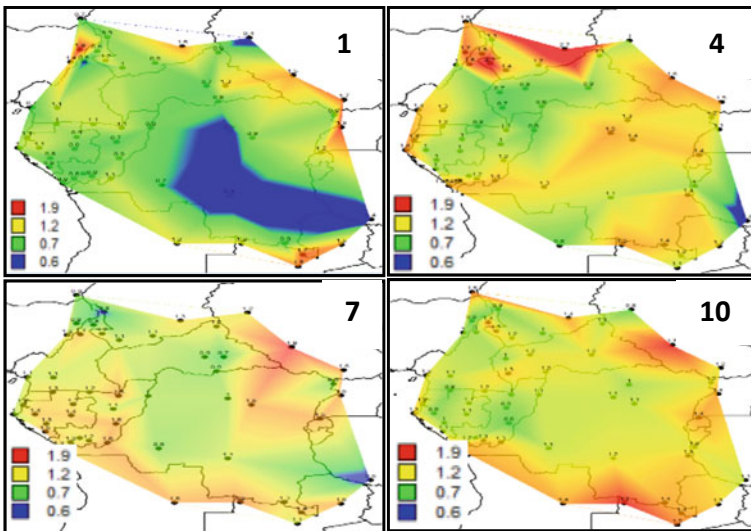


Fig. 5 Spatial distributions of the growth of average long-term temperatures in the middle months of the seasons of the year in fractions of standard deviations

It follows from Fig. 4 that during the winter monsoon (January), the most significant temperature increases of 1–2 °C occurred in the east and south in the mountains, The smallest temperature increases of 0.5 °C was observed in the central part, and, in the north and in the western coastal areas the temperature increase was 0.6–1.2 °C. During the inter-monsoon spring period (April), the most significant increase in mean multiyear temperatures to 2.2–2.4 °C was observed in the north. It was associated with increased desertification and expansion of the Sahara, and a shift of the Sahel to the south. Over the rest of the territory, the temperature increase ranged from 0.6 to 0.9 °C, with slightly higher values of up to 1.2 °C in the southern mountainous part. During the summer monsoon (July), the greatest temperature increase to 1.8–2.2 °C is observed in the east, and another band of significant temperature increases to 1.0–1.6 °C occurs in the southern mountainous part and in the western coastal part. The increase in the central part of the tropical forests was not more than 0.5–0.6 °C. During the intermonsoon fall period (October), the greatest increase was from 1.1 to 2.1 °C in the northeast and in the southern highlands. In the central part, the increase was also up to 0.5–0.6 °C.

Thus, in all seasons there are two parts of the territory with high temperature growth (the southern mountainous and eastern regions) and the central area of tropical forests, where the temperature growth is almost always (except for the hot spring season) small. In the summer monsoon, the coastal area is also added to the area of high-temperature increase due to the air masses from the central Atlantic, where the ocean surface temperature (OST) increases. And in the hot spring inter-monsoon period, the northern part is added, where the influence of the Sahara moving from the north is already felt.

If we consider Δt_{cp} in relation to RMSD (Fig. 5), the highest excess of RMSD from 1.1 to 1.7–2.1 occurs during intermonsoon periods (spring and autumn). It covers up to 90% of the area, with maximums also in the north and in the mountainous southern region. In January, during the winter monsoon, the multiyear variability is large and the $\Delta t_{cp}/\text{RMSD}$ ratio reaches a maximum of 1.7–1.8, with $\Delta t_{cp}/\text{RMSD} < 1$ for half of the area and < 0.5 –0.6 in the central region. In July during the summer monsoon, the $\Delta t_{cp}/\text{RMSD}$ ratio is approximately the same for the entire area and averages 1.2–1.3.

4.5 Selection of Effective Climate Model for Central Africa

The main research tools, especially for future climate change assessment, are physical and mathematical models of the general atmosphere and ocean circulation (GAOC), which already number more than 50 within CMIP5/CMIP6 projects [32, 33]. These models have different resolutions (number of grid nodes by latitude and longitude and levels by altitude in the atmosphere and depth in the ocean) and different climate characterization schemes in explicit constructions and parameterization on the intra-grid scale [34–36]. As a result, there is uncertainty both in reconstructing today's climate from different climate models and even greater uncertainty in estimating projections

into the future until the end of the twenty-first century. On the other hand, climate models are based on regularities of general atmosphere and ocean circulation. They do not always effectively take into account regional climatic features of a specific territory, for example, extremely hot (Arabian Peninsula) or cold (Sakha Republic (Yakutia)) conditions [33, 34]. Therefore, the main task for assessing current and especially future regional climate changes is choosing the most effective climatic model when comparing modeling and observational data for a specific territory.

The following models were chosen as competing climate models, which have information on the results of ongoing experiments on the CMIP5 project freely available on the Internet [10]:

1. Hadley Centre for Climate Prediction, Met Office, UK, HadCM3 Model.
2. Institute for Numerical Mathematics, Russia, INM CM4.0 Model.
3. Model of the Max Planck Institute for Meteorology, Germany (ECHAM5/MPI OM).
4. The Beijing Climate Center, China, BCC Model.
5. IPSL/LMD/LSCE, France, CM4 V1 model.
6. Meteo-France, Centre National de Recherches Meteorologiques, CNRM, CM3 Model.
7. Bjerknes Centre for Climate Research, Norway, BNU-ESM, BCM2.0 Model.
8. Canadian Centre for Climate Modelling and Analysis, CanESM2, CGCM3.1 Model, T63 resolution.
9. The Japanese high-resolution MIROC3.2 model (CCSR/NIES/FRCGC, Japan, MIROC3.2, high resolution), MIROC-ESM.

The methodology for choosing an effective model is based on comparing the observational data and the data from the historical experiment (Historical experiment 1850–2005) for a joint period. 30 year duration, emphasizing the correspondence of the averages for the last observation period, e.g. 1976–2005. Obviously, those models which show the smallest deviation from the multiyear average of the observational data are the most efficient. Therefore, four-time periods were selected: 1950–1975, 1961–1990 (the period recommended by WMO), 1976–2005, and 1950–2005 and the average air temperatures in typical months of all seasons: January, April, July, October.

4.6 Comparison of Simulation and Observation Data for Different Periods

First, we calculated the differences between the mean multiyear temperatures for the entire joint period between the simulated and observed values. The results of these differences ($\Delta = T_{\text{mod}} - T_{\text{obs}}$) averaged over all 65 weather stations for each month of the year are shown in Table 2.

The data in Table 2 show that the average modulo differences (Δ) range from 2.0 to 5.5 °C, and on average, for all months, the smallest differences for the three models

Table 2 Differences between modeled and observed multiyear average temperatures for all weather stations in Central Africa

Months	Climate models									
	Cmcc-cm	CNRM	Hadley	INM	IPSL-CM5A-MR	Micro5	MPI	NorESM1-M	BCC	
1	2.3	2.2	2.5	3.4	2.0	2.3	2.6	2.8	2.1	
2	3.1	3.1	2.7	4.7	2.6	2.7	3.3	3.6	2.8	
3	4.0	4.1	3.4	5.4	3.4	3.2	4.0	4.5	3.6	
4	4.1	4.2	3.7	5.5	3.5	3.8	4.3	4.7	3.8	
5	3.9	4.0	3.6	5.1	3.4	3.7	4.1	4.4	3.6	
6	3.6	3.6	3.9	4.2	3.5	3.5	3.8	3.8	3.2	
7	3.4	3.4	3.7	4.0	3.3	3.3	3.8	3.3	2.9	
8	2.5	2.7	3.1	3.5	2.7	2.8	2.9	2.7	2.5	
9	2.7	2.8	2.9	4.1	2.3	2.5	3.0	3.0	2.4	
10	2.7	2.7	2.8	4.1	2.3	2.6	2.9	3.1	2.6	
11	2.5	2.5	2.7	3.8	2.2	2.3	2.7	2.9	2.3	
12	2.6	2.6	3.0	3.5	2.3	2.5	2.8	2.9	2.4	
среднее	3.1	3.2	3.2	4.3	2.8	2.9	3.4	3.5	2.9	

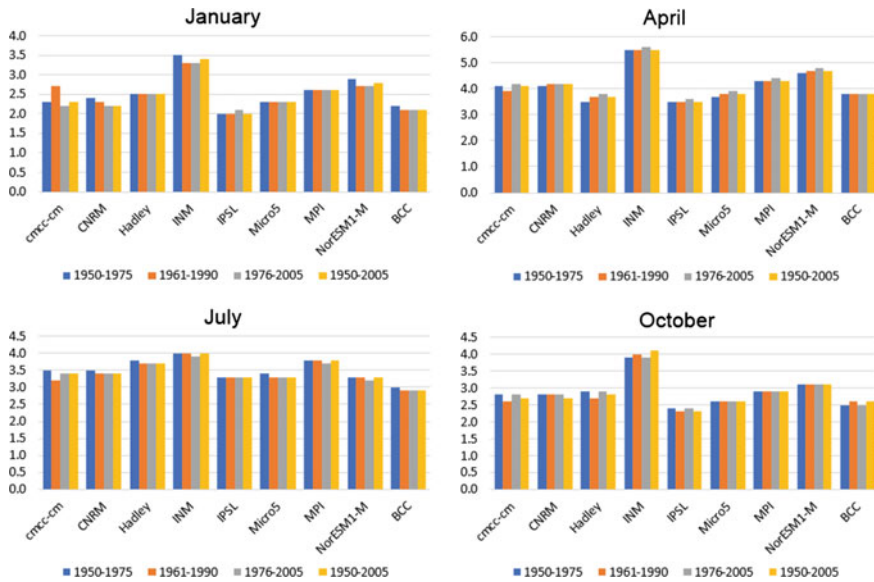


Fig. 6 Differences between modelled and observed mean multiyear temperatures at weather stations in Central Africa

are 2.8–2.9 °C. However, even these smallest (Δ) exceed the natural variability (RMSD), which ranges from 0.6 °C in September to 0.9 °C in January on average for the area, by several times.

Figure 6 shows the differences in the mean multiyear temperatures (modulo) between the simulated and observed data on average for the entire territory of Central Africa for different periods and characteristic months of all year seasons.

Based on the obtained diagrams, we can conclude that the modulo average error is almost independent of the given averaging periods and varies from 2 to 5.5 °C depending on the climate model and season of the year. The smallest errors were obtained using two climate models: IPSL (French Laplace Institute model) and BCC (Beijing Climate Center model, China). The average territorial errors of these models range from 2 °C in autumn and winter to 2–3 °C in spring and summer. For this territory, such errors are significant because they exceed the standard deviation of natural multiyear fluctuations (RMSD) by 2 or more times, which should be considered when adjusting especially the future climate projections.

4.7 Estimation of Errors by Territory

The selected most effective IPSL, and BCC models have the smallest error but average for the whole territory and modulo. At the same time, the spatial distribution of these errors can be heterogeneous both in magnitude and in sign. Therefore, spatial

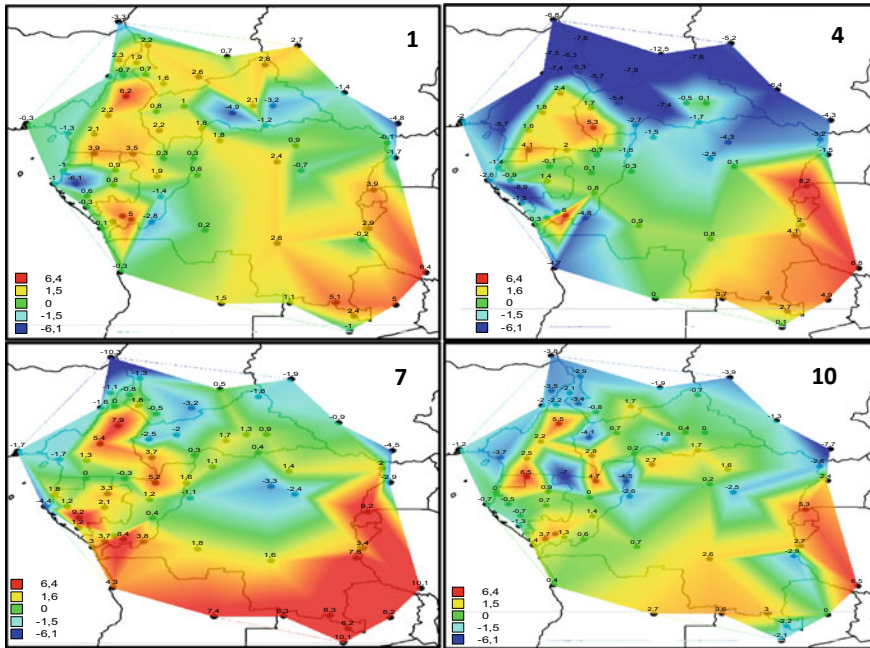


Fig. 7 Spatial distributions of systematic errors of the IPSL model for air temperature in characteristic months (month numbers) of the year

distributions of errors over Central Africa were plotted and analyzed, shown for the IPSL model and characteristic months of all seasons of the year in Fig. 7, and the BCC model in Fig. 8. The differences in the multiyear mean values were considered only for the last 30 year period from 1976 to 2005. Figure 6 shows that these differences practically do not depend on the considered period, and the last period is the closest to the subsequent extrapolation by climate scenarios.

The spatial distributions of the systematic errors of the IPSL model indicate that in winter (January), the deviations are mostly positive and reach their maximum values (up to $+6.4\text{ }^{\circ}\text{C}$) in the southeast, where the mountains are located. A similar situation of local maximum positive errors in the northwest, where mountainous areas are also located. Such a large systematic overestimation of the model data is due to the fact that the historical experiment considered only the surface temperature at sea level. Therefore, in the mountainous regions, either model data at other vertical levels should be taken into account, or a large positive correction for the vertical temperature gradient should be introduced. Negative errors with local maxima of -4 to $-6\text{ }^{\circ}\text{C}$ occur near the coast and in the interior of tropical forests. In these areas, the actual temperature is higher than that calculated by the model, which is associated with the heat effect of the Gulf of Guinea and equatorial forests in the winter and cool phase of the African monsoon. In spring (April), during the hottest inter-monsoon period, the distribution of errors is more differentiated: large negative

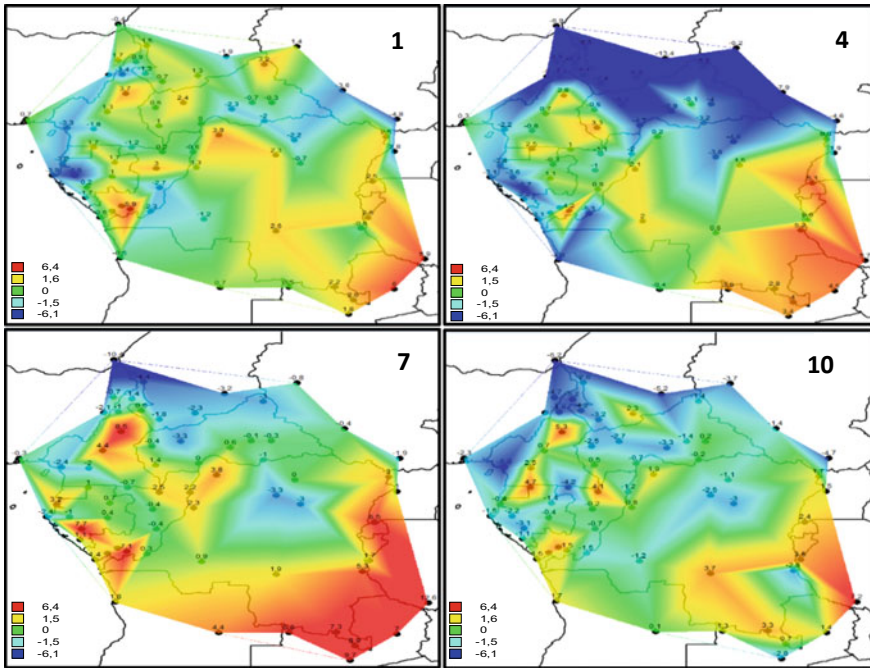


Fig. 8 Spatial distributions of systematic errors of the BCC model for air temperature in characteristic months (month numbers) of the year

errors (up to $-12\text{ }^{\circ}\text{C}$) in the north and large positive errors (up to $+6.8\text{ }^{\circ}\text{C}$) in the south in the mountain regions. The actual temperature in the north is higher than the calculated one due to considerable warming of the territory and the influence of hot air in the Sahel and the Sahara. In summer (July), during the summer phase of the African monsoon, a similar division of territory by errors is preserved, but in the southern mountainous areas, the deviations are larger (up to $+8$ to $+10\text{ }^{\circ}\text{C}$), and in the northern areas smaller (down to $-8\text{ }^{\circ}\text{C}$). In autumn (October) during the intermonsoon period, the spatial distribution of errors is more homogeneous, and their marginal values are smaller. Thus, in the north, negative errors practically do not exceed $-3 \div -4\text{ }^{\circ}\text{C}$ (although there are two local extremes to $-7\text{ }^{\circ}\text{C}$), and in mountainous areas (northwest and south), errors do not exceed $+6.5\text{ }^{\circ}\text{C}$. In some local cases, large deviations from model data can also be caused by large errors in the observational data.

During all seasons of the year in Fig. 8, the largest positive deviations take place in the southern mountainous regions (from $+4$ to $+5\text{ }^{\circ}\text{C}$ in winter to $+10 \div +12\text{ }^{\circ}\text{C}$ in summer), and the largest negative deviations are observed in the northern regions and the gulf coast also throughout the year with the highest values up to $-10 \div -12\text{ }^{\circ}\text{C}$ in spring and with the lowest $-4 \div -6\text{ }^{\circ}\text{C}$ in autumn and winter. In the winter period (January), positive temperature differences (up to $+6\text{ }^{\circ}\text{C}$) occur in the

center, northeast, and southeast of the territory in question, and negative values (up to $-6.6\text{ }^{\circ}\text{C}$)—in the extreme west, northeast, and central south. In the spring period (April), positive differences (up to $+5.7\text{ }^{\circ}\text{C}$) are observed in the southeast, and east, and negative values (up to $-13.4\text{ }^{\circ}\text{C}$) occur from the sea coast in the southwest to the north and northeast. In summer (July), positive temperature differences (up to $+12.6\text{ }^{\circ}\text{C}$) are observed over most of the territory with the highest values in the volcanic region of Cameroon and shifted from the west coast to the south and east. Negative values (from $-10.4\text{ }^{\circ}\text{C}$) are located from the extreme west to the north to the center. In the autumn period (October), the largest temperature differences up to $+7.2\text{ }^{\circ}\text{C}$ are observed in the southeast and east, and negative values up to $-6.2\text{ }^{\circ}\text{C}$ and more are located in the far west, north, and northeast.

5 Conclusions

In particular, the following conclusions were obtained.

1. The observational data are highly heterogeneous in time and space, with the most unreliable observations occurring in the Democratic Republic of Congo, which occupies nearly half Central Africa.
2. A methodology was developed and applied to estimate climatic changes in air temperature in Central Africa, based on a sequential transition from more reliable to less reliable information, an assessment of the stability of no stationarity indicators, on the identification of areas homogeneous in climate change dynamics and on the quantification of changes that have occurred, depending on the type of mean value change model.
3. It is established that changes in average value took place in the second half of the twentieth century, from the middle of 1970 to the beginning of 2000, and the model of stepped changes in average value is more effective than the trend model.
4. On the territory of Central Africa, four areas homogeneous in the dynamics of changes in the mean value were identified, and in two of them, the step temperature rise occurred twice: the first in the late 1970s—early 1980s and the second in the late 1990s—early 2000s, and in the remaining two once: in the mid-1990s or early 2000s.
5. In all seasons, the southern mountainous, and eastern regions of the territory had the highest temperature rise to $2.0\text{--}2.2\text{ }^{\circ}\text{C}$, which is $1.7\text{--}2.1$ RMSD. In the summer monsoon, the western coastal strip is also added to the area of high temperature rise to $1.5\text{--}1.7\text{ }^{\circ}\text{C}$ due to humid and warm air masses from the Atlantic, where OST increases. Another area of high-temperature increases in the north up to $2.2\text{--}2.4\text{ }^{\circ}\text{C}$ occurred during the hottest spring intermonsoon period and is apparently related to the Saharan advance southward. In the central part of the territory, where there are tropical forests, the temperature increase in almost

- all seasons (except spring) is small and does not exceed 0.5–0.6 °C, which is less than RMSD.
6. The French IPSL model of the Laplace Institute and the Chinese BCC model of the Beijing Climate Center proved to be the most efficient models, with average deviations from observational data up to 2–3 °C for the territory in question.
 7. Although average deviations from selected models are small, their spatial distributions show local extremes, which reach $-10 \div -12$ °C and $+10 \div +12$ °C.
 8. Territorial overestimation of air temperatures by models is connected with mountain conditions and high altitudes of weather stations (up to 1800 m). This should be considered when estimating future temperature projections. Temperature overestimation in the mountains is most significant in summer (up to +12 °C) and the least in autumn and winter (up to $+4 \div +6$ °C).
 9. Territorial underestimations of temperatures by models occur mainly in the north and west and are caused by two different causes of warming local character: the influence of the Sahara and Sahel from the north and the Gulf of Guinea from the west. These overestimations also have a seasonal course. The largest negative deviations are observed in the spring, the hottest intermonsoon period, and the smallest in the summer and winter monsoon.

References

1. Amraoul, L.: Characterization of the 1970s climatic shift in Northwest Africa. *Pub. IAHS* **340**, 513–520 (2010).
2. Vissin, E.W.: Impact of climatic variability and surface state dynamics on runoff in the Beninese Niger River Basin, PhD thesis. Hydro climatology. University of Burgundy—Climatology Research Center. CNRS—UMR 5210, version 1, 285 (11 Feb. 2010).
3. Masson-Delmotte, V., P. Zhai, A. Pirani, S. L. Connors, C. Péan, S. Berger, N. Caud, Y. Chen, L. Goldfarb, M. I. Gomis, M. Huang, K. Leitzell, E. Lonnoy, J.B.R. Matthews, T. K. Maycock, T. Waterfield, O. Yelekçi, R. Yu and B. Zhou (eds.). IPCC. *Climate Change 2021: The Physical Science Basis. Contribution of Working Group I to the Sixth Assessment Report of the Intergovernmental Panel on Climate Change*. Cambridge University Press (2012).
4. Stocker, T.F., Qin, D., Plattner, G.-K., Tignor, M., Allen, S.K., Boschung, J., Nauels, A., Xia, Y., Bex, V., Midgley, P.M.: IPCC. *Climate Change 2013: The Physical Science Basis. Contribution of Working Group I to the Fifth Assessment Report of the Intergovernmental Panel on Climate Change/Eds*. Cambridge, United Kingdom and New York, NY, USA: Cambridge University Press (2013).
5. Vtoroy otsenochnyy doklad RosGidrometa ob izmeneniyakh klimata i ikh posledstviyakh na territorii Rossiyskoy Federatsii [The second assessment report of RosHydromet on climate change and its consequences on the territory of the Russian Federation]. Moscow, GU VNIIGMI-WDC, 1400 (2018) [In Russian].
6. Bates, B. C., Kundzewicz, Z. W., Wu, S., Palutikof, J. P.: *Climate Change and Water*, technical paper published by the Intergovernmental Panel on Climate Change. IPCC Secretariat. Geneva, 236 (2008).
7. Acero, F.G., Gracia, J.A., Gallego, M.C.: Peaks-over-threshold study of trends in extreme rainfall over the Iberian Peninsula. *Journal of Climate*. **24**(4), 1089–1105 (2011).

8. Homar, V., Ramis, C., Romero, R., Alonso, S.: Recent trends in temperature and precipitation over the Balearic Islands (Spain). *Climatic Change*. **98**, 199–211 (2010).
9. Amraoui, L.: Recent climate evolution in Northwest Africa (Morocco, Mauritania and their near ocean between 1950 and 2008). Thesis of the University Jean Moulin—Lyon III, 43 (2011).
10. Camberlin, P.: Central Africa in the context of tropical interannual and intra-seasonal climate variability, pp. 25–39 (14 Dec 2010). HAL Id: hal-00320705. <https://hal.archives-ouvertes.fr/hal-00320705/document>
11. Kruger, A. C., Shongwe, S.: Temperature trends in South Africa: 1960–2003. *International Journal of Climatology: A Journal of the Royal Meteorological Society*. **24**(15), 1929–1945 (2004). <https://doi.org/10.1002/joc.1096>
12. <https://public.wmo.int/en/events/meetings/state-of-climate-africa-2019>
13. Diedhiou, A., Bichet, A., Wartenburger, R., Seneviratne, S.I., David, P.: Changes in climate extremes over West and Central Africa at 1.5 °C and 2 °C global warming. *Nature*. **529**, 477–483 (2018).
14. Hulme, M., Doherty, R., Ngara, T., New, M., Lister, D.: African climate change: 1900–2100. *Climate Research*. **17**(2), 145–168 (2001).
15. Aguilar, E., Aziz Barry, A., Brunet, M., Ekan, L., Fernandes, A., Massoukina, M., Zhang, X.: Changes in temperature and precipitation extremes in western central Africa, Guinea Conakry, and Zimbabwe, 1955–2006. *Journal of Geophysical Research: Atmospheres*. **114**(2) (2009).
16. Seneviratne, S. I., Donat, M.G., Pitman, A.J., Knutti, R., Wilby, R. L.: Allowable CO₂ emissions based on regional and impact-related climate targets. *Nature*. **540**, 564–588 (2016).
17. https://report.ipcc.ch/ar6wg2/pdf/IPCC_AR6_WGII_FinalDraft_Chapter09.pdf
18. Pokam, W., Longandjo, G-N., Moufouma-Okia, T., Wilfran, et al.: Consequences of 1.5 °C and 2 °C global warming levels for temperature and precipitation changes over Central Africa. *Environmental Research Letters*. **13**(5), 55–81 (2018).
19. Grossman, D.: The Congo rainforest is losing ability to absorb carbon dioxide. That’s bad for climate change. (2020) 49. <https://rainforestjournalismfund.org/fr/node/20909>
20. Zaks, L.: Statisticheskoye otsenivaniye [Statistical estimation]. M.: Statistics. 598 (1976) [In Russian].
21. Rekomendatsii po statisticheskim metodam analiza odnorodnosti prostranstvenno-vremennykh kolebaniy rechnogo stoka L [Recommendations on Statistical Methods for Analyzing the Homogeneity of Spatio-Temporal Fluctuations in River Flow]. *Gidrometeoizdat*, 78 (1984) [In Russian].
22. Malinin, V.N.: Statisticheskie metody analiza gidrometeorologicheskoy informacii. SPb [Statistical methods for the analysis of hydrometeorological information]. RSHU. 408 (2008) [In Russian].
23. Rekomendatsii po privedeniyu ryadov rechnogo stoka i ikh parametrov k mnogoletnemu periodu [Recommendations for bringing river runoff series and their parameters to a multi-year period]. Leningrad, *Gidrometeoizdat*, 64 (1979) [In Russian].
24. Lobanov, V.A., Lemesheko, N.A., Zhiltsova, E.L., Gorlova, S.A., Reneva, S.A.: Vosstanovleniye mnogoletnikh ryadov temperatury vozdukha na Yevropeyskoy territorii Rossii [Reconstruction of long-term series of air temperature in the European territory of Russia]. *Meteorologiya i gidrologiya [Meteorology and Hydrology]*. **2**, 5–14 (2005) [In Russian].
25. Lobanov, V.A., Shadurskiy, A.Ye.: Vydeleniye zon klimaticheskogo riska na territorii Rossii pri sovremennom izmenenii klimata. Monografiya [Identification of climatic risk zones on the territory of Russia under current climate change. Monograph]. St. Petersburg, Russian State Humanitarian University, 123, (2013) [In Russian].
26. Lobanov, V.A., Toshchakova, G.G.: Osobennosti i prichiny sovremennykh klimaticheskikh izmeneniy v Rossii [Features and causes of modern climate change in Russia]. *Geographic Bulletin, Perm University*, Vol. 38, **3**, 79–89 (2016) [In Russian].
27. Lobanov, V.A., Kirilina, K.S.: Sovremennyye i budushie izmeneniya klimata Respubliki Sakha (Yakutiya) [Current and future climate changes in the Republic of Sakha (Yakutia)]. Monograph—St. Petersburg, RSHU, 157 (2019) [In Russian].

28. Shukri, O.A.A., Lobanov, V.A., Khamid, M.S.: *Sovremennyy i budushiy klimat Araviyskogo poluostrova* [The current and future climate of the Arabian Peninsula]. Monograph—St. Petersburg, RSHU, 190 (2018) [In Russian].
29. Lobanov, V.A., Naurozbayeva, Zh.K.: *Vliyaniye izmeneniya klimata na ledovyy rezhim Severnogo Kaspiya* [Influence of climate change on the ice regime of the Northern Caspian]. Saint-Petersburg, Publishing House of the Russian State Hydrometeorological University, 140 (2021) [In Russian].
30. Lobanov, V.A.: *Leksii po klimatologii. Chast' 2. Dinamika klimata. Kn.2* [Lectures on climatology. Part 2. Climate dynamics. Book 2]. St. Petersburg, Russian State Hydrometeorological University Press, 377 (2018) [In Russian].
31. Lobanov, V.A.: *Uchebnoye posobiye po regional'noy klimatologii* [Textbook on regional climatology]. St. Petersburg, Russian State Hydrometeorological University Press, 170 (2020) [In Russian].
32. About the WCRP CMIP5 Multi-Model Dataset Archive at PCMDI: http://www-pcmdi.llnl.gov/ipcc/about_ipcc.php
33. Atmospheric Model Intercomparison Project: <http://www-pcmdi.llnl.gov/projects/amip/index.php>
34. Gates, W.L., 1992: AMIP: The Atmospheric Model Intercomparison Project. *Bull. Amer. Meteor. Soc.* **73**, 1962–1970.
35. Taylor, K.E., Stouffer, J.R., Meehl, G.A., 2012.: An overview of CMIP5 and experiment design. *Bull. American Meteorological Society*, 485–498 (April 2012).
36. IPCC Standard Output from Coupled Ocean-Atmosphere GCMs. http://www-pcmdi.llnl.gov/ipcc/standard_output.html#Experiments

Electrical Structure and Dynamics of a Thunderstorm with Hail in the North-West of the Russian Federation by Three-Dimensional Simulation data



M. L. Toropova, N. E. Veremei, Yu. P. Mikhailosvkii, and A. A. Sin'kevich

Abstract A numerical study of thunderstorm development using 3D model is presented. An investigation of evolution features of cloud parameters and spatial distribution of the cloud characteristics during development is carried out. It is shown that maxima of studied parameters (cloud top height, vertical velocities, hydrometeor specific contents, lightning frequency, etc.) are reached at 50 min of simulation. The cloud appears in simulation domain after 26 min of simulation, maxima are reached in 25 min of cloud development. It is shown that most intensive convective processes take place during 50–60 min of simulation and reduce thereafter. Multi-layer electrical charge structure is formed in the cloud. A polarity of the cloud inverts shortly after lightning activity beginning and returns back to the structure with main positive charge in the upper part of the cloud at mature stage of Cb development. A coincidence is established between location of regions with main volume charge and regions with highest specific hail content when discharges begin. A predominance of updrafts in velocity field of the studied thunderstorm during development stage is demonstrated. Downdrafts are formed in precipitation regions under the cloud base. At mature stage downdrafts are formed inside cloud and first appears in an anvil.

Keywords Thunderstorm · Numerical model · Hail · Electrification

1 Introduction

Studies of severe convective storms and hail formation remain one of the priorities in research in meteorology. Understanding physical features of development and

M. L. Toropova (✉) · N. E. Veremei · Yu. P. Mikhailosvkii · A. A. Sin'kevich
Voeikov Main Geophysical Observatory, St. Petersburg, Russia
e-mail: marina-toropova@mail.ru

Yu. P. Mikhailosvkii
e-mail: yupalych@yandex.ru

A. A. Sin'kevich
e-mail: sinkevich51@mail.ru

electrification of convective clouds, which are associated with hazardous weather phenomena, should lead to the elaboration of new methods for nowcasting. Moreover, it can be used for the improvement of weather modification methods. The regional component of the analysis is also important as there are features in the structure of atmosphere.

Numerical modelling is one of the most accessible and convenient research tools. In particular, numerical models of convective clouds make it possible to obtain information about the evolution of cloud characteristics, which are not available from regular observational data sources.

Results of a study of the development of a thunderstorm (Cb) in the North-West region of Russia based on numerical simulation data are presented below. A case study of a powerful thunderstorm near St. Petersburg on July 22, 2017, is carried out. Hailstones of a dangerous size were observed. Experiments were performed using a numerical non-stationary three-dimensional model of convective cloud (3D model) developed at Roshydromet (Russia), scientists of the Voeikov Main Geophysical Observatory (MGO) were active participants. The model uses rawinsonde sounding data as initial conditions. As a result of simulation thermodynamic, electrical, and microphysical characteristics of a Cb with a grid step of 200 m (in our study) are obtained. Four hydrometeor fractures are presented in the model: cloud droplets, rain, small ice crystals and hail. The 3D model includes parametric expressions for microphysical processes, detailed description is provided in publications [1, 2].

Earlier, the authors had already performed a set of studies of the chosen thunderstorm. A study of the chosen Cb development using a small-dimensional model was carried out. An investigation of some aspects of Cb evolution, given various accounting for physical processes using 3D model, was carried out [3].

Results of spatial distribution of the electrical characteristics of the Cb at various stages of development using 3D model are presented in [2]. Generally, charge structure in thunderstorms is presented by dipole or three-pole with screening layers [4, 5], with the help of 3D model it was shown that a multilayer charge structure is formed in the cloud, as well as its inverted polarity can take place [2].

Such results match with previous investigations, for example, a presence of multi-layer charge structure in a cloud was confirmed by results of numerical experiments [6–9]. It is known that inverted electrical polarity in Cu can be observed in the cases of high aerosol concentration in atmosphere, presence of extreme updrafts, etc. These parameters impact electrification processes [10–12]. Investigations of the spatial position of the charge regions and regions with the presence of large ice particles (hail and grain) were carried out in [6, 7]. These studies are important for understanding the role of the ice phase in cloud electrification. This role is also considered in presented study.

Another important investigated feature is location of updrafts and downdrafts in the cloud. Strong updrafts with vertical velocities of high values are observed during developing stage of Cb lifecycle in our investigations. Updrafts in Cu are highly variable and their properties depend on environmental conditions (CAPE, moisture, lifting condensation level, cold pools, etc.) [13–18]. Even more challenging

are studies of downdraft formation as they play important role in number of hazardous weather processes (e.g. tornado genesis) and long-lived Cu [19].

The present research is devoted to investigation of an evolution of Cb characteristics: electrical (space charge, electrical field strength), microphysical (specific content of hailstones), and dynamic (regions of updrafts and downdrafts). Particular attention is given to their spatial distribution. Results of numerical simulation of thunderstorm in the northwest of the Russian Federation are under consideration.

2 Dynamics of Thunderstorm Development Based on the Results of Numerical Simulation

Time series of main characteristics of the Cb are demonstrated in Fig. 1. Table 1 presents the maximum estimated values of the Cb parameters at various stages of cloud lifecycle. The simulated Cb appears in the computational domain at the 26 min (vertical line 1 in Fig. 1). The cloud top height (H_{TOP}) increased rather quickly after the Cb appearance and was equal to 6.1 km at 41 min (15 min after the beginning Cb development). H_{TOP} reached 11.5 km at 53 min (vertical line 5 in Fig. 1) and decreased steadily after that. H_{TOP} was 8.3 km to the end of simulation (100 min).

The updraft (W) was 1 m/s (at the time of the appearance of the cloud) and increased rapidly with the cloud development. W reached 14.8 m/s by the time of precipitation beginning (40 min) and 26.4 m/s by the time of discharges beginning (44 min). Maximum W (30.5 m/s) was achieved shortly after beginning of lightning activity (at 45 min), and it decreased thereafter. They were 7.8 m/s by the end of the simulation.

The rain (I_R), hail (I_H) and total (I_{SUM}) precipitation intensities near the earth's surface were considered separately. The dynamics of these intensities were found to be coinciding. Precipitation begins to fall out from the cloud at 40 min of simulation. Its intensity increased rapidly, since the beginning of electrical discharges (46 min). Peak values of I_R , I_{SUM} , I_H were equal to 215, 302 and 101 mm/h, consequently. Results of simulation have demonstrated that these values were reached during a period 50–51 min of simulation. Cloud top height was 10.1–10.5 km at this period and updraft was equal to 17.4 m/s. A decrease of precipitation intensity was observed after an absolute maximum was reached. Then a small local maximum of I_R (188 mm/h), I_H (71 mm/h) and I_{SUM} (251 mm/h) were observed at 60 min. Precipitation still continued to fall out from the cloud (I_R —43 mm/h, I_H —4 mm/h, I_{SUM} —46 mm/h) by the end of the simulation.

The dynamics of changes of specific content of individual cloud fractions is considered: cloud drops— Q_C , raindrops— Q_R , cloud ice crystals— Q_{IC} , hail— Q_I . Maximum Q_C was reached at 39 min of numerical experiment and equaled 2.21×10^{-3} kg/kg while H_{TOP} and updraft velocity were 4.7 km and 14.7 m/s consequently. Maximum of Q_{IC} (1.34×10^{-3} kg/kg) was reached at 43 min. The corresponding

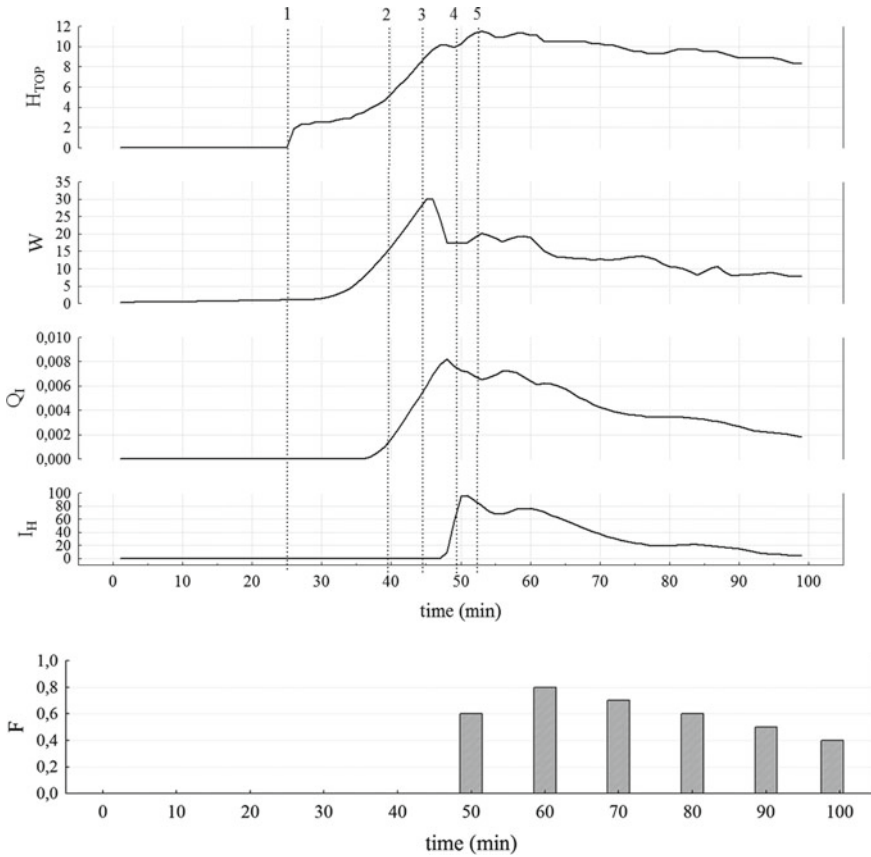


Fig. 1 Time series of simulated thunderstorm parameters: cloud top height (H_{TOP} , km), maximum vertical velocity (W , m/s), maximum specific hail content (Q_I , kg/kg), hail precipitation intensity (I_H , mm/h), lightning frequency (F , min^{-1}). Vertical line indicated specific moment in Cb development: (1) Cb appear in simulation domain, (2) beginning of precipitation, (3) beginning of lightning, (4) maximum precipitation intensity, (5) maximum cloud top height

values of H_{TOP} and W were equal to 7.5 km and 24.5 m/s, an increase in the electrical field strength to critical values and the beginning of lightning flashes were fixed within 1 min after that. Maximum Q_R amounted up to 7.74×10^{-3} kg/kg (at 50 min) and was observed after maximum of liquid precipitation intensity near the earth’s surface and before maximum of total precipitation intensity.

Electrical discharges in the cloud began at 44 min (Fig. 1). Analysis have shown, that during Cb development 36 electrical discharges were fixed. The first electrical discharge in the cloud was fixed at the 44th min of the simulation. The highest lightning frequency F , averaged over 10 min intervals, was 0.8 min^{-1} and corresponded to a period of 50–60 min of simulation. The discharge frequency decreases to 0.4 min^{-1} by the end of the experiment.

Table 1 Maximum values of simulated Cb parameters during its development

Time step	Time (min)	H_{TOP} (km)	W (m/s)	Q_I (kg/kg)	Z_{MAX} (dBZ)	I_R (mm/h)	I_H (mm/h)	I_{SUM} (mm/h)
Cb appearance in simulation domain	26	1.9	1.0	0.0E+00	0.0	0.0	0.0	0.0
Beginning of I_{SUM}	40	4.9	14.8	1.2E-03	49.0	0.0	0.0	0.0
Beginning of electrical discharges	44	8.1	26.4	4.8E-03	61.6	0.7	0.0	0.7
Maximum W	45	9.3	30.5	6.4E-03	65.9	7.4	0.0	7.4
Beginning I_H	45	9.5	30.5	6.6E-03	66.3	9.0	0.0	9.0
Maximum Q_I	48	10.1	19.5	8.3E-03	68.0	88.7	3.6	92.3
Maximum I_R	50	10.1	17.4	7.5E-03	67.7	215	81.6	290

H_{TOP} —cloud top height, W —vertical velocity, Q_I —hail specific content, Z_{MAX} —radar reflectivity, I_R —rain intensity, I_H —hail intensity, I_{SUM} —total precipitation intensity

Summarizing the above data on the temporal changes of extreme values of the main characteristics of the thunderstorm, one can conclude the following. The cloud appeared in the computational domain at 26 min. There was an increase in the values of all considered characteristics up to their maximum values within 25 min. A period between 50 and 60 min of simulation coincides with the time of most intensive cloud development. The highest lightning frequency was recorded during indicated period, further, the cloud passed into the mature stage and, gradually, into the dissipation stage (which is not shown in the results, as the simulation had been performed for fixed period of time—100 min). The obtained values of the Cb characteristics to the end of simulation suggest that the cloud was still in mature stage of lifecycle at that time.

3 Spatial Distribution of Cloud Characteristics

The spatial distribution of the following Cb characteristics is considered: volume charge density τ , electrical field strength E_Z , regions with the highest specific hail content Q_1 , trajectories of air flows, and arrangement of the regions with the most intense updrafts and downdrafts. To perform this analysis, four specific timepoints were selected for the period of Cb evolution: the beginning of electrical discharges, the absolute maximum of Q_1 , the absolute maximum H_{TOP} , and the period, when Cb was in mature stage of development. The detailed study of three-dimensional fields of investigated parameters was carried out for these timepoints, the results are shown in Fig. 2.

The charge in of the cloud (Fig. 2a) had a multilayer structure, where the main dipole had a classical orientation and was clearly distinguished (the area of the main positive charge was on the top and below was negative charge) for the time close to the beginning of the discharges (44 min).

In addition to the main dipole, regions of weaker charges were located above the main dipole (negative and positive) and below the main dipole (positive charge). The positive volume charge τ^+ reached values of $8000 \times 10^{-12} \text{ C/m}^3$, while τ^- was almost twice as large in absolute value and reached $-19,000 \times 10^{-12} \text{ C/m}^3$.

The maximum τ^+ was located at a level 3.7 km, and τ^- at 2.1 km. The electrical field strength varied from -187 up to 341 kV/m ; thus, the largest absolute values corresponded to E_Z^+ . The E_Z^+ center was located at an altitude of 2.5 km (between the centers τ of the main dipole), the E_Z^- center was at an altitude of 1.7 km.

Figure 2a illustrates time period close to appearance of electrical discharge. The values of the volume charge and field strength were quite large. Other parts of the figure (Fig. 2b–d) show fields of investigated parameters related to the period of charge accumulation stage. The charge values were much smaller as these periods are distant in time from the moment of discharge.

The region with the highest values of the specific hail content Q_1 is shown by black markers (isosurface). Its maximum was $4.5 \times 10^{-3} \text{ kg/kg}$ at the period of the

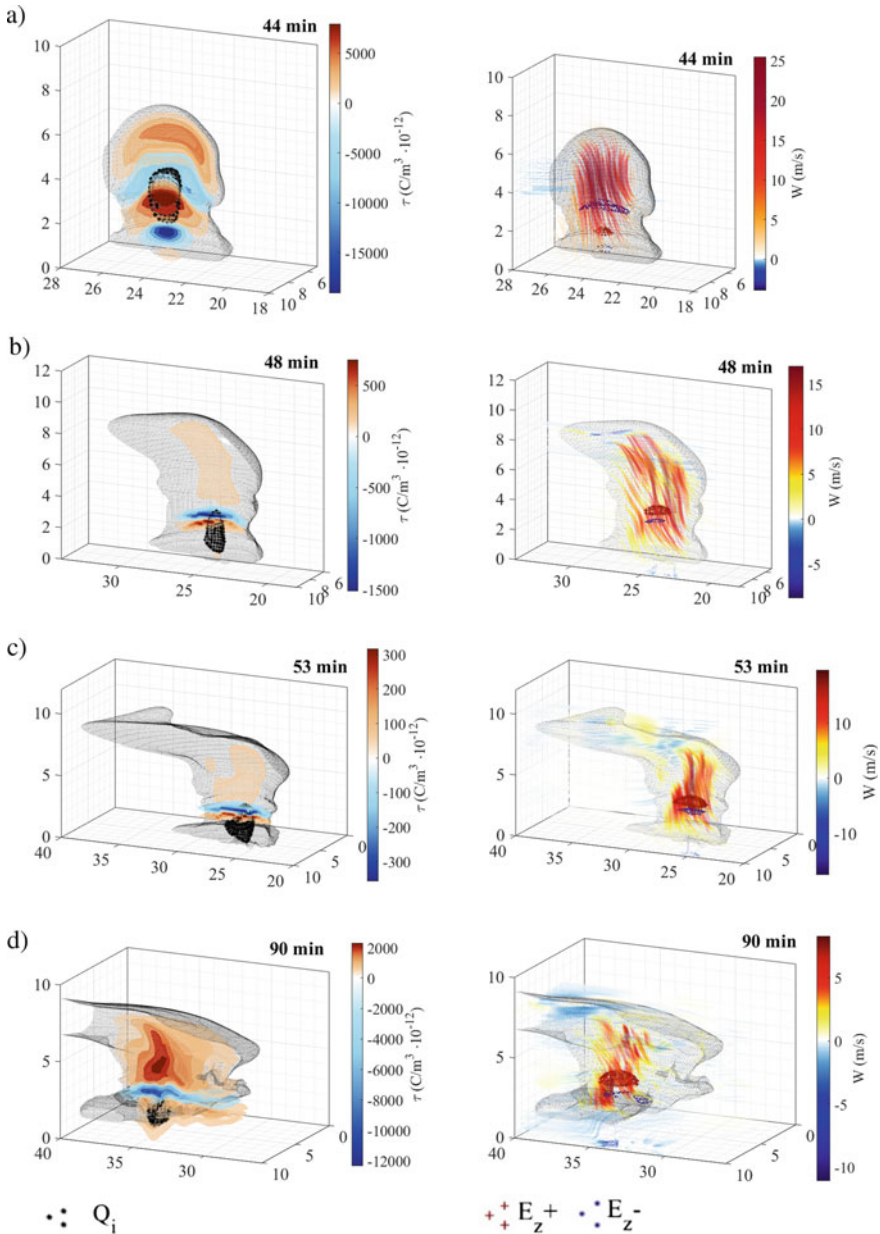


Fig. 2 Spatial distribution of simulated Cb parameters: volume charge density τ (left column, color flood) and regions of highest Q_1 values (left column, markers); updraft (downdraft) trajectories and W (right column, colored trajectories) and regions with extreme E_z (right column, markers). Timesteps: **a** beginning of electrical discharges (44 min), **b** maximum Q_1 (48 min), **c** maximum H_{TOP} (53 min), **d** mature Cb (90 min)

beginning of electrical discharges and had the same location as maximum τ^+ (at height of 3.7 km).

Updrafts occupied almost the entire volume of Cb and reached 25 m/s. The strongest updrafts were observed near the central vertical axis of thunderstorm at an altitude of 5.1 km. The downdrafts in the computational domain did not exceed 4 m/s, the highest values were observed at a height of 5.5 km close to the leeward side of Cb.

Vertical depth of the cloud was 8.8 km at the moment of maximum specific hail content Q_1 (48 min, Fig. 2b) with cloud base at 1.4 km and cloud top at 10.2 km.

The simulated Cb changed its polarity by that time: the upper layer of the main cloud dipole had a negative charge, the lower one had positive charge, both layers were rather thin. The peak τ^+ was located at a height of 3.5 km, and τ^- —at 3.9 km.

Thus, the maximum τ^+ slightly shifted downward relative to the moment of discharges beginning, the volume charge of overlying layer τ^- significantly increased. The negative charge still exceeded the positive one in absolute value. τ varied from -1500×10^{-12} to 750×10^{-12} C/m³ (Fig. 2b). There was a region of a significant vertical extent (about 60% of the cloud) of a weak τ^+ located above the main dipole. E_Z varied from -22 to 14 kV/m. During the discussed period the E_Z^- maximum was located at an altitude of 3.7 km (between the charge layers of the main cloud dipole), the E_Z^+ center was located higher, at an altitude of 4.3 km. Q_1 reached 8.0×10^{-3} kg/kg at 48 min. The absolute maximum was located at a height of 2.3 km. Thus, it shifted downward by almost 1.5 km and moved beneath the main cloud dipole during 4 min after discharges started.

It had been observed that Cb region with the highest values of Q_1 coincided with regions with the main cloud charge. The updrafts in the cloud varied from -10 to 17 m/s; updrafts still prevailed. W maximum was located at a height of 6.7 km. The most intense downdrafts in Cb were observed in the anvil (height 9.9 km) on the leeward side, and downdrafts were also observed near the ground under the central part of the cloud. The downdrafts beneath Cb are apparently caused by precipitation falling from the cloud. The liquid precipitation intensity at that time was 89 mm/h and solid—3.5 mm/h.

At 53th minute of simulation, Cb was in period of most intensive lightning frequency. The thunderstorm depth reached its maximum of 10.0 km (cloud base was at 1.5 km, and cloud top at—11.5 km). The inverse polarity of the cloud preserved during this period.

The absolute maxima of the volume charge coincided in height with those, observed at 44th minute of experiment (τ^+ —3.3 km, τ^- —3.9 km), the center of τ^+ had slightly moved down. The general charge structure of Cb preserved: the main dipole was represented by thin charge layers, most of the cloud (above the main dipole) had a weak positive charge. Absolute values of τ^- still surpassed those of τ^+ . E_Z^+ and E_Z^- centers remained at the same height, as at 48 min (4.3 and 3.7 km, respectively).

The absolute maximum Q_1 was 6.6×10^{-3} kg/kg at 53 min and remained at the same height, slightly shifting upwards to an altitude of 2.5 km. Updrafts dominated in the central part of the cloud, reaching a maximum of 20 m/s at a height of 7.7 km.

Powerful anvil of the thunderstorm was observed at the same time, where downdrafts were also fixed. The strongest downdraft was observed beneath Cb, the velocity equaled to 17 m/s. It was caused by intense precipitation of 156 mm/h.

Thunderstorm was at mature stage at 90 min. Its vertical depth was 7.9 km (cloud base was located at 1.6 and cloud top at 9.4 km).

Cb changed polarity at this stage of lifecycle, the upper charge of the main cloud dipole had positive charge, the lower one had negative. The positive charge prevailed in the spatial structure of the cloud. The absolute maximum τ^+ was located at a height of 5.1 km, and τ^- at—3.7 km. An analysis of the E_Z values had shown the predominance of E_Z^+ (in absolute values), the same was observed at the onset of electrical discharges before the formation of an inverted charge structure. The absolute maximum of E_Z^+ was located at an altitude of 4.3 km, and E_Z^- —at 2.9 km.

The specific content of hail decreased to 2.7×10^{-3} kg/kg, reaching a maximum at a height of 2.1 km. The values of downdrafts decreased to 8 m/s. These values were observed at a lower part of the cloud (height 4.1 km). Downdrafts reached 11 m/s in the zone of falling precipitation under the cloud.

The precipitation intensity decreased as well to 85 mm/h. The number and absolute values of downdraft velocities in the upper and middle parts of Cb have increased.

4 Conclusions

Dynamics of the characteristics of a thunderstorm with hail is analyzed according to the data of three-dimensional numerical simulation. Cb started to develop in the computational domain at 25 min. The cloud passed into the thunderstorm stage at 44 min. Electrical field strength had overcome a threshold value (300 kV/m) and lightning appeared.

The absolute maxima of the updrafts (30 m/s at 45 min) and the specific hail content in the cloud (8.3×10^{-3} kg/kg at 48 min) were reached shortly after the start of the discharges. The period of 50–60 min of simulation corresponds to the most intensive cloud development: the highest cloud top height (11.5 km) and frequency of electrical discharges (0.8 min^{-1}) were fixed. The maxima of the specific content of cloud drops and ice crystals precede the onset of electrical discharges (39 and 43 min, respectively), while the maxima of the content of hailstones and raindrops are reached shortly after the onset of discharges (48 and 50 min). Cloud top height reached 8.3 km by the end of the numerical experiment (100 min), Cb was at mature stage.

An analysis was made of the spatial structure of the electrical characteristics of the cloud, as well as of the specific content of hailstones and regions of updrafts/downdrafts. The cloud had a classic electrical polarity by the time when electrical discharges began: the upper layer of the main cloud dipole had a positive charge. In addition to the main dipole, there were 3 layers with small absolute volume charge density values.

Further development of the cloud resulted in polarity change to reverse one. Most of the cloud (more than 60%) had a weak positive charge. The polarity changed to normal one at mature living stage.

Maximum absolute values of the negative volume charge were greater than those of positive charge at all stages of cloud development.

When charge polarity returned to normal (main upper layer was positive), the absolute maxima of E_Z corresponded to positive values, and vice versa.

An analysis of arrangement of the regions with the highest specific content of hail showed that, there was a coincidence of highest volume charge values and the specific content of hail in the cloud at the beginning of the electrical activity. As Cb developed, the areas of maximum hail content shifted to the lower part of the cloud and solid precipitation started.

The study of updrafts and downdrafts in thunderstorm demonstrated the predominance of ascending air motions at the developing (growth) stage of Cb lifecycle, reaching significant values—30 m/s. This value is significantly less than that estimate from particle theory [20]. It was obtained that $W_{MAX} = (2CAPE)^{0.5}$. Since CAPE according to rawinsonde data for the day of interest was approximately 1350 J/kg, this would result in updraft velocity of 52 m/s. Gridded vertical velocity data analysis allowed us to demonstrate the predominance of ascending air motions during growth stage.

It is shown that the formation of descending air motions in the cloud is primarily associated with precipitation. Subsequently, downdrafts are formed in the upper part of the cloud (anvil), at the mature stage the formation of downdrafts in other parts of the cloud begins. Regions of Cb occupied by updrafts are more localized and reduced by that time.

Thus, the performed study confirms the reproduction by a three-dimensional numerical model of a number of physical patterns known and obtained earlier from observational data and other numerical experiments. It also allows to evaluate the prospects for using the model to refine the cloud seeding methods. The used cloud model provides the possibility to study physical processes of electrification and formation of hazardous weather phenomena.

Acknowledgements The work was prepared with the financial support of the Russian Science Foundation and the Government of St. Petersburg (Proj. № 22-27-2001).

References

1. Veremei, N.E., Dovgaluk, Yu. A., Zatevakhin, M.A., Ignatiev, A.A., Morozov, V.N., Pastushkov, R.S.: Description of the basic numerical nonstationary three-dimensional model of a convective cloud. *Trudy GGO* **582**, 45–91 (2016) [in Russian].
2. Mikhailovsky, Y.P., Toropova, M.L., Veremey, N.E., Dovgalyuk, Yu. A., Sin'kevich, A. A., Yang, J., Lu, J.: Dynamics of the Electrical Structure of Cumulonimbus Clouds. *Radiophys. Quantum Electron.* **64**, 309–320 (2021). <https://doi.org/10.1007/s11141-022-10133-y>

3. Dovgalyuk, Yu. A., Veremei, N. E., Sin'kevich A. A., Mikhailovsky Yu. P., Toropova, M.L.: Investigation of the dynamics of the electrical structure of a thunderstorm cumulonimbus cloud according to three-dimensional numerical simulation data (on the example of the north-west of Russia). *Trudy GGO* **592**, 7–22 (2019) [in Russian].
4. Williams, Earle R.: The Electrification of Thunderstorms. *Scientific American* **259**, **5**, 88–99 (1988). Available at: <http://www.jstor.org/stable/24989265> (Accessed 13 July 2022).
5. Williams, E.R.: The three-pole structure of thunderstorms, *J. Geophys. Res.*, **94**(D11), 13151–13167 (1989). <https://doi.org/10.1029/JD094iD11p13151>
6. Brothers, M.D., Bruning, E.C., Mansell, E.R.: Investigating the relative contributions of charge deposition and turbulence in organizing charge within a thunderstorm. *J. Atm. Sci.* **75**(9), 3265–3284 (2018). <https://doi.org/10.1175/JAS-D-18-0007.1>
7. Mansell, E.R., McGorman, D.R., Ziegler, C.L., Straka, J.M.: Charge structure and lightning sensitivity in a simulated multisell thunderstorm. *J. Geophys. Res.* **110**, D 12101 (2005). <https://doi.org/10.1029/2004JD005287>
8. Zhang, B., Chen, B., Shi, L., Chen, Q.: Modeling of the Stepped Leader Initiation Process in an Altitude Triggered Lightning. *Mathematical Problems in Engineering* **2016** (2016). <https://doi.org/10.1155/2016/9201253>. Available at: <https://www.hindawi.com/journals/mpe/2016/9201253/> (Accessed 13 July 2022).
9. Zheng, T., Tan, Y., Wang, Y.: Numerical Simulation to Evaluate the Effects of Upward Lightning Discharges on Thunderstorm Electrical Parameters. *Adv. Atmos. Sci.* **38**, 446–459 (2021). <https://doi.org/10.1007/s00376-020-0154-z>
10. Xu, L., Zhang, Y., Liu, H. et al.: The role of dynamic transport in the formation of the inverted charge structure in a simulated hailstorm. *Sci. China Earth Sci.* **59**, 1414–1426 (2016). <https://doi.org/10.1007/s11430-016-5293-9>
11. Phillips, V.T.J., Patade, S.: Multiple Environmental Influences on the Lightning of Cold-Based Continental Convection. Part II: Sensitivity Tests for Its Charge Structure and Land–Ocean Contrast. *J. Atm. Sci.* **79**(1), 263–300 (2022). <https://doi.org/10.1175/JAS-D-20-0234.1>
12. Zhao, P., Yin, Y., Xiao, H.: The effects of aerosol on development of thunderstorm electrification: A numerical study. *Atm. Res.* **153**, 376–391 (2015). <https://doi.org/10.1016/j.atmosres.2014.09.011>
13. Knupp, K.R., Cotton, W. R.: Convective cloud downdraft structure: An interpretive survey. *Rev. Geophys.* **23**(2), 183–215 (1985). <https://doi.org/10.1029/RG023i002p00183>
14. Luo, Z.J., Jeyaratnam, J., Iwasaki, S., Takahashi, H., Anderson, R.: Convective vertical velocity and cloud internal vertical structure: An A-Train perspective. *Geophys. Res. Lett.* **41**, 723–729 (2014). <https://doi.org/10.1002/2013GL058922>
15. Glenn, I.B., Krueger, S.K.: Downdrafts in the near cloud environment of deep convective updrafts. *J. Adv. Model. Earth Syst.*, **6**, 1–8 (2014). <https://doi.org/10.1002/2013MS000261>
16. Wang, D., Giangrande, S.E., Feng, Z., Hardin, J.C., Prein, A.F.: Updraft and downdraft core size and intensity as revealed by radar wind profilers: MCS observations and idealized model comparisons. *J. Geophys. Res.: Atm.* **125**, e2019JD031774 (2020). <https://doi.org/10.1029/2019JD031774>
17. van den Heever, S.C., Grant, L.D., Freeman, S.W., Marinescu, P.J. et al.: The Colorado State University Convective Cloud Outflows and UpDrafts Experiment (C3LOUD-Ex). *Bulletin of the American Meteorological Society* **102**, 7 (2021): E1283–E1305. <https://doi.org/10.1175/BAMS-D-19-0013.1>. Available at: <https://journals.ametsoc.org/view/journals/bams/102/7/BAMS-D-19-0013.1.xml> (Accessed 13 July 2022).
18. Barnes, G.M. Updraft Evolution: A Perspective from Cloud Base. *Mon. Wea. Rev.* **123**(9), 2693–2715 (1995). [https://doi.org/10.1175/1520-0493\(1995\)123<2693:UEAPFC>2.0.CO;2](https://doi.org/10.1175/1520-0493(1995)123<2693:UEAPFC>2.0.CO;2)
19. Kirkpatrick, C., McCaul, E.W., Jr., and Cohen, C. Variability of Updraft and Downdraft Characteristics in a Large Parameter Space Study of Convective Storms. *Mon. Wea. Rev.* **137**(5), 1550–1561 (2009). <https://doi.org/10.1175/2008MWR2703.1>
20. Dutton, J.A.: *Dynamics of Atmospheric Motion*. Dover Publications, Inc. (1976).

Measurement of Cloud Water Content from a Research Aircraft



V. V. Volkov, V. V. Petrov, and N. O. Krutikov

Abstract The article is devoted to measuring cloud water content. It considers various designs of sensors to measure liquid and total water content. Algorithms to calculate liquid and total water content are presented. As a result of research flights, data on capture coefficients for sensors of various designs were obtained in mixed-phase and droplet clouds.

Keywords Cloud water content · Research aircraft · Sensors design · Capture coefficients

1 Introduction

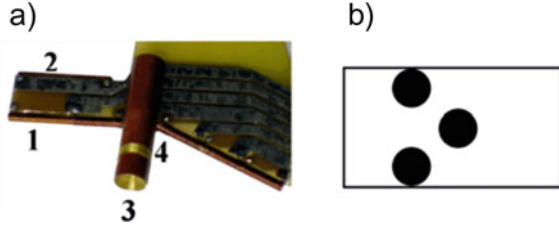
An important integral characteristic of clouds is their water content. At negative temperatures, clouds contain both liquid droplets and ice crystals. To measure cloud water content from board aircraft, a probe constructed by A. Nevzorov is used. The probe determines liquid water and total water content by a method of water droplet and crystal evaporation from a hotwire placed in an incident air flow [1]. With time, the probe has been upgraded [2]. Still, some problems in measuring water content of mixed-phase clouds remain unsolved. The presence in clouds of both droplets and crystals necessitates the development of algorithms that would permit one to account separately for power required for droplet evaporation and that for melting and evaporation of crystals. Neglecting phase composition features would result in systematic errors in water content measurements. Thus, in warm clouds (at positive temperatures) total water content would paradoxically appear to be less than liquid water content. Indefinite capture coefficients for cloud particle sensors can be another source of error in measuring total water content. This paper deals with measuring cloud water and finding ways to determine total water content.

V. V. Volkov (✉) · V. V. Petrov · N. O. Krutikov
Central Aerological Observatory, 3 Pervomayskaya str., 141701 Dolgoprudny, Russia
e-mail: volkov-vv@mail.ru

© The Author(s), under exclusive license to Springer Nature Switzerland AG 2023
R. Zakinyan and A. Zakinyan (eds.), *Physics of the Atmosphere, Climatology and Environmental Monitoring*, Springer Proceedings in Earth and Environmental Sciences, https://doi.org/10.1007/978-3-031-19012-4_32

339

Fig. 1 Nevzorov probe sensors to measure: 1a—liquid water, 3a—total water



2 Sensor Designs

Currently, two designs of Nevzorov probe sensor are employed [1]. To measure the liquid phase of cloud particles, a sensor in the form of a nickel hot wire wound on a copper core is used (Fig. 1a, 1). The sensor evaporates liquid water, while crystals bounce off the core cylinder. A total water sensor is a wire wound on a reverse cone (Fig. 1a, 3) [2]. The authors proposed a sensor of a flow-type design [3] (Fig. 1b) with three cylindrical heating elements arranged in a staggered order. Due to an intricate airflow over the sensing elements, the sensor provides high capture coefficients.

3 Measurement of Water Content

Water content measurement is based on measuring the power spent on maintaining constant temperature of the measuring element. The power balance of the liquid water sensor (P_{LWC}) and total water sensor (P_{TWC}) is given by the expressions

$$P_{LWC} = P_{iLWC} + P_{eLWC} + P_{cLWC}$$

$$P_{TWC} = P_{iTWC} + P_{eTWC} + P_{cTWC}$$

This power is spent on heating and evaporation of P_{LWC} and P_{iTWC} droplets, heating, melting and evaporation of P_{iLWC} and P_{iTWC} crystals, and, partly, on convective heat loss of P_{cLWC} and P_{cTWC} sensors.

Power required for heating, (melting crystals) and evaporation of droplets is calculated by the formulas

$$P_{iLWC} = \varepsilon_{iLWC} \cdot W_i L_i \cdot S_{LWC} U,$$

$$P_{eLWC} = \beta \cdot W_i L_i \cdot S_{LWC} U,$$

$$P_{iTWC} = \varepsilon_{iTWC} \cdot W_i L_i \cdot S_{TWC} U,$$

$$P_{\text{ITWC}} = \varepsilon_{\text{ITWC}} \cdot W_1 L_1 \cdot S_{\text{TWC}} U,$$

where $\varepsilon_{\text{ILWC}}$, $\varepsilon_{\text{ITWC}}$, $\varepsilon_{\text{ITWC}}$ are the coefficients of droplet and crystal capture by the sensor, β is the coefficient of crystal capture by the liquid water sensor, which is close to zero. W_1 , W_i are water content values in liquid and solid phases. L_1 , is the specific heat and vaporization, L_i is the value of specific heat, melting and vaporization. S_{LWC} , S_{TWC} are the areas of the liquid and total water sensors. U is the aircraft airspeed.

Assuming the coefficient $\beta = 0$, water content values are obtained from

$$W_1 = \frac{\Delta P_{\text{LWC}}}{\varepsilon_{\text{ILWC}} \cdot L_1 \cdot S_{\text{LWC}} U}$$

and the values for ice from

$$W_i = \frac{\Delta P_{\text{TWC}} - \varepsilon_{\text{ITWC}} \cdot W_1 L_1 \cdot S_{\text{TWC}} U}{\varepsilon_{\text{ITWC}} \cdot L_i \cdot S_{\text{TWC}} U}$$

$$W_{\text{T}} = W_1 + W_i$$

where ΔP_{LWC} , ΔP_{TWC} designate the difference between the power required for evaporation and convective heat loss; W_{T} is the total water content.

In clouds, at positive temperatures $W_i = 0$. Then, the readings of the total water sensor will be given by the expression

$$\Delta P_{\text{TWC}} - \varepsilon_{\text{ITWC}} \cdot W_1 L_1 \cdot S_{\text{TWC}} U = 0$$

or

$$W_1 = \frac{\Delta P_{\text{TWC}}}{\varepsilon_{\text{ITWC}} \cdot L_1 \cdot S_{\text{TWC}} U}$$

By comparing the readings of Nevzorov probe with those of the instruments that count the spectra of cloud particle sizes, CDP and CIP [4, 5], it is possible to determine the capture coefficients $\varepsilon_{\text{ILWC}}$ and $\varepsilon_{\text{ITWC}}$. Although the capture coefficient $\varepsilon_{\text{ITWC}}$ remains unknown.

4 Accounting for the Power Spent in Dry Air

There are several ways to account for convective heat loss of Nevzorov probe sensors. One method is to determine heat loss on the reference element (Fig. 1a—2) and (Fig. 1a—4) heated to the temperature of the measuring element, the former, however, blown over by an air flow protected from droplets. Since the measuring and reference elements are blown over differently, the heat loss balance changes when the airflow

mode changes. Modern probes of cloud water content are usually digital [6]. Still the measuring sensor contains both the basic measuring element and the reference one. Water content is determined by the values of power loss on both elements. These values are stored in computer memory, and water content can be calculated by processing on the ground. Such instruments no longer require the presence of an operator on board a research aircraft. Another way to account for convective heat loss is a method of measuring power on the measuring element itself in a cloudless atmosphere. Both methods have disadvantages. Since heat losses are a function of the Reynolds number and air temperature, thus depending on flight conditions, aircraft speed and altitude, changes in these parameters during the flight in clouds would lead to a systematic measurement error. A method devoid of these disadvantages is based on the calculation of convective heat losses due to air flowing over a cylindrical body, using the relations known from thermal physics [7]. This method can be effective in the cases when low clouds or a vertically developed cloud layer would prevent measurements of convective heat loss on the measuring element. It is convenient to write the convective heat loss value of the sensor in a dimensionless form using the Nusselt number (Nu)

$$\text{Nu} = \frac{P}{\pi d \lambda (T_1 - T_2)},$$

where P is the convective heat loss, d is the sensor diameter, λ is the thermal conductivity, T_1 is the sensor temperature, T_2 is the ambient air temperature. The magnitude of convective heat loss will primarily depend on the Reynolds number [7]

$$\text{Re} = \frac{\rho d U}{\mu},$$

here ρ is the density of the atmosphere at the flight level, U is the airspeed of the aircraft, μ is the kinematic viscosity. The authors have conducted studies of convective heat losses of the water content sensor in dry air under various flight regimes. Figure 2 shows the results of measuring the logarithm of the Nusselt number obtained during the flight of a research aircraft in dry air.

The resulting dependence of the Nusselt number

$$\text{Nu} = 1.58 \text{Re}^{0.2893}$$

differs from the one known for the airflow over the cylinder [4].

5 Analysis of Water Content Measurements

The Yak 42D research aircraft took off from Stavropol airport at 15:35 LT on 05/25/2020 and climbed to a height of 7800 m. During the flight, the aircraft crossed

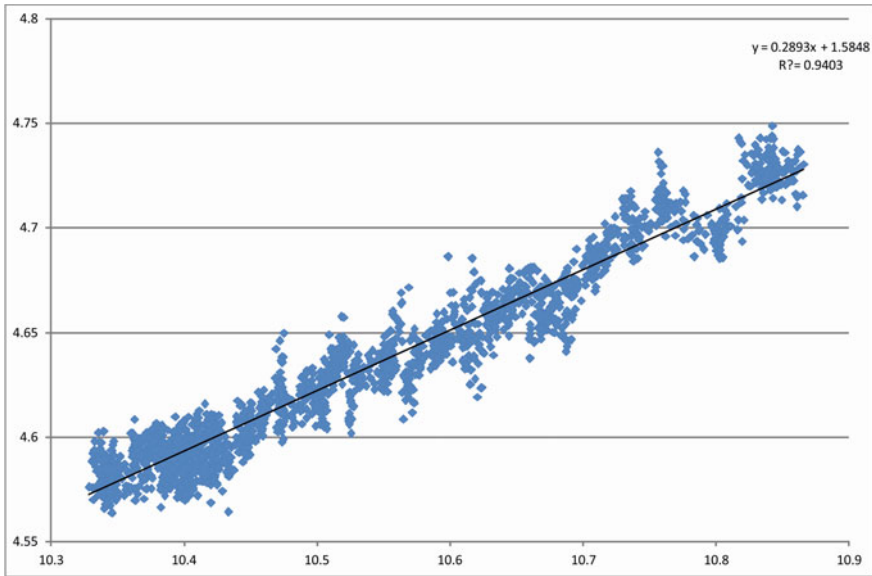


Fig. 2 The dependence of the Nusselt logarithm number on the logarithm of the Reynolds number in the case when the water content sensor is blown over outside clouds (according to the aircraft data)

the tops of cumulus and cirrus–cumulus clouds (Fig. 3). A zero isotherm was observed at an altitude of 3300 m. At an altitude of 3600–4200 the aircraft crossed an Ac cloud layer, and at 1800–2800 m it travelled through stratified cumulus clouds. The aircraft was equipped with systems to measure concentrations and sizes of the PIP, PIP, and CDP cloud particles.

When in stratified cumulus clouds at an altitude of 2200 m, in a layer of positive temperatures, the CDP instrument indicated the presence of cloud particles with sizes from 2 to 15 microns (Fig. 4). Maximum water content calculated from the CDP data was 0.37 g/m^3 . According to the liquid water sensor and the flow-type total water sensor, water content values were 0.27 g/m^3 and 0.35 g/m^3 , respectively. Concurrently, the CIP instrument revealed the presence of small droplets (Fig. 4) with a radius less than $12 \text{ }\mu\text{m}$. Thus, we can assume that in clouds of this type with a large content of small droplets, the capture coefficients for Nevzorov liquid water sensor and a flow-type total water sensor will be 0.73 and 0.94, respectively. Under the same conditions, a reverse-cone total water sensor measured water content of 0.19, which corresponds to a 0.51 capture coefficient.

In the same flight, the aircraft traversed cumuli tops at an altitude of 7800 m. The air temperature was $-27 \text{ }^\circ\text{C}$. Plate-shape crystals of over 1 mm radius were observed (Fig. 5), according to the CIP data. Interestingly, particles of less than 50 microns size were hardly ever observed according to the CDP data. The average water content values for this cloud were liquid water content by the data of Nevzorov probe, total water content from the reverse-cone sensor, total water content from the flow-type

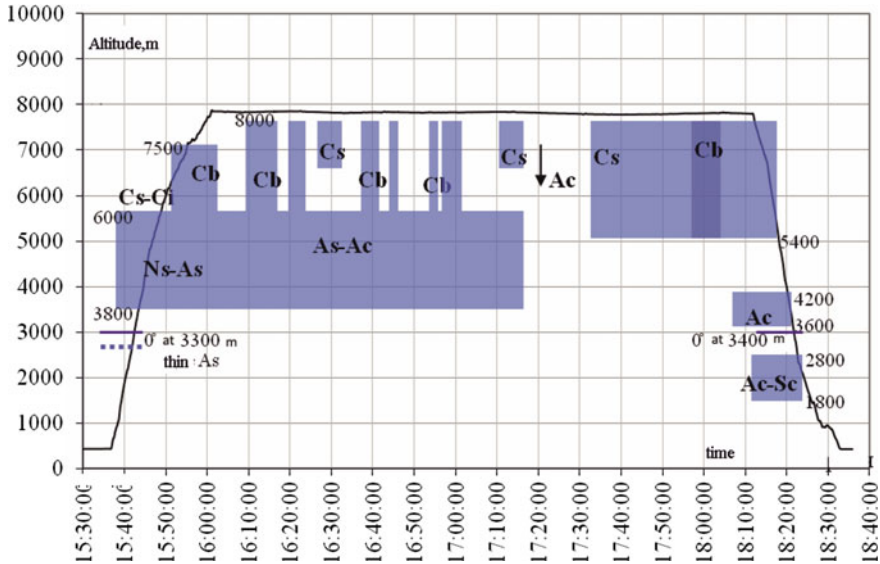


Fig. 3 Flight profile 25.05.2020

sensor, 0.13, 0.37, 0.43 (g/m^3), respectively. Assuming the capture coefficient for the flow-type sensor to be 1, the capture coefficient for the reverse-cone sensor will be 0.86.

6 Conclusions

- A comparison of the performance of two total water sensors—reverse-cone and flow-type sensor—showed a 10% agreement between their measurements.
- The capture coefficients for the reverse-cone sensor and that for the total water flow-type sensor in clouds consisting of droplets with a radius less than 12 microns were 0.78 and 0.94, respectively.
- In mixed-phase clouds with a large number of large crystalline particles, the capture coefficient for the total water reverse-cone sensor was 0.86 relative to the value for the flow-type sensor.

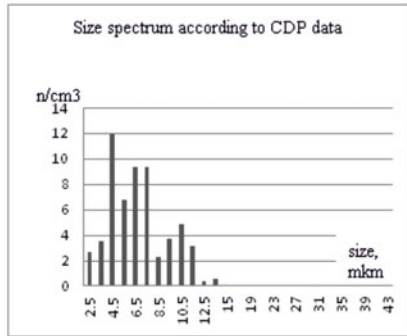
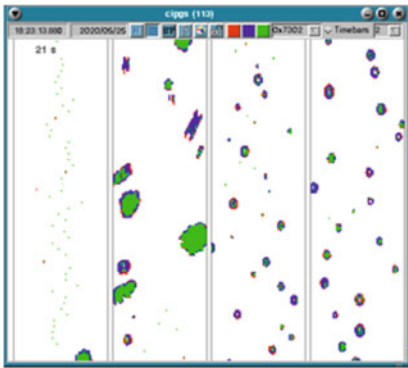
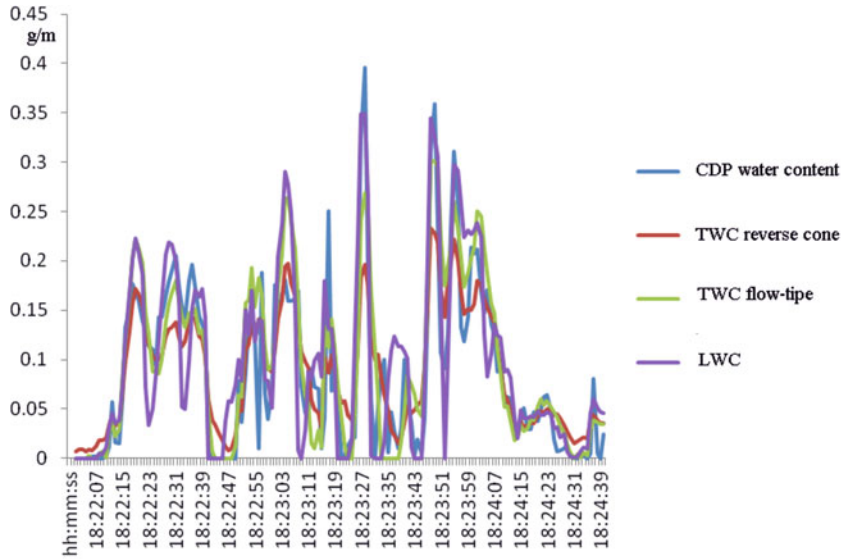


Fig. 4 Water content, cloud particle image and size spectrum in clouds with positive air temperatures. TWC is the total water content, LWC is the liquid water content

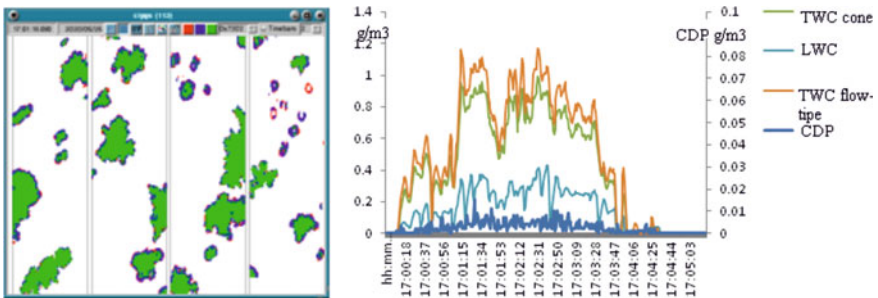


Fig. 5 Cloud particles and water content of mixed-type clouds. TWC is the total water content, LWC is the liquid water content

References

1. Nevzorov, A.N.: Aircraft cloud water content meter. Proceedings of the CAO, vol. 147, 19–26. (1983) [in Russian].
2. Korolev, A.V., Strapp, J.W., Isaac, G.A., Nevzorov, A.N.: The Nevzorov Airborne Hot-Wire LWC–TWC Probe: Principle of Operation and Performance Characteristics, *Journal of Atmospheric and oceanic technology* **15**, 1495–1510, (1998).
3. Volkov, V.V., Krutikov, N.O., Pacianskiy, A.V.: Airplane sensor of total water content. Patent No. 2735908 dated October 31, (2019) [in Russian].
4. Kolokutin, G.E., Volkov, V.V.: The Microphysical Nature of the Glory from Aircraft Measurements, *Atmospheric and Oceanic Optics*. **31**, 157–162 (2018).
5. Volkov, V.V., Kolokutin, G.E., Strunin, M.A. *et al.*: The Onboard Data-Acquisition System of Research Aircraft for Studying Atmospheric Processes. *Instrum. Exp. Tech.* **62**, 401–407 (2019).
6. Korolev, A.V., Isaac, G.A., Cooper S.G., Strapp, J.W., Hallet, J.: Microphysical characterization of mixed-phase clouds, *Q. J. R. Meteorol. Soc.* **129**, 39–65 (2003).
7. Eckert, E.R.G., Dreik, R.M.: *Theory of heat and mass transfer*, McGraw Hill (1957).

Analytical Solution of a Two-Dimensional Model of Dry Air Convection in a Stratified Atmosphere



Robert G. Zakinyan , Arthur R. Zakinyan , and L. M. Kulgina

Abstract In this work, an analytical solution of a two-dimensional model of thermal convection in a stratified atmosphere is obtained. Since the atmosphere is stratified, this leads to the fact that pressure, density and temperature decrease with height in a state of atmospheric statics. As a result of the heating of the Earth's surface, the atmosphere is perturbed and thermal convection occurs. In this work, expressions for the stream function, perturbations of temperature, pressure, and velocity field are obtained.

Keywords Thermal convection in a stratified atmosphere · Analytical solution · Stream function · Temperature perturbation · Pressure perturbation · Velocity field

1 Introduction

The study of thermal convection is the subject of many works, both theoretical and experimental [1]. One of the first experimental studies of thermal convection can be considered the experiments of Benard [2, 3]. These experiments showed that in a liquid layer heated from below, thermal convection occurs at a certain value of the vertical temperature gradient. In this case, convective cells appear in the liquid layer in the vertical plane with alternating clockwise and counterclockwise rotation. These convective cells are called rolls in the form of cylinders, the axis of which is directed perpendicular to the vertical plane. The first theoretical study of thermal convection began with the work of Rayleigh [4]. In this work, Rayleigh

R. G. Zakinyan (✉) · A. R. Zakinyan · L. M. Kulgina
Department of Theoretical and Mathematical Physics, North-Caucasus Federal University, 1
Pushkin Str., 355017 Stavropol, Russia
e-mail: zakinyan@mail.ru

A. R. Zakinyan
e-mail: zakinyan.a.r@mail.ru

R. G. Zakinyan · A. R. Zakinyan
North Caucasus Center for Mathematical Researches, 1 Pushkin Str., 355017 Stavropol, Russia

investigated a linearized system of equations describing thermal convection. Investigating this system of equations for stability, Rayleigh obtained the dispersion relation. Further, solving the eigenvalue problem, Rayleigh obtained an expression for the critical Rayleigh number, which determines the stability of the fluid with respect to convective motion [5].

Rayleigh's approach was developed in the works of many researchers, in particular, Chandrasekhar [3]. However, it should be noted that convection is a purely nonlinear phenomenon [6, 7]. Therefore, Rayleigh's analysis cannot be considered an analytical solution of the system of equations describing thermal convection. Rayleigh's approach is only an analysis of the stability of the state, but not a description of the dynamics of the state itself.

There have been many attempts to find an analytical solution to the system of equations describing thermal convection under various assumptions. In particular, solutions were obtained for an incompressible isothermal fluid [8–12]. However, an analytical solution for the system of equations describing thermal convection in a stratified atmosphere has not been obtained [13].

In this paper, one particular analytical solution of the system of equations describing thermal convection in a stratified atmosphere is given.

2 Free Convection Equations

When describing the thermal convection of air in the atmosphere, we neglect the viscosity of the air. In other words, we will consider air as an ideal fluid. The motion of an ideal fluid is described by the Euler equation. We write it in an inertial frame of reference (without a source of mass and taking into account the rotation of the Earth):

$$\frac{\partial \mathbf{v}}{\partial t} + (\mathbf{v}, \nabla) \mathbf{v} = -\frac{1}{\rho} \nabla p + \mathbf{g}. \quad (1)$$

Let us write the continuity equation (without the source of mass)

$$\frac{\partial \rho}{\partial t} + \operatorname{div}(\rho \mathbf{v}) = 0. \quad (2)$$

In the undisturbed state (atmospheric statics):

$$\mathbf{v} = 0, \quad -\frac{1}{\rho_e} \nabla p_e + \mathbf{g} = 0, \quad \nabla p_e = \rho_e \mathbf{g}, \quad (3)$$

$$\frac{\partial p_e}{\partial x} = 0, \quad \frac{\partial p_e}{\partial z} = -\rho_e g. \quad (4)$$

Equation (3) is the equation of atmospheric statics. Here, ρ is the air density of the disturbed atmosphere; ρ_e is the air density in the state of atmospheric statics; g is acceleration of gravity.

In the state of atmospheric statics, the temperature changes with height according to a linear

$$T_e = T_{e0} - \gamma z, \quad (5)$$

here T_{e0} is the temperature near the earth's surface.

For the distribution of air density with height in the state of atmospheric statics, we obtain

$$\rho_e(z) = \rho_{e0} e^{-\alpha(\gamma_A - \gamma)z}, \quad (6)$$

here $\gamma_A = g/R_d = 34$ °C/KM is the so-called autoconvection gradient, it coincides with the temperature gradient of the atmosphere homogeneous in density; R_d is specific gas constant of dry air; $\alpha = 1/T_{e0} \approx 1/T_0$ is coefficient of thermal expansion, $T_0 = 273$ K.

The pressure in the surrounding atmosphere in a state of statics is determined similarly to the barometric formula

$$p_e(z) = p_{e0} e^{-\alpha\gamma_A z}. \quad (7)$$

Disturbed state of the atmosphere

In the perturbed state, in the general case, the pressure can be written as

$$p = p_e + p', \quad (8)$$

i.e., in the form of the sum of pressures in the state of statics and disturbances relative to it. In the same form, we will represent the remaining parameters: temperature and density.

Over temperature function

We assume that the temperature of the disturbed atmosphere can be represented as:

$$T = T_e + \theta, \quad (9)$$

here

$$\theta = \Delta T + \theta' \quad (10)$$

is over temperature function (temperature disturbance). Here ΔT is some given over temperature function due to adiabatic rise; and θ' is her perturbation, unknown function.

We will assume that

$$\Delta T = \Delta_0 T - \Delta \gamma \cdot z, \quad (11)$$

here $\Delta \gamma = \gamma_a - \gamma$, γ_a is dry adiabatic temperature gradient (lapse rate) of rising air.

Change in density in a disturbed state of the atmosphere

The Boussinesq approximation assumes that one can assume that the pressure perturbation in the equation of state is zero, then

$$\rho' \approx -\rho_e \alpha \theta, \quad (12)$$

For the atmosphere $\alpha \theta \ll 1$. Therefore, below, the expression for the air density of the disturbed atmosphere will be represented as

$$\rho = \rho_e (1 - \alpha \theta). \quad (13)$$

In contrast to the Boussinesq approximation, in expression (13) the air density ρ_e in the state of statics is not a constant value, but is a known function of height (6).

Next, we accept that in the equation of motion $p' \neq 0$ (Boussinesq approximation).

Equations of motion

We obtain for the equation of motion the expression:

$$\frac{\partial \mathbf{v}}{\partial t} + (\mathbf{v}, \nabla) \mathbf{v} = -\frac{1}{\rho_e} \nabla p' + \frac{\rho'}{\rho_e} \mathbf{g}. \quad (14)$$

Continuity equation

$$\frac{1}{\rho_e} \frac{\partial \rho'}{\partial t} + \operatorname{div} \mathbf{v} = \alpha (\gamma_A - \gamma) w + \left(u \frac{\partial \alpha \theta}{\partial x} + w \frac{\partial \alpha \theta}{\partial z} \right). \quad (15)$$

Formulas (14) and (15) in Cartesian coordinates will be written as:

$$\frac{\partial u}{\partial t} + u \frac{\partial u}{\partial x} + w \frac{\partial u}{\partial z} = -\frac{1}{\rho_e} \frac{\partial p'}{\partial x}, \quad (16)$$

$$\frac{\partial w}{\partial t} + u \frac{\partial w}{\partial x} + w \frac{\partial w}{\partial z} = -\frac{1}{\rho_e} \frac{\partial p'}{\partial z} - \frac{\rho'}{\rho_e} g, \quad (17)$$

$$\frac{1}{\rho_e} \frac{\partial \rho'}{\partial t} + \frac{\partial u}{\partial x} + \frac{\partial w}{\partial z} = \alpha (\gamma_A - \gamma) w + \left(u \frac{\partial \alpha \theta}{\partial x} + w \frac{\partial \alpha \theta}{\partial z} \right). \quad (18)$$

Taking into account expression (13), we obtain

$$\frac{\partial w}{\partial t} + u \frac{\partial w}{\partial x} + w \frac{\partial w}{\partial z} = -\frac{1}{\rho_e} \frac{\partial p'}{\partial z} + \alpha g \theta. \quad (19)$$

In the stationary case, the system of equations describing thermal convection takes the form:

$$u \frac{\partial u}{\partial x} + w \frac{\partial u}{\partial z} = -\frac{1}{\rho_e} \frac{\partial p'}{\partial x}, \quad (20)$$

$$u \frac{\partial w}{\partial x} + w \frac{\partial w}{\partial z} = -\frac{1}{\rho_e} \frac{\partial p'}{\partial z} + \alpha g \theta, \quad (21)$$

$$\frac{\partial u}{\partial x} + \frac{\partial w}{\partial z} = \alpha(\gamma_A - \gamma)w + \alpha \left(u \frac{\partial \theta}{\partial x} + w \frac{\partial \theta}{\partial z} \right). \quad (22)$$

Note that although the left side of Eq. (22) contains the expression for the velocity divergence, and the right side is not equal to zero, i.e. the velocity divergence is not equal to zero, it does not follow from this that there is a source of mass. As can be seen from the continuity Eq. (2), there is no source of mass in our consideration. But from expression (22) it follows that there may be a source of streamlines.

Heat equation

In the general case, for the heat equation we obtain

$$\frac{\partial T}{\partial t} + (\mathbf{v}, \nabla)T = -\frac{R_d}{c_V} T(\nabla, \mathbf{v}) + \kappa \nabla^2 T, \quad (23)$$

here κ is thermal diffusivity.

If we accept $\kappa = 0$, which seems reasonable, since in our convection model we consider the movement of inviscid air (ideal fluid) with a viscosity coefficient equal to zero ($\nu = 0$), then we get

$$\frac{\partial \theta}{\partial t} + u \frac{\partial \theta}{\partial x} + w \frac{\partial \theta}{\partial z} = \gamma w - \frac{\gamma_a}{\gamma_A - \gamma_a} T_e(\nabla, \mathbf{v}). \quad (24)$$

Or, taking into account the expression for the velocity divergence (22), for the stationary case, the heat conduction equation can be written in the form:

$$u \frac{\partial \theta}{\partial x} + w \frac{\partial \theta}{\partial z} = -(\gamma_a - \gamma)w. \quad (25)$$

Then the continuity equation can be written in the form

$$\frac{\partial u}{\partial x} + \frac{\partial w}{\partial z} = \alpha(\gamma_A - \gamma_a)w. \tag{26}$$

We see that the velocity divergence is not equal to zero. It is zero, in particular, when the vertical speed is zero: $w = 0$. Thus, streamlines are closed in horizontal motion and not closed in the presence of a vertical velocity component.

Thus, the system of equations describing thermal convection reduces to the form:

$$u \frac{\partial u}{\partial x} + w \frac{\partial u}{\partial z} = -\frac{1}{\rho_e} \frac{\partial p'}{\partial x}, \tag{27}$$

$$u \frac{\partial w}{\partial x} + w \frac{\partial w}{\partial z} = -\frac{1}{\rho_e} \frac{\partial p'}{\partial z} + \alpha g \theta, \tag{28}$$

$$\frac{\partial u}{\partial x} + \frac{\partial w}{\partial z} = \alpha(\gamma_A - \gamma_a)w, \tag{29}$$

$$u \frac{\partial \theta}{\partial x} + w \frac{\partial \theta}{\partial z} = -(\gamma_a - \gamma)w. \tag{30}$$

3 Solution of the Resulting System of Equations

We multiply Eq. (27) by u , and Eq. (28) by w and add the resulting equations:

$$u \frac{\partial}{\partial x} \left(\frac{u^2}{2} + \frac{w^2}{2} \right) + w \frac{\partial}{\partial z} \left(\frac{u^2}{2} + \frac{w^2}{2} \right) = -\frac{1}{\rho_e} \left(u \frac{\partial p'}{\partial x} + w \frac{\partial p'}{\partial z} \right) + \alpha g \theta w. \tag{31}$$

From the heat conduction Eq. (30) we express

$$w = -\frac{1}{\gamma_a - \gamma} \left(u \frac{\partial \theta}{\partial x} + w \frac{\partial \theta}{\partial z} \right). \tag{32}$$

Substituting into (31), we get

$$\begin{aligned} u \frac{\partial}{\partial x} \left(\frac{u^2 + w^2}{2} + \frac{\alpha g}{\gamma_a - \gamma} \frac{\theta^2}{2} \right) + w \frac{\partial}{\partial z} \left(\frac{u^2 + w^2}{2} + \frac{\alpha g}{\gamma_a - \gamma} \frac{\theta^2}{2} \right) \\ = -\frac{1}{\rho_e} \left(u \frac{\partial p'}{\partial x} + w \frac{\partial p'}{\partial z} \right). \end{aligned} \tag{33}$$

We introduce the function Π :

$$\frac{1}{\rho_e} \nabla p' = \nabla \Pi. \tag{34}$$

Then we obtain the law of conservation of energy for perturbations in the form:

$$u \frac{\partial}{\partial x} \left(\frac{u^2 + w^2}{2} + \frac{\alpha g}{\gamma_a - \gamma} \frac{\theta^2}{2} + \Pi \right) + w \frac{\partial}{\partial z} \left(\frac{u^2 + w^2}{2} + \frac{\alpha g}{\gamma_a - \gamma} \frac{\theta^2}{2} + \Pi \right) = 0. \tag{35}$$

From here, the Bernoulli equation can be written as:

$$\frac{u^2 + w^2}{2} + \frac{\alpha g}{\gamma_a - \gamma} \frac{\theta^2}{2} + \Pi = \text{const.} \tag{36}$$

It can be seen from expression (36) that the perturbation of the total energy is the sum of the kinetic, thermal, and potential energies. We take the constant equal to zero, since when the perturbations are zero, then the speed is also zero. Then

$$\frac{u^2 + w^2}{2} + \frac{\alpha g}{\gamma_a - \gamma} \frac{\theta^2}{2} + \Pi = 0. \tag{37}$$

From here

$$\Pi = -\frac{u^2 + w^2}{2} - \frac{\alpha g}{\gamma_a - \gamma} \frac{\theta^2}{2}. \tag{38}$$

We write the equations of motion in the form:

$$u \frac{\partial u}{\partial x} + w \frac{\partial u}{\partial z} = -\frac{\partial \Pi}{\partial x}, \tag{39}$$

$$u \frac{\partial w}{\partial x} + w \frac{\partial w}{\partial z} = -\frac{\partial \Pi}{\partial z} + \alpha g \theta. \tag{40}$$

Let us substitute expression (38) into Eqs. (39) and (40). Then the system of equations describing thermal convection can be written as:

$$w \left(\frac{\partial u}{\partial z} - \frac{\partial w}{\partial x} \right) = \frac{\alpha g}{\gamma_a - \gamma} \theta \frac{\partial \theta}{\partial x}, \tag{41}$$

$$u \left(\frac{\partial u}{\partial z} - \frac{\partial w}{\partial x} \right) = -\frac{\alpha g}{\gamma_a - \gamma} \theta \frac{\partial \theta}{\partial z} - \alpha g \theta. \tag{42}$$

$$\frac{\partial u}{\partial x} + \frac{\partial w}{\partial z} = \alpha (\gamma_A - \gamma_a) w, \tag{43}$$

$$u \frac{\partial \theta}{\partial x} + w \frac{\partial \theta}{\partial z} = -(\gamma_a - \gamma)w. \tag{44}$$

From the heat conduction Eq. (44), it follows

$$u \frac{\partial}{\partial x}(\theta + (\gamma_a - \gamma)z) + w \frac{\partial}{\partial z}(\theta + (\gamma_a - \gamma)z) = 0. \tag{45}$$

This implies

$$u = f'(\tilde{\theta}) \frac{\partial \tilde{\theta}}{\partial z}, \quad w = -f'(\tilde{\theta}) \frac{\partial \tilde{\theta}}{\partial x}, \tag{46}$$

here

$$\tilde{\theta} = \theta + (\gamma_a - \gamma)z. \tag{47}$$

In other words, the function $f(\tilde{\theta})$ plays the role of a stream function. We represent it as a linear function:

$$f(\tilde{\theta}) = \sqrt{\frac{g}{\alpha^3(\gamma_a - \gamma)^3}} \alpha \tilde{\theta}. \tag{48}$$

It follows from the continuity Eq. (43) that we can introduce the functions:

$$\tilde{u} = ue^{-\alpha(\gamma_a - \gamma_a)z}, \quad \tilde{w} = we^{-\alpha(\gamma_a - \gamma_a)z}, \tag{49}$$

for which the divergence will be zero:

$$\frac{\partial \tilde{u}}{\partial x} + \frac{\partial \tilde{w}}{\partial z} = 0. \tag{50}$$

It follows that it is possible to introduce a “stream function” for the “velocity” (49):

$$\tilde{u} = \frac{\partial \tilde{\psi}}{\partial z}, \quad \tilde{w} = -\frac{\partial \tilde{\psi}}{\partial x}. \tag{51}$$

Then for the velocity components we get:

$$u = e^{\alpha(\gamma_a - \gamma_a)z} \frac{\partial \tilde{\psi}}{\partial z}, \quad w = -e^{\alpha(\gamma_a - \gamma_a)z} \frac{\partial \tilde{\psi}}{\partial x}. \tag{52}$$

In a particular case of expression (48), we obtain

$$\frac{\partial^2 \theta}{\partial x^2} + \frac{\partial^2 \theta}{\partial z^2} + \lambda \theta = 0, \quad \lambda = \alpha^2 (\gamma_a - \gamma)^2. \quad (53)$$

Equation (53) is a homogeneous Helmholtz equation.

Particular solutions of the homogeneous Helmholtz equation have the form [14]:

$$\theta = (Ax + B) \cdot (C \cdot \cos \mu z + D \cdot \sin \mu z), \quad \lambda = \mu^2,$$

$$\theta = (A \cdot \cos \mu x + B \cdot \sin \mu x) \cdot (C + D \cdot z), \quad \lambda = \mu^2,$$

$$\theta = (A \cdot \cos \mu_1 x + B \cdot \sin \mu_1 x) \cdot (C \cdot \cos \mu_2 z + D \cdot \sin \mu_2 z), \quad \lambda = \mu_1^2 + \mu_2^2,$$

$$\theta = (A \cdot \cos \mu_1 x + B \cdot \sin \mu_1 x) \cdot (C \cdot \cosh \mu_2 z + D \cdot \sinh \mu_2 z), \quad \lambda = \mu_1^2 - \mu_2^2,$$

$$\theta = (A \cdot \cosh \mu_1 x + B \cdot \sinh \mu_1 x) \cdot (C \cdot \cos \mu_2 z + D \cdot \sin \mu_2 z), \quad \lambda = -\mu_1^2 + \mu_2^2.$$

The fundamental solution has the form:

$$\theta = C_1 \cdot \frac{i}{4} H_0^{(1)}(\mu r) + C_2 \cdot \frac{i}{4} H_0^{(2)}(\mu r),$$

here

$$r = \sqrt{(x - x_0)^2 + (z - z_0)^2},$$

$H_0^{(1)}$, $H_0^{(2)}$ are Hankel functions of the first and second kind of zero order; (x_0, z_0) is an arbitrary point.

$$\theta = \Delta_0 T \cdot \sin \kappa z \cdot \cos kx.$$

The stream function:

$$\tilde{\theta} = \Delta_0 T \cdot \sin \kappa z \cdot \cos kx + (\gamma_a - \gamma)z.$$

Knowing the stream function, one can find the velocity field.

One can find the solution in polar coordinates.

4 Conclusions

Thus, in this work, a particular analytical solution of the system of equations describing thermal convection in a stratified atmosphere is obtained. The solution was obtained under the assumption that the air density perturbation is proportional to the temperature perturbation, according to formula (12). Unlike traditional approaches, the air density in the state of atmospheric statics is considered not constant, but decreasing with height according to the law (6). In the expression for the velocity divergence (18), in addition to the traditional linear term on the right-hand side (deep convection approximation), the nonlinear term due to the temperature perturbation is also taken into account. Since the velocity divergence is not equal to zero, the heat conduction Eq. (24) includes a term related to the work of the gas during thermal expansion. The pressure perturbation is determined from the Bernoulli Eq. (36). A particular solution was obtained under the assumption that the stream function can be represented as a linear dependence (48).

Analytical solutions are obtained under various boundary conditions. Namely, when heating occurs from below, the picture presented in Figs. 1, 2 and 3 is obtained. For a point source, the picture presented in Figs. 4, 5 and 6 is obtained.

Fig. 1 Temperature perturbation field

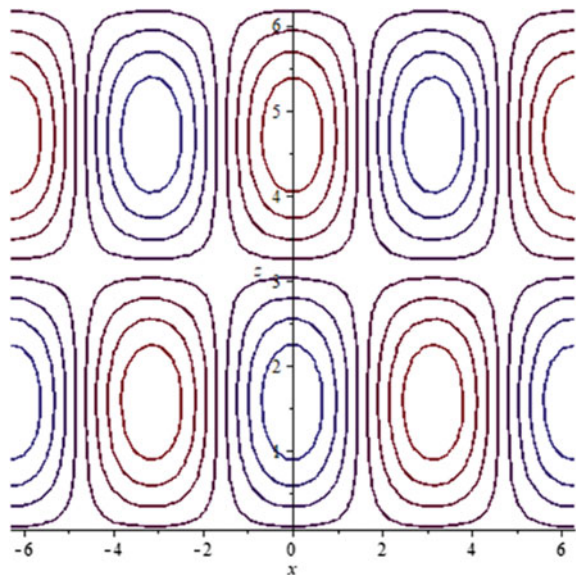


Fig. 2 Stream function

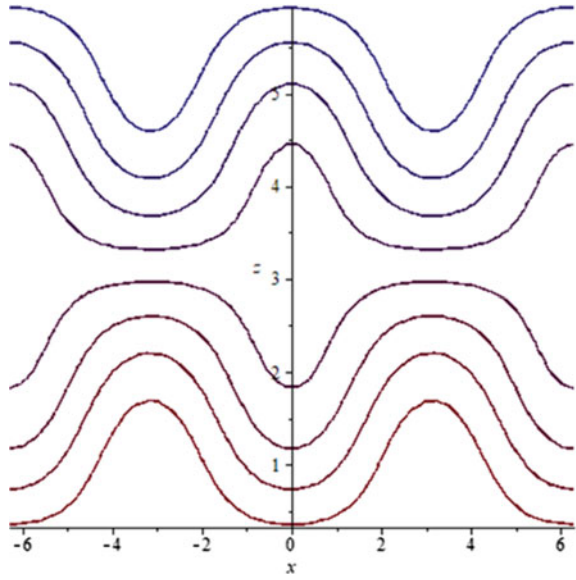


Fig. 3 Velocity field when heating occurs from below

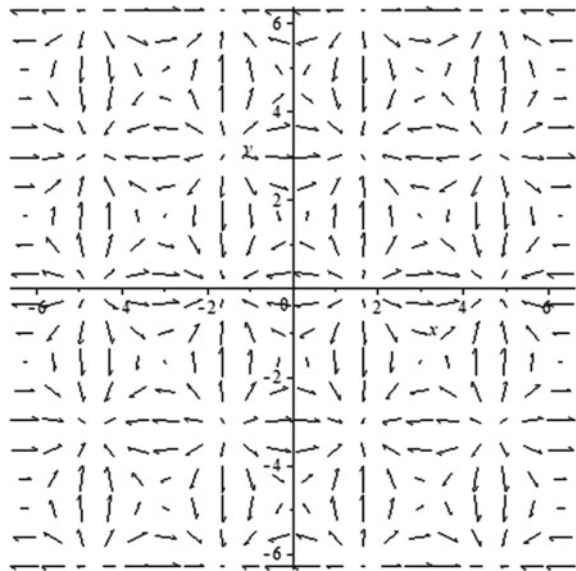


Fig. 4 Isolines of temperature disturbance

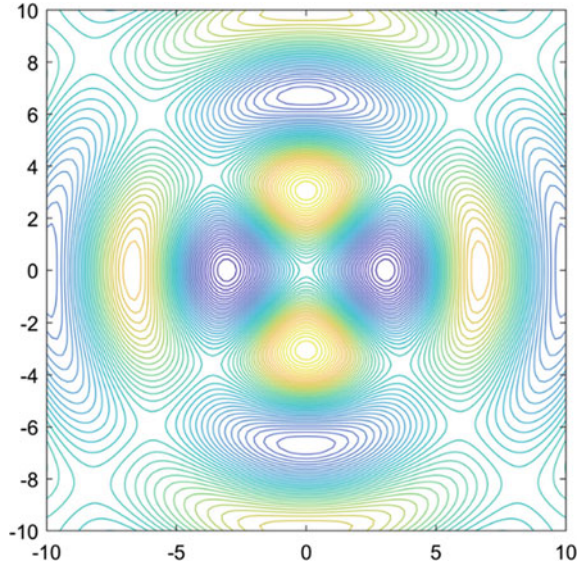
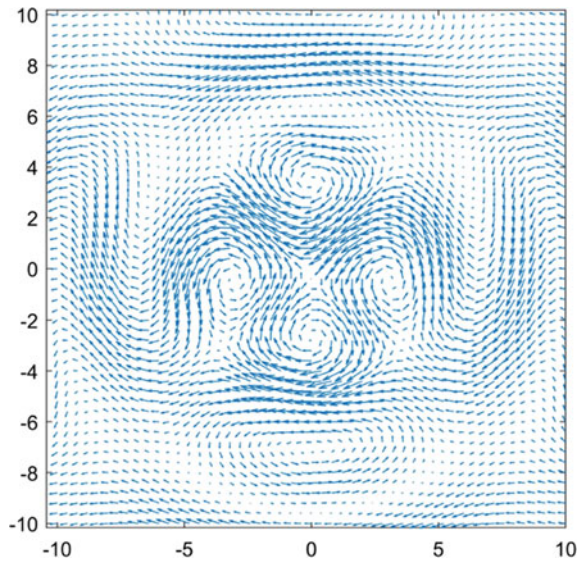


Fig. 5 Velocity field



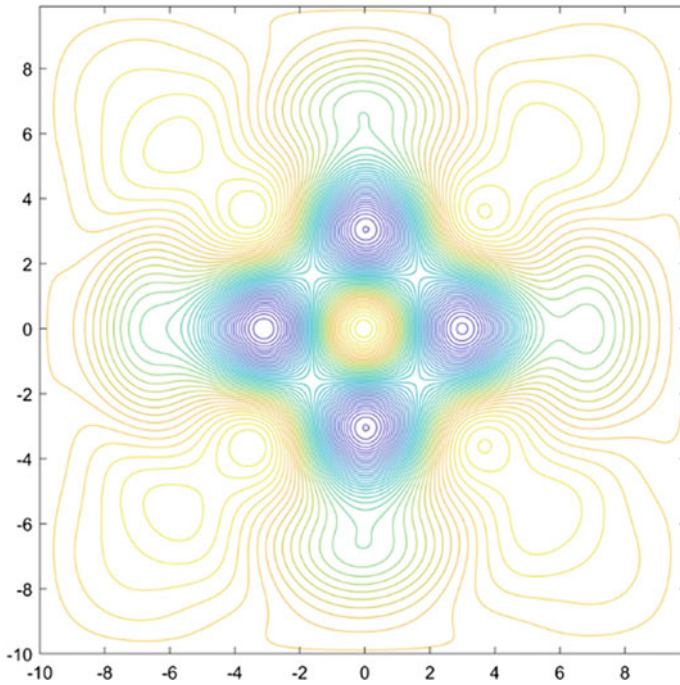


Fig. 6 Pressure perturbation field

Acknowledgements This research was supported by North-Caucasus Center for Mathematical Research under agreement № 075-02-2021-1749 with the Ministry of Science and Higher Education of the Russian Federation.

References

1. Alekseev, V.V., Gusev, A.M.: Free convection in geophysical processes. *Advances in the physical sciences* **141**(2), 311–343 (1983) (in Russian).
2. Garifullin, F.A.: The emergence of convection in horizontal layers of a liquid. *Soros's Educational Journal* **6**(8) (2000) (in Russian).
3. Gershuni, G.Z., Zhukhovitsky, E.M.: *Convective stability of an incompressible fluid*. Nauka. Moscow. (1972) (in Russian).
4. Rayleigh, Lord: On the convection currents in a horizontal layer of fluid when the higher temperature is on the underside. *Philos. Mag.* **32**, 529–546 (1916).
5. Getling, A.V.: Formation of spatial structures of Rayleigh–Benard convection. *Advances in the Physical Sciences* **161**(9) (1991) (in Russian).
6. Busse, F.H.: Nonlinear properties of thermal convection. *Rep. Prog. Phys.* **41**, 1929–1967 (1978).
7. Busse, F.H., Clever, R.M.: An asymptotic model of two-dimensional convection in the limit of low Prandtl number. *J. Fluid Mech.* **102**, 75–83 (1981).

8. Andreev, V.K., Kaptsov, O.V., Pukhnachev, V.V., Rodionov, A.A.: Application of group-theoretic methods in hydrodynamics. Nauka. Novosibirsk. (1994) (in Russian).
9. Aristov, S.N. and Polyanin, A.D.: New classes of exact solutions of the Euler equations. Reports of the Academy of Sciences **419**(3), 1–6 (2008) (in Russian).
10. Polyanin, A.D., Aristov, S.N.: A new method for constructing exact solutions of three-dimensional Navier–Stokes and Euler equations. Theoretical foundations of chem. Technology **45**(6), (2011) (in Russian).
11. Lappa M.: Thermal convection: patterns, evolution and stability. A John Wiley and Sons, Ltd., Publication, Naples, Italy (2010).
12. Wang, C.Y.: Exact solution of the steady Navier-Stokes equations. Annu. Rev. Fluid Mech., **23**, 159–177 (1991).
13. Zakinyan, R.G., Zakinyan, A.R., Lukinov, A.A.: Two-dimensional analytical model of dry air thermal convection. Meteorology and Atmospheric Physics. **127**(4), 451–455 (2015). <https://doi.org/10.1007/s00703-015-0368-2>
14. Polyanin, A.D.: Handbook of linear partial differential equations for engineers and scientists. ISBN 1-58488-299-9 (2002).

Statistical Analysis of Thunderstorm and Hail Activity in the Stavropol Territory



M. V. Zharashuev 

Abstract The article is devoted to the comparison of statistical data of thunderstorm and hail activity on the territory of the Stavropol Region. As a result of data comparison, malfunctions of the North Caucasus lightning Direction Finding network were detected. High-frequency sensors were subject to particularly frequent malfunctions. At the same time, it was found that the discharges of the “cloud-to-earth” type tend to repeat cycles of hail activity.

Keywords Statistical analysis · Thunderstorm · Hail activity · Lightning

1 Introduction

In the last decade, the requirements for the quality of information about thunderstorms have increased markedly. Previously, radar data or data from weather stations and posts were mainly used for statistical studies of thunderstorm activity, but recently thunderstorm direction finding information has been added to them [1]. These data have their advantages and disadvantages. Radar information makes it possible to cover large areas, while the data on thunderstorms obtained as a result of processing such information are probabilistic in nature [1, 2]. Observations of thunderstorms at meteorological stations and posts provide reliable information only in a small radius and are largely determined by the human factor. Lightning direction finding networks, which have been developed relatively recently, provide information from vast areas, and also allow, using instrumental methods, to record and determine the characteristics of discharges [3–5]. Combining different types of meteorological information.

M. V. Zharashuev (✉)
High-Mountain Geophysical Institute, Nalchik, Russia
e-mail: mkg777@mail.ru

2 Measurement Methodology and Analysis of Results

The radar data used in the research were obtained from a stable and continuously operating MRL-5, based on automated systems “Antigrad” and “automated control system MRL”. The lightning direction finding network of the North Caucasus has been operating since 2009. LS8000 is a modern multi-point lightning direction finding system in which the accuracy of determining lightning discharge depends on the density of the stations. The lightning direction finding network of the North Caucasus includes 4 lightning recorders located in the cities of Mikhailovsk and Zelenakumsk, Stavropol Krai, in the village of Islamey (KBR) and Cherkessk (KCHR) [6]. The territory under study is located in the zone of stable bearing of lightning discharges by eight lightning recorders. In the statistical analysis of any information, including lightning direction finding, the volume and reliability of the processed data plays an important role. Within the framework of this work, the program of statistical processing of lightning direction finding information was modified and supplemented [7]. The discrepancy between the readings obtained by low-frequency (LF) and high-frequency (VHF) sensors on specific days indicates failures in their operation. The sharp deviation of the share of lightning discharges in a particular month from its average value for the period from 2009 to 2020 is also indirect evidence of inaccurate fixation of discharges due to lightning direction finding network failures in the period under review. The thunderstorm direction finding information accumulated to date does not allow us to judge the cyclical nature of thunderstorm activity in the North Caucasus. But since hail and thunderstorm are weather phenomena closely related to each other, it can be expected that the dynamics of the time course of thunderstorm activity will be identical to the hail, considered in the author’s work [8], in which hail clouds in the study area for 2002–2018 were identified and accounted for using the method of automatic identification of convective cells.

Data from low-frequency sensors were used to compare lightning direction finding and radar information, since the data received by VHF sensors were subject to more frequent failures what is clearly visible in Table 3 and Fig. 3. Statistical analysis of lightning direction finding and radar information showed that thunderstorm activity, like hail activity, increased from 2011 to 2015, as well as from 2017 to 2018 (Fig. 1). Theoretically, the peak of lightning activity like hail (Fig. 1a) should have occurred in 2016, but in fact significantly more lightning was recorded in 2014 (Fig. 1b). This can be attributed to the unstable operation of LF lightning direction finding network sensors in 2016.

3 Failure Detection of the Lightning Direction Finding Network

The study area is an area of 173 km², the center of which is located in the area of Mikhailovsk, Stavropol Territory. This area includes all types of terrain from

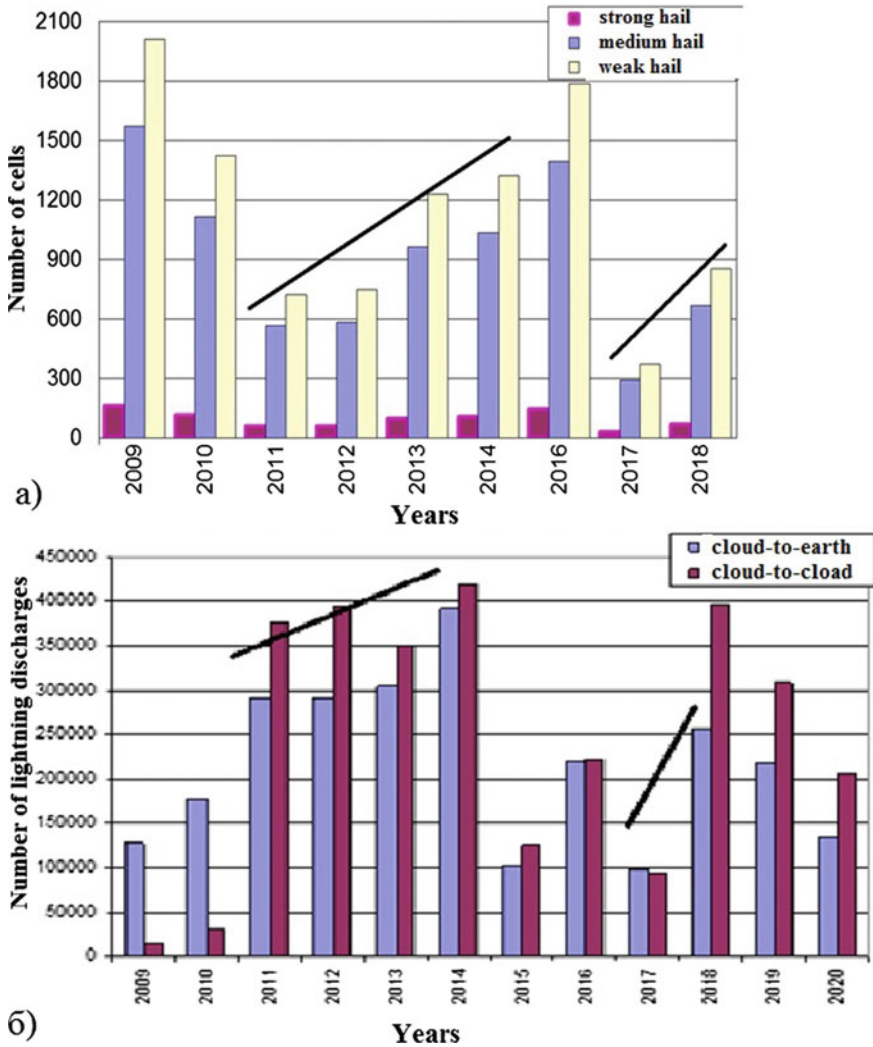


Fig. 1 The number of **a** hail cells according to MRL-5, **b** lightning discharges recorded by low-frequency sensors (LF) in 2009–2020

lowlands to highlands. The inhomogeneous relief imposes additional requirements on the number of sensors involved in the lightning discharges bearing. During the period 2009–2020, high-frequency sensors (VHF) recorded 35,046,305 lightning discharges in the study area, of which two, 18.6%—three, 2.7%—four, 0.25%—5 or more lightning recorders participated in determining 78.4% of the discharges. Low-frequency sensors (LF) recorded 6,419,407 lightning discharges, of which 44.7%, 35.7%, 12.3% of the discharges were recorded by two, three and four sensors,

respectively. Data on the average daily number of recorded discharges are shown in Fig. 2.

Discharges in most cases are recorded by two lightning direction finders, which indicates frequent failures of certain lightning direction finding network sensors. By the deviations of the lightning discharges fraction per month from its long-term average value, it is possible to judge the failures of the LF sensors in certain months or seasons (Table 1). In particular, the results obtained in April 2011, 2013, 2018–2020, May 2009 and 2016, June 2015, July 2009 and 2015, 2018, August 2010, 2016, 2018 and 2019, in September 2010, 2016, 2019, indicate failure lightning direction finding in the North Caucasus.

As a result of the study of lightning activity in the North Caucasus, it was revealed that the most dangerous months for all types of discharges are June and July (Table 2). In 2012–2014, the largest number of lightning discharges of the “cloud-to-cloud” type falls on May. In 2016, the largest number of thunderstorms was recorded in August.

Based on the data on the proportion of cloud-to-cloud lightning discharges per month relative to the total annual number of discharges, according to significant deviations from the average distribution of lightning discharges and according to the annual course of lightning activity, it can be concluded that a violation of the uniformity of lightning direction finding data is possible due to failures in the operation of LF sensors (Table 2). In particular, in April 2011, 2013, 2018–2020, May 2018–2020, June, July 2015, August 2013, 2016, 2017, 2018–2020 and September 2012, 2019.

The number of discharges recorded using the LF sensor cannot exceed the number of discharges recorded using the VHF sensor in the same time period in the same territory. Table 3 shows that in August, September 2018, June, July, August and September

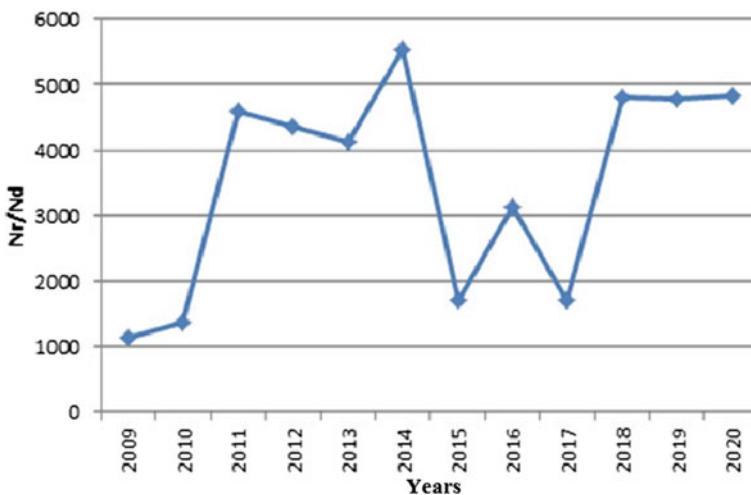


Fig. 2 Average number of cloud-earth discharges per day in the period from April to September

Table 1 The proportion of lightning discharges recorded by low-frequency sensors per month relative to the total number of discharges during the thunderstorm season

Year	April	May	June	July	August	September
2009	1,3	7,6	23,4	37,7	20,6	9,5
2010	1,9	12,1	35,4	19,7	7,9	23
2011	0,1	10,3	30,3	29,2	22,1	8,1
2012	3	28,3	22,9	19,8	23,9	2,0
2013	0,2	21,6	29	25,7	18,6	4,9
2014	4,0	29,4	18,3	23,7	18	6,6
2015	2	10,2	44,4	11,9	24,8	6,8
2016	1,9	10	25,6	17,2	44,1	1,3
2017	1,3	13,5	27,9	22,4	29,9	5
2018	0,3	20,9	13,3	47,4	11,2	6,9
2019	5,5	19,7	31,3	33,4	9,7	0,5
2020	0	20,2	18,2	35,9	13,4	12,3
Average value	1,8	17	26,7	27	20,3	7,2

Table 2 The share (%) of lightning discharges of the “cloud-to-cloud” type, per month relative to the total annual number of discharges recorded in the study area for 2009–2020

Year	April	May	June	July	August	September
2009	1,2	6,9	28,4	24,1	29,9	9,5
2010	5,9	22,1	29,8	20,4	11,9	10
2011	0,1	16,2	32,6	28,3	14,6	8,3
2012	6,1	31,2	19,7	18,2	23,8	1,1
2013	0,5	46,2	27,3	12,1	9,5	4,6
2014	3,6	32,6	21,6	21,0	14,1	7,1
2015	2,9	13,7	48,9	8,0	24,3	2,2
2016	2,2	12,3	30,3	17,0	37,9	0,3
2017	6,9	11,7	17,1	12,7	45,8	5,9
2018	0,3	44,5	22,2	26,0	3,8	3,2
2019	18,5	45,3	11,4	22,8	2,1	0
2020	0	55,8	17,3	10,0	9,4	7,5
Average value	4,00	28,2	25,5	18,4	18,9	5

2019, 2020, there were obvious failures in fixing cloud-to-cloud discharges in the lightning direction finding network of the North Caucasus.

Failures in the operation of high-frequency sensors are particularly well traced in Fig. 3, where it can be seen that the data does not agree well not only with radar information (Fig. 1a) but also with data from low-frequency sensors of the lightning direction finding network (Fig. 1b).

Table 3 The ratio of the number of lightning discharges VHF to the number of LF discharges in the study area

Year	HF/LF					
	April	May	June	July	August	September
2009	24,7	22,9	30,7	16,1	36,7	25,2
2010	55,7	33,2	15,2	18,7	27,2	7,8
2011	7,7	12,7	8,7	7,8	5,3	8,2
2012	16,3	9,1	7,1	7,5	8,2	4,6
2013	13,7	13,4	5,9	2,9	3,2	5,9
2014	3,9	4,8	5,1	3,9	3,4	4,6
2015	13,1	12,1	9,9	6,0	8,8	2,9
2016	6,4	6,8	6,5	5,4	4,7	1,1
2017	10,9	1,8	1,3	1,2	3,2	2,5
2018	1,9	4,2	3,3	1,1	0,7	0,9
2019	1,7	1,1	0,2	0,3	0,1	0
2020	1,5	2,5	0,8	0,2	0,6	0,5
Average	13,1	10,4	7,9	5,9	8,5	5,4

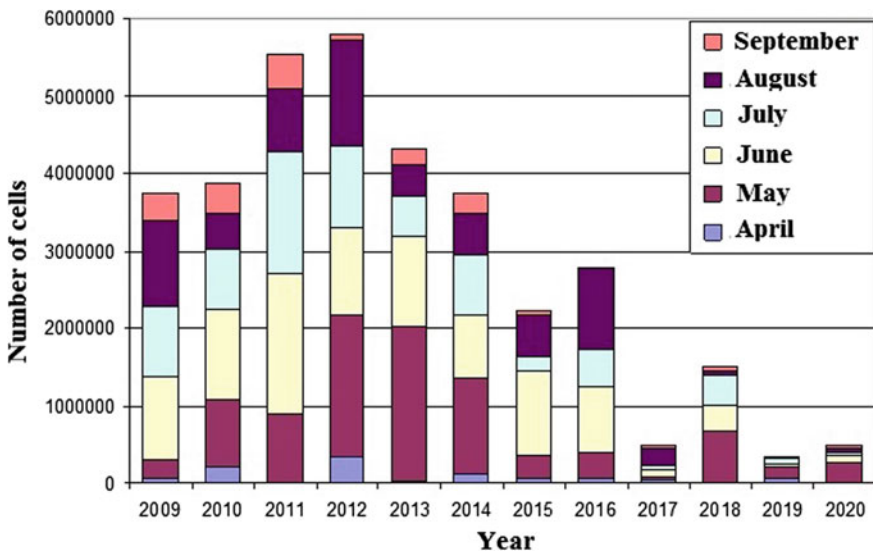


Fig. 3 The annual course of lightning activity, cloud-to-cloud discharges in the period from 2009 to 2020

4 Conclusion

To conduct a study of thunderstorm and hail activity, a methodology and algorithms were developed to control the quality of the processed thunderstorm direction finding information. As a result of the comparison of lightning direction finding and radar information, the facts of failures of the lightning direction finding network of the North Caucasus were revealed, which had a significant impact on the results of the study. VHF sensors were subject to particularly frequent malfunctions. At the same time, it was found that the discharges of the “cloud-to-earth” type tend to repeat cycles of hail activity. The factor preventing the detection of lightning activity cycles is the short period of operation and frequent failures of lightning direction finding network.

References

1. Active-passive radar. Edited by L.G. Kachurin, L.I. Divinsky. Hydrometeoizdat, St. Petersburg (1992) [in Russian].
2. Ilin, N.V., Kuterin, F.A.: Accuracy of Thunderstorm Detection Based on DMRL-C Weather Radar Data. *Russ. Meteorol. Hydrol.* **45**, 669–675 (2020).
3. Adzhiev, A.K., Stasenko, V.N. & Tapaskhanov, V.O.: Lightning detection system in the North Caucasus. *Russ. Meteorol. Hydrol.* **38**, 1–5 (2013).
4. Ivanova, A.R.: International Practices of Thunderstorm Nowcasting. *Russ. Meteorol. Hydrol.* **44**, 756–763 (2019).
5. Snegurov, A.V., Snegurov, V.S.: Comparison of characteristics of multipoint lightning direction finding systems/Proceedings of GGO. **595**, 22–62 (2019) [in Russian].
6. Jarashuev M.V., Tekueva M.T.: Statistical analysis of the lightning type ground-to-cloud in the North Caucasus and the Stavropol territory. *IOP Conf. Ser.: Mater. Sci. Eng.* **698**, 044032 (2019).
7. Zharashuev, M.V.: Cyclicity of hail activity in the North Caucasus. *Proceedings of GGO.* **598**, 197–203. (2020) [in Russian].
8. Zharashuev, M.V.: Program for automatic processing of information from LS8000 lightning direction finders. Certificate of state registration of the computer program. No. 2020663442, 27.10.2020 (2020) [in Russian].